Role of cell monolayer biomechanics in shaping barrier function during bacterial infections

Dissertation

der Mathematisch-Naturwissenschaftlichen Fakultät

der Eberhard Karls Universität Tübingen

zur Erlangung des Grades eines

Doktors der Naturwissenschaften

(Dr. rer. nat.)

vorgelegt von

Marie Münkel

aus Tübingen

Tübingen

2025

Gedruckt mit Genehmigung der Mathematisch-Naturwissenschaftlichen Fakultät der Eberhard Karls Universität Tübingen.

Tag der mündlichen Qualifikation:	23.10.2025
Dekan:	Prof. Dr. Thilo Stehle
1. Berichterstatter/-in:	Dr. Effie E. Bastounis
2. Berichterstatter/-in:	Prof. Dr. Samuel Wagner

Table of Contents

Abstract

Antibiotic-resistant bacteria are a leading cause of mortality worldwide. As a defense mechanism, the human body maintains biophysical barriers to prevent the entry and dissemination of such pathogens. Barrier function relies on force distribution between the cells forming the barrier and their substrate. My PhD thesis focused on understanding how the force exertion of barrier cells is altered during bacterial infection. The outmost skin barrier consists of multi-layered epithelial cells (EPCs) called keratinocytes, which play an important role in detecting the opportunistic pathogen *Staphylococcus aureus* (SA), and in recruiting immune cells to the infection site. While the role of the N-formylated peptide receptor 2 (FPR2) in the recruitment and activation of neutrophils has been extensively characterized, its function on keratinocytes during SA infection was unclear. We found that activation of FPR2 stimulates IL-8 and IL-1α secretion, keratinocyte proliferation and gap wound closure, as well as SA clearance in the skin of mice. In the intestine, the epithelial barrier must fend off bacterial pathogens like food-borne *Listeria monocytogenes* (LM). Once individual cells are infected, LM can spread directly from one cell to another to form infection foci comprised of hundreds of infected cells. EPCs are known to collectively migrate towards the center of the infection focus and extrude infected cells from the monolayer, thus limiting bacterial spread. How this migration is coordinated was not well understood. In two studies we demonstrated that extracellular-signal-regulated kinase (ERK) activation waves propagating in EPC monolayers drive collective cell extrusion, a process that is furthermore promoted by increasing extracellular matrix stiffness. LM can also infect macrophages (MΦs) and use them to spread further throughout the body via the vasculature. How infected MΦs manage to overcome the barrier of the endothelial cells (ECs) lining the inner lumen of the blood vessels is still unknown. We found that an increase in barrier permeability and lack of reinforcement of tractional and monolayer stresses in ECs exposed to LM-infected MΦs promote MΦ transmigration, a process that is partly driven by TNF-α secretion. Similar to LM, the tick-borne pathogen *Borrelia burgdorferi* (BB) can proliferate in and disseminate via the vasculature to distant organs. We found that BB actively modulates the physical forces ECs exert on their substrate and on each other,

which is tightly coupled with innate immune signaling. Our work demonstrates that the regulation of forces between neighboring cells and between cells and their substrate directly modulate the barrier function of endothelial and epithelial barriers, limiting or conversely facilitating dissemination of infection, depending on the pathogen or exact mechanism of spread. Insights into the interplay between biochemical and biomechanics signaling in regulating barrier function can open innovative avenues to fight bacterial infections while limiting the use of antibiotics.

Zusammenfassung

Antibiotikaresistente Bakterien sind eine der Hauptursachen für die Sterblichkeit weltweit. Als Abwehrmechanismus bildet der menschliche Körper biophysikalische Barrieren, um das Eindringen und die Verbreitung solcher Pathogene zu verhindern. Die Barrierefunktion hängt von der Kraftverteilung zwischen den Zellen und ihrem Substrat ab. Meine Doktorarbeit handelt davon, wie die Kraftweiterleitung von Barriere bildenden Zellen während einer bakteriellen Infektion verändert wird. Die äußerste Hautbarriere besteht aus mehrschichtigen epithelialen Zellen (EPCs), den sogenannten Keratinozyten, die eine wichtige Rolle bei der Erkennung des opportunistischen Erregers *Staphylococcus aureus* (SA) und bei der Rekrutierung von Immunzellen an die Infektionsstelle spielen. Während die Rolle des N-formylierten Peptidrezeptors 2 (FPR2) bei der Rekrutierung und Aktivierung von Neutrophilen umfassend charakterisiert wurde, war seine Funktion in Keratinozyten während einer SA-Infektion unklar. Wir fanden heraus, dass die Aktivierung von FPR2 die Sekretion von IL-8 und IL-1α, die Proliferation von Keratinozyten die Wundheilung, sowie die SA-Eliminierung in der Haut von Mäusen stimuliert. Im Darm muss die epitheliale Barriere bakterielle Erreger wie den lebensmittelübertragenen *Listeria monocytogenes* (LM) abwehren. Sobald einzelne Zellen infiziert sind, kann sich LM direkt von einer Zelle zur nächsten ausbreiten und Infektionsherde aus Hunderten infizierter Zellen bilden. Es ist bekannt, dass EPCs kollektiv in Richtung des Zentrums eines solchen Infektionsherds wandern und infizierte Zellen aus dem Monolayer herausdrängen, wodurch die bakterielle Ausbreitung begrenzt wird. Wie diese Migration koordiniert wird, war jedoch nicht gut verstanden. In zwei Studien zeigen wir, dass sich ausbreitende Aktivierungswellen der extrazellulär signalregulierten Kinase (ERK) in EPC-Monolayern kollektive Zell-Extrusion antreiben, ein Prozess, der zudem durch eine erhöhte Festigkeit der extrazellulären Matrix gefördert wird. LM kann auch Makrophagen (MΦs) infizieren und sie nutzen, um sich über das Blutsystem im Körper weiter auszubreiten. Wie es infizierten MΦs gelingt, die Barriere der Endothelzellen (ECs), die den Innenraum der Blutgefäße auskleiden, zu überwinden, ist noch unbekannt. Wir fanden heraus, dass eine erhöhte Barrierepermeabilität und ein ausbleibendes Steigern von Spannung zwischen ECs und zwischen ECs und ihrem Substrat, die LM-infizierten MΦs ausgesetzt sind, die

Transmigration von MΦs fördern, ein Prozess, der teilweise durch die Sekretion von TNF-α gesteuert wird. Ähnlich wie LM kann sich der durch Zecken übertragene Erreger *Borrelia burgdorferi* (BB) vermehren und über das Gefäßsystem zu entfernten Organen verbreiten. Wir fanden heraus, dass BB aktiv die von ECs aufeinander und auf ihr Substrat ausgeübten physikalischen Kräfte moduliert, was eng mit der Beteiligung der angeborenen Immunantwort verknüpft ist. Unsere Arbeit zeigt, dass die Regulation von Kräften zwischen Zellen und zwischen Zellen und ihrem Substrat ein integraler Bestandteil der Barrierefunktion von endothelialen und epithelialen Barrieren ist. Diese zu überwinden, zu umgehen oder zu modulieren, spielt für verschiedene bakterielle Erreger eine zentrale Rolle bei ihrer Ausbreitung und Immunflucht. Ein tieferes Verständnis des Zusammenspiels von biochemischen und biomechanischen Signalen bei der Regulierung der Barrierefunktion kann innovative Wege eröffnen bakterielle Infektionen zu bekämpfen und dabei den Einsatz von Antibiotika zu begrenzen.

Abbreviations

ActA	actine assembly inducing protein
AhR	aryl hydrocarbon receptor
Arp 2/3	actine related protein 2/3
BB	*Borrelia burgdorferi*
BBK32	fibronectin-binding protein
EC	endothelial cell
ECM	extracellular matrix
EPC	epithelial cell
FPR2	N-formylated peptide receptors 2
FRET	Fluorescence resonance energy transfer
HMEC-1	human microvascular endothelial cells
HUVEC	human umbilical vein endothelial cells
ICAM-1	intercellular adhesion molecule 1
IL-1α	Interleukin 1 α
IL-1β	Interleukin 1 β
IL-24	Interleukin 24
IL-6	Interleukin 6
IL-8	Interleukin 8
InlA	Internalin-A
InlB	Internalin-B
JNK	c-Jun N-terminal kinase
LAP	Listeria adhesion protein
LLO	Listeriolysin O
LM	*Listeria monocytoses*
MEK	mitogen activated protein kinase
МΦ	macrophage
NF-κB	nuclear factor kappa light chain of B-cells
NTERT	telomerase reverse transcriptase immortalized keratinocytes
PSM	phenol-soluble modulins
ROS	reactive oxygen species
SA	*Staphylococcus aures*
SELE	gene of P-selectin
SF	*Shigella flexneri*
SFK	Src family kinase
TLR2	toll-like receptor 2
TNF-R1/2	tumor necrosis factor receptor 1/2
TNF-α	Tumor necrosis factor α
VCAM-1	vascular cell adhesion molecule 1

General Introduction

Bacterial pathogens are a global health concern

Bacteria, a domain of prokaryotic organisms, play a central role in all ecosystems. In the human body alone, there are as many bacterial cells as human cells, accumulating to a striking overall mass of 0.2 kg in strikingly diverse body sites, including the digestive system, skin and mouth (Sender et al., 2016). It is known that these commensal bacterial communities are crucial for skin and gut health as they, for example, protect from bacterial infections, a leading cause of hospitalization and mortality worldwide (Balakrishnan, 2022; Gupta & Dey, 2023; Mahmud et al., 2022; Naghavi et al., 2024). Often the lethal outcome of bacterial infections is a result of infections with antibiotic resistance bacterial strains. They render the treatment available as useless and leave patients without effective treatment options. In 2021 700,000 people died due to antibiotic resistant strains and WHO predicted that this number will rise to 10 million by the year 2050 (Mancuso et al., 2021). Bacterial pathogens can either hide within communities of beneficial bacteria, e.g., *Staphylococcus aureus* (SA), or gain access to human body sites via different routes, e.g., the consumption of contaminated food, like *Listeria monocytogenes* (LM) and *Shigella Flexneri* (SF) (Rey et al., 2020) causing food poisoning and systemic infection, via parasites, like the tick-transmitted *Borrelia burgdorferi* (BB) (Kurokawa et al., 2020), the causative agent of Lyme disease, or through direct skin contact with contaminated surfaces or persons, like SA (Taylor & Unakal, 2017). Once they infect the host, these pathogens can cause severe disease, like sepsis, gastrointestinal bleeding, wound healing disorders, meningitis, and multiple-organ failure, especially in immunocompromised individuals. This highlights the need of the body to defend itself against pathogens that it is exposed to in a variety of different ways. The immune system plays an important role in this, with its adaptivity and diversity in detecting, and killing pathogens. Even before infection can be established tissues with barrier functions can prevent the colonization and subsequent infection.

The immune system and biophysical barriers protect the body from infections

As mentioned above, the host's ability to prevent infections from bacterial pathogens is crucial to ensure survival. The human body has evolved strategies to prevent pathogenic

bacteria from entering the system, as well as strategies to kill those that entered and prevent further dissemination and damage. The first line of defense is provided by the epithelial cells lining the interface between the external environment and the inside of the body. They form physical and chemical barriers (e.g. mucus and saliva) that are not easily breached (Citi, 2018), while they additionally secrete antimicrobial peptides that can kill fungi or bacteria, by for examples, forming pores in their outer membranes (Johnstone & Herzberg, 2022). The second line of defense is provided by the adaptive and innate immune system. Phagocytic immune cells like neutrophils and macrophages, which migrate to the site of infection and kill the invading bacteria belong to the innate immune system. They also secrete soluble proinflammatory factors like cytokines, which stimulate and attract further immune cells that will aid the bacteria destruction process. Infected host cells themselves can respond to the infection by undergoing controlled cell death (Li et al., 2023), secreting cytokines to trigger immune cell recruitment (Imanishi, 2000), or releasing antimicrobial peptides to protect surrounding naïve cells (McCormick & Weinberg, 2010). Additionally, to the innate immune system, the adaptive immune system can contribute to bacterial clearance. Its response is more specific and longer lasting. The different types of T cells can secret cytokines, recruiting neutrophils or antigen presenting cells (Curtis & Way, 2009; Shepherd & McLaren, 2020). B cells produce antigen specific antibodies, that bind to the pathogen and facilitate phagocytosis by killer cells, being a substantial part of the complement immune system. The complement system consists of soluble, or membrane bound peptides secreted by various different cell types including cells in the liver, epithelial cells, endothelial cells and immune cells. Its three main functions can be summarized as opsonization, chemotaxis of immune cells and lysis of the pathogen (Lubbers et al., 2017). After the infection is cleared memory cells will retain information about effective antibodies and lead to a faster and precise immune response in a potential second infection (Chi et al., 2024).

The skin is the biggest barrier surface of the human body to protect against bacterial pathogens

The biggest barrier surface of the human body is the skin. If there is no injury beforehand, it prevents bacterial pathogens from entering inner tissues. The external part, the epidermis consists of layered keratinocytes. These terminally differentiated epithelial cells originate from progenitor cells in the basal layer, which proliferate while moving outwards. Towards the skin surface they differentiate further, until they die off and build a topical layer of cornification (Golan, 2019). The skin, as all surface areas of the body, is colonized by a variety of commensal bacteria. Hiding among them is the opportunistic bacterial pathogen *S. aureus* (SA), which poses a serious health risk being the most common cause of (antibiotic–resistant) hospital acquired infections (Golan, 2019).

To detect the presence of pathogenic bacteria and then trigger the appropriate immune response, keratinocytes express toll-like receptor TLR2, which bind cell wall components of SA and activate the NF-κB pathway. That leads to a production of pro-inflammatory cytokines like IL-8 (Mempel et al., 2003). Additionally the aryl hydrocarbon receptor (AhR) induces IL-24, IL-6 and IL-1beta secretion in SA exposed keratinocytes (Stange et al., 2022). The secretion of pro-inflammatory mediators recruits neutrophils to the site of infection. Both neutrophils and keratinocytes, as well as monocytes in the skin express N-formylated peptide receptors (FPR1, FPR2), another pattern recognition receptor. N-formylated peptides are characteristic of bacterial proteins, and their detection leads to cytokine release, phagocytosis, and attraction of immune cells to fight the infection (Weiß et al., 2020).

SA counteracts this by secreting phenol-soluble modulins (PSMs), which act as ligands of FPRs and thus modulate the immune response (Viklund et al., 2022). Depending on their length and folding state, secreted PSMs can activate FPR1 only (short peptides), or antagonize mostly FPR2. This is the case for longer peptides with α-helical, amphipathic folding properties (Kretschmer et al., 2015).

SA is a facultative pathogen that colonizes, for example, the nasal passages of about 30 % of the population, but doesn’t necessarily cause infection. Furthermore, it does not

rely on the host cells to survive (Krismer et al., 2017). Other bacteria, like *Borrelia burgdorferi* (BB), however are obligatory pathogens. In order to spread, survive and proliferate it depends on its host organisms (Kumar et al., 2015). One commonality between SA and BB is that, while both are traditionally considered extracellular pathogens that do not establish a long-term intracellular lifestyle, either pathogen can invade, survive and even proliferate temporarily within its host cells. A strategy both employ to evade their hosts immune system (Fraunholz & Sinha, 2012; Ma et al., 1991). BB relies on vectors to be transmitted to new hosts. Vectors such as ticks, mosquitoes, fleas, and lice, feed on the blood of multiple species or individuals and transmit the pathogens during the feeding process. BB is carried by ticks (Parola & Raoult, 2001), and can afterwards spread directly through the dermal tissue, the lymphatic system or the vasculature causing Lyme disease (Hyde, 2017). BB exploits tick secreted serine protease inhibitors, which inhibit pro-inflammatory proteases secreted by neutrophils and mast cell at the site of entry. This way BB can evade the host innate immunity and establish infection aided by its vector (Bencosme-Cuevas et al., 2023). Lyme disease affects an increasing number of patients, as between 1984 and 1990 140 cases where reported annually to 2,525 in 2022 in Canda (Davidson et al., 2025). Around half of the registered cases develop chronic symptoms including aseptic meningitis, cranial neuropathy, and motor or sensory radiculopathy, cardiac manifestations and arthritis. In later stages, if left untreated musculoskeletal, neurological and cognitive symptoms can emerge (Murison et al., 2023).

Summing up, the skin is one of the most important defensive barrier against pathogenic bacteria colonizing the body amongst commensal bacterial communities. Keratinocytes cornification makes it physically difficult for pathogens to penetrate, while FPR1 and FPR2 recognize bacteria-specific peptides enabling effective detection and clearance. Pathogens like SA and BB have evolved strategies to circumvent these defenses by exploiting host mechanisms or cooperating with other parasitic organisms.

Foodborne bacterial pathogens have to circumvent the gut epithelial barrier

Another entry site is the digestive system. Here epithelial cells line the intestine and, together with a mucus barrier, prevent pathogens from entering the deeper tissue (Martens et al., 2018). However, bacteria that contaminate food like *Listeria*

monocytogenes (LM) have evolved strategies to infect intestinal epithelial cells and cause food poisoning (Rey et al., 2020).

Intestinal epithelial cells form a continuous monolayer with a strong polarization on the apical side, which points to the intestinal lumen, and a basal side that is attached to the underlying collagen rich matrix. Three types of junctions are located towards the apical side and are especially important to make the epithelial monolayer impermeable to pathogens. (1) The tight junctions are directly responsible for permeability by controlling the paracellular distribution of soluble molecules. They also prevent hole formation in the epithelial monolayer by extending below extruding cells and ensuring a stable barrier function during (Higashi et al., 2024). (2) The adherens junctions connect cells with each other via E-cadherin-catenin connections. Those are associated to the actin cytoskeleton, which forms a contractile ring at the apical side of each cell (Citi, 2018). (3) And third, the desmosomes, these cell-cell connections are composed of transmembrane cadherins that are connected to the intermediate filament part of the cytoskeleton, they increase the mechanical load of the monolayer stresses on the adherence junctions, aiding the mechanosensing indirectly by that (Nanavati et al., 2024).

At the basal side, epithelial cells are connected to the underlying substrate by focal adhesions. These adhesions consist of transmembrane proteins called integrins that are connected to the actin cytoskeleton via a protein complex, which includes mechanosensing proteins like vinculin (Atherton et al., 2016).

Cell-matrix junctions (such as focal adhesions in adherent endothelial and epithelial cells) allow the cell to sense substrate stiffness, mechanical stretching, and tension within the cell (De Pascalis & Etienne-Manneville, 2017; Zhou et al., 2015). The protein talin binds directly to the integrins and plays an important role in cellular motility and spreading while vinculin binds to the actomyosin machinery and when it is missing it compromises focal adhesion stability and force transduction (Atherton et al., 2016). Both need tensional forces within the actin cytoskeleton for their activation. Other proteins that are part of the focal adhesions like the focal adhesion kinase (FAK) and paxillin do not sense substrate stiffness directly but are responsible for downstream response by

controlling integrin signaling to the biomechanical cues (Stutchbury et al., 2017). Mild mechanical tensional stresses transmitted through the actomyosin machinery, the actin cytoskeleton and cell-cell connections are known to improve the barrier function of the epithelium (Lee et al., 2023). Moreover, cells can transmit contractile stresses from their cytoskeleton to their substrate (traction forces) via focal adhesions. The interplay between the monolayer stresses and traction forces distributes tensional forces within the monolayer and ensures appropriate localization and stability of junctional tension (Mertz et al., 2013; Rübsam et al., 2017).

Force transmission between cells via cell-cell connections maintains the function and integrity of the tissue by modulating cell fate decisions like entering the cell cycle. In regions of high tensional stresses between cells, proliferation is increased ensuring cohesion during morphogenesis (Vasquez & Martin, 2016). Cell-cell connections are also crucial for long distance collective cell motility during tissue repair. As one cell migrates toward the wound edge, the attached, adjacent cell will be stretched. Stretching will activate the intracellular protein kinase ERK and lead to an anisotropic contraction of the cell between front and rear end, triggering the same stretching response in the next cell (Hino et al., 2020). Sensing and responding to tension in the monolayer are important mechanisms in action that ensure monolayer integrity in a continuously reorganizing cellular network.

Pathogens like LM need to bypass tight junctions between cells to breach the epithelial monolayer barrier. LM does so in two ways, via its adhesion proteins (1) Internalin-A (InlA) and internalin-B (InlB) and (2) Listeria adhesion protein (LAP). InlA binds to E-cadherin, which is only transiently exposed in a confluent monolayer, during senescence cell extrusion or junctional remodeling (Pentecost et al., 2006). InlA allows adhesion of LM to the epithelial surface while InlB binding to host receptor c-MET triggers invasion of LM into the epithelial cell by uptake into a phagosome (Lecuit, 2005). Here LM secretes the listeriolysin O (LLO) to escape into the cytoplasm where it can replicate. Apart from this direct invasion, LM can also spread from one infected cell to another adjacent cell. Using the ActA protein, which is anchored and exposed on LM membrane (Travier & Lecuit, 2014), it recruits the Arp2/3 complex to facilitate actin polymerization, forming actin tails to propel itself within the cell. By pushing a membrane protrusion into the

neighboring cell it can be up taken and escape into the next cell´s cytoplasm, spreading without exposing itself to external immune responses (Gouin et al., 2005; Weddle & Agaisse, 2018). Instead, LAP triggers a redistribution of junction proteins, leading to barrier disfunction and allowing LM to translocate form the intestinal lumen into the tissue (Drolia et al., 2018).

Summing up, gut epithelial cells are the first line of defense against foodborne pathogens. The integrity of this barrier relies on the organization and dynamics of cell-cell junction complexes (i.e., tight junctions and adherens junctions) and of focal adhesions. The actin cytoskeleton generates tensional forces that are transmitted and redistributed across the epithelial monolayer via these adhesion complexes, which is important for barrier permeability regulation. LM has developed strategies to compromise and overcome this barrier, by disrupting the junctional protein distribution and evading the extracellular defenses through intracellular uptake. This is followed by direct cell to cell spread mediated by actin-based motility. By these means, LM further perturbs cellular force transduction by interfering with the actin cytoskeleton's ability to generate and transmit mechanical tension.

Endothelial monolayers provide a barrier to systemic infection

While skin and gut epithelial cells form the body's primary barrier against environmental pathogens, many bacterial pathogens, including BB (Salo et al., 2016), Rickettsia species (Lamason et al., 2016), LM and SF (Weddle & Agaisse, 2018), exploit the vasculature to disseminate further once these initial barriers are breached. Endothelial cells, which line the inner lumen of blood vessels, are the first and key component of vascular barriers like the blood-brain-barrier. After entering the bloodstream, pathogens must evade the host immune system, which includes leukocytes, soluble factors such as antibodies, and the immune responses of endothelial cells themselves (Hickey & Kubes, 2009). To establish infection in secondary sites such as the brain, liver, or placenta, these pathogens must then penetrate or cross the endothelial barrier to gain access to the underlying tissues.

Endothelial barriers are organized in a similar way to the epithelial barrier in the intestine, although there are also key differences between the two (Keshavanarayana et

al., 2025). They both develop tight junctions, adherens junctions, which are connected to the underlying actin cytoskeleton (Lechuga et al., 2024). Either cell type can dynamically change their barrier permeability by reorganizing their junctions in response to pro-inflammatory signaling molecules or mechanical stresses (Keshavanarayana et al., 2025; Lechuga et al., 2024; Mullin et al., 2005). Key differences include that the tight junctions in endothelial cells are less complex and robust than those in epithelial cells, and that endothelial cells are generally flatter and exhibit lower degrees of apicobasal polarity compared to the columnar and strongly polarized in apical and basal side epithelial cells (Castro Dias et al., 2019). Adherens junctions in endothelial cells are composed of VE-cadherin instead of E-cadherin, but also connect neighboring cells via the actin cytoskeleton, while focal adhesions connect them to their substrate. Additionally, gap junctions provide a direct communication by enabling the passage of small signaling molecules between cells (Sluiter et al., 2021). The endothelial barrier permeability is controlled by the forces transmitted to the substrate or intercellularly (Valent et al., 2016). During infection, endothelial cells secrete and react to the pro-inflammatory cytokines like TNF-α by increasing traction and intercellular forces, which is followed by increase permeability for enhanced leukocyte recruitment and transmigration to the infection site (Brandt et al., 2022). The leukocytes themselves are activated and shift from circulating in the blood to making contact with the endothelial cells. In the first step, they roll over the surface, then they adhere to endothelial cell adhesion proteins like ICAM-1 and VCAM-1. Afterwards, they start crawling over the monolayer surface looking for transmigration hotspots created by the endothelia cells. For that, they form membrane protrusions by reorganizing the actin cytoskeleton at cell-cell junctions (Arts et al., 2021). At the same time, they control gap enlargement by increasing their contractility, restricting transmigration in that manner (Alon & van Buul, 2017). Leukocyte transmigration from the blood to adjacent tissues is therefore not only dependent on the leukocyte active migration but is also tightly controlled by the endothelial cells via remodeling of their actin cytoskeleton and contractile force transduction.

Bacterial pathogens like LM have come up with a strategy not only to evade these barrier functions, but even to exploit them to disseminate to other organs via the

bloodstream. While healthy individuals are rarely affected from systemic LM infection, in immunocompromised and elderly people as well as in pregnant women, LM can cross the blood-brain-barrier or the placental barriers, leading to meningitis and even spontaneous abortion (Charlier et al., 2020). LM can be taken up by phagocytic cells like macrophages at the primary infection site, the epithelial cells in the intestine. As it can escape the vacuole it is engulfed in in endothelial cells, it can also escape the phagosome of macrophages and replicate within the cytoplasm (Maudet et al., 2020). As the immune cells travel the vasculature, LM stays hidden from being cleared by leukocytes or targeted by antibiotics and antibodies. Infected macrophages can transmigrate the vascular barrier as described above, acting as a trojan horse and carrying LM to the brain or placenta tissue. Here LM can use its actin based motility to directly spread form infected macrophages to other cells, like for example neurons (Disson & Lecuit, 2012).

While LM can hitch a ride with macrophages to evade interaction with the innate immune system in the blood, BB, after using ticks to breach the skin barrier and suppress the initial immune response exploding tick saliva proteins, has evolved strategies to directly inhibit immune response and transmigrates the endothelial barrier to invade deeper tissues. BB expresses surface proteins, like the fibronectin-binding protein (BBK32), that can bind the C1 complex of the complement system, directly inhibiting clearance by this system (Garcia et al., 2016). BBK32 is also involved in all steps of BB extravasation, from tethering, dragging, stationary adhesion and finally transmigration into the underlying extracellular matrix (Hyde, 2017). BB extravasates preferably into the heart or joint tissue but can also cross the blood-brain barrier. After invasion of the tissue, it inflicts an inflammatory immune response, which ultimately cause carditis, arthritis, and neuroborreliosis (Steere et al., 2004). In *in-vitro* settings, BB has also been observed to invade host cells like fibroblasts directly, maintaining their viability. This is dependent on the reorganization of the actin cytoskeleton and Src family kinases (SFK) of the host cells, and most likely, serves as an immune system evasion strategy making BB not targetable by antibiotics and macrophage clearance (Wu et al., 2011). How that might impact the biomechanics of endothelial cells that are generated by the contractility of the actin cytoskeleton remains unclear.

Although epithelial and endothelial monolayer barriers differ in location and structure, they share the fundamental function of restricting pathogen entry and dissemination within the host. While the chemical aspects of host-pathogen interactions at these barriers have been extensively studied, and targeted by antibiotic therapies, the critical role of biophysical forces within cell monolayers and at their interfaces with the substrate remains far less explored and poorly understood.

Aim of the study

Bacterial pathogens continue to pose a serious global health threat. As a first line of defense, the human body relies on epithelial and endothelial barriers to prevent pathogen invasion and dissemination. Host-pathogen interactions have traditionally been studied with a focus on biochemical aspects, which are the primary targets of current drug treatments like antibiotics. However, the emergence of antibiotic- and treatment-resistant bacterial strains highlights the urgent need to identify alternative mechanisms for infection prevention and control.

The biomechanical aspects of host-pathogen interactions, particularly how bacterial pathogens overcome physical barriers formed by tightly sealed monolayers of epithelial or endothelial cells, remain relatively unexplored and are rarely addressed in treatment strategies. Yet, they may offer promising new avenues for therapeutic interventions.

This study aims to investigate the interactions between host barrier-forming cells, both epithelial and endothelial, and several bacterial pathogens, including *Listeria monocytogenes*, *Borrelia burgdorferi*, *Staphylococcus aureus*, and *Shigella flexneri*. The emphasis will be placed on understanding the biomechanical aspects of these interactions to potentially harnessed them for future antibiotic-independent treatments of bacterial infections.

List of publications

1. **Muenkel M.**, Keskin E., Balmes A., Schäffer T. E., Romer F., Loskill P., Lebtig M., Kretschmer D., Wright K., Mostowy S., Bastounis E.; **(under review)** *Listeria-infected macrophages promote biomechanical alterations in endothelial cell monolayers for transmigration.*

2. Hundsdorfer L, **Muenkel M**, Aparicio-Yuste R, Sánchez Rendón JC, Gomez-Benito MJ, Balmes A, Schäffer TE, Yeh YT, Constantinou I, Wright K, Güler GÖ, Velic A, Maček B, Mostowy S, Bastounis EE (2025). *ERK activation waves coordinate the mechanical cell competition that leads to collective onslaught of bacterially-infected cells.* **Cell Reports**, 44, 1, 115193

3. Aparicio-Yuste R, **Muenkel M**, Clark A, Gómez-Benito M, Bastounis EE (2022). *A stiff extracellular matrix favors the mechanical cell competition that leads to extrusion of bacterially-infected epithelial cells.* **Frontiers in Cell and Developmental Biology** 10.

4. Lebtig, M., Scheurer, J., **Muenkel, M.,** Becker, J., Bastounis, E., Peschel, A., & Kretschmer, D. (2023). *Keratinocytes use FPR2 to detect Staphylococcus aureus and initiate antimicrobial skin defense*. **Frontiers in Immunology**, 14, 1188555.

5. Aparicio-Yuste R, **Muenkel M**, Axarlis K, Reuss A, Gómez-Benito M, Blacker G, Caspi Tal M, Craikzy P, Bastounis EE (2022) *Borrelia burgdorferi modulates the physical forces and immunity signaling in endothelial cells***. iScience** 25, 104793.

6. **Muenkel M**, Aparicio-Yuste, R, Caspi Tal, M, Kraiczy P, Bastounis EE (2022) *Spatiotemporal characterization of endothelial cell motility and physical forces during exposure to Borrelia burgdorferi.* **STAR Protocols** 3, 101832.

7. Aparicio-Yuste R, Serrano-Alcalde F, **Muenkel M**, Gómez-Benito M, Garcia-Aznar J, Bastounis EE, Gómez-Benito M (2022) *Computational modelling of epithelial cell monolayers during bacterial infection: application to Listeria monocytogenes.* **Computer Methods in Applied Mechanics and Engineering**, 115477. **(not included in this thesis)**

8. Marco Lebtig, **Marie Muenkel**, Tobias Votteler, Effie Bastounis, Mark Burian, Andreas Peschel, Dorothee Kretschmer **(In preparation)** *S. aureus activates FPR2 to modulate TLR-2 induced inflammation, differentiation and barrier integrity by keratinocytes.* **(not included in this thesis)**

Contributions to publications

1. **Listeria-infected macrophages promote biomechanical alterations in endothelial cell monolayers for transmigration**

I performed all experiments and analysis of data except for parts of data shown in morphology analysis of Figure 2 A-E (Erva Keskin), ELISA shown in Figure S2 E (Marco Lebtig) and alignment analysis shown in Figure 5 D-E, 2 A,F,J, G, suppl. Figure 2 I, J (Felix Romer), injection of zebrafish larvae (Kathryn Wright) , AFM measurements Figure S4 D-E (Aylin Balmes) and FACS experiments Figure S4 F-I (Erva Keskin). I prepared all figures and collaboratively wrote the manuscript with Effie Bastounis.

2. **ERK activation waves coordinate the mechanical cell competition that leads to collective onslaught of bacterially-infected cells**

I performed all experiments and provided the data and figure design for: Figure 1C-F and Figure 7. I wrote the corresponding methods part of all analyzed data provided by me. I helped revise and edit the final manuscript.

3. **A stiff extracellular matrix favors the mechanical cell competition that leads to extrusion of bacterially-infected epithelial cells**

I performed all experiments and provided the data and figure design for: Figure 1B, Figure 2 and Figure 7. I developed software code in Matlab for analysis of data shown in Figure 7 and wrote the corresponding methods part of all analyzed data provided by me. I helped revise and edit the final manuscript.

4. **Keratinocytes use FPR2 to detect Staphylococcus aureus and initiate antimicrobial skin defense.**

I performed all experiments and provided the data and figure design for Figure 3D-H. I developed software code in Matlab for analysis for obtaining the proliferation rate form live cell imaging cell tracking and wrote the corresponding methods part of all analyzed data provided by me.

5. **Borrelia burgdorferi modulates the physical forces and immunity signaling in endothelial cells**

I performed experiments with heat-inactivated Borrelia burgdorferi and provided the data and figure design for figure 7A-C. I wrote the corresponding methods part of all analyzed data provided by me.

6. **Spatiotemporal characterization of endothelial cell motility and physical forces during exposure to Borrelia burgdorferi**

I performed the TFM/MSM experiments and designed and prepared the graphical abstract and the figures presented, as well as revised and edited the manuscript.

Results and general discussion

Aim and scope of the work presented

Bacterial pathogens pose a global health concern. In the interaction between host cells and bacteria, physical barriers provided by epithelial and endothelial cells play a critical role to prevent infection and dissemination of the pathogenic bacteria throughout the body. While barrier structures vary depending on their location and composition, commonalities can be identified like the requirement for maintaining cell-cell and cell-substrate junctions, and regulating tensional stresses among the monolayer to modulate permeability and barrier functions.

While biochemical aspects of host-pathogen interactions have been studied extensively in the past, yielding different antibiotic treatments, biomechanical aspects of the immune response to pathogens have not equally been explored or leveraged for therapeutic purposes. Understanding how barrier-forming cell monolayers maintain their function is

key for developing new treatment strategies against bacterial infections, which becomes increasingly urgent as the number of antibiotic resistant strains continues to rise.

In this thesis, four distinct host-pathogen interactions have been explored in further detail with an emphasis on host barrier functions and their biomechanical aspects: between (**1**) human keratinocytes and *Staphylococcus aureus* in the paper '**Keratinocytes use FPR2 to detect Staphylococcus aureus and initiate antimicrobial skin defense**' published by Lebtig, M., Scheurer, J., Muenkel, M., Becker, J., Bastounis, E., Peschel, A., & Kretschmer, D. in 2023 in Frontiers in Immunology, (**2**) canine epithelial cells and *Listeria monocytogenes* in the papers '**ERK activation waves coordinate the mechanical cell competition that leads to collective onslaught of bacterially-infected cells** ' published by Hundsdorfer L, Muenkel M, Aparicio-Yuste R, Sánchez Rendón JC, Gomez-Benito MJ, Balmes A, Schäffer TE, Yeh YT, Constantinou I, Wright K, Güler GÖ, Velic A, Maček B, Mostowy S, Bastounis EE in 2025 in Cell Reports and '**A stiff extracellular matrix favors the mechanical cell competition that leads to extrusion of bacterially-infected epithelial cells'** published by Aparicio-Yuste R, Muenkel M, Clark A, Gómez-Benito M, Bastounis EE in 2022 in Frontiers in Cell and Developmental Biology, (**3**) human endothelial cells, macrophages and *Listeria monocytogenes* in the manuscript '**Listeria-infected macrophages promote biomechanical alterations in endothelial cell monolayers for transmigration**' written by Muenkel M., Keskin E., Balmes A., Schäffer T. E., Romer F., Loskill P., Lebtig M., Kretschmer D., Wright K., Mostowy S., Bastounis E.; (under review), and (4) human endothelial cells and *Borrelia burgdorferi* in the papers '**Spatiotemporal characterization of endothelial cell motility and physical forces during exposure to Borrelia burgdorferi**' published by Muenkel M, Aparicio-Yuste, R, Caspi Tal, M, Kraiczy P, Bastounis EE in 2022 in STAR Protocols and '**Borrelia burgdorferi modulates the physical forces and immunity signaling in endothelial cells**' published by Aparicio-Yuste R, Muenkel M, Axarlis K, Reuss A, Gómez-Benito M, Blacker G, Caspi Tal M, Craikzy P, Bastounis EE in 2022 in iScience.

Summary of the key results

The human skin is composed by approximately 90 % epithelial cells, so-called keratinocytes, that form a multi-layer barrier protecting against invasion of pathogenic bacteria. Formyl peptide receptors (FPR) expressed by keratinocytes and neutrophils and are important for detection of short formylated peptides that are secreted by all bacteria. This allows infection of the skin to be detected and inflammation to be promoted. SA additionally secretes large amounts of phenolsoluble modulin (PSM) peptide toxins, which are ligands of the FPR2 receptor as well. While the role of activated FPR1 and FPR2 receptors in neutrophils is known to increase intracellular calcium, chemotaxis and degranulation accompanied by the expression of receptors for phagocytosis, aiding in pathogen clearance, the consequences of activation of FPR receptors on keratinocytes have not been well understood. This may especially be of interest in finding new ways of supporting pathogen clearance in SA infections, as methicillin-resistant strains are prevalent in hospital acquired infections, endangering patience recovery.

In the first study of this thesis (Appendix section 1, (Lebtig et al., 2023)), we discovered that the activation of FPR2 receptor on keratinocytes induces cytokine secretion of IL-8 and IL-1a and increases keratinocyte proliferation, which promotes clearance of SA skin infection in an FPR-dependent manner in mice. Our data indicates that activation of FRP in keratinocytes is an important step in combating SA skin colonization.

We demonstrated that effective communication of and between host cells is essential for clearing pathogens: from sensing infection through the FPR2 receptor to coordinating a collective response of neighboring cells via cytokine secretion. While in this study, intercellular communication relies primarily on soluble cytokines and membrane receptor activation, in the following study we explored how epithelial cells coordinate their response to infection by integrating biomechanical cues to drive pathogen clearance.

In this second project, we investigated how epithelial cell monolayers respond to the presence of large domains of intracellularly LM-infected epithelial cells (infection foci). A distinctive feature of LM is its ability to spread directly from an initially infected cell to neighboring cells, forming infection foci that expand over time to contain hundreds of

infected cells. But how do epithelial monolayers react to the presence of these foci? What defense mechanism do they employ to restrict bacterial spread from cell to cell?

In previous work, Effie Bastounis (Bastounis et al., 2021) showed that cells in these infection foci display reduced contractility, traction forces and stiffness compared to uninfected cell regions. As a consequence, they induce collective migration of surrounding uninfected epithelial cells (‘surrounders’) which with high directionality and speed move towards the center of the infection focus, while simultaneously increasing the traction forces at the interface of the infection focus and surrounders. This collective epithelial cell migration leads to infected cells being mechanically squeezed and subsequently extruded upwards from the monolayer, forming extrusion mounds. Infected cells in the mounds eventually die due to their forcible separation from the basement membrane, The gradient in mechanical cell characteristics such as contractility, force transduction, and stiffness between infected cells in the infection focus and surrounders is a key driver of infected cell extrusion. Therefore, in the following two publications, we focused on how this reaction is coordinated among the surrounder cells and how extracellular mechanics (e.g., matrix stiffness) might regulate this process.

In one of the publications belonging to this thesis (Appendix section 2,(Hundsdorfer et al., 2025)), we showed that this collective migratory behavior is driven by wave-like activation of the ERK kinase. This activation is triggered by cycles of stretching and contraction of neighboring uninfected cells within the monolayer, a process similar to what has been observed before in wound healing (Hino et al., 2020), as if the infection focus were perceived as a wound. Here the cyclic and coordinated activation and deactivation of ERK in individual cells are decisive, as both, constitutively active or inactive ERK prevent extrusion of infected cells, leading to enhanced bacterial spread and bigger infection foci.

Moreover, this extrusion mechanism appears to depend on the stiffness of the underlying substrate. In a second publication on this topic (Appendix section 3,(Aparicio-Yuste et al., 2022)), we developed a computational model that simulates the extrusion of infected cells, while allowing us to systematically vary the stiffness of the extracellular matrix (ECM). The model predicted that higher ECM stiffness increases the compression

and elimination of infected cells, which we could confirm experimentally *in vitro*. Additionally, the model showed that the contrast in stiffness between the softer infected cells and the stiffer uninfected cells within the same monolayer becomes more pronounced with increasing ECM stiffness.

Together, these two studies demonstrate that integrating biomechanical signals, such as matrix stiffness and propagation of contractility waves by ERK activation coordinates collective cellular movement and plays a critical role in the host's defense against LM infection within epithelial tissues.

In the studies described so far, we have looked into chemical and biomechanical integration of intercellular and environmental cues in epithelial cells during infection, which is crucial for a collective response for clearing infection within the tissue. The barrier structure of epithelial cell and endothelial cell monolayers share many commonalities in their reliance on cell-cell connection and regulation of traction- and intercellular forces to maintain their function. In the last two studies, we focused on the collective responses of endothelial cells when confronted with infection.

The uptake of LM through contaminated food can cause infection of the epithelial cells lining the small intestine, as discussed above. However, in a subgroup of patients, immunocompromised individuals or pregnant women, LM can cause systemic infection with severe consequences like meningitis, liver infection or spontaneous abortion. The dissemination of LM is known to occur via the vasculature, either as freely circulating bacteria or bacteria carried within macrophages, which spread the infection to distant organs by interacting with the endothelial cells lining the lumen of the blood vessel during extravasation.

In this work we explored the interactions between LM-infected macrophages and endothelial cell monolayers aiming to shed light on how the infected macrophages subvert the endothelial barriers, facilitating systemic LM spread (Appendix section 4, unpublished manuscript, Muenkel et al.). We discovered that endothelial cells exposed to macrophages become more elongated and collectively aligned, which is accompanied by a sustained decrease in their migration speed over at least 24 h. Interestingly, while endothelial cells exposed to uninfected macrophages transiently increase their traction

forces as well as intercellular stresses and barrier resistance approximately 5-15 h post exposure, these responses could not be observed when macrophages were infected with LM. We identified early TNF-α secretion as a key driver of compromised barrier integrity during infection, which, together with an increase in gene expression of endothelial cell adhesion molecules *ICAM1*, *VCAM1* and *SELE*, and a subsequent increase in macrophage adhesion, facilitates macrophages transmigration. Additionally, in *in vivo* zebrafish model, we observed a systemic increase of vascular permeability and a decrease in macrophage extravasation time.

LM interacts indirectly with the endothelium via macrophages, suppressing their appropriate response to macrophages, which weakens the barrier function. In another study, we explored the mechanisms BB employs to traverse the endothelial barrier as a model pathogen that directly interacts with the endothelial cells instead of relying on host cell-cell interactions.

After BB enters the blood stream, it remains free floating within the vessels, but how it manages to extravasate is not well understood. While the majority of BB infections can be treated well using antibiotics, a subset of patients experiences chronic symptoms like fatigue, neurologic impairment or of cardiac and arthritic nature, persisting up to half a year post-treatment. Understanding how BB interacts with endothelial barriers is crucial in finding better treatment plans to prevent long term damage to affected patients.

We developed a protocol to characterize the spatiotemporal changes in motility and force transduction that BB exposure induces in endothelial cell monolayers (Appendix section 5, (Muenkel et al., 2022)) and discovered that endothelial traction forces and intercellular monolayer forces increase severely right after exposure, and then decrease for around 24 h, which is accompanied by a decrease in endothelial cell motility as well. Only during the early four hours of exposure (4 hpe) innate signaling pathways are upregulated, while after 24 h only few genes (3) of these pathways were still upregulated compared to unexposed endothelial cells. Exposure to heat-inactivated BB did not elicit the same response as viable BB, revealing that BB in part actively modulates the innate immune signaling and force transduction of endothelial host cells during infection (Appendix section 6, (Yuste et al., 2022)).

Context in current state of knowledge

Due to the deadly nature of many bacterial infections, their mode of spread and interactions with the host have been studied several decades now. In the following, our recent findings will be placed in the context of existing literature to better appreciate their significance and implications.

N-formylated peptide receptors FPR2, expressed in neutrophils, was known to be important for neutrophils chemotaxis in response to PSM, ROS production and phagocytosis (Forsman et al., 2012; Weiß et al., 2020). Its inhibition prevents proinflammatory neutrophil infiltration during SA infection of the skin in mice, underlying its role in the innate immune system response to detecting and clearing SA infection (Kretschmer et al., 2010). While it was known to be expressed in keratinocytes, its role here was not as clear as the chemotaxis in neutrophils. We found FPR2, alongside TLR2 and Ahr, to be the third relevant receptor for SA detection in keratinocytes. Its detection of PSMs, SA-secreted peptides, leads to IL-8 secretion, like the activation of TLR2, but additionally to IL-1a secretion. The secreted pro-inflammatory cytokines lead to neutrophil recruitment as well as secretion of antimicrobial peptides, which contribute to bacterial clearance (Miller & Cho, 2011). Therefore, PSM detection via FPR2 on keratinocytes enhances the effect that this has on neutrophils by increasing neutrophil recruitment via additional signaling molecules.

It has been reported that later during the infection process, around 2 days after infection, the affected epidermis and dermis tissue, where SA is not cleared, moves to more superficial locations forming a crust containing necrotic tissue and the pathogen. This crust can be shed and proliferation of epidermis was observed to heal the cutaneous damage (Onunkwo et al., 2010). But how these processes are coordinated has not been shown in greater detail. With the FPR2-dependent increase in keratinocyte proliferation and improvement of wound gap closure, which we could observe, we contributed to fill a gap of knowledge in this aspect of skin repair after infection. FPR2 is not only important for recognizing and combating the infection at an early stage, but also for rapid recovery and prevention of other infections.

Next to the implications of FPR2 involvement in the immune response to SA infections, we identified another signal mediator, ERK, as a key player in coordinating bacterial clearance of LM infections in epithelial cells.

MAPK/ERK pathway spans from the membrane to the nucleus, integrating extracellular signals from soluble mediators to activate or repress specific genes regulating cell proliferation, differentiation, senescence, survival, transformation and migration (Savoia et al., 2019). As a central signaling pathway in cell development, mutations and alterations in its functions have been shown to be a driving force in cancer development, like melanomas. In tumors, the ERK pathways is typically upregulated and MEK inhibitors, the upstream activator of ERK, have been clinically used to block ERK activation, suppressing tumor growth (Kohno & Pouyssegur, 2006), and to enhance the efficacy of radiotherapy and chemotherapeutics in esophageal squamous carcinoma (Song et al., 2023). Beyond oncology, MEK/ERK inhibitors are in pre-clinical trials as treatment for insulin resistance in type 2 diabetes. Here they showed, that a long term activated ERK-pathway is associated with the pathogenesis of type 2 diabetes, which could partially be reverted in mice treated with oral administration of MEK inhibitor (Ozaki et al., 2016). ERK as a potential target against bacterial infections has not been explored yet. Our findings show that spatially and temporally coordinated cycles of ERK activation and inactivation are required for effective clearance of bacteria in epithelial monolayers, whereas both constitutive ERK activation and inactivation prevent the extrusion of infected cells. This suggests that currently available compounds that induce sustained ERK inhibition or activation are unlikely to be beneficial for this process. On the other hand, a high susceptibility of cancer patients to bacterial infections has long since been reported (Worku et al., 2022), but so far it has not been linked directly to MEK inhibitor treatments.

In healthy individuals, epithelial cells in the intestine are subject to periodic stretching called peristalsis, due to wave like contracting and relaxing of muscles in the gastrointestinal tract, moving food through the digestive system (Huizinga & Lammers, 2009). It is known that peristalsis has a great impact on intestinal epithelial cell ERK activity. Cyclic stretch activates ERK and the focal adhesion kinase, which leads to increased proliferation of endothelial cells in vivo and mucosa in vitro (Chaturvedi et al.,

2007). Impaired peristalsis has been associated with a variety of pathologies, including bacterial overgrowth and mucosa atrophy (Husebye, 2005). Both of which can create favorable conditions for bacterial infections. While it is not known how the lack of peristalsis impairs the bacterial clearing via ERK-dependent extrusion we report here, considering its great impact on bacterial overgrowth, wound healing (Dieckgraefe et al., 1997) and endothelial cell proliferation, it appears likely that also ERK-driven bacterial clearance could be affected by the presence or absence of cyclic stretch.

An increase in intestinal tissue stiffness is associated with chronic inflammation and the development of fibrosis. The stiffness of the healthy small intestinal tissue was measured around 3 kPa, while regions affected with fibrosis due to Crohn's disease display increased stiffness of around 28 kPa (Johnson et al., 2013). Chronic inflammation damages the mucosa itself, leading to increased permeability, as well as higher bacterial loads and diversity compared to healthy conditions (Chen et al., 2021; Sun et al., 2021). This starts a cycle of ongoing tissue damage, where pathogens can penetrate the epithelial barrier more easily, increasing inflammation, which leads to more tissue damage. Thus, conditions associated with increased tissue stiffness in the intestine sensitize to infections. Our findings, that increased extracellular matrix stiffness is beneficial for the extrusion process of infected epithelial cells appear contradictory to that. However, the increased susceptibility to bacterial infections in inflammatory bowel disease is most likely caused by the damaged barrier due to inflammation, while in our model we looked at intact epithelial barriers that were only confronted with a stiffened extracellular matrix and not pre-damaged due to chronic inflammation. The increased bacterial clearance response of cells on a fibrotic-like stiff matrix might be an attempt of the body to fight against the damage and improve defense mechanisms.

While tissue stiffness and ERK signaling in epithelial cells open up new discussion pathways about the involvement and potential use of biomechanical mechanisms in bacterial infection treatment, in our study looking into the interaction of LM infected macrophages and endothelial cells, the altered biomechanical aspects of this interactions were in parts mediated by TNF- α secretion.

Tumor necrosis factor α (TNF-α) is a pro-inflammatory protein that is expressed by macrophages, CD4+ cells, mast cells, neutrophils and NK cells. It is at first expressed as a transmembrane protein, which can be cleaved and released, promoting inflammation by triggering MAPK, NF-κB and JNK pathways in cells expressing TNF-R1 or TNF-R2 (Leone et al., 2023). It is known that TNF-α oversecretion plays an important role in several pro-inflammatory autoimmune diseases, like rheumatoid arthritis, Crohn's disease, ulcerative colitis and inflammatory bowel disease(Jang et al., 2021; Leone et al., 2023). Treatment strategies based on TNF-α inhibition have been developed that have proven to be effective in reducing damage in patients. There are several TNF-α antagonists, mostly antibodies, used in clinic to date (Esposito & Cuzzocrea, 2009). It has even been observed that the risk of dementia in patients treated with TNF-α antagonists for inflammatory disease was significantly lower than in the general population, and animal models have hinted towards similar trends, opening discussions about TNF-α targeting as dementia preventive approach in high risk populations (Plantone et al., 2023). After the COVID-19 pandemic, clinical data has shown that patients treated with TNF-α antagonists had lower hospitalization rates and even less severe humoral response to the vaccine (Leone et al., 2023). As we demonstrated that LM-infected macrophages exhibit increased adhesion and transendothelial migration, driven by an early rise in TNF-α secretion, the known beneficial effects of TNF-α inhibition in other inflammatory diseases suggest that such an approach could similarly benefit patients with systemic listeriosis. Paradoxically, it has been shown that the opposite is the case (Peña-Sagredo et al., 2008; Yamada et al., 2000). While the effects on TNF-α blockade have not yet been explored in the context of LM infection, the lack of TNF-α appears to shift the macrophage population from a pro-inflammatory phenotype to an anti-inflammatory phenotype, which seems to make the population as a whole more susceptible to LM. (Li et al., 2020; Peña-Sagredo et al., 2008; Yamada et al., 2000). Hence, the potentially beneficial effect of inhibiting TNF-α on barrier integrity could be overridden by a significantly higher load of infected macrophages in the blood, which might ultimately increase the overall risk of infection. It is also possible that the regulation of the highly heterogeneous macrophage population cannot be influenced by a simple on-off mechanism, similar to how ERK activity during infection must be finely tuned rather than merely switched on or off. Moreover, our work primarily focused on the

barrier function of endothelial cells rather than the susceptibility of macrophages to infection.

Not only in vascular dissemination of LM does the process of immune cell extravasation play a crucial role, but also in BB infections. BB triggers the recruitment of larger numbers of neutrophils, activating the endothelial cells and increasing vascular permeability. While transmigration is essential for pathogen clearance, it creates a transient period of increased vascular permeability, which appears to be exploited by BB to facilitate its spread (Tan et al., 2021). We did not observe an increase in traction forces when endothelial cells were exposed to heat-inactivated BB, suggesting that endothelial cells are not activated in the same manner as compared to when exposed to live BB. This suggests that the activation of endothelial cells by the pathogen, similar to the process of LM dissemination via macrophages, plays a crucial role in BB extravasation.

In vivo BB is hard to study, since, other than atopic infections with SA, it is not easily accessible in biopsies or direct observations. To better understand the mechanisms underlying BB dissemination and find alternative treatment strategies to prevent long term damage in the future, we developed an *in vitro*, live cell imaging-compatible protocol, where individual parameters can be tweaked in a controllable manner.

Limitations of the study

In our research, we are studying host-pathogen interactions with an emphasis on biomechanical aspects to discover novel virulence mechanisms that can hopefully be utilized in the future to find new ways to fight infectious disease. Additionally, we aim to better understand epithelial and endothelial barrier mechanobiology, where observing changes that can be caused by infection is a useful tool to understand which mechanism are important for maintaining their function For this, we employed a variety of different models to study these mechanisms in a quantitative way and with the ability to modulate individual parameters to work out detailed sub-aspects. Models, by nature, are always simplified versions of *in vivo* processes, and as George E. P. Box once phrased it: „All models are wrong, but some are useful.“ (Box et al., 1978). In the following section, the limitations of the models employed in this work will be discussed.

The in vitro model we used to explore the role of FPR2 receptors in keratinocytes during SA infections exhibit two limitations. For once, only one cell type (NTERT) was used as a keratinocyte model. NTERT cells are not primary cells but immortalized, and this might alter their functions compared to skin explants. Additionally, cells were cultured in a monolayer instead of a multi-layer, as it would be *in vivo*. This change in tissue architecture can also have an impact on their behavior. However, part of it was made up for by using mouse models, where a fully developed functional epidermis is present.

While our infection model of epithelial monolayers infected with LM are very useful to understand how infection mound formation is triggered, coordinated and enhanced, several aspects might be neglected compared to the *in vivo* conditions of the complex anatomical structure of the intestinal mucosa. *In vivo* endothelial cells undergo constant cycles of stretching, due to peristalsis. We know that this has an impact on ERK activity, so it is close at hand, that this might also affect the ERK mediated extrusion processes. Additionally, while the mucosa consists of a monolayer of epithelial cells, their 3D structure is not in a flat plane but organized in upwards extended villous and indented crypts. Cells migrate from the crypts into the tips of the villous where they are extruded. How this constant migratory behavior impacts the collective cell motility we observed during infected cell extrusion remains unclear. It also must be noted that all of our *in vitro* experiments were performed using Madin-Darby canine kidney cells, a popular model for the intestinal epithelium. The only second cell type we used were epithelial cells in the tailfin of zebrafish larvae, which exhibited the same behavior. But we have not shown that this applies to human derived cells, though it is highly likely, since we have already demonstrated that the mechanism is preserved across species.

For our studies exploring the interaction of LM infected macrophages or BB with endothelial cells, we used similar vascular models.

In either study we used one type of endothelial cells, namely primary human umbilical vein endothelial cells (HUVECs) for LM studies or human microvascular endothelial cells (HMEC-1) for BB studies. Endothelial cells, depending on their location in the body, can exhibit distinct phenotypes. In the arteries they are thicker, with more robust barriers, are exposed to high oscillatory shear stresses and secrete high amounts of anti-coagulant

and anti-inflammatory molecules. In the veins, they are thinner, more permeable and adapted to lower shear stresses. In the capillary, where most of the nutrient exchanges and extravasation of immune cells take place, their phenotype is highly variable. In the blood-brain barrier junctions are tight and the monolayer is continuous, while in kidney or liver they can be leaky and discontinuous supporting the filter functions of these organs (Aird, 2007). Our findings need to be seen in the context of the origin of the endothelial cells used. HUVEC are macrovascular cells from a big vein in the umbilical cord, and since they are primary, they are expected to have unaltered behavior as compared to in vivo conditions, though variations between donors can be observed. HMEC-1 are microvascular cells from the skin and are genetically altered. While this makes them more uniform, not as donor specific as the HUVECs and easily comparable with other studies, they might also exhibit slightly altered behavior compared to primary cells. In general, the endothelial cell models selected here might limit the impact and generalizability of our findings.

In our setups, when looking at the vascular barrier function, only endothelial cells were considered. *In vivo* however, tissue specific anatomy contributes to the barrier function, implicating other cell types in this process. One important cell type are mural cells, mesenchymal like cells that support endothelial cells, increasing the stability of vessels and keeping tissue homeostasis. Few studies employing 3D vessel-on-chip models have incorporated bone marrow derived mural cells (Alimperti et al., 2017). In the blood-brain barrier, astrocytes are part of the vascular barrier, as they are directly attached to the endothelial monolayer to regulate their function and distribute nutrients from the blood to the neurons in the brain. For incorporating astrocytes into blood-brain-barrier models, microfluidic platforms have been reported (Bang et al., 2017). In the gut, enteric glial cells and pericytes help maintain the vascular barrier by coordinating, together with endothelial cells, permeability and bacterial escape (Jingjie & Jun, 2023). Our studies cannot make a statement about how these additional barrier components would change the vascular barrier function in different tissue types *in vivo*.

Shear stresses are exerted on the apex of endothelial cells in all vascular vessels due to blood flow, although their magnitude, direction and time-dependencies might differ . In the studies presented herein, we have not considered fluid shear stresses in our in vitro

set ups, with exception of the adhesion assay of infected macrophages on endothelial cells, which were perfused with a low shear stress for approximately 24 h. Yet it is known that also shear stresses inflict differential responses depending on the location of the endothelial cells in the body. While HUVEC and other endothelial cells are known to elongate and align under flow while increasing their proliferation (Ajami et al., 2017; Dolan et al., 2011), brain microvascular endothelial cells show none of those characteristics, but increase their contact sites, which makes their tight junction-dependent barrier function more robust under flow (DeStefano et al., 2017). This might alter the response to both, LM infected macrophages as well as free floating BB.

Since we are interested in the interaction of macrophages and endothelial cells, which is partly dependent on the adhesion molecule ICAM-1, disregarding flow might also omit important regulation mechanisms. We showed that ICAM-1 is significantly upregulated in endothelial cells when exposed to LM-infected macrophages versus when exposed to uninfected macrophages. However, the levels of expression in unexposed endothelial cells, that we compared the exposed ones with might be much lower than it would be under flow conditions in general, since it is known that exposure to flow upregulates ICAM-1 expression and promotes leukocyte adhesion as well, while VCAM-1, upregulated in our infection settings, is not directly affected by flow exposure (Morigi et al., 1995; Tsuboi et al., 1995).

Outlook

After discovering the involvement of FPR2 in keratinocytes in SA detection and clearance, it would be very interesting to explore the interplay of FPR2 activation with TLR2 and Ahr. Both are known to play a role in SA detection as well. For example, PSMs, which are ligands of FPR2 lead to the secretion of lipopeptides, which in turn are ligands of TLR2. Most likely these receptors do not act independently. By co-stimulating keratinocytes with PMAs and lipoproteins, one could find out if their activation acts additive, synergistic or maybe even antagonistic. Furthermore, are there specific factors of SA that subvert detection via the FPR2 receptor? By exposing keratinocytes to different SA mutant strains that do not secrete individual peptides, possible evasion strategies of SA could be explored.

To transfer our gained knowledge of the importance of ERK activation waves in clearing infected cells from the monolayer into more in vivo like conditions, similar infection experiments could be performed on a stretch platform that is compatible with live cell imaging. This has been recently developed, and is now available for usage (Jaworski et al., 2025). By repeating experiments using epithelial cells carrying the FRET-ERK sensor used in our previous study, the ERK activation during periodic stretch could be analyzed in spatial and temporal resolution for either uninfected or infected conditions. By building polyacrylamide hydrogels with varying stiffness on the PDMS stretch membrane (Smith et al., 2024), even the effect of altered extracellular matrix stiffness could be further evaluated with an additional parameter at play.

To add even further complexity, one could build gut epithelial organoids, transfecting them with the FRET-ERK sensor carrying plasmid and observe ERK activity in a 3D tissue model. For this, high resolution and fast microscopy techniques like spinning disc microscopy would have to be employed to gain high spatial and temporal imaging resolution. Codes developed in our study for the analysis of ERK activation on a single cell level in 2D would have to be adapted to 3D tissue models.

In our study exploring the interaction of LM-infected macrophages, we focused mostly on the changes that endothelial cells undergo depending on whether they are exposed to infected or uninfected macrophages. We have not looked at the changes the macrophages themselves undergo depending on their infection status. The phenotype upon exposure of endothelial cells to macrophages is very similar to what people have observed in conditions under flow. It would be interesting to perform traction force microscopy of macrophages in substrate coated with endothelia cell adhesion molecules to observe changes in their contractility. Since LM replicates in their cytoplasm and leads to a decrease in cellular contractility and stiffness in other cell types (Bastounis et al., 2021), it might have a similar effect on the macrophages. If that is the case, the forces they apply onto the epithelial cells during the crawling stage of transmigration process might differ depending on their infection status. In our study we could observe that at least part of the development of the elongated and collectively aligned phenotype in endothelial cells after exposure to macrophages is contact-dependent. It is possible that macrophage crawling induces similar shear stresses on the apical surface of the

endothelial cells as flow. The magnitude of flow can change a variety of endothelial cell characteristics, for example their stiffness is increased, similar to what we observe when expose ECs to uninfected macrophages (Silvani et al., 2021). If uninfected macrophages apply higher shear stresses to the endothelial cells, this could in part explain the elevated stiffness.

To also add the aspect of flow directly to the experimental set up, one could use different microfluidic platforms. Endothelial cells can be seeded in microfluidic chips and macrophages can be perfused on their surface. By using more complex set ups allowing the modulation of flow, for example platforms published by (Ansarizadeh et al., 2025) or (Bang et al., 2017) or (Rathod et al., 2017), one could better understand how cellular alignment, macrophages adhesion, transmigration efficiency, vascular permeability and heterotypic spread of LM from infected macrophages to endothelial cells happens under flow conditions, and how higher or lower flow might have an impact on these processes.

Note that one aspect of LM infection was intentionally excluded from all of our experiments: the role of extracellular bacteria. We always employed a gentamicin protection assay during our infection experiment to eliminate extracellular LM. This approach allows us to control the spread of infection and monitor long-term intracellular dynamics without a constant increase in infections over time, particularly important given the absence of an intact immune system in our *in vitro* models. Therefore, free-floating LM released into the cell culture medium either due to cell extrusion and rupture of infected cell in the epithelial monolayer, or due to bursting of infected macrophages in contact with endothelial monolayer, are always killed immediately in the medium. *In vivo* these bacterial cells would have the chance to re-introduce infection and alter the behavior of surrounder epithelial cells or suddenly directly exposed endothelial cells. It would be interesting to observe how the herein described mechanisms would be influenced by the presence of free LM.

We have explored the biomechanical alterations of both epithelial and endothelial barriers in response to differing infection processes. Differences discovered in our studies between distinct endothelial and epithelial cell types could be in part stemming from the unique anatomical location of each cell type in the body and the unique

mechanical stimuli they experience in vivo. Endothelial cells line the inner lumen of the blood vessels and consequently, most prominent environmental mechanical stress comes from the blood flow over their apical surface. They are very sensitive to changes in magnitude and directionality shear stresses, with high laminar stresses promoting an anti-inflammatory phenotype and stabilizing blood vessels, while disturbed or oscillatory flow can lead to NF-κB activation, pro-inflammatory responses and promotion atherogenic progression (Fang et al., 2019; Nakajima & Mochizuki, 2017). Endothelial cells detect flow via receptor tyrosine kinases, like Flk-1, which, upon exposure to shear stresses at the apical surface of the cell associate with adaptor protein Shc. Shc also clusters with integrins in the focal adhesions sites when the cell experience shear stresses, both pathways leading to a downstream activation of the Ras pathway (Chen et al., 1999).

On the contrary, epithelial cells line cavities of different organs, including the airways, the gut and the skin as discussed above. They are very sensitive to cell-cell tension, which can fluctuate during crowding because of compression of the cell monolayer as well as because of substrate stiffness (Aparicio-Yuste et al., 2025).

A common external mechanical cue for both endothelial and epithelial cells is cyclic mechanical stretching. Endothelial cells experience it mostly in the arteries as frictional force tangentially to the blood flow due to the heartbeat (Nakajima & Mochizuki, 2017) or in the pulmonary circulation system during breathing (Fang et al., 2019), Epithelial cells in the lung experience this cyclic stretched as well, but also in the gut during peristalsis (Huizinga & Lammers, 2009).

During infection epithelial cells and endothelial cells can secrete pro-inflammatory mediators (Bauer et al., 2023; Mempel et al., 2003; Stange et al., 2022). We discovered that during bacterial infection endothelial cell monolayers become more permeable, upregulate adhesion molecules and promote infected leucocyte transmigration, while epithelial cells through mechanobiological alterations they undergo force the extrusion of infected cells (Bastounis et al., 2021) via coordinated intracellular ERK signaling. Endothelial cells on the contrary do not extrude infected cells (data from Bastounis lab). Could this difference stem from differences in cell-cell junction dynamics and distinct

intercellular force modulation? We observed two distinct biomechanical responses of endothelial cells and epithelial cells to infection, but both involving differential modulation of their traction forces with different phenotypic outcomes. It would be interesting to find out if this difference is due to the different mechanical cues in their environment which would make the responses appropriate to their location and function.

Next to the different mechanical cues each cell type would experience *in vivo*, the mode of infection in our study was different. Epithelial cells were directly infected and fought against infected cells amongst themselves in the monolayer, while in our endothelial cell models, they were confronted with external infected macrophages. It would be interesting to observe how endothelial cells react to direct infections. As this is relevant as well next to infected leukocytes, since in vivo free floating LM has been observed in the blood (Join-Lambert et al., 2005; Quereda et al., 2016).

Likewise, how would epithelial cells react to the presence of LM infected macrophages? Epithelial cells and macrophages interact for example in the lung alveola, here resident macrophages are always present and during infection approximately after 2-3 day also recruited macrophages can be found (Bhattacharya & Westphalen). Here alveolar epithelial cells are apical exposed to alveolar macrophages that enter the alveolar space coming from the vasculature (Xue et al., 2023). Also while rare, LM is known to cause respiratory infections, including pneumonia, pleural infection, and empyema (Guidi et al., 2021; Morgand et al., 2018)

Is the mode how cells are exposed to infection decisive on how their biomechanical reaction turns out or is it set by the cell type itself?

General conclusions

During skin infection with SA, we observed how membrane bound G-protein coupled receptors (FPR2) in keratinocytes pick up on the presence of bacterial pathogens, alerting neighboring cells via cytokines, which modulate collective cell motility, wound closure and inflammation to clear the infections. During LM infection, we observed how biomechanical cues from the stiffness of the extracellular matrix and contractility of

neighboring cells can direct collective infected cell extrusion within the monolayer by altering the strength of the traction forces. Here cells communicate via direct cell-cell connections, unlike the keratinocytes, which used secreted factors and receptor-mediated responses. Similar to epithelial cells, endothelial cells respond to direct contact with bacteria-infected macrophages as well as bacteria themselves by modulating their traction- and intercellular forces differently from uninfected conditions, particularly early during infection, and promote an increase of barrier permeability most likely aiding bacterial dissemination.

Our findings demonstrate the complex nature of host-pathogen interactions. The tightly controlled interplay between pathogen detection, recruitment of immune cells, coordination of cell-cell and cell-substrate adhesions and force transduction, as well as modulation of monolayer permeability depend on the successful integration of chemical mediators as well as mechanical cues from each host cells environment and neighboring cell.

Acknowledgements

I would like to thank all collaborators and co-authors for the great collaboration, discussions and support. Special thanks to Serge Mostowy for hosting and supporting me during and beyond my research visit in his lab. Thank you to Libera Lo Presti, for all the fruitful discussions, feedback on talks and writings. She also always has advice and time to listen to complains and struggles. Big thank you to my PI Effie Bastounis, for all the effort and time she spent guiding me through my PhD journey, and all the great opportunities for conferences, traveling, projects and talks she provided. I am very grateful for the support of the whole Bastounis Lab (Lara, Julio, Raul, Erva, Nadine, Felix, Ioanna, Jennifer, Sinja), who made working fun and enjoyable, and always lend a helping hand when nothing was working. Thank you to the Peschel Lab for being amazing and fun lab neighbors and exchanging all kinds of resources when needed, you always made it happen. Finally, I would like to thank my friends and family for supporting me beyond the actual PhD work and kept me motivated and going.

Appendix

References

Aird, W. C. (2007). Phenotypic heterogeneity of the endothelium: II. Representative vascular beds. *Circulation research*, *100*(2), 174-190.

Ajami, N. E., Gupta, S., Maurya, M. R., Nguyen, P., Li, J. Y.-S., Shyy, J. Y. J.,...Subramaniam, S. (2017). Systems biology analysis of longitudinal functional response of endothelial cells to shear stress. *Proceedings of the National Academy of Sciences*, *114*(41), 10990-10995.

Alimperti, S., Mirabella, T., Bajaj, V., Polacheck, W., Pirone, D. M., Duffield, J.,...Chen, C. S. (2017). Three-dimensional biomimetic vascular model reveals a RhoA, Rac1, and N-cadherin balance in mural cell-endothelial cell-regulated barrier function. *Proc Natl Acad Sci U S A*, *114*(33), 8758-8763. https://doi.org/10.1073/pnas.1618333114

Alon, R., & van Buul, J. D. (2017). Leukocyte breaching of endothelial barriers: the actin link. *Trends in immunology*, *38*(8), 606-615.

Ansarizadeh, M., Nguyen, H.-T., Lazovic, B., Kettunen, J., De Silva, L., Sivakumar, R.,...Singh, P. (2025). Microfluidic vessel-on-chip platform for investigation of cellular defects in venous malformations and responses to various shear stress and flow conditions. *Lab on a Chip*, *25*(4), 613-630.

Aparicio-Yuste, R., Hundsdorfer, L., Bastounis, E. E., & Gomez-Benito, M. J. (2025). Hybrid model to simulate host cell biomechanics and infection spread during intracellular infection of epithelial monolayers. *Computers in Biology and Medicine*, *185*, 109506. https://doi.org/https://doi.org/10.1016/j.compbiomed.2024.109506

Aparicio-Yuste, R., Muenkel, M., Clark, A. G., Gómez-Benito, M. J., & Bastounis, E. E. (2022). A Stiff Extracellular Matrix Favors the Mechanical Cell Competition that Leads to Extrusion of Bacterially-Infected Epithelial Cells [Original Research]. *Frontiers in Cell and Developmental Biology*, *10*, e912318. https://doi.org/10.3389/fcell.2022.912318

Arts, J. J. G., Mahlandt, E. K., Grönloh, M. L. B., Schimmel, L., Noordstra, I., Gordon, E.,...van Rijssel, J. (2021). Endothelial junctional membrane protrusions serve as hotspots for neutrophil transmigration. *Elife*, *10*, e66074.

Atherton, P., Stutchbury, B., Jethwa, D., & Ballestrem, C. (2016). Mechanosensitive components of integrin adhesions: Role of vinculin. *Experimental cell research*, *343*(1), 21-27.

Balakrishnan, V. S. (2022). WHO's first global infection prevention and control report. *Lancet Infect Dis*, *22*(8), 1122. https://doi.org/10.1016/S1473-3099(22)00459-5

Bang, S., Lee, S.-R., Ko, J., Son, K., Tahk, D., Ahn, J.,...Jeon, N. L. (2017). A low permeability microfluidic blood-brain barrier platform with direct contact between perfusable vascular network and astrocytes. *Scientific reports*, *7*(1), 8083.

Bastounis, E. E., Serrano-Alcalde, F., Radhakrishnan, P., Engström, P., Gómez-Benito, M. J., Oswald, M. S.,...Theriot, J. A. (2021). Mechanical competition triggered by innate immune signaling drives the collective extrusion of bacterially infected epithelial cells. *Developmental Cell*, *56*(4), 443-460.e411. https://doi.org/10.1016/j.devcel.2021.01.012

Bauer, L., Rijsbergen, L. C., Leijten, L., Benavides, F. F. W., Noack, D., Lamers, M. M.,...van Riel, D. (2023). The pro-inflammatory response to influenza A virus infection is fueled by endothelial cells. *Life Science Alliance*, *6*(7).

Bencosme-Cuevas, E., Kim, T. K., Nguyen, T.-T., Berry, J., Li, J., Adams, L. G.,...Kaufmann, S. H. E. (2023). Ixodes scapularis nymph saliva protein blocks host inflammation and complement-mediated killing of Lyme disease agent, Borrelia burgdorferi. *Frontiers in Cellular and Infection Microbiology*, *13*, 1253670.

Bhattacharya, J., & Westphalen, K. (2016). Macrophage-epithelial interactions in pulmonary alveoli.

Box, G. E. P., Hunter, W. H., & Hunter, S. (1978). *Statistics for experimenters* (Vol. 664). John Wiley and sons New York.

Brandt, M., Gerke, V., & Betz, T. (2022). Human endothelial cells display a rapid and fluid flow dependent tensional stress increase in response to tumor necrosis factor-α. *bioRxiv*, 2022.2001.2012.476017. https://doi.org/10.1101/2022.01.12.476017

Castro Dias, M., Mapunda, J. A., Vladymyrov, M., & Engelhardt, B. (2019). Structure and junctional complexes of endothelial, epithelial and glial brain barriers. *International journal of molecular sciences*, *20*(21), 5372.

Charlier, C., Disson, O., & Lecuit, M. (2020). Maternal-neonatal listeriosis. *Virulence*, *11*(1), 391-397.

Chaturvedi, L. S., Marsh, H. M., Shang, X., Zheng, Y., & Basson, M. D. (2007). Repetitive deformation activates focal adhesion kinase and ERK mitogenic signals in human Caco-2 intestinal epithelial cells through Src and Rac1. *Journal of Biological Chemistry*, *282*(1), 14-28.

Chen, K.-D., Li, Y.-S., Kim, M., Li, S., Yuan, S., Chien, S., & Shyy, J. Y. J. (1999). Mechanotransduction in response to shear stress: roles of receptor tyrosine kinases, integrins, and Shc. *Journal of Biological Chemistry*, *274*(26), 18393-18400.

Chen, Y., Cui, W., Li, X., & Yang, H. (2021). Interaction between commensal bacteria, immune response and the intestinal barrier in inflammatory bowel disease. *Frontiers in Immunology*, *12*, 761981.

Chi, H., Pepper, M., & Thomas, P. G. (2024). Principles and therapeutic applications of adaptive immunity. *Cell*, *187*(9), 2052-2078.

Citi, S. (2018). Intestinal barriers protect against disease. *Science*, *359*(6380), 1097-1098. https://doi.org/10.1126/science.aat0835

Curtis, M. M., & Way, S. S. (2009). Interleukin-17 in host defence against bacterial, mycobacterial and fungal pathogens. *Immunology*, *126*(2), 177-185.

Davidson, A., Kelly, P. H., Davis, J., Major, M., Moïsi, J. C., & Stark, J. H. (2025). Historical Summary of Tick and Animal Surveillance Studies for Lyme Disease in Canada, 1975–2023: A Scoping Review. *Zoonoses and Public Health*, *72*(1), 9-22.

De Pascalis, C., & Etienne-Manneville, S. (2017). Single and collective cell migration: the mechanics of adhesions. *Molecular biology of the cell*, *28*(14), 1833-1846.

DeStefano, J. G., Xu, Z. S., Williams, A. J., Yimam, N., & Searson, P. C. (2017). Effect of shear stress on iPSC-derived human brain microvascular endothelial cells (dhBMECs). *Fluids and Barriers of the CNS*, *14*, 1-15.

Dieckgraefe, B. K., Weems, D. M., Santoro, S. A., & Alpers, D. H. (1997). ERK and p38 MAP kinase pathways are mediators of intestinal epithelial wound-induced signal transduction. *Biochemical and biophysical research communications*, *233*(2), 389-394.

Disson, O., & Lecuit, M. (2012). Targeting of the central nervous system by Listeria monocytogenes. *Virulence*, *3*(2), 213-221.

Dolan, J. M., Meng, H., Singh, S., Paluch, R., & Kolega, J. (2011). High fluid shear stress and spatial shear stress gradients affect endothelial proliferation, survival, and alignment. *Annals of biomedical engineering*, *39*(6), 1620-1631. https://doi.org/10.1007/s10439-011-0267-8

Drolia, R., Tenguria, S., Durkes, A. C., Turner, J. R., & Bhunia, A. K. (2018). Listeria adhesion protein induces intestinal epithelial barrier dysfunction for bacterial translocation. *Cell host & microbe*, *23*(4), 470-484.

Esposito, E., & Cuzzocrea, S. (2009). TNF-alpha as a therapeutic target in inflammatory diseases, ischemia-reperfusion injury and trauma. *Current medicinal chemistry*, *16*(24), 3152-3167.

Fang, Y., Wu, D., & Birukov, K. G. (2019). Mechanosensing and mechanoregulation of endothelial cell functions. *Comprehensive physiology*, *9*(2), 873-904.

Forsman, H., Christenson, K., Bylund, J., & Dahlgren, C. (2012). Receptor-dependent and-independent immunomodulatory effects of phenol-soluble modulin peptides from Staphylococcus aureus on human neutrophils are abrogated through peptide inactivation by reactive oxygen species. *Infection and immunity*, *80*(6), 1987-1995.

Fraunholz, M., & Sinha, B. (2012). Intracellular Staphylococcus aureus: live-in and let die. *Frontiers in cellular and infection microbiology*, *2*, 43.

Garcia, B. L., Zhi, H., Wager, B., Höök, M., & Skare, J. T. (2016). Borrelia burgdorferi BBK32 inhibits the classical pathway by blocking activation of the C1 complement complex. *PLoS pathogens*, *12*(1), e1005404.

Golan, Y. (2019). Current treatment options for acute skin and skin-structure infections. *Clinical Infectious Diseases*, *68*(Supplement_3), S206-S212.

Gouin, E., Welch, M. D., & Cossart, P. (2005). Actin-based motility of intracellular pathogens. *Curr Opin Microbiol*, *8*(1), 35-45. https://doi.org/10.1016/j.mib.2004.12.013

Guidi, F., Chiaverini, A., Repetto, A., Lorenzetti, C., Centorotola, G., Bazzucchi, V.,...Blasi, G. (2021). Hyper-virulent Listeria monocytogenes strains associated with respiratory infections in Central Italy. *Frontiers in cellular and infection microbiology*, *11*, 765540.

Gupta, U., & Dey, P. (2023). Rise of the guardians: gut microbial maneuvers in bacterial infections. *Life sciences*, *330*, 121993.

Hickey, M. J., & Kubes, P. (2009). Intravascular immunity: the host–pathogen encounter in blood vessels. *Nature reviews immunology*, *9*(5), 364-375.

Higashi, T., Saito, A. C., & Chiba, H. (2024). Damage control of epithelial barrier function in dynamic environments. *European Journal of Cell Biology*, *103*(2), 151410. https://doi.org/https://doi.org/10.1016/j.ejcb.2024.151410

Hino, N., Rossetti, L., Marín-Llauradó, A., Aoki, K., Trepat, X., Matsuda, M., & Hirashima, T. (2020). ERK-Mediated Mechanochemical Waves Direct Collective Cell Polarization. *Developmental Cell*, *53*(6), 646-660.e648. https://doi.org/10.1016/j.devcel.2020.05.011

Huizinga, J. D., & Lammers, W. J. E. P. (2009). Gut peristalsis is governed by a multitude of cooperating mechanisms. *American Journal of Physiology-Gastrointestinal and Liver Physiology*, *296*(1), G1-G8.

Hundsdorfer, L., Muenkel, M., Aparicio-Yuste, R., Sanchez-Rendon, J. C., Gomez-Benito, M. J., Balmes, A.,...Bastounis, E. E. (2025). ERK activation waves coordinate mechanical cell competition leading to collective elimination via extrusion of bacterially infected cells. *Cell Reports*, *44*(1). https://doi.org/10.1016/j.celrep.2024.115193

Husebye, E. (2005). The pathogenesis of gastrointestinal bacterial overgrowth. *Chemotherapy (0009-3157)*, *51*.

Hyde, J. A. (2017). Borrelia burgdorferi Keeps Moving and Carries on: A Review of Borrelial Dissemination and Invasion [10.3389/fimmu.2017.00114]. *Frontiers in Immunology*, *8*, 114.

Imanishi, J. (2000). Expression of Cytokines in Bacterial and Viral Infections and Their Biochemical Aspects. *The Journal of Biochemistry*, *127*(4), 525-530. https://doi.org/10.1093/oxfordjournals.jbchem.a022636

Jang, D.-i., Lee, A. H., Shin, H.-Y., Song, H.-R., Park, J.-H., Kang, T.-B.,...Yang, S.-H. (2021). The role of tumor necrosis factor alpha (TNF-α) in autoimmune disease and current TNF-α inhibitors in therapeutics. *International journal of molecular sciences*, *22*(5), 2719.

Jaworski, D., Hundsdorfer, L., Bastounis, E., & Constantinou, I. (2025). StretchView - A Multi-Axial Cell-Stretching Device for Long-Term Automated Videomicroscopy of Living Cells. *Adv Sci (Weinh)*, e2408853. https://doi.org/10.1002/advs.202408853

Jingjie, W., & Jun, S. (2023). Gut vascular barrier in the pathogenesis and resolution of Crohn's disease: a novel link from origination to therapy. *Clinical Immunology*, *253*, 109683.

Johnson, L. A., Rodansky, E. S., Haak, A. J., Larsen, S. D., Neubig, R. R., & Higgins, P. D. R. (2014). Novel Rho/MRTF/SRF inhibitors block matrix-stiffness and TGF-β–induced fibrogenesis in human colonic myofibroblasts. *Inflammatory bowel diseases*, *20*(1), 154-165.

Johnson, L. A., Rodansky, E. S., Sauder, K. L., Horowitz, J. C., Mih, J. D., Tschumperlin, D. J., & Higgins, P. D. (2013). Matrix stiffness corresponding to strictured bowel induces a fibrogenic response in human colonic fibroblasts. *Inflammatory bowel diseases*, *19*(5), 891-903. https://doi.org/10.1097/MIB.0b013e3182813297

Johnstone, K. F., & Herzberg, M. C. (2022). Antimicrobial peptides: Defending the mucosal epithelial barrier. *Frontiers in Oral Health*, *3*, 958480.

Join-Lambert, O. F., Ezine, S., Le Monnier, A., Jaubert, F., Okabe, M., Berche, P., & Kayal, S. (2005). Listeria monocytogenes-infected bone marrow myeloid cells promote bacterial invasion of the central nervous system. *Cellular microbiology*, *7*(2), 167-180.

Keshavanarayana, P., Aparicio-Yuste, R., Spill, F., Gomez-Benito, M. J., & Bastounis, E. E. (2025). Leveraging computational modeling to explore epithelial and endothelial cell monolayer mechanobiology. *Trends in Cell Biology*.

Kohno, M., & Pouyssegur, J. (2006). Targeting the ERK signaling pathway in cancer therapy. *Annals of medicine*, *38*(3), 200-211.

Kretschmer, D., Gleske, A.-K., Rautenberg, M., Wang, R., Köberle, M., Bohn, E.,...Klebanoff, S. J. (2010). Human formyl peptide receptor 2 senses highly pathogenic Staphylococcus aureus. *Cell host & microbe*, *7*(6), 463-473.

Kretschmer, D., Rautenberg, M., Linke, D., & Peschel, A. (2015). Peptide length and folding state govern the capacity of staphylococcal β-type phenol-soluble modulins to activate human formyl-peptide receptors 1 or 2. *Journal of Leucocyte Biology*, *97*(4), 689-697.

Krismer, B., Weidenmaier, C., Zipperer, A., & Peschel, A. (2017). The commensal lifestyle of Staphylococcus aureus and its interactions with the nasal microbiota. *Nature reviews microbiology*, *15*(11), 675-687.

Kumar, D., Ristow, L. C., Shi, M., Mukherjee, P., Caine, J. A., Lee, W. Y.,...Chaconas, G. (2015). Intravital Imaging of Vascular Transmigration by the Lyme Spirochete: Requirement for the Integrin Binding Residues of the B. burgdorferi P66 Protein. *PLoS Pathog*, *11*(12), e1005333. https://doi.org/10.1371/journal.ppat.1005333

Kurokawa, C., Lynn, G. E., Pedra, J. H. F., Pal, U., Narasimhan, S., & Fikrig, E. (2020). Interactions between Borrelia burgdorferi and ticks. *Nature Reviews Microbiology*, *18*(10), 587-600.

Lamason, R. L., Bastounis, E., Kafai, N. M., Serrano, R., Del Alamo, J. C., Theriot, J. A., & Welch, M. D. (2016). Rickettsia Sca4 Reduces Vinculin-Mediated Intercellular Tension to Promote Spread. *Cell*, *167*(3), 670-683.e610. https://doi.org/10.1016/j.cell.2016.09.023

Lebtig, M., Scheurer, J., Muenkel, M., Becker, J., Bastounis, E., Peschel, A., & Kretschmer, D. (2023). Keratinocytes use FPR2 to detect Staphylococcus aureus and initiate antimicrobial skin defense [Original Research]. *Frontiers in Immunology*, *14*.

Lechuga, S., Marino-Melendez, A., Naydenov, N. G., Zafar, A., Braga-Neto, M. B., & Ivanov, A. I. (2024). Regulation of epithelial and endothelial barriers by molecular chaperones. *Cells*, *13*(5), 370.

Lecuit, M. (2005). Understanding how Listeria monocytogenes targets and crosses host barriers [https://doi.org/10.1111/j.1469-0691.2005.01146.x]. *Clinical Microbiology and Infection*, *11*(6), 430-436. https://doi.org/https://doi.org/10.1111/j.1469-0691.2005.01146.x

Lee, E.-J., Kim, Y., Salipante, P., Kotula, A. P., Lipshutz, S., Graves, D. T., & Alimperti, S. (2023). Mechanical regulation of oral epithelial barrier function. *Bioengineering*, *10*(5), 517.

Leone, G. M., Mangano, K., Petralia, M. C., Nicoletti, F., & Fagone, P. (2023). Past, present and (foreseeable) future of biological anti-TNF alpha therapy. *Journal of Clinical Medicine*, *12*(4), 1630.

Li, L., Dickinson, M. S., Coers, J., & Miao, E. A. (2023). Pyroptosis in defense against intracellular bacteria. *Seminars in Immunology*, *69*, 101805. https://doi.org/https://doi.org/10.1016/j.smim.2023.101805

Li, X., Körner, H., & Liu, X. (2020). Susceptibility to intracellular infections: contributions of TNF to immune defense. *Frontiers in Microbiology*, *11*, 1643.

Lubbers, R., Van Essen, M. F., Van Kooten, C., & Trouw, L. A. (2017). Production of complement components by cells of the immune system. *Clinical & Experimental Immunology*, *188*(2), 183-194.

Ma, Y., Sturrock, A., & Weis, J. J. (1991). Intracellular localization of Borrelia burgdorferi within human endothelial cells. *Infect Immun*, *59*(2), 671-678. https://doi.org/10.1128/iai.59.2.671-678.1991

Mahmud, M. R., Akter, S., Tamanna, S. K., Mazumder, L., Esti, I. Z., Banerjee, S.,...Hossain, M. S. (2022). Impact of gut microbiome on skin health: gut-skin axis observed through the lenses of therapeutics and skin diseases. *Gut microbes*, *14*(1), 2096995.

Mancuso, G., Midiri, A., Gerace, E., & Biondo, C. (2021). Bacterial antibiotic resistance: the most critical pathogens. *Pathogens*, *10*(10), 1310.

Martens, E. C., Neumann, M., & Desai, M. S. (2018). Interactions of commensal and pathogenic microorganisms with the intestinal mucosal barrier. *Nature Reviews Microbiology*, *16*(8), 457-470.

Maudet, C., Kheloufi, M., Levallois, S., Gaillard, J., Huang, L., Gaultier, C.,...Lecuit, M. (2020). Bacterial inhibition of CD8+ T-cells mediated cell death promotes neuroinvasion and within-host persistence. *bioRxiv*, 2020-2011.

McCormick, T. S., & Weinberg, A. (2010). Epithelial cell-derived antimicrobial peptides are multi-functional agents that bridge innate and adaptive immunity. *Periodontology 2000*, *54*(1), 10-1111.

Mempel, M., Voelcker, V., Köllisch, G., Plank, C., Rad, R., Gerhard, M.,...Ring, J. (2003). Toll-like receptor expression in human keratinocytes: nuclear factor κB controlled gene activation by Staphylococcus aureus is Toll-like receptor 2 but not Toll-like receptor 4 or platelet activating factor receptor dependent. *Journal of Investigative Dermatology*, *121*(6), 1389-1396.

Mertz, A. F., Che, Y., Banerjee, S., Goldstein, J. M., Rosowski, K. A., Revilla, S. F.,...Horsley, V. (2013). Cadherin-based intercellular adhesions organize epithelial cell–matrix traction forces. *Proceedings of the National Academy of Sciences*, *110*(3), 842-847.

Miller, L. S., & Cho, J. S. (2011). Immunity against Staphylococcus aureus cutaneous infections. *Nature Reviews Immunology*, *11*(8), 505-518.

Morgand, M., Leclercq, A., Maury, M. M., Bracq-Dieye, H., Thouvenot, P., Vales, G.,...Charlier, C. (2018). Listeria monocytogenes-associated respiratory infections: a study of 38 consecutive cases. *Clinical Microbiology and Infection*, *24*(12), 1339-e1331.

Morigi, M., Zoja, C., Figliuzzi, M., Foppolo, M., Micheletti, G., Bontempelli, M.,...Remuzzi, A. (1995). Fluid shear stress modulates surface expression of adhesion molecules by endothelial cells.

Muenkel, M., Aparicio-Yuste, R., Tal, M. C., Kraiczy, P., & Bastounis, E. E. (2022). Spatiotemporal characterization of endothelial cell motility and physical forces

during exposure to Borrelia burgdorferi. *STAR Protocols*, *3*(4), 101832. https://doi.org/https://doi.org/10.1016/j.xpro.2022.101832

Mullin, J. M., Agostino, N., Rendon-Huerta, E., & Thornton, J. J. (2005). Keynote review: epithelial and endothelial barriers in human disease. *Drug discovery today*, *10*(6), 395-408.

Murison, K., Wilson, C. H., Clow, K. M., Gasmi, S., Hatchette, T. F., Bourgeois, A.-C.,...Koffi, J. K. (2023). Epidemiology and clinical manifestations of reported Lyme disease cases: Data from the Canadian Lyme disease enhanced surveillance system. *PLoS One*, *18*(12), e0295909.

Naghavi, M., Ong, K. L., Aali, A., Ababneh, H. S., Abate, Y. H., Abbafati, C.,...Abbastabar, H. (2024). Global burden of 288 causes of death and life expectancy decomposition in 204 countries and territories and 811 subnational locations, 1990–2021: a systematic analysis for the Global Burden of Disease Study 2021. *The Lancet*, *403*(10440), 2100-2132.

Nakajima, H., & Mochizuki, N. (2017). Flow pattern-dependent endothelial cell responses through transcriptional regulation. *Cell Cycle*, *16*(20), 1893-1901.

Nanavati, B. N., Noordstra, I., Lwin, A. K. O., Brooks, J. W., Rae, J., Parton, R. G.,...Green, K. J. (2024). The desmosome-intermediate filament system facilitates mechanotransduction at adherens junctions for epithelial homeostasis. *Current Biology*, *34*(17), 4081-4090.

Onunkwo, C. C., Hahn, B. L., & Sohnle, P. G. (2010). Clearance of experimental cutaneous Staphylococcus aureus infections in mice. *Archives of dermatological research*, *302*, 375-382.

Ozaki, K.-i., Awazu, M., Tamiya, M., Iwasaki, Y., Harada, A., Kugisaki, S.,...Kohno, M. (2016). Targeting the ERK signaling pathway as a potential treatment for insulin resistance and type 2 diabetes. *American journal of physiology-endocrinology and metabolism*, *310*(8), E643-E651.

Parola, P., & Raoult, D. (2001). Ticks and Tickborne Bacterial Diseases in Humans: An Emerging Infectious Threat. *Clinical Infectious Diseases*, *32*(6), 897-928. https://doi.org/10.1086/319347

Pentecost, M., Otto, G., Theriot, J. A., & Amieva, M. R. (2006). Listeria monocytogenes Invades the Epithelial Junctions at Sites of Cell Extrusion. *PLOS Pathogens*, *2*(1), e3. https://doi.org/10.1371/journal.ppat.0020003

Peña-Sagredo, J. L., Hernández, M. V., Fernandez-Llanio, N., Giménez-Ubeda, E., Munoz-Fernandez, S., Ortiz, A.,...Biobadaser, G. (2008). Listeria monocytogenes infection in patients with rheumatic diseases on TNF-alpha antagonist therapy: the Spanish Study Group experience. *Clinical & Experimental Rheumatology*, *26*(5), 854.

Plantone, D., Pardini, M., Righi, D., Manco, C., Colombo, B. M., & De Stefano, N. (2023). The role of TNF-α in Alzheimer's disease: a narrative review. *Cells*, *13*(1), 54.

Quereda, J. J., García-del Portillo, F., & Pucciarelli, M. G. (2016). Listeria monocytogenes remodels the cell surface in the blood-stage. *Environmental microbiology reports*, *8*(5), 641-648.

Rathod, M. L., Ahn, J., Jeon, N. L., & Lee, J. (2017). Hybrid polymer microfluidic platform to mimic varying vascular compliance and topology. *Lab on a Chip*, *17*(14), 2508-2516.

Rey, C., Chang, Y.-Y., Latour-Lambert, P., Varet, H., Proux, C., Legendre, R.,...Enninga, J. (2020). Transcytosis subversion by M cell-to-enterocyte spread promotes Shigella flexneri and Listeria monocytogenes intracellular bacterial dissemination. *PLoS pathogens*, *16*(4), e1008446.

Rübsam, M., Mertz, A. F., Kubo, A., Marg, S., Jüngst, C., Goranci-Buzhala, G.,...Moser, M. (2017). E-cadherin integrates mechanotransduction and EGFR signaling to control junctional tissue polarization and tight junction positioning. *Nature communications*, *8*(1), 1250.

Salo, J., Pietikäinen, A., Söderström, M., Auvinen, K., Salmi, M., Ebady, R.,...Hytönen, J. (2016). Flow-tolerant adhesion of a bacterial pathogen to human endothelial cells through interaction with biglycan. *The Journal of infectious diseases*, *213*(10), 1623-1631.

Savoia, P., Fava, P., Casoni, F., & Cremona, O. (2019). Targeting the ERK signaling pathway in melanoma. *International journal of molecular sciences*, *20*(6), 1483.

Sender, R., Fuchs, S., & Milo, R. (2016). Revised estimates for the number of human and bacteria cells in the body. *PLoS biology*, *14*(8), e1002533.

Shepherd, F. R., & McLaren, J. E. (2020). T cell immunity to bacterial pathogens: mechanisms of immune control and bacterial evasion. *International journal of molecular sciences*, *21*(17), 6144.

Silvani, G., Romanov, V., Cox, C. D., & Martinac, B. (2021). Biomechanical characterization of endothelial cells exposed to shear stress using acoustic force spectroscopy. *Frontiers in Bioengineering and Biotechnology*, *9*, 612151.

Sluiter, T. J., van Buul, J. D., Huveneers, S., Quax, P. H. A., & de Vries, M. R. (2021). Endothelial barrier function and leukocyte transmigration in atherosclerosis. *Biomedicines*, *9*(4), 328.

Smith, A. M., Inocencio, D. G., Pardi, B. M., Gopinath, A., & Andresen Eguiluz, R. C. (2024). Facile determination of the Poisson's ratio and Young's modulus of polyacrylamide gels and polydimethylsiloxane. *ACS Applied Polymer Materials*, *6*(4), 2405-2416.

Song, Y., Cheng, Y., Lan, T., Bai, Z., Liu, Y., Bi, Z.,...Wei, X. (2023). ERK inhibitor: A candidate enhancing therapeutic effects of conventional chemo-radiotherapy in esophageal squamous cell carcinoma. *Cancer Letters*, *554*, 216012.

Stange, E.-L., Rademacher, F., Drerup, K. A., Heinemann, N., Möbus, L., Gläser, R., & Harder, J. (2022). Staphylococcus aureus activates the aryl hydrocarbon receptor in human keratinocytes. *Journal of Innate Immunity*, *14*(6), 582-592.

Steere, A. C., Coburn, J., & Glickstein, L. (2004). The emergence of Lyme disease. *The Journal of clinical investigation*, *113*(8), 1093-1101.

Stutchbury, B., Atherton, P., Tsang, R., Wang, D.-Y., & Ballestrem, C. (2017). Distinct focal adhesion protein modules control different aspects of mechanotransduction. *Journal of cell science*, *130*(9), 1612-1624.

Sun, D., Ge, X., Tang, S., Liu, Y., Sun, J., Zhou, Y.,...Sheng, J. (2021). Bacterial characteristics of intestinal tissues from patients with crohn's disease. *Frontiers in cellular and infection microbiology*, *11*, 711680.

Tan, X., Petri, B., DeVinney, R., Jenne, C. N., & Chaconas, G. (2021). The Lyme disease spirochete can hijack the host immune system for extravasation from the

microvasculature. *Mol Microbiol*, *116*(2), 498-515. https://doi.org/10.1111/mmi.14728
Taylor, T. A., & Unakal, C. G. (2017). Staphylococcus aureus infection.
Travier, L., & Lecuit, M. (2014). Listeria monocytogenes ActA: a new function for a 'classic'virulence factor. *Current opinion in microbiology*, *17*, 53-60.
Tsuboi, H., Ando, J., Korenaga, R., Takada, Y., & Kamiya, A. (1995). Flow stimulates ICAM-1 expression time and shear stress dependently in cultured human endothelial cells. *Biochemical and biophysical research communications*, *206*(3), 988-996.
Valent, E. T., van Nieuw Amerongen, G. P., van Hinsbergh, V. W. M., & Hordijk, P. L. (2016). Traction force dynamics predict gap formation in activated endothelium. *Experimental cell research*, *347*(1), 161-170.
Vasquez, C. G., & Martin, A. C. (2016). Force transmission in epithelial tissues. *Developmental Dynamics*, *245*(3), 361-371.
Viklund, M., Fredriksson, J., Holdfeldt, A., Lind, S., Franzyk, H., Dahlgren, C.,...Forsman, H. (2022). Structural Determinants in the Staphylococcus aureus–Derived Phenol-Soluble Modulin α2 Peptide Required for Neutrophil Formyl Peptide Receptor Activation. *The Journal of Immunology*, *208*(7), 1632-1641.
Weddle, E., & Agaisse, H. (2018). Principles of intracellular bacterial pathogen spread from cell to cell. *PLoS pathogens*, *14*(12), e1007380.
Weiß, E., Schlatterer, K., Beck, C., Peschel, A., & Kretschmer, D. (2020). Formyl-peptide receptor activation enhances phagocytosis of community-acquired methicillin-resistant Staphylococcus aureus. *The Journal of Infectious Diseases*, *221*(4), 668-678.
Worku, M., Belay, G., & Tigabu, A. (2022). Bacterial profile and antimicrobial susceptibility patterns in cancer patients. *PLoS One*, *17*(4), e0266919.
Wu, J., Weening, E. H., Faske, J. B., Höök, M., & Skare, J. T. (2011). Invasion of eukaryotic cells by Borrelia burgdorferi requires β1 integrins and Src kinase activity. *Infection and immunity*, *79*(3), 1338-1348.
Xue, Y., Wang, M., & Han, H. (2023). Interaction between alveolar macrophages and epithelial cells during Mycoplasma pneumoniae infection. *Frontiers in Cellular and Infection Microbiology*, *13*, 1052020.
Yamada, K., Yoshino, K., Sekikawa, K., Madarame, H., Yagita, H., & Nakane, A. (2000). Effect of a matrix metalloproteinase inhibitor on host resistance against Listeria monocytogenes infection. *FEMS Immunology & Medical Microbiology*, *29*(3), 187-194.
Yuste, R. A., Muenkel, M., Axarlis, K., Gómez Benito, M. J., Reuss, A., Blacker, G.,...Bastounis, E. E. (2022). Borrelia burgdorferi modulates the physical forces and immunity signaling in endothelial cells. *iScience*, *25*(8), 104793. https://doi.org/https://doi.org/10.1016/j.isci.2022.104793
Zhou, J., Aponte-Santamaría, C., Sturm, S., Bullerjahn, J. T., Bronowska, A., & Gräter, F. (2015). Mechanism of focal adhesion kinase mechanosensing. *PLoS computational biology*, *11*(11), e1004593.

Section 1

Keratinocytes use FPR2 to detect Staphylococcus aureus and initiate antimicrobial skin defense.

Marco Lebtig[1,2], Jasmin Scheurer[3], Marie Muenkel[2,4], Janna Becker[1,2], Effie Bastounis[2,4], Andreas Peschel[1,2] and Dorothee Kretschmer[1,2*]

[1]Department first: Infection Biology, Interfaculty Institute of Microbiology and Infection Medicine, University of Tübingen, Tübingen, Germany,

[2]Cluster of Excellence EXC 2124 Controlling Microbes to Fight Infections, University of Tübingen, Tübingen, Germany,

[3]Department of Dermatology, University of Tübingen, Tübingen, Germany, 4Interfaculty Institute of Microbiology and Infection Medicine, University of Tübingen, Tübingen, Germany

Published 2023 in Frontiers in Immunology, 14, 1188555.

frontiers | Frontiers in Immunology

TYPE Original Research
PUBLISHED 31 May 2023
DOI 10.3389/fimmu.2023.1188555

OPEN ACCESS

EDITED BY
Taylor Sitarik Cohen,
AstraZeneca, United States

REVIEWED BY
Constantin Felix Urban,
Umeå University, Sweden
Meredith Crane,
Brown University, United States

*CORRESPONDENCE
Dorothee Kretschmer
dorothee.kretschmer@uni-tuebingen.de

RECEIVED 17 March 2023
ACCEPTED 16 May 2023
PUBLISHED 31 May 2023

CITATION
Lebtig M, Scheurer J, Muenkel M, Becker J, Bastounis E, Peschel A and Kretschmer D (2023) Keratinocytes use FPR2 to detect *Staphylococcus aureus* and initiate antimicrobial skin defense. *Front. Immunol.* 14:1188555. doi: 10.3389/fimmu.2023.1188555

Keratinocytes use FPR2 to detect *Staphylococcus aureus* and initiate antimicrobial skin defense

Marco Lebtig[1,2], Jasmin Scheurer[3], Marie Muenkel[2,4], Janna Becker[1,2], Effie Bastounis[2,4], Andreas Peschel[1,2] and Dorothee Kretschmer[1,2]*

[1]Department first: Infection Biology, Interfaculty Institute of Microbiology and Infection Medicine, University of Tübingen, Tübingen, Germany, [2]Cluster of Excellence EXC 2124 Controlling Microbes to Fight Infections, University of Tübingen, Tübingen, Germany, [3]Department of Dermatology, University of Tübingen, Tübingen, Germany, [4]Interfaculty Institute of Microbiology and Infection Medicine, University of Tübingen, Tübingen, Germany

Introduction: Keratinocytes form a multilayer barrier that protects the skin from invaders or injuries. The barrier function of keratinocytes is in part mediated by the production of inflammatory modulators that promote immune responses and wound healing. Skin commensals and pathogens such as *Staphylococcus aureus* secrete high amounts of phenol-soluble modulin (PSM) peptides, agonists of formyl-peptide receptor 2 (FPR2). FPR2 is crucial for the recruitment of neutrophils to the sites of infection, and it can influence inflammation. FPR1 and FPR2 are also expressed by keratinocytes but the consequences of FPR activation in skin cells have remained unknown.

Methods: Since an inflammatory environment influences *S. aureus* colonization, e. g. in patients with atopic dermatitis (AD), we hypothesized that interference with FPRs may alter keratinocyte-induced inflammation, proliferation, and bacterial colonization of the skin. To assess this hypothesis, we investigated the effects of FPR activation and inhibition in keratinocytes with respect to chemokine and cytokine release as well as proliferation and skin wound gap closure.

Results: We observed that FPR activation induces the release of IL-8, IL-1α and promotes keratinocyte proliferation in a FPR-dependent manner. To elucidate the consequence of FPR modulation on skin colonization, we used an AD-simulating *S. aureus* skin colonization mouse model using wild-type (WT) or $Fpr2^{-/-}$ mice and demonstrate that inflammation enhances the eradication of *S. aureus* from the skin in a FPR2-dependent way. Consistently, inhibition of FPR2 in the mouse model or in human keratinocytes as well as human skin explants promoted *S. aureus* colonization.

Discussion: Our data indicate that FPR2 ligands promote inflammation and keratinocyte proliferation in a FPR2-dependent manner, which is necessary for eliminating *S. aureus* during skin colonization.

KEYWORDS

keratinocytes, skin colonization, formyl-peptide receptor 2, *Staphylococcus aureus*, inflammation

1 Introduction

The skin acts as a physical and immunological protective barrier with over 90% keratinocytes as the predominant cell type in the epidermis. Keratinocytes respond to pathogenic microorganisms and injury by producing antimicrobial peptides and cytokines (1). During their maturation from the basal to the uppermost layer, epidermal cells undergo a calcium-regulated differentiation. Staphylococci are ubiquitous colonizers of human skin, especially coagulase-negative staphylococci as *S. epidermidis*. A less frequent colonizer of the skin represents the opportunistic pathogen *Staphylococcus aureus* (2). S. aureus causes a wide range of diseases from superficial skin infections to severe invasive infections such as septicemia or endocarditis (3). Acute bacterial skin infections are a common reason to seek healthcare facilities, and *S. aureus* is the most common organism associated with hospital-acquired infections (4). These infections are further complicated by methicillin-resistant *S. aureus* (MRSA) strains, which are prevalent in hospitals. Virulence of pathogenic *S. aureus* depends on various virulence factors, e. g. the phenol-soluble modulin (PSM) peptide toxins. *S. aureus* can not only induce cutaneous infections but it also frequently contributes to flare-up of inflammatory skin diseases such as atopic dermatitis (AD) (5). AD is characterized by acute eczematous, pruritic lesions over dry skin and severely impairs the quality of life of those affected. Under normal circumstances *S. aureus* rarely colonizes human skin. In AD, *S. aureus* frequently colonizes unaffected skin. Interestingly, it has been shown that an inflammatory environment promotes *S. aureus* skin colonization (6, 7).

Formyl-peptide receptors (FPRs) belong to the family of chemoattractant G-protein coupled receptors (GPCRs), which are critical for detecting bacterial infections and are known to influence inflammation (8). All bacteria release short formylated peptides, ligands of FPR1. However, staphylococci, especially highly pathogenic *S. aureus* strains, additionally secrete large amounts of PSMs, which represent FPR2 ligands (9). Neutrophils express FPR1 as well as FPR2 and FPR activation is known to transiently increase intracellular calcium, chemotaxis, degranulation, expression of receptors for phagocytosis and thereby enhance pathogen elimination (8, 10). Although it has been shown that various epithelial cells including keratinocytes also express FPR1 and FPR2 (11), the consequences of FPR activation in these cells are poorly understood. FPR2 ligands such as the synthetic ligand WKYMVM and the human antimicrobial peptide LL-37 were shown to increase keratinocyte proliferation and improve wound healing (12, 13). In contrast, FPR inhibitors attenuated phorbol 12-myristate 13-acetate (PMA)-induced ear edema by reducing local production of cytokines such as MCP-1, CXCL1 as well as IL-6, and thereby possess anti-inflammatory properties (14). Opposite effects were reported in intestinal epithelial cells, whose stimulation with the formylated peptide fMLF, an FPR1 agonist, decreased TNFα-induced NFκB signaling and proinflammatory cytokine production (15). Most AD patients are colonized by *S. aureus* and experience relapses of their skin disorder because of overgrowth of this bacterium (16). Studies revealed that topical administration of anti-inflammatory corticosteroids or tacrolimus lowered *S. aureus* levels in atopic skin (17, 18). *S. aureus* releases high amounts of FPR2 ligands, the PSMs. PSMs are short formylated α-helical, amphipathic peptides and are released in high amounts especially by pathogenic *S. aureus* strains, e. g. USA300 (19). Therefore, we hypothesized that keratinocyte-dependent FPR2 activation induces skin inflammation.

Since it is unclear if and how FPRs influence bacteria-induced skin inflammation such as AD, we investigated the consequences of FPR activation or inhibition in the presence or absence of *S. aureus* colonization in human keratinocytes, and in an animal model of skin inflammation and *S. aureus* colonization using wild-type (WT) and Fpr2-/- mice. We observed that the FPR1 ligand fMLF and the FPR2 ligands PSMα3, PSMα, PSMε and MMK1 induced IL-8 as well as IL-1α and in part MIP-3α, and CXCL10 release by human keratinocytes. The FPR inhibitors tBOC and WRW4 prevented the FPR ligand-induced release of IL-1α and IL-8 as well as proliferation of keratinocytes. In addition, we found enhanced *S. aureus* colonization but not *S. epidermidis* colonization in FPR2 inhibitor-treated keratinocytes and in human skin explants. Accordingly, we observed that FPR2 inhibition in an *in vivo* model simulating human AD enhanced *S. aureus* colonization only in WT but not in $Fpr2^{-/-}$ mice. This enhanced *S. aureus* colonization correlated with a decreased release of inflammatory cytokines IL-1α, IL-1β as well as MIP-2 in WT but not in $FPR2^{-/-}$ mice. Our data show that induction of skin inflammation by *S. aureus* is mediated at least in part by FPR2 activation in keratinocytes leading to enhanced IL-8 as well as IL-1α release and keratinocytes proliferation. Conversely, inhibition of FPR2 in keratinocyte prevents inflammation but promotes *S. aureus* skin colonization.

2 Results

2.1 Expression of FPRs by keratinocytes and activation by bacterial ligands

It has been described that keratinocytes express FPRs (11). To analyze consequences of FPR activation in keratinocytes, we evaluated the suitability of the immortalized human keratinocyte cell line N/TERT-1 for such functional studies since primary human keratinocytes (PHK) have only a limited lifespan. We compared the expression of FPRs on the surface of PHK (Figures 1A, B) with the expression by differentiated N/TERT-1 cells (Figures 1C, D). Fluorescence-activated cell sorting (FACS) analysis confirmed FPR expression on both cell types. In order to elucidate whether FPR ligands can also activate keratinocytes, we stimulated PHK and N/TERT-1 with synthetic FPR1 and FPR2 ligands and included the TLR2 ligand Pam2Cys (P2C) as a positive control. It is well documented that staphylococci release TLR2 ligands (20) and TLR2 activation in keratinocytes leads to IL-8 release (21). We assessed whether FPR activation by the FPR1 ligand fMLF, the staphylococcal FPR2 ligand phenol-soluble modulin α3 (PSMα3), or the synthetic FPR2 ligand MMK1 can trigger the release of proinflammatory cytokines by differentiated PHK. We observed that stimulation of PHK with FPR1 or FPR2 ligands increased the release of IL-8 (Figures 1E–G). However,

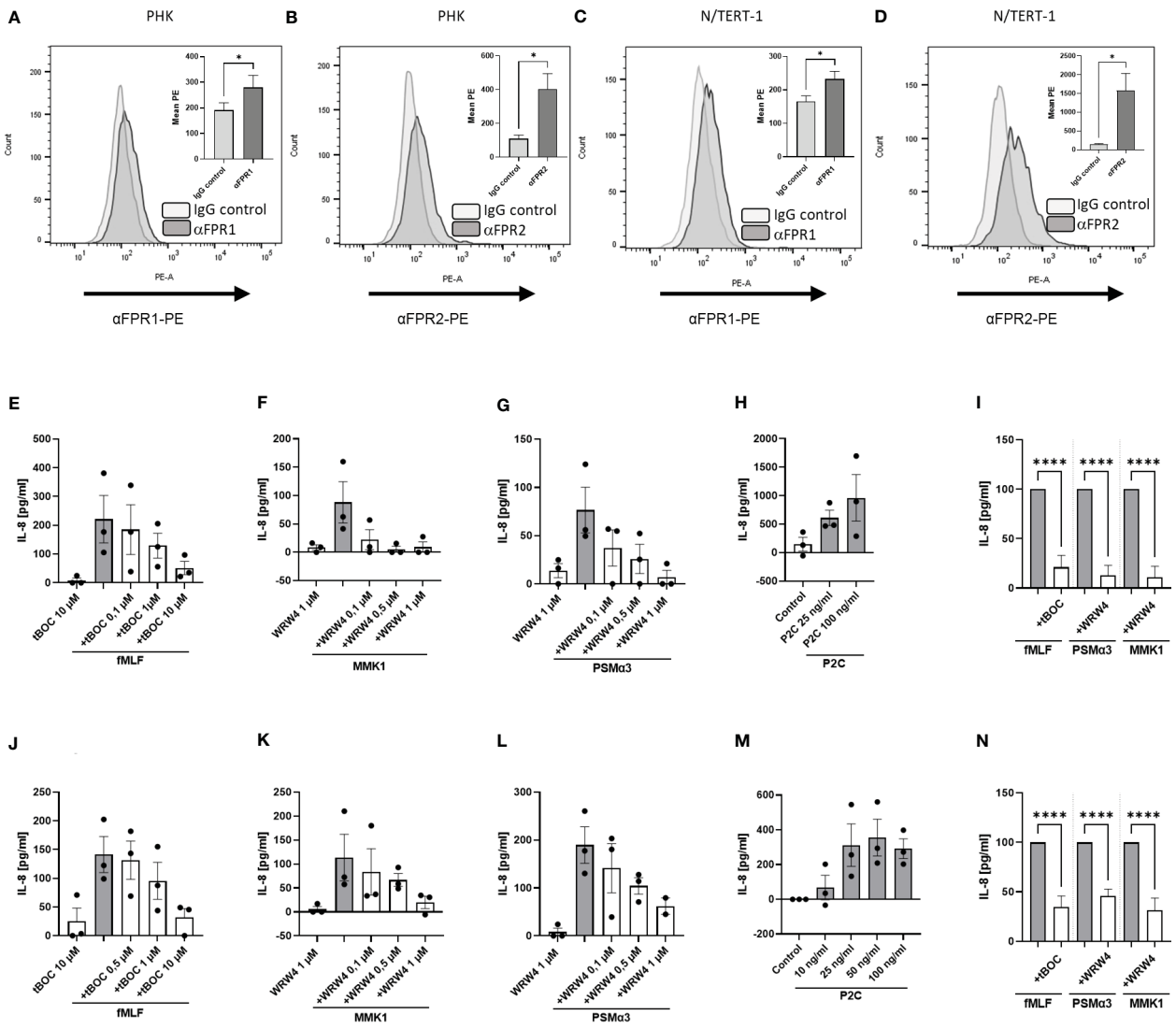

FIGURE 1
FPR expression and activation induce IL-8 release from keratinocytes in a receptor-dependent manner. FACS analysis of FPR1 and FPR2 expression by PHK **(A, B)** as well as by N/TERT-1 keratinocytes **(C, D)**. IL-8 release of differentiated primary PHKs stimulated for 17 h with either fMLF (100 nM) +/- various concentrations of tBOC **(E)**, MMK1 (100 nM) or PSMα3 (10 nM) +/- various concentrations of WRW4 **(F, G)** or control (DMSO) and P2C **(H)**. Relative amount of released IL-8 by FPR inhibitor-treated keratinocytes (WRW4 1µM, tBOC 10µM) compared to indicated FPR ligands alone **(I)**. IL-8 release of differentiated N/TERT-1 keratinocytes stimulated for 17 h with either fMLF (100 nM) +/- tBOC **(J)**, MMK1 (100 nM) +/- WRW4 **(K)**, PSMα3 (10nM) +/- WRW4 **(L)** or control (DMSO) and P2C **(M)**. Relative amount of released IL-8 by FPR inhibitor-treated N/TERT-1 keratinocytes (WRW4 1µM, tBOC 10µM) compared to indicated FPR ligands alone **(N)**. Data represent mean and SEM out of five experiments **(A, B)**, mean and SEM of six experiments **(C, D)**, of at least 3 experiments **(E–H, J–M)**, of 4-6 experiments **(I, N)**. All data in **(E–N)** represent IL-8 release minus IL-8 release by medium treated cells. *P < 0.05; ****P < 0.0001, significant difference versus the indicated FPR ligands as calculated by paired two-tailed Student's t-tests of the mean **(A–D)** or ordinary one-way ANOVA of baseline corrected data **(I, N)**.

activation of TLR2 by the lipopeptide P2C increased the release of these cytokines even stronger (Figure 1H). To confirm that the observed effects are FPR-dependent, we incubated the cells with increasing concentrations of the FPR1- or FPR2-specific inhibitors tBOC or WRW4, respectively, to prevent PHK activation. We observed dose-dependent, significant inhibition of the FPR ligand-induced release of IL-8 (Figure 1I). Moreover, stimulation of differentiated N/TERT-1 cells led to comparable results with respect to IL-8 release (Figures 1J–N). We concluded that these cells can be used as surrogate for PHK and analyzed S. epidermidis-derived FPR2 ligands PSMα and PSMε regarding IL-8 induction in N/TERT-1. Again, IL-8 release was inhibited by WRW4 (Supplementary Figure 1A).

2.2 Activation of FPRs induces expression of IL-1α, CXCL10, and MIP-3α in keratinocytes

Next, we were interested whether keratinocyte FPR activation leads to secretion of other chemokines or cytokines in addition to IL-8. Therefore, we analyzed N/TERT-1 cells for the release of IL-1α, CXCL11, CCL2, CCL3, MIP-3α and CXCL10 (Figure 2; Supplementary Figure 2). Besides the TLR2 ligand P2C, the FPR1 ligand fMLF, the *S. aureus* FPR2 ligand PSMα3, the *S. epidermidis* FPR2 ligands PSMα and PSMε as well as the synthetic FPR2 ligand MMK1 induced IL-1α release from keratinocytes (Figures 2A–D;

Supplementary Figure 1B). Significant inhibition of FPR ligand-induced release of IL-1α was achieved with 1 μM WRWR4 or 10 μM tBOC (Figure 2E; Supplementary Figure 1B), thereby confirming that the induction was mediated by FPR2 and FPR1, respectively. fMLF and PSMα3 also induced MIP3-α and CXCL10 slightly, which did not markedly increase after prolonged stimulation (Figures 2F, I). Whereas induction of these two chemokines by fMLF could be inhibited by tBOC, and reached statistical significance at least for CXCL10 (Figures 2H, K), induction by PSMα3 was not inhibited by WRW4 suggesting that induction of CXCL10 and MIP3-α by PSMα3 is not FPR2-dependent and may be a secondary consequence of the membrane-perturbing properties of PSMα3 (Figures 2G, J).

2.3 Influence of FPRs on keratinocyte proliferation, migration, and gap closure

A typical feature of skin lesions in atopic dermatitis is abnormally enhanced keratinocyte proliferation (22, 23), which may be shaped by skin microbiome members via FPR stimulation. To assess this possibility, we analyzed whether proliferation of non-differentiated PHK may be influenced by FPR activation or inhibition using a proliferation assay, based on the tetrazolium salt WST-1, which can be metabolized by active cells to formazan. We observed that low concentrations of FPR ligands promote the proliferation of PHK in a dose-dependent

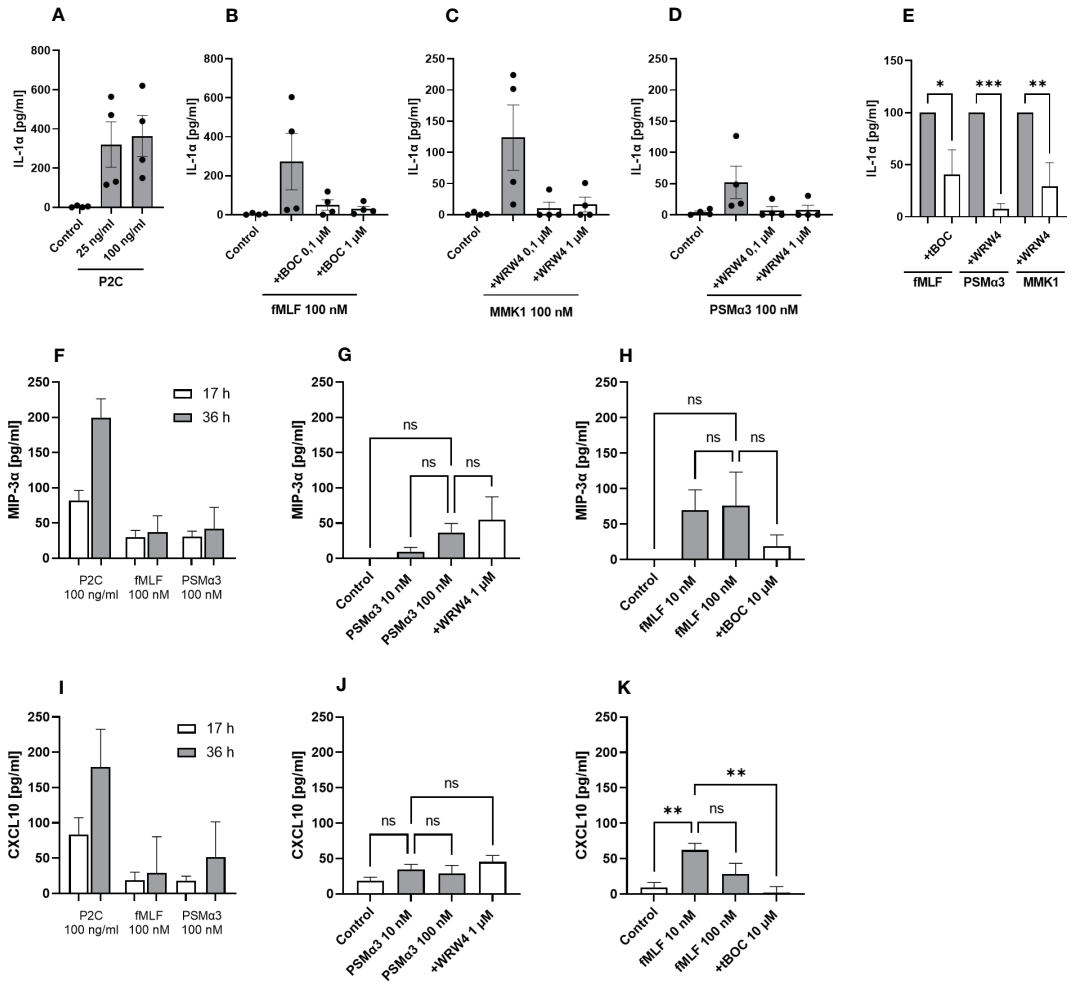

FIGURE 2
Activation by FPR ligands induces IL-1α as well as MIP-3α and CXCL10 release from keratinocytes. IL-1α release of differentiated N/TERT-1 keratinocytes stimulated for 17 h with either P2C **(A)**, fMLF +/- tBOC **(B)**, MMK1 +/- WRW4 **(C)**, or PSMα3 +/- WRW4 **(D)** and control (DMSO). Relative amount of released IL-1α by keratinocytes treated with FPR inhibitors as compared to indicated FPR ligands alone **(E)**. MIP-3α release of differentiated N/TERT-1 keratinocytes stimulated for 17 or 36 h with either P2C, fMLF or PSMα3 **(F)**. MIP-3α release after 36 h stimulation with different concentrations of PSMα3 +/- WRW4 **(G)** or fMLF +/- tBOC **(H)** and control (DMSO). CXCL10 release of differentiated N/TERT-1 keratinocytes stimulated for 17 or 36 h with either P2C, fMLF or PSMα3 **(I)**. CXCL10 release after 36 h stimulation with different concentrations of PSMα3 +/- WRW4 **(J)** or fMLF +/- tBOC **(K)** and control (DMSO). Data in A-K represent means ± SEMs from at least four independent experiments. Data in **(A–H)** represent cytokine release minus cytokine release by medium-stimulated cells. Ns, not significant, *P < 0.05; **P < 0.01; ***P < 0.001, significant difference versus the indicated FPR ligands as calculated by ordinary one-way ANOVA of baseline corrected data **(E)** or one-way ANOVA with Dunnett's multiple comparisons test **(G, H, J, K)**.

trend (Figures 3A, B), whereas inhibitors of FPR1 and FPR2 prevented the proliferation-stimulating activity of FPR ligands (Figure 3C). To assess whether enhanced proliferation may support the skin wound healing process, we monitored wound gap closure in a scratch assay with cells seeded on coverslips. Live-cell imaging of cells populating the wound was performed for 12 hours. Since cultivation of PHK is limited to very few passages, we used N/TERT-1 keratinocytes instead of PHK. We analyzed how fast cells populate the wound either with addition of FPR2 ligand PSMα3 alone or in combination with the FPR2 inhibitor WRW4. To stain the nucleus of living cells, Hoechst was used, which allowed us to segment cell nuclei and follow their tracks during wound healing as well as to determine nuclei splitting events by performing image processing on the microscopy image data (Figure 3G). Significantly improved gap closure, particularly in the case of PSMα3-treated cells compared to medium control, was observed, whereas inhibition of FPR2 by WRW4 delayed PSMα3-mediated enhanced gap closure (Figures 3D, E; Supplementary Movie 1). Furthermore, the mean cell migration speed was significantly increased in cells treated with PSMα3 compared to the medium control, and interestingly, even after closing the gap, when the cells mix to rearrange the cell monolayer, the migration speed of these cells was still higher (Figure 3F, after 7h). Using an orthogonal approach based on tracking cell division events using the imaging data (Figure 3G), we also confirmed enhanced splitting events, *i.e.*, proliferation, only for PSMα3-treated cells as compared to medium control, but not for WRW4-treated or for PSMα3 and WRW4-treated cells (Figure 3H). Thus, we can conclude that PSMα3-treated cells, which exhibit the greatest wound healing efficiency, achieve that by means of both enhanced proliferation and migration.

2.4 FPR2 inhibition prevents inflammation of the skin and enhances colonization by *S. aureus*

S. aureus may reach live keratinocytes in deeper skin areas if the stratum corneum is breached. To analyze if FPR stimulation may affect the capacity of keratinocytes to bind *S. aureus*, we exposed human keratinocytes to *S. aureus* USA300, which produces FPR-activating formylated peptides and PSM peptides, with and without addition of the FPR1 inhibitor tBOC or FPR2 inhibitor WRW4 (Figure 4A). Inhibition of FPR2 in PHK as well as in N/TERT-1 significantly enhanced binding by USA300, but not by *S. epidermidis*, whereas inhibition of FPR1 had no influence on *S. aureus* binding (Figures 4A, B; Supplementary Figure 3). Thus, sensing of PSMs by FPR2 may reduce the capacity of *S. aureus* to bind to keratinocytes, which may help to limit the persistence of *S. aureus* in atopic skin.

Since *S. aureus* skin colonization and subsequent skin inflammation plays a crucial role in atopic dermatitis, we analyzed the influence of FPR2 on *S. aureus* colonization in an *in vivo* model that simulates human atopic dermatitis. We impaired the skin barrier by tape stripping in wild-type and $Fpr2^{-/-}$ mice and applied then PSMs-producing *S. aureus* USA300 with or without WRW4 to the tape-stripped skin (Figure 4C). After 24 hours, $Fpr2^{-/-}$ mice contained approximately tenfold higher bacterial numbers on their skin than wild-type mice, indicating that FPR2 plays a critical role in limiting *S. aureus* skin colonization. In support of this finding, WRW4 treatment also increased the abundance of *S. aureus* on the skin of wild-type mice, but it had no influence on the *S. aureus* growth rate on $Fpr2^{-/-}$ skin (Figure 4D). These increases were accompanied by a reduction in the secretion of MIP-2, IL-1α, and IL-1β (Figures 4E–G) in the skin of $Fpr2^{-/-}$ mice or WRW4-treated wild-type mice compared to untreated wild-type mice. In contrast to the wild-type mice, we observed no difference between WRW4 and mock treatment in the $Fpr2^{-/-}$ mice with respect to release of MIP-2, IL-1α, and IL-1β (Figures 4E–G). Interestingly, also inhibition of FPR2 in human skin explants enhanced *S. aureus* binding and colonization, respectively (Figures 4H, I).

3 Discussion

Secreted bacterial molecules can influence skin homeostasis. Lipopeptides, but also formylated peptides such as PSMs, belong to those molecules that are released by skin colonizing bacteria (19, 20). FPR2 is one of the most promiscuous receptors within the class-A subfamily of GPCRs, not only being able to interact with a variety of ligands but also being expressed by highly diverse cell types (24). In contrast to neutrophils, it was rather unclear if and how FPR2 ligands such as staphylococcal PSMs can influence the physiology of keratinocytes.

It has been described that bacterial colonization promotes wound healing of the skin. Germ-free mice show impaired wound healing compared to specific pathogen-free as well as wild-type mice and treatment of human skin with antibiotics impaired wound healing in an IL-1 receptor-dependent manner (25). Furthermore, FPR ligands were shown to promote cutaneous wound healing (13). Our finding that bacterial FPR ligands promote keratinocyte proliferation in a FPR-dependent manner is in line with these observations (11). Therefore, we speculate that bacterial FPR ligands are responsible for the wound healing-promoting properties of skin bacteria. *S. aureus* skin colonization in patients with AD activates keratinocytes (26) leading to enhanced chemokine and IL-1α production, keratinocyte proliferation, as well as antimicrobial activity. Since we show that all these responses can be triggered by FPR activation and since *S. aureus* is known to produce high amounts of PSMs, we suggest that this is most probably driven by FPR2 (19). This is supported by the fact that expression of a functional Agr global regulatory system in *S. aureus* was not only required for PSM production, but also for epidermal colonization and the induction of AD-like inflammation in mice (27). The enhanced chemokine production could lead to recruitment of leukocytes, which may then promote the elimination of bacteria from infected wounds (28).

However, since the skin barrier of AD patients is frequently impaired, constant FPR activation could be a reason for the observed hyperproliferation of keratinocytes in AD (23), thereby supporting chronic *S. aureus* colonization and maintaining inflammation.

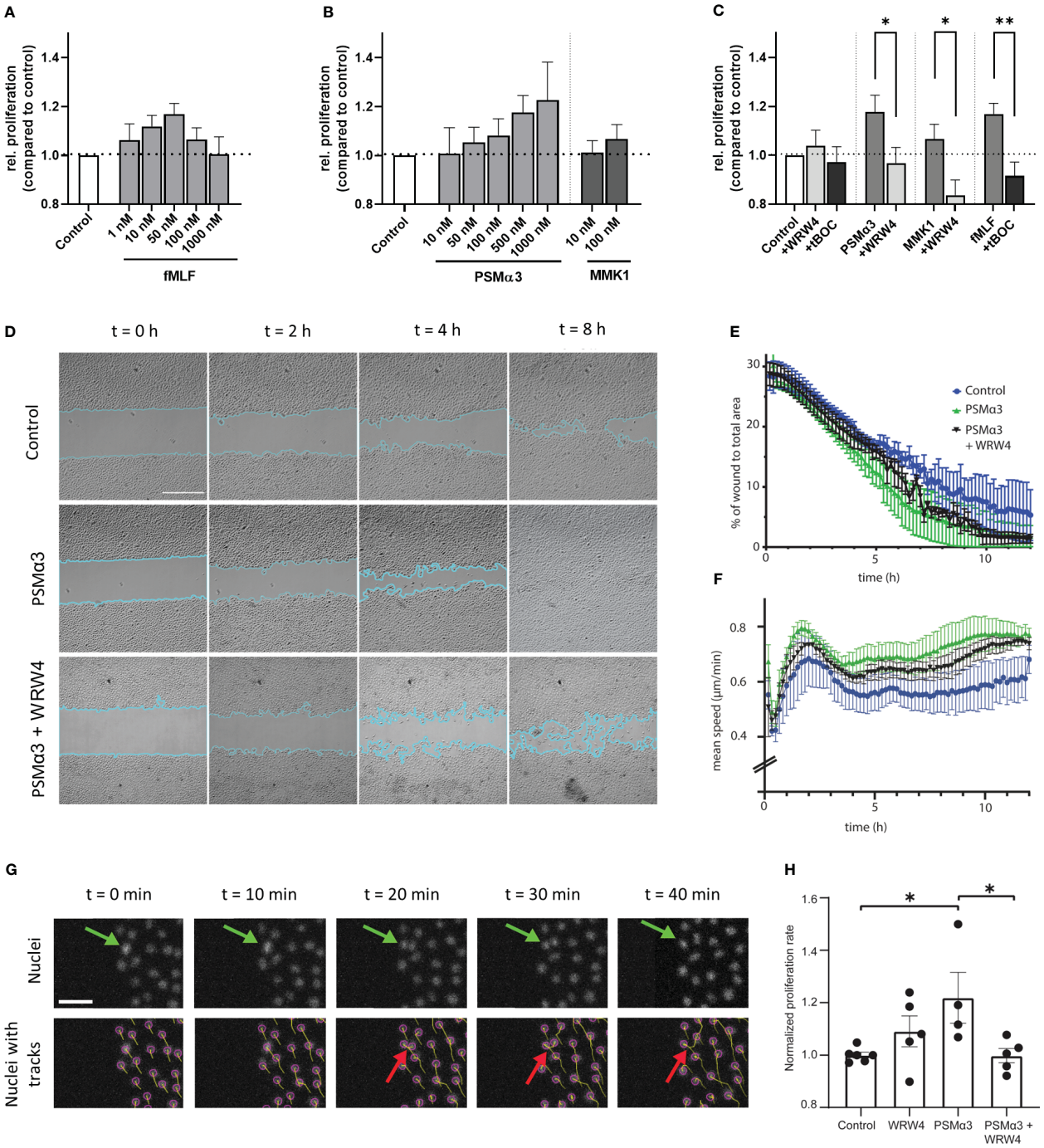

FIGURE 3
Influence of FPR ligands and inhibitors on proliferation, wound closure efficiency and migration speed. Relative proliferation of 24 h stimulated PHKs either treated with different concentrations of fMLF **(A)** or different concentrations of FPR2 ligands PSMα3 and MMK1 **(B)** compared to untreated (medium) control. Influence of FPR1 inhibitor tBOC (10 µM) on fMLF (50 nM) enhanced proliferation or FPR2 inhibitor WRW4 (1 µM) on PSMα3 (500 nM) or MMK1 (100 nM) induced proliferation **(C)**. Representative phase contrast images of wound closure of undifferentiated N/TERT-1 keratinocytes treated with vehicle control (top row), 10 nM PSMα3 (middle row) or 10 nM PSMα3 plus 1 µM WRW4 (bottom row). Scale bar: 500 µm. Cyan line traces the wound edges **(D)**. Percentage of gap (i.e., wound) area compared to the area of the whole field of view (y-axis) as a function of time (x-axis, h) **(E)**. Mean migration speed (y-axis, µm/h) of N/TERT-1 cells as a function of time (x-axis, h) for cells repopulating the wound as in previous panels **(F)**. Exemplary epifluorescence images of N/TERT-1 keratinocytes' nuclei stained with live-cell DNA dye (Hoechst) during wound closure. Top row shows nuclei without tracks, while bottom row shows the same images with superimposed object detection (purple circles) and tracks (cumulative displacements of the nuclei). Green arrows mark a dividing cell (on top) and cell division as detected by the nuclear segmentation and tracking (bottom row, red arrows) **(G)**. Using Trackmate Fiji plugin, cells were tracked for 12 h, split events were counted and divided by the total number of nuclei. Cells were treated with PSMα3 (10 nM), WRW4 (1 µM), both or vehicle control. Proliferation rate was normalized with respect to the mean of cells treated with vehicle control **(H)**. Data represent mean and SEM of six independent experiments of three different donors, **(A-C)** or three independent experiments **(D-H)**. *P < 0.05; **P < 0.01, significant difference versus the indicated FPR ligands as calculated by paired two-tailed Student's t-test **(C)**. A one-way ANOVA followed by a Dunnett's multiple comparison test was performed and control (*P = 0.02) and PSMα3 plus WRW4 treated cells' proliferation rate (*P = 0.02) was determined to be significantly altered compared to PSMα3 treated cells only **(H)**.

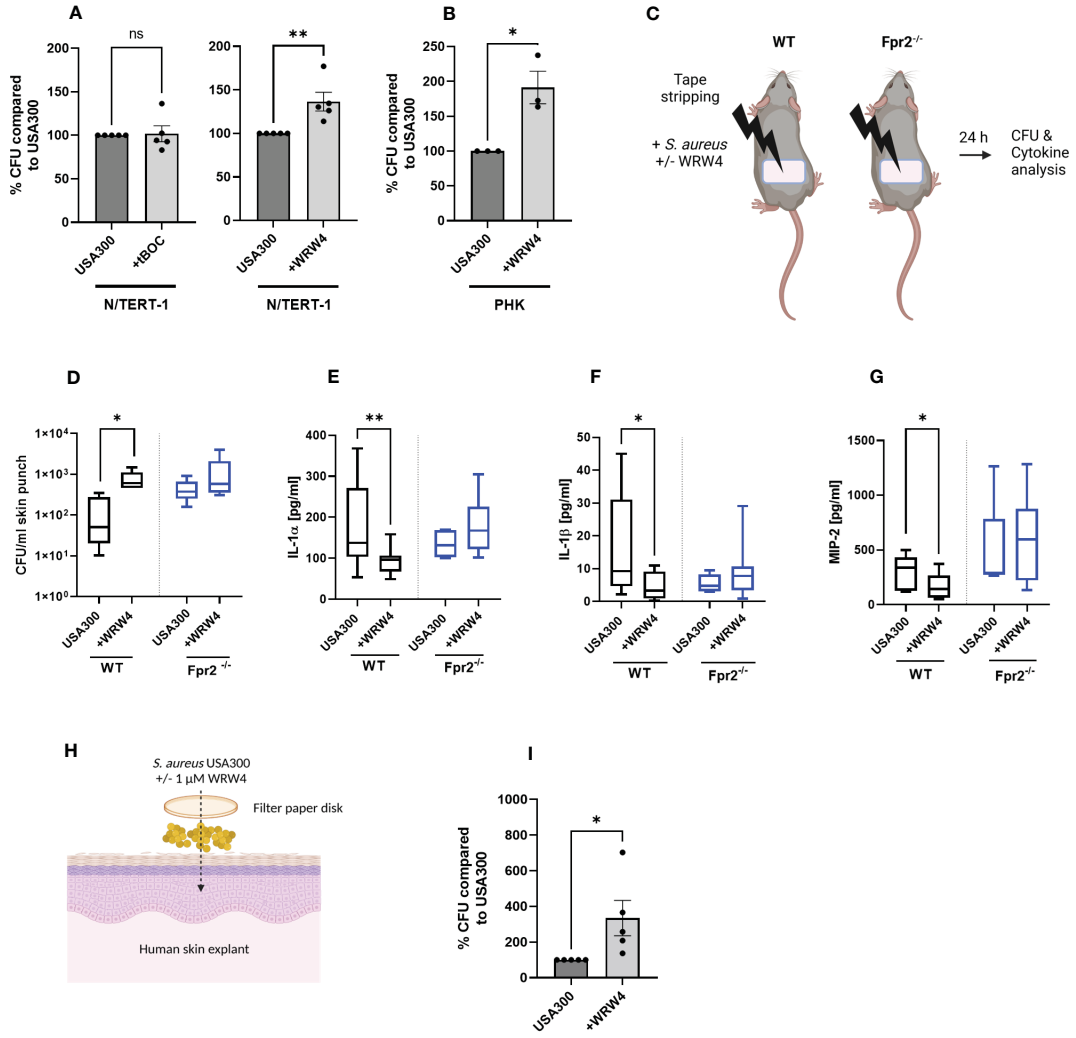

FIGURE 4
FPR2 inhibition prevents inflammation of the skin and enhances colonization by *S. aureus*. CFUs of *S. aureus* recovered from infected N/TERT-1 **(A)** treated either with USA300 +/- tBOC (10 µM) (left) or USA300 +/- WRW4 (1 µM) (right), or CFU of *S. aureus* recovered from infected PHK +/- WRW4 (1 µM) **(B)**. Skin of tape stripped wild-type and Fpr2$^{-/-}$ were colonized for 24 h with *S. aureus* either with addition of WRW4 or PBS **(C)**. Recovered *S. aureus* **(D)** and IL-1α **(E)**, IL-1β **(F)** or MIP-2 **(G)** derived from supernatants of skin punches of *S. aureus* colonized skin. Model of colonization of human skin explants with *S. aureus* **(H)**. Bacteria derived from human skin explants after *S. aureus* colonization in combination with DMSO or WRW4 (1 µM), **(H, I)**. Data represent mean and SEM of five independent experiments of baseline-corrected data **(A)**, of three independent experiments of three different donors **(B)** of three/four mice per group (WT) and three mice per group Fpr2$^{-/-}$ **(D)** six mice per group (WT) and three mice per group of Fpr2$^{-/-}$ **(E–G)**, two tapes per mouse and of five independent experiments with skin explants from 5 donors **(I)**. *P < 0.05; **P < 0.01, significant difference versus the indicated controls as calculated by paired or two-tailed Student's t-tests **(A, B, G, I)** or Mann-Whitney test **(D, E)**.

In summary, our data indicate that *S. aureus* furthers skin colonization by modulating a keratinocyte-induced, pro-inflammatory milieu as assessed by cytokine levels via FPRs. Neutrophils also express FPR2 and play a crucial role during skin infection (28). Therefore, in our *in vivo* model it cannot be excluded that cytokine release could be due to leukocyte-derived cytokines, but our *in vitro* data with primary keratinocytes and skin explants suggest that this is rather unlikely. *S. aureus*-triggered chemokine production is accompanied by significant secretion of IL-1α and IL-1β in the skin of wild-type mice after *S. aureus* colonization as observed by us and others (25). It has been described that inhibition of FPRs prevents inflammation of the skin (29). Our data support these observations since inhibition of FPR2 by WRW4 or lack of Fpr2 prevented the release of IL-1α, IL-1β and MIP-2. However, the reduced inflammation led to enhanced skin colonization of *S. aureus*. Hence, it is tempting to speculate that by secreting inhibitors of FPRs, *S. aureus* tries to reduce inflammation. Indeed, *S. aureus* frequently releases inhibitors of FPRs, namely, the proteins CHIPS (30), FLIPr (31) or FLIPr-like (32). Since these inhibitors are human specific, only the *S. aureus*-released agonists of FPRs, i.e., the PSMs, but not the antagonists can be analyzed in animal models. Our data regarding application of the synthetic FPR2 inhibitor WRW4 to the skin of mice, human keratinocytes, or skin explants support the hypothesis that *S. aureus* could use FPR inhibitors to promote skin colonization. The production of FPR ligands and inhibitors may contribute to the ability of *S. aureus* to adjust a favorable balance between activation and inhibition. Our data regarding *S. epidermidis* show that their PSMs also activate

keratinocytes in a FPR2-dependent manner. Since colonization of keratinocytes by *S. epidermidis* could not be influenced by the addition of WRW4, the amount of PSMs released by these bacteria might be too low for FPR2 activation. This is consistent with the fact that coagulase-negative staphylococci generally release lower amounts of FPR2 ligands compared to highly pathogenic *S. aureus* strains (9).

It has been shown that mice spontaneously developing AD symptoms due to the lack of cathepsin E exhibit increased susceptibility to infection with *S. aureus* and *Porphyromonas gingivalis* (33). In AD patients with secondary *S. aureus* infections, combination therapy with anti-staphylococcal medicines and topical immunosuppressive corticosteroids improves clinical outcomes more than therapy using topical corticosteroids alone, supporting the significance of a co-occurring *S. aureus* infection in exacerbating the symptomatology of AD patients. Interestingly, FPR-encoding genes belong to the most important hub genes involved in the pathogenesis of acne (34), thus providing further evidence for a role of FPR in the maintenance of inflammatory skin conditions. Our data imply that FPR2 inhibition reduces local activation and cytokine secretion of keratinocytes via FPR2, allowing *S. aureus* to initially colonize better. This increased colonization could then result in the permanent recruitment of more leukocytes, which tend to promote inflammation and *S. aureus* colonization (6).

Based on our findings, topical FPR2 inhibition could be useful as a therapeutic option to reduce sterile inflammation of the skin as described (14). On the contrary, in patients with atopic dermatitis, inhibition of FPR2 in keratinocytes promotes chronic *S. aureus* colonization.

4 Material and methods

4.1 Bacterial strains, culture conditions and peptides

For this study, *S. aureus* USA300 LAC and *S. epidermidis* 1457 were used and cultured in tryptic soy broth (TSB) at 37°C for 17 h over-night under agitation at 160 rpm. All assays were performed with logarithmically growing bacteria. Various agonists and antagonists were used for this study. As FPR2 agonists PSMα3, PSMα, PSMε (35) and MMK1 were used and WRW4 as FPR2 antagonist. Formylated PSMα3 was kindly provided by Stefan Stevanovic (Dep. of Immunology, Tuebingen). MMK1 (LESIFRSLLFRVM), PSMα, PSMε and WRW4 were purchased (EMC microcollections). fMLF (SIGMA Life Science) was used as FPR1 agonist and N-tert-butoxycarbonyl-methionyl-leucyl-phenylalanine (tBOC; Bachem) as antagonist. For stimulation of TLR2, Pam_2Cys-SKKKK (P2C, Invivogen) was used.

4.2 Cell culture

Primary human keratinocytes (PHK) were isolated from juvenile human foreskin after routine circumcision from the Loretto Clinic in Tübingen, as previously described (7, 36). Primary human keratinocytes were cultured in collagen-coated tissue flasks in CnT-BM.1 Basal Medium 1 with supplements (CELLnTEC) at 37°C and 5% CO_2. Cell passage 2-4 were used for stimulation and adherence experiments. PHK isolation from human foreskin were approved by the ethics committee of the Medical Faculty of the University Tübingen (750/2018BO2). PHK were differentiated by stimulation for 17 h with 1.7 mM $CaCl_2$ in keratinocyte base medium without additional supplements (CELLnTEC). Cytokine release by the medium treated cells was subtracted from all values unless otherwise stated.

The immortalized human keratinocyte cell line N/TERT-1 was kindly provided by J. G. Rheinwald (37). N/TERT-1 cells were cultured in cell culture flasks (Greiner Bio-One GmbH, CELLSTAR® TC) in CnT-BM.1 Basal Medium 1 with supplements (CELLnTEC) at 37°C, 5% CO_2. Forty-eight hours prior to experiments, as well as during experiments, N/TERT-1 cells were differentiated with 1.7 mM $CaCl_2$ in epidermal keratinocyte base medium (CELLnTEC).

4.3 Stimulation of keratinocytes with agonists and antagonists for GPCRs

Before stimulation, 250 µl/well of N/TERT-1 cells with a concentration of 0,02 × 10^6 cells/ml were seeded in epidermal keratinocyte medium containing supplements (CELLnTEC) into 48-well plates coated with 25 µg/ml rat tail collagen I (Corning). After incubation for 72 h at 37°C, 5% CO_2, cells were differentiated for 48 h with 1.7 mM $CaCl_2$ in epidermal keratinocyte base medium (CELLnTEC). PHKs from passage three were seeded into collagen coated 48-well plates in a concentration of 0.04 × 10^6 cells/ml and incubated 72 h in epidermal keratinocyte medium containing supplements (CELLnTEC). No further differentiation prior to experiments was performed for PHKs. Agonist and antagonists were applied to the PHKs and N/TERT-1 cells in fresh epidermal keratinocyte base medium (CELLnTEC) with 1.7 mM $CaCl_2$. Agonist and their respective antagonists were applied individually as well as in combination. Cells were stimulated at 37°C, 5% CO_2 for 17 h or 36 h. After incubation, plates were centrifuged at 200 × g for 5 min. Supernatant was transferred to polypropylene freezing plates (Thermo Scientific) and stored at -80°C until further analysis via ELISA or Bio-Plex® multiplex assay.

4.4 Enzyme-linked immunosorbent assay and multiplex cytokine analysis

Typical cytokines and chemokines released by keratinocytes during inflammation and wound healing were analyzed (38–40). For the detection of IL-8 and IL-1α in cell culture supernatant, ELISAs (R&D Systems) were performed according to the manufacturer's instruction. For the detection of further chemokines in cell culture supernatants, a customized panel for human chemokines was used (GM-CSF, CCL1, CXCL11, CXCL10, MCP-1, CCL22, CXCL9, MIP-1α, MIP-3α, CCL17) and analyzed

according to the manufacturer's instruction (BioRad, Bio-Plex Pro Human Chemokines Standard, Bio-Plex Pro Human Cytokine Screening Panel Standards). For cell culture samples, 50 µl of a 1:4 dilution was used for analysis. For samples originated from mice, customized panels for mice cytokines and chemokines (IL-1α, IL-1β, IL-10, CXCL10, CXCL11, M-CSF, MCP-1, MIP-1α, MIP-2) were used (BioRad, Bio-Plex Pro Mouse Cytokine 1 and 2 standards). Skin wash samples were used undiluted. All samples were measured with the Bio-Plex™ 200 System (BioRad) and analyzed via the Bio-Plex Manager™ Software (Version 6.2, Build 175 by BioRad).

4.5 Analysis of keratinocyte proliferation

For the proliferation assay, PHK were seeded at a concentration of 4 x 10^5 cells/ml in 100 µl basal medium with supplements (CELLnTEC) into 96-well microtiter flat bottom plates. After 24 h incubation at 37°C and 5% CO_2, 95% H_2O, cell supernatants were removed and PHK were stimulated either with FPR1, FPR2, or TLR2 ligands (fMLF, PSMα3, P2C) or inhibitors (WRW4, tBOC) alone or in combination at the indicated concentrations for further 24 h. Triton X100 (1%) was used as negative control and medium as proliferation control. Then WST-1 [2-(4-Iodophenyl)-3-(4-nitrophenyl)-5-(2,4-disulfophenyl)-2H-tetrazolium] Proliferation reagent (10 µl/well) (Merck, Germany) was added and incubated for further three hours at 37°C and 5% CO_2. WST-1 produces a highly water-soluble formazan upon metabolically active cells, allowing a direct colorimetric measurement of cell viability and proliferation. Then the microtiter plate was shaken at 300 rpm for 1 hour in a microplate reader (Clariostar, BMG Labtech Germany) and absorbance was measured according to manufacturer's instructions. Proliferation was calculated relative to the medium control.

4.6 Scratch assay and video microscopy

Glass bottom 12-well plates (Cellvis P12-1.5H-N) were coated with rat tail collagen I (Thermofisher, A1048301). Culture-inserts 2 well for self-insertion (80209, Ibidi) were glued onto the glass coverslips of each well. 2.8 x 10^5 N/TERT-1 cells resuspended in 70 µl of complete cell medium were seeded into each well of a culture-insert 2 well µ-Dish (35 mm, Ibidi, 80206). After incubation at 37°C and 5% CO_2 for 24 h, the cells were stained with Hoechst (1 µg/ml, INVITROGEN CORP, H3570) for 10 min at 37°C, then the culture insert was removed, and cells were washed twice with PBS. Each dish was filled with 2 ml Leibovitz L-15 medium with supplements (CELLnTEC, 11540556, Fisher). Depending on the condition, either FPR2 ligand PSMα3 (10 nM), or FPR2 inhibitor WRW4 (1 µM), or both, was added. Multi-channel time-lapse sequences were acquired of the phase contrast image of cells as well as fluorescence of the Hoechst-stained cell nuclei. Images were taken every 10 min for 12 h using an inverted Nikon Eclipse Ti2 with a Prime 95B camera (Teledyne Photometrics) using a 40X 0.60NA super plan fluor ADM ELWD air objective and the NIS-Elements (RRID : SCR_014329) software package. The microscope was surrounded by a box-type incubator (OKOlab) maintained at 37°C.

4.7 Image processing and quantitation of cell speed, scratch area, and cell proliferation rate

For each scratch segment imaged, the area of the scratch (area not covered by cells) was determined at each instance of time using ImageJ (version 1.53t 24, 2022) and in particular a plugin for image analysis of *in vitro* scratch wound assays (41). The Trackmate plugin (42) was used to track the nuclei of the cells using a LAP tracker, which also allowed to count nuclei split events for each given track. Using custom-written MATLAB (MathWorks) scripts, only cells present in the first-time frame were considered, and based on their tracks, we calculated the mean speed of those cells overtime. We also calculated the percentage of this cell sub-population that divided within the 12-h time frame to determine average cell proliferation rates. The codes with example data can be found at https://github.com/ebastoun/N/TERT_1_kinematics. All scripts and functions are written in MATLAB (MathWorks). Averaging across different independent experiments as well as subsequent statistical analysis was performed using the commercial software Prism (GraphPad).

4.8 Keratinocyte adhesion and invasion assay

For adhesion assays, PHK were seeded onto 24-well plates 0.4 µm, (Sarstedt) coated with 25 µg/ml collagen I (rat tail, Corning). When cells were 100% confluent, PHKs were differentiated with differentiation medium (1.7 mM $CaCl_2$ in CnT-BM.1 basal medium 1 (CELLnTEC) without supplements) for 24 h at 37°C and 5% CO_2. PHKs were treated with 1 µM WRW4 or DMSO and were incubated with *S. aureus* USA300 in differentiation medium (multiplicity of infection= 30 (MOI30); optical density (OD)= 0.5) for 1.5 hours at 37°C. After two washing steps with 1x PBS, keratinocytes were lysed with saponin (0,5% in PBS), and serial dilutions of the lysate were plated onto blood agar plates. After overnight incubation at 37°C, colony forming units (CFUs) were counted.

2 ml of N/TERT-1 cells with a concentration of 0.04 x 10^6 cells/ml were seeded into 6-well plates (Greiner bio-one) coated with 25 µg/ml collagen I (rat tail, Corning). When N/TERT-1 cells were confluent, they were differentiated for 48 h with 1.7 mM $CaCl_2$. On the day of infection, USA300 or *S. epidermidis* 1457 over-night culture (17 h) was diluted in TSB to OD_{600} 0.1 and incubated (37°C, 160 rpm) to regrow to OD_{600} 1. The bacteria were further diluted in keratinocyte basal medium with 1.7 mM $CaCl_2$ to a MOI of five. Keratinocytes were infected with USA300 either alone or in combination with 1 µM WRW4 or DMSO (medium) as control for 2 h (37°C, 5% CO_2). After 2 h, supernatant was removed, and cells were washed two times with PBS and lysed with 0.5% saponin.

Serial dilutions of the cell lysate as well as a bacterial control incubated without N/TERT-1 cells were plated on TSA plates using an IUL EDDY Jet 2 spiral plater. Plates were incubated over-night at 37°C and CFUs were counted using the IUL Flash & Go instrument.

4.9 FPR expression

For FPR surface expression analysis, 2 x 10^5 PHK or N/TERT-1 cells were incubated in a 96-well V-bottom plate either with the isotype control (mouse IgG1, Becton Dickinson), anti-FPR1 mouse anti-human FPR1 (BD Bioscience) or anti-FPR2, each 5 µl (mouse anti-human FPRL1, Alvedron Freiburg) for 40 min on ice in PBS, after two washing steps, each time using 250 µl PBS. Cells were stained with a second fluorescently labelled antibody (goat anti mouse IgG-PE, Abcam) for 25 min on ice in the dark. After two washing steps, cells were analyzed by flowcytometry (Fortessa X-20, Becton Dickinson) and FlowJo™ software.

4.10 Infection of human skin explants

Human skin explants were prepared from juvenile human foreskin after routine circumcision. Fat and vascular tissue were removed, and the skin was cut into small 1-cm^2 pieces. 30 min before infection, 1 µM WRW4 diluted in PBS or DMSO (1:45000) in PBS, was topically applied onto human skin explants by using 8-mm filter paper discs (Smart Practice). Human skin explants were then infected with 10^8 *S. aureus* USA300 for 3 h at 37°C. Using a biopsy punch, 8-mm skin punches from infected skin were prepared and washed twice with 1x PBS. Subsequently, human skin explants were cut into small pieces and scraped, and serial dilutions of the skin lysate were plated onto blood agar plates. After over-night incubation at 37°C, CFUs were counted. Experimental procedures for PHK and skin explants were approved by the local medical ethical committee (reference numbers 750/2018BO2, 054/2017BO2).

4.11 *In vivo* skin colonization model

Animal studies were performed with 6-8 week-old female C57BL/6J WT and $Fpr2^{-/-}$ mice. *S. aureus* USA300 was inoculated in TSB and grown for 17 h under aerobic conditions followed by two washing steps with PBS. The mouse skin was shaved before experiments under isoflurane anaesthesia. Tape-stripping was conducted as described bevor (7). Therefore, skin of mice was superficially disrupted by repeated stripping with an adhesive tape (7 times) before *S. aureus* application. To analyze *S. aureus* skin colonization, 15 µl of a bacterial suspension containing 10^8 *S. aureus* and 5 µl PBS or WRW4 (10 µM) was applied epicutaneously for 24 h on the shaved dorsal skin of mice using filter papers and Finn Chambers (Smart Practice, Barsbuttel, Germany) under isoflurane anaesthesia. After 24 h, the mice were euthanized, and 4 mm skin punches were used for analysis of *S. aureus* CFUs as previously described (6, 7). Washing of the skin punch (vortex for 10 s) in PBS yielded the "wash" fraction used for CFU and cytokine/chemokine Multiplex analysis described above. Experimental procedures involving mice were approved by the local authorities (Regierungspräsidium Tübingen, IMIT 3/18G).

4.12 Statistics

All statistical analyses were performed with GraphPad Prism 9.0 (GraphPad Software, La Jolla, USA). The amount of cytokine (Figures 1I, N, Figure 2E) or number of CFUs (Figures 4A, B, I; Supplementary Figure 3A) released by keratinocytes stimulated with fMLF, MMK1 or PSMα3 was normalized to 100% (baseline corrected) and the inhibition of cytokine release or CFUs by WRW4 related thereto. An unpaired two-tailed Student's t-test or Mann-Whitney Test (for the animal experiments) was performed to compare two data groups, while more than two data groups were analyzed by one-way ANOVA with Dunnett's multiple comparisons test if not otherwise noted.

Figures 4C, 4H were created with BioRender.com.

Data availability statement

The original contributions presented in the study are included in the article/Supplementary Material. Further inquiries can be directed to the corresponding author.

Ethics statement

The studies involving human participants were reviewed and approved by local medical ethical committee (reference numbers 750/2018BO2, 054/2017BO2). The patients/participants provided their written informed consent to participate in this study. The animal study was reviewed and approved by Regierungspräsidium Tübingen.

Author contributions

ML, MM and DK designed the experiments. ML, MM, JB, DK and JS performed the experiments. ML, AP, EB and DK edited the manuscript and interpreted the data. All authors contributed to the article and approved the submitted version.

Funding

This study was funded by grants from the German Research Foundation (TRR261 to AP project ID 398967434; TRR156 project ID 246807620 (DK, AP); individual project 234105777 to AP; project 426823561 to DK and DFG GZ : KR4395/3-1 to ML) and the German Center for Infection Research (DZIF) to AP and DK. AP and EB is supported by the Cluster of Excellence EXC 2124 'Controlling Microbes to Fight Infections' project ID 390838134.

Acknowledgments

We thank Cosima Hirt for technical support, Birgit Schittek for kindly providing primary human keratinocytes, Ji Ming Wang for kindly providing the Fpr2$^{-/-}$ mice, as well as Stefan Stevanović for synthesizing PSM peptides and Libera Lo Presti for critical reading/editing the manuscript.

Conflict of interest

The authors declare that the research was conducted in the absence of any commercial or financial relationships that could be construed as a potential conflict of interest.

Publisher's note

Supplementary material

The Supplementary Material for this article can be found online at: https://www.frontiersin.org/articles/10.3389/fimmu.2023.1188555/full#supplementary-material

SUPPLEMENTARY FIGURE 1
Activation of N/TERT-1 by *S. epidermidis* PSMα and PSMε induces IL-8 and IL-1α release from keratinocytes in a FPR2-dependent manner. IL-8 **(A)** or IL-1α release **(B)** of differentiated N/TERT-1 keratinocytes stimulated for 17 h with either PSMα (1000 nM) +/- WRW4 (1 μM) or PSMε (500 nM) +/- WRW4 (1 μM). Data represent cytokine release minus cytokine release by medium-treated cells. *P < 0.05; **, P < 0.01 ***, significant difference versus the indicated controls as calculated by unpaired Student's t-tests.

SUPPLEMENTARY FIGURE 2
Release of cytokines an chemokines by N/TERT-1. CXCL11, MCP-1, GM-CSF and MIP-1α release of differentiated N/TERT-1 keratinocytes stimulated for 17 h with either P2C (100 ng/ml), fMLF (100 nM) or PSMα3 (100 nM). Release of CCL22, CXCL9 and CCL17 were below the detection level. Data represent means ± SEMs from at least four independent experiments.

SUPPLEMENTARY FIGURE 3
Inhibition of FPR2 does not affect colonization by *S. epidermidis*. CFUs of *S. epidermidis* 1457 recovered from infected N/TERT-1 treated +/- WRW4 (1 μM). Data represent mean and SEM of five independent experiments of baseline-corrected data. Ns = not significantly different versus the indicated control as calculated by paired Student's t-tests.

SUPPLEMENTARY MOVIE 1
Influence of FPR ligands on keratinocyte wound closure. Top row: phase contrast video of N/TERT-1 cells over 12 h period (frame rate: 10 min), treated with vehicle control (left), or 10 nM PSMα3 (middle), or 10 nM PSMα3 plus 1 μM WRW4 (right) as they migrate to close a wound. Scale bar: 500 μm. Bottom row: video of fluorescently labelled N/TERT-1 cell nuclei stained with a DNA dye (Hoechst), corresponding to the same cells as in the top row. Superimposed are the displacement tracks of all individual cells color-coded for the total distance travelled by each nucleus (blue = 0 μm, red = 500 μm) within the span of the video (12 h).

References

1. Bitschar K, Wolz C, Krismer B, Peschel A, Schittek B. Keratinocytes as sensors and central players in the immune defense against staphylococcus aureus in the skin. *J Dermatol Sci* (2017) 87(3):215–20. doi: 10.1016/j.jdermsci.2017.06.003

2. Byrd AL, Belkaid Y, Segre JA. The human skin microbiome. *Nat Rev Microbiol* (2018) 16(3):143–55. doi: 10.1038/nrmicro.2017.157

3. Cheung GYC, Bae JS, Otto M. Pathogenicity and virulence of staphylococcus aureus. *Virulence* (2021) 12(1):547–69. doi: 10.1080/21505594.2021.1878688

4. Golan Y. Current treatment options for acute skin and skin-structure infections. *Clin Infect Dis* (2019) 68(Suppl 3):S206–S12. doi: 10.1093/cid/ciz004

5. Chung EJ, Luo CH, Thio CL, Chang YJ. Immunomodulatory role of staphylococcus aureus in atopic dermatitis. *Pathogens* (2022) 11(4):1–10. doi: 10.3390/pathogens11040422

6. Bitschar K, Staudenmaier L, Klink L, Focken J, Sauer B, Fehrenbacher B, et al. Staphylococcus aureus skin colonization is enhanced by the interaction of neutrophil extracellular traps with keratinocytes. *J Invest Dermatol* (2020) 140(5):1054–65 e4. doi: 10.1016/j.jid.2019.10.017

7. Burian M, Bitschar K, Dylus B, Peschel A, Schittek B. The protective effect of microbiota on *S. aureus* skin colonization depends on the integrity of the epithelial barrier. *J Invest Dermatol* (2017) 137(4):976–9. doi: 10.1016/j.jid.2016.11.024

8. Weiss E, Kretschmer D. Formyl-peptide receptors in infection, inflammation, and cancer. *Trends Immunol* (2018) 39(10):815–29. doi: 10.1016/j.it.2018.08.005

9. Rautenberg M, Joo HS, Otto M, Peschel A. Neutrophil responses to staphylococcal pathogens and commensals via the formyl peptide receptor 2 relates to phenol-soluble modulin release and virulence. *FASEB J* (2011) 25(4):1254–63. doi: 10.1096/fj.10-175208

10. Weiss E, Schlatterer K, Beck C, Peschel A, Kretschmer D. Formyl-peptide receptor activation enhances phagocytosis of community-acquired methicillin-resistant staphylococcus aureus. *J Infect Dis* (2019) 221(4):668–678. doi: 10.1093/infdis/jiz498

11. Yu N, Zhang S, Lu J, Li Y, Yi X, Tang L, et al. An acute phase protein, stimulates proliferative and proinflammatory responses of keratinocytes. *Cell Prolif* (2017) 50 (3):1–10. doi: 10.1111/cpr.12320

12. Carretero M, Escamez MJ, Garcia M, Duarte B, Holguin A, Retamosa L, et al. *In vitro* and *in vivo* wound healing-promoting activities of human cathelicidin LL-37. *J Invest Dermatol* (2008) 128(1):223–36. doi: 10.1038/sj.jid.5701043

13. Kwon YW, Heo SC, Jang IH, Jeong GO, Yoon JW, Mun JH, et al. Stimulation of cutaneous wound healing by an FPR2-specific peptide agonist WKYMVm. *Wound Repair Regen* (2015) 23(4):575–82. doi: 10.1111/wrr.12315

14. Wu BC, Skovbakke SL, Masoudi H, Hancock REW, Franzyk H. *In vivo* anti-inflammatory activity of lipidated peptidomimetics Pam-(Lys-betaNspe)6-NH2 and lau-(Lys-betaNspe)6-NH2 against PMA-induced acute inflammation. *Front Immunol* (2020) 11:2102. doi: 10.3389/fimmu.2020.02102

15. Carlson RM, Vavricka SR, Eloranta JJ, Musch MW, Arvans DL, Kles KA, et al. fMLP induces Hsp27 expression, attenuates NF-kappaB activation, and confers intestinal epithelial cell protection. *Am J Physiol Gastrointest Liver Physiol* (2007) 292(4):G1070–8. doi: 10.1152/ajpgi.00417.2006

16. Leung DY. Infection in atopic dermatitis. *Curr Opin Pediatr* (2003) 15(4):399–404. doi: 10.1097/00008480-200308000-00008

17. Hung SH, Lin YT, Chu CY, Lee CC, Liang TC, Yang YH, et al. Staphylococcus colonization in atopic dermatitis treated with fluticasone or tacrolimus with or without antibiotics. *Ann Allergy Asthma Immunol* (2007) 98(1):51–6. doi: 10.1016/S1081-1206(10)60859-9

18. Breuer K, HA S, Kapp A, Werfel T. Staphylococcus aureus: colonizing features and influence of an antibacterial treatment in adults with atopic dermatitis. *Br J Dermatol* (2002) 147(1):55–61. doi: 10.1046/j.1365-2133.2002.04872.x

19. Wang R, Braughton KR, Kretschmer D, Bach TH, Queck SY, Li M, et al. Identification of novel cytolytic peptides as key virulence determinants for community-associated MRSA. *Nat Med* (2007) 13(12):1510–4. doi: 10.1038/nm1656

20. Hanzelmann D, Joo HS, Franz-Wachtel M, Hertlein T, Stevanovic S, Macek B, et al. Toll-like receptor 2 activation depends on lipopeptide shedding by bacterial surfactants. *Nat Commun* (2016) 7:12304. doi: 10.1038/ncomms12304

21. Staudenmaier L, Focken J, Schlatterer K, Kretschmer D, Schittek B. Bacterial membrane vesicles shape staphylococcus aureus skin colonization and induction of innate immune responses. *Exp Dermatol* (2022) 31(3):349–61. doi: 10.1111/exd.14478

22. Koch M, Kockmann T, Rodriguez E, Wehkamp U, Hiebert P, Ben-Yehuda Greenwald M, et al. Quantitative proteomics identifies reduced NRF2 activity and mitochondrial dysfunction in atopic dermatitis. *J Invest Dermatol* (2022) 143:220–231. doi: 10.1016/j.jid.2022.08.048

23. Goleva E, Berdyshev E, Leung DY. Epithelial barrier repair and prevention of allergy. *J Clin Invest* (2019) 129(4):1463–74. doi: 10.1172/JCI124608

24. Krepel SA, Wang JM. Chemotactic ligands that activate G-Protein-Coupled formylpeptide receptors. *Int J Mol Sci* (2019) 20(14):1–18. doi: 10.3390/ijms20143426

25. Wang G, Sweren E, Liu H, Wier E, Alphonse MP, Chen R, et al. Bacteria induce skin regeneration via IL-1beta signaling. *Cell Host Microbe* (2021) 29(5):777–91 e6. doi: 10.1016/j.chom.2021.03.003

26. Nguyen MT, Kraft B, Yu W, Demircioglu DD, Hertlein T, Burian M, et al. The nuSaalpha specific lipoprotein like cluster (lpl) of *S. aureus* USA300 contributes to immune stimulation and invasion in human cells. *PloS Pathog* (2015) 11(6):e1004984. doi: 10.1371/journal.ppat.1004984

27. Nakamura Y, Takahashi H, Takaya A, Inoue Y, Katayama Y, Kusuya Y, et al. Staphylococcus agr virulence is critical for epidermal colonization and associates with atopic dermatitis development. *Sci Transl Med* (2020) 12(551):1–11. doi: 10.1126/scitranslmed.aay4068

28. Nguyen TH, Cheung GYC, Rigby KM, Kamenyeva O, Kabat J, Sturdevant DE, et al. Rapid pathogen-specific recruitment of immune effector cells in the skin by secreted toxins. *Nat Microbiol* (2022) 7(1):62–72. doi: 10.1038/s41564-021-01012-9

29. Skovbakke SL, Winther M, Gabl M, Holdfeldt A, Linden S, Wang JM, et al. The peptidomimetic lau-(Lys-betaNSpe)6-NH2 antagonizes formyl peptide receptor 2 expressed in mouse neutrophils. *Biochem Pharmacol* (2016) 119:56–65. doi: 10.1016/j.bcp.2016.09.004

30. de Haas CJ, Veldkamp KE, Peschel A, Weerkamp F, Van Wamel WJ, Heezius EC, et al. Chemotaxis inhibitory protein of staphylococcus aureus, a bacterial antiinflammatory agent. *J Exp Med* (2004) 199(5):687–95. doi: 10.1084/jem.20031636

31. Prat C, Bestebroer J, de Haas CJ, van Strijp JA, van Kessel KP. A new staphylococcal anti-inflammatory protein that antagonizes the formyl peptide receptor-like 1. *J Immunol* (2006) 177(11):8017–26. doi: 10.4049/jimmunol.177.11.8017

32. Prat C, Haas PJ, Bestebroer J, de Haas CJ, van Strijp JA, van Kessel KP. A homolog of formyl peptide receptor-like 1 (FPRL1) inhibitor from staphylococcus aureus (FPRL1 inhibitory protein) that inhibits FPRL1 and FPR. *J Immunol* (2009) 183 (10):6569–78. doi: 10.4049/jimmunol.0801523

33. Tsukuba T, Yanagawa M, Okamoto K, Okamoto Y, Yasuda Y, Nakayama KI, et al. Impaired chemotaxis and cell adhesion due to decrease in several cell-surface receptors in cathepsin e-deficient macrophages. *J Biochem* (2009) 145(5):565–73. doi: 10.1093/jb/mvp016

34. Chen B, Zheng Y, Liang Y. Analysis of potential genes and pathways involved in the pathogenesis of acne by bioinformatics. *BioMed Res Int* (2019) 2019:3739086. doi: 10.1155/2019/3739086

35. Cheung GY, Joo HS, Chatterjee SS, Otto M. Phenol-soluble modulins–critical determinants of staphylococcal virulence. *FEMS Microbiol Rev* (2014) 38(4):698–719. doi: 10.1111/1574-6976.12057

36. Bitschar K, Sauer B, Focken J, Dehmer H, Moos S, Konnerth M, et al. Lugdunin amplifies innate immune responses in the skin in synergy with host- and microbiota-derived factors. *Nat Commun* (2019) 10(1):2730. doi: 10.1038/s41467-019-10646-7

37. Dickson MA, Hahn WC, Ino Y, Ronfard V, Wu JY, Weinberg RA, et al. Human keratinocytes that express hTERT and also bypass a p16(INK4a)-enforced mechanism that limits life span become immortal yet retain normal growth and differentiation characteristics. *Mol Cell Biol* (2000) 20(4):1436–47. doi: 10.1128/MCB.20.4.1436-1447.2000

38. Behm B, Babilas P, Landthaler M, Schreml S. Cytokines, chemokines and growth factors in wound healing. *J Eur Acad Dermatol Venereol* (2012) 26(7):812–20. doi: 10.1111/j.1468-3083.2011.04415.x

39. Grone A. Keratinocytes and cytokines. *Vet Immunol Immunopathol* (2002) 88 (1-2):1–12. doi: 10.1016/S0165-2427(02)00136-8

40. Uchi H, Terao H, Koga T, Furue M. Cytokines and chemokines in the epidermis. *J Dermatol Sci* (2000) 24 Suppl 1:S29–38. doi: 10.1016/S0923-1811(00)00138-9

41. Suarez-Arnedo A, Torres Figueroa F, Clavijo C, Arbelaez P, Cruz JC, Munoz-Camargo C. An image J plugin for the high throughput image analysis of *in vitro* scratch wound healing assays. *PloS One* (2020) 15(7):e0232565. doi: 10.1371/journal.pone.0232565

42. Ershov D, Phan M-S, Pylvänäinen JW, Rigaud SU, Le Blanc L, Charles-Orszag A, et al. TrackMate 7: integrating state-of-the-art segmentation algorithms into tracking pipelines. *Nat Methods* (2022) 19(7):829–32. doi: 10.1038/s41592-022-01507-1

Section 2

ERK activation waves coordinate the mechanical cell competition that leads to collective onslaught of bacterially-infected cells

Lara Hundsdorfer,[1,2] Marie Muenkel,[1,2] Raul Aparicio-Yuste,[3] Julio Cesar Sanchez-Rendon,[1,2] Maria Jose Gomez-Benito,[3] Aylin Balmes,[4] Tilman E. Schäffer,[4] Ana Velic,[5] Yi-Ting Yeh,[6] Iordania Constantinou,[7,8] Kathryn Wright,[9] Gizem Özbaykal Güler,[9] Dominik Brokatzky,[9] Boris Maček,[5] Serge Mostowy,[9] and Effie E. Bastounis[1,2,10,*]

[1]Interfaculty Institute of Microbiology and Infection Medicine, University of Tübingen, 72076 Tübingen, Baden-Württemberg, Germany

[2]Cluster of Excellence EXC 2124 Controlling Microbes to Fight Infections, University of Tübingen, 72076 Tübingen, Baden-Württemberg, Germany

[3]Engineering Research Institute of Aragon (I3A), Department of Mechanical Engineering, University of Zaragoza, 50018 Zaragoza, Aragon, Spain

[4]Institute of Applied Physics, University of Tübingen, 72076 Tübingen, Baden-Württemberg, Germany

[5]Proteome Center Tübingen, University of Tübingen, 72076 Tübingen, Baden-Württemberg, Germany

[6]Department of Mechanical Engineering, University of Washington, Seattle, WA 98195, USA

[7]Institute of Microtechnology, Technische Universität Brauschweig, 38106 Braunschweig, Lower Saxony, Germany

[8]Center of Pharmaceutical Engineering (PVZ), Technische Universität Braunschweig, 38106 Braunschweig, Lower Saxony, Germany

[9]Department of Infection Biology, London School of Hygiene and Tropical Medicine, London WC1E 7HT, UK

Published 2025 in Cell Reports, 44, 1, 115193.

Cell Reports

Article

ERK activation waves coordinate mechanical cell competition leading to collective elimination via extrusion of bacterially infected cells

Graphical abstract

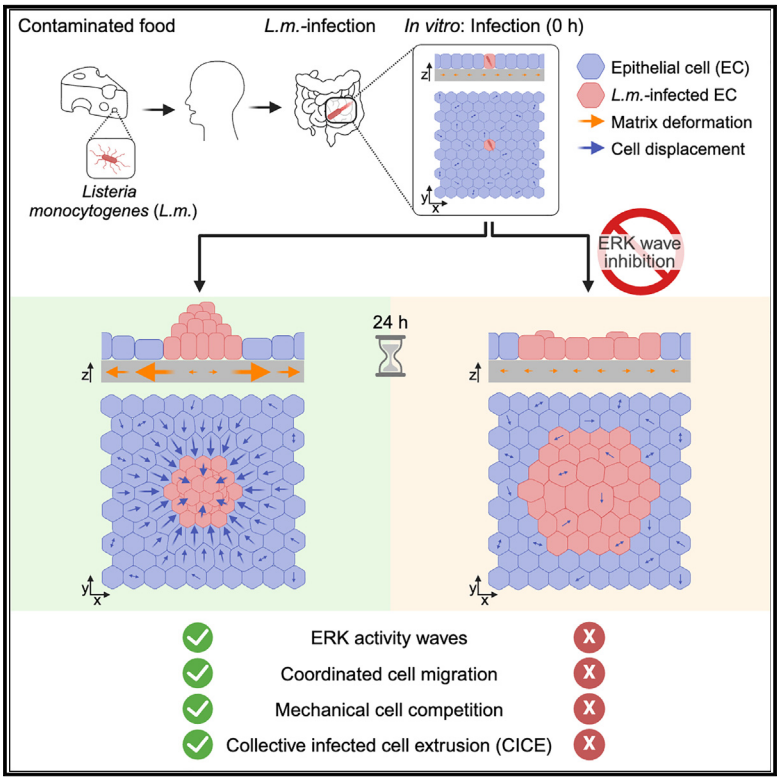

Highlights

- Increased frequency ERK waves travel between epithelial cells during infection
- ERK waves enable surrounder cells to polarize and reinforce monolayer stresses
- Epithelial cells' altered mechanics drive collective infected cell extrusion (CICE)
- In the absence of ERK waves, CICE is diminished and bacterial spread is enhanced

Authors

Lara Hundsdorfer, Marie Muenkel, Raul Aparicio-Yuste, ..., Boris Maček, Serge Mostowy, Effie E. Bastounis

Correspondence

effie.bastounis@uni-tuebingen.de

In brief

Collective infected cell extrusion (CICE) enables uninfected epithelial cells to eliminate adjacent infected cells and limit infection spread. Hundsdorfer et al. show that during infection with the intracellular bacterium *Listeria monocytogenes*, CICE depends on the propagation of ERK waves across the epithelium monolayer, triggering key changes in host cell biomechanics.

Hundsdorfer et al., 2025, Cell Reports *44*, 115193
January 28, 2025
https://doi.org/10.1016/j.celrep.2024.115193

CellPress

Cell Reports

CellPress
OPEN ACCESS

Article

ERK activation waves coordinate mechanical cell competition leading to collective elimination via extrusion of bacterially infected cells

Lara Hundsdorfer,[1,2] Marie Muenkel,[1,2] Raul Aparicio-Yuste,[3] Julio Cesar Sanchez-Rendon,[1,2] Maria Jose Gomez-Benito,[3] Aylin Balmes,[4] Tilman E. Schäffer,[4] Ana Velic,[5] Yi-Ting Yeh,[6] Iordania Constantinou,[7,8] Kathryn Wright,[9] Gizem Özbaykal Güler,[9] Dominik Brokatzky,[9] Boris Maček,[5] Serge Mostowy,[9] and Effie E. Bastounis[1,2,10,*]

[1]Interfaculty Institute of Microbiology and Infection Medicine, University of Tübingen, 72076 Tübingen, Baden-Württemberg, Germany
[2]Cluster of Excellence EXC 2124 Controlling Microbes to Fight Infections, University of Tübingen, 72076 Tübingen, Baden-Württemberg, Germany
[3]Engineering Research Institute of Aragon (I3A), Department of Mechanical Engineering, University of Zaragoza, 50018 Zaragoza, Aragon, Spain
[4]Institute of Applied Physics, University of Tübingen, 72076 Tübingen, Baden-Württemberg, Germany
[5]Proteome Center Tübingen, University of Tübingen, 72076 Tübingen, Baden-Württemberg, Germany
[6]Department of Mechanical Engineering, University of Washington, Seattle, WA 98195, USA
[7]Institute of Microtechnology, Technische Universität Brauschweig, 38106 Braunschweig, Lower Saxony, Germany
[8]Center of Pharmaceutical Engineering (PVZ), Technische Universität Braunschweig, 38106 Braunschweig, Lower Saxony, Germany
[9]Department of Infection Biology, London School of Hygiene and Tropical Medicine, London WC1E 7HT, UK
[10]Lead contact
*Correspondence: effie.bastounis@uni-tuebingen.de
https://doi.org/10.1016/j.celrep.2024.115193

SUMMARY

Epithelial cells respond to infection with the intracellular bacterial pathogen *Listeria monocytogenes* by altering their mechanics to promote collective infected cell extrusion (CICE) and limit infection spread across cell monolayers. However, the underlying biochemical pathways remain elusive. Here, using *in vitro* (epithelial monolayers) and *in vivo* (zebrafish larvae) models of infection with *L. monocytogenes* or *Shigella flexneri*, we explored the role of extracellular-signal-regulated kinase (ERK) activity waves in coordinating the mechanical battle between infected and surrounder uninfected cells that leads to CICE. We discovered that when ERK waves are suppressed, cells fail to exhibit alterations in cell shape and kinematics associated with CICE and behave more like quiescent uninfected monolayers. In particular, uninfected cells surrounding infection foci are unable to polarize, reinforce their monolayer stresses, and promote CICE. Our findings reveal that crosstalk between ERK waves and cell mechanics is key to collective elimination of large domains of infected cells.

INTRODUCTION

The food-borne facultative intracellular bacterial pathogen *Listeria monocytogenes* (*L.m.*), like other bacterial and viral pathogens, can non-lytically spread from cell to cell by triggering rapid assembly of host cell actin filaments at one bacterial pole, forming "actin comet tails."[1,2] Similar but distinct strategies are employed by other bacterial pathogens like tick-borne *Rickettsia parkeri* (*R.p.*) and enteropathogenic *Shigella flexneri* (*S.f.*).[3,4] After initial invasion of a single epithelial cell, pathogens employing actin-based motility replicate and spread to neighboring cells, leading to formation of large domains of infected cells (infection foci) comprising hundreds of cells.[5] In response, host cells alter their biomechanics to counteract bacterial spread.[4,6,7] For example, when epithelial cells in monolayer are infected with low doses of *L.m.*, a mechanical battle takes place, whereby stiffer and more contractile uninfected surrounder cells (surrounders) collectively move toward domains of infected cells, squeezing them and promoting collective infected cell extrusion (CICE), ultimately leading to infected cell death.[8]

CICE depends on alterations in cell contractility, cell stiffness, and intercellular adhesions between infected and surrounder uninfected cells, but little is known about the interplay between cell mechanics and biochemical signaling during this process.[8] A role for NF-κB signaling is supported by evidence that CICE occurs only in epithelia infected with a *Rickettsia* mutant strain that fails to inactivate NF-κB.[8,9] Nevertheless, NF-κB inhibition only partially reduces CICE (25%), suggesting that additional pathways are involved.[8] This hypothesis is further supported by the upregulation of markers associated with epithelial-to-mesenchymal transition (EMT) in both infected and surrounder cells and biochemical and biomechanical changes that are reminiscent

of EMT.[8] Besides NF-κB, also the extracellular-signal-regulated kinase (ERK) plays a role in this process.[10,11] However, whether ERK is involved in the mechanical cell competition driving CICE remains unclear. Seemingly poorly understood is how NF-κB and ERK signaling pathways spatiotemporally interact with host cell biomechanics to regulate CICE and limit infection spread.

In recent years, the ERK pathway has drawn attention and has been characterized as a fast and modular mechanosensitive pathway involved in many processes ranging from wound healing to development and innate immune responses.[12–15] ERK signaling can oscillate autonomously within single cells, modulating their behavior based on internal cues.[16] Additionally, ERK signals can propagate as waves across neighboring cells, coordinating tissue-wide responses.[17,18] This dual mode of ERK activation—both within individual cells and across cell communities—provides a highly adaptable mechanism for cell organization and long-range intercellular communication at orders of magnitude faster than diffusion alone would allow.[18–20] The frequency and amplitude of ERK waves may vary depending on the external stimulus, leading to transient or sustained ERK activation, which in turn results in different cell fates (e.g., differentiation versus proliferation).[21,22] Cytokines and pro-inflammatory ligands also modulate frequency and amplitude of ERK waves, suggesting that changes in ERK dynamics could occur during infection.[23,24] However, despite extensive research in other biological contexts,[18,25,26] the role of ERK waves in facilitating rapid information transmission between epithelial cell monolayers during infection has not been investigated to date.

Based on this, and evidence implicating ERK waves in collective extrusion of UV-treated cells[27] and apoptotic cells,[28] we speculated that ERK waves could regulate fast collective migration of surrounder cells toward infection foci (the driving force behind CICE). Monitoring ERK activity dynamics across epithelial monolayers infected with *L.m.* or *S.f.*, we found that ERK activity waves coordinate alterations in host cell shapes, kinematics, and dynamics that occur during infection and are key in driving CICE. Importantly, ERK is key to CICE also in *S.f.*-infected zebrafish larvae. Our findings highlight ERK waves as a spatial alarm signal propagating across monolayers to modulate cell biomechanics, thus enabling fast coordinated action against the threat of infection spread.

RESULTS

ERK is activated by EGFR signaling during epithelial cell infection with *L.m.* and is important for CICE

To determine whether ERK signaling is altered during *L.m.* infection of epithelial cells, we infected Madin-Darby Canine Kidney (MDCK) epithelial cells with *L.m.* for 24 h until CICE occurrence.[8] Western blot analysis revealed that the levels of the two ERK isoforms ERK1 and ERK2 (ERK1/2) remained constant during infection, while phosphorylated ERK1/2 (*p*-ERK1/2), a proxy for ERK activation, increased in infected compared to uninfected cells (Figures 1A and 1B). Consistently, the levels of auto-phosphorylated EGFR and phosphorylated MEK1/2 were significantly higher in infected than in uninfected cells (Figures 1A and 1B). These findings demonstrate that *L.m.* infection activates EGFR and its downstream signaling kinases, MEK1/2 and ERK1/2.

Next, to determine whether ERK is involved in CICE, we treated infected MDCK cells with a MEK inhibitor (PD0325901) to inhibit ERK activation (Figure S1A). Under these conditions, CICE was suppressed, with mound volume decreasing by 60% compared to control samples (Figures 1C and 1D), and infected cells and their nuclei appeared no longer squeezed but regularly organized (Figures 1C and S1B). Treatment with an EGFR inhibitor (PD153035) similarly reduced mound volume by 70% (Figures S1C and S1D). Consistent with our previous findings, reduced mound volume was associated with an increase in infection foci area and bacterial load (Figures 1E and 1F; Video S1).

To explore whether ERK inhibition affects pathways related to the cytoskeleton, contractility, and cell adhesion—essential for CICE—we performed phosphoproteomics followed by Gene Ontology (GO) analysis.[29] While uninfected samples treated with MEK inhibitor displayed only a few differentially phosphorylated proteins compared to untreated/uninfected samples (Figures 1H, S1E and S1F), in infected samples, MEK inhibition led to a significant increase in differentially phosphorylated proteins (Figure 1H). Notably, multiple GO terms related to cell contractility and cell-cell or cell-ECM adhesion were differentially regulated in infected samples, at both 8 and 24 hours post-infection (hpi) (see magenta-labeled in Figure 1I). These findings suggested a link between ERK activation and cell biomechanics (e.g., contractility, motility) during infection, which we further explored.

ERK inhibition prevents the polarization and collective alignment of uninfected surrounder cells and the squeezing of infected cells

Infected cells and their uninfected surrounders undergo distinct changes in shape that are crucial for CICE.[8] To determine whether ERK inhibition affects cell shape, we first analyzed shape descriptors in uninfected monolayers. Both ERK-inhibited and control MDCK cells formed regularly packed polygons with random orientation, although in ERK-inhibited samples radial alignment was even lower than in controls (Figure S2A). However, there were no significant differences in mean cell area, aspect ratio, radial alignment, or shape factor q (cell perimeter to square root of area)[30] between the two conditions (Figure S2B), ruling out ERK may impact cell shape.

By contrast, ERK inhibition significantly altered the shape of cells in *L.m.*-infected monolayers: infected cells appeared enlarged rather than squeezed, while surrounder cells failed to polarize and looked like cells in non-infected wells (Figures 2A–2C). Additionally, surrounder cells failed to align their long axes with neighboring cells, lacking the nematic order observed in control infected monolayers (Figures 2D and 2E). Also, no increase in shape factor q, a measure of tissue fluidity, was observed in uninfected surrounders upon MEK inhibition (Figures 2F and S2B). This suggests that ERK inhibition disrupts polarization, nematic ordering, and tissue fluidity necessary for surrounder cells to collectively take action and squeeze infected cells.

ERK inhibition abrogates increases in host cell speed and migration coordination during *L.m.* infection

To determine whether ERK inhibition affects cell motility during infection, we tracked MDCK cells infected with a low dose of

CellPress
OPEN ACCESS

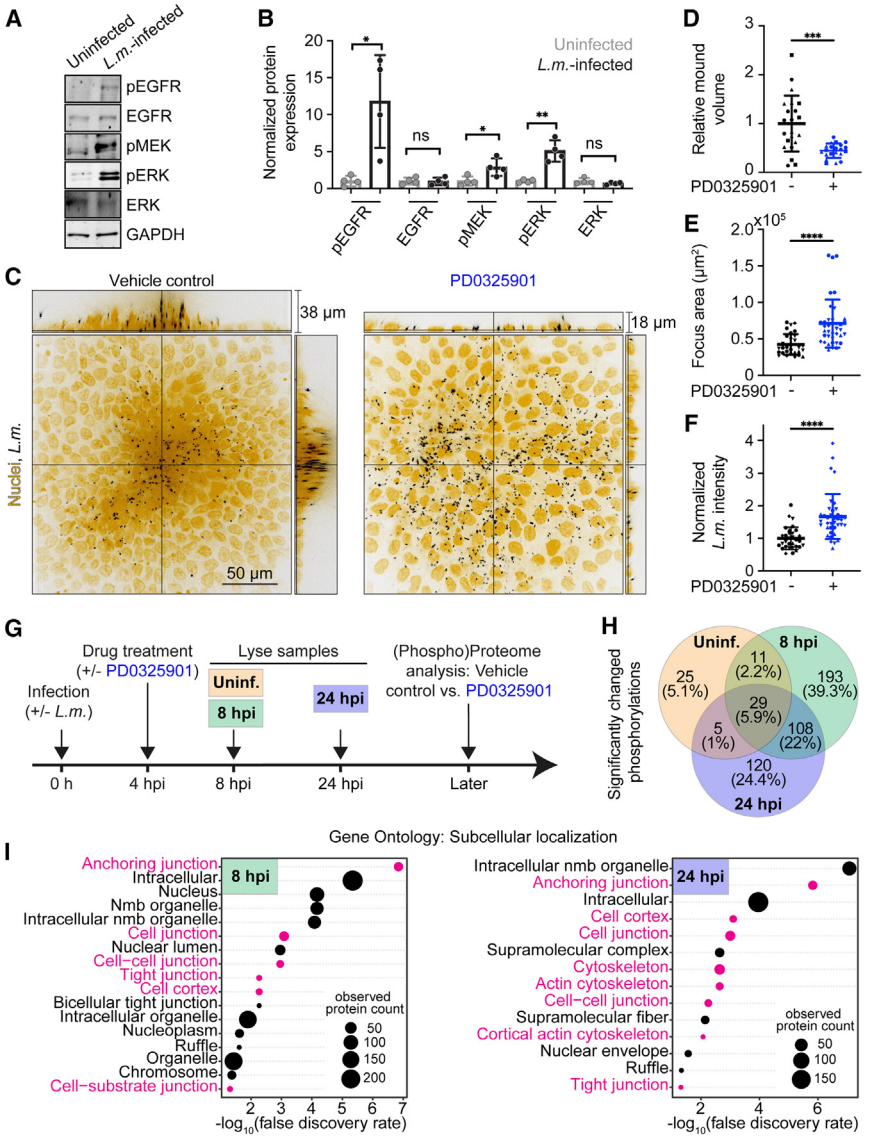

Figure 1. ERK activation increases in host cells during *L.m.* infection and is required for mound formation

(A) Representative cropped western blots from lysates of uninfected and *L.m.*-infected MDCK cell monolayers at 24 hpi. Total or phosphorylated levels (p) of the indicated proteins were probed for pEGFR, EGFR, pMEK, pERK, ERK, and GAPDH.

(B) Bar plots of relative expression of proteins probed in (A). Measurements normalized to GAPDH expression of each condition and expressed as fold change relative to mean uninfected cells' expression level. Lines: mean ± SD, unpaired t test: $*p < 0.05$, $**p < 0.01$.

(C) Orthogonal views of *L.m.*-infected MDCK cells at 24 hpi treated with vehicle control (left) or 50 µM PD0325901 (right) at 4 hpi. Host nuclei: yellow; *L.m.*: black.

(D–F) Quantification of *L.m.* infection focus properties of the conditions shown in (C): (D) relative mound volume, (E) focus area (µm^2), (F) relative *L.m.* fluorescence intensity. D, F normalized to mean of control cells. Lines: mean ± SD, WRST: $***p < 0.001$, $****p < 0.0001$; different shapes indicate data from $N = 3$ independent experiments.

(G) Sketch of phosphoproteomics experimental setup. Uninfected samples (orange) or *L.m.*-infected samples at 8 (green) and 24 (blue) hpi treated with vehicle control or PD0325901 are compared.

(H) Venn diagram displaying the number and percentage of significantly changed protein phosphorylation levels comparing control to PD0325901-treated cell samples as explained in (G).

(I) Functional enrichment analysis of differentially phosphorylated proteins of samples shown in (G), displaying in bubble plots the GO cellular components significantly altered between control versus PD0325901-treated samples. Cell-mechanics-related GO components are in magenta. Left: *L.m.*-infected for 8 h, right: *L.m.*-infected for 24 h. See also Figure S1, Video S1, and Table S1.

L.m., treated or not with MEK inhibitor. We started live-cell imaging at around 6 hpi and centered the imaged field of view around a given infection focus to also monitor its growth (Figures 3A, 3B, S3A, and S3B; Video S2). To ensure imaging of intracellular bacteria only, we used an *L.m.* strain expressing mtagRFP under the ActA promoter control,[31] which is active when *L.m.* enters the host cell cytosol, and maintained the cells in gentamicin-containing medium to eliminate extracellular bacteria and prevent further host cell invasion events.[32] We also imaged control uninfected cells under same conditions. Using particle image velocimetry (PIV) on the cell nuclei images, we calculated cell displacements over time (Figures 3A, 3B, S3C, and S3D; Video S2). The average migration speed of uninfected monolayers was 4 µm/h, consistent with previous studies and reflecting the quiescent state of these confluent cells (Figures 3C and S3E). ERK inhibition did not significantly affect uninfected cells' migration speed, although this was consistently lower than in controls. Thus, ERK has only a modest impact on cell movement in dense, confluent cell monolayers, possibly related to the mild reduction in collective cell alignment (Figures S2A and S3C–S3F).

In contrast, *L.m.*-infected cell monolayers showed a quasi-linear increase in migration speed, starting 14 hpi and peaking at 25 hpi (Figures 3A and 3C). The correlation length of movement, a measure of how far the motion of individual cells remains correlated to each other, also increased, highlighting the collective response of surrounder cells migrating toward the infection focus (Figures 3D and S3F). Accordingly, displacement vector maps showed that surrounder cells collectively moved toward the infection focus (Figure 3A), as highlighted in the rose plots (Figures 3E and 3F). However, ERK-inhibited infected monolayers exhibited no increase in migration speed and correlation length over time post-infection (Figures 3B–3D, and 3G), indicating that upon ERK inhibition, cells in infected monolayers behave like those in non-infected samples.

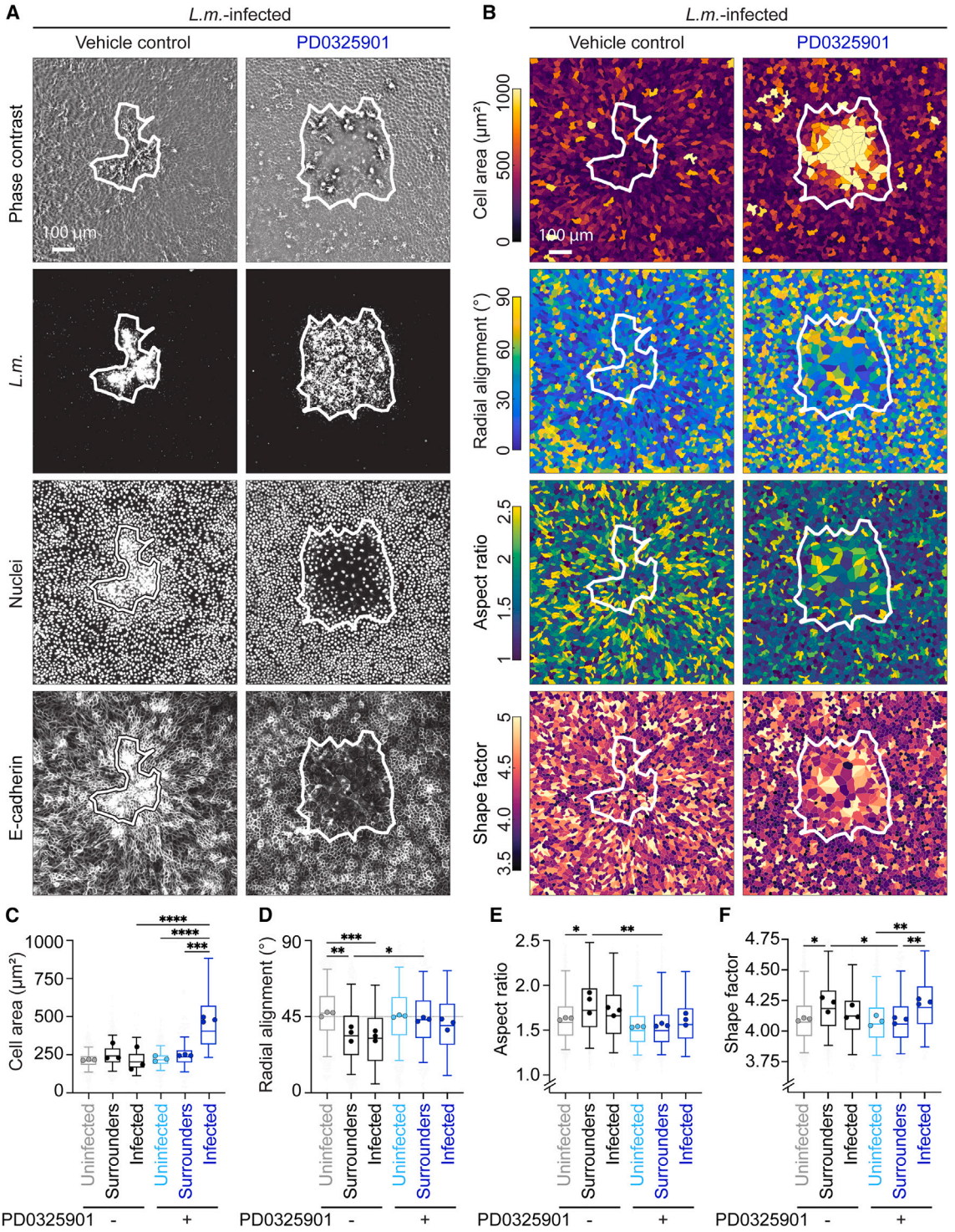

Figure 2. ERK inhibition abrogates collective alignment of surrounder cells and alters the shape of infected cells

(A) *L.m.*-infected MDCK cells at 24 hpi, treated at 4 hpi with vehicle control (1st column) or 50 µM PD0325901 (2nd column). Rows: phase contrast, *L.m.*, cell nuclei, E-cadherin fluorescence. White outline: infection focus contour.

(B) Same images as in (A) with cells in rows color-coded for: cell area (µm²), radial alignment (°) of major cell axis, cell aspect ratio, shape factor (see STAR Methods).

(legend continued on next page)

Infection induces dynamic ERK activation waves that travel between neighboring cells and are essential for CICE

The lack of coordinated cell migration in *L.m.*-infected, ERK-inhibited samples suggested that ERK activation waves might drive these behavioral changes. To test this, we treated cells with phorbol-12-myristate-13-acetate (PMA), which acutely and constitutively activates ERK,[20,33] thus abrogating ERK activation waves. Under these conditions, the volume of infection mounds was significantly diminished (Figures S4A and S4B), and cells showed random migration, similar to ERK-inhibited cells, lacking the directional movement seen in untreated cells (Figure S4C). Conversely, treatment with epidermal growth factor (EGF), which was previously shown to increase single-cell ERK activity pulses and wave frequency occurrence,[15,23] led to faster formation of mounds and thus significantly smaller infection foci than untreated infected samples, although the precise factors driving accelerated CICE were not investigated further (Figures S4B and S4D). Collectively, these findings suggest that ERK waves, and not constitutive ERK activity, are crucial for the directional migration of surrounder cells toward the infection focus and subsequent CICE.

To examine the spatiotemporal modulation of ERK activation during infection, we performed Förster resonance energy transfer (FRET) imaging on EKARE-NLS-expressing MDCK cells and measured the increase in the FRET/CFP ratio in the cells' nuclei as proxy for ERK activation.[15,34] In absence of infection, the frequency of ERK waves propagating from one cell to neighboring cells in densely packed MDCK cell monolayers was low. This is consistent with previous findings suggesting that when monolayer cell density is increased, basal ERK activity and frequency of waves are diminished (Figures S4E and S4F; Video S3).[16] Moreover, when cells were treated with MEK inhibitor, ERK activity levels were decreased, and waves were completely abolished (Video S3). In contrast, when cells were infected with *L.m.*, we observed a significant increase in the frequency of ERK waves propagating through the monolayer, seemingly traveling along both infected and surrounder cells (Figure 4A; Video S3). To better quantify single-cell ERK activity and wave propagation, we first constructed kymographs by considering the infection focus center as the center of the new polar coordinate system and averaging ERK activity radially while plotting it over time (Figures S4F and S4G). We also constructed kymographs by following individual cells ordered based on the distance from the focus center (or field of view center for uninfected cells) and plotted their mean ERK activity over time (Figures 4B and 4C). In both cases, the baseline ERK activity in single cells of infected monolayers was increased as compared to non-infected samples but decreased over time as confluence increased, similar to uninfected samples (Figures 4B, S4F and S4G). Median ERK activity was considerably lower in ERK-inhibited (with MEK inhibitor) samples and higher in activated (with PMA) samples, irrespective of whether they were infected or not. Moreover, cells displayed neither single-cell oscillations in ERK activity (see median single-cell ERK activity in Figure 4B) nor waves (Video S3). To ensure that cells did not photobleach, we performed FRET recordings every 1 h instead of every 10 min in some wells, but even under these imaging conditions, ERK activity decreased over time (Video S3).

Using the ARCOS algorithm to analyze ERK waves from 8 to 16 hpi, we found that ERK wave frequency was significantly higher in infected than in non-infected cell samples (Figures 4D and S4H).[19] However, the size of ERK-activated cell clusters did not significantly differ in infected compared to non-infected cell samples (Figure 4E).[19] At around 14–16 hpi, when extrusion starts, we did not observe clear radial ERK waves traveling away from the infection focus, consistent with these cells not being apoptotic.[8,28] Nevertheless, cell displacement vectors and spontaneous ERK waves suggested a connection between the two processes, consistent with previous findings from non-infectious contexts (Figure 4A).[15] To investigate whether the increase in ERK waves during infection is a global phenomenon, we performed additional FRET imaging on an expanded field of view imaged to capture surrounder cells up to 700 μm away from the infection focus center. Under these conditions, we observed no reduction in ERK activity or the frequency of ERK-activated cell clusters with increasing distance from the infection site, suggesting a global regulation of ERK waves rather than a strictly local effect (Video S3 and Figure S4I). Moreover, upon inhibition (marimastat) of matrix metalloproteases (MMPs),[15] previously involved in ERK wave propagation, we observed a slight decrease in ERK activation waves during infection and suppression of CICE, resulting in larger infection foci than controls (Figures S4J and S4K). These observations suggest that MMPs also contribute to ERK wave dynamics and thus to CICE. Overall, we provide evidence for that a global increase in baseline ERK activity and ERK waves is crucial for the alterations in cell kinematics that occur during infection, and lead to CICE.

Simulations predict that the inability of proximal surrounders to increase their monolayer stresses may be responsible for the lack of CICE in ERK-inhibited infected cells

Since absence of ERK waves suppresses cell morphology and kinematics' alterations arising during L.m. infection, it is likely surrounder and infected cells fail to engage in effective mechanical competition.[8] To test this and determine the mechanical parameters that lead to CICE suppression, we employed a hybrid computational approach, combining agent-based and finite element models. This model simulates epithelial monolayer dynamics, accounting for infection spread by considering the increasing number of infected cells over time (Figure S5). We assumed that surrounder cells can vary their degree of protrusion based on our findings that ERK inhibition reduces polarization of surrounder cells and migration speed (Figure 5A left). We

(C–F) Box plots of cell area (C), radial alignment (D), cell aspect ratio (E), shape factor (F) of cells originating from uninfected wells, uninfected surrounders and infected cells treated with vehicle control (grayscale) or 50 μM PD0325901 (bluescale). $N = 4908 \pm 778$ single cells were analyzed per condition. Dots show mean of each of $N = 3$ independent replicates; ANOVA followed by Tukey's multiple comparisons test: $^{*}p < 0.05$, $^{**}p < 0.01$, $^{***}p < 0.001$, $^{****}p < 0.0001$. See also Figure S2.

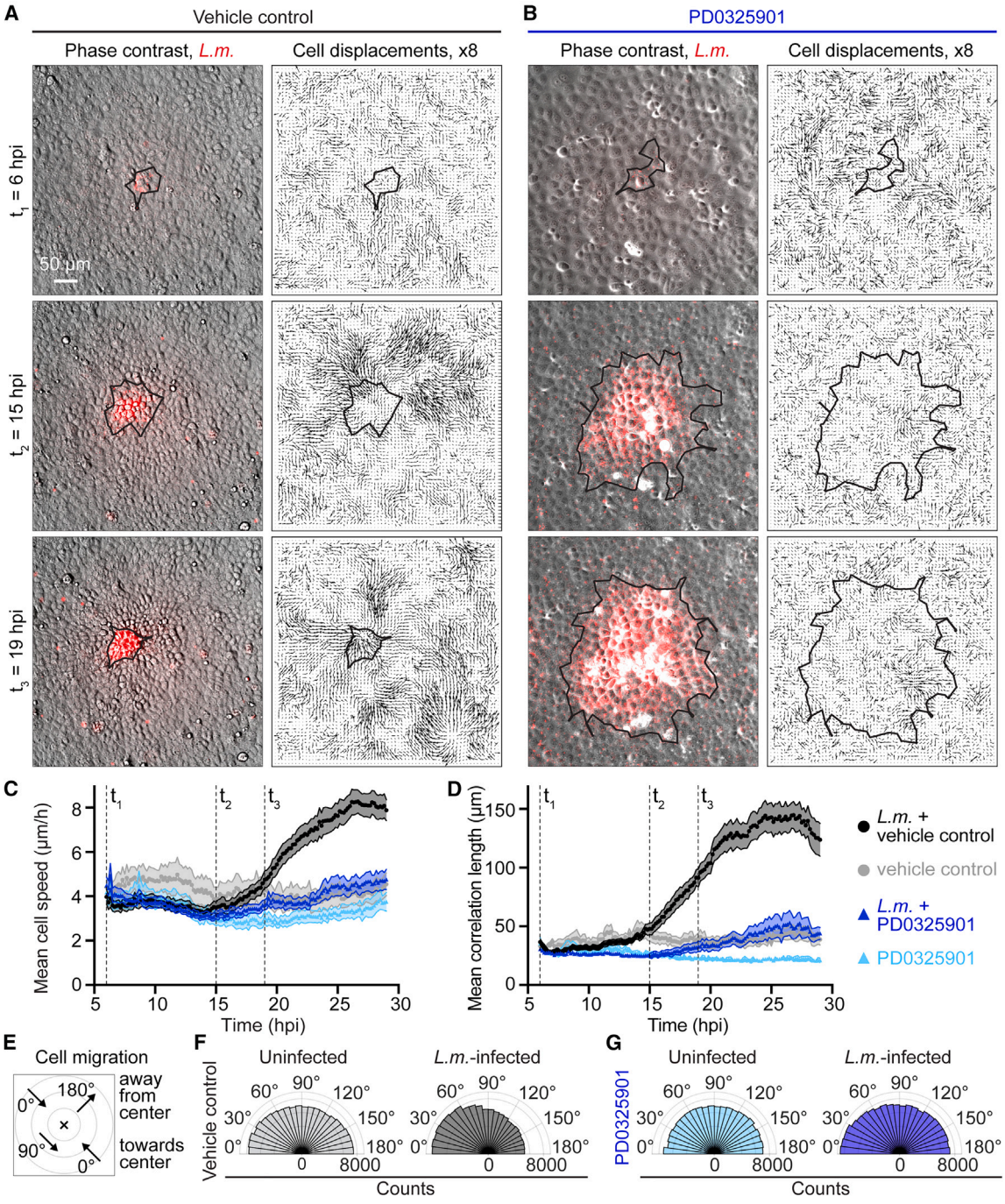

Figure 3. ERK inhibition stalls the increase in cell speed and coordinated migration of MDCK cells during *L.m.* infection

(A and B) Representative video microscopy images of *L.m.*-infected MDCK cell monolayers treated with vehicle control (A) or 50 μM PD0325901 (B) at three indicated time points (rows). Columns: overlay of phase-contrast image with *L.m.* fluorescence, cell displacements (arrows, scaled 8x). Black outline: infection focus contour.

(C and D) Mean cell speed (μm/h, C) and correlation length (μm, D) over time (hpi) shown for uninfected or *L.m.*-infected cells treated or not at 4 hpi with 50 μM PD0325901 (see color legend). Solid line: mean, shaded area: SEM for three independent experiments, $N = 7$ and $N = 18$ recordings for uninfected and *L.m.*-infected conditions, respectively. Dashed lines indicate representative time points shown in (A-B).

(E) Sketch of cell migration directionality angles quantified in (F-G). 0° and 180° correspond to cells moving toward or away from the center of the infection focus (or field of view for uninfected cells), respectively.

(F and G) Rose plots showing cell displacement directionality angle (angle between radial direction and cell displacement, see STAR Methods) for uninfected (left) or *L.m.*-infected cells in monolayer (right), treated with vehicle control (F) or 50 μM PD0325901 (G). See also Figure S3 and Video S2.

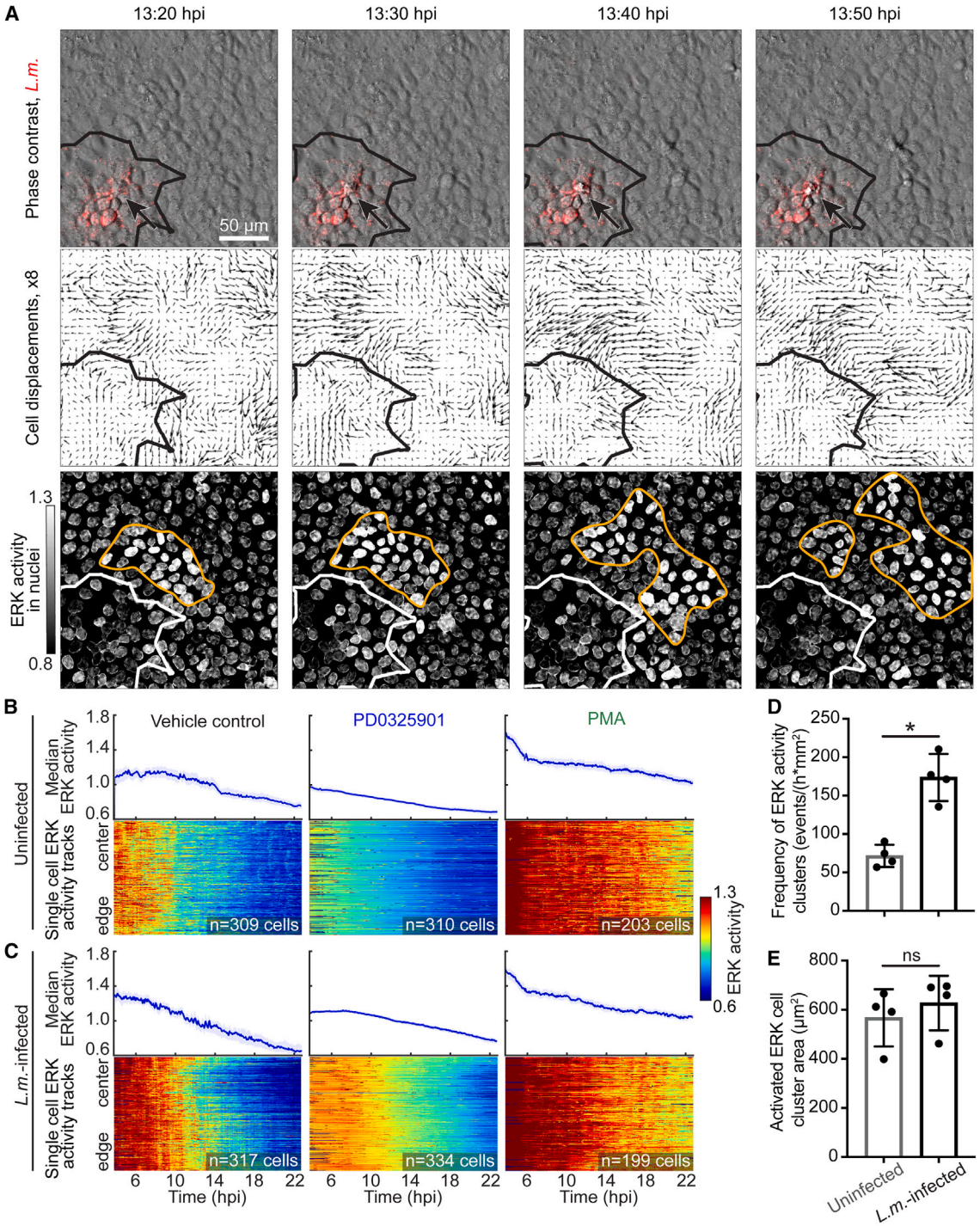

Figure 4. ERK inhibition or constitutive activation abolishes ERK activation waves traveling between MDCK cells during *L.m.* infection

(A) Representative time-lapse images (columns) of *L.m.*-infected MDCK cells monolayers when extrusion of infected cells first occurs. Rows: overlay of phase contrast and *L.m.* fluorescence (red), cell displacements (arrows, scaled 8x), ERK activity in cell nuclei with orange outline indicating ERK activity wave. Black/white outlines: infection focus contour. Arrows point on first extruded infected cell.

(legend continued on next page)

also assumed that contractility and stiffness of infected cells can vary compared to surrounders (Figure 5A middle and right).[8]

We simulated four different cases (Figure 5; Video S4). In case 1, infected cells exhibit lower stiffness (250 Pa) than surrounder cells (500 Pa), leading to polarization of surrounders toward the infection focus because they protrude toward the site of minimum stress, the focus[8] (Figure 5B). As a result, monolayer stresses of uninfected cells surrounding the focus (proximal surrounder) increase, leading to squeezing of infected cells, a prerequisite for CICE. In case 2, we simulated *in vitro* ERK wave inhibition by reducing the surrounder cell force (F^s) so that surrounder cells cannot polarize effectively toward the focus, resulting in loss of infected cell squeezing and reduction of monolayer stresses in proximal surrounders compared to case 1 (Figure 5B). In case 3, we simulated case 2 but also assumed that infected cells have the same stiffness as surrounders (500 Pa). This makes surrounders less competent in squeezing infected cells compared to case 2 (Figure 5B). As in case 2, monolayer stresses of proximal surrounder cells fail to increase. Finally, in case 4, we simulated case 2 but also assumed reduced contractility of infected compared to surrounder cells. As a result, instead of being squeezed, infected cells increase their area (Figure 5B). Similar to cases 2 and 3, monolayer stresses of proximal surrounder cells are weakened.

To summarize, our model predicts that impairing surrounder cell polarization (cases 2–4 versus 1) reduces infected cell squeezing and monolayer stresses reinforcement. Additionally, eliminating stiffness differences between surrounder versus infected cells (case 3 versus 2) further decreases squeezing, albeit slightly. Only when both surrounder cell force and infected cell contractility are reduced (case 4), infected cells enlarge rather than being squeezed.

ERK inhibition deescalates the mechanical competition between infected and surrounder uninfected cells

The model suggested that for infected cell squeezing and CICE to stall (as observed when ERK waves are abrogated), the reinforcement of monolayer stress in surrounder cells must disappear. Additionally, a further reduction in contractility of infected cells may result in cell enlargement rather than squeezing. To confirm these findings *in vitro*, we first performed TFM to measure traction stresses exerted by cells on their matrix. These stresses serve as proxy for how well focal adhesions are organized and connected to the underlying contractile cytoskeleton. We found that the traction stress magnitude was always increased during infection (Figures 6A–6C; Video S5) compared to uninfected cells, which remained at steady state with minimal fluctuations (Figures S6A–S6D). Although the average traction stress magnitude appeared lower in ERK-inhibited versus control samples, this difference was not statistically significant. We also measured transepithelial electrical resistance (TEER) to examine changes in monolayer barrier integrity and permeability (Figure S6E). Infected samples exhibited reduced TEER compared to non-infected samples, regardless of pharmacological treatment, indicating that infection compromises monolayer barrier integrity independently of ERK waves. However, since TEER provides only a scalar value representing the overall permeability of the entire monolayer without offering spatial information, this conclusion should be interpreted with caution.

Since we have established that infected and surrounder cells exhibit different mechanical properties, we quantified average traction stresses for each cell population separately and found that infected cells exerted 30% less traction compared to surrounders, while ERK inhibition attenuated this difference by 10% (Figure 6D). Monolayer stress microscopy[35] revealed that proximal surrounders failed to increase their monolayer stresses when ERK was inhibited, consistent with the model predictions that stress reinforcement is crucial for infected cell squeezing (Figures 6A and 6E). Accordingly, control infected cells displayed an approximately 30% decrease in monolayer stresses as compared to surrounder cells, while in ERK-inhibited samples, both surrounders and infected cells exhibited lower monolayer stresses than control samples (Figures 6A, 6E, and S6C and S6D). This is consistent with the model prediction, suggesting that an increase in monolayer stresses of proximal surrounders is required for infected cell squeezing (case 2). However, we do not have direct evidence that infected cell contractility is decreased (case 4), which would explain the enlargement of infected cells when ERK waves are absent.

Consistent with our previous findings,[8] the *in silico* model also predicts that differences in stiffness between infected versus surrounder cells promote squeezing, though the effect is subtle (case 2 versus 3). To further investigate this, we examined whether stiffness differences between infected versus surrounder cells at 24 hpi persist when ERK is inhibited at 4 hpi. We found that both infected and surrounder cells exhibited stiffness levels similar to uninfected samples (Figure 6F). Similar results were obtained when ERK is constitutively activated with PMA to abrogate waves (Figure S6F). Collectively, we discovered that in the absence of ERK waves, infected and surrounder cells display similar stiffness and attenuated differences in traction stress exertion. Under these conditions, proximal surrounders are unable to reinforce their monolayer stresses, a prerequisite for infected cell squeezing and CICE to occur.

ERK activation waves drive CICE in *S.f.*-infected epithelial cells *in vitro* and *in vivo*

Intracellular bacterial pathogens such as *S.f.*, which, like *L.m.,* use actin-based motility to move within host cells, have been shown to trigger ERK activation in other host cell types.[36,37] We thus examined whether *S.f.* infection of epithelial cells would also induce ERK waves and CICE. Thus, we monitored ERK

(B and C) Median (top) and heatmap plots (bottom) of ERK activity over time for uninfected (B) and *L.m.*-infected (C) MDCK cells monolayers treated with vehicle control (left), 50 μM PD0325901 (middle), or 200 nM PMA (right). Heatmap plots show individual cells' ERK activity over time (h or hpi), and cells are ordered as a function of distance from the center of the field of view (for uninfected) or the infection focus center (infected).
(D and E) Bar plots of mean frequency of ERK waves (events/(h•mm^2), (D) and ERK-activated cell cluster area (μm^2, (E) for uninfected and *L.m.*-infected MDCK cell monolayers. $N = 4$ independent experiments, the median of which is shown as a circle overlayed on the box plot. Lines: mean ± SD, WRST: $^*p < 0.05$, ns:$p > 0.05$. See also Figure S4 and Video S3.

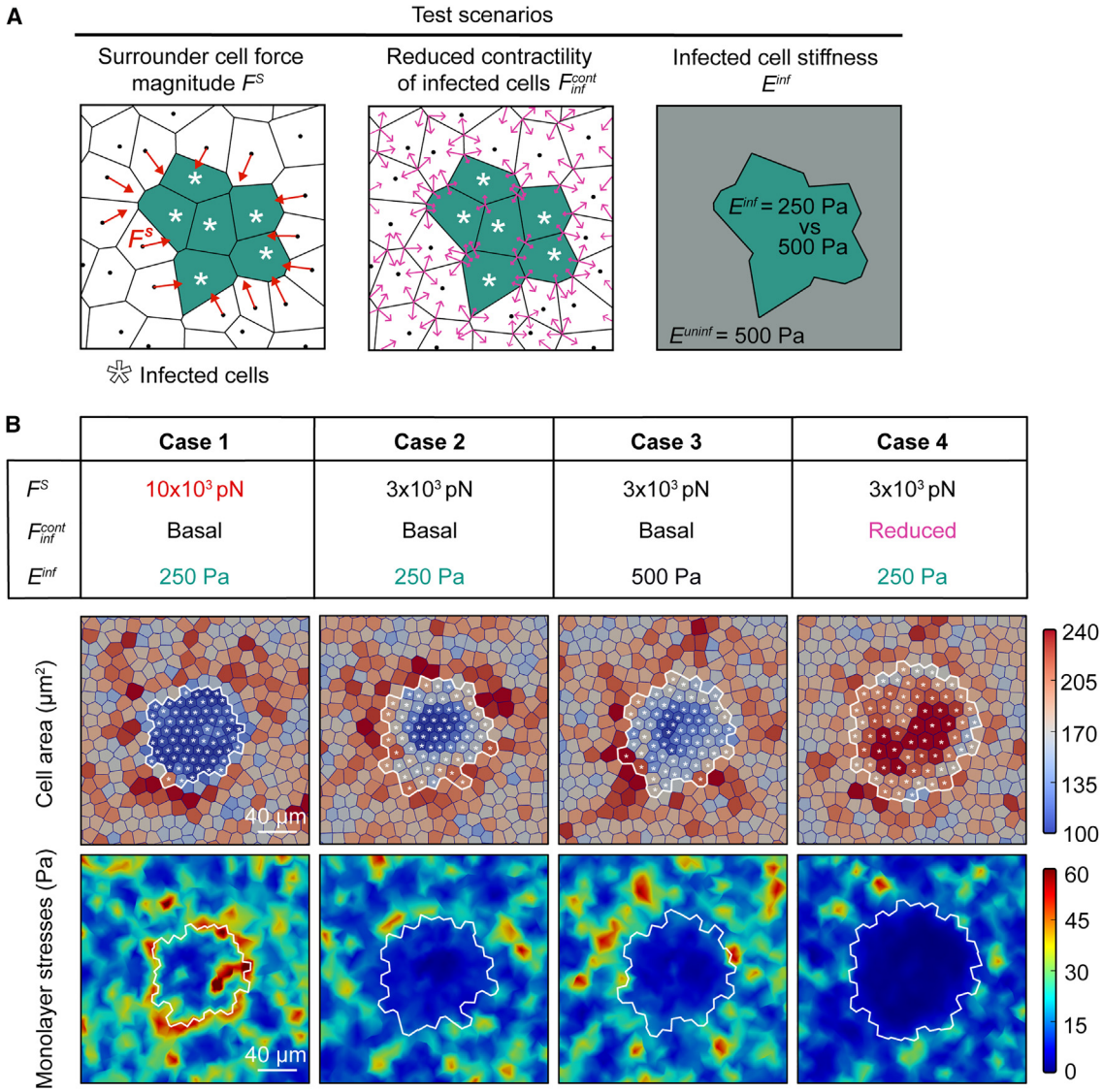

Figure 5. Modeling reveals that monolayer stress reinforcement of proximal surrounders is necessary for infected cell squeezing

(A) Schematic of hybrid model. Infected cells are denoted by green asterisk. Proximal surrounders exert force F_s pointing toward the focus (left), infected cells versus surrounders can have varying contractility (middle) or varying cell stiffness (right).

(B) Four cases were simulated (columns) by varying the parameters shown in (A). In each case, shown are the cell topology with cells color-coded by area (μm^2, top), and monolayer stresses (Pa, bottom). (1) Infected cells contract, their stiffness is half compared to surrounders, $F_s = 10 \times 10^3$ pN. (2) Infected cells contract, their stiffness is half compared to surrounders, $F_s = 3 \times 10^3$ pN. (3) Infected cells contract, their stiffness is the same as for surrounders, $F_s = 3 \times 10^3$ pN. (4) Infected cells contract less, their stiffness is half compared to surrounders, $F_s = 3 \times 10^3$ pN. White line: infection focus contour. Asterisks: infected cells. See also Figure S5 and Video S4.

activity using our FRET-based biosensor in *S.f.*-infected and uninfected MDCK cell monolayers. We observed increased ERK activity and waves during *S.f.* infection compared to uninfected cells (Figures 7A and 7B) and formation of large infection mounds and CICE in control but not ERK-inhibited *S.f.*-infected MDCK cells at 16 hpi (Figures 7C and 7D). These results showcase that changes in cell mechanics associated with ERK waves and leading to CICE likely play a crucial role in intracellular bacterial infections that trigger ERK activation and involve intercellular bacterial spread (such as *S.f.* infection).

To complement our *in vitro* and *in silico* experiments, we infected the two-layered skin epithelium of zebrafish larvae tails with *S.f.*, with or without MEK inhibitor treatment (Figure 7E). CICE occurred at 6 hpi in control infected samples but was significantly reduced in ERK-inhibited samples (Figure 7F). Additionally, in the controls, the surrounding cells were more polarized, radially aligned, and had higher shape factor than ERK-inhibited cells, consistent with the shape of surrounding MDCK cells in similar *in vitro* experiments (Figures 7E and S7A–S7F). This suggests that CICE driven by ERK-based mechanochemical competition

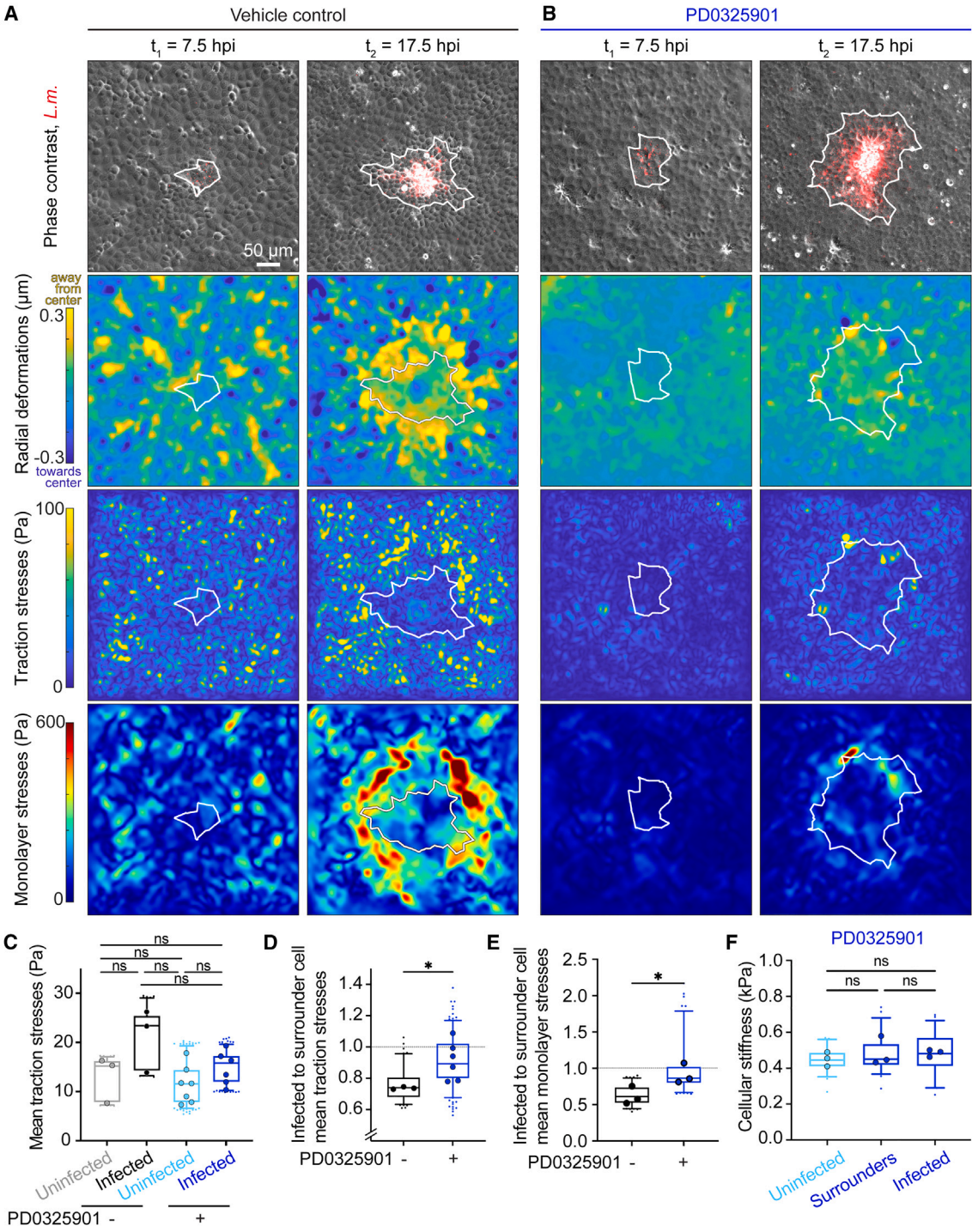

Figure 6. ERK inhibition stalls the increase in monolayer stresses in proximal surrounders and abolishes differences in stiffness between surrounders and infected cells

(A and B) TFM and MSM on MDCK cells adherent on 3-kPa gels and infected at low MOI with *L.m.* such that single-infection foci emerge. Cells were treated with vehicle control (A) or 50 μM PD0325901 (B) at 4 hpi. Rows: overlay of phase contrast with *L.m.* fluorescence, radial deformations that cells impart on their matrix (μm), traction stresses (Pa), and monolayer stresses (Pa). Columns: time (hpi). White line: infection focus contour.

(legend continued on next page)

is relevant *in vivo* and potentially in other cell types in monolayer and tissues.

DISCUSSION

Efficient clearance of bacterially infected cells from epithelial cell monolayers is critical, especially at the delicate intestine surface, where a single monolayer of cells separates the intestinal lumen from the external milieu. CICE can facilitate remodeling of the monolayer to limit infection dissemination. Here we show that ERK activation exhibits spatiotemporal variations during infection and travels in the form of waves of increased frequency between neighboring cells. The presence of these waves tilts the outcome of the mechanical battle in favor of the host and regulates CICE. In the absence of ERK waves, CICE does not occur, and the morphological and kinematical signatures of host cells associated with CICE are completely absent. Moreover, characterization of cell mechanics *in vitro* and *in silico* revealed that reinforcement of monolayer stresses of surrounder cells proximal to the infection focus is key in eliciting infected cell squeezing and CICE and does not occur in absence of ERK waves.

The implications of this work go far beyond *L.m.* infection as we demonstrated that CICE also occurs during *S.f.* infection of epithelial cells and zebrafish larvae. This provides evidence of *in vivo* CICE and opens the gates for similar investigations using other *in vivo* models. Furthermore, the proposed mechanism could be relevant in infections with pathogens other than bacteria. Supporting this idea, in monolayers of HeLa cells infected with vaccinia virus—where still images suggest the occurrence of CICE and ERK activation—it is highly likely that a similar mechanical process modulated by ERK activation waves takes place to enhance infection spread.[38] In infections with *L.m.*, we showed that ERK activation limits infection spread along the monolayer via CICE, potentially due to geometry since extruded cells cannot spread bacteria through the monolayer. Additionally, we speculate that since extruded cells eventually die due to detachment from the basement membrane, *in vivo* in the intestine they would just be discarded from the host via the fecal route.[8] This is further supported by studies on other bacterial pathogens where ERK activation occurs. For example, a study examining still images of immunostained cells showed that ERK activation in infected cells can propagate to neighboring cells, making them produce higher amounts of cytokines like IL-8, which amplifies innate immunity against infection with *L.m.*, *S.f.*, and *Salmonella typhimurium*.[36] However, infected cell squeezing or CICE was not examined or reported in this study. Interestingly, a recent clinical study involving COVID-19 also supports a model whereby ERK activation acts in favor of the host to limit infection spread.[39]

ERK wave propagation allows for fast and long-range intercellular communication in various biological contexts, including wound healing and tissue morphogenesis.[12] Here, we discovered that ERK wave propagation is also important during infection processes, such as when intracellular bacterial disseminate through epithelia, and shed light into its spatiotemporal modulation. ERK waves traveling between cells have been termed "mechanochemical" because they are closely coordinated with cell mechanics. For instance, during wound healing, ERK activation waves are synchronized with cell strain and cooperate with cell polarization to drive collective cell migration.[15] Additionally, ERK is mechanosensitive, meaning that cell extension, including mechanical stretch applied to cells, leads to ERK activation and subsequent cell contraction. We observed a similar pattern when analyzing displacements of cells during ERK wave propagation, and also that abrogation of waves results in lack of polarization of surrounder uninfected cells, necessary for CICE.

Intercellular adhesions are essential for propagation of ERK waves from cell to cell. For instance, in αE-catenin knockout (KO) cells, which are unable to form robust intercellular junctions in monolayer, ERK oscillates within individual cells but fails to propagate between them in waves.[15] We previously found that in αE-catenin KO cells, CICE is inhibited.[8] This finding, along with additional evidence presented herein where ERK is either inhibited or constitutively activated, supports the idea that ERK activity waves—rather than baseline ERK activity alone—regulate CICE. Interestingly, a study on mammary epithelial cells found that ERK activity is heightened when cells reside on stiffer matrices compared to softer ones, although the study did not assess ERK wave propagation.[40] We also previously observed that MDCK cells residing on stiffer matrices exhibit enhanced CICE as compared to those on softer matrices due to stronger traction and monolayer stresses in uninfected cells surrounding the infection focus.[41] Herein we consistently show that in the absence of ERK waves, the monolayer stress reinforcement in surrounding cells is absent, and CICE does not occur.

In vitro and *in vivo* studies have shown that during apoptosis, ERK activation propagates from the apoptotic cell(s) and then spreads to neighboring cells in waves as a mechanism to ensure the removal of damaged cells while maintaining homeostasis during tissue remodeling or in response to damage.[16,42] During infection, when CICE occurs, we did not observe clear radial waves traveling away from the infection mound toward the surrounders.[8] Accordingly, the infected cells that get extruded are not apoptotic and blocking apoptosis using different pharmacological agents does not decrease the volume of infection mounds.[41] Instead, cell death appears to be a consequence of extrusion rather than the cause of it. The question that remains unanswered is what triggers ERK activation ERK to begin with and its propagation subsequently. We speculate that the trigger could be secreted pro-inflammatory ligands for EGFR and other receptors, as recently shown.[19,23] Indeed, we previously showed that various cytokines that can activate ERK, including IL-8 and

(C) Box plots of mean traction stresses of *L.m.*-infected or not MDCK cells, treated or not with 50 μM PD0325901. ANOVA, ns: $p > 0.05$. (D and E) Box plots of ratio of traction stresses (D) or monolayer stresses (E) of infected to surrounder cells. WRST: *$p < 0.05$. For (C-E) $N = 3$ independent experiments were analyzed for cells followed from 10 to 16 hpi, dots show the mean of each sample.

(F) Box plots of cell stiffness (kPa) at 24 hpi for uninfected, surrounder cells, and infected cells, for samples treated with 50 μM PD0325901 at 4 hpi. $N = 58 \pm 3$ cells were analyzed in each case originating from three independent experiments. ANOVA: ns: $p > 0.05$. See also Figure S6 and Video S5.

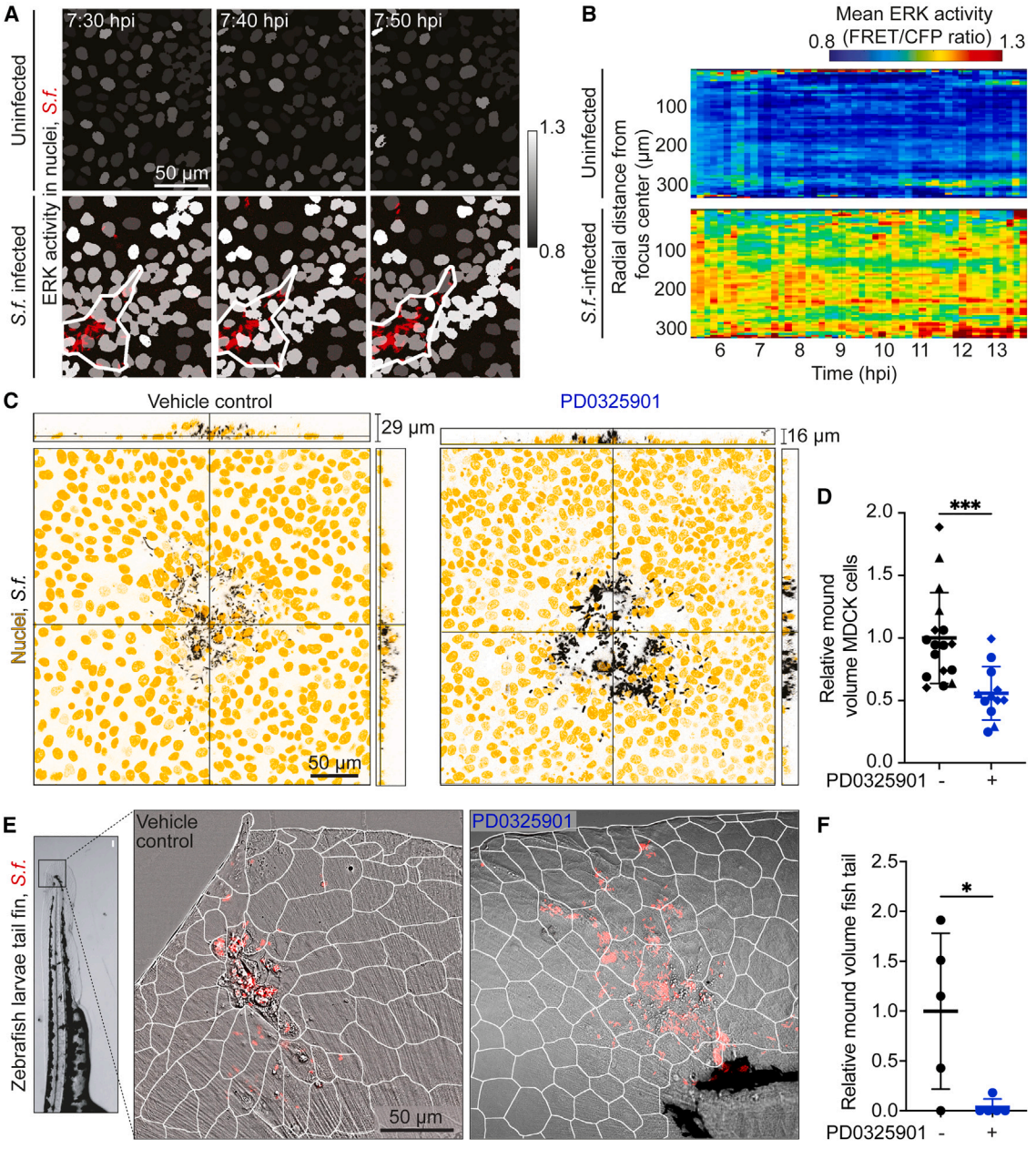

Figure 7. ERK waves also drive collective extrusion of *S.f.*-infected cells *in vitro* and *in vivo*

(A) Representative snapshots of ERK activity in the nuclei of uninfected (top) and *S.f.*-infected MDCK cells (bottom) overlayed with *S.f.* fluorescence (red). Columns: three consecutive time points (hpi).

(B) Kymograph of mean radial ERK activity (y axis) versus time (hpi, x axis) for uninfected (top) or *S.f.*-infected MDCK cells (bottom) (see Figure S4F).

(C) Orthogonal views of *S.f.*-infected MDCK cells 16 hpi treated with vehicle control (left) or 50 μM PD0325901 (right) at 4 hpi. Host nuclei: yellow; *S.f.*: black.

(D) Relative mound volume of *S.f.*-infected MDCK cells treated with vehicle control or 50 μM PD0325901. Normalization to mean of control cells. Mean ± SD, WRST: ***$p < 0.001$.

(E) Representative overlay of phase-contrast images with *S.f.* fluorescence (red) of zebrafish larvae fin tails treated with vehicle control or 41 μM PD0325901. White lines: cell contours. Image on left shows the location of the area imaged in zebrafish larvae.

(F) Relative mound volume of *S.f.*-infected extruded epithelial cells from the skin of zebrafish larvae fin tails. Samples inspected at 6 hpi. Normalization with respect to mean of control zebrafish fin tails. Mean ± SD, WRST: *$p < 0.05$. See also Figure S7.

MCP-1,[8] are present in large amounts in infected samples, and these same cytokines can increase ERK wave frequency also in non-infected cell monolayers.[23,43] However, various additional molecular mechanisms could lead to ERK activation,[12] namely (1) decrease in intercellular space volume, increasing ligand concentration and triggering EGFR-MEK/ERK signaling[44]; (2) opening of stretch-activated ion channels, leading to calcium influx and ERK activation[14]; (3) disruption of E-cadherin/EGFR heterotrimeric complex due to elevated intercellular tension, enabling EGFR dimerization and downstream signaling upon ligand binding[45]; (4) decreased membrane tension, leading to increased endocytic ERK signaling[46]; and (5) increased integrin clustering at focal adhesions.[47] The increase in traction stresses in infected cell samples from the onset of our recordings (early infection) corroborates integrin-mediated ERK activation (5). Opening of stretch-activated ion channels (2) or disruption of E-cadherin/EGFR complex due to increased monolayer stresses (3) could play a role later in infection, when uninfected surrounders become polarized and increase their cell stiffness and monolayer tension. Further experiments are required to confirm these hypotheses.

Our discovery that ERK waves orchestrate the mechanical cell competition occurring during infection and leading to CICE highlights that the interplay between cell-generated physical forces and biochemical signaling critically dictates infection outcomes.

Limitations of the study

We used the EKAREV biosensor to spatiotemporally track ERK activity during epithelial cell infection via FRET. A limitation of this biosensor is its potential responsiveness to cyclin-dependent kinase 1 (CDK1) in addition to ERK, which can lead to increased FRET/CFP signals during mitosis, even when MEK inhibitors are present.[18] Therefore, the observed decrease in ERK activity over time may partly reflect CDK1 activity during cell division. While we demonstrated the occurrence of CICE in zebrafish larvae skin epithelia, we did not explore this process in other relevant tissues, such as the intestine or lung (common entry points for pathogens), nor did we explore the role of host immune cells like macrophages and neutrophils. This could be explored in the future by using zebrafish deficient in immune cells,[48] and considering other sites of infection, including the zebrafish gut. Additionally, we did not account for the influence of extracellular physical cues in our assays, such as cell stretching[41] and ECM stiffness,[41] which could impact CICE dynamics by modulating ERK waves. Incorporating organotypic devices that simulate these conditions will be useful for understanding how biomechanical factors regulate CICE.

RESOURCE AVAILABILITY

Lead contact

Further information and requests for reagents may be directed to and will be fulfilled by the lead contact Effie Bastounis effie.bastounis@uni-tuebingen.de (E.E.B.).

Materials availability

Materials developed in this study are available on request to the corresponding authors.

Data and code availability

Data collected are available on request to the corresponding authors. The (phospho)proteomics data (raw files) generated during this study and subsequent analysis are available on the PRIDE repository[49] of proteomeXchange (https://proteomecentral.proteomexchange.org/ui) with identifier PRIDE: PXD055809. Analyzed (phospho)proteomic data and differential expression analysis are in Table S1. All codes are uploaded in our GitHub repository with the corresponding accession numbers as listed as follows: (1) ERK waves analysis using ARCOS (https://doi.org/10.5281/zenodo.14287824); (2) Calculation of volume of extruded infected cells calculation (https://doi.org/10.5281/zenodo.14287679); (3) Calculation of infection focus area (https://doi.org/10.5281/zenodo.14287812); (4) Cell kinematics analysis (https://doi.org/10.5281/zenodo.7155531) (5) Monolayer stresses calculation (https://doi.org/10.5281/zenodo.7155523); and (6) Hybrid computational model (https://doi.org/10.5281/zenodo.14289212).

ACKNOWLEDGMENTS

We are grateful to Julie A. Theriot for sharing her resources when this project started, Tsuyoshi Hirashima for sharing the EKAREV-NLS plasmid and his insights into several occasions, Matthew Footer for experimental support, and Libera Lo Presti for discussions and revising the manuscript. We acknowledge that part of our MSM codes is based on the original code written by Siva Srinivas Kolukula. The graphical abstract was created with BioRender.com. We acknowledge the Proteome Center Tübingen for measurement and analysis of the (phospho)proteomics data. This work was supported in part by the Deutsche Forschungsgemeinschaft under Germany's Excellence Strategy – EXC 2124 – 390838134 (E.E.B., M.M., J.S.R., and L.H.), DFG grant with Project number 490839690 (E.E.B, L.H., and I.C.), and DFG grant with Project number 335549539/GRK2381 (A.B. and T.E.S.). A.B. is supported by the Add-on Fellowship for Interdisciplinary Life Science of the Joachim Herz Foundation. We also thank EMBO for the Scientific Exchange Grant 10245 (M.M.) and LSHTM Biological Services Facility for the work and care of our zebrafish stocks. G.Ö.G. is funded by the Human Frontier Science Program (LT000436/2021-L). Research in the SM laboratory is supported by a European Research Council Consolidator Grant (772853 - ENTRAPMENT) and Wellcome Discovery Award (226644/Z/22/Z). R.A.-Y. and M.J.G.-B. were supported by the MCIN/AEI/10.13039/501100011033 and ERDF A way of making Europe under the grant agreement No. PID2021-124271OB-I00, and R.A.-Y. would also like to acknowledge support of the Spanish Ministry of Universities (grant No. FPU 20/05274). Finally, we acknowledge support by Open Access Publishing Fund of the University of Tübingen.

AUTHOR CONTRIBUTIONS

Conceptualization, E.E.B. and L.H.; methodology, E.E.B., M.J.G.-B., S.M., B.M., T.E.S., L.H., M.M., R.A.-Y.; software, E.E.B; L.H., M.M., R.A.-Y., J.C.S.R., A.V.; investigation, E.E.B., L.H., M.M., R.A.-Y., A.B., A.V., Y.-T.Y., K.W., D.B., G.Ö.G.; writing – original draft, E.E.B., L.H., M.J.G.-B.; writing – review & editing, E.E.B., L.H., I.C., M.J.G.-B., R.A-Y.; resources, E.E.B., M.J.G-B., S.M., B.M., T.E.S.; supervision, E.E.B., M.J.G-B., S.M., B.M., T.E.S.

DECLARATION OF INTERESTS

The authors declare no competing interests.

STAR★METHODS

Detailed methods are provided in the online version of this paper and include the following:

- KEY RESOURCES TABLE
- EXPERIMENTAL MODEL AND STUDY PARTICIPANT DETAILS
  - Mammalian cell culture
  - Establishment of MDCK cells expressing the FRET-based ERK activity biosensor
  - Bacterial strains used in this study

SUPPLEMENTAL INFORMATION

Supplemental information can be found online at https://doi.org/10.1016/j.celrep.2024.115193.

Received: September 23, 2024
Revised: November 22, 2024
Accepted: December 19, 2024
Published: January 14, 2025

REFERENCES

1. Gouin, E., Welch, M.D., and Cossart, P. (2005). Actin-based motility of intracellular pathogens. Curr. Opin. Microbiol. *8*, 35–45. https://doi.org/10.1016/j.mib.2004.12.013.
2. Stevens, J.M., Galyov, E.E., and Stevens, M.P. (2006). Actin-dependent movement of bacterial pathogens. Nat. Rev. Microbiol. *4*, 91–101. https://doi.org/10.1038/nrmicro1320.
3. Duncan-Lowey, J.K., Wiscovitch, A.L., Wood, T.E., Goldberg, M.B., and Russo, B.C. (2020). Shigella flexneri disruption of cellular tension promotes intercellular spread. Cell Rep. *33*, 108409. https://doi.org/10.1016/j.celrep.2020.108409.
4. Lamason, R.L., Bastounis, E., Kafai, N.M., Serrano, R., Del Álamo, J.C., Theriot, J.A., and Welch, M.D. (2016). Rickettsia Sca4 reduces vinculin-mediated intercellular tension to promote spread. Cell *167*, 670–683.e10. https://doi.org/10.1016/j.cell.2016.09.023.
5. Ortega, F.E., Koslover, E.F., and Theriot, J.A. (2019). Listeria monocytogenes cell-to-cell spread in epithelia is heterogeneous and dominated by rare pioneer bacteria. Elife *8*, e40032. https://doi.org/10.7554/eLife.40032.
6. Bastounis, E.E., Radhakrishnan, P., Prinz, C.K., and Theriot, J.A. (2022). Mechanical forces govern interactions of host cells with intracellular bacterial oathogens. Microbiol. Mol. Biol. Rev. *86*, e0009420. https://doi.org/10.1128/mmbr.00094-20.
7. Rajabian, T., Gavicherla, B., Heisig, M., Müller-Altrock, S., Goebel, W., Gray-Owen, S.D., and Ireton, K. (2009). The bacterial virulence factor InlC perturbs apical cell junctions and promotes cell-to-cell spread of Listeria. Nat. Cell Biol. *11*, 1212–1218. https://doi.org/10.1038/ncb1964.
8. Bastounis, E.E., Serrano-Alcalde, F., Radhakrishnan, P., Engström, P., Gómez-Benito, M.J., Oswald, M.S., Yeh, Y.-T., Smith, J.G., Welch, M.D., García-Aznar, J.M., and Theriot, J.A. (2021). Mechanical competition triggered by innate immune signaling drives the collective extrusion of bacterially infected epithelial cells. Dev. Cell *56*, 443–460.e11. https://doi.org/10.1016/j.devcel.2021.01.012.
9. Engstrom, P., Burke, T.P., Mitchell, G., Ingabire, N., Mark, K.G., Golovkine, G., Iavarone, A.T., Rape, M., Cox, J.S., and Welch, M.D. (2019). Evasion of autophagy mediated by Rickettsia surface protein OmpB is critical for virulence. Nat. Microbiol. *4*, 2538–2551. https://doi.org/10.1038/s41564-019-0583-6.
10. Yang, J., Antin, P., Berx, G., Blanpain, C., Brabletz, T., Bronner, M., Campbell, K., Cano, A., Casanova, J., Christofori, G., et al. (2020). Guidelines and definitions for research on epithelial–mesenchymal transition. Nat. Rev. Mol. Cell Biol. *21*, 341–352. https://doi.org/10.1038/s41580-020-0237-9.
11. Olea-Flores, M., Zuñiga-Eulogio, M.D., Mendoza-Catalán, M.A., Rodríguez-Ruiz, H.A., Castañeda-Saucedo, E., Ortuño-Pineda, C., Padilla-Benavides, T., and Navarro-Tito, N. (2019). Extracellular-signal regulated kinase: A central molecule driving epithelial-mesenchymal transition in cancer. Int. J. Mol. Sci. *20*, 2885. https://doi.org/10.3390/ijms20122885.
12. Crozet, F., and Levayer, R. (2023). Emerging roles and mechanisms of ERK pathway mechanosensing. Cell. Mol. Life Sci. *80*, 355. https://doi.org/10.1007/s00018-023-05007-z.
13. Sano, T., Kobayashi, T., Negoro, H., Sengiku, A., Hiratsuka, T., Kamioka, Y., Liou, L.S., Ogawa, O., and Matsuda, M. (2016). Intravital imaging of mouse urothelium reveals activation of extracellular signal-regulated kinase by stretch-induced intravesical release of ATP. Phys. Rep. *4*, e13033. https://doi.org/10.14814/phy2.13033.
14. Gudipaty, S.A., Lindblom, J., Loftus, P.D., Redd, M.J., Edes, K., Davey, C.F., Krishnegowda, V., and Rosenblatt, J. (2017). Mechanical stretch triggers rapid epithelial cell division through Piezo1. Nature *543*, 118–121. https://doi.org/10.1038/nature21407.
15. Hino, N., Rossetti, L., Marín-Llauradó, A., Aoki, K., Trepat, X., Matsuda, M., and Hirashima, T. (2020). ERK-Mediated mechanochemical waves direct collective cell polarization. Dev. Cell *53*, 646–660.e8. https://doi.org/10.1016/j.devcel.2020.05.011.
16. Aoki, K., Kumagai, Y., Sakurai, A., Komatsu, N., Fujita, Y., Shionyu, C., and Matsuda, M. (2013). Stochastic ERK activation induced by noise and cell-to-cell propagation regulates cell density-dependent proliferation. Mol. Cell *52*, 529–540. https://doi.org/10.1016/j.molcel.2013.09.015.
17. Aoki, K., Kondo, Y., Naoki, H., Hiratsuka, T., Itoh, R.E., and Matsuda, M. (2017). Propagating wave of ERK activation orients collective cell migration. Dev. Cell *43*, 305–317.e5. https://doi.org/10.1016/j.devcel.2017.10.016.
18. Ishii, M., Tateya, T., Matsuda, M., and Hirashima, T. (2021). Retrograde ERK activation waves drive base-to-apex multicellular flow in murine cochlear duct morphogenesis. Elife *10*, e61092. https://doi.org/10.7554/eLife.61092.
19. Gagliardi, P.A., Grädel, B., Jacques, M.-A., Hinderling, L., Ender, P., Cohen, A.R., Kastberger, G., Pertz, O., and Dobrzyński, M. (2023). Automatic detection of spatio-temporal signaling patterns in cell collectives. J. Cell Biol. *222*, e202207048. https://doi.org/10.1083/jcb.202207048.
20. Boocock, D., Hino, N., Ruzickova, N., Hirashima, T., and Hannezo, E. (2021). Theory of mechanochemical patterning and optimal migration in cell monolayers. Nat. Phys. *17*, 267–274. https://doi.org/10.1038/s41567-020-01037-7.
21. Ram, A., Murphy, D., DeCuzzi, N., Patankar, M., Hu, J., Pargett, M., and Albeck, J.G. (2023). A guide to ERK dynamics, part 1: mechanisms and models. Biochem. J. *480*, 1887–1907. https://doi.org/10.1042/bcj20230276.
22. Davies, A.E., Pargett, M., Siebert, S., Gillies, T.E., Choi, Y., Tobin, S.J., Ram, A.R., Murthy, V., Juliano, C., Quon, G., et al. (2020). Systems-level properties of EGFR-RAS-ERK signaling amplify local signals to generate

dynamic gene expression heterogeneity. Cell Syst. *11*, 161–175.e5. https://doi.org/10.1016/j.cels.2020.07.004.

23. DeCuzzi, N.L., Oberbauer, D., Chmiel, K.J., Pargett, M., Ferguson, J.M., Murphy, D., Hardy, M., Ram, A., Zeki, A.A., and Albeck, J.G. (2024). Spatiotemporal clusters of ERK activity coordinate cytokine-induced Inflammatory responses in human airway epithelial cells. Am. J. Resp. Cell Mol. https://doi.org/10.1165/rcmb.2024-0256OC.
24. Wang, W., Zhang, Y., Dettinger, P., Reimann, A., Kull, T., Loeffler, D., Manz, M.G., Lengerke, C., and Schroeder, T. (2021). Cytokine combinations for human blood stem cell expansion induce cell-type- and cytokine-specific signaling dynamics. Blood *138*, 847–857. https://doi.org/10.1182/blood.2020008386.
25. Kinoshita, N., Hashimoto, Y., Yasue, N., Suzuki, M., Cristea, I.M., and Ueno, N. (2020). Mechanical stress regulates epithelial tissue integrity and stiffness through the FGFR/Erk2 signaling pathway during embryogenesis. Cell Rep. *30*, 3875–3888.E3. https://doi.org/10.1016/j.celrep.2020.02.074.
26. Moreno, E., Valon, L., Levillayer, F., and Levayer, R. (2019). Competition for Space Induces Cell Elimination through Compaction-Driven ERK Downregulation. Curr. Biol. *29*, 23–34.E8. https://doi.org/10.1016/j.cub.2018.11.007.
27. Aikin, T.J., Peterson, A.F., Pokrass, M.J., Clark, H.R., and Regot, S. (2020). MAPK activity dynamics regulate non-cell autonomous effects of oncogene expression. Elife *9*, e60541. https://doi.org/10.7554/eLife.60541.
28. Gagliardi, P.A., Dobrzyński, M., Jacques, M.-A., Dessauges, C., Ender, P., Blum, Y., Hughes, R.M., Cohen, A.R., and Pertz, O. (2021). Collective ERK/Akt activity waves orchestrate epithelial homeostasis by driving apoptosis-induced survival. Dev. Cell *56*, 1712–1726.E6. https://doi.org/10.1016/j.devcel.2021.05.007.
29. Young, M.D., Wakefield, M.J., Smyth, G.K., and Oshlack, A. (2010). Gene ontology analysis for RNA-seq: accounting for selection bias. Genome Biol. *11*, R14. https://doi.org/10.1186/gb-2010-11-2-r14.
30. Mitchel, J.A., Das, A., O'Sullivan, M.J., Stancil, I.T., DeCamp, S.J., Koehler, S., Ocaña, O.H., Butler, J.P., Fredberg, J.J., Nieto, M.A., et al. (2020). In primary airway epithelial cells, the unjamming transition is distinct from the epithelial-to-mesenchymal transition. Nat. Commun. *11*, 5053. https://doi.org/10.1038/s41467-020-18841-7.
31. Zeldovich, V.B., Robbins, J.R., Kapidzic, M., Lauer, P., and Bakardjiev, A.I. (2011). Invasive extravillous trophoblasts restrict intracellular growth and spread of Listeria monocytogenes. PLoS Pathog. *7*, e1002005. https://doi.org/10.1371/journal.ppat.1002005.
32. Ortega, F.E., Rengarajan, M., Chavez, N., Radhakrishnan, P., Gloerich, M., Bianchini, J., Siemers, K., Luckett, W.S., Lauer, P., Nelson, W.J., and Theriot, J.A. (2017). Adhesion to the host cell surface is sufficient to mediate Listeria monocytogenes entry into epithelial cells. Mol. Biol. Cell *28*, 2945–2957. https://doi.org/10.1091/mbc.E16-12-0851.
33. Pond, K.W., Morris, J.M., Alkhimenok, O., Varghese, R.P., Cabel, C.R., Ellis, N.A., Chakrabarti, J., Zavros, Y., Merchant, J.L., Thorne, C.A., and Paek, A.L. (2022). Live-cell imaging in human colonic monolayers reveals ERK waves limit the stem cell compartment to maintain epithelial homeostasis. Elife *11*, e78837. https://doi.org/10.7554/eLife.78837.
34. Komatsu, N., Aoki, K., Yamada, M., Yukinaga, H., Fujita, Y., Kamioka, Y., and Matsuda, M. (2011). Development of an optimized backbone of FRET biosensors for kinases and GTPases. Mol. Biol. Cell *22*, 4647–4656. https://doi.org/10.1091/mbc.e11-01-0072.
35. Bazellières, E., Conte, V., Elosegui-Artola, A., Serra-Picamal, X., Bintanel-Morcillo, M., Roca-Cusachs, P., Muñoz, J.J., Sales-Pardo, M., Guimerà, R., and Trepat, X. (2015). Control of cell–cell forces and collective cell dynamics by the intercellular adhesome. Nat. Cell Biol. *17*, 409–420. https://doi.org/10.1038/ncb3135.
36. Kasper, C.A., Sorg, I., Schmutz, C., Tschon, T., Wischnewski, H., Kim, M.L., and Arrieumerlou, C. (2010). Cell-cell propagation of NF-kappaB transcription factor and MAP kinase activation amplifies innate immunity against bacterial infection. Immunity *33*, 804–816. https://doi.org/10.1016/j.immuni.2010.10.015.
37. Köhler, H., Rodrigues, S.P., and McCormick, B.A. (2002). Shigella flexneri Interactions with the Basolateral Membrane Domain of Polarized Model Intestinal Epithelium: Role of Lipopolysaccharide in Cell Invasion and in Activation of the Mitogen-Activated Protein Kinase ERK. Infect. Immun. *70*, 1150–1158. https://doi.org/10.1128/iai.70.3.1150-1158.2002.
38. Beerli, C., Yakimovich, A., Kilcher, S., Reynoso, G.V., Fläschner, G., Müller, D.J., Hickman, H.D., and Mercer, J. (2019). Vaccinia virus hijacks EGFR signalling to enhance virus spread through rapid and directed infected cell motility. Nat. Microbiol. *4*, 216–225. https://doi.org/10.1038/s41564-018-0288-2.
39. Witowski, A., Palmowski, L., Rahmel, T., Nowak, H., Ehrentraut, S.F., Putensen, C., von Groote, T., Zarbock, A., Babel, N., Anft, M., et al. (2024). Activation of the MAPK network provides a survival advantage during the course of COVID-19-induced sepsis: a real-world evidence analysis of a multicenter COVID-19 Sepsis Cohort. Infection. https://doi.org/10.1007/s15010-024-02325-7.
40. Farahani, P.E., Lemke, S.B., Dine, E., Uribe, G., Toettcher, J.E., and Nelson, C.M. (2021). Substratum stiffness regulates Erk signaling dynamics through receptor-level control. Cell Rep. *37*, 110181. https://doi.org/10.1016/j.celrep.2021.110181.
41. Aparicio-Yuste, R., Muenkel, M., Clark, A.G., Gómez-Benito, M.J., and Bastounis, E.E. (2022). A Stiff Extracellular Matrix Favors the Mechanical Cell Competition that Leads to Extrusion of Bacterially-Infected Epithelial Cells. Front. Cell Dev. Biol. *10*, 912318. https://doi.org/10.3389/fcell.2022.912318.
42. Hiratsuka, T., Fujita, Y., Naoki, H., Aoki, K., Kamioka, Y., and Matsuda, M. (2015). Intercellular propagation of extracellular signal-regulated kinase activation revealed by in vivo imaging of mouse skin. Elife *4*, e05178. https://doi.org/10.7554/eLife.05178.
43. Werle, M., Schmal, U., Hanna, K., and Kreuzer, J. (2002). MCP-1 induces activation of MAP-kinases ERK, JNK and p38 MAPK in human endothelial cells. Cardiovasc. Res. *56*, 284–292. https://doi.org/10.1016/S0008-6363(02)00600-4.
44. Tschumperlin, D.J., Dai, G., Maly, I.V., Kikuchi, T., Laiho, L.H., McVittie, A.K., Haley, K.J., Lilly, C.M., So, P.T.C., Lauffenburger, D.A., et al. (2004). Mechanotransduction through growth-factor shedding into the extracellular space. Nature *429*, 83–86. https://doi.org/10.1038/nature02543.
45. Sullivan, B., Light, T., Vu, V., Kapustka, A., Hristova, K., and Leckband, D. (2022). Mechanical disruption of E-cadherin complexes with epidermal growth factor receptor actuates growth factor-dependent signaling. Proc. Natl. Acad. Sci. USA *119*, e2100679119. https://doi.org/10.1073/pnas.2100679119.
46. De Belly, H., Stubb, A., Yanagida, A., Labouesse, C., Jones, P.H., Paluch, E.K., and Chalut, K.J. (2021). membrane tension gates ERK-mediated regulation of pluripotent cell fate. Cell Stem Cell *28*, 273–284.e6. https://doi.org/10.1016/j.stem.2020.10.018.
47. Guo, W.h., and Wang, Y.l. (2007). Retrograde fluxes of focal adhesion proteins in response to cell migration and mechanical signals. Mol. Biol. Cell *18*, 4519–4527. https://doi.org/10.1091/mbc.e07-06-0582.
48. Shiau, C.E., Kaufman, Z., Meireles, A.M., and Talbot, W.S. (2015). Differential requirement for irf8 in formation of embryonic and adult macrophages in zebrafish. PLoS One *10*, e0117513. https://doi.org/10.1371/journal.pone.0117513.
49. Perez-Riverol, Y., Bai, J., Bandla, C., García-Seisdedos, D., Hewapathirana, S., Kamatchinathan, S., Kundu, D.J., Prakash, A., Frericks-Zipper, A., Eisenacher, M., et al. (2022). The PRIDE database resources in 2022: a hub for mass spectrometry-based proteomics evidences. Nucleic Acids Res. *50*, D543–D552. https://doi.org/10.1093/nar/gkab1038.
50. Bernardini, M.L., Mounier, J., d'Hauteville, H., Coquis-Rondon, M., and Sansonetti, P.J. (1989). Identification of icsA, a plasmid locus of Shigella flexneri that governs bacterial intra- and intercellular spread through

interaction with F-actin. Proc. Natl. Acad. Sci. USA *86*, 3867–3871. https://doi.org/10.1073/pnas.86.10.3867.

51. Perez, T.D., Tamada, M., Sheetz, M.P., and Nelson, W.J. (2008). Immediate-early signaling induced by E-cadherin engagement and adhesion. J. Biol. Chem. *283*, 5014–5022. https://doi.org/10.1074/jbc.M705209200.
52. Ellett, F., Pase, L., Hayman, J.W., Andrianopoulos, A., and Lieschke, G.J. (2011). mpeg1 promoter transgenes direct macrophage-lineage expression in zebrafish. Blood *117*, e49–e56. https://doi.org/10.1182/blood-2010-10-314120.
53. Kawabata, N., and Matsuda, M. (2016). cell density-dependent increase in tyrosine-monophosphorylated ERK2 in MDCK cells expressing active Ras or Raf. PLoS One *11*, e0167940. https://doi.org/10.1371/journal.pone.0167940.
54. Schindelin, J., Arganda-Carreras, I., Frise, E., Kaynig, V., Longair, M., Pietzsch, T., Preibisch, S., Rueden, C., Saalfeld, S., Schmid, B., et al. (2012). Fiji: an open-source platform for biological-image analysis. Nat. Methods *9*, 676–682.
55. Cox, J., and Mann, M. (2008). MaxQuant enables high peptide identification rates, individualized p.p.b.-range mass accuracies and proteome-wide protein quantification. Nat. Biotechnol. *26*, 1367–1372. https://doi.org/10.1038/nbt.1511.
56. Tyanova, S., Temu, T., Sinitcyn, P., Carlson, A., Hein, M.Y., Geiger, T., Mann, M., and Cox, J. (2016). The Perseus computational platform for comprehensive analysis of (prote)omics data. Nat. Methods *13*, 731–740. https://doi.org/10.1038/nmeth.3901.
57. Franceschini, A., Szklarczyk, D., Frankild, S., Kuhn, M., Simonovic, M., Roth, A., Lin, J., Minguez, P., Bork, P., Von Mering, C., and Jensen, L.J. (2013). STRING v9. 1: protein-protein interaction networks, with increased coverage and integration. Nucleic Acids Res. *41*, D808–D815. https://doi.org/10.1093/nar/gks1094.
58. Wilkinson, L. (2011). ggplot2: Elegant Graphics for Data Analysis (Springer).
59. Mostowy, S., Boucontet, L., Mazon Moya, M.J., Sirianni, A., Boudinot, P., Hollinshead, M., Cossart, P., Herbomel, P., Levraud, J.P., and Colucci-Guyon, E. (2013). The zebrafish as a new model for the in vivo study of Shigella flexneri interaction with phagocytes and bacterial autophagy. PLoS Pathog. *9*, e1003588. https://doi.org/10.1371/journal.ppat.1003588.
60. Bastounis, E.E., Radhakrishnan, P., Prinz, C.K., and Theriot, J.A. (2021). Volume measurement and biophysical characterization of mounds in epithelial monolayers after intracellular bacterial infection. STAR Protoc. *2*, 100551. https://doi.org/10.1016/j.xpro.2021.100551.
61. Pentecost, M., Kumaran, J., Ghosh, P., and Amieva, M.R. (2010). Listeria monocytogenes Internalin B activates junctional endocytosis to accelerate intestinal invasion. PLoS Pathog. *6*, e1000900. https://doi.org/10.1371/journal.ppat.1000900.
62. Wang, X., Merkel, M., Sutter, L.B., Erdemci-Tandogan, G., Manning, M.L., and Kasza, K.E. (2020). Anisotropy links cell shapes to tissue flow during convergent extension. Proc. Natl. Acad. Sci. USA *117*, 13541–13551. https://doi.org/10.1073/pnas.1916418117.
63. Gui, L., and Wereley, S.T. (2002). A correlation-based continuous window-shift technique to reduce the peak-locking effect in digital PIV image evaluation. Exp. Fluids *32*, 506–517. https://doi.org/10.1007/s00348-001-0396-1.
64. Angelini, T.E., Hannezo, E., Trepat, X., Fredberg, J.J., and Weitz, D.A. (2010). Cell migration driven by cooperative substrate deformation patterns. Phys. Rev. Lett. *104*, 168104. https://doi.org/10.1103/PhysRevLett.104.168104.
65. del Álamo, J.C., Meili, R., Alonso-Latorre, B., Rodríguez-Rodríguez, J., Aliseda, A., Firtel, R.A., and Lasheras, J.C. (2007). Spatio-temporal analysis of eukaryotic cell motility by improved force cytometry. Proc. Nat. Acad. Sci. USA *104*, 13343–13348. https://doi.org/10.1073/pnas.0705815104.
66. Bastounis, E.E., Ortega, F.E., Serrano, R., and Theriot, J.A. (2018). a multi-well format polyacrylamide-based assay for studying the effect of extracellular matrix stiffness on the bacterial infection of adherent cells. J. Vis. Exp. *137*, 57361. https://doi.org/10.3791/57361.
67. Muenkel, M., Aparicio-Yuste, R., Tal, M.C., Kraiczy, P., and Bastounis, E.E. (2022). Spatiotemporal characterization of endothelial cell motility and physical forces during exposure to Borrelia burgdorferi. STAR Protoc. *3*, 101832. https://doi.org/10.1016/j.xpro.2022.101832.
68. Yuste, R.A., Muenkel, M., Axarlis, K., Gómez Benito, M.J., Reuss, A., Blacker, G., Tal, M.C., Kraiczy, P., and Bastounis, E.E. (2022). Borrelia burgdorferi modulates the physical forces and immunity signaling in endothelial cells. iScience *25*, 104793. https://doi.org/10.1016/j.isci.2022.104793.
69. Bastounis, E., Meili, R., Álvarez-González, B., Francois, J., del Álamo, J.C., Firtel, R.A., and Lasheras, J.C. (2014). Both contractile axial and lateral traction force dynamics drive amoeboid cell motility. J. Cell Biol. *204*, 1045–1061. https://doi.org/10.1083/jcb.201307106.
70. Tambe, D.T., Hardin, C.C., Angelini, T.E., Rajendran, K., Park, C.Y., Serra-Picamal, X., Zhou, E.H., Zaman, M.H., Butler, J.P., Weitz, D.A., et al. (2011). Collective cell guidance by cooperative intercellular forces. Nat. Mater. *10*, 469–475. https://doi.org/10.1038/nmat3025.
71. Zittlau, K.I., Lechado-Terradas, A., Nalpas, N., Geisler, S., Kahle, P.J., and Macek, B. (2022). temporal analysis of protein ubiquitylation and phosphorylation during parkin-dependent mitophagy. Mol. Cell. Proteomics *21*, 100191. https://doi.org/10.1016/j.mcpro.2021.100191.
72. Boersema, P.J., Raijmakers, R., Lemeer, S., Mohammed, S., and Heck, A.J.R. (2009). Multiplex peptide stable isotope dimethyl labeling for quantitative proteomics. Nat. Protoc. *4*, 484–494. https://doi.org/10.1038/nprot.2009.21.
73. Gonzalez-Valverde, I., and Garcia-Aznar, J.M. (2017). A hybrid computational model to explore the topological characteristics of epithelial tissues. Int. J. Numer. Method Biomed. Eng *33*, e2877. https://doi.org/10.1002/cnm.2877.
74. Sarkar, D., Gompper, G., and Elgeti, J. (2021). A minimal model for structure, dynamics, and tension of monolayered cell colonies. Commun. Phys. *4*, 36. https://doi.org/10.1038/s42005-020-00515-x.

STAR★METHODS

KEY RESOURCES TABLE

REAGENT or RESOURCE	SOURCE	IDENTIFIER
Antibodies		
Anti-EGFR rabbit antibody	Cell Signaling	Cat#4267;RRID:AB_2797654
Anti-pEGFR rabbit antibody	Cell Signaling	Cat#3777;RRID:AB_2096270
Anti-pERK1/2 rabbit antibody	Cell Signaling	Cat#9101;RRID:AB_331646
Anti-ERK mouse antibody	BD Biosciences	Cat#610124;RRID:AB_397530
Anti-pMEK1/2 rabbit antibody	Cell Signaling	Cat#9121;RRID:AB_331648
Anti-MEK1/2 rabbit antibody	Cell Signaling	Cat#9122;RRID:AB_823567
Human anti-GAPDH antibody	Bio-Rad	Cat#12004168;RRID:AB_2941791
IRDye 680RD Goat anti-mouse	Li-Cor	Cat#92568070;RRID:AB_2651128
IRDye 800CW Goat anti-rabbit	Li-Cor	Cat#92632211;RRID:AB_621843
Bacterial and virus strains		
L. monocytogenes: *L.m.*-ActAp:mTagRFP	Ortega et al.[32]	N/A
L. monocytogenes: *L.m.*-GFP	Ortega et al.[32]	N/A
S. flexneri M90T	Bernardini et al.[50]	N/A
Chemicals, peptides, and recombinant proteins		
DMEM	Thermo Fisher	Cat#41965039
FluoroBrite DMEM	Thermo Fisher	Cat#A1896701
Phosphate buffered saline (PBS)	Thermo Fisher	Cat#10010023
Fetal bovine serum (FBS)	Thermo Fisher	Cat#10270106
L-glutamine	PanReac-AppliChem	Cat#A3704
Blasticidin S	Sigma	Cat#SBR00022
MS-222 (tricaine)	Sigma-Aldrich	Cat#A5040
PTU	Sigma-Aldrich	Cat#P7629
BBL Brain Heart Infusion (BHI)	BD	Cat#211059
Difco Agar, granulated	BD	Cat#214530
Streptomycin sulfate	Thermo Fisher	Cat#455340050
Chloramphenicol	Corning	Cat#56-75-7
Gentamicin	Fisher	Cat#15820243
Tryptone soya agar (TSA)	Sigma-Aldrich	Cat#22091
Carbenicillin	Sigma-Aldrich	Cat#C1389
Congo red solution	Sigma-Aldrich	Cat# C6767
Tryptone soya broth (TSB)	Sigma-Aldrich	Cat#T8907
Phenol red	Sigma-Aldrich	Cat#P0290
Polyvinyl-pyrrolidone (PVP)	Sigma-Aldrich	Cat#PVP40
NaCl	Sigma	Cat#S7653
KCl	Sigma	Cat#P9541
CaCl dihydrate	Sigma	Cat#21102
MgSO4 hexahydrate	Sigma	Cat#M2670
MEK inhibitor PD0325901	Sigma	Cat#PZ0162
Dimethyl sulfoxide (DMSO)	Sigma	Cat#D2650
Low-melting point agarose	Thermo Fisher	Cat#R0801
Sulfo-SANPAH	Fisher	Cat#10474005
Collagen I, rat tail	Thermo Fisher	Cat#A1048301
Phorbol 12-myristate 13-acetate (PMA)	Sigma	Cat#P1585

(*Continued on next page*)

Continued

REAGENT or RESOURCE	SOURCE	IDENTIFIER
MEK inhibitor trametinib	Selleckchem	Cat#S2673
Human EGF	Sigma	Cat#E9644
EGFR inhibitor PD153035	Sigma	Cat#SML0564
Hoechst 33342	Invitrogen	Cat#H3570
Formaldehyde 16% methanol-free	Thermo Fisher	Cat#28906
Bovine serum albumin (BSA)	AppliChem	Cat#A6588
(3-Aminopropyl)triethoxysilane	Sigma	Cat#A3648
40% Acrylamide	Sigma	Cat#A4058-100ML
Bis-acrylamide solution (2%w/v)	Fisher Scientific	Cat#BP1404-250
FluoSpheres carboxylate-modified microspheres, 0.2 μm, yellow-green fluorescent (505/515)	Invitrogen	Cat#F8803
Ammonium persulfate	Fisher	Cat#BP17925
TEMED	Sigma	Cat#T9281-25ML
HEPES, free acid	J.T. Baker	Cat#4018-04
0.25% trypsin-EDTA, phenol red	Thermo Fisher	Cat#25200056
Benzonase	Merck	Cat#70746
SCH772984	Selleckchem	Cat# S7156
Marimastat	Selleckchem	Cat# S7156
Deposited data		
Phosphoproteomic data	This paper	ProteomeXchange, PRIDE: PXD055809
Experimental models: Cell lines		
MDCK II	Perez et al.[51]	N/A
MDCK II E-cadherin-GFP	Perez et al.[51]	N/A
Experimental models: Organisms/strains		
WT AB strain zebrafish	Ellett et al.[52]	N/A
Recombinant DNA		
pT2A-EKAREV-NLS plasmid	Kawabata et al.[53]	N/A
Software and algorithms		
Fiji	Schindelin et al.[54]	RRID:SCR_002285 https://imagej.net/
MATLAB	The MathWorks Inc.	RRID:SCR_001622 https://de.mathworks.com/products/matlab.html
GraphPad Prism	GraphPad	RRID:SCR_002798 http://www.graphpad.com/scientific-software/prism/
NIS-Elements software package	Nikon	RRID:SCR_014329 https://www.nikoninstruments.com/Products/Software
Igor Pro	WaveMetrics, Lake Oswego, OR, USA	RRID:SCR_000325 http://www.wavemetrics.com/products/igorpro/igorpro.htm
MaxQuant software suite (version 1.6.14.0)	Cox et al.[55]	RRID:SCR_014485 https://www.maxquant.org/
Perseus software (version 1.6.3.2)	Tyanova et al.[56]	RRID:SCR_015753 https://maxquant.net/perseus/
STRING software	Franceschini et al.[57]	RRID:SCR_005223 http://string.embl.de/

(*Continued on next page*)

Continued

REAGENT or RESOURCE	SOURCE	IDENTIFIER
R package ggplot2	Wilkinson et al.[58]	RRID:SCR_014601 https://cran.r-project.org/web/packages/ggplot2/index.html
ERK waves analysis using ARCOS	This paper	https://doi.org/10.5281/zenodo.14287824
Calculation of volume of extruded infected cells	This paper	https://doi.org/10.5281/zenodo.14287679
Calculation of infection focus area	This paper	https://doi.org/10.5281/zenodo.14287812
Cell kinematics analysis	This paper	https://doi.org/10.5281/zenodo.7155531
Monolayer stresses calculation	Aparicio-Yuste et al.[68]	https://doi.org/10.5281/zenodo.7155523
Hybrid computational model	This paper	https://doi.org/10.5281/zenodo.14289212

EXPERIMENTAL MODEL AND STUDY PARTICIPANT DETAILS

Mammalian cell culture

Epithelial type II Madin-Darby Canine Kidney (MDCK) cells (originally provided by Nelson lab, Stanford University) were cultured in high glucose DMEM medium (Thermo Fisher, 41965039) containing 4.5 g/L glucose and supplemented with 10% fetal bovine serum (FBS, Thermo Fisher, 10270106) in a 5% CO_2 humidified incubator at 37°C. The cell passages were between P10-P50. During image acquisition, the cells were cultured under the same conditions as indicated above, except that FluoroBrite DMEM (Thermo Fisher, A1896701) supplemented with 580 mg/L L-glutamine (PanReac-AppliChem, A3704) and 10% FBS was used as cell culture medium. To image the localization of E-cadherin over time with live-cell time-lapse microscopy, we used type II MDCK E-cadherin GFP expressing cells (MDCK E-cadherin-GFP, kindly provided by the Nelson lab, Stanford University).[51] For FRET-based time-lapse imaging of ERK activity in the nuclei of MDCK cells, we used cells transfected with the pT2A-EKAREV-NLS (kindly provided by Hirashima lab, Mechanobiology Institute, Singapore).[15,34,53]

Establishment of MDCK cells expressing the FRET-based ERK activity biosensor

For the establishment of EKAREV-NLS-expressing MDCK cells, type II MDCK cells were transfected with the plasmid pT2A-EKAREV-NLS using the Neon transfection system (Invitrogen, MPK5000). Briefly, type II MDCK cells were resuspended in the resuspension buffer at a concentration of $1x10^6$ cells in 100 μL and gently pipetted to get a single-cell suspension. Twenty-four-well glass bottom plates were filled with 0.5 mL of complete cell culture medium and preincubated in the incubator at 37°C with 5% CO_2. Ten microliters of the plasmid at a concentration of 1.5 μg/mL was added in the cell suspension and cells were electroporated in 10-μL tips using the following electroporation parameters: pulse voltage: 1650 V; pulse width: 20 ms; pulse number: 1. Following electroporation, the 10 μL of cell and plasmid suspension was added in one well of the 24-well plate. Medium was replenished the following day and two days later when cells had proliferated, 10 μg/mL blasticidin (Sigma, SBR00022) was added for selection. Once cells formed a monolayer, fluorescence microscopy was used to confirm that approximately 90% of cells were expressing the plasmid. To obtain a pure population of MDCK cells expressing the pT2A-EKAREV-NLS plasmid the transfected cells were flow-sorted with the MA900 cell sorter. Thereon, the cells were propagated in medium always supplemented with 10 μg/mL of blasticidin.

Bacterial strains used in this study

The *Listeria monocytogenes* (*L.m.*) strains used in this study are as follows: JAT607 (Species: *L.m.* 1043S, Genotype/Description: ActApmTagRFP),[32] and JAT605 (Species: *L.m.* 1043S, Genotype/Description: Constitutive GFP).[32] The *Shigella flexneri* (*S.f.*) strain used in this study is *S.f.* srv. 5a str. M90T constitutively expressing mCherry.[59]

Zebrafish larvae used in this study

Animal experiments were performed according to the Animals (Scientific Procedures) Act 1986 and approved by the Home Office (Project license: PPL P4E664E3C). Zebrafish embryos were obtained by natural spawning, and larvae were maintained at 28.5°C in E3 embryo medium unless otherwise stated. E3 medium contained 5 mM NaCl (Sigma, S7653), 0.17 mM KCl (Sigma, P9541), 0.33 mM CaCl dihydrate (Sigma, 21102), and 0.33 mM MgSO4 hexahydrate (Sigma, M2670) in distilled water. The AB wildtype zebrafish strain was used. For injections and live imaging, embryos were anesthetized in 200 μg/mL MS-222 (tricaine) (Sigma-Aldrich, A5040) in E3 and recovered into fresh E3 supplemented with 0.036 g/L PTU (Sigma-Aldrich, P7629).

METHOD DETAILS

Bacterial infections of MDCK cells in monolayer

Listeria monocytogenes (*L.m.*) infection of MDCK cells in monolayer was performed as described previously[60] using the *L.m.* 10403S strain JAT607 ActApmTagRFP. This strain expresses mTagRFP under the control of the ActA promoter, which is activated once the

bacteria have invaded the host cell, leading to intracellular fluorescent bacteria approximately 4 hpi.[5] In few assays where an alternative fluorescent protein was needed (e.g., when staining cells with propidium iodine to assess cell death), infection was done using the 10403S *L.m.* strain constitutively expressing GFP.[61] Briefly, the bacteria were streaked out from a frozen glycerol stock onto BHI (BD, 211059) agar (BD, 214530) plates with 0.2 mg/mL streptomycin (Thermo Fisher Scientific, 455340050) and 7.5 μg/mL chloramphenicol (Corning, 56-75-7) and then maintained at 37°C for 2 days. To get flagellated *L.m.* prior to infection, cultures of 2 mL of 37 g/L BHI, 0.2 mg/mL streptomycin and 7.5 μg/mL chloramphenicol were inoculated from colonies on the BHI agar plates, and kept in the dark at room temperature without shaking for ∼16 h, that is, until the cultures had reached an optical density (OD_{600}) of approximately 0.5. Afterward, the cultures were centrifuged at 2000 x *g* at room temperature for 5 min and resuspended in 2.5 mL DMEM cell culture medium. The bacterial L.*m.*-suspension was diluted 1:16 in medium to get a multiplicity of infection (MOI) of 100–200 bacteria/host cell, as determined by plating different dilutions of the *L.m.*-suspension on BHI agar plates and counting the colonies formed after 1–2 days. The volume of *L.m.*-suspension added on the cell monolayers depended on the assay: we used 0.25 mL per 24-well transwell insert, 1 mL per 24-well plate well, 1.5 mL per AFM cell culture dish, 2 mL per 6-well plate well, and 12 mL per T-175 flask. The confluent host cell monolayers were incubated with the *L.m.*-suspension in a 5% CO_2 humidified incubator at 37°C for 30 min. Afterward, host cells were washed four times with phosphate buffered saline (PBS, Thermo Fisher, 10010023) and finally DMEM was added containing 20 μg/mL gentamicin (Fisher, 15820243).

The *Shigella flexneri* (*S.f.*) infection was performed like *L.m.*-infections with pathogen specific modifications. The *S.f.* strain srv. 5a str. M90T constitutively expressing mCherry was streaked out from a frozen glycerol stock on 40 g/L tryptone soya agar (TSA, Sigma-Aldrich, 22091) with 100 μg/mL carbenicillin (Sigma-Aldrich, C1389) and 1% Congo red solution (Sigma-Aldrich, C6767) which identifies colonies containing the virulence plasmid. For the overnight culture, 5 mL of tryptone soya broth (TSB, Sigma-Aldrich, T8907) containing 100 μg/mL carbenicillin were inoculated with a virulent red colony. The bacterial *S.f.*-suspension for infection was prepared 2–2.5 h before infection by inoculating 100 μL of *S.f.* overnight culture in 5 mL TSB containing 100 μg/mL of carbenicillin, followed by incubation at 37°C and 200 rpm until the cultures reached an OD_{600} of about 0.6 (1.5–2 h). As with infection of MDCK with *L.m.*, 100% confluent MDCK cell monolayers were infected with 1 mL *S.f.*-infection mix, which corresponded to a MOI of 5 bacteria/host cell. This was followed by centrifugation at 200 x *g* for 10 min, incubation for 30 min, washing away extracellular bacteria four times and finally adding medium containing 50 μg/mL of gentamicin, to ensure killing of extracellular bacteria in the cell culture medium that might result from lysis of infected cells. The MDCK monolayers were only infected for 16 h before being fixed, since we found that *S.f.* spread intercellularly faster than *L.m*. and first extruded infected cells were observed at approx. 6 hpi as opposed to approx. 15 h when infected with *L.m.*

Injection of zebrafish larvae tail fin with *S.f*

S.f. cultures for injection were prepared as mentioned earlier, with minor adjustments. Following overnight growth, 5 mL of TSB containing 100 μg/mL of carbenicillin was inoculated with 100 μL of the overnight culture and incubated at 37°C, shaking at 200 rpm until the OD_{600} reached approximately 0.3-0.5. Bacteria were then pelleted by centrifugation at 4000 x *g* for 4 min at room temperature. Bacteria were washed in PBS resuspended in a mixture of phenol red (Sigma-Aldrich, P0290) and polyvinyl-pyrrolidone (PVP, Sigma-Aldrich, PVP40) (final concentration 0.25% phenol red and 2% PVP) to a concentration of 10,000 CFU/nL. Embryos were injected into the tail fin with 1–2 nL of inoculum and recovered into petri dishes containing either E3 + 41 μM PD0325901 (Sigma, PZ0162) or E3 + DMSO (Sigma, D2650) as a vehicle control. At 6 hpi, *S.f.* infected embryos were immobilized in 1% low-melting point agarose (Thermo Fisher, R0801) and positioned on glass-bottom MatTek dishes. Imaging was performed with a Zeiss LSM 880 with Fast Airyscan and 63x/1.4 NA oil objective. For fixed samples, *S.f.* infected embryos were collected at 6 hpi and fixed in 4% methanol-free paraformaldehyde (PFA, Thermo Fisher, 28906) at 4°C overnight. Embryos were washed in PBS and imaged as above.

Reagents for pharmacological perturbations

Pharmacological perturbations were applied on MDCK cells at 4 hpi or later when indicated, by replacing the cell culture medium with medium containing either vehicle control or the indicated pharmacological inhibitor or molecule. For MEK inhibition, we cultured cells in 50 μM PD0325901. Stock concentration was 41 mM in DMSO, and we used as vehicle control the same volume of DMSO. ERK was activated in cell culture with 200 nM Phorbol 12-Myristate 13-Acetate (PMA, Sigma, P1585) and stock concentration was 1.62 mM in DMSO. Trametinib (MEK inhibitor, Selleckchem, S2673) concentration used in cell culture was 200 nM and the stock concentration was 10 mM. EGF (Sigma, E9644-.2MG) was used in cell culture at a concentration of 10 and 25 ng/mL and the stock concentration was 10 μg/mL. PD153035 (EGFR inhibitor, Sigma, SML0564-5MG) was used in cell culture at a concentration of 4 μM and stock concentration was 5 mM in DMSO.

Fixation of MDCK cells and quantitative microscopy for calculation of infection mound volume, infection focus area, and total bacterial fluorescence intensity

For analysis of infection foci, MDCK cell nuclei were stained by replacing the medium with 5 μg/mL Hoechst (Invitrogen, H3570) containing cell culture medium at 4 hpi (more details in section "Bacterial infections of MDCK cells in monolayer"). Samples were incubated at 37°C and 5% CO_2 for 10 min. Subsequently, samples were washed once with pre-warmed PBS and cell culture medium containing 20 μg/mL of gentamicin was added. The samples were fixed 24 hpi or 16 hpi for *L.m.*- or *S.f.*- infected MDCK samples,

respectively, by carefully washing once with warm PBS, then adding 500 μL of 4% PFA diluted in PBS per well for 10 min, followed by washing with and storing the samples in PBS at 4°C until imaging.

For 3D imaging of infection mounds different spinning disk confocal microscopes were used, depending on where and when the experiments where performed. Infection mounds (resulting from *L.m.* infection) were initially imaged with a Zeiss AxioObserver SD Spinning Disk microscope, with an Axiocam 503 mono CCD camera and a Plan-Apochromat 40x/1.4 NA Oil DIC objective (University of Stuttgart). Samples infected with *L.m.* and treated with TPA, EGF, PMA, trametinib, and the EGFR inhibitor were imaged with our newly installed spinning disk confocal microscope, a Nikon Eclipse Ti2 microscope equipped with a CSU-W1 spinning disc with 50-μm Disk and a digital camera C15440 (Hamamatsu), using a 40x/1.25 NA silicon oil objective. Finally, infection mounds resulting from *S.f.* infection of MDCKs were imaged using a Zeiss LSM 880 with Fast Airyscan and 40x/1.2 NA oil immersion objectives.

In all cases described earlier and irrespective of the microscope, z stack confocal images of the bacterial fluorescence and host MDCK nuclei fluorescence were acquired with a z-spacing between 0.2 and 1 μm. Fields of view were selected so that the whole mound could be imaged in all conditions investigated. To quantify the infection mound volume (i.e., the volume occupied by collectively extruded infected cells) from the resulting images, we used custom written MATLAB (The MathWorks Inc., RRID:SCR_001622) codes available at: https://github.com/ebastoun/Infection_mound_volume. In brief, the nuclei fluorescence images were first background corrected, then binarized and finally the MATLAB function alphaShape was applied to calculate the area covered by extruded nuclei per z-plane, disregarding the basal cell monolayer. The alpha radius used was 50 px. The volume of the extruded infected cells was determined by adding up the area of each z slice and multiplying by the increment between each z slice as described previously.[41,60] The calculated mound volumes were normalized to the mean of the control condition (without pharmacological perturbations, i.e., vehicle control) for each independent experiment.

To quantify the area of the infection foci (i.e., the domain occupied by neighboring infected cells) and the total *L.m.* fluorescence intensity of the infection foci (proxy of bacterial load within each focus), we performed epifluorescence imaging of the fixed samples. We used an inverted Nikon Eclipse Ti2 microscope with a Prime 95B camera (Teledyne Photometrics) using a 40x/0.6 NA air objective and the NIS-Elements (RRID:SCR_014329) software package. The bacterial fluorescence images were analyzed with the alphaShape function (alpha radius 50 px) to infer the area of the infection foci, as described previously[5] and using custom-written codes in MATLAB available at: https://github.com/ebastoun/Infection_mound_area_over_time. The bacterial load of each infection focus was calculated by integrating the bacterial fluorescence intensity values within the infection focus area. For each independent experiment values were normalized relative to the mean of the control condition (i.e., to the condition without pharmacological perturbations).

Fixation and quantitative microscopy for characterization of cell shape

For cell shape quantification of MDCK cells in the uninfected and *L.m.*-infected monolayers, the infection assay was performed using MDCK E-cadherin-GFP cells because E-cadherin localizes at the cell-cell junctions and thus enables accurate segmentation of the cells comprising the monolayer (more details in section "Bacterial infections of MDCK cells in monolayer"). As described in the section above, the live-cell samples were Hoechst-stained and then fixed 24 hpi. Phase-contrast and epifluorescence imaging (of nuclei, E-cadherin, and bacterial fluorescence) was performed with an inverted Nikon Eclipse Ti2 microscope with a Prime 95B camera using a 20X/0.7 NA super plan fluor LWD ADM air objective and the NIS-Elements software package. The E-cadherin fluorescence images were segmented with the Fiji plugin Tissue Analyzer.[54] The segmented image was then used as input for a custom written MATLAB code to determine for each cell in the image: (1) the cell area, (2) the radial alignment angle of the major axis of the cell, (3) the aspect ratio of the cell (ratio of the length of the major axis to minor axis), (4) the shape factor determined as the ratio of the cell perimeter to square root of cell area. The radial alignment angle is defined as the angle formed between the radial direction (center of field of view which in the infected samples coincides approximately with the center of the infection focus) and direction of the major axis of the cell. Moreover, while the aspect ratio quantifies the elongation/polarization of each cell, the shape factor parameter is an indicator of the shear rigidity (or tissue fluidity) of the cells, with a shape factor of 3.81 indicating cells behaving more like solids and higher values more fluid-like cells.[62] To discriminate between infected cells and their uninfected surrounders in the *L.m.*-infected MDCK monolayers, we used the bacterial fluorescence images and cells were classified as infected if their maximum bacterial fluorescence intensity exceeded a threshold value empirically determined.

Time-lapse (FRET) microscopy imaging

To characterize cell migration and ERK activity of uninfected and *L.m.*-infected MDCK monolayers, live-cell epifluorescence microscopy imaging and FRET imaging was performed. To that end, glass-bottom 24-well plates (Cellvis, P24-1.5H-N) were coated with 30 μg/mL rat-tail collagen I at 37°C for 30 min. Then, we seeded $2*10^5$ MDCK EKAREV-NLS expressing cells per well for 24 h to form a confluent monolayer. The confluent monolayers were then infected with 1 mL/well of the bacterial *L.m.*-suspension (more details in section "Bacterial infections of MDCK cells in monolayer"). Four hpi, we washed the uninfected and *L.m.*-infected monolayers once with PBS, added FluoroBrite DMEM with pharmacological treatment or vehicle control, and started the multi-channel imaging. Phase-contrast and epifluorescence (nuclei and bacterial fluorescence) live cell imaging was performed with an inverted Nikon Eclipse Ti2 microscope with a Prime 95B camera using a 40x/0.6 NA air objective and the NIS-Elements software package. The microscope was surrounded by a box-type incubator (OKOlab) maintained at 37°C and humidified with 5% CO_2. We took images for 20–30 h every 2.5, 5, or 10 min. For FRET imaging of the ERK activity, first the CFP signal was imaged by using CFP 436/20 excitation

and 480/40 emission filters. Then, the FRET signal was imaged with CFP 436/20 excitation and YFP 535/30 emission filters. From here on, those images are referred to as CFP and FRET image, respectively. For imaging propagation of *L.m.* expressing mtagRFP, we used an mCherry filter with 560/40 excitation and 630/75 emission. For imaging of *S.f.*-infected MDCK EKAREV-NLS expressing or control uninfected cells, a similar approach was used, with the exception that a different microscopy system, the Zeiss LSM 880 with Fast Airyscan with a 20x/0.8 NA air objective, was used.

Characterization of cell kinematics and migration coordination

The time-lapse MDCK nuclei fluorescence images were used to compute the cell migration speed of the MDCK cells in monolayer and coordination of their migration. To do so, particle image velocimetry (PIV) with a window size and overlap of 48 px and 24 px, respectively, was applied on the nuclei fluorescence images.[63] We calculated the speed of migration of cells by dividing the resulting displacements to the time interval between frames, which was always 10 min. The coordination of migration was approximated by the calculation of the correlation length of movement as done previously.[64] We first calculated the spatial correlation function $C_{dd}(R)$ that averages the scalar product of all displacement vector pairs separated by a distance R. The correlation values show an exponential decay over distance that could be fitted to the function $C_{dd}(R) = \exp(-R/R_0)$, where $2R_0$ indicates the maximum non-random correlated distance.[64] The custom-written codes to calculate the correlation length were written in MATLAB and are available at: https://github.com/ebastoun/Correlation_length_of_movement_of_epithelial_cells_in_monolayer. To calculate the directionality of movement of surrounder cells and create the rose plots (Figures 3E and 3F), we tracked the movement of the cell nuclei with the Fiji v2.14.0 plugin TrackMate v7.13.2 over the duration of the time-lapse recording. The cell migration directionality angle at each instance of time was defined as the angle between the displacement of the cell nucleus, and the radial direction. For the radial direction the center of the polar coordinate system was defined either as the center of the field of view or in the case of infection as the center of the infection focus. For the construction of the histogram plots, we binned the calculated angles ranging from 0° to 180° in groups of 7.5°, where 0°/180° corresponds to a nucleus moving toward/away from the infection focus, respectively.

Characterization of ERK activity dynamics in (infected) MDCK cells in monolayer

To obtain the ERK activity in the nuclei of MDCK cells expressing EKAREV-NLS, which is represented by the FRET efficiency, the CFP (CFP/CFP) and FRET (CFP/YFP) images were background-corrected by subtracting from them the CFP and FRET fluorescence images of an empty position also imaged overtime but not containing cells. Then, the ratio of background-corrected FRET to CFP image was calculated, followed by multiplication with a binary mask of the cell nuclei to exclude regions not containing cell nuclei. That was performed with the ImageJ/Fiji binarization method ''Huang''. The resulting images containing the ERK activity in the nuclei of cells over time were further analyzed with two different approaches.

First, we created kymographs of the mean radial ERK activity as a function of distance away from the center of the field of view imaged (y axis) and over time (x axis). To that end, we moved to a radial coordinate system whose origin is at the center of the field of view imaged, which for infected samples coincides approximately with the center of the infection focus (see Figure S4F).

Second, instead of averaging ERK activity to create kymographs, for all the cells one-by-one (y axis, cell count) we plotted the median of ERK activity in the cell nucleus at each given instance of time (x axis) (Figure 4B). To that end, live-cell images were pre-processed with Fiji, and subsequent image processing was performed using a custom-written MATLAB script. Briefly, accurate nuclei segmentation and subsequent individual nucleus tracking was performed with the Stardist detector and TrackMate plugin v.7.12.2, respectively, in Fiji. Correction of false connections between nuclei in the segmentation mask was done with the ''watershed irregular features'' option, while the convexity threshold value was set to 0.99 (Biovoxxel plugin v2.6.0). A custom MATLAB script was used to read the TrackMate output file with the coordinates of each nucleus track, process the individual tracks to quantify cell orientation and match ERK intensity to nuclei tracks. The segmentation mask and ERK signal image were matched for each nucleus position at every frame. ERK activity for a single nucleus was calculated as the median of the values contained in the region of the ERK signal image defined by the segmentation mask of that nucleus. Thus, kymographic heatmaps of single cell ERK activity display ERK activity over time, where the single cell tracks of the nuclei are vertically organized by closest distance to the center of the image (Top: center; bottom: edge of the image).

We further processed the single cell ERK activity signals (code available at: https://github.com/ebastoun/Single_cell_ERK_signal_analysis) to identify clusters of ERK activated cells as well as how ERK activity propagates to neighboring cells in the form of waves. To that end, we used MATLAB v2023b and the ARCOS v0.3.0, ggplot2 v3.5.1 and sf v1.0-16 packages in R v4.4.1, as previously proposed for automatically characterizing the spatiotemporal ERK signaling patterns in cell collectives.[19] We performed this analysis in two steps. First, we performed some ERK activity signal filtering, then, the collective ERK activation events were detected and the ERK wave characteristics were quantified, as described in detail below. To accurately detect an ERK activation event in a single cell nucleus, we used a custom MATLAB script to remove the global long-term trend in ERK fluorescence intensity and also the intrinsic noise from the single cell ERK fluorescence intensity signals. The global trend was calculated with a long moving median filter (50 time points) considering the ERK signal intensity for all the cell nuclei in a given time point, and then subtracted from the single cell ERK fluorescence intensity signal. The intrinsic noise of the global-trend-filtered single cell ERK fluorescence intensity signal was calculated with a short moving median filter (30 time points) and subtracted from itself. A threshold was applied to the resulting single cell ERK fluorescence intensity signal (value of 0.02) so that values equal or higher than the threshold were considered as single cell ERK activations. The results were saved in a.csv file and then read by a custom R script to quantify the ERK activation waves with the

ARCOS algorithm as done previously.[19] Briefly, the ARCOS algorithm finds clusters of activated cell nuclei (defined as collective events) at every time point through the DBSCAN algorithm, which depends upon a search distance parameter. Then, the ARCOS algorithm groups the clusters based on its members. We chose a search distance parameter of 25.8 μm based on the distribution of distances among the cell nuclei in the first time point. For further analysis, we filtered out collective events with less than four nuclei and considered events that persist for at least two consecutive frames. Moreover, for the analysis in Figures 4D and 4E images taken from 8 to 16 hpi were considered. Using this approach we calculated (1) mean ERK activated cell cluster area for each condition under study and (2) frequency of ERK activated cell collective events, defined as the number of events per hour and normalized to the area of the field of view examined, as done previously.[19]

Polyacrylamide hydrogel fabrication and 2D traction force microscopy

How well cell-ECM adhesions are organized and connected to the underlying cytoskeleton was assessed with TFM which allows the calculation of the traction stresses that cells exert on their extracellular matrix (ECM). To perform TFM, two-layered soft elastic polyacrylamide hydrogels were prepared, where the uppermost one contained fluorescent tracer beads and was collagen I-coated to enable subsequent cell adhesion. As cells adhere, move and contract on the hydrogel, they deform it inducing traceable movement of the beads. By measuring the beads' displacements, we then calculated the traction stresses that cells exert, as described previously.[4,65,66] Using the calculated traction stresses one can infer the monolayer stresses (intra- and inter-cellular stresses) using monolayer stress microscopy, as discussed in the section below.[67,68]

Briefly, we first manufactured polayacrylamide hydrogels to serve as the cells' ECM. To that end, wells from a 24-well glass bottom plate were pretreated by incubating at room temperature with 0.5 M NaOH for 30 min, 2% APTES in 95% EtOH for 5 min and 0.5% glutaraldehyde for 30 min to 2 h, rinsed with distilled water in between each pretreating step and finally dried at 60°C. A 3 kPa stiff polyacrylamide hydrogel was prepared by mixing 5% acrylamide (Sigma, A4058-100ML) with 0.1% bis-acrylamide (Fisher BioReagents, BP1404250) in distilled water. For the preparation of the second layer, we also added 0.03% of 0.2 μm fluorescent beads to the mixture (Thermo Fisher, F8807). To initiate polymerization 0.43% TEMED (Sigma-Aldrich, 1107320100) and 0.06% ammonium persulfate (APS) were added to the first mixture. Per well, 3.6 μL of the polyacrylamide solution mixture was added on the pretreated glass surface. Immediately after, untreated 12 mm glass coverslips were pressed on top to flatten the gels. After 20 min polymerization, the glass cover slips were removed, and polymerization of the second layer mixture containing the fluorescent beads was initiated with TEMED and APS. Per well, 2.5 μL of the second layer mixture was added on top of the first layer, followed by flattening with 12 mm glass coverslips. The coverslips were removed after 20 min polymerization, the hydrogels were covered with 50 mM HEPES pH 8.5, sterilized 1h with UV, and stored at 4°C. The hydrogels were washed once with 50 mM HEPES, then activated by addition of 200 μL/well of 0.1% w/v Sulfo-SANPAH (Thermo Scientific, 10474005) with 1% DMSO in 50 mM HEPES, and UV radiation for 10 min. This was immediately followed by washing with 50 mM HEPES and addition of 200 μL/well of 0.25 mg/mL Collagen I (Thermo Fisher, A1048301) diluted in 50 mM HEPES. The plate was incubated overnight at room temperature. Before seeding of the cells on hydrogels, the hydrogels were washed with PBS and equilibrated with cell culture medium at 37°C for 30 min. To achieve confluent cell monolayers $2.5*10^5$ MDCK cells expressing EKAREV-NLS cells per well were seeded on the hydrogels and placed in a 5% CO_2 humidified incubator at 37°C. After 24 h, when MDCK had formed confluent monolayers, some wells were infected with 1 mL/well of the bacterial *L.m.*-suspension for 30 min (more details in section "Bacterial infections of MDCK cells in monolayer").

After 4 hpi, the uninfected and *L.m.*-infected monolayers were washed once with PBS and FluoroBrite DMEM with drugs or vehicle control was added, directly before the multi-channel live-cell epifluorescence microscopy imaging was to start. For imaging in all cases, we used an inverted Nikon Eclipse Ti2 microscope with a Prime 95B camera using a 40x/0.6 NA air objective and the NIS-Elements software package. The microscope was surrounded by a box-type incubator (OKOlab) maintained at 37°C, humidified and with 5% CO_2. Every 10 min for a period of 20–24 h we took the phase-contrast image of cells, the bacterial fluorescence image and the fluorescence image of the tracer beads. At the end of the TFM recording, cells were detached using 10% SDS to obtain the reference images of the fluorescent beads in the hydrogels in their undeformed configuration.

The 2D displacements of the beads were calculated in MATLAB by comparing the fluorescence bead image to the undeformed reference image at each instance of time using a method similar to particle image velocimetry (PIV).[63] The used window size and overlap of the interrogation window were 32 px and 16 px, respectively. Using these displacements the traction stresses exerted by the cell monolayers on the hydrogels were calculated in MATLAB as described before.[4,69] To differentiate the traction stresses exerted by the infected cells versus their uninfected surrounders, a custom written MATLAB code was used (available at: https://github.com/ebastoun/Infection_mound_area_over_time) to border the infected area over time. This was done with the built-in alphaShape function using an alpha radius of 50 px. With the resulting binary mask containing the area of the infected cells, the traction stresses were allocated to surrounder or infected cells.

Calculation of cell monolayer stresses

We calculated inter- and intra-cellular stresses, herein referred to as monolayer stresses, using the technique Monolayer Stress Microscopy (MSM).[70] MSM makes use of the traction forces exerted by cells on their ECM as input and assumes that these traction forces are perfectly transmitted between the monolayer and the ECM, i.e., cell-ECM adhesions are perfect. This results in cells being subjected to a force equal to traction forces but in opposite directions (third Newton's Law). Furthermore, we only consider traction forces in the plane of the monolayer, neglecting those in the vertical direction (out of plane). It is also assumed that the thickness of the

monolayer is constant and uniform. Cell-cell adhesions are assumed to be perfect (the monolayer is considered as a continuum), the mechanical properties of the monolayer are assumed to be uniform, so that cells within the monolayer can be modeled as linear elastic isotropic materials.[70] Another assumption MSM takes is that cell deformations are small, i.e., the displacements that occur between two consecutive time frames and the changes in cell shapes and areas are small. These assumptions greatly simplify the formulation of the problem, as a two-dimensional framework is adopted, with a plane stress formulation. In this case, the equilibrium equations, compatibility, and constitutive equations yield the Beltrami differential formulation. This formulation, together with Newton's equilibrium equations, formulated at each point of the monolayer in a differential way, yield the distribution of the stresses in the monolayer. The model equations are solved using the finite element formulation in a custom-built software.[68] The monolayer was discretized with square elements of size 4.5 μm × 4.5 μm, forming a finite element mesh of 10,000 elements. The Poisson's coefficient was set to 0.49. The source code is available at: https://github.com/ebastoun/Monolayer-Stress-Microscopy.

Transepithelial electrical resistance (TEER) measurements of MDCK cells in monolayer

To assess barrier integrity of (infected) MDCK cells in monolayer overtime we performed TEER measurements, using the cellZscope system (NanoAnalytics, Münster, Germany). For this, 24-well transwell inserts (0.4 μm pore size, cellQuart, 9320402) were coated with 400 μL of 30 μg/mL collagen I solution in PBS at 37°C for 30 min. This was followed by washing with PBS and seeding of $0.5*10^5$ MDCKs per insert one day before infection. Two inserts were not seeded with cells and served as blank positions. Twenty-four hours after cell seeding, when cell monolayers had formed, some were infected with 0.25 mL/insert of the bacterial *L.m.*-suspension for 30 min (more details in section "Bacterial infections of MDCK cells in monolayer"). After washing four times with PBS, all inserts were transferred from the 24-well plate to the chambers of the cellZscope system. Four hundred μL of cell culture medium supplemented with 20 μg/mL gentamicin was added in each insert and 800 μL in the chamber outside of each insert. The part of the cellZscope system containing the cells was placed in a 5% CO_2 humidified incubator at 37°C and the TEER was measured every 30 min. For drug treatment the measurement was paused 4 hpi to add 50 μM PD0325901 and DMSO as vehicle control. The TEER was monitored for 30 to 40 h.

Western blotting analysis

To determine protein expression and phosphorylation of EGFR, MEK, and ERK, in uninfected and *L.m.*-infected MDCK monolayers, western blotting was performed. First, glass-bottom 6 well plates (Cellvis, P06-1.5H-N) were coated with 2 mL of 30 μg/mL collagen I in PBS at 37°C for 30 min, washed once with PBS, and then $10*10^5$ MDCK cells/well were seeded. After 24 h, the MDCK cell monolayers were 100% confluent and were either infected with 1.5 mL/well of bacterial *L.m.*-suspension for 30 min (more details in section "Bacterial infections of MDCK cells in monolayer") or not (control uninfected monolayers). Twenty-four hours after infection, the cell samples were lysed with a buffer containing 0.5 M Tris-HCl, pH 7.4, 1.5 M NaCl, 2.5% deoxycholic acid, 10% NP-40, 10 mM EDTA and a protease inhibitor mixture (phenylmethylsulfonyl fluoride (PMSF), leupeptin, aprotinin, and sodium orthovanadate). The total cell lysate was separated on an SDS-PAGE (4% stacking, 10% running), followed by transfer onto a nitrocellulose membrane (Immobilon P, 0.45-mm pore size). Then, the membrane was incubated with the designated antibodies as follows anti-phospho-EGF receptor (EGFR, Tyr1068, Clone D7A5) rabbit monoclonal antibody (Cell Signaling, #3777, RRID:AB_2096270); anti-EGF receptor (EGFR, Clone D38B1) rabbit monoclonal antibody (Cell Signaling, #4267, RRID:AB_2797654); anti-phospho-p44/42 MAPK (Erk1/2) (Thr202/Tyr204) rabbit monoclonal antibody (Cell Signaling, #9101, RRID:AB_331646); anti-ERK (pan Erk, Clone 16/ERK) mouse monoclonal antibody (BD Biosciences, #610124, RRID:AB_397530); anti-phospho-MEK1/2 (Ser217/221) rabbit polyclonal antibody (Cell Signaling, #9121, RRID:AB_331648); anti-MEK1/2 rabbit polyclonal antibody (Cell Signaling, #9122, RRID:AB_823567); anti-GAPDH human Fab rhodamine antibody (BioRad, #12004168, RRID:AB_2941791). Immunodetection was performed using the IRDye 680RD and 800CW-labeled secondary antibodies (Li-Cor, #925–68070, RRID:AB_2651128 and #926–32211, RRID:AB_61843) under the Bio-Rad ChemiDoc imaging system. GAPDH was used as reference protein. Quantification was performed using Fiji.

To verify that 50 μM of the MEK inhibitor PD0325901 abrogates phosphorylation of ERK, we performed western blotting of *L.m.*-infected MDCK monolayers treated or not with PD0325901, using a slightly modified protocol since these experiments were performed in a different laboratory/institution. The cells were lysed 24 hpi with RIPA buffer (Thermo Fisher Scientific, 89900) supplemented with phosphatase/protease inhibitor cocktail (1:100, Cell Signaling, 5872) on ice. The lysate was transferred to precooled tubes and centrifuged at 14000 x *g* at 4°C for 20 min. The proteins in the supernatant were separated by SDS-PAGE with 15-well Bolt Mini Gels 4–12% (Invitrogen, NW04125BOX). Semi dry blotting was used to transfer the proteins from the gel to the PVDF transfer membranes (0.45 μm, Thermo Fisher, 88518). The membrane was blocked with 5% bovine serum albumin (BSA, AppliChem, A6588) in tris-buffered saline with 1% Tween (TBST) at 4°C overnight. Incubation with primary and secondary antibodies and imaging was performed as indicated in the paragraph just above.

Determination of bulk cell stiffness using atomic force microscopy (AFM)

To measure the stiffness of *L.m.*-infected cells and their uninfected surrounder cells and to compare those to the stiffness of cells originating from uninfected wells, we conducted AFM. For sample preparation, we first added 1.5 mL/dish of 30 μg/mL collagen I in PBS to glass-bottom cell culture dishes (50 mm, WPI, FD5040-100) and incubated them at 37°C for 30 min. Dishes were then washed with PBS, cells seeded with $4.6*10^5$ MDCK cells/dish and incubated for 24 h until 100% confluent monolayers had formed.

At that point, monolayers were infected with 1.5 mL/dish bacterial suspension (more details in section "Bacterial infections of MDCK cells in monolayer") or were left untreated (uninfected controls). For ERK inhibition or activation, we added 50 μM PD0325901 or 200 nM PMA to the cell culture medium at 4 hpi. After 24 hpi the AFM measurements were performed using a commercial AFM setup (MFP3D-BIO, Asylum Research, Santa Barbara, CA, USA) mounted on an inverted optical microscope (Ti-S, Nikon, Tokyo, Japan). Cantilevers with 2 μm diameter spherical tips and a nominal spring constant of 200 pN/nm (biosphere B1000-CONT, nanotools, München, Germany) were used. Before each measurement, the spring constant was calibrated using thermal calibration. Force maps (50 × 50 μm^2, 30x30 px^2) were recorded. The retract distance was set to 3 μm, the sampling rate to 2 Hz and the trigger force to 500 pN. Typical sample indentations were several hundred nanometers. Data were analyzed in Igor Pro (WaveMetrics, Lake Oswego, OR, USA, RRID:SCR_000325) using the Hertz Model. Force maps typically contained several cells. Regions of interest (ROIs) of individual cells were drawn manually and the median stiffness value for each cell was calculated.

Sample preparation for phosphoproteomics, nano LC-MS/MS analysis and data processing

Samples were prepared using the protocol for "in-solution protein digestion" as previously described for two biological replicates.[71] Briefly, to extract a high enough amount of proteins, we lysed one T175-flask (Sarstedt, 833.912.002) per condition. 100% confluent MDCK cell monolayers residing on T175-flasks (3.68x10^7 cells per flask) were infected with 12 mL of *L.m.* bacterial suspension (more details in section "Bacterial infections of MDCK cells in monolayer") or not (uninfected controls). At 4 hpi *L.m.*-infected and control monolayers were either treated with 50 μM PD0325901 or vehicle control (DMSO). Lysis of L.*m.*-infected monolayers was performed either at 8 hpi or 24 hpi, while control uninfected monolayers were lysed and collected together with the 8 hpi infected sample.

For lysis, the cells were washed once with PBS, placed on ice, and immediately after, 1 mL lysis-buffer (4% w/v sodium dodecyl sulfate (SDS), in 100 mM tris(hydroxymethyl)aminomethane (Tris)/HCl, pH 8.0, 1:100 protease/phosphatase inhibitor cocktail (Cell signaling, #5872) was added. After 10 min, the cells were scraped with a cell scraper (Sigma, CLS3010-100EA) and transferred to a falcon tube. To degrade DNA and RNA, 0.5 μL/sample benzonase (Merck, 70746) was added to the samples, which were then vortexed, incubated at room temperature for 10 min, and transferred to screw cap microtubes (Sarstedt, 72.694.700) containing 500 μL glass beads (Roth, N033.1) for homogenization. The cells were homogenized at 6.5 m/s for 40 s twice by using a FastPrep-24 (MP Biomedicals) and incubated on ice for 2 min in between. Afterward, samples were centrifuged at the maximum speed 21300 x *g* for 1 min and the supernatant was collected. For reduction of cysteine disulfide bonds, 10 mM dithiothreitol (DTT, Roth, 6908.1) was added and samples were incubated at room temperature shaking (Thermomixer C, Eppendorf) for 45 min. For alkylation of cysteine thiol groups, 5.5 mM iodoacetamide (IAA, Sigma, I6125-10G) was added and samples were incubated in dark again at room temperature shaking for 45 min. Then, the suspensions were centrifuged at 12000 x *g* for 15 min. To precipitate the proteins, the supernatant was diluted 1:8 with ice-cold acetone/methanol mixture (8:1 v/v) and incubated overnight at −20°C. The next morning, the samples were centrifuged at 1000 x *g* for 5 min, followed by washing, resuspension of the protein pellet in 80% v/v acetone aq. and thoroughly vortexing. These steps were repeated two more times. The protein pellet was air dried for 10 min, rehydrated in 100 μL denaturation buffer (6 M urea, 2 M thiourea in 10 mM Tris/HCl, pH 8), and frozen at −80°C.

For the proteome analysis, for each experiment (MDCK monolayers infected for 8 h, 24 h and uninfected) mixtures with a ratio of 1:1 of samples treated with either 50 μM PD0325901 or DMSO (vehicle control) were prepared. This resulted in a total protein amount of 600 μg, of which one part was used for proteome analysis (10 μg). Dimethyl-labeling was performed[72] followed by label efficiency and label channel mixing checks in separate LC–MS/MS runs. Phosphopeptides were enriched using MagReSyn Ti-IMAC (titanium-immobilized metal affinity chromatography, ReSyn Bioscience) in two consecutive rounds of enrichment using total amount of 600 μg proteins per mix.[71]

The phosphoproteome and proteome of all samples were analyzed on an Q Exactive HF-X mass spectrometer (Thermo Fisher Scientific). An online-coupled Easy-nLC 1200 UHPLC (Thermo Fisher Scientific) was used to separate peptides on a 20 cm analytical column (75 μm ID PicoTip fused silica emitter) in-house packed with ReproSil-Pur C18-AQ 1.9 μm resin (Dr Maisch GmbH Ltd). Phosphopeptides and dimethyl-labeled proteomes were eluted using a 90 min and a 130 min gradient, respectively.

Raw files were processed with the MaxQuant software suite (Version 1.6.14.0).[55] MS/MS data were searched against UniProt *Canis lupus familiaris* (containing 43678 entries) and *L.m.* databases, containing commonly observed contaminants. The mass tolerance for precursor ions was set to 4.5 ppm and for fragment ions to 20 p.m. All search parameters were kept to default values except for the following: dimethylation for light (28.03 Da), intermediate (32.06 Da), and heavy (36.08 Da) labels was allowed on lysine residues and peptide N termini for phosphoproteome data. For all phospho raw files, phosphorylation on STY was defined as variable modification, while oxidation of methionine and protein N-terminal acetylation were set as variable modifications. Carbamidomethylation of cysteine residues was allowed as fixed modification. All searches were performed in trypsin/P-specific digestion mode. Data analyses were performed using Perseus software (Version 1.6.2.3)[56] to identify significantly changed phosphorylation sites (Threshold $p < 0.05$). The significantly changed phosphorylation sites that occurred in at least one replicate were analyzed with STRING software to perform functional enrichment analysis.[57] The resulting significant enriched GO subcellular localizations (Compartments) were visualized in a bubble plot using the R package ggplot2.[58]

Hybrid computational model to simulate infection *in silico*

A hybrid computational model was employed to simulate a two-dimensional (2-D) epithelial cell monolayer, integrating discrete and continuum modeling approaches, namely, an agent-based model (ABM) to simulate cells as individual entities and a finite element

model (FEM) to simulate the monolayer as a continuum.[73] Both techniques are integrated in an iterative loop, thus allowing the simulation of epithelial cells in monolayer over several time steps. In this framework, cell centroids are first represented as independent particles in the ABM, which are randomly distributed in the cell monolayer. Given the distribution of cells, we compute the balance of cell forces by assuming a quasistatic equilibrium and considering cell-cell interaction forces ($F_{ji}^{cell-cell}$). These forces depend on the distance between cell centroids, and we assume that when cells are in close proximity, they repel each other (contact inhibition), whereas two cells are pulled apart, there are attractive forces acting in both cells. This force-dependent behavior is assumed to follow the Lennard-Jones potential.[74] Additionally, we consider that cells are able to sense the stresses they are subjected to, responding in an active manner by generating additional loads (mechanosensing mechanism). This cell mechanical response entails cell actomyosin contraction and cell protrusion. Regarding the actomyosin contraction force (F_i^{contr}), we assume that the greater the tensile stress sensed by a given cell is, the more the cell contracts. Regarding the protrusion load (F_i^{protr}), it is assumed that the cell protrudes in the direction of lower tensile stress, which defines the direction of polarization of the cell. The magnitude of this force is proportional to the tensile stresses acting on the cell. Finally, it is assumed that surrounder cells proximal to the infection focus (proximal surrounders) exert forces pointing toward the infection focus ($F_{k,i}^{s}$), which reproduces the migration of surrounder uninfected cells during the mechanical competition that occurs during bacterial infection with *L.m.*

Cell centroids are then used to determine the Voronoi tessellation, which provides a distribution of cell polygons in the monolayer (polygons formed by the bisection of the connecting lines between neighboring points/cell centroids). It is assumed that each cell occupies the area of the polygon associated with its centroid. These polygons are discretised with triangles to generate a finite element mesh. Due to the geometrical properties of the cell (i.e., the thickness is much lower than the in-plane dimensions) we assume that the cell monolayer can be modeled in the FEM as a plane stress model. The cell monolayer is assumed to behave as a linear elastic isotropic material. We distinguish between infected and uninfected cells with varying elastic modulus (500 Pa for uninfected cells and 250 or 500 Pa for infected cells,[8] depending on the assumed scenario) and a Poisson's ratio of 0.49 for both of them. The forces computed in the ABM are then introduced in the FEM as concentrated forces in the cell centroids and in the vertices of the Voronoi polygons. To define the boundary conditions of the cell monolayer, we assume conditions of symmetry. The forces previously computed induce new deformations in the monolayer, which causes the movement of cells. The displacements of the cell centroids and the stress distribution inside each cell are used as new inputs for the ABM in the new iteration of the loop. This process is repeated until the end of the simulated period. The evolution of cell area, cell stresses and the displacements of the cells are then compared against experimental results. The ABM is implemented through custom made MATLAB files and the FEM is calculated with the commercial software ABAQUS CAE (Dassault systèmes Simulia Corporation).

QUANTIFICATION AND STATISTICAL ANALYSIS

We performed statistical analysis with Graphpad Prism 10 (Graphpad, RRID:SCR_002798). All box plots in the manuscript (unless otherwise indicated in the corresponding figure legends) show the following: horizontal line is the distribution's median, boxes indicate the 25% and 75% quartiles, whiskers indicate the 5 and 95% quantiles. Outliers are represented as dots unless the sample size is very high in which case they are not shown (that is the case only in Figures 2C–2F). The mean parameter values per independent recording are overlayed on the box plots and indicated with a circle (e.g., Figure 6C). Always at least three independent experiments are performed unless otherwise indicated. In the box plots showing cell stiffness measured via AFM (i.e., Figure 6F), the mean stiffness value is also superimposed on the box plots and indicated as dot. The figure legends indicate statistical test performed, *p*-values, and sample size. For comparison of two samples, we either used the non-parametric test Wilcoxon Rank-sum test (denoted as WRST) or the parametric Student's t-test (denoted as t test). To analyze more than two samples simultaneously, we first performed an ordinary one-way ANOVA to test whether there were significant differences among the samples ($p < 0.05$). If this was the case and the normality test was passed, we performed multiple comparisons using a Tukey test, comparing each column with the mean of every other column. The family-wise alpha threshold was 0.05 to get a 95% confidence interval.

Cell Reports, Volume *44*

Supplemental information

ERK activation waves coordinate mechanical cell competition leading to collective elimination via extrusion of bacterially infected cells

Lara Hundsdorfer, Marie Muenkel, Raul Aparicio-Yuste, Julio Cesar Sanchez-Rendon, Maria Jose Gomez-Benito, Aylin Balmes, Tilman E. Schäffer, Ana Velic, Yi-Ting Yeh, Iordania Constantinou, Kathryn Wright, Gizem Özbaykal Güler, Dominik Brokatzky, Boris Maček, Serge Mostowy, and Effie E. Bastounis

Figure S1

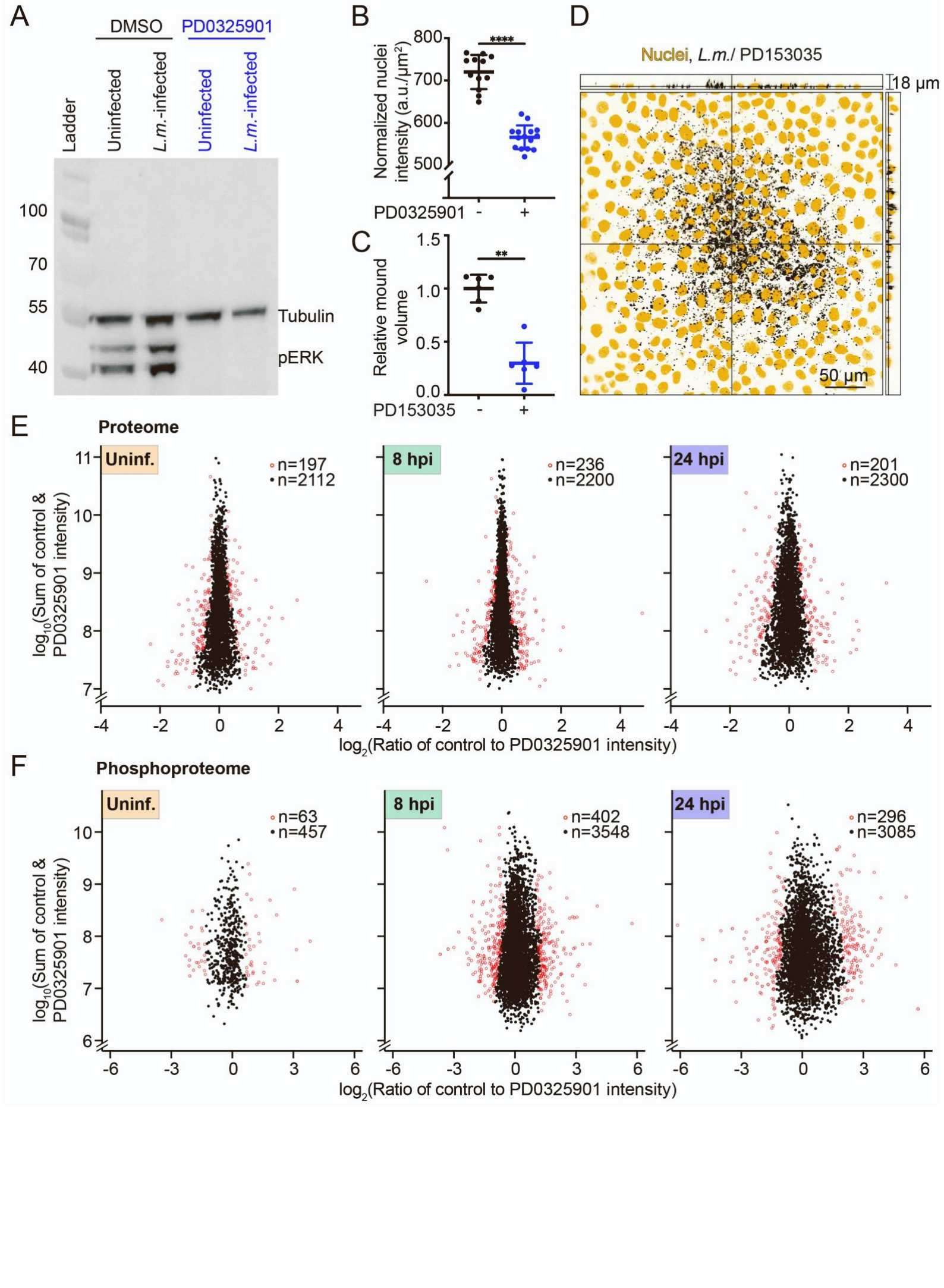
A
DMSO
PD0325901
Ladder
Uninfected
L.m.-infected
Uninfected
L.m.-infected
100
70
55
40
Tubulin
pERK
B
Normalized nuclei intensity (a.u./μm²)
800
700
600
500
****
PD0325901 - +
C
Relative mound volume
1.5
1.0
0.5
0.0
**
PD153035 - +
D
Nuclei, L.m./ PD153035
18 μm
50 μm
E
Proteome
Uninf.
n=197
n=2112
8 hpi
n=236
n=2200
24 hpi
n=201
n=2300
log10(Sum of control & PD0325901 intensity)
log2(Ratio of control to PD0325901 intensity)
F
Phosphoproteome
Uninf.
n=63
n=457
8 hpi
n=402
n=3548
24 hpi
n=296
n=3085
log10(Sum of control & PD0325901 intensity)
log2(Ratio of control to PD0325901 intensity)

Figure S2

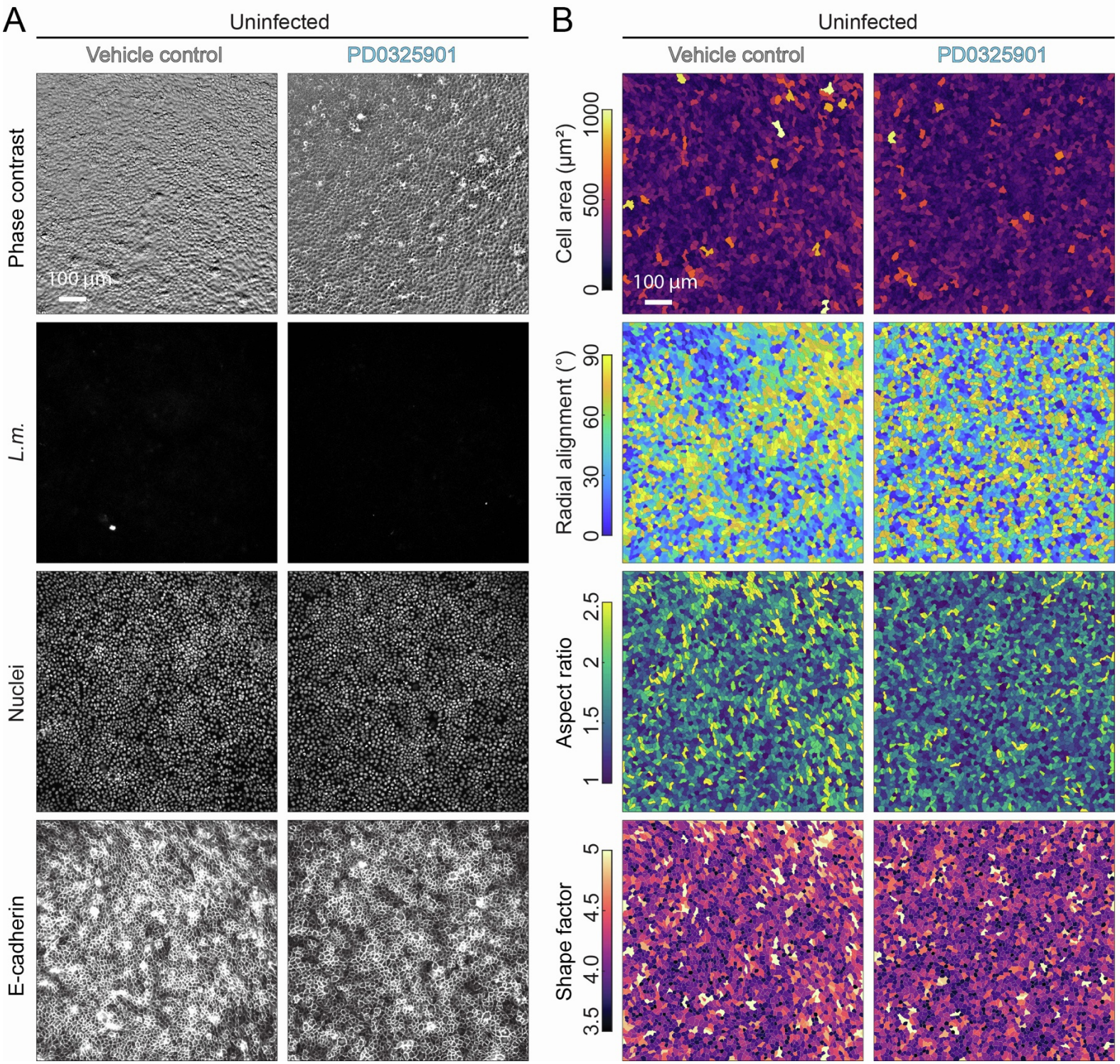
A
Uninfected
Vehicle control
PD0325901
Phase contrast
L.m.
Nuclei
E-cadherin
100 µm
B
Uninfected
Vehicle control
PD0325901
Cell area (µm²)
0
500
1000
Radial alignment (°)
0
30
60
90
Aspect ratio
1
1.5
2
2.5
Shape factor
3.5
4.0
4.5
5
100 µm

Figure S3

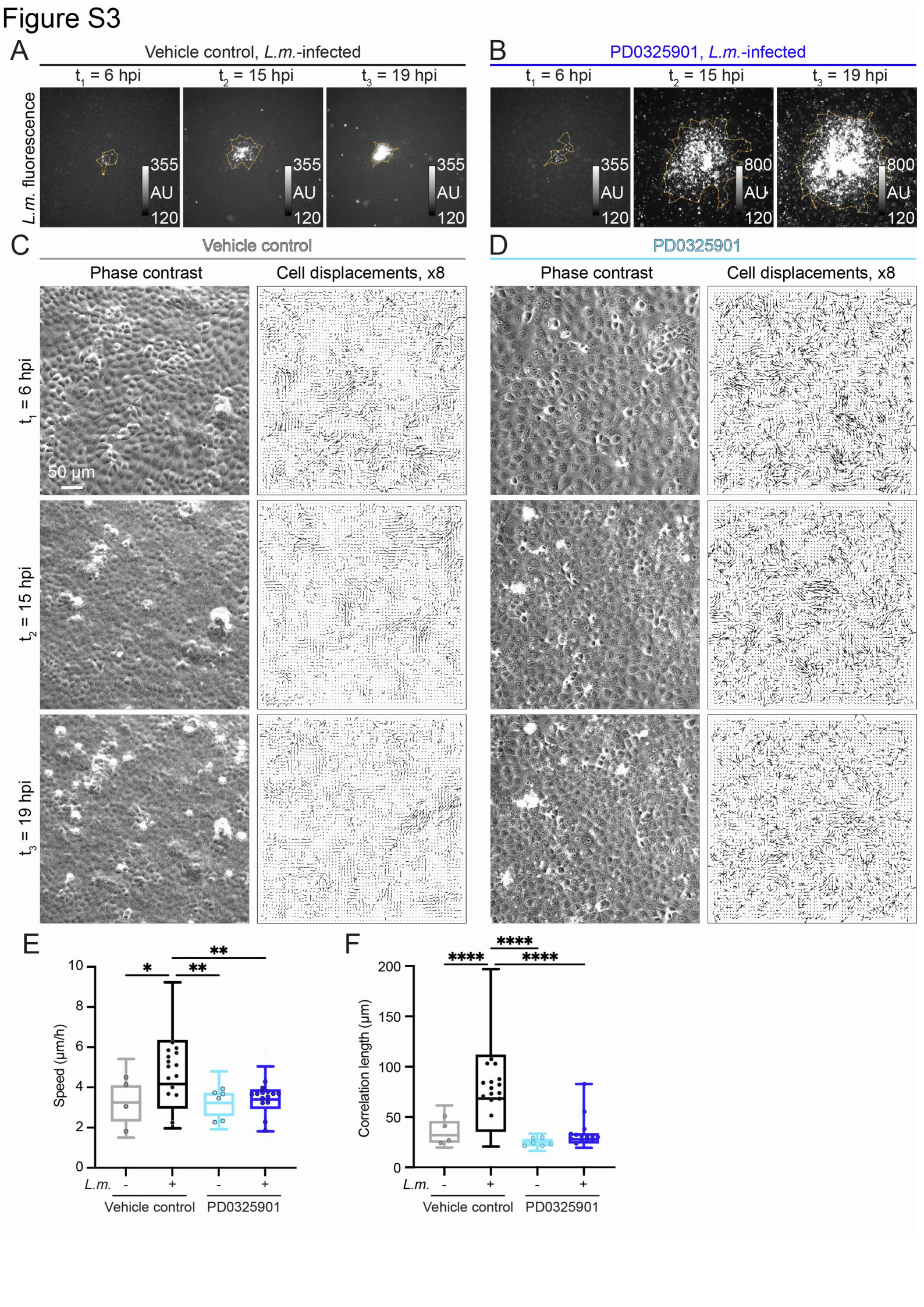
A
Vehicle control, L.m.-infected
t1 = 6 hpi
t2 = 15 hpi
t3 = 19 hpi
L.m. fluorescence
355
AU
120
B
PD0325901, L.m.-infected
800
C
Vehicle control
Phase contrast
Cell displacements, x8
t1 = 6 hpi
t2 = 15 hpi
t3 = 19 hpi
50 µm
D
PD0325901
E
Speed (µm/h)
L.m.
Vehicle control
PD0325901
F
Correlation length (µm)

Figure S4

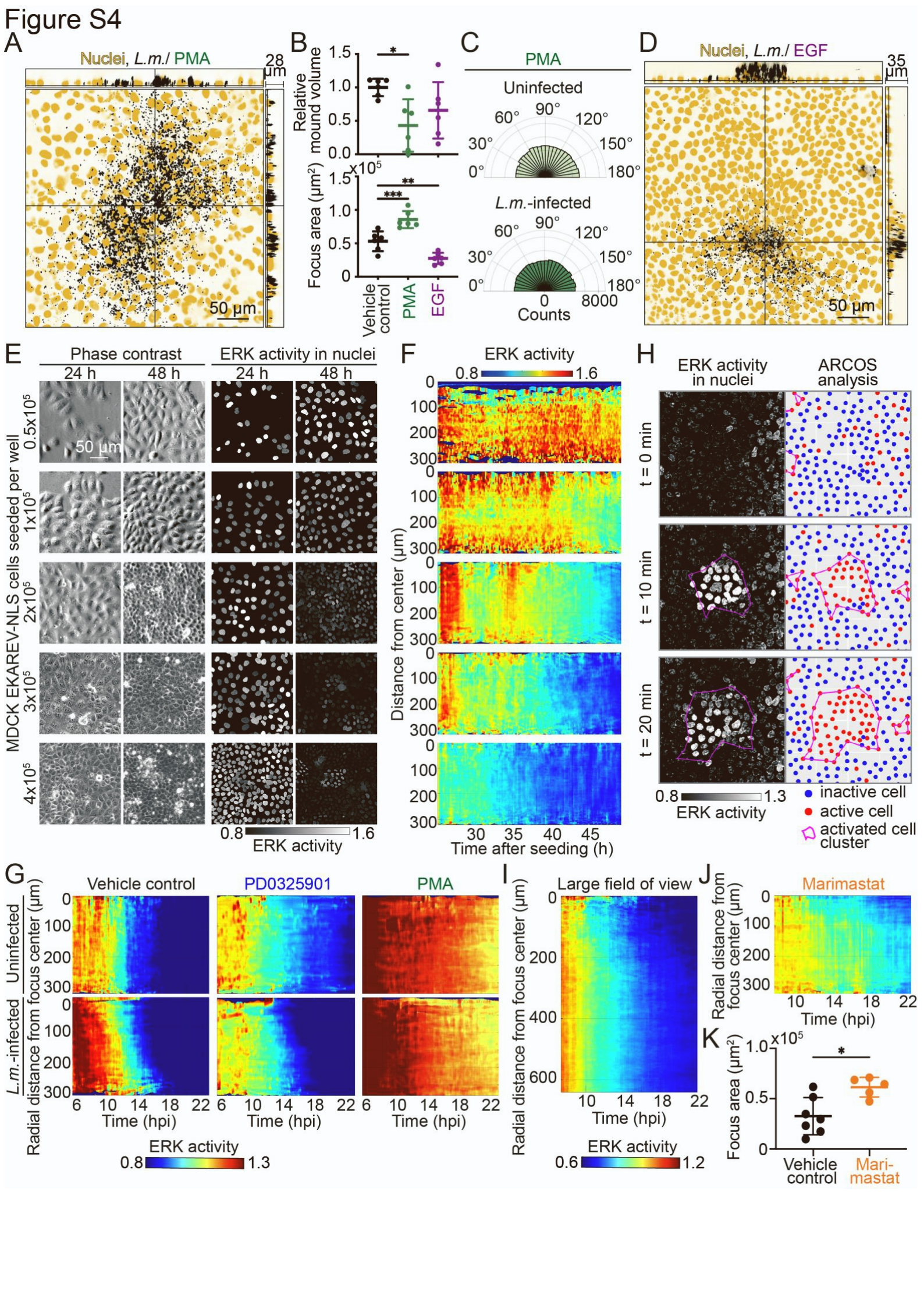
A
Nuclei, L.m./ PMA
28 µm
50 µm
B
Relative mound volume
Focus area (µm²)
x10⁵
Vehicle control
PMA
EGF
C
PMA
Uninfected
L.m.-infected
Counts
D
Nuclei, L.m./ EGF
35 µm
50 µm
E
Phase contrast
ERK activity in nuclei
24 h
48 h
MDCK EKAREV-NLS cells seeded per well
0.5x10⁵
1x10⁵
2x10⁵
3x10⁵
4x10⁵
50 µm
ERK activity
F
ERK activity
Distance from center (µm)
Time after seeding (h)
H
ERK activity in nuclei
ARCOS analysis
t = 0 min
t = 10 min
t = 20 min
inactive cell
active cell
activated cell cluster
G
Vehicle control
PD0325901
PMA
Uninfected
L.m.-infected
Radial distance from focus center (µm)
Time (hpi)
I
Large field of view
J
Marimastat
K
Vehicle control
Mari-mastat

Figure S5

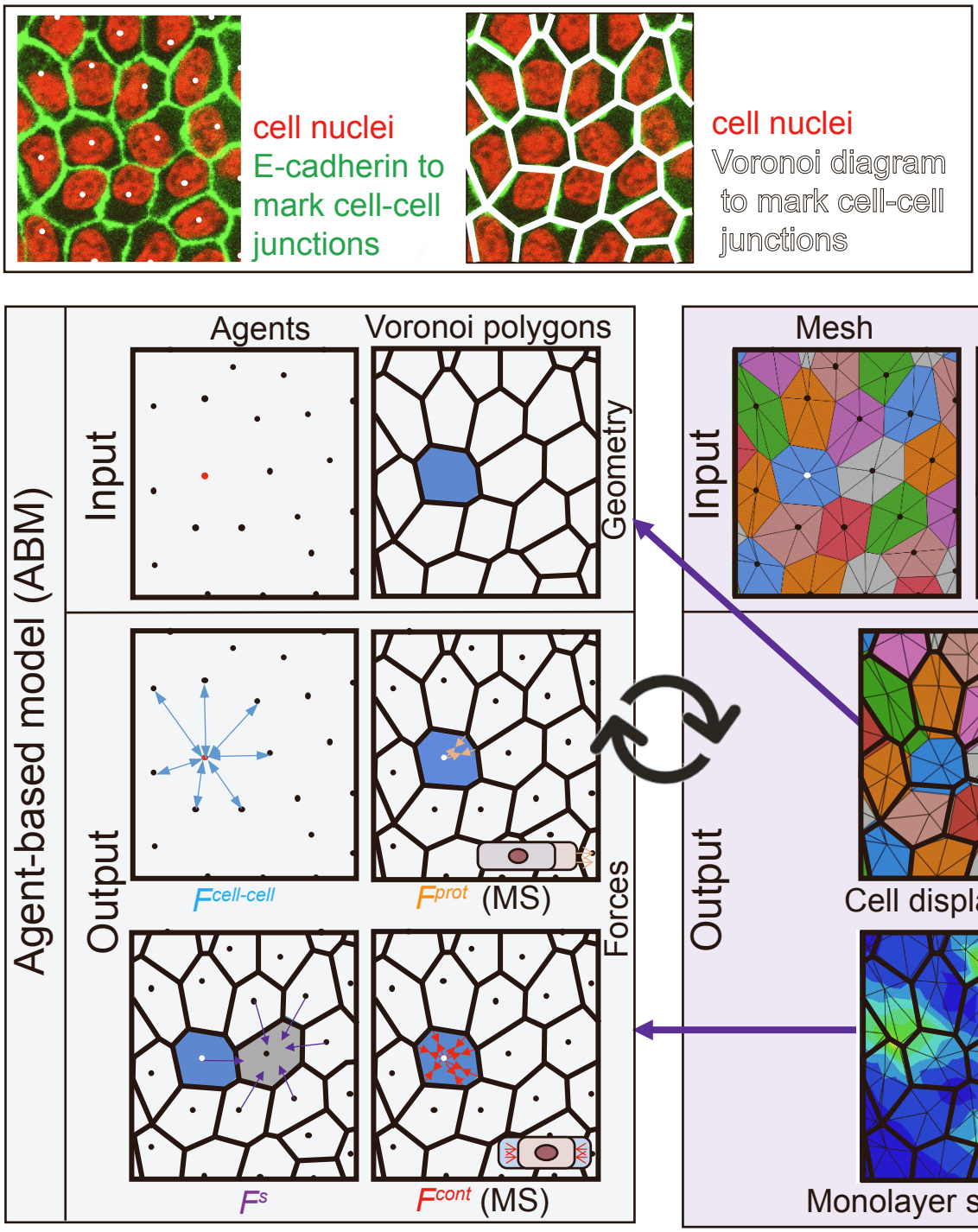
A
cell nuclei
E-cadherin to mark cell-cell junctions
cell nuclei
Voronoi diagram to mark cell-cell junctions
B
Agent-based model (ABM)
Agents
Voronoi polygons
Input
Geometry
Output
Forces
$F^{cell-cell}$
F^{prot} (MS)
F^{s}
F^{cont} (MS)
Finite element model (FEM)
Mesh
Forces
Input
Output
Cell displacements
Monolayer stresses (MS)

Figure S6

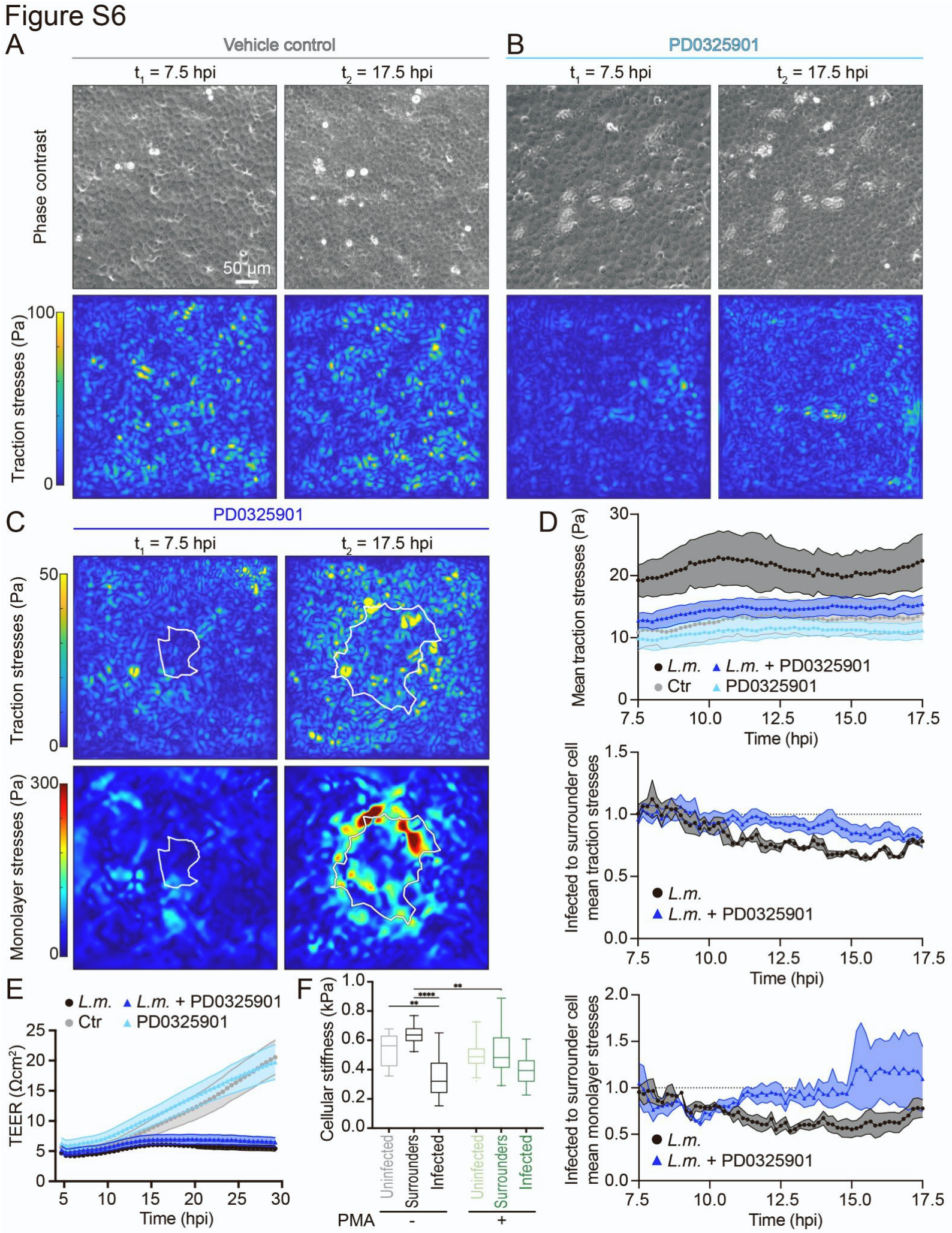
A
Vehicle control
B
PD0325901
t1 = 7.5 hpi
t2 = 17.5 hpi
Phase contrast
50 µm
Traction stresses (Pa)
100
0
C
PD0325901
Monolayer stresses (Pa)
300
50
D
Mean traction stresses (Pa)
L.m.
L.m. + PD0325901
Ctr
PD0325901
Time (hpi)
Infected to surrounder cell mean traction stresses
Infected to surrounder cell mean monolayer stresses
E
TEER (Ωcm²)
F
Cellular stiffness (kPa)
Uninfected
Surrounders
Infected
PMA
-
+

Figure S7

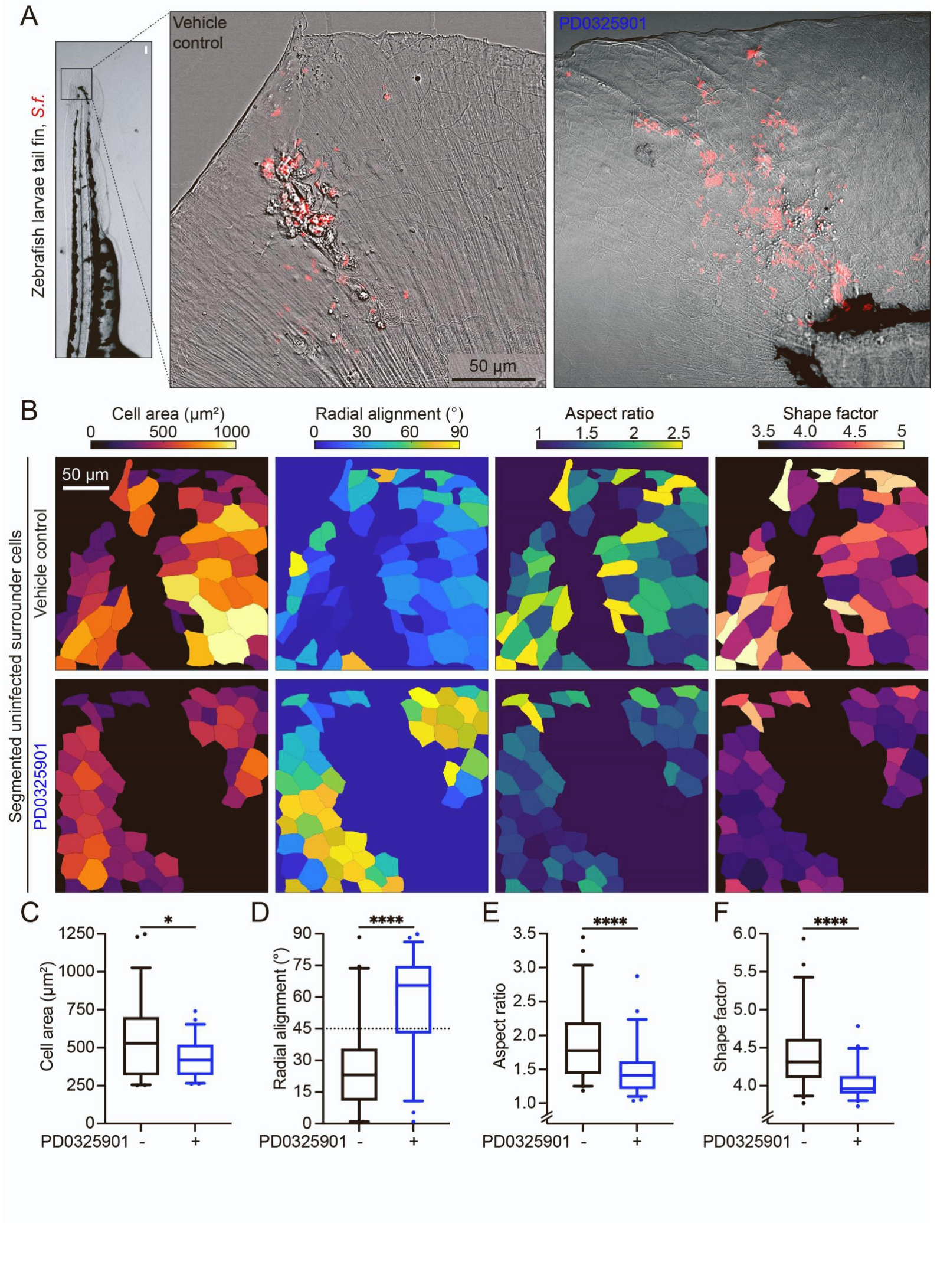
A
Zebrafish larvae tail fin, S.f.
Vehicle control
PD0325901
50 µm
B
Cell area (µm²)
0 500 1000
Radial alignment (°)
0 30 60 90
Aspect ratio
1 1.5 2 2.5
Shape factor
3.5 4.0 4.5 5
50 µm
Vehicle control
PD0325901
Segmented uninfected surrounder cells
C
Cell area (µm²)
1250 1000 750 500 250 0
*
PD0325901 - +
D
Radial alignment (°)
90 75 60 45 30 15 0
****
PD0325901 - +
E
Aspect ratio
3.5 3.0 2.5 2.0 1.5 1.0
****
PD0325901 - +
F
Shape factor
6.0 5.5 5.0 4.5 4.0
****
PD0325901 - +

SUPPLEMENTAL INFORMATION

SUPPLEMENTAL FIGURE LEGENDS

Figure S1 PD0325901 inhibits ERK in MDCK cells without altering much the phosphoproteome of uninfected cells, while EGFR inhibition abrogates mounds. Related to Figure 1. (**A**) Representative whole western blot from lysates of uninfected and *L.m.*-infected MDCK cells in monolayer at 24 hpi treated or not with vehicle control (1st and 2nd lanes) or 50 μM PD0325901 at 4 hpi (3rd and 4th lanes). ERK protein phosphorylation was probed, and tubulin was used as a loading control. (**B**) Quantification of integral of host MDCK cell nuclei fluorescence intensity within an *L.m.* infection focus at 24 hpi, for MDCK cells treated at 4 hpi with vehicle control (black) or 50 μM PD0325901 (blue). Data are normalized relative to the area of each infection focus; hence units are in a.u./μm^2. Dots refer to distinct images analyzed originating from one experiment. Lines: mean±SD, WRST: ****p<0.0001. (**C**) Mound volume of MDCK cells fixed at 24 hpi and treated at 4 hpi with vehicle control (left) or 4 μM PD153035 (right). Values have been normalized to the mean mound volume of control infected cells. Lines indicate mean±SD, WRST: **p<0.01. (**D**) Orthogonal views of *L.m.*-infected MDCK cells 24 hpi treated with 4 μM PD153035 (EGFR inhibitor). Host nuclei: yellow; *L.m.*: black. (**E-F**) Scatter plots of proteome (E) and phosphoproteome (F) summed intensity of the sample treated with vehicle control and PD0325901 over their intensity ratio, for data collected from uninfected (left), L.m.-infected samples 8 hpi (middle) and 24 hpi (right) as shown in Figure 1G. Dots indicate measured expression (E) or phosphorylation (F) of proteins, with those displaying significant changes (Significance B, $p < 0.05$) highlighted in red.

Figure S2 Cell shape morphometrics and E-cadherin localization do not change when ERK is inhibited in uninfected MDCK cell monolayers. Related to Figure 2. (**A**) MDCK cells in monolayer 48 h post-seeding and previously treated at 28 h post-seeding with vehicle control (1st column) or 50 μM PD0325901 (2nd column). Rows: phase contrast image, *L.m.* fluorescence, cell nuclei fluorescence, and E-cadherin fluorescence. (**B**) Same images as in (A) with cells in different rows color-coded for: cell area (μm^2), radial alignment (°) of the major cell axis, cell aspect ratio, and shape factor (see STAR methods).

Figure S3 Cell kinematics of MDCK cells originating from uninfected monolayers remain unaltered when ERK is inhibited. Related to Figure 3. (**A-B**) Representative video-microscopy images of *L.m.* fluorescence (AU) shown in Figure 3A-B but without the overlayed phase contrast, for inspection of bacterial fluorescence. For better visualization colorbar limits were not kept

constant. Colorbar axis limits are displayed in the right bottom of each image. (**C-D**) Representative video-microscopy images of MDCK cells in monolayer originating from uninfected wells treated with vehicle control (C) or 50 μM PD0325901 (D) at the three indicated time points (rows). Columns show phase contrast image (left) and the cell displacements (arrows, scaled 8x). (**E-F**) Boxplots of cell speed (E, μm/h), and correlation length (F, μm) of cells from uninfected or *L.m.*-infected wells, treated with vehicle control (grayscale) or 50 μM PD0325901 (bluescale). The same data is shown in figure 3 over time. Dots show the time average of each replicate originating from three independent experiments; ANOVA followed by Tukey's multiple comparisons test: *p<0.05, **p<0.01, ****p<0.0001.

Figure S4 Constitutive ERK activation stalls formation of mounds and increasing density of MDCK cells in monolayer decreases ERK activation. Related to Figure 4. (**A**) Orthogonal views of *L.m.*-infected MDCK cells at 24 hpi treated at 4 hpi with 200 nM of PMA (activates ERK). Host nuclei: yellow; *L.m.*: black. (**B**) *L.m.* mound volume (top) and infection focus area (bottom, μm^2) at 24 hpi for MDCK cells treated at 4 hpi with 200 nM of PMA (green) or with 25 ng/mL EGF (purple). Only the mound volumes are plotted relative to control mound volumes. Lines indicate mean±SD, ANOVA followed by Tukey's multiple comparisons test: *p<0.05, **p<0.01, ***p<0.001. (**C**) Rose plots showing cell displacement directionality angle (angle between radial direction and cell displacement, see STAR methods) for uninfected (top) or *L.m.*-infected cells in monolayer (bottom), treated with 200 nM of PMA. 0^o and 180^o correspond to cells moving towards or away from the center of the infection focus (or field of view for uninfected cells), respectively. (**D**) Orthogonal views of *L.m.*-infected MDCK cells at 24 hpi treated at 4 hpi with 25 ng/mL EGF. Host nuclei: yellow; *L.m.*: black. (**E-F**) ERK activation depend on cell confluency. In (E) columns 1 and 2 show phase contrast images of uninfected MDCK cells expressing EKAREV-NLS at 24 and 48 h post-cell seeding. Columns 3 and 4 show the corresponding ERK activity in the nuclei of cells while panel F displays the corresponding ERK activity summarized by the kymographs of mean radial ERK activity (y-axis) versus time (hpi, x-axis). Rows indicate different seeding densities. (**G**) Kymographs of mean radial ERK activity (y-axis) versus time (hpi, x-axis) for uninfected (top) or *L.m.*-infected MDCK cells (bottom). The center of the polar coordinate system was considered the center of the infection focus or of the field of view for uninfected cells. Columns show samples treated at 4 hpi with vehicle control (left), 50 μM of PD0235901 (middle) or 200 nM of PMA (right). (**H**) Representative images (left column) of ERK activity in the nuclei of MDCK cells in monolayer expressing EKAREV-NLS. Three consecutive time points separated by 10 min are shown. Right column shows the detected cell nuclei as red or blue dots indicating ERK activation or not,

respectively. Magenta contours show the boundary of detected clusters of cells with higher ERK activity as they propagate in forms of waves between consecutive frames. Quantification of ERK wave characteristics like cluster size and frequency of ERK activation cluster events is based on this type of analysis (see also STAR methods). (**I**) Kymograph of mean radial ERK activity (y-axis) versus time (hpi, x-axis) for *L.m.*-infected MDCK cells depicted as in panel G but over a longer distance (>600 μm away from the infection focus), since the imaged field of view is three times larger. **(J)** Kymograph of mean radial ERK activity (y-axis) versus time (hpi, x-axis) for *L.m.*-infected MDCK cells treated at 4 hpi with 10 μM marimastat to inhibit MMPs. The polar coordinate system is as described in panel G. Note that panels I and J share the same colorbar. (**K**) *L.m.* infection focus area (μm^2) at 24 hpi for MDCK cells treated at 4 hpi with 10 μM marimastat or vehicle control. Lines: mean±SD, WRST: $^{*}p<0.05$.

Figure S5 Schematic of the hybrid computational model to simulate the biomechanics of epithelial cells in monolayer infected with *L.m.* Related to Figure 5. (**A**) Superimposed epifluorescence images of MDCK cell nuclei (red) and E-cadherin (green) marking cell-cell junctions. On the left image, the cell centroids are marked with a white dot. On the right image, cell boundaries are marked with white lines and are concordant with the resulting Voronoi tessellation of cell nuclei centres. These boundaries are in good agreement with the actual cell-cell junctions, supporting the use of a hybrid computational model in which cell centres act as agents for the agent-based model (ABM) and the Voronoi diagram supplies the geometry required for the finite element model (FEM). (**B**) Pipeline showing how the hybrid computational model works. Left: ABM is depicted, the input of which is the actual geometry of the monolayer, and the outputs are the resulting calculated cellular forces (cell-cell interaction force, $F^{cell-cell}$; protrusion force, F^{prot}; surrounder cell force, F^{s}; and contraction force, F^{cont}). These cell-generated forces are shown in the sketch for just a specific cell denoted in blue. Additionally, surrounder cell forces, F^{s} are shown as they act on just one specific infected cell denoted in grey. Right: FEM model, for which the inputs are the Voronoi polygons, which are meshed with triangular elements. In addition, the forces calculated in the ABM are shown, which are applied as concentrated forces. The FEM analysis is performed, and the outputs of the model are the displacements that cells within the monolayer undergo and the cell monolayers stresses (denoted as MS). Calculated cell displacements are used as inputs in the ABM geometry to update agent position (left top), and monolayer stresses are used for the calculation of forces (F^{prot} and F^{cont}, left bottom). Both models form an iterative loop that allows the simulation of cell monolayers over time.

Figure S6 Traction forces of uninfected MDCK cells in monolayer remain unaltered when ERK is inhibited while barrier function is compromised in *L.m.*-infected samples irrespective of ERK inhibition as evidenced by TEER. Related to Figure 6. (A-B) TFM on uninfected MDCK cells adherent on 3 kPa gel. Cells were treated with vehicle control (A) or 50 μM PD0325901 (B). Rows indicate phase contrast image and traction stresses (Pa). Columns indicate time (h) post-imaging initiation. (**C**) Images of traction stresses (Pa, top) and monolayer stresses (Pa, bottom) of *L.m.*-infected MDCK cells treated with 50 μM PD0235901. Same representative experiment as shown in Figure 6B but color map is adapted so that the contrast is similar to Figure 6A and the differences between surrounder cells' stresses versus infected cells' can be better visualized. (**D**) Evolution of traction and monolayer stresses of uninfected or *L.m.*-infected MDCK cells in monolayer treated with vehicle control or 50 μM PD0325901 at 4 hpi. Top plot: traction stresses (Pa, y-axis) over time (hpi, x-axis). Middle plot: ratio of infected to uninfected surrounder cells traction stresses over time (hpi, x-axis). Bottom plot: ratio of infected to uninfected surrounder cells monolayer stresses over time (hpi, x-axis). Three independent experiments were performed and an average of N=5 recordings were performed per condition. Mean±SEM (shaded area). (**E**) Transepithelial electrical resistance (TEER) (Ωcm^2, y-axis) as a function of time (hpi, x-axis) for uninfected and *L.m.*-infected MDCK cells in monolayer treated with vehicle control or PD0325901 at 4 hpi (immediately before recording started). Three independent experiments were performed, and an average of N=13 wells per condition were monitored in total. (**F**) Boxplots of cell stiffness (kPa) at 24 hpi for uninfected cells, surrounder cells, and infected MDCK cells, treated with 200 nM PMA at 4 hpi. N=22±6 cells were analyzed per condition, one experiment performed, ANOVA followed by Tukey's multiple comparisons test: **p<0.01, ****p<0.0001.

Figure S7 *S.f.*-infected cell extrusion occurs *in vivo* in zebrafish larvae skin epithelia cells with surrounder cells exhibiting higher polarization during mounding. Related to Figure 7. (**A**) Same representative overlay of phase contrast images with *S.f.* fluorescence (red) of zebrafish larvae fin tails treated with vehicle control or 41 μM PD0325901 as shown in Figure 7E but without the overlay of white cell contours. Images added for better visualization of the accuracy of cell outlines added in Figure 7E. (**B**) Segmented surrounder uninfected cells originating from images of zebrafish larvae fin tails treated with vehicle control (top) or 41 μM PD0325901 (bottom) and also shown in Figure 7E and panel A. Columns show cells color-coded for: cell area (μm^2), radial alignment (°) of the major cell axis, cell aspect ratio, and shape factor (see STAR methods).

(**C-F**) Boxplots of cell area (μm^2, C), radial alignment angle (^{o,} D), cell aspect ratio (E), and shape factor (F) of uninfected surrounder cells from zebrafish larvae fin tails treated with vehicle control (black) or 41 μM PD0325901 (blue). A mean of N=54 single cells were analyzed per condition. WRST: *p<0.05, ****p<0.0001.

Section 3

A stiff extracellular matrix favors the mechanical cell competition that leads to extrusion of bacterially-infected epithelial cells

Raúl Aparicio-Yuste[1,2], Marie Muenkel[2], Andrew G. Clark[3,4], María J. Gómez-Benito[1*] and Effie E. Bastounis[2*]

[1]Department of Mechanical Engineering, Multiscale in Mechanical and Biological Engineering (M2BE), Instituto de Investigaciónen Ingeniería de Aragón (I3A), University of Zaragoza, Zaragoza, Spain,

[2]Interfaculty Institute of Microbiology and Infection Medicine, Cluster of Excellence “Controlling Microbes to Fight Infections” (CMFI, EXC 2124), University of Tübingen, Tübingen, Germany,

[3]Institute of Cell Biology and Immunology/Stuttgart Research Center Systems Biology, University of Stuttgart, Stuttgart, Germany,

[4]Center for Personalized Medicine, University of Tübingen, Tübingen, Germany

Published 2022 in Frontiers in Cell and Developmental Biology 10.

frontiers | Frontiers in Cell and Developmental Biology

ORIGINAL RESEARCH
published: 22 June 2022
doi: 10.3389/fcell.2022.912318

A Stiff Extracellular Matrix Favors the Mechanical Cell Competition that Leads to Extrusion of Bacterially-Infected Epithelial Cells

Raúl Aparicio-Yuste[1,2], *Marie Muenkel*[2], *Andrew G. Clark*[3,4], *María J. Gómez-Benito*[1]* and *Effie E. Bastounis*[2]*

[1]Department of Mechanical Engineering, Multiscale in Mechanical and Biological Engineering (M2BE), Instituto de Investigación en Ingeniería de Aragón (I3A), University of Zaragoza, Zaragoza, Spain, [2]Interfaculty Institute of Microbiology and Infection Medicine, Cluster of Excellence "Controlling Microbes to Fight Infections" (CMFI, EXC 2124), University of Tübingen, Tübingen, Germany, [3]Institute of Cell Biology and Immunology/Stuttgart Research Center Systems Biology, University of Stuttgart, Stuttgart, Germany, [4]Center for Personalized Medicine, University of Tübingen, Tübingen, Germany

OPEN ACCESS

Edited by:
Tsuyoshi Hirashima,
Kyoto University, Japan

Reviewed by:
Takumi Kawaue,
Kyoto University, Japan
Tamal Das,
Max Planck Institute for Intelligent Systems, Germany

***Correspondence:**
María J. Gómez-Benito
gomezmj@unizar.es
Effie E. Bastounis
effie.bastounis@uni-tuebingen.de

Specialty section:
This article was submitted to Cell Adhesion and Migration, a section of the journal Frontiers in Cell and Developmental Biology

Received: 05 April 2022
Accepted: 31 May 2022
Published: 22 June 2022

Citation:
Aparicio-Yuste R, Muenkel M, Clark AG, Gómez-Benito MJ and Bastounis EE (2022) A Stiff Extracellular Matrix Favors the Mechanical Cell Competition that Leads to Extrusion of Bacterially-Infected Epithelial Cells. Front. Cell Dev. Biol. 10:912318. doi: 10.3389/fcell.2022.912318

Cell competition refers to the mechanism whereby less fit cells ("losers") are sensed and eliminated by more fit neighboring cells ("winners") and arises during many processes including intracellular bacterial infection. Extracellular matrix (ECM) stiffness can regulate important cellular functions, such as motility, by modulating the physical forces that cells transduce and could thus modulate the output of cellular competitions. Herein, we employ a computational model to investigate the previously overlooked role of ECM stiffness in modulating the forceful extrusion of infected "loser" cells by uninfected "winner" cells. We find that increasing ECM stiffness promotes the collective squeezing and subsequent extrusion of infected cells due to differential cell displacements and cellular force generation. Moreover, we discover that an increase in the ratio of uninfected to infected cell stiffness as well as a smaller infection focus size, independently promote squeezing of infected cells, and this phenomenon is more prominent on stiffer compared to softer matrices. Our experimental findings validate the computational predictions by demonstrating increased collective cell extrusion on stiff matrices and glass as opposed to softer matrices, which is associated with decreased bacterial spread in the basal cell monolayer *in vitro*. Collectively, our results suggest that ECM stiffness plays a major role in modulating the competition between infected and uninfected cells, with stiffer matrices promoting this battle through differential modulation of cell mechanics between the two cell populations.

Keywords: finite element analysis, cell competition, cell mechanics, traction and monolayer stresses, infection, *Listeria monocytogenes*, epithelial cells, cell extrusion

1 INTRODUCTION

Cell competition refers to the process whereby less fit cells, often denoted "losers", are sensed and eliminated by more fit neighboring cells, accordingly referred to as "winners" (Gradeci et al., 2021). This competition between losers and winners is essential for tissue homeostasis but it also emerges during tissue development and can play a role in various pathologies including tumor development

(Meyer et al., 2014; Moreno et al., 2019). Although the chemical signals driving the battle between two different cell populations are relatively more explored, an increasing number of studies showcases that mechanical signals such as differential sensitivity to compression during cell crowding are also crucial in driving such interactions (Gradeci et al., 2019; Matamoro-Vidal and Levayer, 2019; Moreno et al., 2019; Bastounis et al., 2021b).

We recently showed that a mechanical competition during late infection drives the collective onslaught and elimination of infected cells out of the epithelial monolayer (Bastounis et al., 2021b). When epithelial cells in monolayer get exposed to low dosage of *Listeria monocytogenes* (*L.m.*), a food-borne facultative intracellular bacterial pathogen, some sparse cells in the monolayer get infected. Within several hours *L.m.* has the ability to replicate intracellularly and spread intercellularly to larger domains containing hundreds of cells. However, at later times post-infection (~16 h post-infection, hpi), we discovered that surrounding uninfected cells ("winners") responding to innate immune signals, migrate actively and in a coordinated fashion towards the infection focus, squeezing the infected cells and eventually forcing their massive extrusion (mounding) out of the monolayer (~24 hpi). Infected cells ultimately die, possibly due to their forceful separation out of their basement membrane, thus suggesting that the "infection mounding" process is a beneficial for the host process in that it obstructs infection dissemination through the cell monolayer. Interestingly, this competition that leads to infected cell elimination is mechanical in nature, and depends on: 1) a decrease in contractility (i.e., traction stresses exerted by the cells on their matrix) of infected as opposed to uninfected neighbors; 2) a lowering in the passive stiffness of infected as opposed to uninfected neighbors, and 3) the presence of cell-cell adhesions since lack of those completely stalls mound formation. Thus, it appears that cell-matrix and cell-cell force transduction as well as cellular stiffness are crucial determinants in driving the mechanical competition that emerges during infection (Bastounis et al., 2022).

Studies conducted over the last decades have underlined the importance of extracellular matrix (ECM) stiffness in regulating important cellular functions such as cell motility, by modulating the cellular traction forces, the intercellular forces and/or the bulk stiffness of cells (Solon et al., 2007; Califano and Reinhart-King, 2010; Borau et al., 2011; Bastounis et al., 2019; Doss et al., 2020). In many different cell types, as ECM stiffness increases, cellular traction force generation also increases, and this effect is particularly prominent in single cells and to a lesser degree in cellular monolayers (Lampi et al., 2016; Zhao et al., 2018; Bastounis et al., 2019). Given that ECM stiffness increases in certain pathologies including fibrotic diseases, cancer and inflammatory bowel diseases (IBD) (Lampi and Reinhart-King, 2018; Onfroy-Roy et al., 2020), it remains still an open question whether varying ECM stiffness would promote or limit infected cell extrusion and, if so, what would be the physical and molecular mechanisms involved. Interestingly, Gradeci et al., showed that changes in the ratio of winner-to-loser cell stiffness altered the kinetics of cell competition between wild-type MDCK cells and cells depleted for the polarity protein scribble, although ECM stiffness was not addressed in this study (Gradeci et al., 2021). Another study on competition between wild-type cells and oncogenically-transformed ones did show that increasing ECM stiffness attenuates extrusion of transformed cells by tuning the dynamic localization of filamin, an important F-actin crosslinking protein (Pothapragada et al., 2022). Thus, it remains unclear whether there are generalizable mechanisms that could predict how ECM stiffness impacts cell behavior and thus the outcome of a cell competition, and whether those would apply to epithelial cells that are infected with intracellular bacterial pathogens, which can replicate intracellularly and also dynamically spread from cell to cell.

To explore such questions, studies often rely on *in vitro* experiments. Such experiments have provided great insight into how intracellular bacteria efficiently spread through epithelial cells in monolayer and on the physical cellular processes that bacteria often hijack to promote their dissemination (Lamason et al., 2016; Faralla et al., 2018). However, *in silico* cellular models and simulations can complement *in vitro* experiments and even facilitate the design of future *in vitro* experiments (Brodland, 2015; Gradeci et al., 2021). Such models present several advantages such as that they are controllable, time-efficient, and cost-effective. Moreover, one can tweak one parameter at a time, thus making it easier to reach causal conclusions. Nevertheless, they do need *in vitro* and *in vivo* models to be properly validated and calibrated. Most infection computational models have focused on the dynamics of bacterial spread in colonies considering contact forces, bacterial growth or the interaction between bacteria and biomaterials (Delarue et al., 2016). Others have focused on the dynamics of intracellular bacterial spread, with the bacteria modeled as particles within two-dimensional (2-D) rigid host cells (Ortega et al., 2019). Recently, we developed a computational, three-dimensional (3-D) finite element model (FEM) to explore the physical mechanisms that drive the squeezing and extrusion of bacterially infected cells during their competition with surrounding uninfected cells (Bastounis et al., 2021b). This simplified model not only validated our experimental results but also predicted that cell-cell adhesions between infected cells and immediate surrounders are necessary for mound formation, a result that we then confirmed experimentally.

Herein, we introduce an extension to our infection computational model with the aim to investigate the previously overlooked role of ECM stiffness in potentially modulating the forceful extrusion of infected cells by uninfected surrounders (Bastounis et al., 2021b). The parameters of our model are selected based on our experimental observations. We find that increasing ECM stiffness promotes the collective squeezing and subsequent extrusion of infected cells due to differential cellular displacements and cellular force generation. Moreover, we discover that an increase in the ratio of uninfected to infected cell stiffness as well as a smaller infection focus size, both promote squeezing of infected cells, and this phenomenon is more prominent on stiffer as opposed to softer matrices. Our experimental findings validate the computational predictions by demonstrating increased collective cell extrusion on stiff

matrices and glass as opposed to softer matrices, accompanied by decreased bacterial spread in the basal cell monolayer *in vitro*. Collectively, our results suggest that ECM stiffness plays a major role in modulating the competition between "winner" uninfected cells and "loser" infected cells with stiffer matrices promoting this battle through differential modulation of cell mechanics between the two cell populations.

2 MATERIALS AND METHODS

2.1 *In vitro* Experiments

2.1.1 Cell Culture

Epithelial cells type II MDCK cells and type II MDCK cells that express E-cadherin-RFP were a generous gift of the Nelson lab, Stanford University (Perez et al., 2008). MDCK cells were cultured in high glucose DMEM medium (Thermofisher; 10741574) containing 4.5 g/L glucose and supplemented with 10% fetal bovine serum (Thermofisher, 10270106), further referred to as DMEM. They were kept at a temperature of 37°C with 5% CO_2.

2.1.2 Bacterial Infections and Fixation of Samples for Imaging Mound Volumes

Infection of MDCK cells with *L.m.* was performed as described previously (Bastounis et al., 2021a) using *L.m.* strain JAT607 (Species: *L.m.* 1043S, Genotype/Description: ActAp::mTagRFP) (Ortega et al., 2017). JAT607 *L.m.* express mtagRFP under the control of the ActA promoter which makes them fluoresce only few hours (approximately 4 h) after host cell internalization. The infection assays were performed as follows. Three days prior to infection frozen glycerol stocks of JAT607 were streaked on BHI agar plates containing 7.5 μg/ml chloramphenicol and 0.2 mg/ml streptomycin and incubated at 37°C for approximately 1 day until colonies formed. 16 h prior to infection a 2 ml BHI solution supplemented with 7.5 μg/ml chloramphenicol and 0.2 mg/ml streptomycin was inoculated with JAT607 bacteria from the BHI agar plates and incubated for approximately 16 h in the dark, without shaking at room temperature (RT). The optical density (OD_{600}) of the overnight culture was then measured (approximately 0.4), the bacterial cultures were centrifuged at 2000 g for 5 min at RT and re-suspended in 2 ml PBS. 0.5 ml of this bacterial suspension was added to 24 ml DMEM medium. MDCK cells were washed once with PBS and 1 ml of the bacterial-containing DMEM solution was added to each well, so that the resulting multiplicity of infection (MOI) was approximately ~ 250 bacteria/cell. After 30 min incubation at 37°C with 5% CO_2 the bacterial-containing medium was exchanged with DMEM containing 5 μg/ml Hoechst (Fisher, 11534886) to stain the host cell nuclei. After 10 min incubation under the previous conditions MDCK cells were washed with PBS three times and DMEM containing 20 μg/ml gentamycin (Fisher, 15820243) was added. 24 h post-infection MDCK cells were washed once again with PBS after which 4% methanol free paraformaldehyde (Thermofisher, 28906) in PBS was added in each well for 10 min. Samples were then washed once in PBS and stored in PBS at 4°C until microscopy imaging was performed.

2.1.3 Mound Volume Calculations, Infection Focus Area and Total Bacterial Fluorescence

Volumes of infected extruded cell domains were calculated using custom MATLAB scripts as previously explained in detail (Bastounis et al., 2021a). Briefly, images of Hoechst-stained MDCK nuclei and of the bacterial fluorescence in and around a given infection focus were taken using a z-spacing of 0.2 μm. For imaging, we used a Zeiss AxioObserver SD Spinning Disk microscope, equipped with an Axiocam 503 mono CCD camera and a Plan-Apochromat 40x/1.4 Oil DIC objective. For imaging the Hoechst-stained host cell nuclei, we used the blue channel (excitation laser 405 nm, emission filter 450/50 nm) and for the mtagRFP-expressing bacteria, we used the red channel: (excitation laser 561 nm, emission filter 600/50 nm). Nuclei located at the basal cell monolayer were disregarded, and only z-stacks of nuclei of cells extruded from that monolayer were considered. We calculated the area occupied by cells in each z-stack slice individually and then determined the total volume of the extruded area using this information. As a proxy of space occupied by cells, we used the signal of the nuclei and applied an alpha shape for area calculations (MATLAB (MathWorks) function alphaShape). First, the individual z-stack images were flatfield and background corrected and then a multi-threshold (between 5 and 3 thresholds per image) was applied to create a binary mask of the nuclei. The area occupied by cells in each z-stack was then multiplied by the height between z-stack slices, in order to determine the volume of the entire extruded domain. The codes used are written in Matlab (Mathworks) and can be found at https://github.com/ebastoun/Infection_mound_volume. For calculating the size of infection foci, we used epifluorescence imaging, and specifically an inverted Nikon Eclipse Ti2 with an EMCCD camera (Andor Technologies) and a 40 × 0.60 NA Plan Fluor air objective. The system was controlled by the MicroManager software. To characterize the efficiency of *L.m.* spread from cell-to-cell through the MDCK cell monolayer, we measured the size of infection foci as previously described (Ortega et al., 2019). The codes used are written in Matlab (Mathworks) and can be found at https://github.com/Fabianjr90/Listeria_focus_shape_analysis.

2.1.4 Fabrication of Polyacrylamide Hydrogels

Polyacrylamide hydrogels were prepared on glass bottom 24-well plates (MatTek, P24G-1.5-13-F) as previously described in (Bastounis et al., 2021a). Briefly, glass coverslips were pretreated with 0.5 M NaOH for 30 min at RT, rinsed with water and then incubated for 5 min at RT with 2% APTS ((3-Aminopropyl)triethoxysilane, Sigma, A3648-100ML) in 95% EtOH. After a rinsing step with water, the coverslips were incubated for another 30 min with 0.5% Glutaraldehyde (Sigma, G6257-100ML), rinsed again with water and finally dried at RT. Polyacrylamide hydrogels were built in two layers to achieve a sufficiently thin layer of fluorescent beads on the surface. 3 kPa hydrogels were prepared by mixing 5% acrylamide (Sigma, A4058-100ML) and 0.1% bis-acrylamide (Fisher, 10193523). 35 kPa hydrogels were prepared by mixing 8% acrylamide and 0.26% bis-acrylamide. Polymerization was

initiated by addition of 0.06% ammonium persulfate and 0.43% TEMED. The first layer was created by adding 3.6 μL of the acrylamide mix on the glass coverslip and covering it with a 12 mm round cover glass which was gently pressed on top to create a flat surface. During the polymerization of the first layer, an additional 0.03% of 0.2 μm fluorescent beads (Thermofisher, F8810) was added to the second layer solution. 2.4 μL of the second layer solution were then added on top of the first layer after removing the glass coverslip. A 12 mm round cover glass was again placed on top to generate a flat polyacrylamide layer containing tracer beads. After polymerization and removal of the round cover glass the gels maintained in 50 mM Hepes, pH 7.5 were UV sterilized for 1 h. Gels were then activated by addition of 200 μL of 0.5% w/v heterobifunctional cross-linker Sulfo-SANPAH (Fisher; 10474005) in 1% dimethyl sulfoxide (DMSO, Sigma, D2650-5X10ML) in 50 mM HEPES, pH 7.5, and exposure to UV light (λ = 302 nm) for 10 min. The Sulfo-SANPAH was then removed, and the gels were washed with 50 mM HEPES, pH 7.5. Gels were incubated overnight with 200 μL of 0.25 mg/ml rat tail collagen (Thermofisher, A1048301) and the following day washed once with 50 mM HEPES, pH 7.5 and stored in the same buffer.

2.1.5 Traction Force Microscopy (TFM)

TFM was performed as previously described (Lamason et al., 2016; Bastounis et al., 2021a). More specifically, polyacrylamide hydrogels were equilibrated for 30 min at 37°C with cell media prior to cell seeding. Subsequently, 4×10^5 MDCK cells were seeded on the hydrogels. 24 h post-seeding, cells were stained with 5 μg/ml Hoechst stain (Fisher, 11534886) for 10 min. Cells were washed once in PBS, and 1 ml of Leibovitz's L-15 Medium, without phenol red (Fisher, 21083027) and supplemented with 10% fetal bovine serum was added in each well. The multi-well plate was then transferred to the microscope stage for initiation of time-lapse acquisition. For imaging we used an inverted Nikon Eclipse Ti2-E with a Prime BSI sCMOS camera (Teledyne Photometrics) using a ×40 CFI Super Plan Fluor ADM ELWD objective with a NA 0.60 and the NIS-Elements Microscope Imaging Software (Nikon Metrology). Multi-channel images of the phase contrast image of cells, the nuclei fluorescence and the tracer beads' fluorescence were taken every 10 min. After approximately 8 h of imaging, the acquisition was stopped and 10% SDS was added to the wells to detach the cells from their matrix. Reference images of the beads in the undisturbed hydrogel surface were acquired. We used a particle image velocimetry-like technique to compare the image of the tracer beads at each instance of time with the reference image to determine the beads' displacements in MATLAB (MathWorks) (Gui and Wereley, 2002). We used interrogation windows of 48 × 24 pixels (window size × overlap). Calculations of the two-dimensional traction stresses that MDCK cells in monolayer exert on the hydrogel are described elsewhere (Bastounis et al., 2014; Lamason et al., 2016) and were performed also in MATLAB. For calculation of the number of nuclei in each recording the images of Hoechst-stained nuclei were used and the Fiji (ImageJ) plugin Trackmate was used for segmentation of cell nuclei and tracking. Output data from Trackmate were exported as xml files and read in Matlab to calculate cell speed based on nuclear motion (Hayer et al., 2016).

2.1.6 Monolayer Stress Microscopy (MSM)

Traction stresses were retrieved from the TFM measurements described above. We assumed perfect cell-substrate adhesions and complete confluence of the monolayer. We neglected the components of the traction forces perpendicular to the plane of the monolayer. We considered the traction forces exerted by the cells on their substrate are equal to the forces applied by the substrate on the cells but pointing in the opposite direction (third Newton's law). We also assumed that the monolayer displayed a uniform and constant thickness, which was much smaller than the dimensions of the monolayer. Thus, this methodology is only valid at the early stages of intercellular bacterial spread, just before mounding occurs (approximately 16 h post-infection). The domain was discretized with a finite element mesh (element size 28.352 μm) and monolayer stresses (that is inter- and intra-cellular stresses) were computed under the hypothesis of plane stress [for more details of the methodology see Tambe et al. (2011); Aparicio-Yuste et al. (2022)]. We initially considered that the stiffness of both uninfected surrounders and infected cells is the same ($R_E = 1$) but also ran MSM for the case where infected cells are four-fold softer than uninfected surrounders ($R_E = 4$) and confirmed that qualitatively the tangential monolayer stresses did not look significantly different. Custom-written scripts are publicly available at https://github.com/ebastoun/Monolayer-Stress-Microscopy.

2.2 *In silico* Experiments

We built an *in silico* model of the epithelial monolayer considering both infected and uninfected surrounder cells as well as cell-cell and cell-ECM adhesion contacts. The monolayer resided on either a 3 kPa, 10 kPa, 20 or 35 kPa ECM or on a 2 GPa glass coverslip.

2.2.1 The Geometry and Material Properties of our Model

Although the ECM microstructural composition and mechanical properties are highly complex and vary at different length scales (Sun, 2021), for simplicity we assumed that the matrix where cells reside is a continuum medium and as such an average value of its mechanical properties was chosen. We also assumed that the matrix is an elastic isotropic material, as proposed previously (Kandemir et al., 2018). Epithelial cells were simulated in this work as individual components. Although the cell monolayer structure and functions arise from individual entities or cells, we assumed that cells in the monolayer act as a collective since every given cell interacts with its neighbors through cell-cell junctions. Cells were simulated as regular hexagonal prisms despite the more diverse topology they show in a monolayer. This hexagonal pattern is the most frequent polygon type in cell monolayers since it maximizes the space filled by cells in a tissue (Lecuit and Lenne, 2007). Each individual cell was divided into three domains: the contractile, the adhesive and the expanding/protrusive (Bastounis et al., 2021b). This enabled us to simplify the cell architecture and allowed us to simulate computationally cell dynamic changes,

such as cellular deformations, cell-ECM traction adhesions and cell protrusions. Additionally, both active and passive cell behaviors were considered in our model. The passive was simulated so to account for the stiffness arising from the cellular cytoskeleton (e.g., the microtubules or intermediate filament network), whereas the active accounted for the actomyosin contractile apparatus and actin polymerization (Moreo et al., 2008; Borau et al., 2011).

2.2.2 Cell-ECM and Cell-Cell Mechanical Interactions Considered

The mechanical interactions of cells with their ECM and between each other were taken into account in our model through cell-ECM contact and cell-cell interactions, respectively. Cell-cell interactions were considered through a continuum approach, assuming perfect adhesions through a linear elastic thin element that transmits the loads between cells. Thus, cells were able to sense forces from their neighbors and interact with them. Cell-ECM adhesions were simulated by a cohesive contact interaction between two surfaces, the given cell and the ECM. The higher the stiffness of the contact, the more difficult the relative displacement between the two surfaces. Furthermore, we worked under the assumption of perfect cell-ECM adhesions, meaning that all the force is transmitted from the cell to the ECM and vice versa.

2.2.3 Assumed Mechanotransduction Scheme Used by Non-infected Cells to Detect Infection

To better examine the impact of infection on the collective squeezing that leads to extrusion of infected epithelial cells, we simulated a cellular cycle where certain cells (e.g., infected) are allowed to experience different degrees of protrusion or strength of adhesion to their ECM. In settings not involving infection (uninfected case), all cells presented the same mechanical behavior. To simulate infection, cells infected with bacteria were assumed to have distinct mechanical properties as compared to neighboring uninfected cells (infected case). More specifically and based on previous experimental findings, infected cells were considered softer and with decreased active stiffness as compared to neighboring uninfected cells (Bastounis et al., 2021b).

For simplicity, bacterial infection was considered fixed, that is, bacteria did not spread or replicate intracellularly during the simulation period. For both infected and uninfected monolayers, we analyzed the cellular behavior over the course of this cellular cycle and according to a mechanotransduction scheme. Briefly, all cells were first exposed to a round of contraction in order to sense and bear loads from their neighboring cells and their ECM. This contraction resulted in cell-ECM displacements and allowed the cells to move with respect to their ECM. If the cell-ECM displacements were large when cells contract, we assumed new cell-ECM adhesions would form, followed by a new cycle of contraction. Once new adhesions were formed, cellular protrusion would occur only if the given cell exhibited asymmetry in its tensional distribution (in the direction of the stress gradient). This means that the cell actively responded to the non-symmetrical distribution of the stresses by protruding. In our simulations, this occurred only during infection and was observed only in uninfected cells close to the infection focus. These cells exhibited tensional asymmetry and thus protruded towards the direction of minimum stress, which lied at the edge of the infection focus.

To summarize, we simulated and examined the 3D dynamics of a cell monolayer residing on a flat ECM of a given stiffness in two particular cases: uninfected and infected condition. We considered that in the uninfected case, all cells in the monolayer exhibited similar mechanical properties and interactions with their ECM. However, under conditions involving infection, cell-ECM traction adhesions of infected cells were weakened compared to uninfected surrounder cells, and new strong traction adhesions were formed along surrounding uninfected cells (where the cells sense there was a large relative displacement with respect to the ECM). In turn, the uninfected cells protruded towards the infection focus due to their tensional asymmetry.

2.2.4 Implementation

The mechanical interactions of infected cells with surrounding uninfected cells in a monolayer were analyzed with a three-dimensional, finite element model using the commercial software ABAQUS CAE 6.14 (Dassault systèmes Simulia Corporation). The general model is described elsewhere (Bastounis et al., 2021b). Based on this model, we built here a FEM of infected and uninfected cell monolayers taking into account additional considerations as outlined below. Regarding the geometry, we assumed two main entities: the ECM and the cells. The parameters characterizing the cells and ECM domains are summarized (**Table 1**) and were chosen based on previous *in vitro* studies (O'Dea and King, 2012; Schmedt et al., 2012; Escribano et al., 2019). Overall, 217 individual cells and their junctions coexisted, collectively forming a hexagonal monolayer. This hexagonal pattern of the monolayer was selected to avoid artifacts arising from asymmetries.

Our model is composed by four main domains: uninfected cells (Ω_{uninf}), infected cells (Ω_{inf}), cell-cell junctions ($\Omega_{junction}$) and ECM (Ω_{ECM}). Concerning material properties, cells and ECM were assumed to behave as linear elastic materials (Escribano et al., 2018); as we were not interested in long-term effects, we just simulated a short period of time (one contraction-protrusion cycle). The Young's modulus (measure of stiffness) of uninfected surrounder cells was considered of the order of 1,000 Pa, while that of infected cells of 250 Pa, as previously measured by Atomic Force Microscopy (AFM) experiments (Bastounis et al., 2021b). Cell-cell junctions were assumed to have a Young's modulus of 1,000 Pa, and this value was selected so that the continuity of the mechanical properties of the monolayer is preserved. To interrogate the role of ECM stiffness on infected cell squeezing, we considered different ECM stiffnesses in our simulations, namely: soft, stiff and glass matrices with elastic moduli of 3 kPa, 10 kPa, 20 kPa, 35 kPa, and 2 GPa, respectively, values corresponding to the polyacrylamide hydrogels we built for our *in vitro* experiments and the glass coverslips commonly used. The Poisson's ratios were set to 0.48 (Moreo et al., 2008) and 0.45 (Alvarez-González

TABLE 1 | Summary of the features of the computational model.

Domain	Geometry	Dimensions (μm)	Mechanical properties
ECM	Rectangular prism	220 × 220 × 20 (LxWxH)	E = 3, 10, 20, 35 kPa and 2 GPa (glass); ν = 0.45
Cell	Hexagonal prism	Hexagon side length = 7; Height = 7	E = 1 kPa (uninfected cells); ν = 0.48
Cell-cell junction	Thin sheet	7 × 0.01 × 7 (LxWxH)	E = 1 kPa; ν = 0

TABLE 2 | Mechanical parameters in our computational model.

	Uninfected		Infected	
	E (Pa)	ν (–)	E (Pa)	ν (–)
Passive	500	0.48	125	0.48
Active	500	0	125	0
Cell	1,000	—	250	—

et al., 2017) for cells and ECM, respectively, since both are nearly incompressible. We modeled the cells' active and passive behavior through two different meshes in the model with shared nodes. This strategy allowed us to separate active protrusion and contraction from passive contractility.

In order to simulate cell contraction and expansion/protrusion, we followed the analogy of the thermoelastic expansion equations governing volumetric changes in both contraction and expansions processes (Vujošević and Lubarda, 2002; Hervás-Raluy et al., 2019; Nieto et al., 2020). We assumed the contractile part of the cell was exposed to a negative volumetric change, decreasing its volume. On the contrary, the protruding part of the cell was subjected to a positive volumetric change, increasing its volume. According to our experimental observations, minimal change in cell height was observed during contraction, remarking the importance of cell contraction in the plane of the monolayer. Therefore, we assumed non-isotropic contraction, i.e., the contraction occurred just in the plane of the monolayer to avoid changes in cell height. In such manner, we generated area changes in the plane of the monolayer, but not in the normal direction, thus the Poisson's coefficient of the active part was set to zero and the same was applied to cell-cell junctions (**Table 1** and **Table 2**).

Cell-cell interactions were simulated in ABAQUS through a contact interaction, where the normal direction of the contact behaved as a "hard" contact and the tangential direction acted as a frictionless surface. However, we used surface-to-surface contacts to model cell-ECM adhesions under the assumption of perfect cell-ECM adhesions. The domain of the cell referred to as adhesion site was attached to the ECM surface via a cohesive contact. The strength of the traction adhesions (active cellular adhesion sites that transmit traction forces to the ECM) was determined by the stiffness of the matrix **K** and its stiffness coefficients (K_x, K_y, K_z), where K_x and K_y are the two shear traction adhesions in the plane of the ECM and K_z the normal traction adhesion to the plane of the ECM. The higher the stiffness coefficients K_i, the stronger the traction adhesion between the cell and the ECM is and the lower the K_i, the weaker the traction adhesion is. By tuning these parameters, we differentiated three types of cell-ECM contacts. The first type of contact described the formation of new adhesions at the edge of the infection focus on the side of the surrounding uninfected cells, with the stiffness coefficients (K_x, K_y, K_z) = (10, 10, 10) kPa. These high values created a strong cell-ECM contact which is one of the mechanisms that uninfected cells use to fight against infected cells, by squeezing them and eventually eliciting their extrusion. The second type of contact is a general cell-ECM contact whose stiffness coefficients were set to (0,0,0.1) kPa. This condition represented a general cell-ECM attachment, meaning that cells could move in the plane but they could not be separated from the ECM. The third contact concerned infected cells which present weaker cell-ECM traction adhesions and therefore, we assumed their stiffness coefficients were (0,0,0.001) kPa. This distinction between infected and uninfected traction adhesion coefficients was not considered in our previous model (Bastounis et al., 2021b).

The ECM was meshed with standard linear hexahedral solid elements, whose mesh density was higher at the center of the upper surface. Both cell-cell junctions, regions of the cell referred to as protrusion and adhesion, were meshed with linear hexahedral solid elements in order to obtain coincident nodes and regular connectivity. The cell contraction part was meshed with linear triangular prisms to keep the continuity of the mesh. Additionally, to account for the passive and active behavior of the cell, we used two superimposed meshes to which we associated the mechanical properties of the active and passive part of the cell (**Table 2**). The model resulted in 93.948 nodes and 148.239 elements. As boundary conditions, we assumed all displacements were prevented at the bottom surface of the ECM. In addition, the displacements of all the cells that were at the edge of the monolayer were restricted. These conditions were consistent with our experimental setup. Furthermore, our *in vitro* experiments were performed by choosing the field of view to be near the center of the well on which the cellular monolayer was formed, thus edge effects should be negligible.

To provide novel insight into the role of ECM stiffness in promoting infected cell squeezing, we run simulations using our computational model. First, we tested the impact of ECM stiffness in mound formation by assigning distinct values of ECM stiffness. We considered matrices that are soft, stiff and infinitely stiff (i.e., glass) with an elastic modulus of 3 kPa, 10 kPa, 20 kPa, 35 kPa and 2 GPa, respectively. Second, we investigated how infection spread affects mounding by considering different size infection foci comprised by varying number of infected cells on both soft and stiff

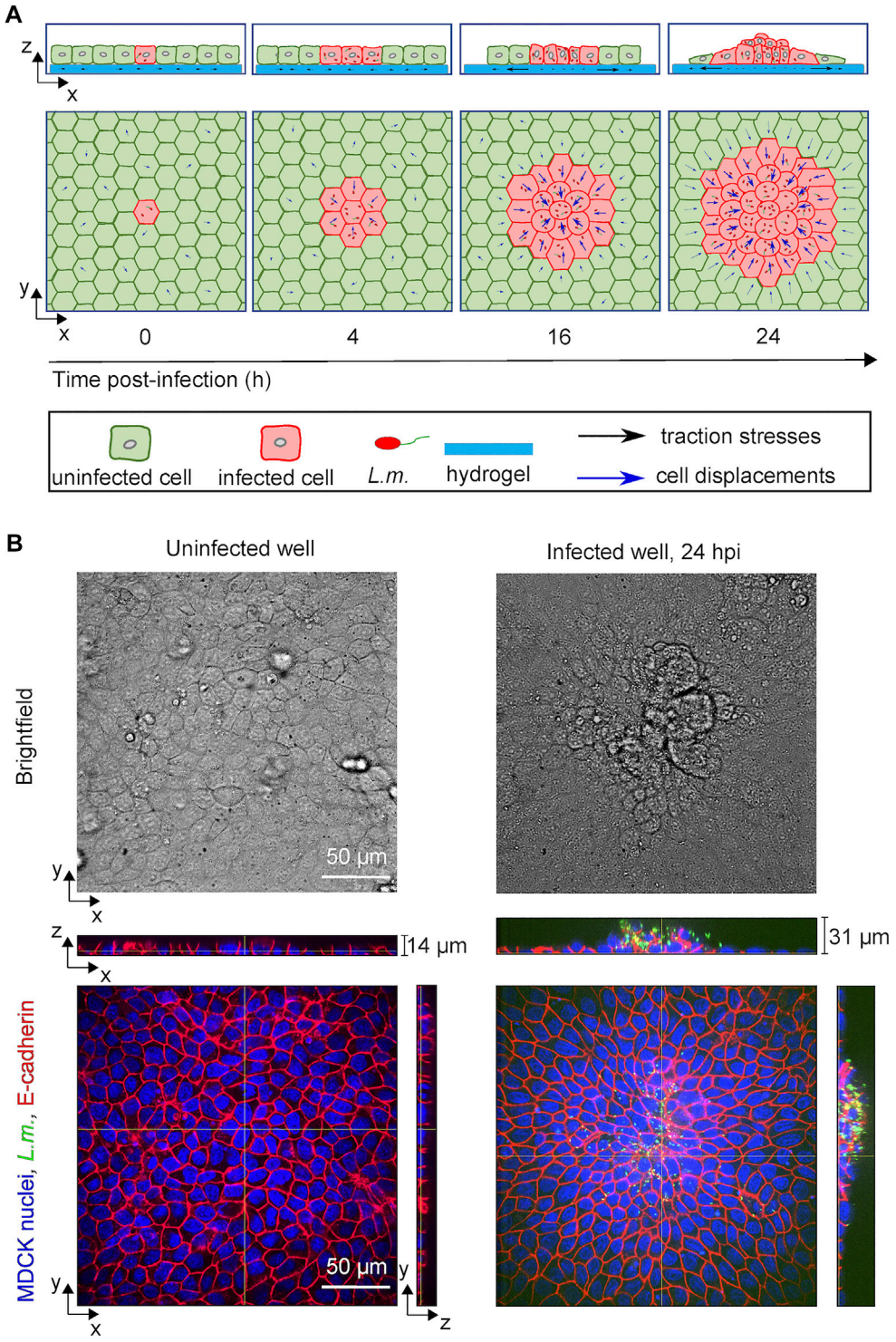

FIGURE 1 | *L.m.*-infected epithelial cells in monolayer get collectively extruded at late infection. **(A)** Schematic illustration showing the time course of *in vitro* infection of host epithelial cells with *L.m.* so that infection mounds emerge at late infection (24 hpi). Initially a single cell gets infected by *L.m.* (0 hpi), but as time proceeds bacteria replicate and spread to neighboring cells (4 hpi). Uninfected surrounder cells (green) start actively migrating towards the infection focus comprised by several infected cells (red), while softer and less contractile infected cells get squeezed (16 hpi) and eventually extruded (24 hpi) out of the cellular monolayer. **(B)** Representative brightfield image (top row) and orthogonal views (bottom row) of *L.m.* fluorescence in green, E-cadherin in red and MDCK nuclei in blue for cells originating from an uninfected well (left column) and from a *L.m.*-infected well with the field of view shown focused around and infection focus at 24 hpi (right column).

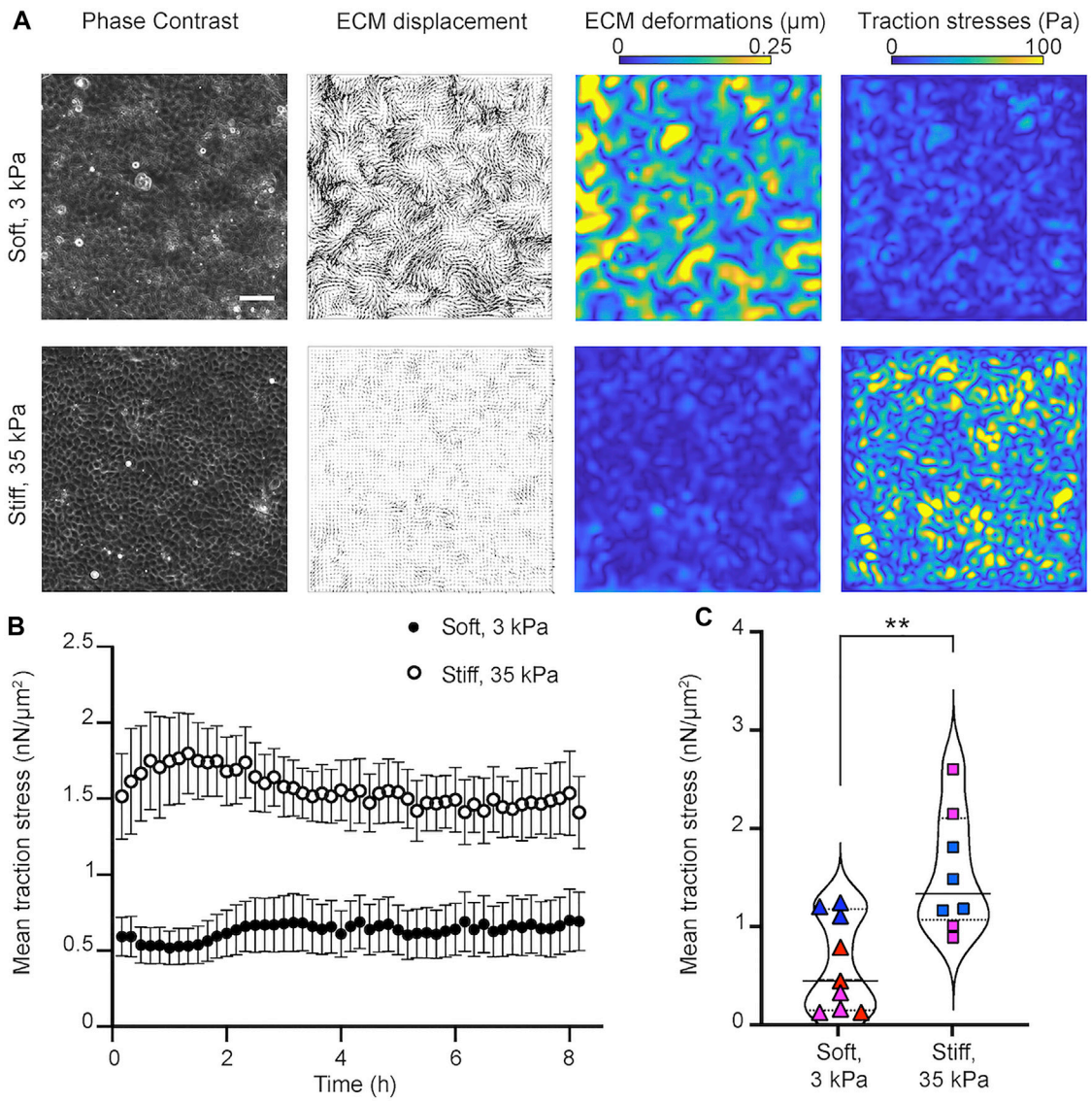

FIGURE 2 | Epithelial cells in monolayer exert higher traction stresses when residing on stiff as opposed to softer matrices. **(A)** Traction force microscopy performed on MDCK cells residing on soft, 3 kPa (upper row) and stiff, 35 kPa (bottom row) hydrogels. Columns of a representative time instance show: phase contrast image of cells, displacements imparted by the cells on the hydrogel (vectors), corresponding deformations (colormap shows magnitude, μm) and traction stresses exerted by cells (colormap shows magnitude, Pa). Scale bar is 50 μm. **(B)** Plot of the mean traction stress magnitude (*y*-axis) versus time (*x*-axis). Mean ± SEM are shown for $N = 8$ and $N = 9$ TFM recordings performed on stiff 35 kPa and soft 3 kPa gels, respectively. **(C)** Violin plots of the mean traction stress magnitude for all recordings and time points shown in panel **(B)**. Symbols show the time average of the mean traction stress for each recording. Same color points correspond to recordings performed the same day on different wells. Solid line indicates the mean and dotted the STD of all time averages. **: $p < 0.001$, Wilcoxon Ran Sum test.

matrices. Lastly, we examined how the ratio of uninfected to infected cell passive and active stiffness affects mound formation when ECM stiffness varies. We ran several cases within the same range of the ratio of uninfected to infected cell stiffness (R_E), which we defined as:

$$R_E = \frac{E_{uninf}}{E_{\text{inf}}} \tag{1}$$

where E_{uninf} the Young's modulus of uninfected cells and E_{inf} the Young's modulus of infected cells.

3 RESULTS

3.1 Epithelial Cells Exert Higher Traction Stresses When Residing on Stiff as Compared to Soft Matrices

We have shown that during late infection of epithelial cells with *L.m.* (> 16 hpi) a mechanical competition takes place leading to squeezing of softer and less contractile infected cells by stiffer and more contractile uninfected surrounder cells, which actively

migrate with high speeds towards the infection focus (Bastounis et al., 2021b) (**Figure 1A**). As a result of this mechanical battle, infected cells are extruded out of the basal monolayer and pile up forming large 3D "mounds" whose height typically exceeds 30 μm, which is at least three-fold higher than the typical height of cells in non-infected cell monolayers (**Figure 1B**). Given that it is well known that cell mechanics are modulated by ECM stiffness, we hypothesized that ECM stiffness will impact cellular stiffness and traction force generation and that these, in turn, would impact formation of infection mounds. To assess whether ECM stiffness affects the traction stress-generating ability of cells and whether the magnitude of traction stresses is modulated based on ECM stiffness, we cultured Madin-Darby Canine Kidney (MDCK) epithelial cells as confluent monolayers on hydrogels of varying stiffness. We chose this cell line because it forms polarized and homogeneous monolayers in tissue culture and have broadly been used in studies examining *L.m.* infection (Ortega et al., 2019; Bastounis et al., 2021b). Cells were placed on collagen-I coated soft polyacrylamide hydrogels of 3 kPa or stiff hydrogels of 35 kPa. These values were chosen based on previous studies reporting that the elasticity of intestinal ECM broadly ranges from 1 to 68 kPa (Onfroy-Roy et al., 2020). Hydrogels were embedded with tracer beads such that, as cells in the monolayer pull on the hydrogels via their focal adhesions and on each other via cell-cell adhesions, tracer bead movement can be monitored via time-lapse microscopy. Using the fluorescence images of the beads we inferred the deformations that cells imparted on the gels and the traction stresses they exerted on to it through Traction Force Microscopy (TFM) (**Figure 2A** and **Supplementary Movie S1**). 3 kPa is the lowest stiffness we examined since as reported, MDCK on low stiffness gels (< 3 kPa) do not form monolayers but rather aggregate-like structures (Balcioglu et al., 2020). 35 kPa gels are considered as our stiffest condition, since this was found to be the highest stiffness on which the cells can still deform the gels at enough resolution to be measured accurately with TFM (data not shown).

By seeding MDCK cells at a concentration of 4×10^5 cells per well, on wells from a 24-well plate, we found that MDCK were able to form confluent monolayers with similar number of cells on soft 3 kPa and stiff 35 kPa gels 24 h post-seeding (**Supplementary Figure S1A**). Moreover, at these high cell confluence conditions, the speed of migration of cells was minimal (~ 0.08 μm/min) and similar on soft and stiff hydrogels (**Supplementary Figure S1B**). Nevertheless, MDCK residing on stiff 35 kPa gels generated significantly higher traction stresses but imparted reduced deformations as opposed to the softer 3 kPa gels where deformations were higher but traction stresses were overall lower. As expected, the average traction stresses generated by cells pertaining in a field of view were significantly higher for cells residing on stiff as compared to softer matrices (**Figures 2B,C**). Therefore, we conclude that under conditions that do not involve infection and where epithelial cells form a highly confluent monolayer, that is, at steady state, cells exert higher traction forces on stiff 35 kPa hydrogels as opposed to softer 3 kPa ones.

3.2 Considerations and Assumptions of the Infection Computational Model That Accounts for the ECM Stiffness

Our experimental results demonstrate that epithelial cells in monolayer exert higher traction stresses when residing on stiff as opposed to softer matrices. Given this finding, we wondered whether ECM stiffness would similarly impact cell produced traction stresses if we were to use and further develop our model to run *in silico* infection experiments (Bastounis et al., 2021b). Using this model, in turn, we could examine how cellular traction stresses vary as a function of ECM stiffness also when a focus of infected cells is present within the monolayer.

Our computational model relies on certain simplifications, namely, the cells are considered as linear elastic hexagonal prisms and are divided in three domains: the contractile, the adhesive and the expanding/protrusive (**Figure 3A**). We model cell-cell junctions as linear elastic elements in contact to each other (**Figure 3B**), and cell-ECM traction adhesions (i.e., focal areas at the ventral side of cells where traction stresses are exerted onto the underlying matrix) as surface-to-surface contacts (**Figure 3C**). The strength of the traction adhesions is characterized by the matrix parameter **K**, which links cellular traction stresses to cell and matrix displacements in all three different directions. Given our previous study, we also take into account that uninfected surrounding cells exert higher traction stresses as compared to nearby infected cells (**Figure 3C**). In the case of infection, for simplicity we assume that bacteria cannot replicate intracellularly or spread from cell to cell, so cells are either infected (red) or not (green) and their total number is fixed. In our *in silico* 3D monolayer the mechanical parameters of cells are based on previous experimental measurements (Bastounis et al., 2021b), and ECM stiffness is chosen so that it matches our experimental results and *in vitro* measurements (**Figure 3D**). The simulations were run using a finite element method (FEM) approach which allowed us to analyze the cell displacements and stresses in the whole considered geometry and according to the mechanotransduction mechanism depicted in **Figure 3E**.

3.3 *In silico* Model Predicts That Increased ECM Stiffness Promotes Mounding by Enhancing Cell Displacements and the Traction Stresses That are Generated by Nearby Uninfected Cells

Through our *in silico* model, we examined first whether cells on soft 3 kPa ECM as compared to stiff 35 kPa ECM would impart increased ECM displacements and exert reduced traction stresses *in silico* similar to what we previously determined *in vitro* (**Figure 2**). Not only were we able to validate our computational model but given the time efficiency of running *in silico* experiments, we sought to predict how would cells behave on ECM of intermediate stiffness (namely 10 and 20 kPa) and on stiff (~2 GPa) glass typically used for *in vitro* experiments

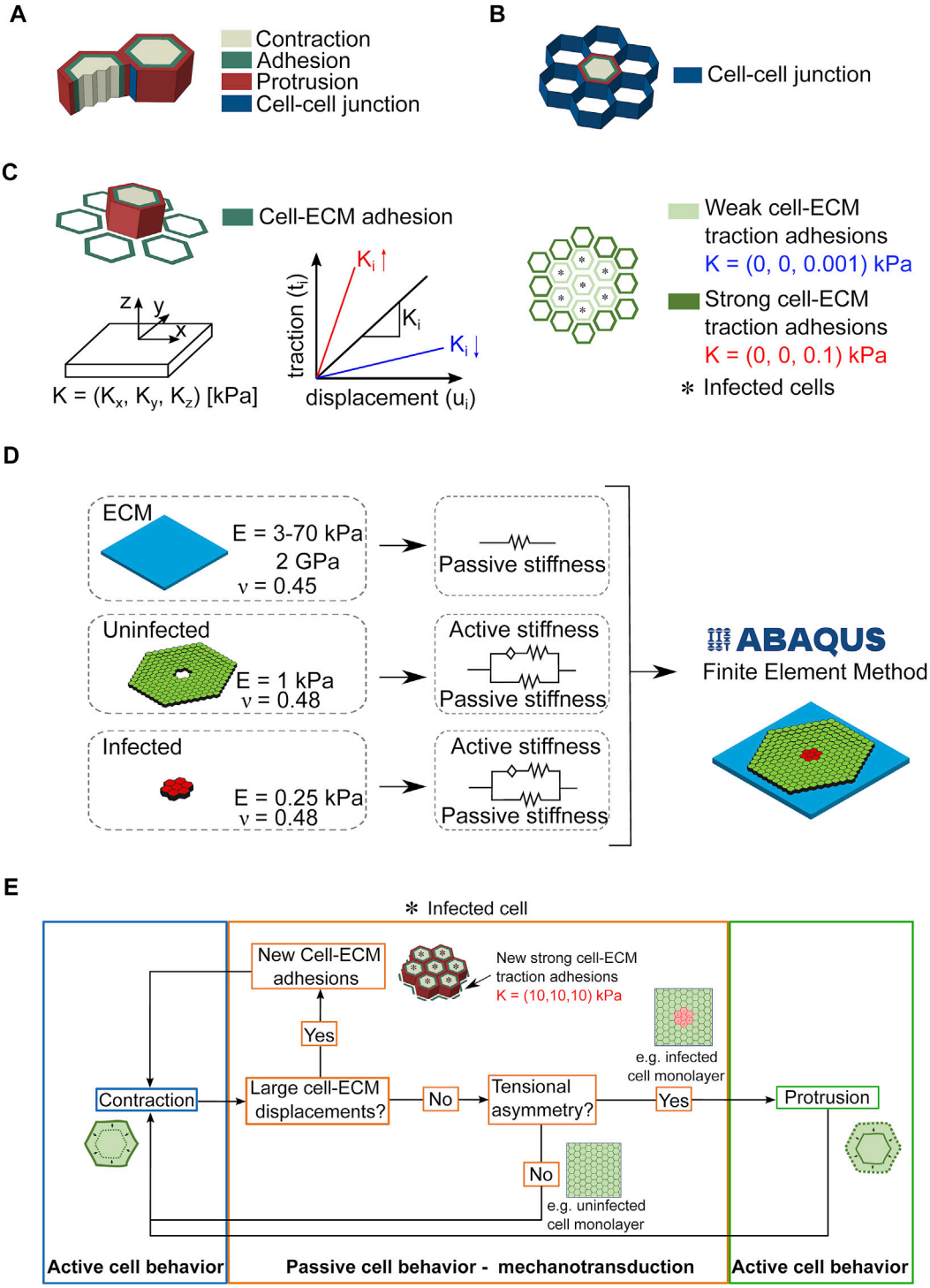

FIGURE 3 | Considerations and assumptions of the infection computational model. **(A,B)**. Sketch showing that cells are approximated in the computational model as hexagonal prisms that form cell-cell junctions with six neighboring cells and are partitioned in three domains: contractile, adhesive and protrusive **(A)**. Cell-cell junctions are modeled as linear thin elastic elements **(B)**. **(C)** Left schematic illustration shows how the cell produced traction stresses exerted to the ECM are modeled through surface-to-surface contacts between the cell and its ECM. The strength of the traction adhesions is characterized by **K** through its stiffness coefficients (K_x, K_y, K_z), with z being the normal direction to the surface, and x and y the directions in the plane of the surface. The higher (lower) the value of K_i (for i equal to x, y or z), the stronger (weaker) the traction adhesions shown in red (blue). Right schematic illustrates an *in silico* infection focus with infected cells denoted by an asterisk. In our model, unlike surrounding uninfected cells, infected cells form very weak traction adhesions with the ECM. **(D)** Sketch depicting the domains of the Finite Element Model (FEM) used to compute cellular displacements and traction stresses exerted by cells on their ECM over time and during bacterial infection. The mechanical properties characterizing the domains are also shown. **(E)** Diagram illustrating the cell mechanotransduction mechanism that drives cell kinematics and dynamics in the cell computational model.

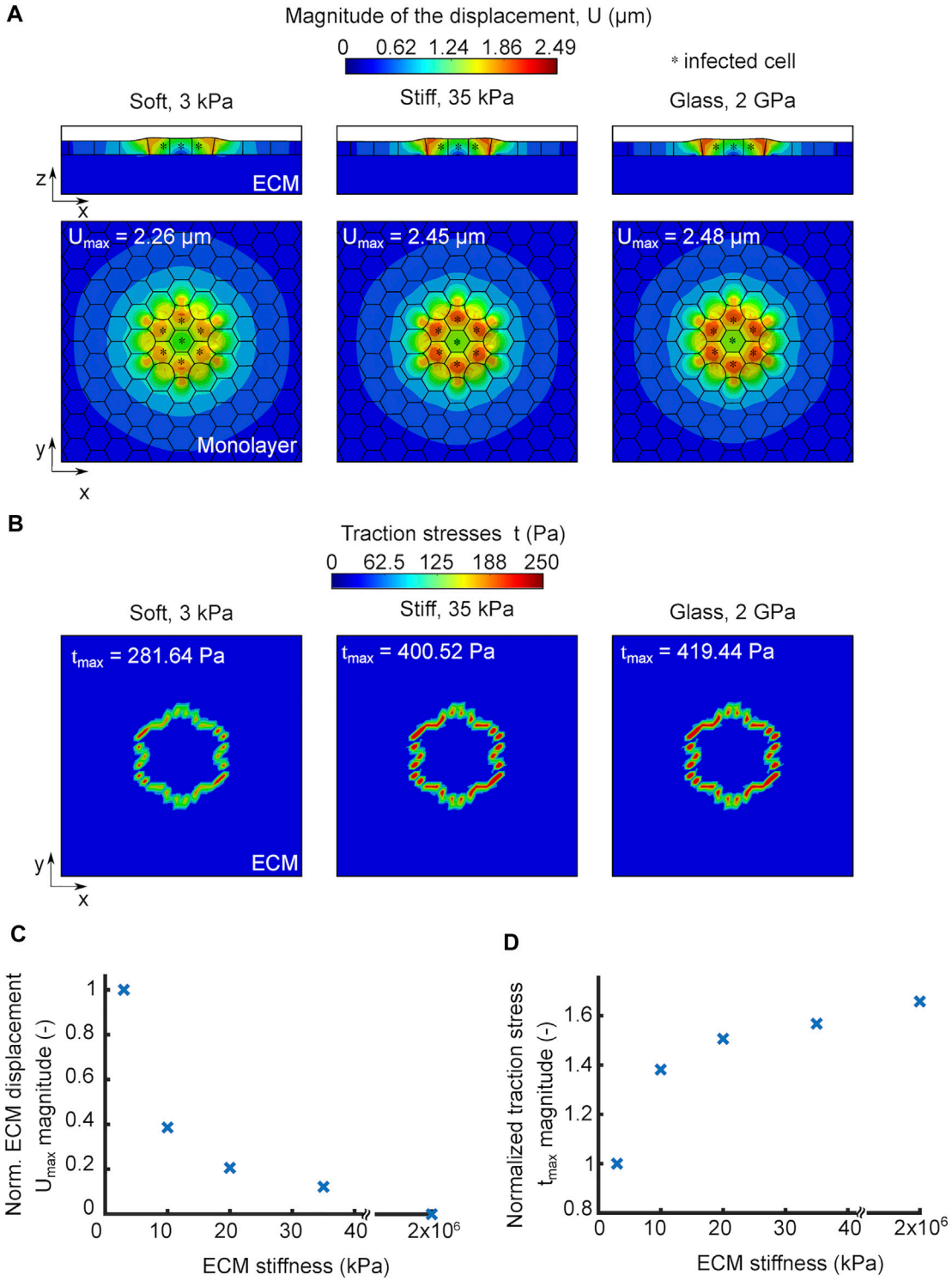

FIGURE 4 | *In silico* model predicts that increased ECM stiffness promotes infected cell squeezing by enhancing cell displacements and traction stresses of nearby uninfected cells. **(A)** Orthogonal view maps of the magnitude of cellular displacements U (μm) of *in silico* infected cells residing on soft 3 kPa gel (left), stiff 35 kPa gel (middle) and 2 GPa glass substrate (right). Top (x–y) and side (x–z) views are shown in all three cases, and infected cells are denoted by an asterisk. An infection focus comprised by 7 cells is considered. The maximum cell displacement is indicated. **(B)** Orthogonal view maps of traction stresses exerted onto the ECM by the cells shown in panel A which have been exposed to *in silico* infection and reside on soft, stiff and glass matrices. The maximum traction stress is indicated. **(C)** Plot showing magnitude of maximum cell displacement (U_{max}, *y*-axis) versus ECM stiffness (*x*-axis) for *in silico* cells in an infected monolayer. U_{max} values are normalized relative to U_{max} for cells residing on soft 3 kPa ECM. **(D)** Plot showing the magnitude of maximum traction stress (t_{max}, *y*-axis) versus ECM stiffness (*x*-axis) for *in silico* cells in an infected monolayer. t_{max} values are normalized relative to t_{max} for cells residing on soft 3 kPa ECM. For C-D the infection focus consists of $N = 7$ infected cells.

(**Supplementary Figures S2A,B**). We found that ECM displacements imparted by cells decreased following an exponential decay with increasing matrix stiffness. On the contrary, traction stresses increased monotonically reaching an asymptotic value at higher ECM stiffness.

We used our *in silico* model, to examine whether ECM stiffness would play a role in infection impacting the traction stress generating capacity of uninfected surrounder cells and, in turn, their mechanical competition with infected cells. We simulated infection by considering a cell monolayer residing on an ECM of a given stiffness and comprised by an infection focus containing just seven infected cells. We considered three different cases where the only parameter we varied was the ECM stiffness. Similar to our TFM experiments, we simulated infection in three different conditions, that is, with cells residing on 3 kPa ECM (soft), on 35 kPa ECM (stiff) or on a 2 GPa glass coverslip (glass), and let the simulations run for the same amount of time (one contraction-protrusion cycle). We noticed that cells in monolayers residing on a stiff matrix or glass exhibited larger cellular displacements compared to those residing on a soft matrix (**Figure 4A**). The maximum displacements observed in the simulations were 2.26, 2.45 and 2.48 μm for cells residing on soft matrix, stiff matrix and glass, respectively. Therefore, we can conclude that *in silico* cells within and near infection foci undergo larger displacements (directly related to squeezing of infected cells and subsequent mounding) when residing on stiff as opposed to softer ECM.

We previously showed that the ability of uninfected surrounders to produce strong traction stresses as they migrate towards the infected cells is key in squeezing the latter and eventually eliciting their extrusion. We thus wondered whether the more pronounced cellular displacements observed on stiff ECMs are driven by the increased traction stress generating capacity of uninfected, surrounding cells. To test that, we computed the traction stresses that cells exert on all three scenarios presented in **Figure 4A** and found the magnitude of traction stresses was higher for cells residing on stiffer matrices and predominantly high for surrounding, uninfected cells just at the edge of the focus since those are the ones that form protrusions in our model due to their tensional asymmetry (**Figure 4B**). The maximum traction stresses exerted by cells on the substrate were 281.64, 400.52 and 419.44 Pa for the soft, stiff and glass matrices, respectively. It is interesting that a 10-fold difference in ECM stiffness, when one compares cells residing on soft 3 kPa to stiff 35 kPa matrices, results in 42% increase in traction stresses, while a five order of magnitude increase in ECM stiffness, when comparing cells residing on 35 kPa hydrogels to 2 GPa glass, results in only 5% increase in the traction stress magnitude, suggesting that this mechanosensing mechanism is highly non-linear. Consistent with this, the change in maximum cellular displacements when comparing soft to stiff ECM is larger than when comparing stiff ECM to glass. When we ran simulations to examine the modulation of ECM displacements and traction stresses in a range of ECM stiffnesses for *in silico* cells during infection, we found the same trend as for non-infected cells (**Supplementary Figures S2A,B** and **Figures 4C,D**). The only difference between infected versus non-infected monolayers is that the extent to which traction forces increased with increasing ECM stiffness was larger during infection, likely because cells in this case are able to undergo protrusion due to development of stress asymmetries. Altogether, we conclude that increasing ECM stiffness gives rise to stronger cell-ECM traction stresses and enhanced cellular displacements, which is expected to increase infected cell squeezing and subsequent extrusion.

3.4 A Smaller Infection Focus or a Larger Difference in Stiffness of Uninfected Surrounders Relative to Infected Cells (Mounders) Increases the Squeezing of Infected Cells

Previous studies on endothelial cells infected with *L.m.* suggest that intercellular bacterial spread is enhanced when cells reside on softer ECM where enlarged infection foci are observed as compared to a stiffer ECM (Bastounis et al., 2018). To examine how the size of infection foci might impact cellular displacements and infected cell squeezing, we considered in our simulations two scenarios: 1) an infection focus comprised of just seven infected cells (small) and 2) a larger infection focus comprised of 19 infected cells (large). We also considered that these foci can be present on soft, stiff or glass ECM and run our simulations to compute the resulting cellular displacements (**Figure 5A**). We found that, independent of ECM stiffness, smaller infection foci result in cells undergoing larger cellular displacements and therefore, infected cell squeezing as compared to larger infection foci (**Figure 5B**). However, the percentage of reduction in maximum cell displacement when comparing small to large infection foci is more pronounced on stiffer as opposed to softer matrices, although the difference is subtle (**Figure 5C**).

An additional mechanical property that could change when host cells reside on soft versus stiff ECM is their passive stiffness arising from the organization of their cytoskeleton. Previous AFM measurements we conducted showed that, when residing on soft 3 kPa gels, infected cells at the edge of mounds exhibit a mean stiffness of 350 Pa while uninfected surrounding cells are 1,000 Pa stiff (Bastounis et al., 2021b). We also showed that changes in the ratio of uninfected to infected cell stiffness between the two populations are sufficient to lead to infected cell extrusion. Here we sought to determine whether and how changes in the ratio of uninfected to infected cell stiffness influence infected cell squeezing depending on ECM stiffness. To that end, we considered three distinct values of stiffness for uninfected surrounder cells, namely, 500, 1,000 and 2,000 Pa (left, center and right plot in **Figure 5D**). For each of these fixed values we ranged the stiffness of infected cells so that R_E (the ratio of uninfected to infected cell stiffness) ranges from 1 to 16. In addition, as in previous *in silico* experiments, we considered three different degrees of ECM stiffness, namely, soft, stiff and glass. We found that, irrespective of the stiffness of surrounder cells, the larger the value of R_E, the higher the cellular displacements and thus infected cell squeezing. However, once R_E becomes higher than approximately 5, a slightly asymptotic behavior emerges, and the displacements stop increasing monotonically as if they

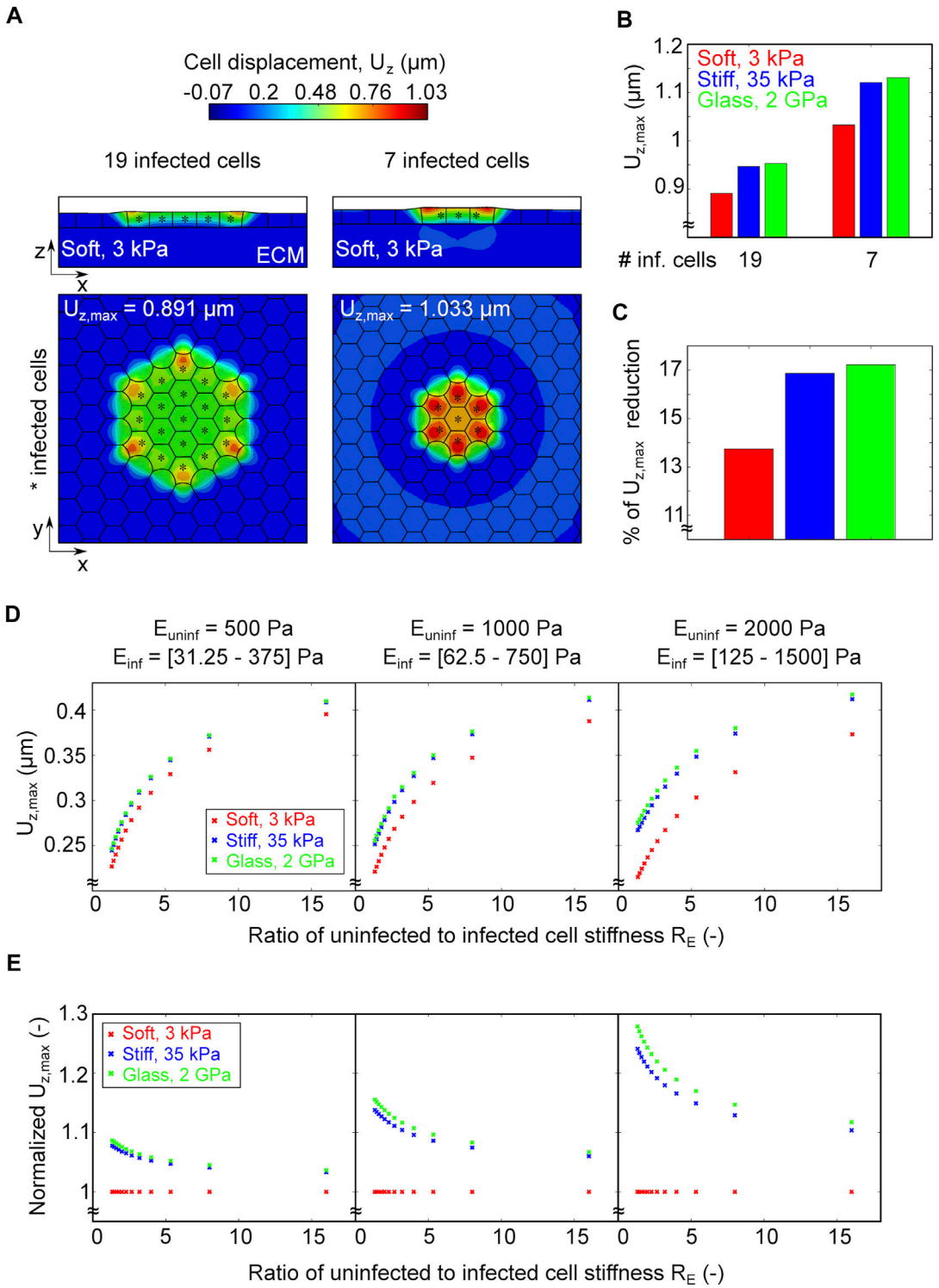

FIGURE 5 | A smaller infection focus or a larger difference in the ratio of uninfected to infected cell stiffness increase infected cell squeezing. **(A)** Ortoghonal view maps of the magnitude of cellular displacements in the vertical axis U_z (μm) of *in silico* infected cells residing on a soft 3 kPa gel. On the left panel the focus is comprised by 19 infected cells denoted by asterisk, whereas on the right by 7. Top (x–y) and side (x–z) views are shown in both cases. **(B)** Barplot of the maximum vertical displacement $U_{z,max}$ of cells residing on soft (red), stiff (blue) and glass (green) matrices in the case of a focus comprised by 19 or 7 infected cells. **(C)** Barplot of the relative decrease in $U_{z,max}$ when comparing foci comprised of 7 relative to 19 infected cells for each of the varying stiffness matrices indicated in the panels above. **(D)** Plots of the maximum vertical displacement $U_{z,max}$ (μm, vertical axis) versus the ratio of uninfected to infected cell stiffness (R_E, horizontal axis) for *in silico* infection foci comprised of 7 infected cells and cells reside on soft 3 kPa (red), stiff 35 kPa (blue) and 2 GPa glass (green) matrix. In the simulations we assumed that the stiffness of the uninfected surrounder cells was fixed and equal to 500 Pa (left), or 1,000 Pa (middle), or 2,000 Pa (right), while infected cells could experience a range of stiffness shown below the plots (R_E = 1–16). **(E)** Same as panel D but *y*-axis shows $U_{z,max}$ normalized to $U_{z,max}$ exhibited by cells on a soft 3 kPa matrix.

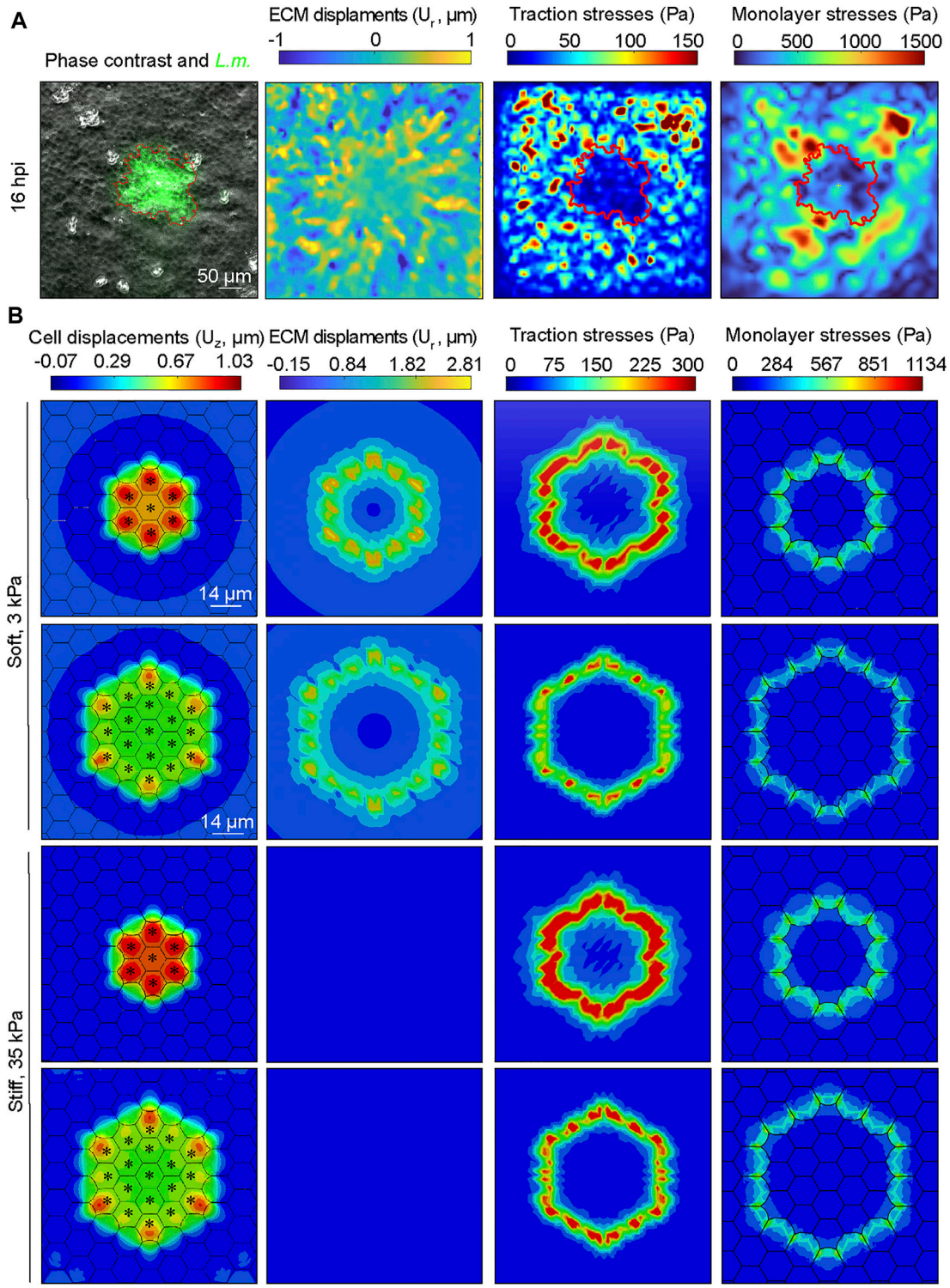

FIGURE 6 | Monolayer stresses are concentrated at the interface between infected and surrounding uninfected cells both experimentally and in our computational model. **(A)** Exemplary image of MDCK cells residing on a soft 3 kPa hydrogel and infected with *L.m.* Time point shown refers to 16 h. p.i. Field of view imaged is centered around an infection focus. Columns show from left to right: phase contrast image overlayed with *L.m.* fluorescence (green), radial ECM displacements (U_r: positive values indicate displacements pointing away from the focus center, µm), magnitude of traction stresses exerted by cells on the ECM (Pa), and magnitude of maximum monolayer tangential stresses (Pa). Red contour line indicates the area covered by infected cells (infection focus). **(B)** Same as panel A but the images depict the corresponding results of the infection computational simulations, with the exception of the first column which shows the configuration of the monolayer, the cell vertical displacements (µm) and where infected cells are denoted by an asterisk. First (second) row refers to a small (large) focus consisting of $N = 7$ ($N = 19$) infected cells residing on a soft 3 kPa ECM. Third (fourth) row refers to a small (large) focus consisting of $N = 7$ ($N = 19$) infected cells and cells reside on a stiff 35 kPa ECM.

had reached some plateau (**Figure 5E**). Moreover, we discovered that, irrespective of the stiffness of surrounder cells, for any given R_E the maximum cell displacements are lower for cells residing on soft matrices, while the displacements for cells residing on stiff matrix or glass are approximately the same, with those exhibited on glass being slightly higher than on stiff 35 kPa ECM. Interestingly, we found that the higher the absolute value of stiffness of uninfected surrounder cells, the stronger the difference in cellular displacements that cells undergo depending on ECM stiffness (**Figures 5D,E**). That is, for a given R_E, if the stiffness of uninfected surrounders is larger (e.g., 2000 versus 500 Pa) then the effect of increased ECM stiffness in enhancing cellular displacements and therefore infected cell squeezing will be more prominent (**Figure 5E**). Altogether, these results suggest that a smaller infection focus and/or large differences in stiffness between surrounders and mounders, both promote large cell displacements and enhance infected cell squeezing. In addition, both these effects will be stronger if the ECM stiffness is increased, although for larger ECM stiffness the increase in cellular displacements stops being monotonic reaching asymptotic values which indicate a saturation in the cell mechanical sensitivity to its surrounding environment.

3.5 Monolayer Stresses are Concentrated at the Interface Between Infected and Surrounding Uninfected Cells Both Experimentally and in Our Computational Model

Our simulations indicate that increasing the ratio of uninfected to infected cell stiffness between uninfected and infected cells enhances cellular displacements and squeezing of infected cells pertaining in the focus. This suggests that inter- and intra-cellular stresses at the interface between the two cell populations might play a critical role in promoting mounding. To test this, we first calculated the radial ECM displacements imparted by cells, the traction stresses they exert and the cell-cell stresses *in vitro* in an actual infection experiment focusing our attention on a single growing *L.m.* infection focus. We used TFM and Monolayer Stress Microscopy (MSM) to measure traction stresses as well as intra- and inter-cellular stresses (referred from here on as monolayer stresses) of cells residing on a soft 3 kPa hydrogel, prior to infected cell extrusion (**Figure 6A** and **Supplementary Figure S3A**). As previously shown, we noticed that the radial deformations U_r of surrounders just at the edge of the mound were large, indicative of them grabbing the ECM and pulling it away from the mound as they move directionally towards it. This traction stress orientation is not consistent with extrusion generated by a "purse-string" but is consistent with lamellipodial protrusion and directed cell migration (Kocgozlu et al., 2016). Thus, mounds are not caused by contraction of infected cells but rather by active crawling of uninfected surrounders that migrate toward the focus, squeezing and extruding the infected cells. Infected cells exerted reduced traction stresses compared to uninfected surrounders cells, consistent with previous findings (Bastounis et al., 2021b). Maximum monolayer tangential stresses were also lower for infected cells compared to uninfected surrounders (**Figure 6A**, fourth column). Interestingly, the maximum monolayer tangential stresses were localized at the edge of the infection focus, exactly where uninfected surrounder cells forcefully and actively moved towards the infection focus while pulling the ECM away from it, to eventually squeeze and extrude infected cells (**Figure 6A**, fourth column).

We then sought to examine whether similar behavior would be observed in our *in silico* model and used this opportunity as a means to validate our model but also to examine how monolayer stresses would be modulated *in silico* under conditions of varying ECM stiffness and focus size (**Figure 6B** and **Supplementary Figure S3B**). Consistent with the *in vitro* observations, radial ECM displacements were positive for the surrounder uninfected cells proximal to the infection focus and much larger for cells residing on soft as opposed to stiffer ECM, (**Figure 6B**, see second column). Moreover, both cellular traction stresses and monolayer tangential stresses exhibited the same tendency as in the *in vitro* experiment, including a high concentration of monolayer stresses at the interface of infected and non-infected cells (**Figure 6B**, see third and fourth columns). The range of values was within the same order of magnitude as that of the *in vitro* experiment, which validates our model despite the large variability in experimental observations. When inspecting the stress maps at the interface between infected and surrounding uninfected cells for cells residing on soft 3 kPa ECM, we found that both traction and monolayer stresses are increased to a higher extent around small as compared to large infection foci (t_{max} increases 13%, and σ_{max} increases 6%). We then wondered how stresses would be modulated at small as compared to large infection foci, for cells residing on stiff 35 kPa ECM. We discovered the same trend as when cells reside on soft ECM, with the exception that the relative differences in the magnitude of the maximum traction stress and monolayer stress were higher when comparing small versus large infection foci for cells residing on 35 kPa ECM (t_{max} increases 21%, and σ_{max} increases 8%). Altogether, these findings reveal that at least *in silico* both traction stresses and monolayer stresses are increased for uninfected surrounder cells proximal to the infection focus when the focus size is smaller as opposed to larger, and that this effect is stronger for cells residing on stiff 35 kPa as compared to soft 3 kPa ECM.

3.6 *In vitro* Experiments Validate *In silico* Predictions Showing That Infected Cell Extrusion is Enhanced When Epithelial Cells Reside on Stiff as Opposed to Softer Matrices

Our *in silico* infection experiments suggest that cells residing on stiffer matrices will undergo more prominent infected cell squeezing and subsequent extrusion as opposed to cells residing on softer matrices. To test whether the predictions of our computational model are correct, we seeded MDCK cells in monolayer on soft 3 kPa hydrogels, or stiff 35 kPa hydrogels, or on glass coverslips and infected them with low dosage of *L.m.* At 24 hpi samples were fixed and confocal microscopy imaging was

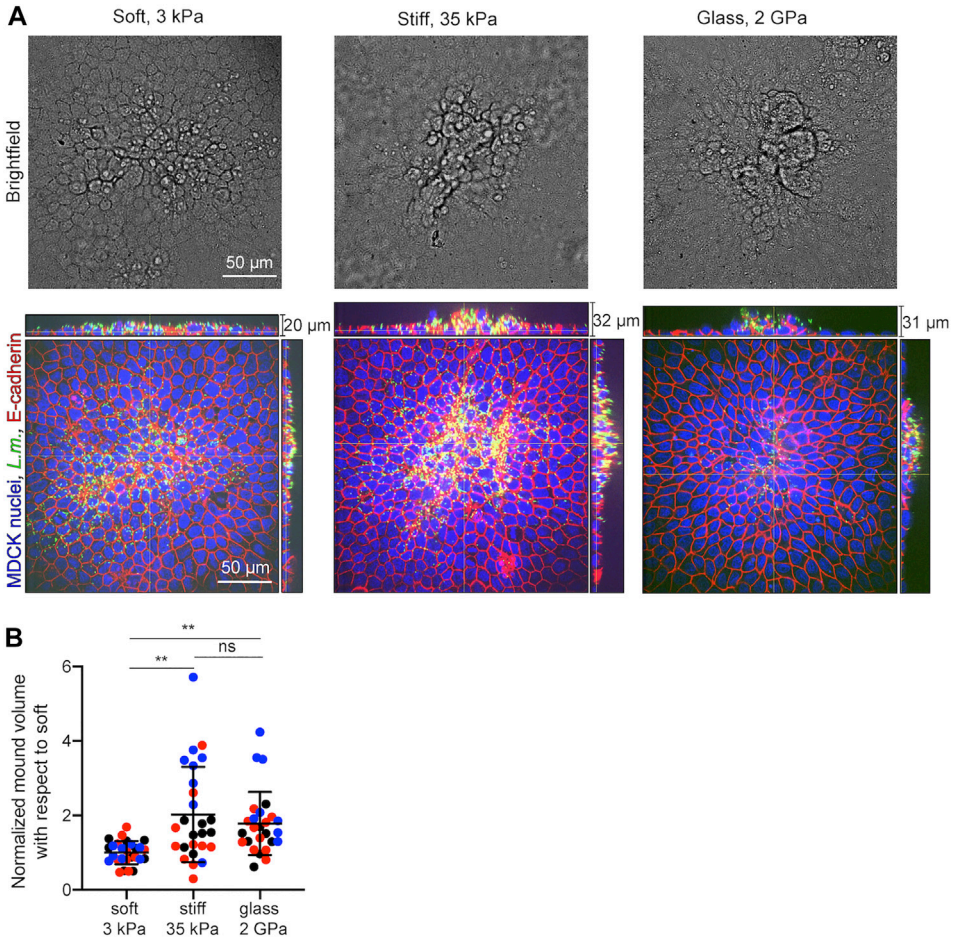

FIGURE 7 | *In vitro* infection experiments validate the computational finding of increased infection mounding when cells reside on stiffer matrices. **(A)** Representative brightfield image (top row) and orthogonal views (bottom row) of *L.m.* fluorescence in green, E-cadherin in red and MDCK nuclei in blue for cells originated from a *L.m.*-infected well with the field of view shown focused around and infection focus at 24 hpi. MDCK cells resided on soft 3 kPa hydrogels (left), or stiff 35 kPa hydrogels (middle), or on glass coverslips (right). **(B)** Barplots of relative *L.m.*-infection mound volume at 24 hpi for MDCK cells residing on soft 3 kPa hydrogels, on stiff 35 kPa hydrogels, or on glass. For each of $N = 3$ independent experiments (shown in different color), values have been normalized relative to the mean mound volume of cells residing on a soft 3 kPa matrix and each circle corresponds to a distinct mound (N = 26 or 27 mound volumes quantified for each condition). (mean ± SD, Wilcoxon Rank Sum test: **: $p < 0.01$, ns: non-significant).

performed to obtain z-stacks around infection foci. Although infected cell squeezing and extrusion were observed under all conditions, they were much more prominent for cells residing on stiff 35 kPa hydrogels or glass coverslips as opposed to soft 3 kPa hydrogels (**Figures 7A,B**). Moreover, especially on glass coverslips, surrounding uninfected cells appeared much more polarized as compared to the other two conditions (**Figure 7A**). When we quantified the volume of extruded cell domains relative to that which infected cells exhibit on a soft 3 kPa matrix using alpha shapes (Bastounis et al., 2021a), we found it to be 2-fold increased for cells residing on stiff 35 kPa matrices and 1.78-fold for cells residing on glass. Therefore, we can conclude that both computationally and experimentally a stiffer ECM promotes infection mounding and also that above a certain stiffness threshold an asymptotic behavior is reached and further increase in stiffness does not lead to further increase in mounding. Moreover, increased mounding observed for cells residing on stiffer ECM and glass was associated to decreased bacterial load (as evidence by the integral of the bacterial fluorescence) and decreased area of the infection focus (**Supplementary Figure S4**), reinforcing that infection mounding may limit bacterial spread across the basal cell monolayer as previously suggested (Bastounis et al., 2021b).

4 DISCUSSION

The stiffness of the extracellular matrix (ECM) on which cells reside is a crucial determinant in modulating a variety of cellular functions such as cell motility, proliferation, and differentiation (Lo et al., 2000; Engler et al., 2006; LaValley et al., 2017). Here we showed that ECM stiffness also modulates the outcome of the cell competition that arises during intracellular bacterial infection of epithelial cells in monolayer and leads to the collective onslaught

via extrusion of infected cells. Both our *in silico* model and the *in vitro* experiments show that increased ECM stiffness promotes the collective extrusion of infected cells as compared to a softer ECM. Through our *in silico* model, we found that the larger the difference in the ratio of stiffness between infected and uninfected surrounder cells, the larger will be the displacements that cells undergo and that lead to squeezing of infected cells and their subsequent extrusion. Moreover, through our computational model, we discovered that this effect is more prominent for cells residing on stiffer as opposed to softer ECM. Although *in vitro* experiments measuring cellular displacements, traction stresses or stiffness of infected versus non-infected cells and how those vary overtime as the infection focus grows on varying stiffness ECM were not conducted (we solely examined traction stress dynamics for infected cells at 3 kPa ECM *in vitro*), they could be the focus of future studies. Nevertheless, our *in vitro* measurements that reveal increased mounding for cells residing on stiff as opposed to softer ECM concern the computational predictions. Previous studies not involving infection have explored the role of physical cues in modulating the outcome of a mechanical cell competition (Matamoro-Vidal and Levayer, 2019; Gradeci et al., 2021). Consistent with our results, Gradeci et al. through a computational approach, showed that the higher stiffness of winner as opposed to loser cells during crowding leads to the compression of losers and an increase in their local density which is a prerequisite for their subsequent elimination (Gradeci et al., 2021). This study also showed that decreasing the ratio of stiffness of winner to loser cells will delay the kinetics of the ongoing competition rather than the final outcome. It is plausible to speculate that infection mounding could also occur for cells residing on soft matrices to the same extent as on stiff, if one was to inspect mounds at a later time point post-infection (> 24 hpi). However, unlike the case of cell competition between wild-type and transformed cells where, only two cell populations are present, in the case of infection the landscape is more complex with some cells remaining uninfected, some being infected with few bacteria and others in the center of the focus being filled with bacteria. Moreover, it remains to be explored if delayed mounding means that bacteria can spread more at the basal cell monolayer (since cells are not extruded to the same extent) and thus, the number of infected cells still adhering to the substratum will increase faster than in the case when those are rapidly extruded, as occurs on a stiffer ECM.

Quite some studies have highlighted the importance of the relative difference in cell stiffness, adhesion strength, contractility and/or motility between two cell populations in regulating the outcome of a mechanical cell competition (Levayer et al., 2015; Matamoro-Vidal and Levayer, 2019). At the same time, it is well established that in many cell types, bulk cell stiffness and traction force generation tend to increase with increased ECM stiffness, as supported by our computational and experimental data for MDCK (Wells, 2008; Han et al., 2012). However, to our knowledge very few studies so far have explicitly tried to address the role of ECM stiffness in regulating any type of cell competition. Pothapragada et al. recently found that stiffening of the ECM attenuates extrusion of oncogenically transformed MDCK cells driven by their wild-type neighbors, which is the opposite of what we find in the case of infection (Pothapragada et al., 2022). In this study, however, which involves only two cell populations, cellular biomechanics were not characterized and the reasoning behind the enhanced elimination observed on soft ECM was the dynamic localization of the actin crosslinking protein filamin. On soft ECM filamin was found to localize at cell-cell contacts between transformed and non-transformed cells and that was necessary for driving the extrusion of the former. On stiffer ECM, instead, filamin localized perinuclearly. It is also worth noting that Pothapragada and colleagues documented a low number of extruded cells, which is distinct from the massive extrusion of infected cells we observe *in vitro*. It is likely that the mechanical mechanism driving extrusion in this case is different which could be due to the distinct biological process studied. Moreover, the authors of this study documented a bimodal extrusion pattern where extrusion counts were similar up to ECM stiffness of 11 kPa and then dropped to 50% less on ECMs 23 kPa or higher. On the contrary, we found significantly less infected cell extrusion when comparing soft 3 kPa ECM to stiff 35 kPa ECM, however the difference between stiff 35 kPa ECM and non-physiologically stiff glass coverslips is minimal, suggesting that, above a certain value, mechanical competition arising during infection becomes insensitive to stiffness and that saturation is reached above a stiffness around 35 kPa.

Our computational model suggests that ECM stiffness modulates the relative cell stiffness between infected and non-infected cells and that by itself it is sufficient to enhance infected cell squeezing on stiffer ECM. Moreover, the model predicts that a larger focus size will limit squeezing of infected cells as compared to a smaller focus size. These results raise the question of whether decreased infected cell squeezing observed on soft ECM is due to: 1) *L.m.* spreading more efficiently when cells reside on soft ECM; 2) the fact that the relative difference in stiffness of winners to losers is not as high as on a stiff ECM; or 3) both. Previous studies on endothelial cells showed that, when host cells resided on soft ECM, *L.m.* spread was favored, likely because of the decreased monolayer tension favoring the formation of bacterial protrusions and engulfment from the donor to the recipient cell (Bastounis et al., 2018). Thus, it is plausible that *L.m.* may also spread more efficiently between epithelial cells residing on soft as opposed to stiff ECM, leading to decreased ability of surrounders to squeeze infected cells since the infection focus becomes larger. This is consistent with the increased focus size we measure at 24 hpi. However, the increased relative stiffness difference between infected and non-infected cells could also play a role in promoting infected cell squeezing on stiffer ECM. Future studies could measure explicitly infected or not cell stiffness depending on ECM stiffness through atomic force microscopy (Buxboim et al., 2010; Bastounis et al., 2021b). Moreover, our computational model considers a fixed number of infected cells in each simulation, a simplification since *in vitro* the number of infected cells changes due to *L.m.* replicating and spreading intercellularly over time. Future studies could focus on incorporating the bacterial dynamics into the current computational model. Finally, it is worth mentioning that in our model we simulate one mechanotransduction cycle due to convergence issues arising while solving the relevant equations governing the dynamics of cell movement otherwise. *In vitro*, though, cells constantly sense and transmit forces from the microenvironment, thus going through multiple such cycles.

Despite this limitation, the protrusion of uninfected surrounding cells is sufficient to allow us to inspect how infected cell squeezing and formation of mounds will be governed by the physical cues that cells display depending on their ECM stiffness. Finally, an additional limitation of the model is that the size and frequency of cell-cell and cell-ECM adhesions are considered constant regardless of the stiffness of the ECM on which cells reside. However, it was recently shown that cells can adapt their focal adhesion size and number based on ECM stiffness (Cao et al., 2017; Yeh et al., 2017). A more elaborate, future version of the computational model could account for changes in cell-cell and cell-ECM adhesion size as well as frequency. However, prior *in vitro* experiments will be necessary to investigate whether those change in a differential manner for uninfected surrounders versus infected cells.

Our discovery underscores the importance of ECM stiffness in regulating the cellular mechanical competition that arises during infection and leads to elimination of bacterially-infected cells. Intriguingly, in the small intestine, where food-borne infections like the one triggered by *L.m.* take place, ECM stiffness can increase significantly from typical values of few kPa in healthy conditions to several tenths of kPa in pathological states (*e.g.*, fibrosis) (Stewart et al., 2018; Onfroy-Roy et al., 2020). Studying further the dynamics of biochemical and (extra)-cellular physical signals during infection including using more elaborate computational models and live-cell biosensors will further reveal how those signals spatiotemporally crosstalk in health and during infection. This, in turn, will be critical to enhance our understanding of how healthy cells eliminate unfit ones during infection but also during other (patho)physiological processes involving cell competition.

DATA AVAILABILITY STATEMENT

Data collected and computer codes are available on request to the corresponding authors, and also available for public download as indicated in the methods section. MSM codes can be downloaded here: https://github.com/ebastoun/Monolayer-Stress-Microscopy. The codes for calculating volume of extruded cell domains (mounds) can be downloaded here: https://github.com/ebastoun/Infection_mound_volume.

AUTHOR CONTRIBUTIONS

Conceptualization, EB and MG-B; Methodology, EB and MG-B; Software, EB, MG-B, RA-Y, and MM; Investigation, EB, MG-B, RA-Y, and MM; Writing—Original Draft, EB, MG-B, RA-Y; Writing—Review and Editing, EB, MG-B, RA-Y, MM, and AC; Resources, EB, MG-B, and AC; Supervision, EB, MG-B.

FUNDING

This work was supported by the Deutsche Forschungsgemeinschaft (DFG, German Research Foundation) under Germany's Excellence Strategy—EXC2124—390838134 (EB and MM), the European Research council [ICoMICS Adg grant agreement: 1,01018587, (RA-Y and MG-B)], the Spanish Ministry of Universities [grant FPU 20/05274 (RA-Y)] and Grant PID2021-124271OB-I00 founded by MCIN/AEI/10.13039/501100011033 (RA-Y and MG-B) and ERDF A way of making Europe (RA-Y and MG-B).

ACKNOWLEDGMENTS

We are grateful to Julie A. Theriot for her insight, scientific discussions and sharing her resources. We thank José M. García-Aznar for the scientific discussion on the computational model. We also thank Libera Lo Presti for discussions and for revising the manuscript and rest of the materials. We acknowledge that part of our MSM codes are based on the original code (plane stress problem) written by Siva Srinivas Kolukula and we hence used some functions from his code.

SUPPLEMENTARY MATERIAL

The Supplementary Material for this article can be found online at: https://www.frontiersin.org/articles/10.3389/fcell.2022.912318/full#supplementary-material

REFERENCES

Álvarez-González, B., Zhang, S., Gómez-González, M., Meili, R., Firtel, R. A., Lasheras, J. C., et al. (2017). Two-layer Elastographic 3-d Traction Force Microscopy. *Sci. Rep.* 7, 39315. doi:10.1038/srep39315

Aparicio-Yuste, R., Gómez-Benito, M. J., Reuss, A., Blacker, G., Tal, M. C., and Bastounis, E. (2022). *Borrelia Burgdorferi* Induces Changes in the Physical Forces and Immunity Signaling Pathways of Endothelial Cells Early but Not Late during *In Vitro* Infection. Available at SSRN: https://ssrn.com/abstract=4024544.

Balcioglu, H. E., Balasubramaniam, L., Stirbat, T. V., Doss, B. L., Fardin, M.-A., Mège, R.-M., et al. (2020). A Subtle Relationship between Substrate Stiffness and Collective Migration of Cell Clusters. *Soft Matter* 16, 1825–1839. doi:10.1039/C9SM01893J

Bastounis, E. E., Ortega, F. E., Serrano, R., and Theriot, J. A. (2018). A Multi-Well Format Polyacrylamide-Based Assay for Studying the Effect of Extracellular Matrix Stiffness on the Bacterial Infection of Adherent Cells. *JoVE* e57361. doi:10.3791/57361

Bastounis, E. E., Radhakrishnan, P., Prinz, C. K., and Theriot, J. A. (2022). Mechanical Forces Govern Interactions of Host Cells with Intracellular Bacterial Pathogens. *Microbiol. Mol. Biol. Rev.* 0, e00094–20. doi:10.1128/mmbr.00094-20

Bastounis, E. E., Radhakrishnan, P., Prinz, C. K., and Theriot, J. A. (2021a). Volume Measurement and Biophysical Characterization of Mounds in Epithelial Monolayers after Intracellular Bacterial Infection. *Star. Protoc.* 2, 100551. doi:10.1016/j.xpro.2021.100551

Bastounis, E. E., Serrano-Alcalde, F., Radhakrishnan, P., Engström, P., Gómez-Benito, M. J., Oswald, M. S., et al. (2021b). Mechanical Competition Triggered by Innate Immune Signaling Drives the Collective Extrusion of Bacterially Infected Epithelial Cells. *Dev. Cell* 56, 443–460. e11. doi:10.1016/j.devcel.2021.01.012

Bastounis, E. E., Yeh, Y.-T., and Theriot, J. A. (2019). Subendothelial Stiffness Alters Endothelial Cell Traction Force Generation while Exerting a Minimal Effect on the Transcriptome. *Sci. Rep.* 9, 18209. doi:10.1038/s41598-019-54336-2

Bastounis, E., Meili, R., Álvarez-González, B., Francois, J., del Álamo, J. C., Firtel, R. A., et al. (2014). Both contractile Axial and Lateral Traction Force Dynamics Drive Amoeboid Cell Motility. *J. cell Biol.* 204, 1045–1061. doi:10.1083/jcb.201307106

Borau, C., Kamm, R. D., and García-Aznar, J. M. (2011). Mechano-sensing and Cell Migration: a 3d Model Approach. *Phys. Biol.* 8, 066008. doi:10.1088/1478-3975/8/6/066008

Brodland, G. W. (2015). How Computational Models Can Help Unlock Biological Systems. *Seminars Cell & Dev. Biol.* 47-48, 62–73. doi:10.1016/j.semcdb.2015.07.001

Buxboim, A., Rajagopal, K., Brown, A. E. X., and Discher, D. E. (2010). How Deeply Cells Feel: Methods for Thin Gels. *J. Phys. Condens. Matter* 22, 194116. doi:10.1088/0953-8984/22/19/194116

Califano, J. P., and Reinhart-King, C. A. (2010). Substrate Stiffness and Cell Area Predict Cellular Traction Stresses in Single Cells and Cells in Contact. *Cel. Mol. Bioeng.* 3, 68–75. doi:10.1007/s12195-010-0102-6

Cao, X., Ban, E., Baker, B. M., Lin, Y., Burdick, J. A., Chen, C. S., et al. (2017). Multiscale Model Predicts Increasing Focal Adhesion Size with Decreasing Stiffness in Fibrous Matrices. *Proc. Natl. Acad. Sci. U.S.A.* 114, E4549–E4555. doi:10.1073/pnas.1620486114

Delarue, M., Hartung, J., Schreck, C., Gniewek, P., Hu, L., Herminghaus, S., et al. (2016). Self-driven Jamming in Growing Microbial Populations. *Nat. Phys.* 12, 762–766. doi:10.1038/nphys3741

Doss, B. L., Pan, M., Gupta, M., Grenci, G., Mège, R.-M., Lim, C. T., et al. (2020). Cell Response to Substrate Rigidity Is Regulated by Active and Passive Cytoskeletal Stress. *Proc. Natl. Acad. Sci. U.S.A.* 117, 12817–12825. doi:10.1073/pnas.1917555117

Engler, A. J., Sen, S., Sweeney, H. L., and Discher, D. E. (2006). Matrix Elasticity Directs Stem Cell Lineage Specification. *Cell* 126, 677–689. doi:10.1016/j.cell.2006.06.044

Escribano, J., Chen, M. B., Moeendarbary, E., Cao, X., Shenoy, V., Garcia-Aznar, J. M., et al. (2019). Balance of Mechanical Forces Drives Endothelial Gap Formation and May Facilitate Cancer and Immune-Cell Extravasation. *PLoS Comput. Biol.* 15, e1006395–21. doi:10.1371/journal.pcbi.1006395

Escribano, J., Sunyer, R., Sánchez, M. T., Trepat, X., Roca-Cusachs, P., and García-Aznar, J. M. (2018). A Hybrid Computational Model for Collective Cell Durotaxis. *Biomech. Model Mechanobiol.* 17, 1037–1052. doi:10.1007/s10237-018-1010-2

Faralla, C., Bastounis, E. E., Ortega, F. E., Light, S. H., Rizzuto, G., Gao, L., et al. (2018). *Listeria Monocytogenes* Inlp Interacts with Afadin and Facilitates Basement Membrane Crossing. *PLoS Pathog.* 14, e1007094–26. doi:10.1371/journal.ppat.1007094

Gradeci, D., Bove, A., Vallardi, G., Lowe, A. R., Banerjee, S., and Charras, G. (2019). Cell-scale Biophysical Determinants of Cell Competition in Epithelia. *bioRxiv*. doi:10.1101/729731

Gradeci, D., Bove, A., Vallardi, G., Lowe, A. R., Banerjee, S., and Charras, G. (2021). Cell-scale Biophysical Determinants of Cell Competition in Epithelia. *eLife Sci.* 10, e61011. doi:10.7554/eLife.61011

Gui, L., and Wereley, S. T. (2002). A Correlation-Based Continuous Window-Shift Technique to Reduce the Peak-Locking Effect in Digital PIV Image Evaluation. *Exp. Fluids* 32, 506–517. doi:10.1007/s00348-001-0396-1

Han, S. J., Bielawski, K. S., Ting, L. H., Rodriguez, M. L., and Sniadecki, N. J. (2012). Decoupling Substrate Stiffness, Spread Area, and Micropost Density: A Close Spatial Relationship between Traction Forces and Focal Adhesions. *Biophysical J.* 103, 640–648. doi:10.1016/j.bpj.2012.07.023

Hayer, A., Shao, L., Chung, M., Joubert, L.-M., Yang, H. W., Tsai, F.-C., et al. (2016). Engulfed Cadherin Fingers Are Polarized Junctional Structures between Collectively Migrating Endothelial Cells. *Nat. Cell Biol.* 18, 1311–1323. doi:10.1038/ncb3438

Hervás-Raluy, S., García-Aznar, J. M., and Gómez-Benito, M. J. (2019). Modelling Actin Polymerization: the Effect on Confined Cell Migration. *Biomech. Model Mechanobiol.* 18, 1177–1187. doi:10.1007/s10237-019-01136-2

Kandemir, N., Vollmer, W., Jakubovics, N. S., and Chen, J. (2018). Mechanical Interactions between Bacteria and Hydrogels. *Sci. Rep.* 8, 10893. doi:10.1038/s41598-018-29269-x

Kocgozlu, L., Saw, T. B., Le, A. P., Yow, I., Shagirov, M., Wong, E., et al. (2016). Epithelial Cell Packing Induces Distinct Modes of Cell Extrusions. *Curr. Biol.* 26, 2942–2950. doi:10.1016/j.cub.2016.08.057

Lamason, R. L., Bastounis, E., Kafai, N. M., Serrano, R., del Álamo, J. C., Theriot, J. A., et al. (2016). Rickettsia Sca4 Reduces Vinculin-Mediated Intercellular Tension to Promote Spread. *Cell* 167, 670–683. e10. doi:10.1016/j.cell.2016.09.023

Lampi, M. C., Faber, C. J., Huynh, J., Bordeleau, F., Zanotelli, M. R., and Reinhart-King, C. A. (2016). Simvastatin Ameliorates Matrix Stiffness-Mediated Endothelial Monolayer Disruption. *PLOS ONE* 11, e0147033–20. doi:10.1371/journal.pone.0147033

Lampi, M. C., and Reinhart-King, C. A. (2018). Targeting Extracellular Matrix Stiffness to Attenuate Disease: From Molecular Mechanisms to Clinical Trials. *Sci. Transl. Med.* 10, eaao0475. doi:10.1126/scitranslmed.aao0475

LaValley, D. J., Zanotelli, M. R., Bordeleau, F., Wang, W., Schwager, S. C., and Reinhart-King, C. A. (2017). Matrix Stiffness Enhances VEGFR-2 Internalization, Signaling, and Proliferation in Endothelial Cells. *Converg. Sci. Phys. Oncol.* 3, 044001. doi:10.1088/2057-1739/aa9263

Lecuit, T., and Lenne, P.-F. (2007). Cell Surface Mechanics and the Control of Cell Shape, Tissue Patterns and Morphogenesis. *Nat. Rev. Mol. Cell Biol.* 8, 633–644. doi:10.1038/nrm2222

Levayer, R., Hauert, B., and Moreno, E. (2015). Cell Mixing Induced by *Myc* Is Required for Competitive Tissue Invasion and Destruction. *Nature* 524, 476–480. doi:10.1038/nature14684

Lo, C.-M., Wang, H.-B., Dembo, M., and Wang, Y.-l. (2000). Cell Movement Is Guided by the Rigidity of the Substrate. *Biophysical J.* 79, 144–152. doi:10.1016/S0006-3495(00)76279-5

Matamoro-Vidal, A., and Levayer, R. (2019). Multiple Influences of Mechanical Forces on Cell Competition. *Curr. Biol.* 29, R762–R774. doi:10.1016/j.cub.2019.06.030

Meyer, S. N., Amoyel, M., Bergantiños, C., de la Cova, C., Schertel, C., Basler, K., et al. (2014). An Ancient Defense System Eliminates Unfit Cells from Developing Tissues during Cell Competition. *Science* 346, 1258236. doi:10.1126/science.1258236

Moreno, E., Valon, L., Levillayer, F., and Levayer, R. (2019). Competition for Space Induces Cell Elimination through Compaction-Driven ERK Downregulation. *Curr. Biol.* 29, 23–34. e8. doi:10.1016/j.cub.2018.11.007

Moreo, P., García-Aznar, J. M., and Doblaré, M. (2008). Modeling Mechanosensing and its Effect on the Migration and Proliferation of Adherent Cells. *Acta Biomater.* 4, 613–621. doi:10.1016/j.actbio.2007.10.014

Nieto, A., Escribano, J., Spill, F., Garcia-Aznar, J. M., and Gomez-Benito, M. J. (2020). Finite Element Simulation of the Structural Integrity of Endothelial Cell Monolayers: A Step for Tumor Cell Extravasation. *Eng. Fract. Mech.* 224, 106718. doi:10.1016/j.engfracmech.2019.106718

O'Dea, R. D., and King, J. R. (2012). Continuum Limits of Pattern Formation in Hexagonal-Cell Monolayers. *J. Math. Biol.* 64, 579–610. doi:10.1007/s00285-011-0427-3

Onfroy-Roy, L., Hamel, D., Foncy, J., Malaquin, L., and Ferrand, A. (2020). Extracellular Matrix Mechanical Properties and Regulation of the Intestinal Stem Cells: When Mechanics Control Fate. *Cells* 9, 2629. doi:10.3390/cells9122629

Ortega, F. E., Koslover, E. F., and Theriot, J. A. (2019). *Listeria Monocytogenes* Cell-To-Cell Spread in Epithelia Is Heterogeneous and Dominated by Rare Pioneer Bacteria. *eLife* 8, e40032. doi:10.7554/eLife.40032.001

Ortega, F. E., Rengarajan, M., Chavez, N., Radhakrishnan, P., Gloerich, M., Bianchini, J., et al. (2017). Adhesion to the Host Cell Surface Is Sufficient to mediateListeria Monocytogenesentry into Epithelial Cells. *MBoC* 28, 2945–2957. doi:10.1091/mbc.e16-12-0851

Perez, T. D., Tamada, M., Sheetz, M. P., and Nelson, W. J. (2008). Immediate-early Signaling Induced by E-Cadherin Engagement and Adhesion. *J. Biol. Chem.* 283, 5014–5022. doi:10.1074/jbc.M705209200

Pothapragada, S. P., Gupta, P., Mukherjee, S., Das, T., and Das, T. (2022). Matrix Mechanics Regulates Epithelial Defence against Cancer by Tuning Dynamic Localization of Filamin. *Nat. Commun.* 13, 218. doi:10.1038/s41467-021-27896-z

Schmedt, T., Chen, Y., Nguyen, T. T., Li, S., Bonanno, J. A., and Jurkunas, U. V. (2012). Telomerase Immortalization of Human Corneal Endothelial Cells Yields Functional Hexagonal Monolayers. *PLOS ONE* 7, e51427–11. doi:10.1371/journal.pone.0051427

Solon, J., Levental, I., Sengupta, K., Georges, P. C., and Janmey, P. A. (2007). Fibroblast Adaptation and Stiffness Matching to Soft Elastic Substrates. *Biophysical J.* 93, 4453–4461. doi:10.1529/biophysj.106.101386

Stewart, D. C., Berrie, D., Li, J., Liu, X., Rickerson, C., Mkoji, D., et al. (2018). Quantitative Assessment of Intestinal Stiffness and Associations with Fibrosis in Human Inflammatory Bowel Disease. *PLOS ONE* 13, e0200377–16. doi:10.1371/journal.pone.0200377

Sun, B. (2021). The Mechanics of Fibrillar Collagen Extracellular Matrix. *Cell Rep. Phys. Sci.* 2, 100515. doi:10.1016/j.xcrp.2021.100515

Tambe, D. T., Corey Hardin, C., Angelini, T. E., Rajendran, K., Park, C. Y., Serra-Picamal, X., et al. (2011). Collective Cell Guidance by Cooperative Intercellular Forces. *Nat. Mater* 10, 469–475. doi:10.1038/nmat3025

Vujosevic, L., and Lubarda, V. A. (2002). Finite-strain Thermoelasticity Based on Multiplicative Decomposition of Deformation Gradient. *Theor. Appl. Mech. (Belgr)* 379, 379–399. doi:10.2298/TAM0229379V

Wells, R. G. (2008). The Role of Matrix Stiffness in Regulating Cell Behavior. *Hepatology* 47, 1394–1400. doi:10.1002/hep.22193

Yeh, Y.-C., Ling, J.-Y., Chen, W.-C., Lin, H.-H., and Tang, M.-J. (2017). Mechanotransduction of Matrix Stiffness in Regulation of Focal Adhesion Size and Number: Reciprocal Regulation of Caveolin-1 and β1 Integrin. *Sci. Rep.* 7, 2045–2322. doi:10.1038/s41598-017-14932-6

Zhao, T., Zhang, Y., Wei, Q., Shi, X., Zhao, P., Chen, L.-Q., et al. (2018). Active Cell-Matrix Coupling Regulates Cellular Force Landscapes of Cohesive Epithelial Monolayers. *npj Comput. Mater* 4, 10. doi:10.1038/s41524-018-0069-8

Conflict of Interest: The authors declare that the research was conducted in the absence of any commercial or financial relationships that could be construed as a potential conflict of interest.

Publisher's Note: All claims expressed in this article are solely those of the authors and do not necessarily represent those of their affiliated organizations, or those of the publisher, the editors and the reviewers. Any product that may be evaluated in this article, or claim that may be made by its manufacturer, is not guaranteed or endorsed by the publisher.

Section 4

Listeria-infected macrophages promote biomechanical alterations in endothelial cell monolayers for transmigration

M. Muenkel[1,2], E. Keskin[1,2], A. Balmes[3], T. E. Schäffer[3], F. Romer[1,2], M. Lebtig[1,2], D. Kretschmer[1,2], K. Wright[4], P. Loskill[2,5,6,7], S. Mostowy[4], E. Bastounis[1,2,*]

[1]Interfaculty Institute of Microbiology and Infection Medicine, University of Tübingen, Tübingen, 72076, Germany

[2]Cluster of Excellence EXC 2124 Controlling Microbes to Fight Infections, University of Tübingen, Tübingen, 72076, Germany

[3]Institute of Applied Physics, University of Tübingen, Tübingen, 72076, Germany

[4]Department of Infection Biology, London School of Hygiene and Tropical Medicine, London, WC1E 7HT, UK

[5]NMI Natural and Medical Sciences Institute at the University of Tübingen, Reutlingen, 72770, Germany

[6]Department for Microphysiological Systems, Institute of Biomedical Engineering, Faculty of Medicine, University Tübingen, Tübingen, 72074, Germany

[7]3R Center for In Vitro Models and Alternatives to Animal Testing, University Tübingen, Tübingen, 72074, Germany

Manuscript under revision.

Listeria-infected macrophages promote biomechanical alterations in endothelial cell monolayers for transmigration

M. Muenkel[1,2], E. Keskin[1,2], A. Balmes[3], T. E. Schäffer[3], F. Romer[1,2], M. Lebtig[1,2], D. Kretschmer[1,2], K. Wright[4], P. Loskill[2,5,6,7], S. Mostowy[4], E. Bastounis[1,2,] *

[1]*Interfaculty Institute of Microbiology and Infection Medicine, University of Tübingen, Tübingen, 72076, Germany*

[2]*Cluster of Excellence EXC 2124 Controlling Microbes to Fight Infections, University of Tübingen, Tübingen, 72076, Germany*

[3]*Institute of Applied Physics, University of Tübingen, Tübingen, 72076, Germany*

[4]*Department of Infection Biology, London School of Hygiene and Tropical Medicine, London, WC1E 7HT, UK*

[5]NMI *Natural and Medical Sciences Institute at the University of Tübingen, Reutlingen, 72770, Germany*

[6]*Department for Microphysiological Systems, Institute of Biomedical Engineering, Faculty of Medicine, University Tübingen, Tübingen, 72074, Germany*

[7]*3R Center for In Vitro Models and Alternatives to Animal Testing, University Tübingen, Tübingen, 72074, Germany*

* Corresponding Author and Lead Contact:

Effie E. Bastounis, Ph.D.
Interfaculty Institute of Microbiology and Infection Medicine
University of Tübingen
Auf der Morgenstelle 28/ E8, Room P03
72076, Tübingen
Germany

Email: effie.bastounis@uni-tuebingen.de
Phone: +49 (0) 7071 2978867

SUMMARY

Intracellular pathogens, like *Listeria monocytogenes* (LM), manipulate host cells to spread from the initial infection site to distant organs through the bloodstream. For that, LM hijacks mononuclear phagocytes to traverse vascular endothelial cell (EC) linings, but how transmigration is regulated by ECs is poorly understood. Here, we show that EC biomechanical responses to macrophages (MΦs) differ markedly with infection, decisively impacting their transmigration. Long-term videomicroscopy reveals that MΦ exposure increases EC polarization and alignment while reducing migration speed. However, only uninfected MΦ-exposed ECs increase their traction forces, monolayer stresses, and barrier integrity; responses significantly attenuated during infection. We show that TNF-α secretion during infection compromises EC barrier integrity and, combined with increased MΦ-EC adhesion, facilitates MΦ transmigration. Using zebrafish, we find that infection increases endothelial permeability, enhancing phagocyte extravasation *in vivo*. Thus, infection overrides MΦ-induced EC barrier strengthening for pathogen spread, remarkable feature that could be harnessed for infection control.

KEYWORDS

cell biomechanics, endothelial cells, infected macrophage, host-pathogen interactions, *Listeria monocytogenes*, traction force microscopy, cell adhesion, vascular permeability, transmigration, bacterial infection, zebrafish models

INTRODUCTION

Many human pathogens can spread from the initial site of infection to distal organs through the bloodstream, causing systemic infection. Systemic dissemination requires direct interaction of pathogens with endothelial cells (ECs). Alternatively, some viruses and bacterial pathogens such as *Listeria monocytogenes* (LM) can hitch a ride with mononuclear phagocytes to travel through the bloodstream, cross endothelial barriers, and reach a distant tissue.[1,2] In this case, intracellular pathogens can be transferred directly from infected phagocytes, such as monocytes, to nearby uninfected ECs without exposure to the extracellular milieu.[2,3] However, more commonly, it is the infected mononuclear phagocytes that cross endothelial barriers and transport pathogens into deeper tissues. In such cases, phagocytes (serving as Trojan horses) forcefully manage to squeeze themselves through the vascular EC linings as they transmigrate and spread to the underlying parenchyma and adjacent tissues.[4,5]

Transmigration is a multistep process during which immune cells first adhere to the vascular EC lining (composed of a single continuous layer of cells), then roll and crawl along the ECs until they reach their exit site typically undergoing paracellular diapedesis (i.e., pass between ECs rather than through them).[6] These sequential steps are orchestrated by both soluble inflammatory mediators and direct heterotypic cell-cell contacts.[7] Phagocytes and other immune cells secrete cytokines and chemokines, such as TNF-α, IL-6, and MCP-1, which can activate ECs, often resulting in increased permeability and expression of adhesion molecules such as ICAM-1 and VCAM-1.[8] The firm adhesion of mononuclear phagocytes to ICAM-1 occurs via integrins, primarily LFA-1 and Mac-1, which undergo conformational changes to increase their binding affinity to ICAM-1.[9] Beyond serving as a passive barrier, ECs actively respond to infection and other inflammatory stimuli by secreting pro-inflammatory signals that recruit and activate immune cells. This localized inflammatory environment can either aid bacterial clearance or facilitate pathogen dissemination.[8,10,11] A central, yet unresolved, question is whether immune cell transmigration is predominantly driven by phagocyte-intrinsic mechanical forces, endothelial biomechanical remodeling, or both.

Physical forces resulting from dynamic regulation of the cytoskeleton play a crucial role in allowing immune cells but also metastatic cancers cells to transmigrate across endothelial linings.[12-14] Using traction force microscopy (TFM), a technique that allows measuring the traction stresses that adherent cells exert on their extracellular matrix (ECM), previous work showed that while ECs increase their own junctional tension, neutrophils use contractile forces to actively open endothelial junctions for transmigration.[15] Proinflammatory signals (e.g., thrombin) that increase

VEC contractility to the extent of compromising barrier integrity also facilitate neutrophil diapedesis. An *in vivo* study using live-cell imaging on zebrafish brains suggested that immune cells (in this case macrophages (MΦs)) can actively generate large traction stresses to physically pull together brain ECs and facilitate repair after cerebrovascular rupture.[16] While these studies indicate that immune cells are physically active players in bringing neighboring ECs together or apart by disrupting or restoring intercellular junctions of ECs, other works suggest that ECs autonomously form gaps due to their intrinsic mechanical activities (e.g., monolayer stresses), thereby impacting transmigration of other cells types.[17] Thus, the relative contribution of ECs and immune cells to transmigration remains controversial, particularly in the context of a bloodstream infection.

Among pathogens that exploit mononuclear phagocytes for dissemination, *Listeria monocytogenes* (LM) is a well-characterized model. The food-borne, facultative intracellular bacterial pathogen LM initiates infection by invading epithelial cells lining the intestinal lumen.[18] Once inside a host cell, LM escapes the phagocytic vacuole, replicates in the cytoplasm, and hijacks the host actin cytoskeleton to spread from cell to cell.[19] Systemic dissemination occurs when bacteria exit epithelial layers, are “captured” by mononuclear phagocytes and enter the bloodstream. By means of circulating phagocytes, LM can cross EC barriers and spread from the intestine to distal organs such as the liver, spleen, brain, and placenta.[2,5,20] The transfer of LM from mononuclear phagocytes to ECs via actin-based motility and transmigration of infected immune cells through ECs are both possible.

In this study, we used long-term videomicroscopy to examine how LM infection alters the biomechanical interactions of MΦ-like cells with ECs. We found that exposure to MΦs (whether LM-infected or not) decreased EC migration speed and increased EC polarization and collective alignment. However, only ECs exposed to uninfected MΦs showed features that correlate with enhanced barrier integrity, i.e. a linear increase in traction forces and monolayer stresses, suggesting that LM infection disrupts the ability of MΦs to modulate EC biomechanical responses. These changes resulted in a higher rate of LM-infected MΦ transmigration through the EC monolayer. In agreement, we observed enhanced transmigration of MΦs *in vivo* using zebrafish infection models. Both released cytokines and increased adhesion between infected MΦs and ECs contributed to efficient transmigration, highlighting the crucial role of MΦ and EC biomechanical alterations in this process.

RESULTS

ECs decrease their migration speed when exposed to MΦs

To investigate the dynamics of EC-immune cell interactions, we used primary HUVEC as our EC model. As our MΦ model, we used PMA-differentiated U937 monocytes, a well-established model for studying LM pathophysiology.[20-23] Unless stated otherwise, we refer to these differentiated cells as MΦs. HUVEC were seeded onto collagen-I coated glass coverslips and allowed to form a monolayer. Simultaneously, MΦs were infected with LM constitutively expressing GFP. To enrich for infected MΦs, we performed fluorescence-activated cell sorting (FACS) before adding them to the HUVEC monolayer in the presence of gentamicin (Figure S1A). The antibiotic ensures that any LM escaping from MΦs due to host cell lysis are eliminated. We then conducted live-cell videomicroscopy over 24 h using RFP-expressing HUVEC under three conditions: HUVEC alone (unexposed); HUVEC exposed to MΦs; and HUVEC exposed to LM-infected MΦs (Movie S1 part 1). To quantify the alterations in cell motility, we used particle image velocimetry (PIV) comparing consecutive fluorescence frames of the RFP expressing HUVEC (Figure 1A-B). Importantly, all recordings began with HUVEC alone, and MΦs were introduced ~2.5 h after imaging started. This design allowed us to compare cell behavior before and after MΦ exposure within the same sample, in addition to using separate unexposed HUVEC controls. We found that at steady state, unexposed HUVEC displayed minimal fluctuations in their migration velocity over time, having an average migration speed of 10 μm/h (Figure 1C-D). However, within 40 min of adding either uninfected or LM-infected MΦs, HUVEC migration speed dropped sharply by 30% and remained suppressed for the full duration of the 24 h recording. This reduction occurred regardless of MΦ infection status and correlated with increased HUVEC polarization and collective alignment. Note that the decrease in HUVEC motility and elongation persisted even when cells were seeded at sub-confluent densities, preventing direct EC-EC contacts (Figure S1B-C and Movie S1, part 2). This suggests that MΦ-induced changes in HUVEC morphology and migration occur independently of HUVEC cell-cell interactions.

MΦ-driven EC alignment requires both soluble cues and direct contact

Live-cell imaging revealed pronounced morphological changes in HUVEC during exposure to MΦs (Movie S1 part 1). To systematically quantify these alterations, we performed immunostaining 24 h post-exposure (hpe) to MΦs, when shape changes were most evident, followed by quantitative microscopy. HUVEC were segmented based on VE-cadherin localization, and various cell shape descriptors were characterized (Figure 2A). HUVEC exposed to (un)infected MΦs exhibited a 15% decrease in cell density and 13% increase in cell area

compared to unexposed controls, due to decreased HUVEC proliferation as evidenced by immunostaining for the Ki-67 proliferation marker (Figure 2B and Figure S2A-C). Exposure to (un)infected MΦ significantly increased HUVEC aspect ratio (i.e., polarization) compared to unexposed controls (Figure 2C). These elongated cells also had fewer neighboring cells within the monolayer and a higher shape factor (cell perimeter divided by square root of area), a metric associated with tissue fluidity (Figure 2D-E).[24] In line with HUVEC becoming more fluid-like when interacting with MΦ, their orientation angle with respect to neighboring cells was larger compared to unexposed HUVEC, indicative of an increase in collective cell alignment (i.e., nematic ordering) (Figure 2A, F). Variance analysis of HUVEC aspect ratio, cell area, and shape factor revealed greater cell shape heterogeneity in MΦ-exposed HUVEC compared to unexposed (Figure S2F-H). Collectively, these findings demonstrate that HUVEC undergo dramatic morphological and organizational remodeling when interacting with MΦs, irrespective of MΦ infection status. This remodeling results in increased HUVEC polarization, enhanced collective alignment and greater heterogeneity in cell shapes.

To dissect the contributions of secreted factors versus direct MΦ-EC contact on the alterations in HUVEC morphology, we performed transwell co-culture experiments. HUVEC were seeded both on transwell inserts and on the glass coverslip of the plate below, while (un)infected MΦ were added only to the upper layer for 24 h (Figure S2D). This setup ensured that the bottom-layer HUVEC were exposed only to the conditioned media from the upper chamber, without direct contact with MΦ. IL-8 measurements confirmed effective cytokine exchange between chambers (Figure S2E). We found that compared to unexposed controls, HUVEC in the bottom layer (i.e., exposed solely to conditioned media) exhibited no change in their aspect ratio but did show a significant increase in their shape factor and collective alignment, although not as pronounced as when HUVEC are in contact with MΦ (Figure 2G-J and Figure S2I-J). These findings suggest that while secreted factors contribute to HUVEC shape alterations during co-culture with MΦs, direct MΦ-EC interactions also play a role.

Upregulation of cytoskeletal remodelling pathways only in ECs exposed to uninfected MΦs

To determine whether the observed changes in HUVEC shape and kinematics are associated with changes in gene expression, between HUVEC exposed to uninfected versus LM-infected MΦs, we performed RNA sequencing. Since morphological changes of HUVEC in response to MΦ first appear at ~ 8 hpe and culminate at ~ 24 hpe, we performed RNA sequencing at these two time points (Figure 3A-B and Movie S1). Analysis revealed a significant number of

differentially expressed genes (DEGs) across conditions and time points (Figure 3A and Table S1). Both infected and uninfected MΦ-exposed HUVEC showed significant upregulation of genes involved in canonical innate immune pathways, including NF-κB and TNF signaling, as well as broader stress-responsive pathways such as MAPK (Figure 3B). Notably, the TNF signaling pathway was strongly upregulated in HUVEC exposed to infected MΦs at both 8 and 24 hpe compared to unexposed controls, whereas in uninfected MΦ-exposed HUVEC this pathway was only mildly induced at 8 hpe and not at 24 hpe. This distinction is critical considering that TNF-α has strong impact in EC biomechanics and regulation of barrier integrity.[25-27] Several pathways regulating the EC cytoskeleton and mechanics, such as VEGF, PI3K-AKT, and RAS signaling, were transiently upregulated at 8 hpe in HUVEC under both MΦ exposure conditions, but not at 24 hpe, suggesting an early but temporary EC response to MΦ interaction. Strikingly, pathways directly involved in cytoskeletal remodeling and adhesion, namely the 'focal adhesion' and 'regulation of actin cytoskeleton' pathways, were exclusively upregulated in HUVEC exposed to uninfected but not infected MΦ at 8 hpe (Figure 3B and Figure S3A-B). These findings suggest that uninfected MΦs trigger transient cytoskeletal alterations in HUVEC that are attenuated or suppressed in infected conditions, and that such changes are most prominent early after MΦ exposure.

To determine whether the transcriptional changes at 8 hpe translated into altered cytoskeletal organization, we immunostained HUVEC exposed to infected or uninfected MΦs and unexposed controls for F-actin and vinculin, a focal adhesion protein linking integrins to the actin cytoskeleton (Figure 3C).[28,29] HUVEC exposed to (un)infected MΦs showed increased F-actin stress fibers, and more vinculin puncta compared to unexposed controls, consistent with enhanced cytoskeletal engagement. However, no discernible differences were observed between infected and uninfected MΦ conditions at 8 hpe, as confirmed by both fixed and live-cell imaging (Figure 3C and Movie S3). Together, RNA sequencing and cytoskeletal staining revealed that both uninfected and infected MΦs induce robust cytoskeletal remodeling in HUVEC.

Increased EC traction and monolayer stresses upon exposure to uninfected but not LM-infected MΦs

Since immunostaining did not reveal major differences between HUVEC exposed to uninfected versus infected MΦs, we turned to traction force microscopy (TFM) to obtain spatially and temporally resolved insight into focal adhesion activity and their mechanical coupling to the underlying actomyosin cytoskeleton.[30] The measured traction stresses can then be used to

calculate inter- and intra-cellular stresses (from now on referred as monolayer stresses), which can serve as a proxy of the monolayer barrier integrity (Figure S4A). First, to determine whether MΦ exposure alters HUVEC traction stresses, we performed TFM on HUVEC cultured on elastic polyacrylamide hydrogels. Across all conditions (i.e., unexposed HUVEC, HUVEC exposed to uninfected MΦ, and HUVEC exposed to infected MΦ), traction stresses displayed high spatial fluctuations (Figure 4 A-B and Movie S3), consistent with previous studies on unexposed HUVEC.[15] While traction stresses and strain energy (i.e., mechanical work imparted by HUVEC to deform their matrix) remained stable in unexposed HUVEC over 24 h, HUVEC exposed to uninfected MΦ exhibited a quasi-linear increase in traction stresses, which peaked at approximately 8 hpe before returning to baseline by 20 hpe. This increase was absent in HUVEC exposed to infected MΦ, despite their overall strain energy being also higher than unexposed controls (Figure 4 A-D and Movie S3). When we calculated the monolayer tensile stresses, we found a similar trend as with the traction stresses (i.e., they significantly increased over the first 13 hpe), but only in HUVEC exposed to uninfected MΦ (Figure 4 E-F, Figure S4B-C). These findings suggest that uninfected MΦ but not infected MΦ exposure leads to increase in EC traction and monolayer stresses, potentially strengthening the EC barrier.

Given that MΦ transmigration requires squeezing between adjacent ECs[31], we next examined whether the observed biomechanical changes are consistent with changes in HUVEC stiffness (i.e., resistance to deformation based on a given force applied). Using atomic force microscopy (AFM), we found that HUVEC exposed to uninfected MΦ were significantly stiffer (30% more) than unexposed HUVEC or HUVEC exposed to infected MΦ (Figure S4D-E). This result prompted us to investigate whether the decreased HUVEC stiffness, traction, and monolayer stresses in HUVEC exposed to infected as opposed to uninfected MΦ could be due to direct bacterial infection of HUVEC, as previously shown to occur in LM-infected epithelial cells.[32,33] Therefore, we measured the percentage of infected HUVEC 24 hpe to infected MΦ using flow cytometry (Figure S4F) and observed a very low (2%) HUVEC infection rate. From this, we conclude that direct infection is not causing the observed decrease in stiffness, traction, and monolayer stresses in HUVEC exposed to bacterially infected MΦ (Figure S4F-I).

EC exposure to infected MΦs results in increased transmigration

The significant increase in the monolayer tensile stresses of HUVEC only in response to uninfected MΦ suggested the presence of a tighter endothelial barrier than upon exposure to

infected MΦ. We hypothesized this difference could directly influence MΦ transmigration efficiency. To test this, we measured transendothelial electrical resistance (TEER) of the monolayers, a measure of barrier permeability or integrity. TEER values were significantly higher (by 33%) in HUVEC exposed to uninfected MΦ compared to those exposed to infected MΦ, when averaged over 3–15 hpe (Figure 5A and Figure S5A). TEER in HUVEC exposed to infected MΦ was comparable to unexposed controls. These findings indicate that increased monolayer tensile stresses in the presence of uninfected MΦ are associated with a tight barrier.

To assess whether the inability of infected MΦ to strengthen the endothelial barrier impacts their transmigration through the HUVEC monolayer, we performed a transmigration assay using (LM-infected) U937, and also a second MΦ-like cell line, THP-1 (human monocytic cell line), as well as primary MΦ (Figure 5B). As expected, over the course of 24 h, transmigration efficiency of infected U937 was nearly 100% higher than that of uninfected U937 (Figure 5C). A similar increase (70%) was observed when using PMA-differentiated THP-1 cells and a slightly lower increase (20%) with primary MΦ (Figure 5C and Figure S5B). For the cell lines, a HUVEC:MΦ ratio of 40:1 was used; however, when using primary MΦ, the maximum achievable ratio was 700:1 due to technical constraints (specifically the limited volume of blood that could be drawn from a human donor). This limitation may partly explain the lower observed percentage. Interestingly, the increase in transmigration of infected MΦ is not specific to LM infection, as we observed a 96% increase in transmigration of *S. aureus*-infected MΦ (U937) compared to uninfected MΦ (Figure S5C).

While the increased transmigration of infected MΦ correlates with altered HUVEC dynamics and failure to tighten the endothelial barrier, it is likely that intrinsic changes in the MΦ themselves, including enhanced adhesion, also contribute to this process. To test whether bacterial infection modulates MΦ adhesion to the endothelium, we performed a perfusion-based adhesion assay under low shear stress in a microfluidic system. After 2 h of flow, we observed a ~2-fold increase in the number of LM-infected MΦ adhering to the HUVEC monolayer compared to uninfected controls (Figure 5D-E and Figure S5D). Consistently, RNA sequencing analysis revealed that compared to HUVEC exposed to uninfected MΦ and relative to unexposed controls, HUVEC exposed to LM-infected MΦ for 8 h showed a pronounced transcriptional upregulation of adhesion molecules, including E-selectin (10-fold), VCAM-1 (4-fold), and ICAM-1 (2.7-fold) (Figure 5F-H). Together, these data suggest that the enhanced transmigration of infected MΦ is not solely due to intrinsic properties of the endothelial barrier but is also driven by increased MΦ adhesion.

Cytokine-mediated weakening of EC barrier integrity promotes infected MΦ transmigration

Our data suggest that HUVEC biomechanical remodeling in response to MΦs involves both direct contact and soluble factors, including cytokines, key regulators of endothelial barrier integrity.[34,35] To investigate whether cytokines are differentially secreted in HUVEC-MΦ co-cultures, we measured the concentrations of 13 cytokines in their supernatant at 8 and 24 hpe using multiplex ELISA. All cytokines were markedly elevated at both time points examined for the infected co-cultures, except for IFN-y and IL-7 which were below detection limits (Figure S6A, C). In the uninfected co-cultures only at 8 hpe, CXCL1, MCP-1, and GM-CSF were modestly elevated compared to unexposed controls (Figure 6A-F and Figure S6B, D-G). Interestingly, all detectable cytokines examined showed higher levels at 24 hpe compared to 8 hpe for the infected co-cultures, other than TNF-α which peaked early at 8 hpe and declined by 24 hpe (Figure 6A-F). These findings are consistent with our RNA sequencing results and in accordance with prior works showing that CXCL1, IL-6, IL-8, and MCP-1 are induced in HUVEC downstream of TNF-α [36,37], and suggest that early TNF-α release may induce the later upregulation of the additional cytokines examined herein.

Given the established role of TNF-α in regulating endothelial traction forces[27,38] and barrier integrity[25,26], we hypothesized that the early burst of TNF-α secretion may weaken the endothelial barrier function and enhance infected MΦ transmigration across HUVEC monolayers. This effect may be further amplified by TNF-α–induced secretion of additional cytokines, including CXCL1, IL-6, IL-8, and MCP-1, which collectively promote barrier destabilization and monocyte recruitment. Supporting this, RNA sequencing analysis confirmed upregulation of TNF pathway genes and also showed an increase in *TNF* transcript levels (i.e., the gene encoding TNF-α) in HUVEC exposed to infected, but not uninfected, MΦs (Figure 6G). This increase was most prominent at 8 hpe (1.4-fold higher than at 24 hpe), mirroring the temporal profile of secreted TNF-α. To functionally assess the role of TNF-α in modulating endothelial barrier properties and MΦ transmigration, we treated HUVEC monolayers with recombinant TNF-α and measured uninfected MΦ transmigration. TNF-α treatment resulted in a ~50% increase in transmigrating uninfected MΦs compared to vehicle controls (Figure 6H), along with a significant reduction in TEER, consistent with barrier weakening (Figure 6I). These findings align with previous studies linking TNF-α to endothelial barrier dysfunction.[27,38-40]

Thus, our data indicate that TNF-α, secreted early and specifically in response to infected MΦs, contributes to loosening the HUVEC monolayer barrier and facilitating MΦ transmigration.

LM-infected zebrafish show increased vascular permeability and MΦ transmigration

Our *in vitro* experiments have shown that in the presence of LM-infected MΦs, HUVEC permeability and MΦ transmigration is increased. To determine whether these findings could be recapitulated *in vivo*, we employed a zebrafish infection model. Zebrafish larvae possess a fully developed innate immune system, including MΦs, making them an excellent model for studying host-pathogen interactions and vascular dynamics.[41] To generate LM-infected MΦs while avoiding systemic dissemination of free LM, LM was locally injected into the trunk muscle. In our model we observed that MΦs at the injection site internalized LM and re-entered the bloodstream, thereby circulating and interacting with ECs at sites distal to the primary infection site, such as the tail fin (Movie S4).

We first sought to examine whether the presence of infected MΦs would have any impact on vascular permeability, as occurs *in vitro*. To this end, we performed a dextran leakage assay to determine whether increased permeability would occur only at the primary infection site as previously reported[42,43] or also at the tail fin indirectly exposed to LM through circulating infected MΦs. At 6 h post LM (or mock) infection, GFP labeled dextran was injected into the heart of the zebrafish larvae and fluorescence microscopy images of the vasculature were acquired (Figure 7A and Figure S7A). Vascular leakage was quantified by calculating the ratio of dextran fluorescence intensity within the tailfin blood vessels (vascular signal) to that in adjacent surrounding tissue (leak signal). This leak/vascular signal ratio was significantly higher in LM-infected larvae compared to mock-infected controls (Figure 7B), consistent with compromised endothelial barrier at distal sites from the site of infection.

Next, we asked whether MΦ transmigration was enhanced in LM-infected versus mock-infected zebrafish larvae. Using a similar infection setup, we performed a tail fin incision to induce MΦ transendothelial migration at the tailfin of zebrafish larvae containing RFP-expressing MΦs (Figure S7B). Confocal videomicroscopy was performed to quantify the time between MΦ-EC attachment and successful transmigration into surrounding extravascular tissue (Movie S4). In LM-infected larvae, MΦ transmigration time was 30% shorter compared to mock-infected controls (Figure 7C-D), indicating increased transmigration efficiency in the presence of LM infection. Together, these *in vivo* findings support our *in vitro* observations demonstrating that circulating MΦs exhibit enhanced transmigration during infection with LM. This reveals a mechanism by which infected MΦs may facilitate LM dissemination to distal tissues via increased EC permeability.

DISCUSSION

Heterotypic interactions between infected immune cells, such as mononuclear phagocytes, and vascular ECs are pivotal for bacterial dissemination through host tissues and evasion of immune surveillance. Yet, the precise mechanisms by which infected mononuclear phagocytes, particularly MΦs, traverse the endothelial barrier, and the potential role of EC mechanotransduction in regulating this process, were poorly understood. Here, we report the unexpected finding that ECs play an active role in monitoring immune cell transit by reinforcing monolayer tension and barrier integrity to restrict uncontrolled MΦ passage. This surveillance mechanism is subverted during infection, compromising the barrier and allowing greater immune cell transmigration, an outcome likely detrimental to the host.

Since our study focused on LM, it is unclear whether our findings generalize to other pathogens, but lines of evidence suggest this is likely. First, we show that the suppression of EC mechanotransduction in response to infected MΦs, which facilitates their transmigration, is at least partially mediated by cytokines. This implies that other pathogens capable of inducing similar cytokine signatures in MΦs may trigger comparable biomechanical changes in ECs, promoting immune cell transmigration. Second, in experiments using *S. aureus* as a model pathogen, we observed a similar increase in the transmigration of *S. aureus*-infected MΦs as compared to uninfected MΦs. These results support the possibility that other bacterial pathogens that persist within mononuclear phagocytes to promote systemic infection, including *Salmonella*, *Streptococcus*, and *Legionella*, may similarly modulate EC biomechanics to sustain their vascular crossing.[44-47]

Under conditions not involving infection, we observe that the mere presence of MΦ reinforces monolayer stresses and endothelial barrier integrity, particularly during the first ~10 hpe. A question that remains is what triggers this response. One intriguing possibility is that the mechanical forces exerted by adhering and migrating MΦs are sensed by ECs in a manner analogous to frictional forces exerted on ECs due to fluid shear stresses, which lead to elevation of traction and monolayer stresses.[48,49] While this analogy remains speculative, it raises mechanistic questions that can be addressed in future studies. Supporting the idea that ECs are active responders during immune cell contact, prior studies have shown that both neutrophils and even interaction with ICAM-1-coated beads are sufficient to elicit an EC biomechanical response, including increased traction force generation.[15,50]

While we focused on the biomechanical responses of ECs, it is important to consider that MΦs themselves may also actively contribute to their own transmigration by exerting mechanical forces

on the endothelium, a possibility we did not directly explore (though we find that infected MΦs adhere more readily on ECs as opposed to uninfected MΦs). For example, work on neutrophils shows that they exert forces locally at the endothelial sites they try to breach; these forces are strong enough to open EC-EC junctional gaps, allowing neutrophils to subsequently push themselves into the underlying subendothelial matrix to thrust an invasive protrusion [15,51]. However, neutrophil diapedesis is also mechanically facilitated by proinflammatory signals that modulate vascular EC (VEC) contractility, leading to spatial heterogeneities in VEC monolayer tensions and thus facilitating diapedesis[15], in line with our findings with MΦ-EC interactions. MΦs have also been shown to generate substantial traction forces during migration, particularly at their leading edge, with force magnitude increasing quasi-linearly with substrate stiffness.[52] Given our AFM data showing that ECs are stiffer in uninfected versus infected settings, it remains an open question whether MΦs exert greater traction forces on stiffer, less permissive EC monolayers, and whether this mechanical input aids their transmigration under non-infected settings. Additionally, MΦ-generated forces can serve reparative functions. For example, MΦs have been shown to physically bridge ruptured brain vasculature by mechanically pulling opposing endothelial edges together to facilitate wound closure.[16] This highlights their potential as active mechanical participants in vascular remodeling.

Whether infection alters MΦ contractility and traction generation, and how these changes might synergize with the altered mechanical state of ECs to facilitate transmigration, remains to be determined. The development and use of optogenetic tools to modulate cell contractility which can be targeted specifically to MΦs could provide a powerful approach to probe with spatiotemporal precision the role of MΦ force generation in promoting their transmigration through endothelia.[53] In parallel, single-cell RNA sequencing of ECs co-cultured with either uninfected or infected MΦs could provide valuable insight into infection-induced cytoskeletal reprogramming in both cell types. Specifically, transcriptomic changes in genes involved in actin dynamics, adhesion, and mechanotransduction may help infer how MΦ motility and traction force generation are modulated during transmigration. Several lines of evidence using MΦ alone infected with other bacterial pathogens (e.g. *L. pneumophila*, *S.* Typhimurium) suggest that various cell biomechanical aspects such migration speed and directionality as well as stiffness can be altered during infection.[54-57] However, none of those were probed during interaction of MΦs with ECs as we report here.

Enhanced collective cell alignment within a monolayer confers mechanical stability by enabling more uniform distribution and balance of intercellular forces.[58,59] Conversely, disruptions in

nematic ordering of cells have been shown to destabilize monolayers, promoting events such as cell extrusion and compromising barrier integrity.[58] In line with these studies, our findings are suggestive of ECs actively responding to the presence of MΦs by reinforcing structural order, likely as a protective mechanism to limit uncontrolled immune cell passage. This response appears to be attenuated in response to infected MΦs, in part due to infection-induced cytokine signaling interfering with (or overriding) this biomechanical reinforcement. We also show that among all the secreted cytokines, TNF-α plays a pivotal role in increasing transmigration of MΦs, consistent with previous studies reporting a role for TNF-α in increasing barrier permeability.[60] Unlike TNF-α, which was upregulated at 8 hpe, the rest of the cytokines tested were significantly upregulated at 24 hpe. These cytokines are often induced by TNF-α and contribute to modulating barrier integrity: e.g., CXCL1 promotes recruitment and transmigration of THP-1 cells;[61] IL-6 increases HUVEC permeability,[62,63] as does the potent monocyte chemoattractant MCP-1, leading to increased monocyte transmigration to the subendothelium;[64] IL-8 regulates endothelial permeability by down-regulation of tight junctions.[65,66] We should, however, note that the weakening of endothelial barrier integrity could also be due to additional factors we did not explore in this study, for example increased presence or reactive oxygen species (ROS) or nitric oxide (NO production) due to infection.

Under infected conditions, we observed strong upregulation of VCAM-1, ICAM-1, and E-selectin expression in HUVEC, indicating that enhanced MΦ transmigration may, in part, be driven by increased MΦ-EC adhesion. Supporting this, we also measured a ~2-fold increase in MΦ–EC adhesion when MΦs where infected versus not. These findings are consistent with prior studies showing that TNF-α, either through direct treatment or via the induction of downstream pro-inflammatory cytokines, leads to elevated expression of these adhesion molecules on ECs.[36,67-69]

Our *in vitro* experiments showed that in the presence of infected MΦs, ECs' increase in monolayer stresses and barrier integrity is attenuated, facilitating MΦ transmigration compared to uninfected MΦ settings. To determine whether this phenomenon also occurs in a more complex *in vivo* setting, we employed a zebrafish infection model, which has been extensively used to study how infected macrophages traverse vascular barriers to spread infection to distant tissues, as shown in the context of *Mycobacterium marinum* (MM) infection.[70,71] In our model, infection of the zebrafish trunk muscle with LM led to a systemic increase in vascular permeability, even though bacterial infection remained largely confined to the initial site. The only exception was the presence of circulating infected MΦs, which were observed in the bloodstream. In turn, this

increase in permeability facilitated faster MΦ transmigration in response to a distal wound, reducing the time required for MΦ recruitment compared to mock-infected larvae. A key question that arises is what drives this systemic vascular permeability. We can reasonably exclude the possibility of free, circulating LM as the cause. Videomicroscopy failed to detect extracellular LM in circulation, and previous studies have shown that LM introduced directly into the zebrafish bloodstream is rapidly phagocytosed and cleared by MΦs within 1 h post-injection.[72] This suggests that the systemic permeability increase is more likely due either to a strong innate immune response or to the presence of circulating infected immune cells. This systemic response differs from what has been reported for other bacterial infections in zebrafish larvae. For example, in MM infection, the increase in vascular permeability appears to be localized to the infection site.[42] This discrepancy may reflect differences in the biology of the pathogens. MM has a significantly slower intracellular doubling time and tends to remain confined within phagosomes, while LM rapidly escapes the phagosome and can actively spread from cell to cell, promoting more aggressive dissemination.[73-76]

Our discovery that the presence of infected MΦs suppresses the typical increase in EC monolayer stresses and barrier integrity, which are the responses observed with uninfected MΦs, highlights the active role of ECs in regulating immune cell transmigration. This suppression is partly cytokine-mediated, reflecting infection-driven alterations that compromise EC biomechanical defenses. Far from being passive barriers, ECs dynamically regulate their cytoskeletal dynamics, traction forces, and intercellular stresses in response to immune cues. Infection, however, disrupts these protective responses, enabling pathogens to exploit infected MΦs to weaken EC mechanics and promote barrier breach. While it is well established that pathogens use MΦs to disseminate systemically, the mechanobiological impact on ECs during MΦ-EC encounters remains poorly understood. Revealing the bacterial effectors and host pathways that alter EC cytoskeletal dynamics and junctional integrity will be key to understanding how vascular barriers are compromised during infection and may reveal new targets to restrict pathogen systemic spread by specifically targeting the vasculature. [43,77,78]

LIMITATIONS OF THE STUDY

While we maintained a stable EC-to-MΦ ratio in most experiments, variations in this ratio could influence EC mechanobiological responses and thus MΦ transmigration efficiency, especially given the cytokine-mediated nature of these interactions during infection. Most experiments

presented herein were conducted with ECs cultured on collagen-I coated glass coverslips, which are approximately six orders of magnitude stiffer than native subendothelial matrices.[79,80] Matrix stiffness is a well-established regulator of EC behavior, known to enhance EC traction forces and monolayer stresses on stiffer substrates.[81] However, how varying levels of subendothelial stiffness modulate EC biomechanics and MΦ transmigration remains an open question. *In vivo*, ECs are also subject to shear stresses from blood flow, which is a critical determinant of EC function and mechanotransduction.[82] Although our EC-MΦ adhesion assay included low magnitude perfusion, we did not systematically examine the role of shear flow in modulating EC-MΦ interactions, something that could be pursued in future studies. Finally, in this work we employed three experimental models: ECs cultured on static glass substrates, ECs within a vessel-on-chip device exposed to low shear stress, and the zebrafish infection model. Future work could include different EC types and/or next-generation vessel-on-chip platforms that better recapitulate human vascular microenvironments.[83,84] Accounting for both extracellular mechanical cues and additional tissue-specific supporting cells (such as pericytes and astrocytes in brain microvasculature) will be essential for dissecting how those modulate EC-MΦ interactions in a more (patho)physiologically-relevant context.

RESOURCE AVAILABILITY

Lead contact

Further information and requests for reagents may be directed to and will be fulfilled by the lead contact Effie Bastounis effie.bastounis@uni-tuebingen.de (E.E.B.).

Materials availability

Materials developed in this study are available on request to the corresponding author.

Data and code availability

Data collected are available on request to the corresponding author. The accession number of the RNA sequencing data (FASTq files) generated during this study and subsequent analysis reported in this paper are available from the lead contact and on the NCBI Gene Expression Omnibus (GEO) archive (accession ID GEO: GSE296345). All differential expression analysis results of this study are included as a supplementary table in this article (Table S1). All codes are uploaded in our GitHub repository with the corresponding accession numbers as listed as follows: (1) Characterization of cell shape descriptors using cell masks generated via Tissue Analyzer Fiji plugin[85] (DOI: 10.5281/zenodo.15703769); (2) Quantification of degree of cell alignment for cells in monolayer (DOI:10.5281/zenodo.15495798);[86] (3) Cell kinematics analysis (DOI: 10.5281/zenodo.7155531); (4) Monolayer stresses calculation (DOI: 10.5281/zenodo.7155523).

AUTHOR CONTRIBUTIONS

Conceptualization, E.E.B. and M.M.; Methodology, E.E.B., M.M., S.M., P.L.; Software, E.E.B; M.M., Investigation, E.E.B., M.M., E.K., A.B., M.L., K.W., S.M., Writing – Original Draft, E.E.B., M.M.; Writing – Review & Editing, E.E.B., S.M., P.L., T.E.S.; Resources, E.E.B., P.L., S.M., T.E.S., D.K.; Supervision, E.E.B., S.M., T.E.S., D.K., P.L.

ACKNOWLEDGEMENTS

We are grateful to Julie A. Theriot for her insight, scientific discussions and sharing her resources when some preliminary experiments were conducted with the help of Michelle Rengarajan involving endothelial cells exposed to (infected) MΦs back in 2016. We also thank Matthew Footer for discussions and experimental support. We thank Libera Lo Presti for discussions and for

revising the manuscript and rest of the materials. We acknowledge that part of our MSM codes is based on the original code (plane stress problem) written by Siva Srinivas Kolukula. We acknowledge Ioanna Pasalidou for assisting Marie Muenkel with microscopy imaging, during conduction of her BSc thesis in the Bastounis lab. The graphical abstract was created with BioRender.com. This research was supported by the Core Facility Flow Cytometry Berg at the Universitätsklinikum Tübingen. RNA sequencing was performed by Arraystar Inc. Immunoassays were performed by the Natural and Medical Sciences Institute (NMI). This work was supported in part by the American Heart Association, award number: 18CDA34070047 (E.E.B.) and the Deutsche Forschungsgemeinschaft (DFG, German Research Foundation) under Germany´s Excellence Strategy – EXC 2124 – 390838134 (E.E.B., M.M., E.K., P.L., F.R.), DFG grant with Project number 335549539/GRK2381 (A.B., T.E.S.). A.B. is supported by the Add-on Fellowship for Interdisciplinary Life Science of the Joachim Herz Foundation. We also thank EMBO for the Scientific Exchange Grant 10245 (M.M.). We thank the LSHTM Biological Services Facility for the work and care of our zebrafish stocks. Research in the S.M. laboratory is supported by a European Research Council Consolidator Grant (772853 - ENTRAPMENT) and Wellcome Discovery Award (226644/Z/22/Z). Finally, we acknowledge support by Open Access Publishing Fund of the University of Tübingen.

DECLARATIONS OF INTEREST

The authors declare no competing interests.

FIGURES

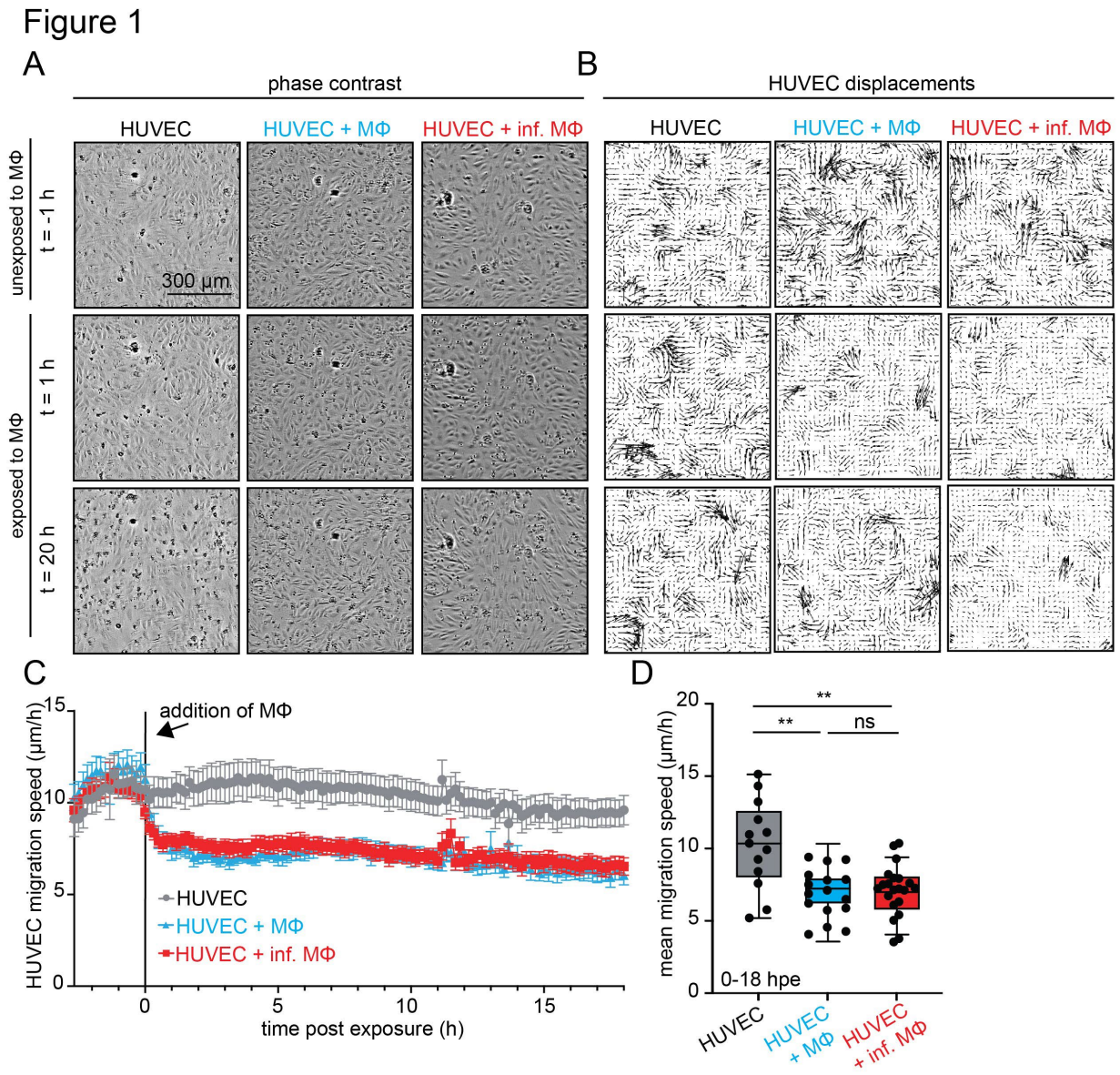

Figure 1 ECs decrease their migration speed by 30% in an acute and sustained manner when exposed to (un)infected U937. (**A**) Columns show representative time-lapse phase contrast images of HUVEC in monolayer unexposed (HUVEC), exposed to uninfected U937 (HUVEC + MΦ), or to LM-infected U937 (HUVEC + inf. MΦ). Rows show representative time points, namely: 1 h before exposure to U937, 1 h (2nd row) and 20 h (3rd row) after exposure to U937. (**B**) Same as A but showing corresponding HUVEC displacement vectors scaled 20x. (**C**) HUVEC migration speed (µm/h) over time post-MΦ exposure (h) for the three conditions shown in A-B. For each condition, mean +/- SEM is plotted for three independent experiments and N=16-21 replicates per condition. Black line marks time of MΦ addition. (**D**) Time-averaged migration

speed for the same conditions and samples as in C. KWTD, ns, non-significant: p>0.05; *: p< 0.05; **: p<0.01.***: p<0.001. See also Figure S1 and Movie S1.

Figure 2

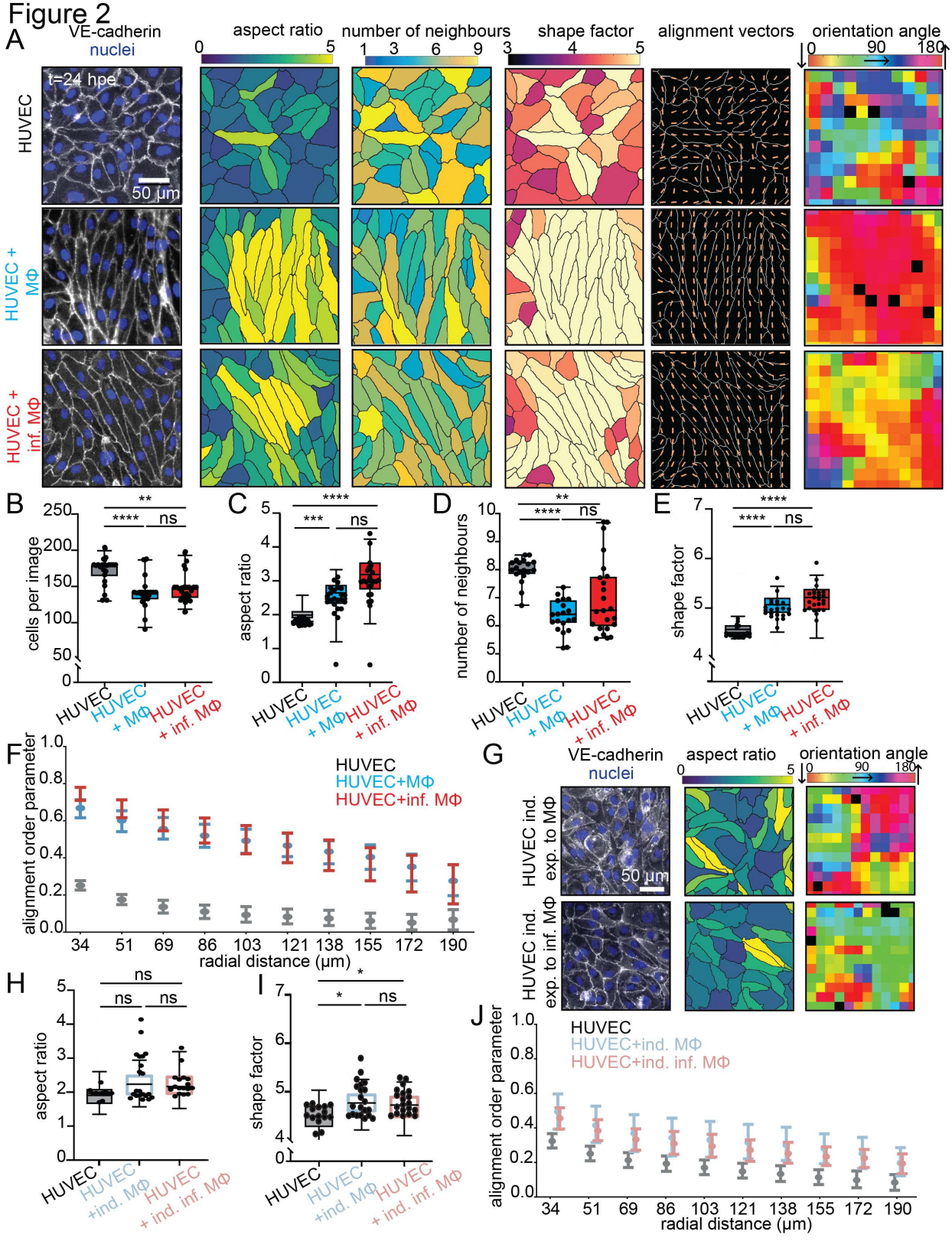

Figure 2 ECs increase their polarization and collective alignment in the presence of MΦs. (**A**) Rows show immunostained samples of HUVEC in monolayer, fixed at 24 h after exposure to PMA-differentiated, uninfected (HUVEC+MΦ) or LM-infected (HUVEC + inf. MΦ) U937 (MΦ). Unexposed HUVEC (HUVEC; top row) served as control. Columns 1-4 show superimposed images of HUVEC nuclei and VE-cadherin fluorescence (1), and segmented HUVEC color-coded based on their aspect ratio (2), number of neighboring cells (3) and shape factor (4). Columns 5-6 show HUVEC contours in white superimposed with cell alignment vectors in orange (5) and maps of the orientation angle of cells (6). (**B-E**) For the three conditions shown in A, boxplots show number of cells per field of view (**B**), mean aspect ratio (**C**), number of neighbors (**D**), shape factor (**E**). Superimposed dots represent average values per image analyzed (12 in total per condition) originating from 3 independent experiments. (**F**) Alignment order parameter between neighboring HUVEC as a function of the radial distance that separates them (μm). Mean and 95% CI is plotted for the three conditions and experiments shown in B. (**G**) Rows show immunostained samples of HUVEC in monolayer alone, fixed at 24 h after being indirectly exposed to uninfected (HUVEC indirectly exposed to MΦ) or LM-infected MΦ (HUVEC indirectly exposed to inf. MΦ) (See text for details). Columns 1-3 show superimposed images of HUVEC nuclei and VE-cadherin fluorescence (1), segmented HUVEC color-coded based on their aspect ratio (2), and maps of the orientation angle of HUVEC (3). (**H-I**) For the two conditions in G and for unexposed HUVEC, boxplots show mean aspect ratio (**H**), and shape factor (**I**). Superimposed dots represent average values per image analyzed (average of 13 images per condition) originating from 3 independent experiments. (**J**) Same as F but for the conditions shown in H-I. For (B-E, H-I), KWTD, ns, non-significant: $p>0.05$; *: $p< 0.05$; **: $p<0.01$.***: $p<0.001$. See also Figure S2.

Figure 3

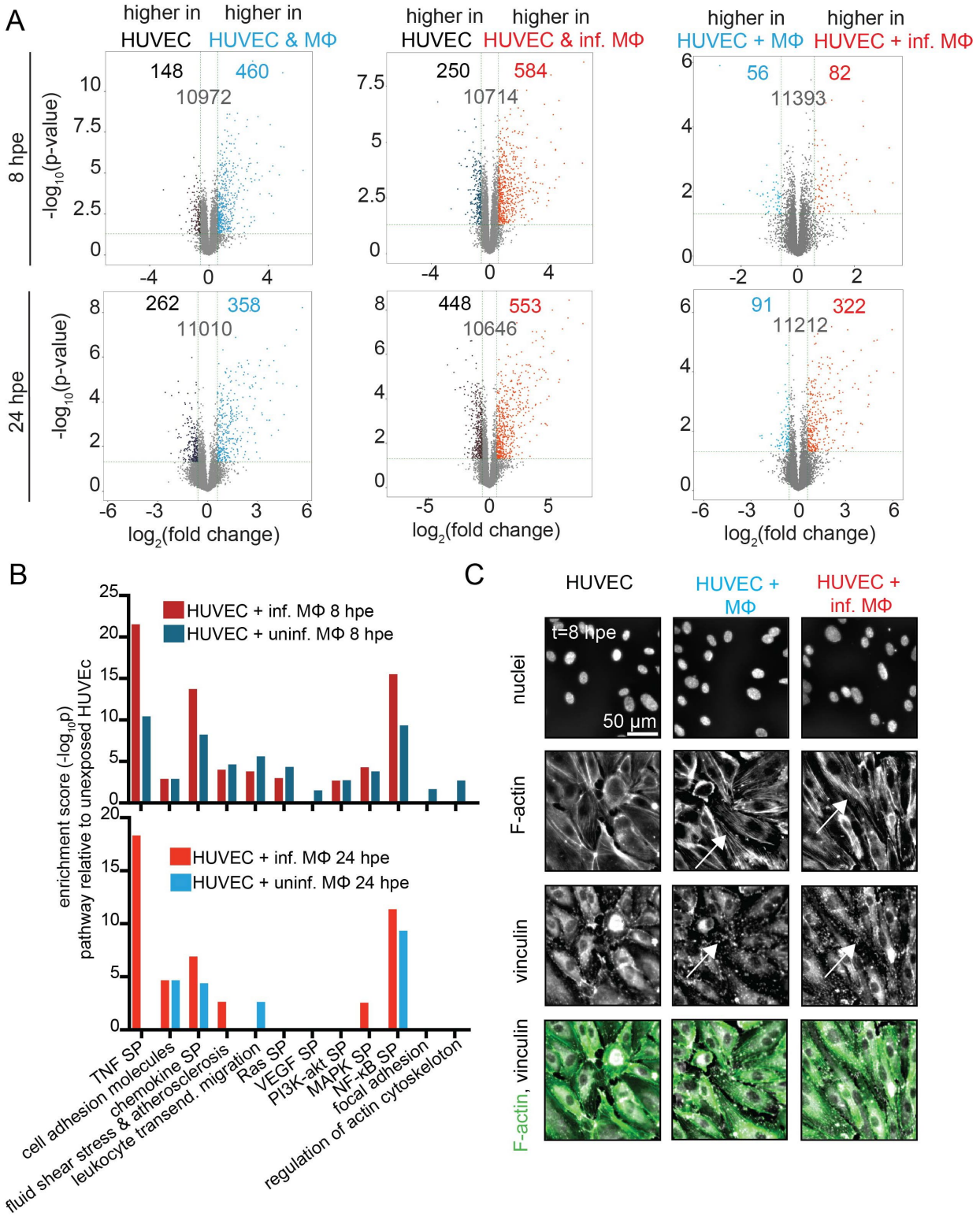

Figure 3 RNA sequencing reveals upregulation of pathways related to focal adhesions and the actin cytoskeleton in HUVEC exposed to uninfected but not LM-infected MΦ. (**A**)

Volcano plots of DEGs based on RNA sequencing of (i) unexposed HUVEC (HUVEC, black), (ii) MΦ-exposed HUVEC (HUVEC+MΦ, blue); (iii) infected MΦ-exposed HUVEC (HUVEC+ inf. MΦ, red). For each pairwise comparison, upregulated genes in each condition are shown in the corresponding color. Non DEGs are colored in gray. Top (bottom) row shows comparison at 8 h (24 h) post MΦ-exposure (hpe). The $-\log_{10}$ p values are plotted against the average $\log_2$-fold changes in gene expression. (**B)** Pathway enrichment analysis. HUVEC+MΦ (blue) and HUVEC+ inf. MΦ (red) are compared with unexposed HUVEC based on their enrichment score ($-log_{10}p$, y-axis). X-axis shows selection of pathways differentially regulated. SP: signaling pathway. Top (bottom) plots refer to HUVEC at 8 hpe (24 hpe). (**C**) Representative immunofluorescence images of HUVEC nuclei (1st row), F-actin (2nd row), vinculin (3rd row) and overlay of the aforementioned (4th row) for unexposed HUVEC (left), HUVEC+MΦ (middle) and HUVEC + inf. MΦ (right) fixed at 8 hpe. Scale bar 50 μm. See also Figure S3 and Movie S2.

Figure 4

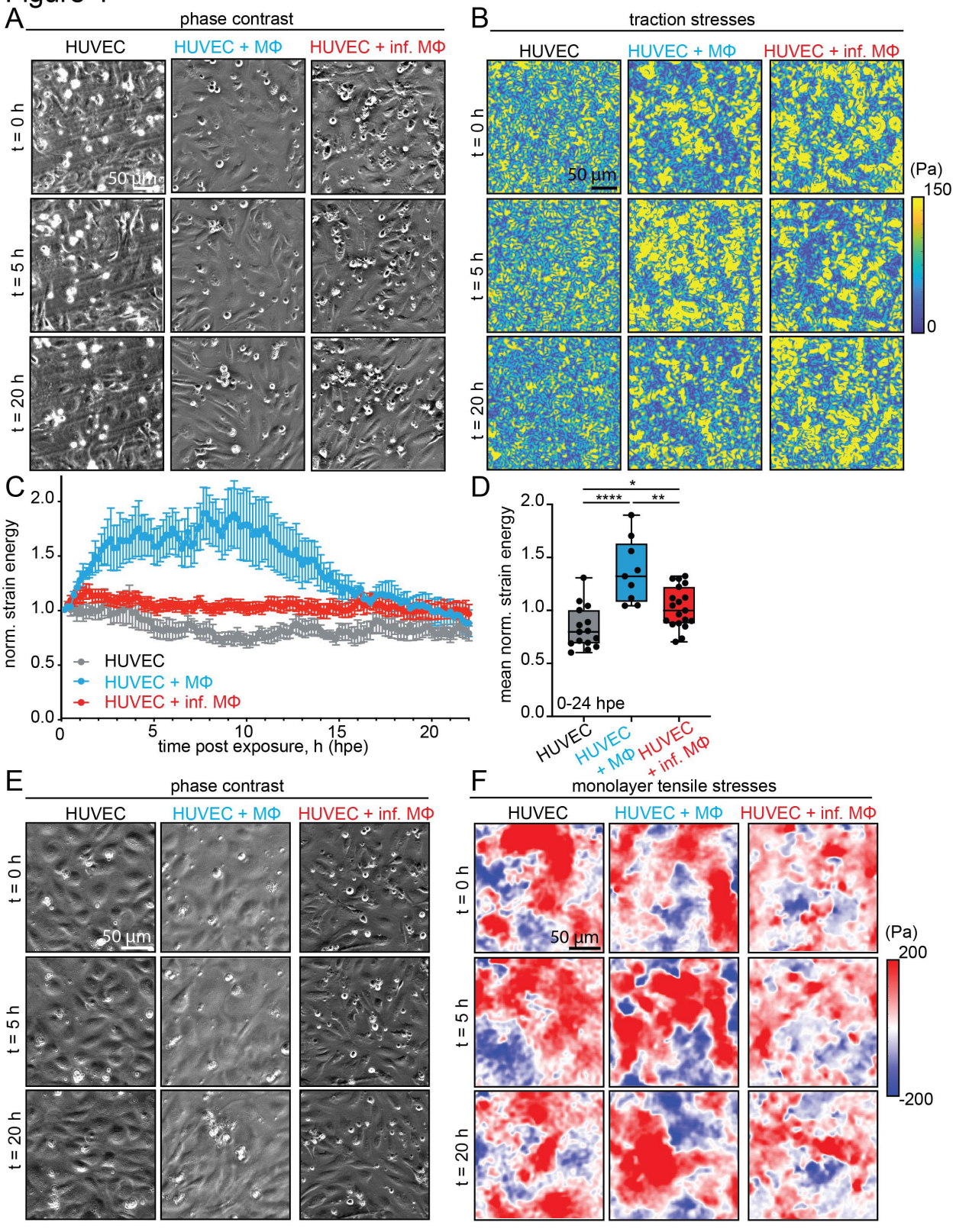
A
phase contrast
HUVEC
HUVEC + MΦ
HUVEC + inf. MΦ
t = 0 h
t = 5 h
t = 20 h
50 µm
B
traction stresses
(Pa)
150
0
C
norm. strain energy
time post exposure, h (hpe)
D
mean norm. strain energy
0-24 hpe
E
phase contrast
F
monolayer tensile stresses
200
-200

Figure 4 Strain energy increases dramatically in ECs exposed to uninfected MΦ, but to a lesser degree in LM-infected MΦ, as compared to unexposed ECs. (**A**) Columns show representative time-lapse phase contrast images of HUVEC in monolayer unexposed (HUVEC), exposed to uninfected U937 (HUVEC + MΦ), or to LM-infected U937 (HUVEC + inf. MΦ). Rows show representative time points, namely: upon addition of U937 (0 h), 5 h and 20 h after exposure to U937. Cells reside on 35 kPa hydrogels. (**B**) Same as A but showing the corresponding traction stresses that cells exert (magnitude in Pa). (**C**) Mean normalized strain energy imparted by cells to deform their matrix for the conditions shown in A-B. Normalization with respect to first time point of each recording. Time in h relative to exposure of HUVEC to MΦ (hpe). Three independent experiments, 9-19 recordings per condition in total. (**D**) Time-averaged normalized strain energy for the same conditions and samples as in C. Superimposed dots show the mean of different recordings. (**E**) Columns show representative time-lapse phase contrast images of the same conditions as in A. Rows show representative time points, namely: upon addition of U937 (0 h), 5 h and 20 h after exposure to U937. Cells reside on 35 kPa hydrogel in all cases. (**F**) Same as A but showing the corresponding monolayer tensile stresses (σ_I, Pa) that cells in the monolayer exert on each other. KWTD, ns, non-significant: p>0.05; *: p< 0.05; **: p<0.001, ****: p<0.0001. See also Figure S4 and Movie S3.

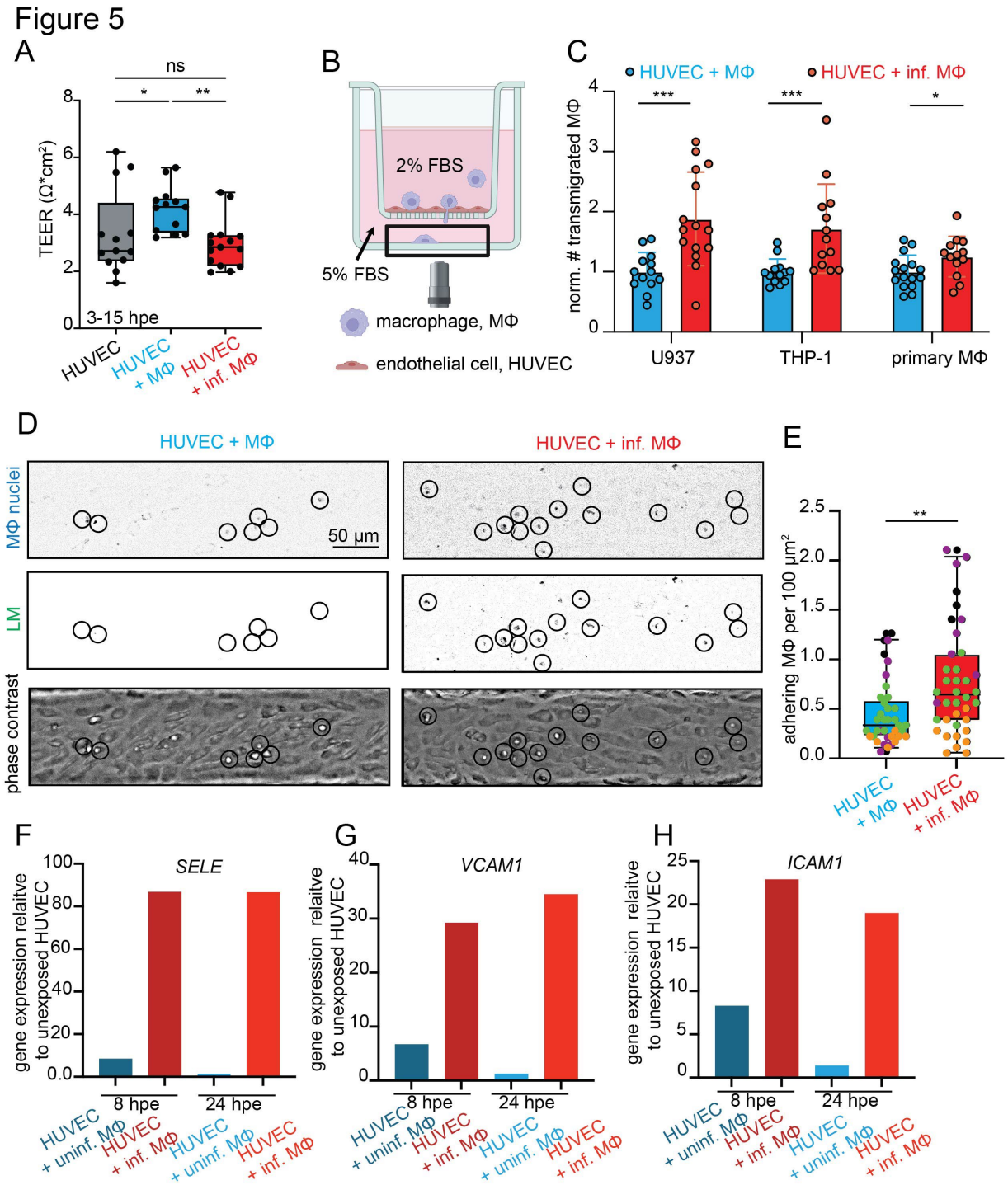

Figure 5 The weaker barrier integrity of ECs exposed to infected as opposed to uninfected MΦs promotes increased transmigration of bacterially-infected MΦs. (**A**) Boxplot of time-averaged mean transendothelial electrical resistance (TEER, W*cm^2) of HUVEC exposed to uninfected (HUVEC+MΦ), LM-infected (HUVEC + inf. MΦ) or no (HUVEC) PMA-differentiated U937 cells (MΦ). Time averaging performed between 3-15 hpe. Dots represent the individual

monolayers analyzed. Three independent experiments and a total of 13-15 samples per condition. (**B**) Schematic of the experimental setup for MΦ transmigration assay. HUVEC are grown in monolayer for 24 h on transwell insert. Uninfected or LM-infected MΦs are added on the insert. After 24 h MΦs in bottom chamber are imaged and counted. Transmigration is induced by fetal bovine serum (FBS) gradient. (**C**) Barplots of number of transmigrated MΦs within 24 h post exposure to HUVEC monolayer. Mean+/SEM. Blue: uninfected MΦ; red: LM-infected MΦ. Three independent experiments with a total of 13-16 replicates per condition for U937, 13 replicates for THP-1, and 12 replicates for primary MΦ. (D) Top row shows MΦ nuclei adhering to HUVEC monolayer in microfluidic chip. Second row shows LM fluorescence in infected MΦs. Third row shows phase contrast image of HUVEC exposed to uninfected (HUVEC+MΦ) or LM infected (HUVEC + inf. MΦ) MΦs. Circles indicate adhering MΦ. (**E**) Boxplot of number of adhering MΦ after 2 h perfusion over HUVEC monolayer normalized to 100 μm^2 of surface area in microfluidic channel shown in D. Dots represent individual samples, colors represent individual replicates (4 independent experiments, with total of 27 samples analyzed per condition). (**F-H**) Barplots of fold change in gene expression of *SELE* (**F**), *VCAM1* (**G**) and *ICAM1* (**H**) for HUVEC 8 and 24 h post exposure to (un)infected MΦ compared to unexposed HUVEC, as determined via RNA seq (N=4 replicates). KWTD, ns, non-significant: $p>0.05$; *: $p< 0.05$; **: $p<0.01$.***: $p<0.001$. See also Figure S5.

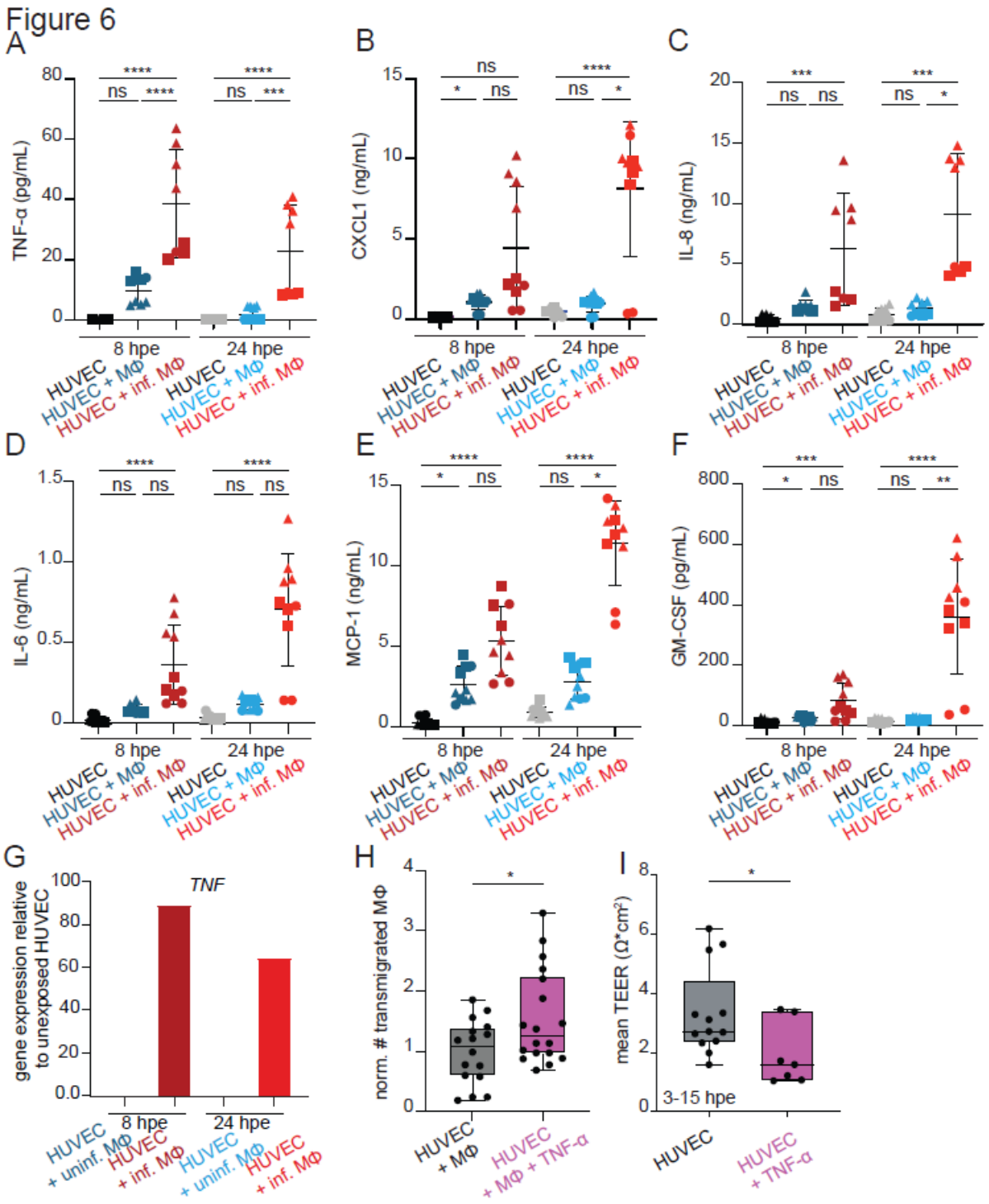

Figure 6 Differential cytokine secretion of HUVEC exposed to uninfected versus LM-infected MΦs. (**A-F**) Scatter plots of cytokine concentration in the supernatant of unexposed HUVEC (HUVEC), HUVEC exposed to uninfected (HUVEC+MΦ), or LM infected (HUVEC + inf. MΦ) MΦs. Scatter plots 1-3 (4-6) refer to samples collected at 8 (24) hpe to MΦ (N =10 samples originating from 3 independent experiments, mean ± SD). Each panel refers to a different

cytokine, namely: TNF-α (**A**), CXCL1 (**B**), IL-8 (**C**), IL-6 (**D**), MCP-1 (**E**), GM-CSF (**F**). (**G**) Barplot of fold change in gene expression of *TNF* in HUVEC 8 and 24 h post exposure to (un)infected MΦ compared to unexposed HUVEC, as determined through RNA seq (N=4 replicates). (**H**) Boxplot of number of transmigrated MΦs (PMA-differentiated U937) 24 h post-exposure to HUVEC in monolayer, with and without addition of 10 ng/mL TNF-α. Mean+/-SEM, N=9 samples originating from 3 independent experiments per condition. (**I**) Boxplot of time-averaged mean transendothelial electrical resistance (TEER, $W*cm^2$) for HUVEC treated with vehicle control or 10 ng/mL TNF-α. Time averaging performed between 3-15 post exposure to MΦs (hpe). Dots represent individual monolayers analyzed. N=13 samples originating from 3 independent experiments per condition. For (A), ANOVA was performed, for (B-F, H-I), KWTD was performed. ns: non-significant, $p>0.05$; *: $p< 0.05$; **: $p<0.01$.***: $p<0.001$, ****: $p<0.0001$. See also Figure S6.

Figure 7

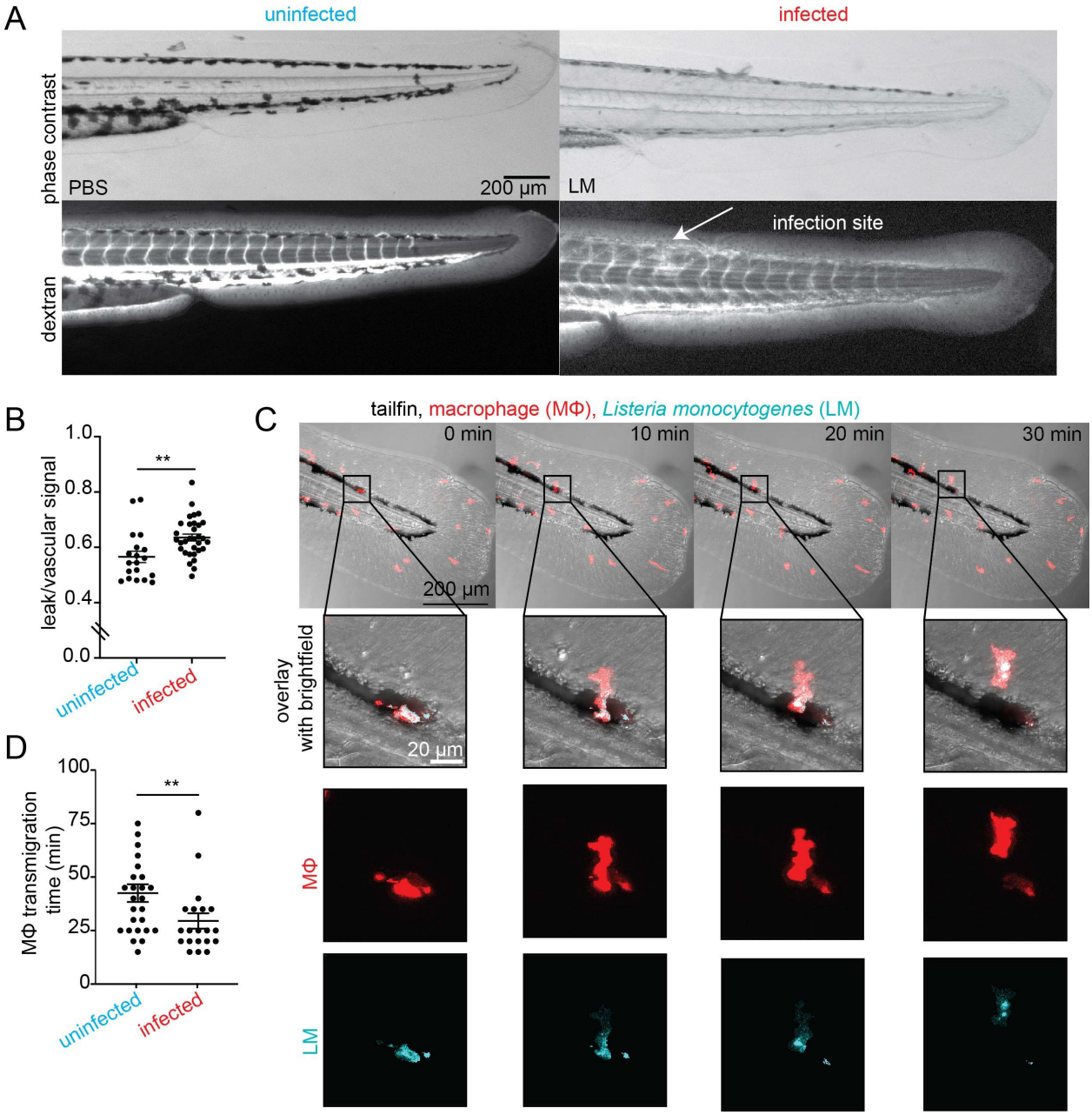

Figure 7 LM infection in trunk muscle of zebrafish larvae leads to systemic increase of vascular leakage and decrease of MΦ transmigration time. (**A**) Representative phase contrast images (1st row) and dextran fluorescence (2nd row) for uninfected (i.e., mock-injected with PBS) and LM-infected zebrafish larvae (24-48 h post-fertilization) at 6 hpi. Arrow points to the LM infection site in the trunk muscle. (**B**) Ratio of leak to vascular signal for uninfected and LM-infected zebrafish larvae, determined via imaging and calculating the integral of the intensity of fluorescent dextran at regions distal to the infection site. Colors represent 3 independent biological replicates; dots represent individual larvae. (**C**) Representative time-lapse brightfield images of

LM-infected zebrafish larvae tail fin (24-48 hpf) overlay with MΦ fluorescence (red) and LM fluorescence (cyan). Zoomed insets show MΦ transmigration from tail vein into the tailfin. Rows show: overlay of brightfield image with MΦ fluorescence (red) and LM fluorescence (cyan); MΦ fluorescence; and LM fluorescence. (**D**) MΦ transmigration time (min) for uninfected and LM-infected zebrafish larvae. N=7 fish on average per condition were analyzed, and a total average of 25 MΦs were tracked as they migrated from tail vein into the tailfin. WRST, **: p< 0.01. See also Figure S7 and Movie S4.

STAR★Methods

Key resources table

REAGENT or RESOURCE	SOURCE	IDENTIFIER
Antibodies and dyes		
anti-VE-cadherin phycoerythrin E (PE)-coated antibody	BD biosciences	Cat #: 560410, RRID: AB_1645502
Alexa Fluor™ 488 phalloidin	Thermofisher	Cat #: A12379
Alexa Fluor™ 647 phalloidin	Thermofisher	Cat #: A30107
DAPI solution	Sigma	Cat #: 10236276001
Hoechst solution	Fisher	Cat #: 11534886
anti-vinculin antibody	Sigma	Cat #: V9131 RRID: AB_477629
Ki-67 Recombinant Rabbit Monoclonal Antibody	Invitrogen	Cat #: MA514520 RRID: AB_10979488

Donkey anti-Rabbit IgG, Alexa Fluor™ Plus 647	Thermofisher	Cat #: A32795 RRID: AB_2762835
Goat anti-Mouse IgG, Alexa Fluor™ 488	Thermofisher	Cat #: A-11001 RRID: AB_2534069
SPY650-FastAct	Spirochrome	Cat #: SC505
CD45 Monoclonal Antibody (30-F11), Alexa Fluor™ 488	eBioscience™	Cat #: 53-0451-82 RRID: AB_2848416
Fluorescein isothiocyanate–dextran	Sigma	Cat # FD70S
Bacterial strains		
L. monocytogenes: LM-GFP	F. Ortega[87]	N/A
S. aureus USA300 Lac-sGFP	N. de Jong[88]	N/A
Chemicals, peptides, and recombinant proteins		
Phosphate buffered saline (PBS)	Thermofisher	Cat#10010023
Fetal Bovine Serum (FBS)	Thermofisher	Cat#10270106
EGMTM-2 BulletKitTM Medium (MEDIUM CC-3156 and Kit CC-4176)	Lonza	Cat# CC-3162
Human GM-CSF Recombinant Protein	Thermofisher	Cat# 300-03-50UG
Leibovitz L-Medium, ohne Phenolrot	Thermofisher	Cat# 21083027
RPMI 1640 Medium, HEPES (Gibco)	Thermofisher	Cat#11594506
RNeasy Plus Micro Kit (50)	Qiagen	Cat#74034
QIAshredder (250)	Qiagen	Cat#79656
Cell Culture Inserts	nanaAnalytics	Cat#9320402
BBL TM Brain-heart infusion (BHI)	BD	Cat#211059
DifcoTM Agar, Granulated	BD	Cat#214530
Streptomycin sulfate	Thermofisher	Cat#455340050
Chloramphenicol	Corning	Cat#56-75-7
Gentamicin	Fisher	Cat#15820243
Dimethyl Sulfoxide (DMSO)	Sigma	Cat#D2650
Sulfo-SANPAH	Fisher	Cat#10474005

Collagen I, rat tail	Thermofisher	Cat#A1048301
Phorbol 12-myristate 13-acetate (PMA)	Sigma	Cat#P1585
Formaldehyde 16% methanol-free	Thermofisher	Cat#28906
Bovine serum albumin (BSA)	AppliChem	Cat#A6588
(3-Aminopropyl)triethoxysilane	Sigma	Cat#A3648
40% Acrylamide	Sigma	Cat#A4058-100ML
Bis-acrylamide solution (2%w/v)	Fisher Scientific	Cat#BP1404-250
Fluorospheres carboxylate-modified microspheres, 0.2 µm, yellow-green fluorescent (505/515)	Invitrogen	Cat#F8803
Ammonium persulfate	Fisher	Cat#BP17925
TEMED	Sigma	Cat#T9281-25ML
HEPES, Free acid	J.T. Baker	Cat#4018-04
0.25% trypsin-EDTA, phenol red	Thermofischer	Cat#25200056
0.05% trypsin-EDTA, phenol red	Thermofischer	Cat#5300054
2-Mercaptoethanol	Roth	Cat# 4227.1
SDS	Roth	Cat# 2326.2
custom multiplex Human Magnetic Luminex (R) Assay	R&D Systems	Cat#LXSAHM-13
Antibiotic-Antimycotic	Thermofisher	Cat#15240062
Deposited data		
RNA sequencing data	This paper	GSE296345, NCBI tracking system #25152039
Experimental models: Cell lines		
HUVEC single Donor in EGM2	Lonza	Cat #: C2517A
RFP HUVEC	Pelobiotech	Cat #: 14600
U937	Theriot lab, University of Washington, USA	N/A
THP-1	Peschel/Kretschmer Lab (University of Tuebingen)	N/A
peripheral blood mononuclear cell	Peschel/Kretschmer Lab (University of Tuebingen)	Project license: 082/2025BO2
Experimental models: Organisms/strains		

Tg(mpeg1::Gal4-FF)^{gl25}/Tg(UASE1b::nfsB.mCherry)^{c264} zebrafish	S. Mostowy[89]	Project license: PPL P4E664E3C and PP5900632
Software and algorithms		
Fiji	[90]	RRID:SCR_002285 https://imagej.net/
MATLAB	The MathWorks Inc.	RRID:SCR_001622 https://de.mathworks.com/products/matlab.html
GraphPad Prism	GraphPad	RRID:SCR_002798 http://www.graphpad.com/scientific-software/prism/
NIS-Elements software package	Nikon	RRID:SCR_014329 https://www.nikoninstruments.com/Products/Software
Cell kinematics analysis	This paper	DOI:10.5281/zenodo.7155531
Monolayer stresses calculation	R. Aparicio-Yuste[68]	DOI:10.5281/zenodo.7155523
Cell morphology quantification analysis	This paper	DOI: 10.5281/zenodo.15703769
Cell alignment analysis	[86]	DOI:10.5281/zenodo.15495798
BD FACSDiva Software	BD Bioscience	RRID:SCR_001456
FlowJo	Flowjo	RRID:SCR_008520
Fiji Plugin Tissue analyzer	[85]	DOI:10.1007/978-1-4939-6371-3_13

Experimental model and study participant details

Mammalian cell culture

Primary human umbilical vein endothelial cells (HUVEC) were purchased from Lonza (C2517A) at P0 and cultured in tissue culture-treated flasks (Sarstedt 833.912.002) in 500 mL of Endothelial Cell Growth Basal Medium-2 (EBM™-2), supplemented with EGMTM-2 BulletKitTM Medium (Lonza, MEDIUM CC-3156 and Kit CC-4176) up until P10. RFP expressing HUVEC were purchased from Pelobiotech at P3 and were cultured in cell culture flasks (Sarstedt 833.912.002) coated with Quick Coating Solution (cAP-01) in Endothelial Basal Medium (EBM, cAP-03) containing 5% fetal bovine serum (FBS). Cells of passages 3-12 were used only.

U937 pro-monocytic human cells (cell line, generous gift from the Theriot Lab, University of Washington) were kept in suspension cell tissue culture flasks (Sarstedt 83.3911.502) in RPMI 1640 medium, HEPES (Gibco) supplemented with 10% FBS and antibiotic-antimycotic solution (Thermofisher, 15240062) at a density of 2-10*10^5 cells/mL. THP-1 human monocyte cells (cell line, generous gift from Andreas Peschel/Dorothee Kretschmer lab, University of Tübingen) were kept in suspension cell tissue culture flasks (Sarstedt 83.3911.502) in RPMI 1640 medium, HEPES (Gibco) supplemented with 10% FBS, antibiotic-antimycotic solution (Thermofisher, 15240062), and 1% sodium pyruvate solution (Sigma, S8636, 100 mM) at a density of 2-10*10^5 cells/mL. Peripheral blood mononuclear cells were isolated from donor blood and differentiated in 6 well plates (Greiner, M9062-100EA) in RPMI 1640 medium, HEPES (Gibco) supplemented with 10% FBS, antibiotic-antimycotic solution (Thermofisher, 15240062) and 100 nM GM-CSF (Thermofisher, 300-03-50UG) at a density of 2*10^6 cells/mL and referred to as primary MΦs. All cells were kept at 37°C and 5% CO_2. Regarding primary MΦ used in this study derived from blood of human donors: The institutional review board (IRB) of the University of Tübingen approved the study and all adult subjects donating blood provided informed consent. This study was done in accordance with the ethics committee of the medical faculty of the University of Tübingen that approved the study, Approval number 082/2025BO2.

Bacterial strains used in this study

The *Listeria monocytogenes* (LM) strain used in this study is JAT606 (Species: LM 1043S, Genotype/Description: Constitutive GFP expression).[87]

For experiments using *S. aureus*, *S. aureus* USA300 was cultured in tryptic soy broth (TSB, Oxoid, CM0129T) at 37°C for 17 h over-night under agitation at 160 rpm.[88]

Zebrafish larvae used in this study

Animal experiments were performed according to the Animals (Scientific Procedures) Act 1986 and approved by the Home Office (Project license: PPL P4E664E3C and PP5900632). Zebrafish embryos were obtained by natural spawning, and larvae were maintained at 28.5 °C in E3 embryo medium unless otherwise stated. E3 medium contained 5 mM NaCl (Sigma, S7653), 0.17 mM KCl (Sigma, P9541), 0.33 mM CaCl dihydrate (Sigma, 21102), and 0.33 mM MgSO4 hexahydrate (Sigma, M2670) in distilled water. Either AB wildtype or Tg(*mpeg1*::Gal4-FF)^{gl25}/Tg(UASE1b::*nfsB.mCherry*)^{c264} zebrafish were used. For injections and live imaging,

embryos were anaesthetized in 200 μg/ml MS-222 (tricaine) (Sigma-Aldrich, A5040) in E3 and recovered into fresh E3 supplemented with 0.036 g/l PTU (Sigma-Aldrich, P7629).

Method details

Differentiation of U937 and THP-1 to MΦ-like cells, MΦ infection and flow sorting

U937 or THP-1 monocyte cells were differentiated to macrophage-like cells prior to infection by addition of 500 ng/ml phorbol 12-myristate 13-acetate (PMA) (Sigma, P1585-1MG) in RPMI 1640 medium, HEPES (Gibco) supplemented with 10% FBS (referred to as RPMI from now on) and antibiotic-antimycotic solution. The cells were incubated for 48 h at 37°C and 5% CO_2.
GFP expressing *Listeria monocytogenes* (LM) strain JAT606 was streaked from a glycerol stock on a BHI agar plate (10006334, Fisher) containing 7.5 ng/mL chloramphenicol (15353771, Fisher Scientific) and 100 ng/mL streptomycin (15424871, Fisher Scientific), and incubated for 3 days at 37°C. The evening before infection a single colony was picked and incubated at room temperature overnight in BHI (53286, Sigma) supplemented with 7.5 ng/mL chloramphenicol and 100ng/ml streptomycin. For experiments using *S. aureus, S. aureus* USA300 was cultured in tryptic soy broth (TSB, Oxoid, CM0129T) at 37°C for 17 h over-night under agitation at 160 rpm. The next morning the liquid cultures, were centrifuged at 2000xg for 5 min at room temperature. The pellet was washed 1x with PBS (10010023, Thermofisher) and 5x the original volume of RPMI, then diluted to a concentration of approximately $1.6*10^3$ bacteria per U937 cell and added to the differentiated U937 cells (12 mL per T175 flask). For THP-1 cells and primary MΦs, the infection mix was diluted 2x fold as compared to that for U937 cells. For primary MΦs, 2 mL of infection mix was added per 6-well plate well. Primary MΦs were then centrifuged for 5 min at 200xg and incubated for another 25 min in the incubator as previously done [91]. U937 and THP-1 were incubated for 40 min at 37°C. Afterwards, the bacterial suspension was removed, cells were washed 1x with PBS and resuspended in RPMI supplemented with 20 μg/mL gentamycin (15820243, Fisher). U937/ THP-1/ primary MΦs were then incubated for 2.5-3.5 h. Prior to flow sorting, cells were washed 1x with PBS, detached using 0.25% trypsin EDTA (25200056, Thermofischer), and suspended in Leibovitz's L-15 CO_2 independent medium (21083027, Thermofisher) during flow sorting with the multi-application cell sorter MA 900 (Sony Biotechnology). GFP positive cells were collected for further experiments.

Fabrication of polyacrylamide hydrogels, traction force microscopy (TFM) and monolayer stress microscopy (MSM)

We manufactured 35 kPa polyacrylamide hydrogels to serve as the cells' ECM and to be able to subsequently perform TFM, as previously performed.[81] For that, wells from a 24-well glass bottom plate were pretreated by incubating at room temperature with 0.5 M NaOH (Roth, 0214.1) for 30 min, 2% APTES (3-Aminopropyl)triethoxysilan, Sigma, A3648-100ML) in 95% ethanol for 5 min and 0.5% glutaraldehyde (Sigma, G6257-100ML) for 30 min to 2 h, rinsed with distilled water in between each pretreating step and finally dried at 60°C. The 35 kPa polyacrylamide hydrogels were prepared by mixing 10% acrylamide (Sigma, A4058-100ML) with 0.3% bis-acrylamide (Fisher BioReagents, BP1404250) in distilled water. For the preparation of the second layer, we also added 0.03% of 0.2 µm fluorescent beads to the mixture (Thermo Fisher, F8826). To initiate polymerization 0.43% TEMED (Sigma-Aldrich, 1107320100) and 0.06% ammonium persulfate (APS) (Fisher, BP17925) were added to the first mixture and then per well, 3.6 µL of the polyacrylamide solution mixture was added on the pretreated glass surface. Following that, untreated 12 mm glass coverslips were pressed on top to flatten the gels and let polymerize for 20 min, after which the glass cover slips were removed, and polymerization of the second layer mixture containing the fluorescent beads was initiated with TEMED and APS. For the second layer only 2.5 µL of the mixture (containing tracer beads) was added on top of the first layer, followed by flattening with 12 mm glass coverslips. Solutions polymerized and then coverslips were removed after 20 min, and hydrogels were covered with 50 mM HEPES (cat. # HN78.3, Roth) pH 8.5. Samples were sterilized via 1 h exposure to UV and stored at 4°C until activation was to occur (two days prior to TFM experiment). Activation was performed by washing first hydrogels with 50 mM HEPES, and then activating them via addition of 200 µL/well of 0.1% w/v Sulfo-SANPAH (Thermo Scientific, 10474005) in 1% DMSO (Sigma, D2650-5X10ML) in 50 mM HEPES, and UV radiation for 10 min. Immediately after samples were washed with 50 mM HEPES and 200 µL/well of 0.25 mg/mL rat tail collagen I (Thermo Fisher, A1048301) diluted in 50 mM HEPES was added. The plate was incubated overnight at 24ºC. Before seeding of the HUVEC on hydrogels, the hydrogels were washed with PBS and equilibrated with cell culture medium at 37°C for 30 min. To achieve confluent HUVEC monolayers, $2.5*10^5$ HUVEC per well were seeded on the hydrogels and placed in a 5% CO_2 humidified incubator at 37°C for 24 h, or until confluent monolayers were formed. After 24 h, HUVEC were either exposed or not, to $2.5*10^4$ LM-infected or not PMA-differentiated (and sorted) U937 cells prior or during the TFM recording as indicated.

30 min prior to the TFM recording, cell culture media was changed to L-15 CO_2-independent medium supplemented with EGMTM-2 BulletKit™ Medium (Lonza, MEDIUM CC-3156 and Kit CC-4176). Samples in the 24-well plate were then transferred to the insert stage of an inverted Nikon Eclipse Ti2 epifluorescence microscope equipped with a Prime 95B camera for imaging. We used a 40x CFI Super Plan Fluor ADM ELWD (NA= 0.60) air objective and the NIS-Elements software package for the acquisition. The microscope was surrounded by a box-type incubator (OKOlab) maintained at 37°C. Every 10 min for a period of 24 h we acquired the phase contrast image of cells, and the fluorescence image of tracer beads embedded in the hydrogel. After finishing the acquisition, cells were detached using 10% SDS (cat. # 2326.2, Roth) to obtain the reference fluorescence image of the tracer beads of the undeformed hydrogel.

The 2D displacements of the beads were calculated in MATLAB by comparing the fluorescence bead image to the undeformed reference image at each instance of time using a method similar to particle image velocimetry (PIV).[92] The used window size and overlap of the interrogation window were 32 px and 16 px (width and overlap), respectively. Using these displacements the traction stresses exerted by the cell monolayers on the hydrogels were calculated in MATLAB as well as the strain energy (mechanical work) imparted by cells to deform their matrix, as described before.[15,30]

The monolayer stresses were calculated by using the traction stresses as input for monolayer stress microscopy (MSM) codes previously described in detail.[93] The monolayer tensile stresses (σ_I, Pa) shown in Figure 4F and Figure S4A-C are the maximum tensile stresses acting in the plane of the monolayer.

Atomic force microscopy

For sample preparation in ibidi µ-dishes (50 mm, low 81136), rat tail collagen I (A1048301, Thermofisher) diluted in PBS at 3 µg/mL was added to the µ-dishes and incubated at 37°C for 30 min. Dishes were then washed with PBS once. HUVEC were detached using trypsin-EDTA 0.05% and suspended in 500 µL of EBM™-2 (Lonza, CC-3156), supplemented with EGMTM-2 BulletKit™ Medium (Lonza CC-4176). 6×10^5 HUVEC were added to the dishes and left to attach and form a monolayer overnight. The next day, the medium was removed, cells were washed once with PBS, and, depending on the condition, either 3 mL of medium only (unexposed), 3 mL of medium containing uninfected MΦs (see preparation above), or 3 mL containing LM-infected MΦs were added at a ratio of HUVEC:MΦ of 20:1. The co-culture was placed in the incubator for 24 h. Afterwards, the medium was removed and replaced by CO_2-indepedent L-15 medium (Thermofisher 25200056). AFM measurements were performed with a commercial AFM setup

(MFP3D-BIO, Asylum Research, Santa Barbara, CA) mounted on an inverted optical microscope (Ti-S, Nikon, Tokio, Japan). Cantilevers with a 1 µm radius spherical tip and a nominal spring constant of 200 pN/nm (biosphere B1000-CONT, nanotools, Munich, Germany) were used. The actual spring constant of each cantilever was determined via thermal calibration. The force distance was set to 2 µm, the force rate to 2 Hz, and the trigger force to 1 nN. Force maps (90×90 μm^2 with 20×20 px or 30×30 px) were recorded. Data were analyzed in Igor Pro (Wavemetrics, Lake Oswego, OR, USA) using the Hertz Model to obtain the Young's modulus ("stiffness"). Only data points with a height of 1 µm and above were included to determine the cell stiffness.

Immunostaining for cell segmentation, calculation of cell shape descriptors and collective alignment of cells, and inspection of the cells' cytoskeleton

HUVEC were seeded on collagen I-coated glass bottoms of 24-well plates (Cellvis, P24-1.5H-N) at $2.5*10^5$ cells/well for 24 h until they form a confluent monolayer. PMA-differentiated U937 cells infected or not with LM were added at a concentration of $2.5*10^4$ cells/well (or not for unexposed HUVEC controls). Co-cultured cells were incubated for additional 24 h after which immunostaining was performed.

For the indirect exposure experiments, described in Figure 2G-J and Figure S2D-E, $2.5*10^5$ HUVEC were added at the collagen I-coated glass bottom of each well and $2.5*10^5$ HUVEC on the insert of the transwells used (24-Well Insert 0.4 µm PET clear, CellQuart, 9320412,). Here samples too were incubated for 24 h, after which PMA-differentiated U937 cells infected or not with LM were added at $2.5*10^4$ cells/well in each insert (i.e., ratio of HUVEC:MΦ of 20:1). Co-cultured cells were incubated for 24 h after which immunostaining was performed.

For immunostaining, cells were washed 1x with PBS and fixed by adding 4% methanol-free formaldehyde (Thermofisher, 28906) for 10 min. Samples were then washed 3x with PBS and incubated in 200 µL of 5% BSA (AppliChem, A6588) in PBS for 30 min for blocking. To immunostain for the cell-cell junction protein VE-cadherin, stain for F-actin and for DNA the following mixture was prepared: 1:10 diluted anti-VE-cadherin phycoerythrin E (PE)-coated antibody (RRID: AB_1645502, BD biosciences, 560410), 1:100 phalloidin 488 (Thermofisher, A12379 Alexa Fluor™ 488 phalloidin), and 0.5 µL DAPI solution (Sigma, 10236276001) in total of 400 µL of 2% BSA in PBS per well. Incubation was 1 h long, performed in the dark at 24°C. Samples were washed 3x with PBS and stored at 4°C, in the dark until imaging.

Note that for immunostaining for vinculin and F-actin (shown in Figure 3C) the following modifications in the immunostaining protocol were performed. For F-actin staining 1:100

phalloidin 488 was used (Thermofisher, A12379) mixed with 1:100 anti-vinculin antibody (RRID:AB_477629, Sigma, V9131) and 0.5 µL DAPI solution (Sigma, 10236276001) in total of 400 µL of 2% BSA in PBS per well. After 1 h long incubation at 24°C in the dark, samples were washed 3x with PBS. Afterwards 1:250 dilution of Donkey anti-Rabbit IgG, Alexa Fluor™ Plus 647 (RRID: AB_2762835, Thermofisher, A32795) in 2% BSA in PBS was added in a total of 400 µL per well.

Fluorescence images of immunostained samples were acquired using an inverted Nikon Eclipse Ti2 with a Prime 95B camera (Teledyne Photometrics), and 40x CFI Super Plan Fluor ADM ELWD (NA= 0.60) objective. We used the VE-cadherin fluorescence images to segment HUVEC and label them using the FIJI plugin Tissue Analyser, 'Segmentation' section and "Detect Bonds" feature, with manual adjustment when needed.[85] Based on this segmentation/labeling, custom Matlab scripts were then used to extract the following cell shape characteristics from the labelled images: (1) aspect ratio (minor to major axis of each cell); (2) area (μm^2); (3) shape factor defines as cell perimeter per square root of area, and serves as a measure of tissue fluidity.[24] For calculation of number of neighboring cells for each given cell a custom Matlab script was used, as well as to perform the calculations of the number of F-actin stress fibers normalized along the minor axis of HUVEC (using the fluorescence images of F-actin).

In order to calculate the alignment angle of neighboring cells a method previously published was used [86]. Briefly, nematic ordering (i.e. collective alignment) of HUVEC was quantified using the scientific software AFT – Alignment by Fourier Transform.[86] Each image was divided into overlapping windows with a size of 125 pixels (approximately 34 µm) and a 50 % overlap between windows. The parameter_search function was used to calculate the median orientation parameter for various neighborhood radii. The custom Python script nematic_ordering.ipynb was used to further analyze and visualize the results. Within each window, a 2D Fast Fourier Transformation determined the orientation of the cell outlines. This orientation was compared to those in neighboring windows, defined by a neighborhood-specific radius and quantified as the order parameter. This order parameter ranges from -1 (vertical alignment) to 1 (horizontal alignment), with 0 representing random orientation. By taking the order parameters of all windows of an image into account, the median order parameter for the entire image was determined as it is shown in Figure 2A, F, J and Figure S2I-J.

Immunostaining for assessing changes in cell proliferation

To assess whether the proliferation rate of HUVEC changes due to MΦ exposure, we first performed immunostaining for the proliferation marker Ki-67. To that end, fixed HUVEC samples were prepared as described directly above. After fixation, cells were permeabilized with 0.2% Triton X-100 (Roth, 3051.4) in PBS for 5 min and washed with PBS. Subsequently, samples were blocked with 5% BSA in PBS for 30 min and incubated with the primary anti-Ki-67 rabbit antibody (RRID: AB_10979488, Invitrogen, MA514520) at a 1:100 dilution in 2% BSA in PBS for 1 h. The samples were washed three times with PBS and blocked again with 5% BSA for 30 min. Finally, the cells were incubated with a donkey anti-Rabbit-647 antibody (1:250) (RRID: AB_2762835, Thermofisher, A-132795) and DAPI (1:1000) for 45 min. After washing twice with PBS, the samples were stored in PBS and imaged as described in the section just above.

Enzyme-linked immunosorbent assay (ELISA)

$2.5*10^5$ HUVEC per well of a 24-well plate were seeded on collagen I-coated glass coverslips and left to form a monolayer by being placed in a 5% CO_2 humidified incubator at 37°C for 24 h. After 24 h, HUVEC were either exposed or not, to $2.5*10^4$ LM-infected or not PMA-differentiated (and sorted) U937 cells, in 1 mL and co-cultures were incubated for additional 24 h. After this point the whole supernatant was used to determine cytokine concentrations. Cytokine concentrations were analyzed in cell culture supernatants using a custom multiplex Human Magnetic Luminex (R) Assay (R&D Systems, LXSAHM-13) to determine the presence and concentrations of CCL2, CXCL1, GM-CSF, IFN-y, IL-2, IL-6, IL-7, IL-8, IL-10, IL-15, IL-18, IP-10 and TNF-α. All steps were performed at room temperature and as per the manufacturer's instructions. In brief, 50 µL of bead solution was mixed with 50 µL of Standard/Control/Sample in the appropriate wells, covered with a foil seal and incubated for 2 h, 21°C, 800 rpm. The plate was then washed 3x with 100 µL Wash Buffer using an automated plate washer (Biotek Multiflo FX). 50 µL of biotinylated antibody cocktail was added to each well, covered with a foil seal and incubated for 1 h, 21°C, 800 rpm. After washing 3x with 100 µL Wash Buffer, 50 µL of diluted Strep-PE was added to each well, covered with a foil seal and incubated for 30 min, 21°C, 800 rpm. After a final 3x wash with 100 µL Wash Buffer, the beads were resuspended in 100 µL Wash Buffer, covered and shaken for 2 min at 800 rpm. The plate was then analyzed on a FLEXMAP 3D (Luminex) using the following settings: sample size 50 µL, 50 events, gate 8000-16000, Standard PMT. Samples were measured at two dilution factors (1:2 and 1:100) as single measurements. Data analysis was performed using Bio-Plex Manager using a 5PL log-fit to generate a standard curve. Sample measurement values were then interpolated against the standard curve and adjusted for dilution

factor. ULOQ and LLOQ for each analyte were defined as the highest and lowest concentrations respectively, that could be accurately quantified.

Note that cytokines released by infected and uninfected MΦs during co-cultivation with HUVEC shown in Figure S2E specifically were detected via ELISA (R&D Systems) following the manufacturer's instructions. To determine the concentration of IL-8, cell supernatants were measured diluted 1:4.

Characterization of kinematics of HUVEC in monolayer

To measure the kinematics of HUVEC in monolayer exposed (or not) to LM-infected or uninfected U937 cells, HUVEC were placed on glass bottom 24-well plates coated with collagen I as described above. To be able to differentiate between endothelial cells and MΦs, HUVEC used in this case were RFP expressing (Cat #: 14600, Pelobiotech) and growing in Endothelial Basal Medium (EBM, cAP-03) containing 5% FBS as per manufacturer's instructions. Cells were seeded in this case at a concentration of $2*10^5$ cells/well and let to form a monolayer for 24 h. After the 24 h period, image acquisition was started using an inverted Nikon Eclipse Ti2 and a Prime 95B camera (Teledyne Photometrics) with a 10X CFI Plan Fluor DL air objective (N.A.=0.13) unless otherwise indicated. Cells were maintained inside an incubator at 37° C and with 5% CO_2 while imaging. The microscope was controlled by the NIS-Elements (RRID:SCR_014329) software package. Images were taken every 10 min. After 3 h of imaging unexposed HUVEC, $2.5*10^4$ sorted LM-infected (or not) differentiated U937 were added to the HUVEC monolayers. Image acquisition was stopped 24 h later. HUVEC were calculated using the RFP fluorescence time-lapse images and performing particle image velocimetry on subsequent frames using interrogation windows of 48 px x 24 px size (width x overlap) in Matlab (MathWorks) as previously described [94]. The mean HUVEC migration speed was calculated by averaging the magnitude of the displacements in the field of view imaged and dividing by the frame interval (10 min).

Transmigration assay

Transmigration of sorted, LM-infected or uninfected MΦ, namely: PMA-differentiated U937; PMA-differentiated THP-1; or primary MΦ, through a confluent monolayer of HUVEC was measured by seeding $6.25*10^4$ HUVEC in a 6.5 mm-diameter transwell insert with 5.0 µm pore size (Corning, 10107341) and letting them sit for 24 h until a monolayer is formed. After the 24 h period elapsed, LM- or *S. aureus*-infected or uninfected MΦs were suspended in full EBM2 medium and added to the insert, on the apical side of the HUVEC monolayer. To use the same HUVEC:MΦ ratio in all

assays, namely 20:1, we used $6.25*10^3$ U937/well and $6.25*10^3$ THP-1 cells. In the case of primary MΦ only $7*10^2$ cells/well were added (i.e., ratio of HUVEC:MΦ of 89:1), because it was impossible to get more cells per donor and have the same number of replicates (six) in each experiment. For the transmigration assay with uninfected U937 (MΦ) and TNF-α , medium in the insert and in the bottom chamber were exchanged for full EBM2 medium containing 10 µg/mL TNF-α prior to adding MΦ in the insert. In the bottom chamber EBM2 containing 5% FBS was added. After 24 h at 37°C and 5% CO_2, U937 (THP-1 or primary MΦs) that had transmigrated to the lower compartment bottom chamber were stained with 1 µM Hoechst (11534886, Invitrogen, Fisher) and imaged using an inverted Nikon Eclipse Ti2 and a Prime 95B camera (Teledyne Photometrics) with a 40x CFI Super Plan Fluor ADM ELWD objective (NA= 0.60). An average of N=9 fluorescence images of the Hoechst-stained nuclei of transmigrated MΦ were taken per bottom chamber well and always per condition 6 wells were imaged. The images were duplicated using FIJI, and then a gaussian filter at a radius of 50 was applied. The filtered and original images were subtracted to correct for uneven illumination. Flatfield-corrected images were used to segment the cell nuclei using constant threshold-based segmentation and objects (i.e. nuclei) per image were measured using the FIJI plugin TrackMate Log Detector.[95] For each independent experiment the number of transmigrated infected MΦs was normalized with the mean value of transmigrated uninfected MΦs, so that comparison between independent experiments is clearer.

Live-cell imaging of F-actin in HUVEC using the SPY650-FastAct dye

For live-cell imaging of F-actin in HUVEC, we used the SPY650-FastAct dye. Briefly, we used an 8-chamber chip (Nunc™ Lab-Tek™ II Chambered Coverglass, Cat #: 155409PK, Nunc) for cell seeding. First, 200 µl of 1:100 collagen I in PBS (0.03 mg/mL) was added in each chamber for 30 min at 37ºC. Following two washed with PBS, 500 µL of $5*10^5$ HUVEC/mL per added in each chamber. Cells were left to attach for 24 h to form a monolayer, and then $1.25*10^5$ infected or not U937 were added on top. 1:5000 SPY650-FastAct (Tebubio, SC505) dye was added in each chamber so that the final concentration was 20 ng/mL (stock concentration was 100 µg/mL). Chip was then brough to the insert stage of an inverted Nikon Eclipse Ti2 microscope equipped with a CSU-W1 spinning disc with 50-µm Disk and a digital camera C15440 (Hamamatsu), using a 40x/1.25 NA silicon oil objective for subsequent imaging. Images were taken at 20 min intervals and focal plane was placed at the basal side of cells, close to the interface with the glass coverslip so that F-actin near the cell-matrix adhesions of HUVEC was imaged. The microscope was controlled by the NIS-Elements (RRID:SCR_014329) software package.

Transendothelial electrical resistance measurements

To assess alterations in endothelial cell barrier integrity, we measured transendothelial electrical resistance (TEER) of HUVEC monolayers exposed to LM-infected or uninfected U937 (or unexposed HUVEC), overtime using the cellZscope system (NanoAnalytics, Münster, Germany). For this, 24-well transwell inserts (0.4 µm pore size, cellQuart, 9320402) were coated with 400 µL of 30 µg/mL collagen I solution in PBS at 37 °C for 30 min. This was followed by washing with PBS and seeding of $1.6*10^4$ cells/cm^2 for 24 h, until monolayers are formed. Two inserts without cells served as blank positions. 24 h after cell seeding, when cell monolayers had formed, HUVEC were washed 1x with PBS and transferred into the TEER device. The top chamber was filled with 400 µL of EBM2 containing LM-infected, uninfected or no U937 cells or 10 µg/mL TNF-α and the bottom with 800 µL of EMB2 full medium supplemented with gentamicin (50 µg/mL) and in case of TNF-α samples also 10 µg/mL TNF-α. Three empty inserts with the same amount of medium were measured as well and used to subtract the electrical resistance of insert and medium from the measured sample values. TEER was measured every 30 min for 24 h.

Measurements of vascular permeability in (LM-infected) zebrafish larvae

To measure the vascular permeability in the tail vain of zebrafish larvae injected with LM in the trunk muscle, Tg(*mpeg1*::Gal4-FF)^{gl25}/Tg(UAS-E1b::*nfsB.mCherry*)^{c264} zebrafish larvae (24-48 hpf) were used. Larvae were maintained in E3 medium at 28.5°C. Overnight cultures of LM strain JAT606 were prepared as described above ("Infection of MΦs and flow sorting"). The day after, the OD600 was measured, and the liquid cultures were centrifuged at 2000 rpm for 4 min. The supernatant was discarded, and the pellet resuspended in a 1:1 solution of PBS and phenol red to an OD600 of 5. Four nL of either LM solution or 50% phenol red in PBS was injected into the trunk muscle of the larvae. Five hours after injection, a solution of 5:1 dextran green and phenol red was injected into the ventricle of the larvae. One hour afterwards, images of the tail vein were taken using a fluorescent stereomicroscope Leica M205FA. During injections and imaging zebrafish larvae were anesthetized using 200 µg/mL tricaine. Vascular permeability was quantified using FIJI by dividing the fluorescence intensity of the dextran in the tail vain distant to the LM injection site and the fluorescence intensity of the adjacent tissue by manually gating the areas of interest.

Transmigration time of MΦs in (infected) zebrafish larvae

To quantify the extravasation time of MΦs in zebrafish larvae, the same zebrafish larvae strain and infection method were used as described above. Four hours after injection, a tail cut was performed to evoke transmigration of MΦs in the tail vain. Zebrafish were placed in 1% agarose and imaged for 15 h every 5 min using a Zeiss Celldiscoverer (CD7) microscope equipped with a 5x/0.35 Plan-Apochromat objective and 1x Tubelens. Using the Fiji plugin TrackMate Manual Tracking the time MΦs took from attaching to the tail vain wall and leaving the vessel was measured and averaged in each zebrafish larva.

Assessment of MΦ adhesion on HUVEC monolayers residing on a vessel-on-chip device

To fabricate a microfluidic chip device, SYLGARD 184 silicon elastomer was mixed with 10% SYLGARD 184 silicon elastomer cure. Mixture was degassed in a vacuum chamber for 40 min. A PDMS mixture (Biesterfeld, 5498840000) was poured into custom made molds (Peter Loskill lab, University of Tübingen) and backed at 80°C for 2 h. PDMS molds were punctured using a dosing tip needle (RS Components, 400-3895) to create in- and outlets for each channel. After cleaning the chips with isopropanol and pressured air, PDMS was activated using a Zepto-BRS plasma activator (Diener electronic GmbH & Co. KG) under O_2 atmosphere and bonded to a glass coverslip. The device was cured overnight at 60°C, was again activated in the same manner and sterilized by adding 70% ethanol for 10 min. Ethanol was removed by washing twice with PBS, rat-tail collagen I in PBS (100 mg/mL) was added in each channel and the device was incubated at 37°C, 5% CO_2 for 2 h. In the meantime, HUVEC were detached from the flasks using 0.05% trypsin/EDTA and suspended in EBM2 full medium at a density of $9*10^6$ cells/mL. Collagen solution was removed, and channels were washed 2x with PBS. Ten µL of HUVEC suspension was added into each channel and cells were left to adhere for 2 h at 37°C and 5% CO_2. Channels were connected to LA-190 syringe pump (Landgraf Laborsysteme) via tubing (VWR/Avantor, VERNAAD04103) filled with full EBM2 and flow was initiated at 10 µL/h (shear stresses 0.01 dyn/cm²). The next day, $5*10^4$ infected or non-infected U937 cells were added to the inlet using a 200 µl pipette tip and washed through the channel at a flow rate of 20 µL/h (shear stresses 0.02 dyn/cm²). After 2 h, flow was ceased, and chips were fixed using 4% PFA for 20 min. Channels were washed 2x with PBS and blocked with 5% BSA in PBS for 30 min. Then, cells were incubated overnight at 4°C with 1:100 CD45 antibody (Cat #: 53-0451-82, RRID: AB_2848416; Thermofisher), 1:100 phalloidin 647 (Cat #: A30107, Thermofisher), 1:100 DAPI in 2% BSA. The next day cells were washed 3x with PBS and stored submerged in PBS at 4°C until they were to

be imaged. Chips were imaged with an inverted Nikon Eclipse Ti2 microscope equipped with a CSU-W1 spinning disc with 50-µm Disk and a digital camera C15440 (Hamamatsu), using a 20X objective and z-stacks were taken at 2 µm intervals. The microscope was controlled by the NIS-Elements (RRID:SCR_014329) software package.

RNA isolation and RNA sequencing

Sample Preparation: 4th passage HUVEC were placed at a concentration of $2.5*10^5$ cells/well on glass collagen I coated coverslips of 24-well plates for 24 h until monolayer are formed. Subsequently PMA-differentiated U937 cells infected or not with LM were added at a concentration of $2.5*10^4$ cells/well (or not for unexposed HUVEC controls). Co-cultured cells were incubated for additional 8 or 24 h as indicated. At the correct time points (8 h or 24 h post-exposure to MΦs), three thorough washes with warm PBS were performed to get rid of floating or loosely adhering MΦs, and then the remaining cells adhering on glass (mostly HUVEC) were harvested and lysed using the QIAshredder Kit (Qiagen; 79656). mRNA was harvested using the RNeasy Plus Micro Kit (Qiagen; 74004) and eluted in 15 µL RNAase free water. RNA concentrations were measured using the nanodrop spectrophotometer and found to be comparable between conditions. Agarose gel electrophoresis was used to check the integrality of total RNA samples (performed by Arraystar Inc.).

For library preparation and RNA sequencing the procedure described below was as followed. The total RNA was depleted of rRNAs by Arraystar rRNA Removal Kit. We used Illumina kits for the RNA-seq library preparation, which included procedures of RNA fragmentation, random hexamer primed first strand cDNA synthesis, dUTP based second strand cDNA synthesis, end-repairing, A-tailing, adaptor ligation and library PCR amplification. Finally, the prepared RNA-seq libraries were qualified using Agilent 2100 Bioanalyzer and quantified by qPCR absolute quantification method. The sequencing was performed using Illumina NovaSeq 6000 using the High-Output Kit with 2x150 read length. We had an average of 40 million reads per sample. The DNA fragments in well mixed libraries were denatured with 0.1M NaOH to generate single-stranded DNA molecules, loaded onto channels of the flow cell at 8 pM concentration, and amplified in situ using TruSeq SR Cluster Kit v3-cBot-HS (#GD-401-3001, Illumina). Sequencing was carried out using the Illumina X- ten/NovaSeq according to the manufacturer's instructions. Sequencing was carried out by running 150 cycles.

Raw sequencing data generated from Illumina X-ten/NovaSeq that pass the Illumina chastity filter were used for following analysis. Trimmed reads (trimmed 5', 3'-adaptor bases) were aligned to the reference genome (CanFam3). Based on alignment statistical analysis (mapp.i.ng ratio, rRNA/mtRNA content, fragment sequence bias), we determined whether the results can be used for subsequent data analysis. To examine the sequencing quality, the quality score plot of each sample was plotted. Quality score Q is logarithmically related to the base calling error probability (P): $Q = -10\log_{10}(P)$. For example, Q30 means the incorrect base calling probability to be 0.001 or 99.9% base calling accuracy. After quality control, the fragments were 5', 3'-adaptor trimmed and filtered ≤ 20 bp reads with Cutadapt software. The trimmed reads were aligned to the reference genome with Hisat 2 software. In a typical experiment, it is possible to align 40 ~ 90% of the fragments to the reference genome. However, this percentage depends on multiple factors, including sample quality, library quality and sequencing quality. Sequencing reads are classified into the following classes: (1) Mapped: reads aligned to the reference genome (including mRNA, pre-mRNA, poly-A tailed lncRNA and pri-miRNA); (2) mtRNA and rRNA: fragments aligned to rRNA, mtRNA; and (3) Unmapped: Reads that are not aligned.

Differentially expressed genes and differentially expressed transcripts are calculated. The novel genes and transcripts are also predicted. The expression level (FPKM value) of known genes and transcripts were calculated using ballgown through the transcript abundances estimated with StringTie. The number of identified genes and transcripts per group was calculated based on the mean of FPKM in group ≥ 0.5. Fragments per kilobase of transcript per million mapped reads (FPKM) is calculated with the formula: $\boldsymbol{FPMK} = \frac{\boldsymbol{C} \times \mathbf{10^6}}{\boldsymbol{L} \times \boldsymbol{N}}$, where C is the number of fragments that map to a certain gene/ transcript, L is the length of the gene/transcript in Kb and N is the fragment number that map to all genes/transcripts. Differentially expressed gene and transcript analyses were performed with R package ballgown. Fold change (cutoff 1.5), p-value (≤ 0.05) and FPKM (≥ 0.5 mean in one group) were used for filtering differentially expressed genes and transcripts.

Pathway enrichment (KEGG) and gene ontology (GO) analysis

Kyoto Encyclopedia of Genes and Genomes (KEGG) pathway and Gene Ontology (GO) term analyses of the whole data set of DEG were performed using the R package GAGE "Generally Acceptable Gene set Enrichment" (GAGE v.2.22.0) package implemented in R. Briefly, default parameter settings were used for comparisons of log-scaled gene set expression (i.e. enrichment) data between different flow conditions (q-value <0.01). Gene sets were defined using annotations obtained from GAGE v2.22.0, go.db v3.2.2, and kegg.db v3.2.2. The R

package “Pathview” v.1.12.0 and KEGGGraph v1.30.0 were used to visualize gene set expression data in the context of functional pathways.

Rate of heterotypic bacterial transfer from LM-infected MΦ to HUVEC using flow cytometry

MΦ infections with LM-GFP were performed, infected MΦs were flow sorted and exposed to HUVEC in monolayer as described above. Co-cultures were incubated at 37°C, 5% CO_2 for 24 h. After the incubation time of the co-culture, HUVEC were stained for VE-cadherin using a anti VE-cadherin-PE antibody (Cat #: 560410, RRID: AB_1645502, BD Bioscience). Briefly, the antibody was diluted 1:10 in PBS. The cell culture medium was aspirated from the co-cultures, and HUVEC were incubated in 100 µL of antibody dilution. The plate was incubated 20 min on ice to prevent antibody internalization. Afterwards, the wells were washed twice with PBS. After VE-cadherin-PE staining cells from the co-cultures were detached using 0.05% trypsin/EDTA and resuspended in L-15 media supplemented with the appropriate HUVEC supplements as indicated above. The cells were strained into 5 mL using polystyrene test tubes through a cell strainer snap cap with a 35 µm nylon mesh to get single cells. The flow cytometry acquisition was performed on a BD LSRFortessa X-20. Compensation was performed automatically by the FACSDiva software by measuring unstained HUVEC first. Here the main population was gated in an SSC-FSC scatter plot. The gate was propagated to the PE-positive only control and the GFP-positive only controls were the PE and GFP peaks were gated, respectively. With these measurements, the software automatically calculated the compensation value (which was zero for the used fluorophores) and applied to the fluorescence channels. After performing the compensation, the samples were acquired. The main population gated in the SSC-FSC scatter plot was further gated for singlets in SSC-A vs SSC-H scatter plot. The singlets were plotted in a PE vs GFP plot and the PE+/GFP+ events were monitored. $1*10^4$ events in the main population were acquired. Data analysis was conducted in FlowJo applying the same gating strategy as described on the unexposed HUVEC and propagating the respective gates to HUVEC exposed to infected and uninfected MΦ.

Quantification and statistical analysis

All statistical analyses were performed with Graphpad Prism 10 (Graphpad, RRID:SCR_002798). In all boxplots of the manuscript horizontal line represents the distribution’s median, boxes

indicate the 25% and 75% quartiles, whiskers indicate the 5 and 95% quantiles. Superimposed dots show the individual values per experiment. For experiments were more than two samples were compared to each other Kruskal-Wallis test with Dunn's multiple comparison test (denoted as KWTD) was performed unless otherwise indicated in the figure legend. If normality test was passed an ordinary one-way ANOVA with Šídák's multiple comparisons (denoted as ANOVA) test was used. If two samples were compared the non-parametric test Wilcoxon Ranksum test (denoted as WRST) or the parametric Student's t-test (denoted as t-test) were performed. For all assays at least three independent experiments were performed unless otherwise indicated. In all figure legends the statistical test performed, p-values, and sample size are indicated. For KWTD, ANOVA, WRST, t-test the following p-value significance values were used: ns: non-significant, $p>0.05$; *: $p< 0.05$; **: $p<0.01$.***: $p<0.001$, ****: $p<0.0001$.

SUPPLEMENTAL INFORMATION

SUPPLEMENTAL FIGURE LEGENDS

Figure S1

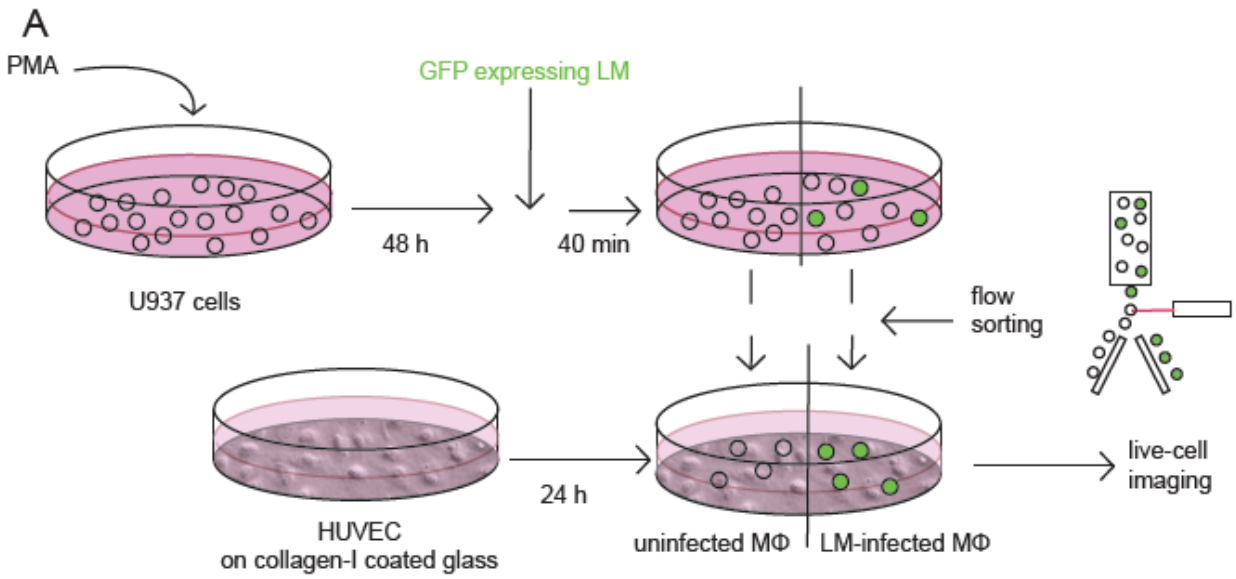
A
PMA
GFP expressing LM
48 h
40 min
U937 cells
flow
sorting
live-cell
imaging
24 h
HUVEC
on collagen-I coated glass
uninfected MΦ
LM-infected MΦ

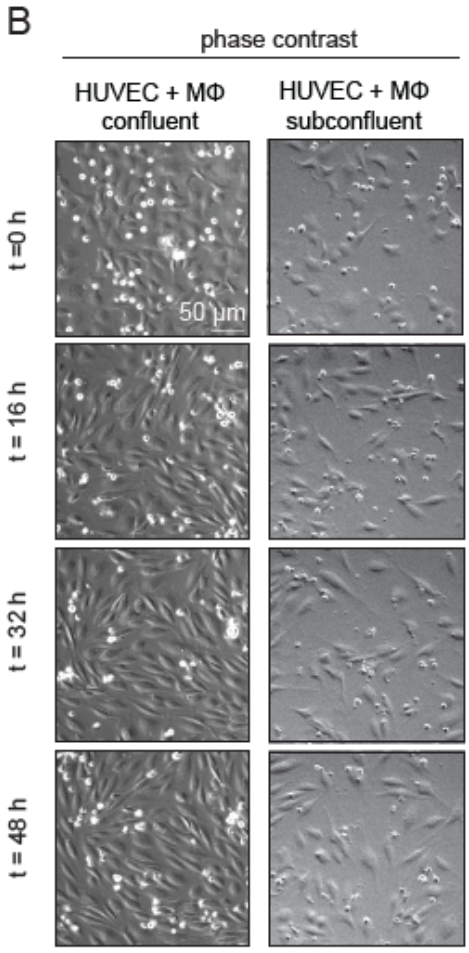
B
phase contrast
HUVEC + MΦ
confluent
HUVEC + MΦ
subconfluent
t =0 h
t = 16 h
t = 32 h
t = 48 h
50 µm

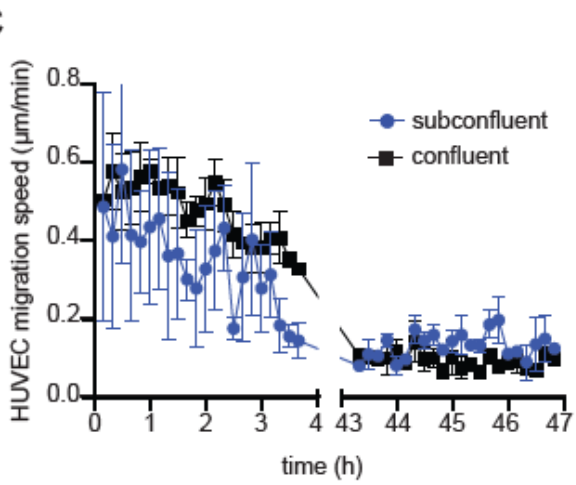
C
HUVEC migration speed (µm/min)
0.8
0.6
0.4
0.2
0.0
0
1
2
3
4
43
44
45
46
47
time (h)
subconfluent
confluent

Figure S1 The decrease in HUVEC migration speed and increase in polarization when exposed to U937 is not EC-EC contact dependent. Related to Figure 1. (**A**) Schematic of the experimental setup. HUVEC are grown in monolayer for 24 h. U937 are differentiated with PMA and then infected or not with LM expressing GFP. Following flow sorting to gain pure population of LM-infected U937, MΦs (infected or not) are co-cultured together with HUVEC. (**B**) Representative time-lapse phase contrast images of HUVEC in monolayer exposed to uninfected PMA-differentiated U937 (left column). Rows show representative time points post-MΦ exposure (h). Right column shows same as left, but for subconfluent HUVEC that do not readily form cell-cell contacts. (**C**) Plot of mean cell migration speed (μm/min) over time (h), for HUVEC tracked either during the first 4 h post-MΦ addition, or between 43 to 47 h post-MΦ addition. An average number of N=10 cells were tracked for HUVEC in monolayer (black) or under subconfluent conditions (blue) as shown in B.

Figure S2

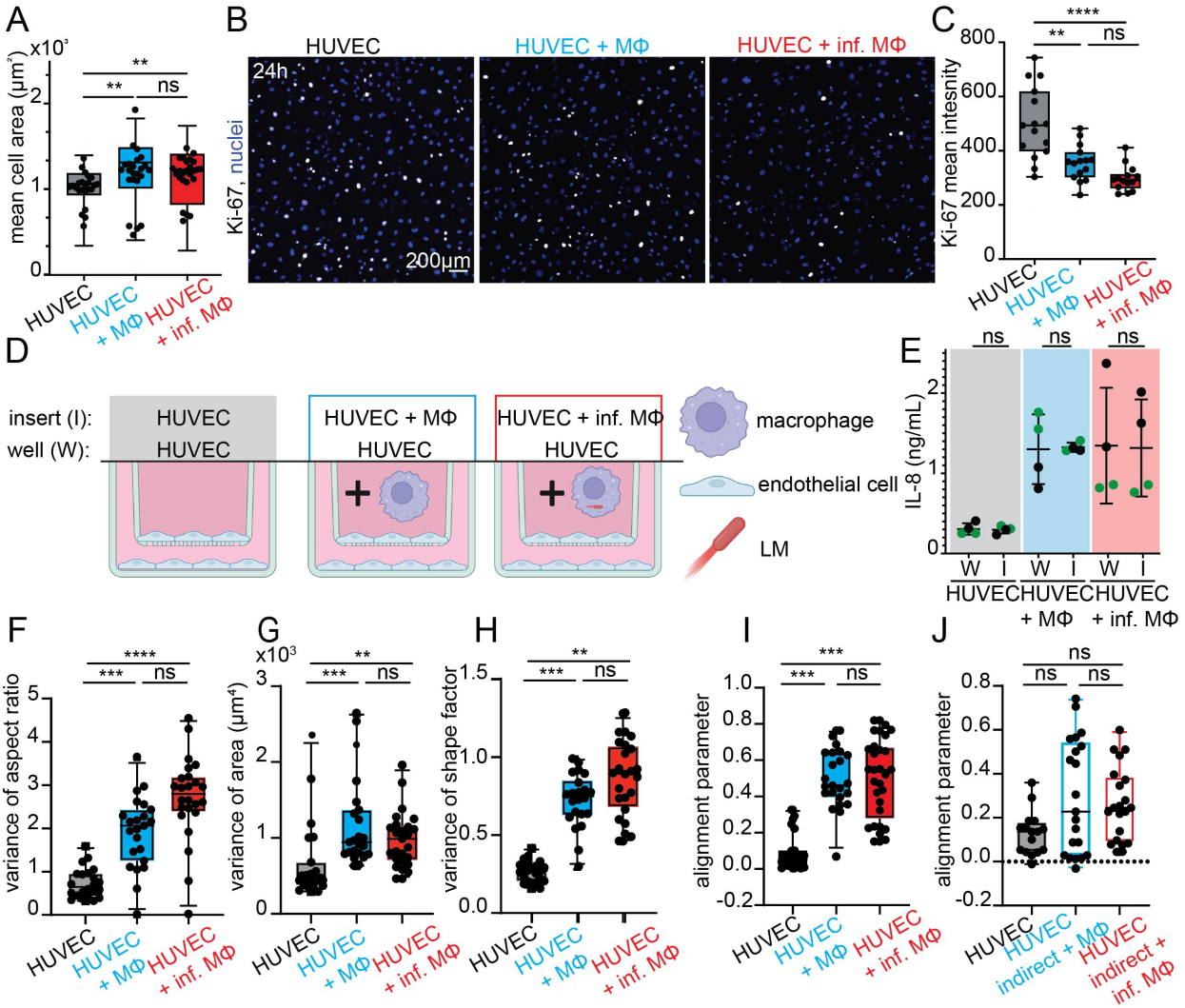

Figure S2 ECs collective alignment is increased and cell proliferation decreased when exposed to (un)infected MΦs. **Related to Figure 2.** (**A**) Boxplots as in Figure 2B-E but showing mean cell area (μm^2). (**B**) Exemplary superimposed images of stained nuclei (blue) and Ki-67 fluorescence (white), a marker for cell proliferation. Samples were fixed and immunostained 24 h after exposure to uninfected (HUVEC+MΦ), LM-infected (HUVEC + inf. MΦ) PMA-differentiated U937 (MΦ) or to nothing (HUVEC). (**C)** Boxplots of mean intensity per field of view Ki-67 fluorescence for the conditions shown in A. Each superimposed dot represents the mean fluorescence of one image (two independent experiments). (**D**) Schematic overview of experimental design for the data presented in Figure 2G-J involving indirect exposure of HUVEC to HUVEC exposed to (Infected) U937. (**E**) For each of the three conditions shown in D, IL-8 concentration (ng/mL) was measured in the medium from both the transwell (I) and the well (W) to ensure that cytokines are homogeneously distributed (two independent experiments). Same color dots refer to samples from same experiment. (**F-H**) Boxplots same as in Figure 2B-E but showing variance of aspect ratio (**F**), variance of area (**G**), and variance of shape factor (**H**). (**I**) Boxplots of the alignment order parameter of cells separated by a distance of 103 μm, comparing the same data and conditions as in Figure 2F. (**J**) Same as panel I, but comparing the same data and conditions as in Figure 2J. Mean +/- SD. KWTD, ns, non-significant: $p>0.05$; *: $p< 0.05$; **: $p<0.01$.***: $p<0.001$.

Figure S3

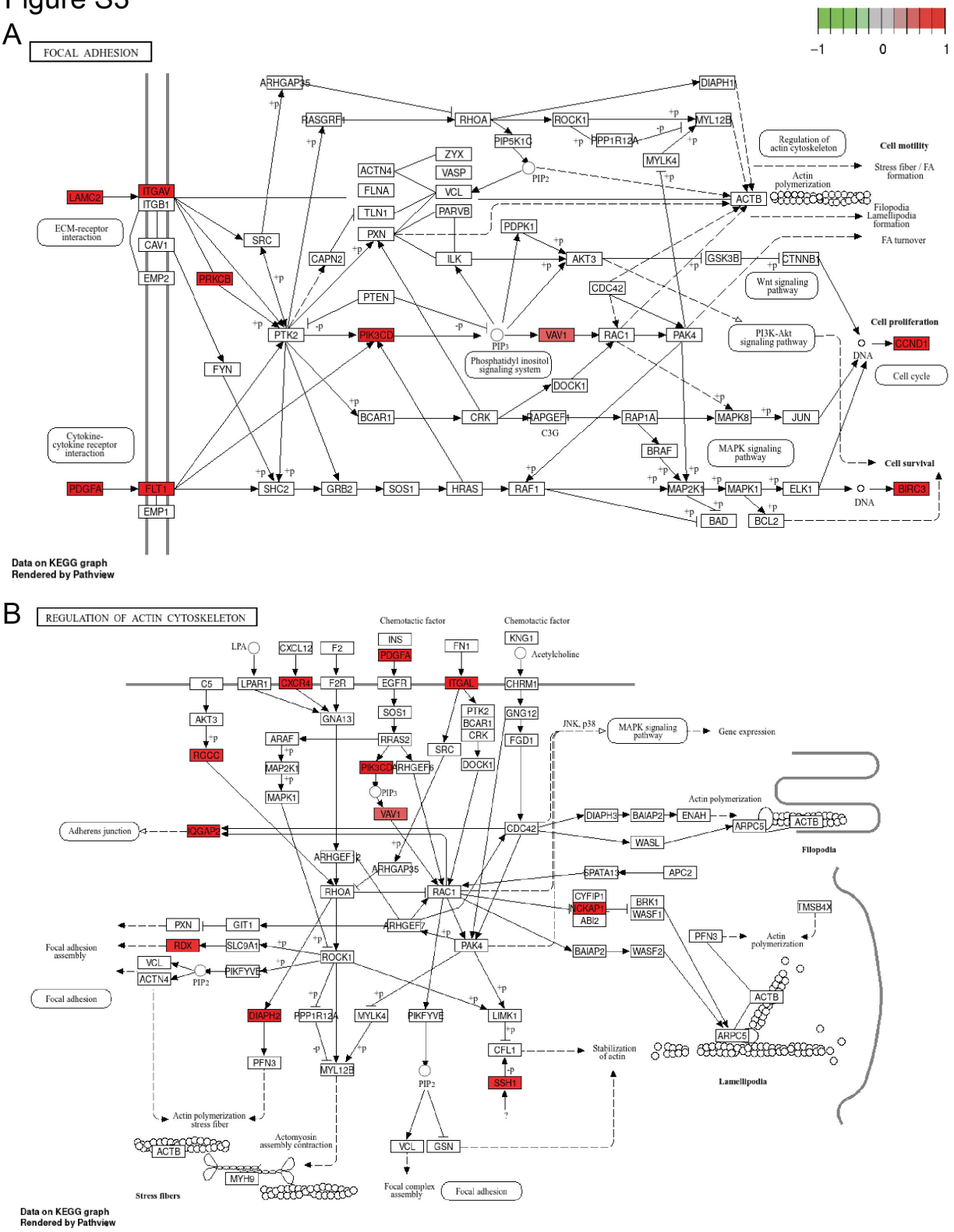

Figure S3 Functional pathways related to actin cytoskeleton and focal adhesions differing only between HUVEC exposed to uninfected MΦ and unexposed HUVEC. Related to Figure

3. (**A-B**) Signaling pathway visualization maps showing the signaling pathways that are differentially regulated only when comparing HUVEC exposed to uninfected MΦ with unexposed HUVEC and only at 8 hpe. The pathways are (A) Focal adhesions and (B) Regulation of the actin cytoskeleton. Detected DEGs are shown in red and color-coded based on their normalized enrichment score. Note there are no downregulated (green) genes.

Figure S4

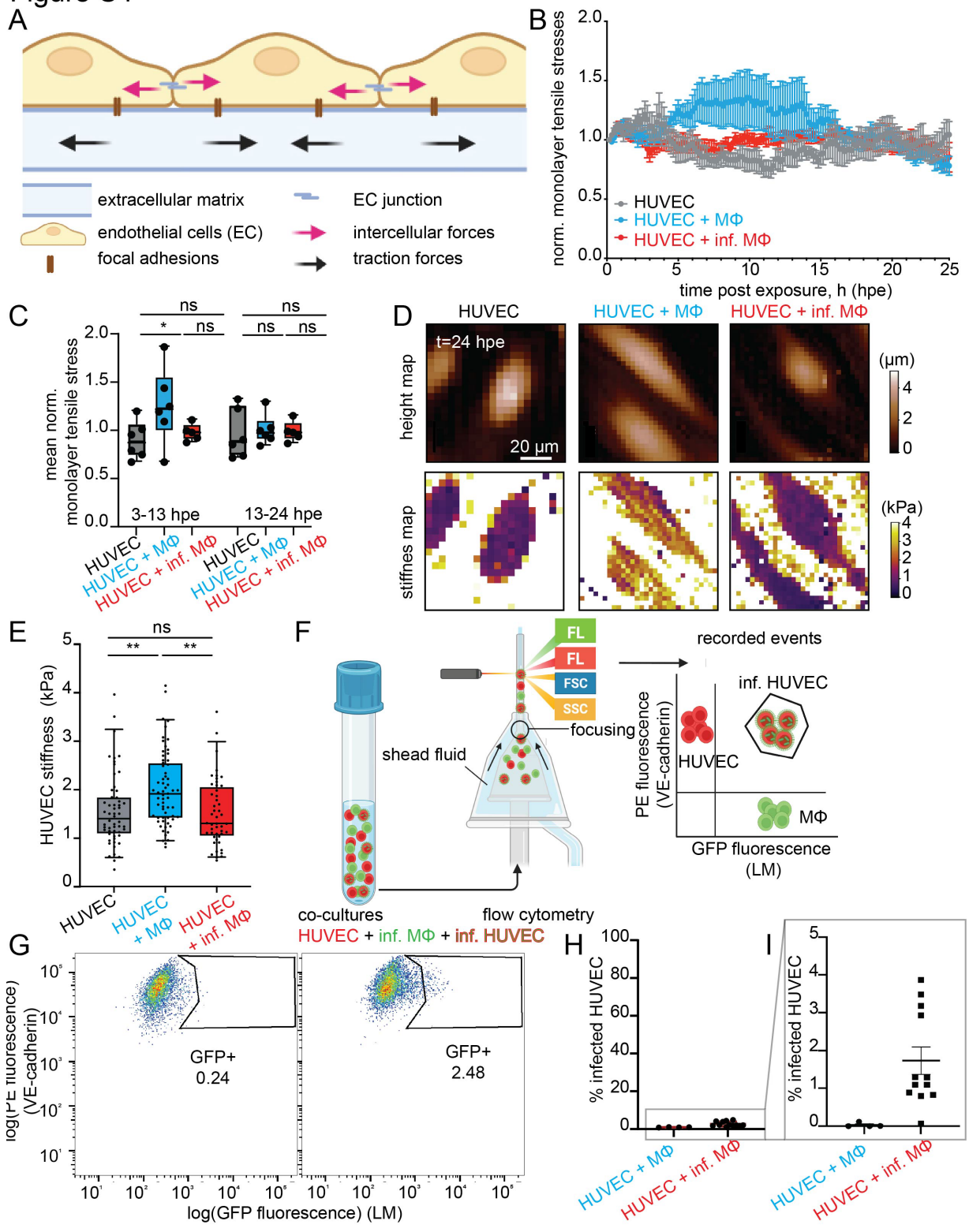

Figure S4 EC monolayer tensile stresses are increased for EC exposed to uninfected and to a lesser degree infected MΦ. Related to Figure 4. (**A**) Schematic depiction of an EC

monolayer (side view) residing on a soft matrix on which ECs exert traction stresses (black arrows). ECs also exert monolayer stresses (i.e., inter- and intra-cellular stresses, depicted via magenta arrows). (**B**) Normalized mean monolayer tensile stresses (σ_I) that HUVEC exert when on 35 kPa matrix as a function of time post MΦ-addition (hpe). Normalization with respect to first timepoint for each experiment. Three conditions are shown: HUVEC in monolayer unexposed (HUVEC), exposed to uninfected U937 (HUVEC + MΦ), or to LM-infected U937 (HUVEC + inf. MΦ). An average of 6 experiments were performed per condition. Mean +/- SEM. (**C**) Time-averaged normalized monolayer tensile stresses (σ_I) for the same conditions and samples as in B. Time averaging was performed either between 3-13 hpe (boxplots 1-3) or between 13-24 hpe (boxplots 4-6). Superimposed dots show the mean of different experiments. (**D**) Representative height and stiffness maps obtained by AFM under the same conditions as in B. (**E**) Boxplot of bulk stiffness of unexposed HUVEC, HUVEC + MΦ, and HUVEC + inf. MΦ (3 independent replicates, 48-63 HUVEC measured per condition). Dots represent the individual stiffness values per HUVEC. (**F**) Schematic of the experimental setup. HUVEC are co-cultured with uninfected MΦ (HUVEC+MΦ, serving as control) or LM-infected MΦ (HUVEC + inf. MΦ) for 24 h. LM constitutively express GFP. MΦ are PMA-differentiated U937 cells. Cells from co-cultures are detached from culture dish and HUVEC are stained with anti-VE-cadherin-PE antibody. Samples are measured using flow cytometry. Gate is drawn around VE-cadherin positive (red), LM positive (green) cells. (**G**) Scatter plot of the logarithm of VE-cadherin fluorescence versus LM-GFP fluorescence in HUVEC exposed to either uninfected (HUVEC+MΦ), or LM infected (HUVEC + inf. MΦ) MΦs. Gate shows LM positive subpopulation of VE-cadherin positive HUVEC. (**H**) Boxplot of infected HUVEC after 24 h co-culturing with (un)infected MΦs. Dots represent individual samples (3 replicates, on average 8 samples per condition). (**I**) same as H but zoomed in on y-axis section between 0-5%. KWTD, ns: non-significant, $p > 0.05$; *: $p > 0.05$; **: $p < 0.001$.

Figure S5

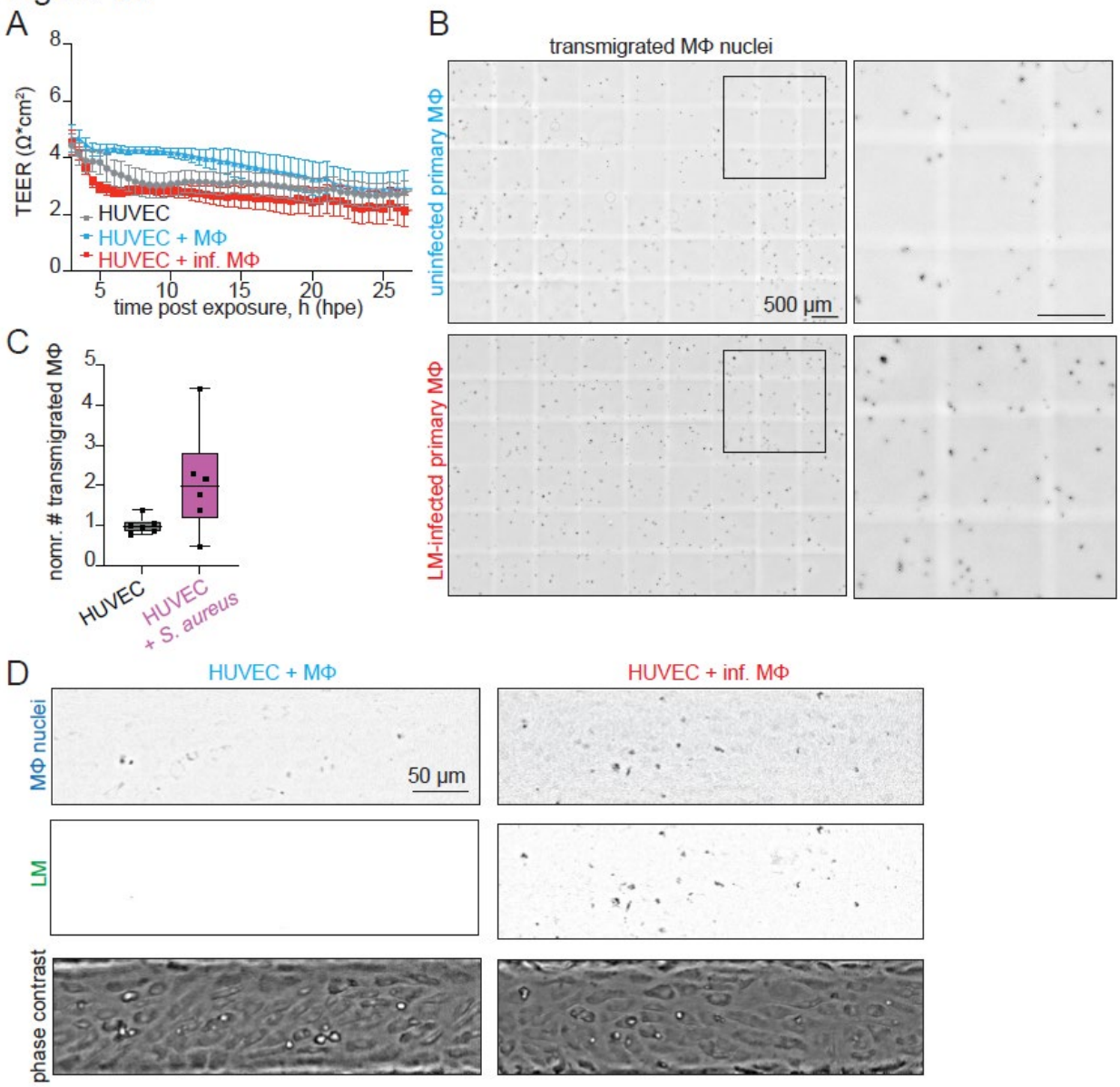

Figure S5 Infected MΦ adhere more and transmigrate more through ECs, compared to their uninfected counterparts. Related to Figure 5. (**A**) Plot of transendothelial electrical resistance (TEER, W*cm^2) over time post TNF- α exposure (hpe) for the same samples as shown in Figure 5A. Mean +/- SEM for N= 14 samples per condition are shown. (**B**) Left column show images of primary MΦ nuclei (from peripheral blood mononuclear cells, differentiated with GM-CSF to MΦ-like cells) in the bottom chamber of a transwell after they have undergone transmigration through HUVEC monolayer residing on the transwell. Refers to data shown in Figure 5B-C. Images on the right are zoomed in portions of the images on the left (see black squares). (**C**) Boxplots of number of transmigrated U937 MΦ-like cells (MΦ) during 24 h exposure to HUVEC in monolayer,

for uninfected MΦs (HUVEC + MΦ) or *S. aureus*-infected MΦs (HUVEC + *S. aureus*-inf. MΦ). (**D**) same as Figure 5D without marker rings.

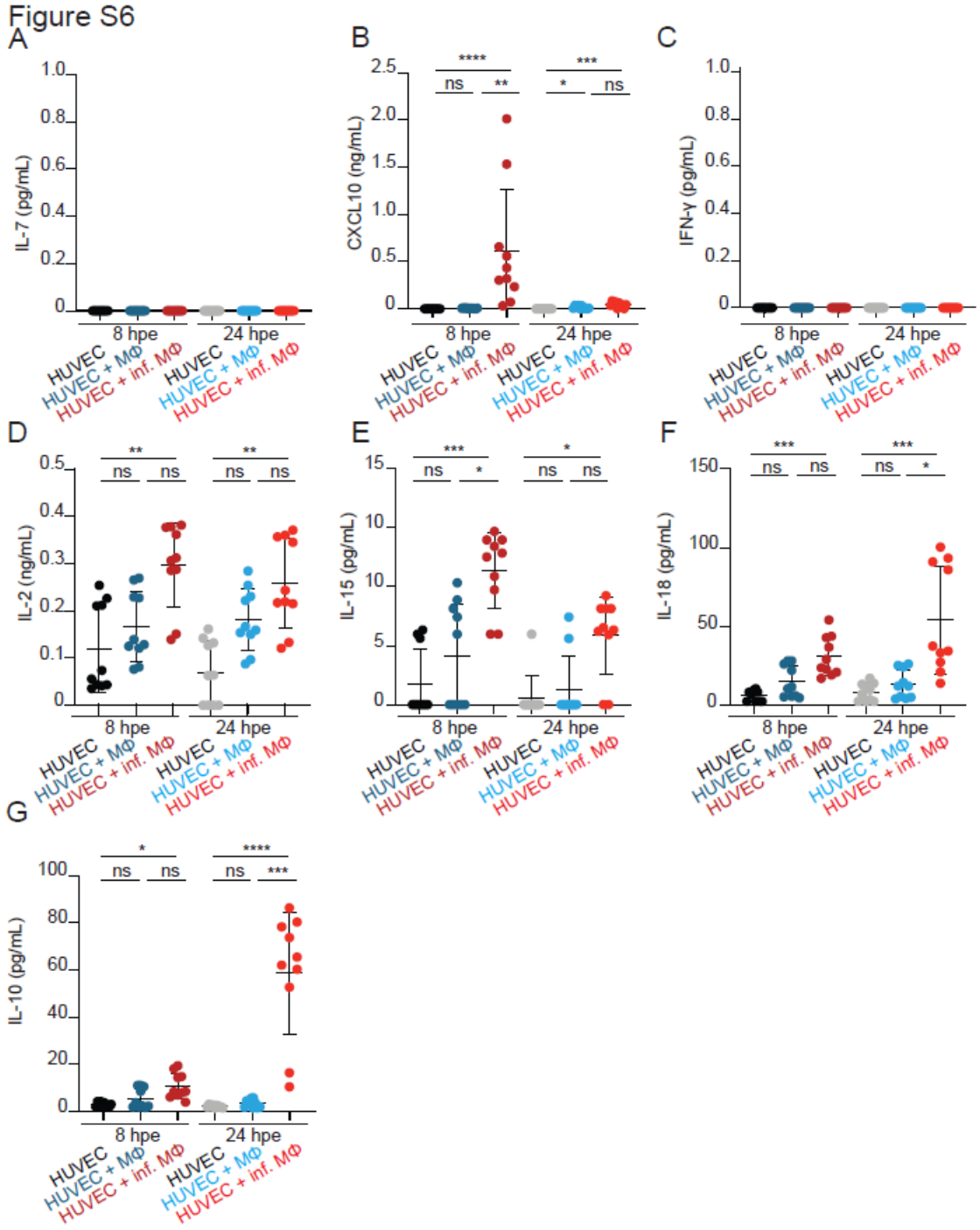

Figure S6 Differential cytokine secretion of HUVEC exposed to uninfected versus LM-infected MΦ also depends on time examined post MΦ exposure. **Related to Figure 6.** (**A-G**) Scatter plots of cytokine concentration in the supernatant of unexposed HUVEC (HUVEC), HUVEC exposed to uninfected (HUVEC+MΦ), or LM infected (HUVEC + inf. MΦ) MΦ. Scatter

plots 1-3 (4-6) refer to samples collected at 8 (24) hpe to MΦ (n =10 samples originating from 3 independent experiments, mean +/- SD, KWTD, ns, non-significant: p>0.05; *: p< 0.05; **: p<0.01, ***: p<0.001, ****: p<0.0001). Each panel refers to a different cytokine, namely: IL-7 (**A**), CXCL10 (**B**), INF-γ (**C**), IL-2 (**D**), IL-15 (**E**), IL-18 (**F**), IL-10 (**G**).

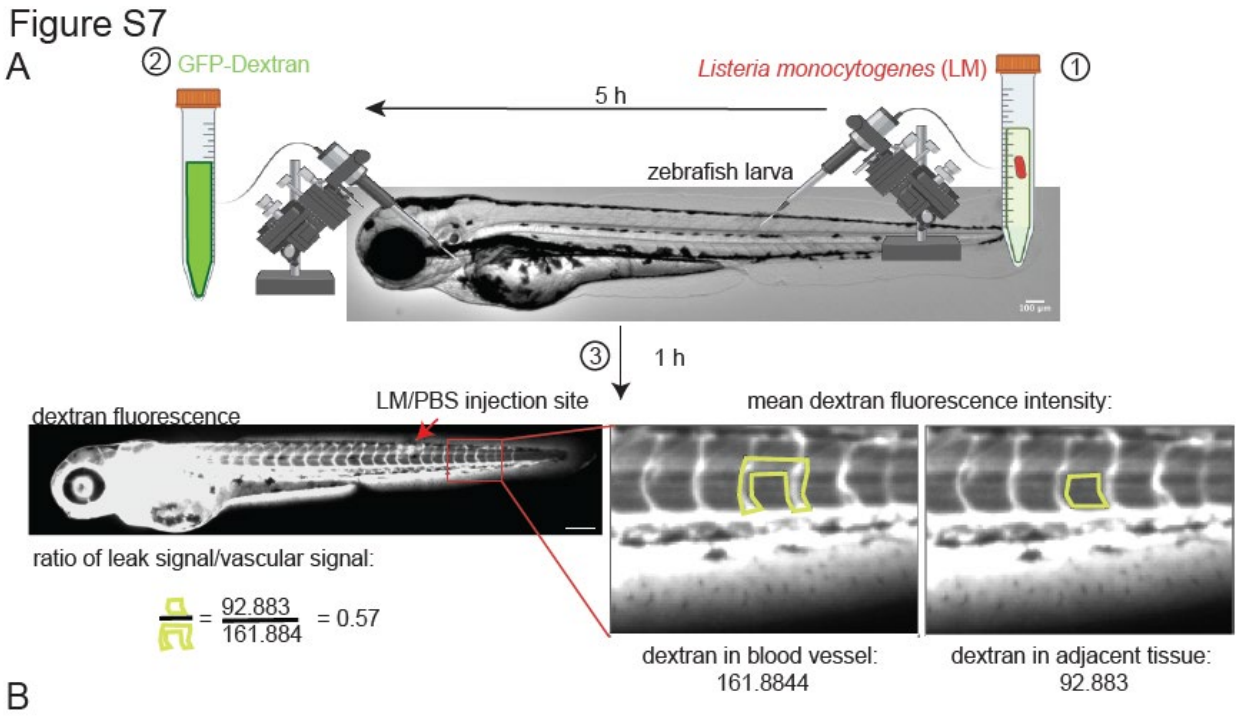

Figure S7 Schematic depiction of experimental setup for vascular leakage assay and measurement of transmigration time of MΦ in zebrafish larvae. Related to Figure 7. (**A**) Schematic depiction of experimental setup to measure vascular leakage in zebrafish larvae. First LM is injected into the trunk muscle of the zebrafish larva. 5 h post-infection FITC-labeled dextran is injected into the ventricle of the larva. One hour later fluorescence images of dextran are taken and dextran fluorescence intensity between vessels and adjacent tissue are compared. (**B**)

Exemplary overlay image of zebrafish larva with MΦ-RFP fluorescence (magenta) and LM-GFP fluorescence (green). Primary LM infection site in the trunk muscle is highlighted with a red box. After infection a cut at the tip of the tailfin is performed to elicit transmigration of MΦ from the vasculature to the wound at the tailfin.

SUPPLEMENTAL MOVIE LEGENDS

Movie S1 HUVEC decrease their migration speed after exposure to (LM-infected) U937 and increase polarization in non-contact dependent manner. Related to Figure 1. The first part of the movie shows time-lapse videomicroscopy of HUVEC in monolayer residing on glass collagen I-coated substrate and are either unexposed (1st column), or exposed to uninfected MΦ (2nd column), or to LM-infected MΦ (3rd column). The top row shows phase contrast images. Inset plot in the right corner of each image shows mean HUVEC migration speed per time point relative to recording start. Time point of MΦ addition is indicated with a black line. Bottom row shows the corresponding HUVEC displacement vectors. Scale bar: 300 μm, arrows: scaled 20x. The second part of the movie shows time-lapse phase contrast images of HUVEC exposed to uninfected MΦ, with HUVEC being either in monolayer (left) or sparsely seeded and hence devoid of cell-cell contacts. Note that over the course of this 97 h-long recording HUVEC get polarized and decrease their migration speed in a process that does not depend on cell-cell contacts.

Movie S2 F-actin stress fibers are increased in EC exposed to uninfected MΦs as opposed to unexposed HUVEC or HUVEC exposed to LM-infected MΦs. **Related to Figure 3.** Videomicroscopy of HUVEC monolayers unexposed (left) or exposed for 24 h to uninfected (HUVEC+MΦ, middle) or LM-infected MΦs (HUVEC + inf. MΦ, right). MΦs are PMA-differentiated U937 cells. Time post macrophage addition (h) is indicated. Scale bar: 100 μm. The F-actin dye FastAct was used.

Movie S3 Traction stresses increase dramatically in HUVEC exposed to uninfected MΦ, and to lesser degree to infected one, but not in unexposed HUVEC. Related to Figure 4. Top row panels show time-lapse phase contrast images of HUVEC in monolayer residing on 35 kPa hydrogels alone (left) or exposed to uninfected PMA-differentiated U937 cells (MΦ) (middle) or to LM-infected MΦ (right). Inset plot shows mean traction stresses (Pa) per field of view as a function of time (h) post exposure to MΦ. Bottom row shows the corresponding magnitude of traction stresses that cells exert (Pa). Scale bar: 100 μm.

Movie S4 Videomicroscopy of LM-infected zebrafish larva tailfin showing MΦs transmigrating through EC linings and migrating towards the wound site at the tailfin. Related to Figure 7. Primary LM infection site of the zebrafish larva in the trunk muscle. After infection a cut at the tip of the tailfin is performed to elicit transmigration of MΦ (red) from the vasculature to the wound at the tailfin. LM-GFP used for the infections is shown in cyan. Time of recording (h) is indicated. Scale bar: 50 μm. Transmigration event of LM-infected MΦ from dorsal vein into tailfin tissue is highlighted by a white box.

SUPPLEMENTAL TABLE LEGENDS

Table S1. Differentially expressed genes and KEGG pathways between uninfected MΦ-exposed HUVEC versus unexposed HUVEC, LM-infected MΦ-exposed HUVEC versus unexposed HUVEC, and LM-infected versus uninfected MΦ-exposed HUVEC at 8 and 24 hpe. Related to Figure 4. Sheets 1-3 of the table present the DEGs identified when comparing the transcriptome of uninfected MΦ-exposed HUVEC versus unexposed HUVEC (Sheet 1), LM-infected MΦ-exposed HUVEC versus unexposed HUVEC (Sheet 2), and LM-infected versus uninfected MΦ-exposed HUVEC (Sheet 3) at 8 hpe. In an analogous manner Sheets 4-6 refer to similar samples at 24 hpe. In each sheet rows correspond to the genes identified and columns A-K correspond to different parameters explained within the table. Columns L-S provide the FPMK (see STAR methods) of genes in samples for each sample from the corresponding groups compared. Sheets 7-9 of the table show KEGG pathways significantly perturbed when comparing the transcriptome uninfected MΦ-exposed HUVEC versus unexposed HUVEC (Sheet 7), LM-infected MΦ-exposed HUVEC versus unexposed HUVEC (Sheet 8), and LM-infected versus uninfected MΦ-exposed HUVEC (Sheet 9) at 8 hpe. In an analogous manner Sheets 10-12 refer to similar samples at 24 hpe. For each comparison pathways that are upregulated (downregulated) in are highlighted in blue (green). The gage package was used for pathway analysis which has precompiled databases for mapping genes to KEGG pathways so to perform pathway enrichment analysis of DEGs between all three populations. KEGG pathways upregulated for each group are indicated. Rows show the KEGG pathways and column different parameters explained in the table including upregulated genes of each category. Note that everywhere unexposed HUVEC are labeled as "UE"; HUVEC exposed to uninfected macrophages are labeled as "UI"; HUVEC exposed to infected macrophages are labeled as "I".

REFERENCES

1. Santiago-Tirado, F.H., and Doering, T.L. (2017). False friends: Phagocytes as Trojan horses in microbial brain infections. PLoS Pathog *13*, e1006680. 10.1371/journal.ppat.1006680.
2. Maudet, C., Kheloufi, M., Levallois, S., Gaillard, J., Huang, L., Gaultier, C., Tsai, Y.-H., Disson, O., and Lecuit, M. (2022). Bacterial inhibition of Fas-mediated killing promotes neuroinvasion and persistence. Nature *603*, 900-906. 10.1038/s41586-022-04505-7.
3. Zhong, P., Agosto, L.M., Munro, J.B., and Mothes, W. (2013). Cell-to-cell transmission of viruses. Curr Opin Virol *3*, 44-50. 10.1016/j.coviro.2012.11.004.
4. Schroeder, G.N., and Hilbi, H. (2008). Molecular pathogenesis of Shigella spp.: controlling host cell signaling, invasion, and death by type III secretion. Clin Microbiol Rev *21*, 134-156. 10.1128/cmr.00032-07.
5. Bakardjiev, A.I., Theriot, J.A., and Portnoy, D.A. (2006). Listeria monocytogenes traffics from maternal organs to the placenta and back. PLoS Pathog *2*, e66. 10.1371/journal.ppat.0020066.
6. Dupas, A., Goetz, J.G., and Osmani, N. (2024). Extravasation of immune and tumor cells from an endothelial perspective. J Cell Sci *137*. 10.1242/jcs.262066.
7. Medrano-Bosch, M., Simón-Codina, B., Jiménez, W., Edelman, E.R., and Melgar-Lesmes, P. (2023). Monocyte-endothelial cell interactions in vascular and tissue remodeling. Front Immunol *14*, 1196033. 10.3389/fimmu.2023.1196033.
8. Pober, J.S., and Sessa, W.C. (2007). Evolving functions of endothelial cells in inflammation. Nature Reviews Immunology *7*, 803-815. 10.1038/nri2171.
9. Sumagin, R., Prizant, H., Lomakina, E., Waugh, R.E., and Sarelius, I.H. (2010). LFA-1 and Mac-1 define characteristically different intralumenal crawling and emigration patterns for monocytes and neutrophils in situ. J Immunol *185*, 7057-7066. 10.4049/jimmunol.1001638.
10. Lemichez, E., Lecuit, M., Nassif, X., and Bourdoulous, S. (2010). Breaking the wall: targeting of the endothelium by pathogenic bacteria. Nature reviews. Microbiology *8*, 93-104. 10.1038/nrmicro2269.
11. Joffre, J., Hellman, J., Ince, C., and Ait-Oufella, H. (2020). Endothelial Responses in Sepsis. Am J Respir Crit Care Med *202*, 361-370. 10.1164/rccm.201910-1911TR.
12. Cambria, E., Coughlin, M.F., Floryan, M.A., Offeddu, G.S., Shelton, S.E., and Kamm, R.D. (2024). Linking cell mechanical memory and cancer metastasis. Nature Reviews Cancer *24*, 216-228. 10.1038/s41568-023-00656-5.
13. Schwartz, A.B., Kandasamy, A., Del Álamo, J.C., and Yeh, Y.T. (2024). Neutrophils exhibit distinct migration phenotypes that are regulated by transendothelial migration. bioRxiv. 10.1101/2024.10.17.618860.
14. Schwartz, A.B., Campos, O.A., Criado-Hidalgo, E., Chien, S., Del Álamo, J.C., Lasheras, J.C., and Yeh, Y.T. (2021). Elucidating the Biomechanics of Leukocyte Transendothelial Migration by Quantitative Imaging. Front Cell Dev Biol *9*, 635263. 10.3389/fcell.2021.635263.
15. Yeh, Y.T., Serrano, R., François, J., Chiu, J.J., Li, Y.J., Del Álamo, J.C., Chien, S., and Lasheras, J.C. (2018). Three-dimensional forces exerted by leukocytes and vascular endothelial cells dynamically facilitate diapedesis. Proc Natl Acad Sci U S A *115*, 133-138. 10.1073/pnas.1717489115.
16. Liu, C., Wu, C., Yang, Q., Gao, J., Li, L., Yang, D., and Luo, L. (2016). Macrophages Mediate the Repair of Brain Vascular Rupture through Direct Physical Adhesion and Mechanical Traction. Immunity *44*, 1162-1176. 10.1016/j.immuni.2016.03.008.

17. Escribano, J., Chen, M.B., Moeendarbary, E., Cao, X., Shenoy, V., Garcia-Aznar, J.M., Kamm, R.D., and Spill, F. (2019). Balance of mechanical forces drives endothelial gap formation and may facilitate cancer and immune-cell extravasation. PLoS computational biology *15*, e1006395-e1006395. 10.1371/journal.pcbi.1006395.
18. Vazquez-Boland, J.A., Kuhn, M., Berche, P., Chakraborty, T., Dominguez-Bernal, G., Goebel, W., Gonzalez-Zorn, B., Wehland, J., and Kreft, J. (2001). Listeria pathogenesis and molecular virulence determinants. Clin Microbiol Rev *14*, 584-640. 10.1128/CMR.14.3.584-640.2001 [doi].
19. Moreau, V., Frischknecht, F., Reckmann, I., Vincentelli, R., Rabut, G., Stewart, D., and Way, M. (2000). A complex of N-WASP and WIP integrates signalling cascades that lead to actin polymerization. Nat Cell Biol *2*, 441-448.
20. Drevets, D.A., Jelinek, T.A., and Freitag, N.E. (2001). Listeria monocytogenes-infected phagocytes can initiate central nervous system infection in mice. Infect Immun *69*, 1344-1350. 10.1128/iai.69.3.1344-1350.2001.
21. Nambu, M., Morita, M., Watanabe, H., Uenoyama, Y., Kim, K.M., Tanaka, M., Iwai, Y., Kimata, H., Mayumi, M., and Mikawa, H. (1989). Regulation of Fc gamma receptor expression and phagocytosis of a human monoblast cell line U937. Participation of cAMP and protein kinase C in the effects of IFN-gamma and phorbol ester. J Immunol *143*, 4158-4165.
22. Harris, P., and Ralph, P. (1985). Human Leukemic Models of Myelomonocytic Development: A Review of the HL-60 and U937 Cell Lines. Journal of Leukocyte Biology *37*, 407-422. 10.1002/jlb.37.4.407.
23. Dramsi, S., Lévi, S., Triller, A., and Cossart, P. (1998). Entry of Listeria monocytogenesinto Neurons Occurs by Cell-to-Cell Spread: an In Vitro Study. Infection and Immunity *66*, 4461-4468. 10.1128/iai.66.9.4461-4468.1998.
24. Mitchel, J.A., Das, A., O'Sullivan, M.J., Stancil, I.T., DeCamp, S.J., Koehler, S., Ocaña, O.H., Butler, J.P., Fredberg, J.J., Nieto, M.A., et al. (2020). In primary airway epithelial cells, the unjamming transition is distinct from the epithelial-to-mesenchymal transition. Nat Commun *11*, 5053. 10.1038/s41467-020-18841-7.
25. Cheng, Y., Desse, S., Martinez, A., Worthen, R.J., Jope, R.S., and Beurel, E. (2018). TNFα disrupts blood brain barrier integrity to maintain prolonged depressive-like behavior in mice. Brain, Behavior, and Immunity *69*, 556-567. 10.1016/j.bbi.2018.02.003.
26. Dewi, B.E., Takasaki, T., and Kurane, I. (2004). In vitro assessment of human endothelial cell permeability: effects of inflammatory cytokines and dengue virus infection. Journal of Virological Methods *121*, 171-180. 10.1016/j.jviromet.2004.06.013.
27. Brandt, M., Gerke, V., and Betz, T. (2022). Human endothelial cells display a rapid and fluid flow dependent tensional stress increase in response to tumor necrosis factor-α. bioRxiv, 2022.2001.2012.476017. 10.1101/2022.01.12.476017.
28. Guo, W., and Wang, Y. (2007). Retrograde fluxes of focal adhesion proteins in response to cell migration and mechanical signals. Mol Biol Cell *18*, 4519-4527.
29. Geiger, B., Bershadsky, A., Pankov, R., and Yamada, K.M. (2001). Transmembrane crosstalk between the extracellular matrix--cytoskeleton crosstalk. Nat Rev Mol Cell Biol *2*, 793-805. 10.1038/35099066.
30. Lamason, R.L., Bastounis, E., Kafai, N.M., Serrano, R., Del Alamo, J.C., Theriot, J.A., and Welch, M.D. (2016). Rickettsia Sca4 Reduces Vinculin-Mediated Intercellular Tension to Promote Spread. Cell *167*, 670-683.e610. 10.1016/j.cell.2016.09.023.
31. Muller, W.A. (2003). Leukocyte–endothelial-cell interactions in leukocyte transmigration and the inflammatory response. Trends in Immunology *24*, 326-333. 10.1016/S1471-4906(03)00117-0.
32. Bastounis, E.E., Serrano-Alcalde, F., Radhakrishnan, P., Engström, P., Gómez-Benito, M.J., Oswald, M.S., Yeh, Y.-T., Smith, J.G., Welch, M.D., García-Aznar, J.M., and Theriot, J.A. (2021). Mechanical competition triggered by innate immune signaling drives the collective

extrusion of bacterially infected epithelial cells. Developmental Cell *56*, 443-460.e411. 10.1016/j.devcel.2021.01.012.
33. Hundsdorfer, L., Muenkel, M., Aparicio-Yuste, R., Sanchez-Rendon, J.C., Gomez-Benito, M.J., Balmes, A., Schäffer, T.E., Velic, A., Yeh, Y.-T., Constantinou, I., et al. (2025). ERK activation waves coordinate mechanical cell competition leading to collective elimination via extrusion of bacterially infected cells. Cell Reports *44*. 10.1016/j.celrep.2024.115193.
34. Cromer, W.E., Zawieja, S.D., Tharakan, B., Childs, E.W., Newell, M.K., and Zawieja, D.C. (2014). The effects of inflammatory cytokines on lymphatic endothelial barrier function. Angiogenesis *17*, 395-406. 10.1007/s10456-013-9393-2.
35. Claesson-Welsh, L., Dejana, E., and McDonald, D.M. (2021). Permeability of the Endothelial Barrier: Identifying and Reconciling Controversies. Trends Mol Med *27*, 314-331. 10.1016/j.molmed.2020.11.006.
36. Makó, V., Czúcz, J., Weiszhár, Z., Herczenik, E., Matkó, J., Prohászka, Z., and Cervenak, L. (2010). Proinflammatory activation pattern of human umbilical vein endothelial cells induced by IL-1β, TNF-α, and LPS. Cytometry A *77*, 962-970. 10.1002/cyto.a.20952.
37. Zhou, P., Lu, S., Luo, Y., Wang, S., Yang, K., Zhai, Y., Sun, G., and Sun, X. (2017). Attenuation of TNF-α-Induced Inflammatory Injury in Endothelial Cells by Ginsenoside Rb1 via Inhibiting NF-κB, JNK and p38 Signaling Pathways. Front Pharmacol *8*, 464. 10.3389/fphar.2017.00464.
38. Stroka, K.M., Vaitkus, J.A., and Aranda-Espinoza, H. (2012). Endothelial cells undergo morphological, biomechanical, and dynamic changes in response to tumor necrosis factor-α. European biophysics journal : EBJ *41*, 939-947. 10.1007/s00249-012-0851-3.
39. Goldblum, S.E., Ding, X., and Campbell-Washington, J. (1993). TNF-alpha induces endothelial cell F-actin depolymerization, new actin synthesis, and barrier dysfunction. Am J Physiol *264*, C894-905. 10.1152/ajpcell.1993.264.4.C894.
40. Petrache, I., Birukova, A., Ramirez, S.I., Garcia, J.G., and Verin, A.D. (2003). The role of the microtubules in tumor necrosis factor-alpha-induced endothelial cell permeability. Am J Respir Cell Mol Biol *28*, 574-581. 10.1165/rcmb.2002-0075OC.
41. Gomes, M.C., and Mostowy, S. (2020). The Case for Modeling Human Infection in Zebrafish. Trends Microbiol *28*, 10-18. 10.1016/j.tim.2019.08.005.
42. Oehlers, S.H., Cronan, M.R., Scott, N.R., Thomas, M.I., Okuda, K.S., Walton, E.M., Beerman, R.W., Crosier, P.S., and Tobin, D.M. (2015). Interception of host angiogenic signalling limits mycobacterial growth. Nature *517*, 612-615. 10.1038/nature13967.
43. Oehlers, S.H., Cronan, M.R., Beerman, R.W., Johnson, M.G., Huang, J., Kontos, C.D., Stout, J.E., and Tobin, D.M. (2017). Infection-Induced Vascular Permeability Aids Mycobacterial Growth. The Journal of Infectious Diseases *215*, 813-817. 10.1093/infdis/jiw355.
44. Ehrhardt, K., Becker, A.-L., and Grassl, G.A. (2023). Determinants of persistent Salmonella infections. Curr Opin Immunol *82*, 102306.10.1016/j.coi.2023.102306.
45. Goldmann, O., Rohde, M., Chhatwal, G.S., and Medina, E. (2004). Role of macrophages in host resistance to group A streptococci. Infect Immun *72*, 2956-2963. 10.1128/iai.72.5.2956-2963.2004.
46. Duclos, S., and Desjardins, M. (2000). Subversion of a young phagosome: the survival strategies of intracellular pathogens. Cell Microbiol *2*, 365-377.
47. Pidwill, G.R., Gibson, J.F., Cole, J., Renshaw, S.A., and Foster, S.J. (2020). The Role of Macrophages in Staphylococcus aureus Infection. Front Immunol *11*, 620339. 10.3389/fimmu.2020.620339.
48. Perrault, C.M., Brugues, A., Bazellieres, E., Ricco, P., Lacroix, D., and Trepat, X. (2015). Traction Forces of Endothelial Cells under Slow Shear Flow. Biophys J *109*, 1533-1536. 10.1016/j.bpj.2015.08.036.
49. Hur, S.S., del Alamo, J.C., Park, J.S., Li, Y.S., Nguyen, H.A., Teng, D., Wang, K.C., Flores, L., Alonso-Latorre, B., Lasheras, J.C., and Chien, S. (2012). Roles of cell confluency

and fluid shear in 3-dimensional intracellular forces in endothelial cells. Proc Natl Acad Sci U S A *109*, 11110-11115. 1207326109 [pii]
10.1073/pnas.1207326109 [doi].
50. Liu, Z., Sniadecki, N.J., and Chen, C.S. (2010). Mechanical Forces in Endothelial Cells during Firm Adhesion and Early Transmigration of Human Monocytes. Cell Mol Bioeng *3*, 50-59. 10.1007/s12195-010-0105-3.
51. Rabodzey, A., Alcaide, P., Luscinskas, F.W., and Ladoux, B. (2008). Mechanical Forces Induced by the Transendothelial Migration of Human Neutrophils. Biophysical Journal *95*, 1428-1438. 10.1529/biophysj.107.119156.
52. Hind, L.E., Dembo, M., and Hammer, D.A. (2015). Macrophage motility is driven by frontal-towing with a force magnitude dependent on substrate stiffness. Integrative Biology *7*, 447-453. 10.1039/c4ib00260a.
53. Valon, L., Marin-Llaurado, A., Wyatt, T., Charras, G., and Trepat, X. (2017). Optogenetic control of cellular forces and mechanotransduction. Nat Commun *8*, 14396. 10.1038/ncomms14396.
54. Bastounis, E.E., Radhakrishnan, P., Prinz, C.K., and Theriot, J.A. (2022). Mechanical Forces Govern Interactions of Host Cells with Intracellular Bacterial Pathogens. Microbiol Mol Biol Rev, e0009420. 10.1128/mmbr.00094-20.
55. Simon, S., Wagner, M.A., Rothmeier, E., Müller-Taubenberger, A., and Hilbi, H. (2014). Icm/Dot-dependent inhibition of phagocyte migration by Legionella is antagonized by a translocated Ran GTPase activator. Cellular Microbiology *16*, 977-992. 10.1111/cmi.12258.
56. McLaughlin, L.M., Govoni, G.R., Gerke, C., Gopinath, S., Peng, K., Laidlaw, G., Chien, Y.-H., Jeong, H.-W., Li, Z., Brown, M.D., et al. (2009). The Salmonella SPI2 effector SseI mediates long-term systemic infection by modulating host cell migration. PLoS pathogens *5*, e1000671-e1000671. 10.1371/journal.ppat.1000671.
57. Velan, B., Bar-Haim, E., Zauberman, A., Mamroud, E., Shafferman, A., and Cohen, S. (2006). Discordance in the Effects of Yersinia pestis on the Dendritic Cell Functions Manifested by Induction of Maturation and Paralysis of Migration. Infection and Immunity *74*, 6365. 10.1128/IAI.00974-06.
58. Saw, T.B., Doostmohammadi, A., Nier, V., Kocgozlu, L., Thampi, S., Toyama, Y., Marcq, P., Lim, C.T., Yeomans, J.M., and Ladoux, B. (2017). Topological defects in epithelia govern cell death and extrusion. Nature *544*, 212. 10.1038/nature21718.
59. Chiang, M., Hopkins, A., Loewe, B., Marchetti, M.C., and Marenduzzo, D. (2024). Intercellular friction and motility drive orientational order in cell monolayers. Proc Natl Acad Sci U S A *121*, e2319310121. 10.1073/pnas.2319310121.
60. Marcos-Ramiro, B., García-Weber, D., and Millán, J. (2014). TNF-induced endothelial barrier disruption: beyond actin and Rho. Thromb Haemost *112*, 1088-1102. 10.1160/th14-04-0299.
61. Lo, H.M., Lai, T.H., Li, C.H., and Wu, W.B. (2014). TNF-α induces CXCL1 chemokine expression and release in human vascular endothelial cells in vitro via two distinct signaling pathways. Acta Pharmacol Sin *35*, 339-350. 10.1038/aps.2013.182.
62. Alsaffar, H., Martino, N., Garrett, J.P., and Adam, A.P. (2018). Interleukin-6 promotes a sustained loss of endothelial barrier function via Janus kinase-mediated STAT3 phosphorylation and de novo protein synthesis. Am J Physiol Cell Physiol *314*, C589-c602. 10.1152/ajpcell.00235.2017.
63. De Cesaris, P., Starace, D., Riccioli, A., Padula, F., Filippini, A., and Ziparo, E. (1998). Tumor Necrosis Factor-α Induces Interleukin-6 Production and Integrin Ligand Expression by Distinct Transduction Pathways *. Journal of Biological Chemistry *273*, 7566-7571. 10.1074/jbc.273.13.7566.

64. Zhang, X., Liu, X., Shang, H., Xu, Y., and Qian, M. (2011). Monocyte chemoattractant protein-1 induces endothelial cell apoptosis in vitro through a p53-dependent mitochondrial pathway. Acta Biochimica et Biophysica Sinica *43*, 787-795. 10.1093/abbs/gmr072.
65. Yu, H., Huang, X., Ma, Y., Gao, M., Wang, O., Gao, T., Shen, Y., and Liu, X. (2013). Interleukin-8 regulates endothelial permeability by down-regulation of tight junction but not dependent on integrins induced focal adhesions. Int J Biol Sci *9*, 966-979. 10.7150/ijbs.6996.
66. Osawa, Y., Nagaki, M., Banno, Y., Brenner, D.A., Asano, T., Nozawa, Y., Moriwaki, H., and Nakashima, S. (2002). Tumor necrosis factor alpha-induced interleukin-8 production via NF-kappaB and phosphatidylinositol 3-kinase/Akt pathways inhibits cell apoptosis in human hepatocytes. Infect Immun *70*, 6294-6301. 10.1128/iai.70.11.6294-6301.2002.
67. Min, J.K., Kim, Y.M., Kim, S.W., Kwon, M.C., Kong, Y.Y., Hwang, I.K., Won, M.H., Rho, J., and Kwon, Y.G. (2005). TNF-related activation-induced cytokine enhances leukocyte adhesiveness: induction of ICAM-1 and VCAM-1 via TNF receptor-associated factor and protein kinase C-dependent NF-kappaB activation in endothelial cells. J Immunol *175*, 531-540. 10.4049/jimmunol.175.1.531.
68. Clark, P.R., Manes, T.D., Pober, J.S., and Kluger, M.S. (2007). Increased ICAM-1 expression causes endothelial cell leakiness, cytoskeletal reorganization and junctional alterations. J Invest Dermatol *127*, 762-774. 10.1038/sj.jid.5700670.
69. van Steen, A.C.I., Kempers, L., Schoppmeyer, R., Blokker, M., Beebe, D.J., Nolte, M.A., and van Buul, J.D. (2021). Transendothelial migration induces differential migration dynamics of leukocytes in tissue matrix. J Cell Sci *134*. 10.1242/jcs.258690.
70. Cambier, C.J., O'Leary, S.M., O'Sullivan, M.P., Keane, J., and Ramakrishnan, L. (2017). Phenolic Glycolipid Facilitates Mycobacterial Escape from Microbicidal Tissue-Resident Macrophages. Immunity *47*, 552-565.e554. 10.1016/j.immuni.2017.08.003.
71. Varela, M., and Meijer, A.H. (2022). A fresh look at mycobacterial pathogenicity with the zebrafish host model. Molecular Microbiology *117*, 661-669. 10.1111/mmi.14838.
72. Levraud, J.P., Disson, O., Kissa, K., Bonne, I., Cossart, P., Herbomel, P., and Lecuit, M. (2009). Real-time observation of listeria monocytogenes-phagocyte interactions in living zebrafish larvae. Infect Immun *77*, 3651-3660. 10.1128/iai.00408-09.
73. Portnoy, D.A., Jacks, P.S., and Hinrichs, D.J. (1988). Role of hemolysin for the intracellular growth of Listeria monocytogenes. Journal of Experimental Medicine *167*, 1459-1471. 10.1084/jem.167.4.1459.
74. Barker, L.P., Porcella, S.F., Wyatt, R.G., and Small, P.L.C. (1999). The Mycobacterium marinum G13 promoter is a strong sigma 70-like promoter that is expressed in Escherichia coli and mycobacteria species. FEMS Microbiology Letters *175*, 79-85. 10.1111/j.1574-6968.1999.tb13604.x.
75. Lamason, R.L., and Welch, M.D. (2017). Actin-based motility and cell-to-cell spread of bacterial pathogens. Current opinion in microbiology *35*, 48-57. 10.1016/j.mib.2016.11.007.
76. Nguyen, L., and Pieters, J. (2005). The Trojan horse: survival tactics of pathogenic mycobacteria in macrophages. Trends in Cell Biology *15*, 269-276. 10.1016/j.tcb.2005.03.009.
77. Kam, J.Y., Cheng, T., Garland, D.C., Britton, W.J., Tobin, D.M., and Oehlers, S.H. (2022). Inhibition of infection-induced vascular permeability modulates host leukocyte recruitment to Mycobacterium marinum granulomas in zebrafish. Pathogens and Disease *80*, ftac009. 10.1093/femspd/ftac009.
78. Kam, J.Y., Wright, K., Britton, W.J., and Oehlers, S.H. (2022). Treatment of infection-induced vascular pathologies is protective against persistent rough morphotype Mycobacterium abscessus infection in zebrafish. Microbial pathogenesis *167*, 105590. 10.1016/j.micpath.2022.105590.
79. Peloquin, J., Huynh, J., Williams, R.M., and Reinhart-King, C.A. (2011). Indentation measurements of the subendothelial matrix in bovine carotid arteries. J Biomech *44*, 815-821. 10.1016/j.jbiomech.2010.12.018.

80. Wood, J.A., Liliensiek, S.J., Russell, P., Nealey, P.F., and Murphy, C.J. (2010). Biophysical Cueing and Vascular Endothelial Cell Behavior. Materials *3*. 10.3390/ma3031620.
81. Bastounis, E.E., Yeh, Y.T., and Theriot, J.A. (2019). Subendothelial stiffness alters endothelial cell traction force generation while exerting a minimal effect on the transcriptome. Sci Rep *9*, 18209. 10.1038/s41598-019-54336-2.
82. White, C.R., and Frangos, J.A. (2007). The shear stress of it all: the cell membrane and mechanochemical transduction. Philos Trans R Soc Lond B Biol Sci *362*, 1459-1467. 10.1098/rstb.2007.2128.
83. Ahn, S.I., Sei, Y.J., Park, H.-J., Kim, J., Ryu, Y., Choi, J.J., Sung, H.-J., MacDonald, T.J., Levey, A.I., and Kim, Y. (2020). Microengineered human blood–brain barrier platform for understanding nanoparticle transport mechanisms. Nature Communications *11*, 175. 10.1038/s41467-019-13896-7.
84. Deli, M.A., Porkoláb, G., Kincses, A., Mészáros, M., Szecskó, A., Kocsis, A.E., Vigh, J.P., Valkai, S., Veszelka, S., Walter, F.R., and Dér, A. (2024). Lab-on-a-chip models of the blood–brain barrier: evolution, problems, perspectives. Lab on a Chip *24*, 1030-1063. 10.1039/D3LC00996C.
85. Aigouy, B., Umetsu, D., and Eaton, S. (2016). Segmentation and Quantitative Analysis of Epithelial Tissues. Methods Mol Biol *1478*, 227-239. 10.1007/978-1-4939-6371-3_13.
86. Marcotti, S., de Freitas, D.B., Troughton, L.D., Kenny, F.N., Shaw, T.J., Stramer, B.M., and Oakes, P.W. (2021). A workflow for rapid unbiased quantification of fibrillar feature alignment in biological images. Front Comput Sci *3*. 10.3389/fcomp.2021.745831.
87. Ortega, F.E., Rengarajan, M., Chavez, N., Radhakrishnan, P., Gloerich, M., Bianchini, J., Siemers, K., Luckett, W.S., Lauer, P., Nelson, W.J., and Theriot, J.A. (2017). Adhesion to the host cell surface is sufficient to mediate Listeria monocytogenes entry into epithelial cells. Mol Biol Cell. 10.1091/mbc.E16-12-0851.
88. de Jong, N.W.M., van der Horst, T., van Strijp, J.A.G., and Nijland, R. (2017). Fluorescent reporters for markerless genomic integration in Staphylococcus aureus. Scientific Reports *7*, 43889. 10.1038/srep43889.
89. Ellett, F., Pase, L., Hayman, J.W., Andrianopoulos, A., and Lieschke, G.J. (2011). mpeg1 promoter transgenes direct macrophage-lineage expression in zebrafish. Blood *117*, e49-e56. 10.1182/blood-2010-10-314120.
90. Schindelin, J., Arganda-Carreras, I., Frise, E., Kaynig, V., Longair, M., Pietzsch, T., Preibisch, S., Rueden, C., Saalfeld, S., and Schmid, B. (2012). Fiji: an open-source platform for biological-image analysis. Nature methods *9*, 676-682.
91. Bayer, J., Becker, J., Liu, X., Gritsch, L., Daiber, E., Korn, N., Oesterhelt, F., Fraunholz, M., Weber, A., and Wolz, C. (2024). Differential survival of Staphylococcal species in macrophages. Mol Microbiol *121*, 470-480. 10.1111/mmi.15184.
92. Gui, L., and Wereley, S.T. (2002). A correlation-based continuous window-shift technique to reduce the peak-locking effect in digital PIV image evaluation. Exp. Fluids *32*, 506-517. 10.1007/s00348-001-0396-1.
93. Yuste, R.A., Muenkel, M., Axarlis, K., Gómez Benito, M.J., Reuss, A., Blacker, G., Tal, M.C., Kraiczy, P., and Bastounis, E.E. (2022). Borrelia burgdorferi modulates the physical forces and immunity signaling in endothelial cells. iScience *25*, 104793. 10.1016/j.isci.2022.104793.
94. Muenkel, M., Aparicio-Yuste, R., Tal, M.C., Kraiczy, P., and Bastounis, E.E. (2022). Spatiotemporal characterization of endothelial cell motility and physical forces during exposure to Borrelia burgdorferi. STAR Protocols *3*, 101832. 10.1016/j.xpro.2022.101832.
95. Ershov, D., Phan, M.-S., Pylvänäinen, J.W., Rigaud, S.U., Le Blanc, L., Charles-Orszag, A., Conway, J.R.W., Laine, R.F., Roy, N.H., Bonazzi, D., et al. (2022). TrackMate 7: integrating state-of-the-art segmentation algorithms into tracking pipelines. Nature Methods *19*, 829-832. 10.1038/s41592-022-01507-1.

Section 5

Borrelia burgdorferi modulates the physical forces and immunity signaling in endothelial cells

Raúl Aparicio Yuste,[1,2] Marie Muenkel,[1,6] Konstantinos Axarlis,[1,6] María J. Gómez-Benito,[2] Annalena Reuss,[1] Grace Blacker,[3] Michal Caspi Tal,[3,4] Peter Kraiczy,[5] and Effie E. Bastounis[1,7,*]

[1]Interfaculty Institute of Microbiology and Infection Medicine, Cluster of Excellence "Controlling Microbes to Fight Infections" (CMFI, EXC 2124), Eberhard Karls University of Tübingen, Auf der Morgenstelle 28/E7, Tübingen 72076, Germany

[2]Department of Mechanical Engineering, University of Zaragoza, Zaragoza, Spain

[3]Institute for Stem Cell Biology and Regenerative Medicine, Stanford University School of Medicine, Stanford, CA, USA

[4]Department of Biological Engineering, Massachusetts Institute of Technology, Cambridge, MA, USA

[5]Institute of Medical Microbiology and Infection Control, University Hospital of Frankfurt, Goethe University Frankfurt, Frankfurt am Main, Germany

[6]These authors contributed equally

[7]Lead contact

Published 2022 in iScience 25, 104793.

iScience

CellPress
OPEN ACCESS

Article

Borrelia burgdorferi modulates the physical forces and immunity signaling in endothelial cells

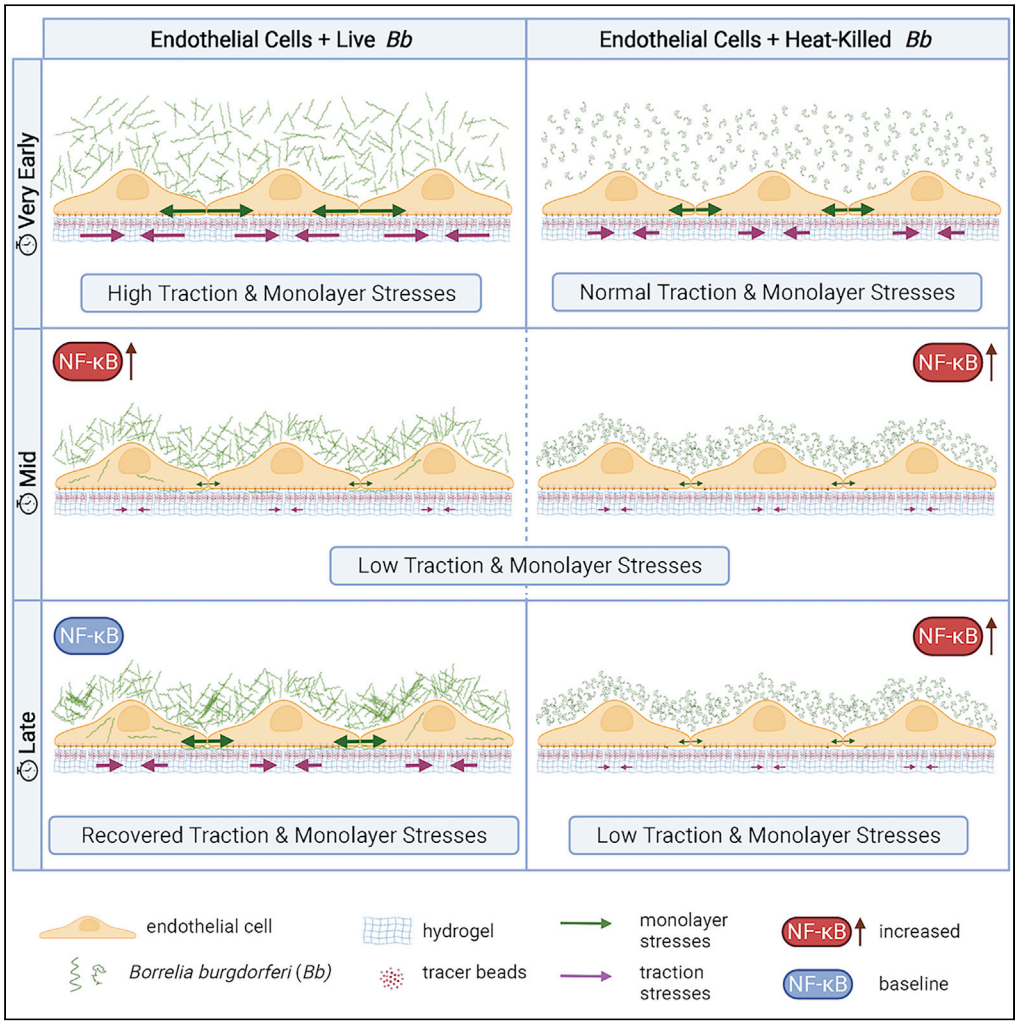

Raúl Aparicio Yuste, Marie Muenkel, Konstantinos Axarlis, ..., Michal Caspi Tal, Peter Kraiczy, Effie E. Bastounis

effie.bastounis@uni-tuebingen.de

Highlights

Early exposure to *Borrelia* decreases endothelial cell motility and physical forces

Early exposure to *Borrelia* also upregulates the host's innate immune signaling pathways

Host cell mechanics and signaling return to steady state at late exposure times

Exposure to dead bacteria steadily reduces motility and physical forces of host cells

Yuste et al., iScience 25, 104793
August 19, 2022
https://doi.org/10.1016/j.isci.2022.104793

iScience

CellPress
OPEN ACCESS

Article

Borrelia burgdorferi modulates the physical forces and immunity signaling in endothelial cells

Raúl Aparicio Yuste,[1,2] Marie Muenkel,[1,6] Konstantinos Axarlis,[1,6] María J. Gómez Benito,[2] Annalena Reuss,[1] Grace Blacker,[3] Michal Caspi Tal,[3,4] Peter Kraiczy,[5] and Effie E. Bastounis[1,7,*]

SUMMARY

***Borrelia burgdorferi* (*Bb*), a vector-borne bacterial pathogen and the causative agent of Lyme disease, can spread to distant tissues in the human host by traveling in and through monolayers of endothelial cells (ECs) lining the vasculature. To examine whether *Bb* alters the physical forces of ECs to promote its dissemination, we exposed ECs to *Bb* and observed a sharp and transient increase in EC traction and intercellular forces, followed by a prolonged decrease in EC motility and physical forces. All variables returned to baseline at 24 h after exposure. RNA sequencing analysis revealed an upregulation of innate immune signaling pathways during early but not late *Bb* exposure. Exposure of ECs to heat-inactivated *Bb* recapitulated only the early weakening of EC mechanotransduction. The differential responses to live versus heat-inactivated *Bb* indicate a tight interplay between innate immune signaling and physical forces in host ECs and suggest their active modulation by *Bb*.**

INTRODUCTION

Lyme disease is a multisystem infectious disease and the most common and rapidly growing tick-borne infection in the northern hemisphere (Feria-Arroyo et al., 2014; Meriläinen et al., 2015). It is caused by a group of bacteria that belong to the *Borrelia burgdorferi* (sensu lato) complex, comprised more than 20 genospecies (Shan et al., 2021). In the majority of infected individuals, prompt treatment with antibiotics is sufficient to resolve the infection (CDC Lyme Disease). However, a subset of infected patients does not return to health and experiences symptoms including neurologic impairment, fatigue, cardiac and arthritic hallmarks as well as a progressive atrophy of the skin – which persist for over 6 months after antibiotic treatment. Although the cause of these continued symptoms is unknown, there is evidence of the continued presence of *Bb* antigens and ongoing inflammatory responses (Jutras et al., 2019; Rouse et al., 2021).

Infected ticks transmit *Bb* into the dermal interstitial fluid while feeding, and from there the pathogens can disseminate throughout the body (Coburn et al., 2021). A key step in bacterial dissemination is the ability of *Bb* to bypass the endothelial cell (EC) lining of blood vessels. To maintain their barrier function ECs form protein complexes at their surfaces that allow them to strongly anchor to the extracellular matrix (ECM) through focal adhesions and to each other through cell-cell junction complexes. The actin cytoskeleton connects these anchors to each other forming a network that allows the cells to transmit forces to their ECM (traction forces) and to each other (intercellular forces).

Various advances in biomechanical techniques have recently enabled the characterization of both the kinematics and dynamics of the motion of cells in monolayer in health and disease. For example, traction force microscopy (TFM) allows direct measurement of the traction forces generated by confluent ECs on their matrix through the active engagement of focal (cell-ECM) adhesions and actomyosin contractility (Rokhzan et al., 2019). An additional technique, monolayer stress microscopy (MSM) enables indirect calculation of the forces that cells in monolayer exert on one another, which is critical in revealing how cells regulate intercellular communication and barrier integrity (Bastounis et al., 2022; Bazellières et al., 2015). Calculation of cell-generated forces has also provided key insight into how certain intracellular bacterial pathogens modulate host cell forces to their own benefit, that is, to disseminate better through tissues (Faralla et al., 2018; Lamason et al., 2016). For example, intracellular *Listeria monocytogenes* hijacks host epithelial cell mechanotransduction weakening the traction stresses that host epithelial cells exert on their

[1]Interfaculty Institute of Microbiology and Infection Medicine, Cluster of Excellence "Controlling Microbes to Fight Infections" (CMFI, EXC 2124), Eberhard Karls University of Tübingen, Auf der Morgenstelle 28/E7, Tübingen 72076, Germany

[2]Department of Mechanical Engineering, University of Zaragoza, Zaragoza, Spain

[3]Institute for Stem Cell Biology and Regenerative Medicine, Stanford University School of Medicine, Stanford, CA, USA

[4]Department of Biological Engineering, Massachusetts Institute of Technology, Cambridge, MA, USA

[5]Institute of Medical Microbiology and Infection Control, University Hospital of Frankfurt, Goethe University Frankfurt, Frankfurt am Main, Germany

[6]These authors contributed equally

[7]Lead contact

*Correspondence: effie.bastounis@uni-tuebingen.de

https://doi.org/10.1016/j.isci.2022.104793

ECM, so that it can more efficiently transmigrate through the cell ventral surface and into the underlying basement membrane (Faralla et al., 2018). Although *Bb* is traditionally considered an extracellular pathogen, studies have shown that it can also get internalized within multiple cell types including ECs (Wu et al., 2011; Ma et al., 1991; Livengood and Gilmore, 2006; Larsen et al., 2003; Girschick et al., 1996), suggesting that *Bb* infection may be able to induce similar alterations in host EC biomechanics.

Of interest, gene expression analysis of host cells, including epithelial and endothelial cells, infected with *Bb in vitro* has revealed that many of the pathways that are related to the regulation of the actin cytoskeleton and focal adhesions show differential expression during the early and late stages of infection (LaFrance et al., 2011). Various integral components of host cell focal adhesions, like the integrin heterodimers α5β1 and αvβ3, facilitate adhesion of *Bb* to host cells (Coburn et al., 1998). They also mediate endothelial cell migration and mechanotransduction (Bastounis et al., 2019; Reinhart-King et al., 2005), suggesting that by interfering with integrin signaling *Bb* may alter host cell mechanics. In addition, exposure of different host cell types to *Bb* activates innate immune signaling pathways such as those dependent on the transcription factor NF-κB (Dev et al., 2011). Of interest, we recently showed that activation of innate immune signaling, particularly of NF-κB, by infection can lead to dramatic changes in host cell mechanics including a decrease in traction forces of infected as compared to uninfected cells (Bastounis et al., 2021). In the context of *Bb* infection, a weakening in intercellular force transduction could enhance paracellular permeability favoring bacterial transmigration through the endothelium.

Tick-transmitted *Bb* typically enters into the host bloodstream as single spirochetes whose diameter of 200 nm may be critical for transmigration through the endothelium and other tissues (Meriläinen et al., 2015; Burns et al., 1997). *Bb* can also localize intracellularly in many host cell types, including ECs, from which it can escape clearance and transmigrate transcellularly (Coleman et al., 1995; Tan et al., 2021; Kumar et al., 2015). Moreover, *Bb* can undergo different morphological transitions, forming for example spherical round bodies and aggregates (Anderson and Brissette, 2021; Sapi et al., 2012). Whether these alternative *Bb* forms emerge as a result of the harsh *in vitro* conditions, the multiplicity of infection, or represent a mechanism to evade *in vivo* host immune responses remains controversial (Murgia and Cinco, 2004; Anderson et al., 2003).

To determine whether exposure of ECs to *Bb* alters their biomechanics, we used video-microscopy to monitor EC monolayers for up to two days after exposure to *Bb*. We discovered a sharp and transient increase in EC traction forces and intercellular forces exerted on neighboring ECs, followed by a prolonged decrease in EC motility and physical forces up to 15 h after exposure (hpe). But all variables returned to levels similar to those of unexposed ECs at a later stage (24 hpe). Concomitantly, RNA sequencing analysis of *Bb*-exposed or unexposed ECs revealed that multiple innate immune signaling pathways (*e.g.*, NF-κB, TNFα) were significantly upregulated at early but not late exposure. Of interest, we found that exposure of ECs to heat-inactivated *Bb* recapitulates the early weakening of EC mechanotransduction but not the reversal observed at late exposure. Altogether our findings suggest a tightly regulated interplay between innate immune signaling and physical forces in host ECs and a differential modulation of those processes at early versus late exposure to *Bb*.

RESULTS

Bb are internally localized within ECs in a dosage-dependent manner at early exposure

To infer whether exposure of ECs to *Bb* alters host cell mechanics, we first sought to evaluate how exactly *Bb* interacts with ECs and whether bacteria are localized extracellularly or also intracellularly. To this end, we grew *Bb* constitutively expressing GFP (*Bb-GFP*) in BSK-H media to mid-log phase (Dunham-Ems et al., 2009) and confirmed via microscopy that all *Bb* retained single spirochete morphology and expressed GFP (Figure 1A and Video S1). To quantify internalization efficiency of *Bb* into ECs, we exposed monolayers of human microvascular endothelial cells −1 (HMEC-1) to *Bb-GFP* for 4hat different multiplicities of infection (MOI). We used HMEC-1 as model host cells because they are dermal microvascular ECs and therefore probably the first type of ECs *Bb* interacts with after skin infection through a tick bite. In addition, this cell line has been previously used to interrogate interactions of *Bb* with ECs (LaFrance et al., 2011). Following extensive washing, we trypsinized the cell monolayers and determined the fraction of ECs that were GFP-positive in each well using flow cytometry (Figures 1B and 1C). At a constant host cell density, we found a monotonic increase in the number of *Bb*-infected ECs with increasing MOI. To confirm that *Bb* is internally localized within ECs, we also performed differential labeling of extracellular *Bb-GFP* cells

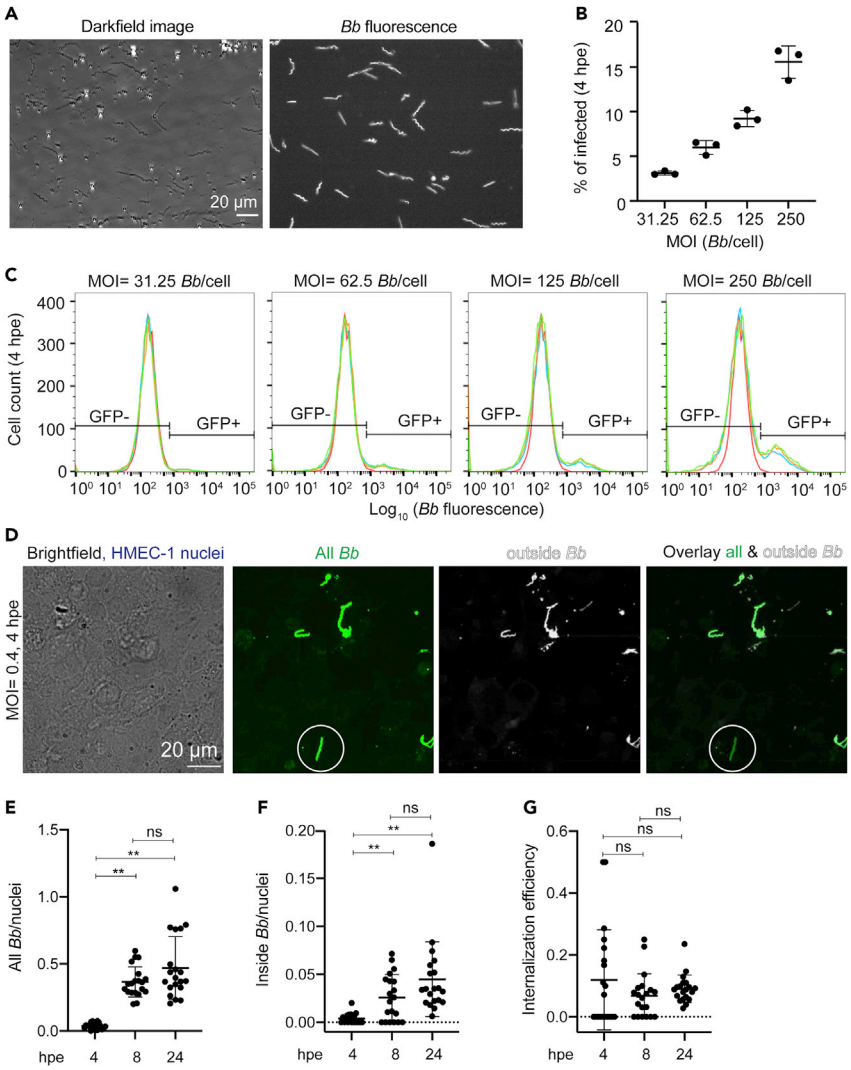

Figure 1. ECs internalize *Bb* in a dose-dependent manner

(A) Darkfield (left) and fluorescence image (right) of *Bb* constitutively expressing GFP (*Bb-GFP*) grown to a concentration of 5 × 10^7 bacteria/mL in BSK-H media.

(B and C) Barplots of percentage of ECs infected with *Bb* versus MOI (mean ± SD) (B) and corresponding histograms of the logarithm of *Bb-GFP* fluorescence intensity per cell for ECs infected with different MOIs of *Bb* (*N* = 3 replicate wells shown in different colors) (C). The histogram of control unexposed cells is shown in red. Based on the autofluorescence of the control group, a gate is defined showing what is considered non-exposed (left, GFP-) and exposed (right, GFP+).

(D) Images of fixed samples of ECs exposed to *Bb-GFP* at a MOI = 11 at 4 hpe. Inside/outside staining was used to confirm internal localization of *Bb*. Left to right: brightfield image superimposed to maximum intensity projection of EC nuclei (blue), *Bb-GFP* fluorescence, antibody fluorescence of non-internalized adhering bacteria and overlay of the last two channels. White circle indicates an internalized spirochete.

(E–G) Barplots of all *Bb-GFP* spirochetes per host cell nucleus (E), inside *Bb*-GFP spirochetes per host cell nucleus (F), and invasion efficiency (inside/outside *Bb*) (mean ± SD, WRST: **p<0.01, ns: non signficant) at different time points after exposure. N = 20 fields of view were segmented and analyzed. See also Figure S1 and Video S1.

(inside/outside labeling) followed by 3D confocal microscopy (Figures 1D and S1A–S1C). Samples were fixed shortly after exposure and specifically labeled with anti-*Bb* antibody under nonpermeabilizing conditions. This inside/outside labeling method allowed us to distinguish between extracellular *Bb* (GFP-positive and antibody-labeled *Bb*) and those that resided within ECs (only GFP-positive). We observed both internally-localized spirochetes as well as spirochetes adhering to the EC surface or that had transmigrated beneath the EC monolayer by 4 hpe. Although the number of bacteria adhering to host cells or being

internally localized significantly increased from 4 to 8 hpe, we found no significant differences between 8 and 24 hpe (Figures 1E and 1F). In addition, the internalization efficiency remained constant irrespective of how long ECs were exposed to *Bb* (Figure 1G). These findings suggest that bacterial adhesion and internalization significantly increase during the first hpe. They also raise the question of whether the lack of changes observed between 8 hpe versus 24 hpe could be because of *Bb* persisting in a viable but not proliferative state onto or within ECs, thus resulting in a constant adhesion rate and internalization efficiency between 8 hpe and 24 hpe.

Host EC motility transiently reduces during early *Bb* exposure

To examine in more detail how do *Bb-GFP* interact spatiotemporally with ECs in monolayer and what changes in EC kinematics those interactions could possibly induce, we monitored ECs exposed to *Bb-GFP* overtime using time-lapse epifluorescence microscopy (Figure 2A and Video S2). EC nuclei were stained with Hoechst so that the motion of ECs could be tracked 7 h before and up to 17 hpe to *Bb-GFP* by applying particle image velocimetry onto successive images of the EC nuclei (Gui and Wereley, 2002). We found that EC displacements and mean speed of motion decreased dramatically during the first few hours after exposure but at later time points ECs recovered their speed to levels just slightly lower than those before exposure (Figures 2A–2C). In our recordings we also observed that at later time points *Bb* formed aggregates. Motivated by these results, we used the *Bb* fluorescence images to calculate the integral *Bb* fluorescence across the whole field of view (FOV) to assess whether *Bb* continue to grow at later time points. We found that the integral of *Bb* fluorescence intensity increased progressively after bacteria had been added on top of the host ECs and reached a peak at a time point that depended on the MOI (the lower the MOI, the earlier this peak was observed, Figure S2A). Thereafter, *Bb* fluorescence decreased overtime until it reached a plateau and remained constant until the end of the recording (~2 days after exposure). Irrespective of the MOI, no changes in mean *Bb* fluorescence or total area occupied by *Bb* occurred at 24 hpe and thereafter (Figures S2A and S2B). To characterize more precisely the changes in *Bb* morphology over the course of exposure to ECs and to identify whether single spirochetes are still present at late exposure, we used image segmentation followed by classification of the *Bb* into three distinct classes namely: single *Bb* (class A, blue); *Bb* networks (class B, magenta); and *Bb* aggregates (class C, green) (Figure S2C). We found that shortly after exposure to *Bb* were mostly in a single spirochete configuration, but overtime spirochetes formed networks and eventually bacterial aggregates although we could still observe motile single *Bb* spirochetes (Figure S2D and Video S2). We then performed propidium iodide (PI) staining of ECs exposed to *Bb* at 4 or 24 hpe to distinguish between live versus dead *Bb* (Figure 2E) (Krämer et al., 2016). Although we found an increase in the total PI fluorescence and in the area in which*Bb*-GFP co-localized with PI, at 24 hpe many of the bacterial aggregates present were PI-negative suggesting they were still viable (Figures S2E and S2F). To further corroborate this and rule out that the recovery of EC motility at late times after exposure was because of *Bb* death, we inspected supernatants of ECs exposed for 4 or 24 h to *Bb-GFP* at either MOI = 200 or MOI = 22 using higher resolution epifluorescence microscopy (Figures S3A and S3B). At 4 hpe at both MOIs most of the spirochetes were motile and no morphological aberrations could be observed either by dark-field or epifluorescence microscopy. At 24 hpe, some spirochetes lacked motility at both MOI = 22 and MOI = 200 and some developed blebs, but single motile spirochetes were still present. This finding was further confirmed when we incubated bacterial supernatants from EC-*Bb* co-cultures at 4 or 24 hpe into BSK-H medium and observed acidification of the medium, indicative of growth of the spirochetes under all conditions tested, albeit to a lesser extent compared to *Bb* never placed into the EC culture medium (data not shown). Thus, we can conclude that the recovery of EC motility at later times after *Bb* exposure is not because of bacterial death since viable spirochetes are still present, although their morphology and proliferation rate differ from those they would exhibit in BSK-H medium.

Traction forces exerted by ECs onto their ECM are attenuated during early *Bb* exposure

Adhesion of *Bb* onto ECs is mediated by the interaction between various bacterial adhesins and ECM components including different integrin subunits (Coburn et al., 1998, 2021; Ebady et al., 2016; Wu et al., 2011). We thus speculated that, during exposure, *Bb* could potentially interfere with focal adhesion organization and traction force generation of ECs in a stage-dependent manner through its interactions with integrin subunits, which could explain the attenuation we previously observed in EC motility. To test this hypothesis, we used TFM to monitor ECs 4 h before exposure and up to 2 days after exposure to a high dosage of *Bb* (MOI = 200) (Figure 3A, left). Although it might not accurately reflect a "normal *in vivo* infection", a high MOI was chosen for this experiment to recognize a discernible effect in EC

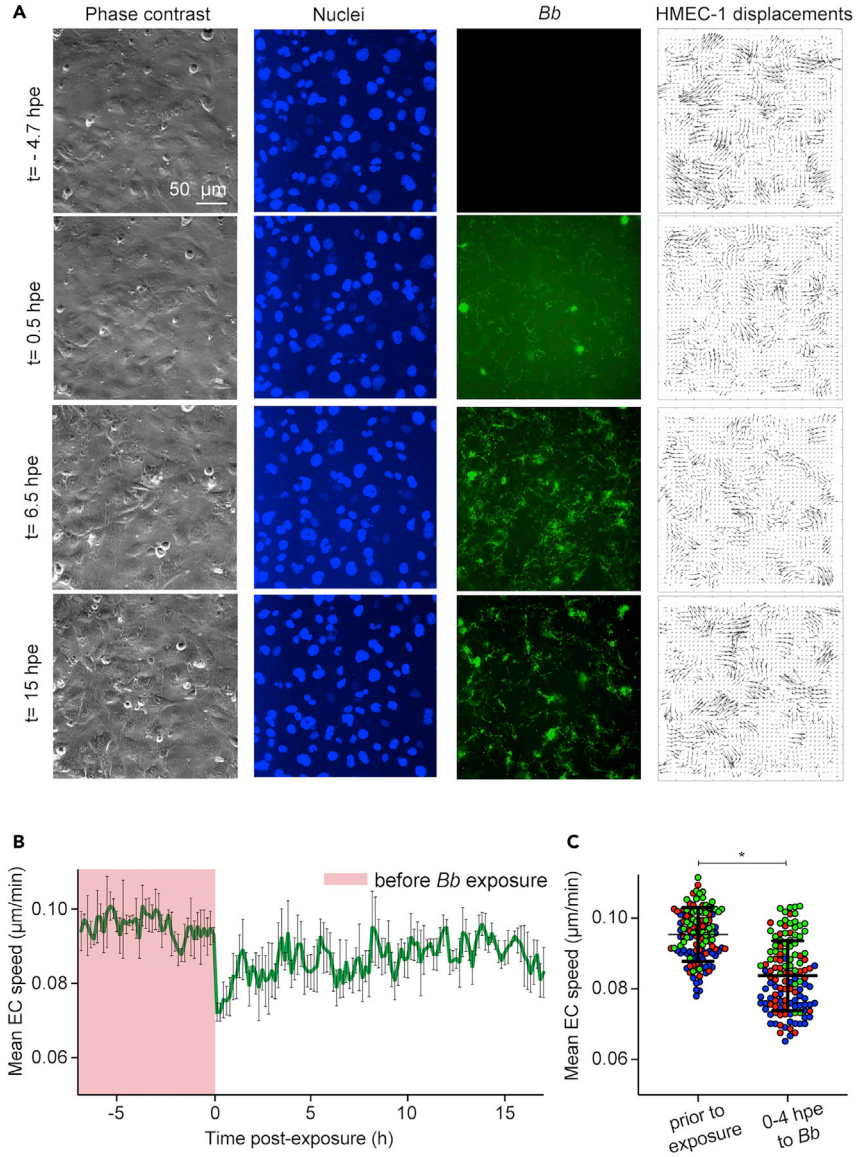

Figure 2. ECs slow down during the early stages of *Bb*-exposure but their motility is recovered at later time points

(A) Representative time-lapse epifluorescence microscopy images of ECs in monolayer during exposure to *Bb* at a MOI =200. Columns show: phase contrast image; Hoechst-stained EC nuclei; *Bb-GFP* fluorescence; cellular displacements. Rows show different time points after exposure.

(B) Plot of mean host cell speed versus time (h) relative to the time point when host cells were exposed to *Bb* (mean ± SD, N = 3 recordings). Magenta dashed line corresponds to the time immediately after addition of *Bb*.

(C) Boxplots of mean EC speed for ECs before *Bb*-exposure (tracked for 4 h) and after exposure to *Bb* at MOI = 200 up to 4 hpe. Different colors correspond to different recordings and circles depict mean spread in the whole field of view (mean ± SD, WRST: *p<0.05). See also Figure S2 and Video S2.

mechanotransduction and thereby gain new mechanistic information as it is often done in such assays. At the same time, we also recorded unexposed ECs to exclude the possibility of changes in traction forces because of an increase in cell confluence that can occur over the course of a day-long recording (Figure 3A, right). We found that upon addition of *Bb*-GFP to ECs, their strain energy (*i.e.*, the mechanical work which ECs impact to deform their ECM) increased abruptly 2-fold within the first 0.5 hpe but decreased over time to 2-fold lower levels as compared to before exposure or to unexposed cells (Figure 3B). The decrease in traction stresses and strain energy as compared to unexposed cells was

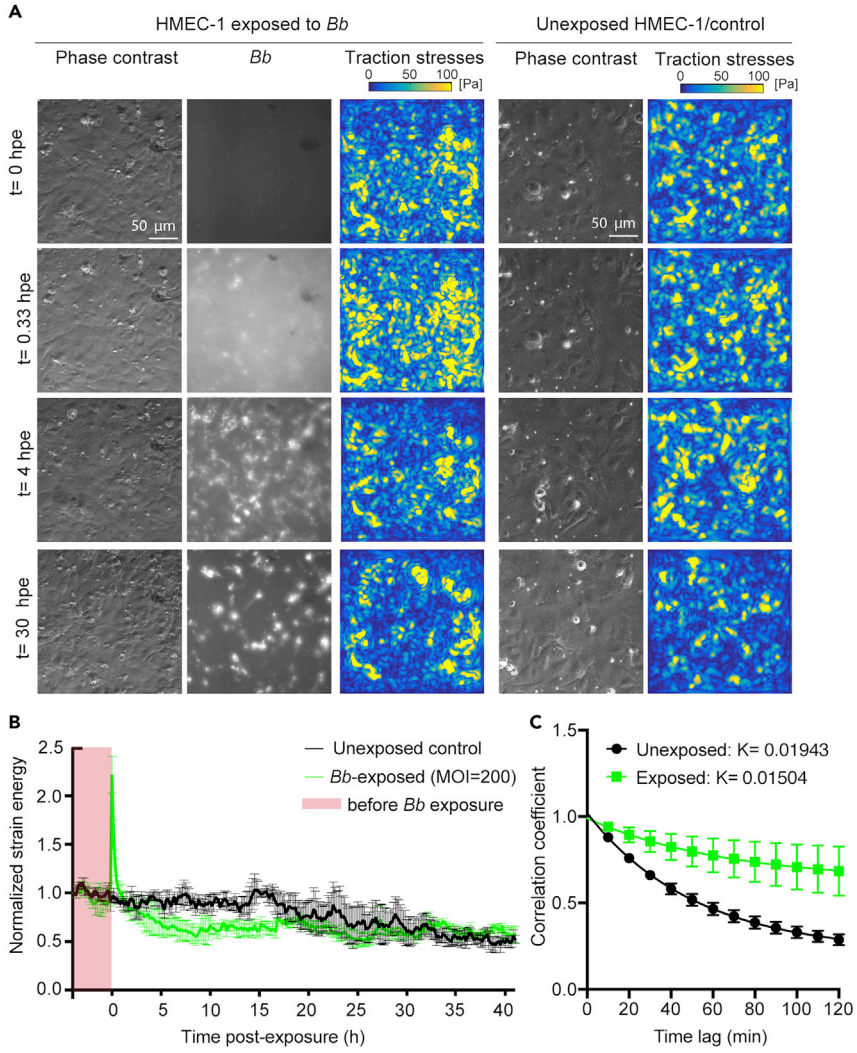

Figure 3. ECs weaken their traction stresses during the early but not late stages of *Bb* exposure

(A) Representative phase contrast image (first column), *Bb-GFP* fluorescence (second column) and cellular traction stress map (third column, Pa) for ECs in monolayer at different time points (rows) after exposure to *Bb-GFP* (MOI =200). TFM was performed for ECs residing on 3 kPa ECM. The fourth and fifth columns show the corresponding phase contrast image and cellular traction stress map for cells not exposed to *Bb*.

(B) Normalized strain energy (mechanical work) imparted by ECs during a TFM recording (mean ± SEM, N = 3 independent experiments). Strain energy has been normalized with respect to the first value at the beginning of each recording. Green: ECs exposed to *Bb-GFP* (MOI = 200); black: unexposed ECs. Time (h) is represented relative with respect to the time at which*Bb* was added. Time before exposure is shaded in red.

(C) Plot showing the cross-correlation coefficient versus time of the cellular deformation maps obtained via TFM for successive frames separated by different time delays for unexposed or *Bb*-exposed ECs (MOI = 200) tracked for 24 hpe. An exponential decay function was fitted into the data yielding a rate constant K= 0.01943 for unexposed ECs and K= 0.01504 for *Bb*-exposed ECs (see STAR Methods). See also Figure S3.

maintained up to approximately 15 hpe. After this point, the normalized strain energy appeared identical in *Bb*-exposed and unexposed cells and, in both cases, lower as compared to the beginning of the recording, likely as a result of increased cell confluence (Hur et al., 2012). Surprisingly, when we correlated the ECM deformation maps, we discovered that the turnover of traction adhesions (active EC adhesions that transduce force to the ECM) of *Bb*-exposed cells was significantly slower and less dynamic compared to that of unexposed cells (Figure 3C), a feature that can also be observed by inspection of the traction stress maps in Figure 3A.

EC monolayer stresses are weakened only at early but not late *Bb* exposure

Our previous findings demonstrated that the traction stresses exerted by ECs on their ECM are weakened during early but not late exposure to *Bb*. However, cells in a monolayer are also able to transduce stresses to each other through their intercellular junctions which are key in regulating barrier function and tissue integrity (Tambe et al., 2011). Those stresses can be tensile or compressive, can result from cells contracting, expanding, or being at rest in different spatial locations and change overtime because of the reorganization of the cytoskeleton and adhesions (Figures 4 and S4A). To measure stresses everywhere within the EC monolayer and to examine how they might change during *Bb* exposure, we used MSM to indirectly estimate intra- and intercellular stresses within a cell monolayer (thereon referred to as monolayer stresses).

ECs not exposed to *Bb*, showed supracellular fluctuations and high heterogeneity in both monolayer tension (σ_I) and compression (σ_{II}), consistent with previous observations in epithelial cell monolayers (Figure 4B, right) (Bazellières et al., 2015). Interestingly, the mean normalized monolayer tension (σ_I) in unexposed ECs remained nearly constant over the first 10 h of imaging and progressively increased over the following 24 h, potentially because of ECs becoming more confluent (Figure 4C). On the contrary, mean normalized monolayer tension (σ_I)exhibited a sharp increase over the first 30 min after *Bb* exposure but remained markedly lower than that of unexposed cells thereafter and up to approximately 20 hpe (Figures 4B and 4C). After that time point, no significant differences were observed between ECs exposed or not to *Bb* (Figure 4C). Collectively, our findings suggest that both the EC traction stresses and monolayer stresses are significantly weakened in cells exposed to *Bb* at early stages (<15 hpe) but they display no differences at later points as compared to cells never exposed to *Bb*.

EC integrins β1 and αvβ3 colocalize with *Bb* but their ventral organization or that of F-actin is comparable to unexposed ECs

We next asked whether the changes in EC motility and traction force generation at early times after exposure were because of alterations in the organization of the cell cytoskeleton or of the focal adhesions. To address that, we grew ECs in monolayer and exposed them (or not) to *Bb-GFP*. Samples were fixed at 8 hpe, immunostained and inspected using 3D confocal microscopy. We first examined the F-actin cytoskeleton using fluorescently labeled phalloidin and observed no major differences when comparing non- or *Bb*-exposed cells (Figures S5A and S5B). Actin stress fibers were present in both cases, although slightly more abundant in unexposed as compared to *Bb*-exposed cells, however, the integral of phalloidin fluorescence intensity in a per cell basis was similar in both conditions (Figure S5C). Given the known involvement of integrins αvβ3 and α5β1 in the attachment of *Bb* to different host cell types (Coburn et al., 1998; Niddam et al., 2017), in the organization of focal adhesions and EC migration (Leavesley et al., 1993), we examined whether their localization or abundance differed between non- or *Bb*-exposed ECs by imaging fixed samples via 3D confocal microscopy (Figures 5A–5D). Inspection of the maximum projection images revealed that some but not all of the spirochetes co-localized with both anti-β1 and anti-αvβ3 antibodies, confirming that the observed signal did not originate from bleed-through fluorescence (Figures 5A and 5D). A more detailed analysis would be needed to conclude whether this co-localization is stochastic or not. The overall organization of those integrin subunits at the basal surface of ECs, from where traction forces are transduced to the extracellular matrix, did not differ dramatically as compared to unexposed ECs, although the integral of anti-β1 antibody fluorescence intensity per cell was increased in the *Bb*-exposed as compared to unexposed ECs (Figures S5D and S5E).

RNA sequencing reveals distinct transcriptional profiles in *Bb*-exposed versus unexposed ECs during early but not late exposure

To better understand which signaling processes might regulate the changes in EC mechanotransduction in response to *Bb*-exposure and how they might differ between early versus late time points after exposure, we analyzed the EC transcriptome. To that end, we exposed ECs in monolayer to *Bb* and extracted their RNA at 4, 24 and 48 hpe. In parallel, at the same time points we also extracted the RNA from unexposed cells (control cells) that were seeded at the same density. We then performed RNA sequencing on these six different populations and used four replicates per condition to determine differentially expressed genes (DE-Gs) when comparing all six populations (Table S1, see Sheets 1–6). As shown by the volcano plot in Figure 6A, at 4 hpe a significant number of genes was upregulated in *Bb*-exposed ECs as compared to controls (78 genes) but only few were downregulated (18 genes). On the contrary, at 24 hpe only 22 and 20 genes were significantly upregulated and downregulated, respectively, in *Bb*-exposed ECs as compared to controls (Figure 6B). Interestingly and paradoxically, at 48 hpe 48 genes were significantly upregulated and 67

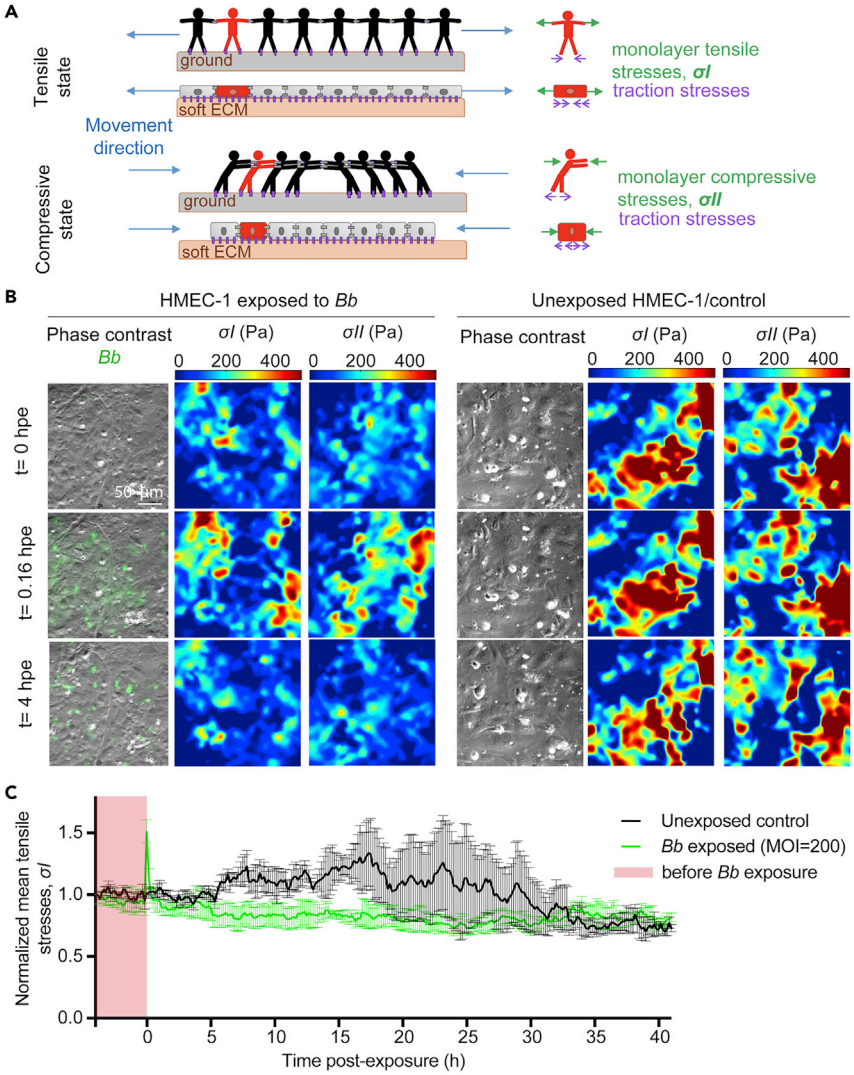

Figure 4. EC monolayer stresses lower during early but not late *Bb*exposure

(A) Sketch of the physical forces present in collectives of cells, and analogue in humans, in 1D. Cells in the monolayer are subjected to tensional and compressive stresses which at any instance balance with the traction stresses on the substrate. Left sketches depict the whole monolayer while right sketches focus on a single cell/human (green). **Top**. Idealized situation in which all cells are pushed by adjacent cells toward the center of the layer. Cells are subjected to compressive stresses while there are no tensile stresses exerted between cells ($\sigma_I = 0, \sigma_{II}$). In the human analogue, humans are subjected to compressive stresses that balance with each other and with the friction exerted in the ground, resulting in a zero net force in each individual when there is no movement. **Bottom.** Idealized situation in which all the cells in the monolayer are pulled by adjacent cells away from the center of the layer and are thus subjected to tensile stresses only ($\sigma_I, \sigma_{II} = 0$). The analogue for humans is also shown.

(B) Representative phase contrast image with *Bb-GFP* fluorescence superimposed (first column), monolayer tensile stresses (σ_I, second column) and compressive stresses (σ_{II}, third column) for ECs in monolayer at different time points (rows) after exposure to *Bb-GFP* (MOI =200). Fourth-sixth columns show the corresponding phase contrast image, monolayer tensile stresses and absolute value of compressive stresses for ECs not exposed to *Bb*.

(C) Normalized mean monolayer tensile stresses (σ_I) as a function of time after exposure (mean ± SEM, N = 3 independent experiments). Mean σ_I has been normalized with respect to the first value at the beginning of each recording. Green: ECs exposed to *Bb-GFP* (MOI = 200); black: unexposed ECs. Time (h) is represented relative to the time at which*Bb* was added. Time before exposure is shaded in red. See also Figure S4.

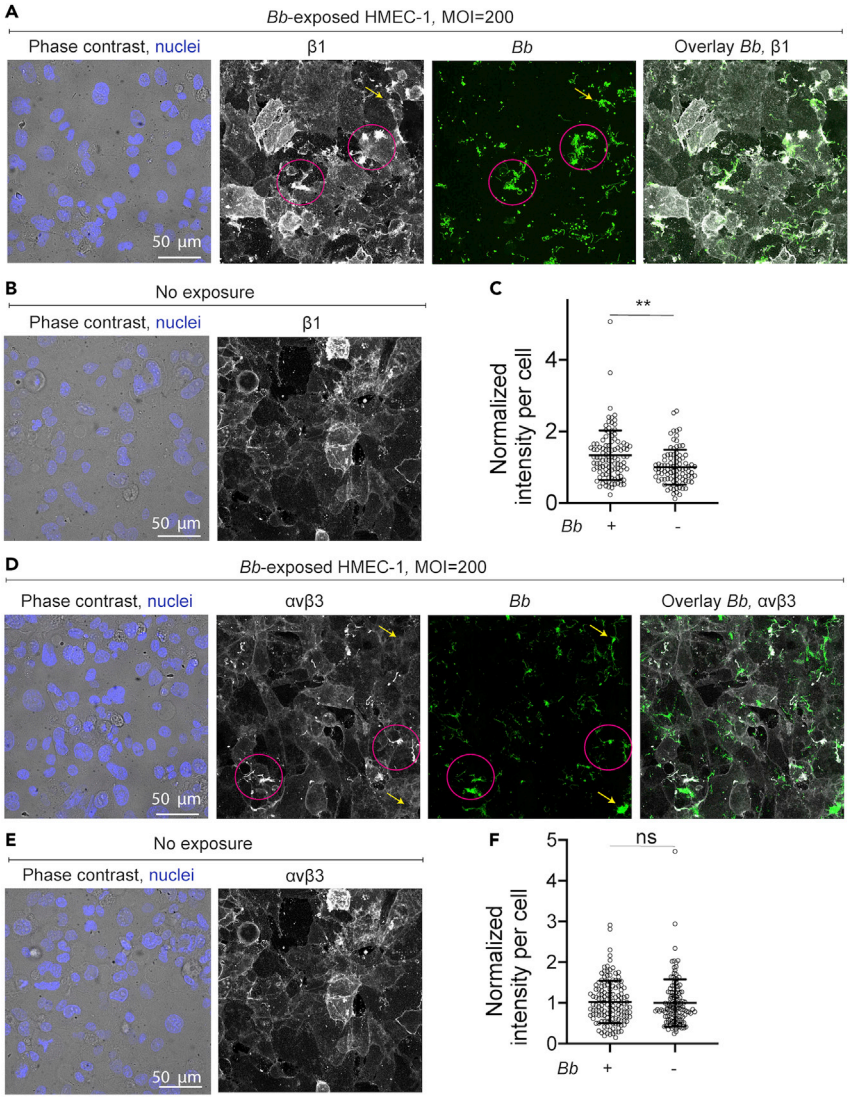

Figure 5. EC integrins β1 and αvβ3 colocalize with *Bb* and β1 shows increased localization compared to unexposed ECs

(A) Representative brightfield image of cells superimposed with the Hoechst-stained nuclei image (first column), anti-β1 integrin antibody fluorescence (second column, maximum intensity projection), *Bb-GFP* fluorescence (third column, maximum intensity projection) and overlay of the last two channels (fourth column) for ECs exposed to *Bb-GFP* for 8 h.

(B) Representative brightfield image of cells superimposed with the Hoechst-stained nuclei image and anti-β1 integrin antibody fluorescence for HMEC-1 not exposed to *Bb*.

(C) Boxplots of normalized mean anti-β1 antibody fluorescence intensity per cell (mean ± SD, dots: individual cells) for ECs exposed to *Bb-GFP* for 8 h or unexposed ECs. Normalization is done with respect to the mean intensity of unexposed ECs. **: $p<0.01$, ns: not significant (Wilcoxon rank-sum test).

(D–F) Same as in (A–C) but showing anti-αvβ3 integrin antibody fluorescence. In panels (A) and (D) pink circles denote co-localization of *Bb-GFP* and the indicated integrins while arrows point to *Bb-GFP* cells that do not colocalize with integrins. See also Figure S5.

genes were significantly downregulated in *Bb*-exposed cells as compared to controls (Figure 6C). However, when we performed principal components analysis (PCA) on our samples (N = 4 replicates per condition), we observed two distinct clusters in the PCA space only for the *Bb*-exposed versus unexposed samples at 4 hpe, whereas the rest of the samples overlapped in the PCA space (Figure 6D). Moreover, as expected, the unexposed ECs at 4 hpe clustered closer to the rest of the samples in the PCA space whereas the *Bb*-exposed ECs at 4 hpe were the only group that clustered on its own as compared to the other samples.

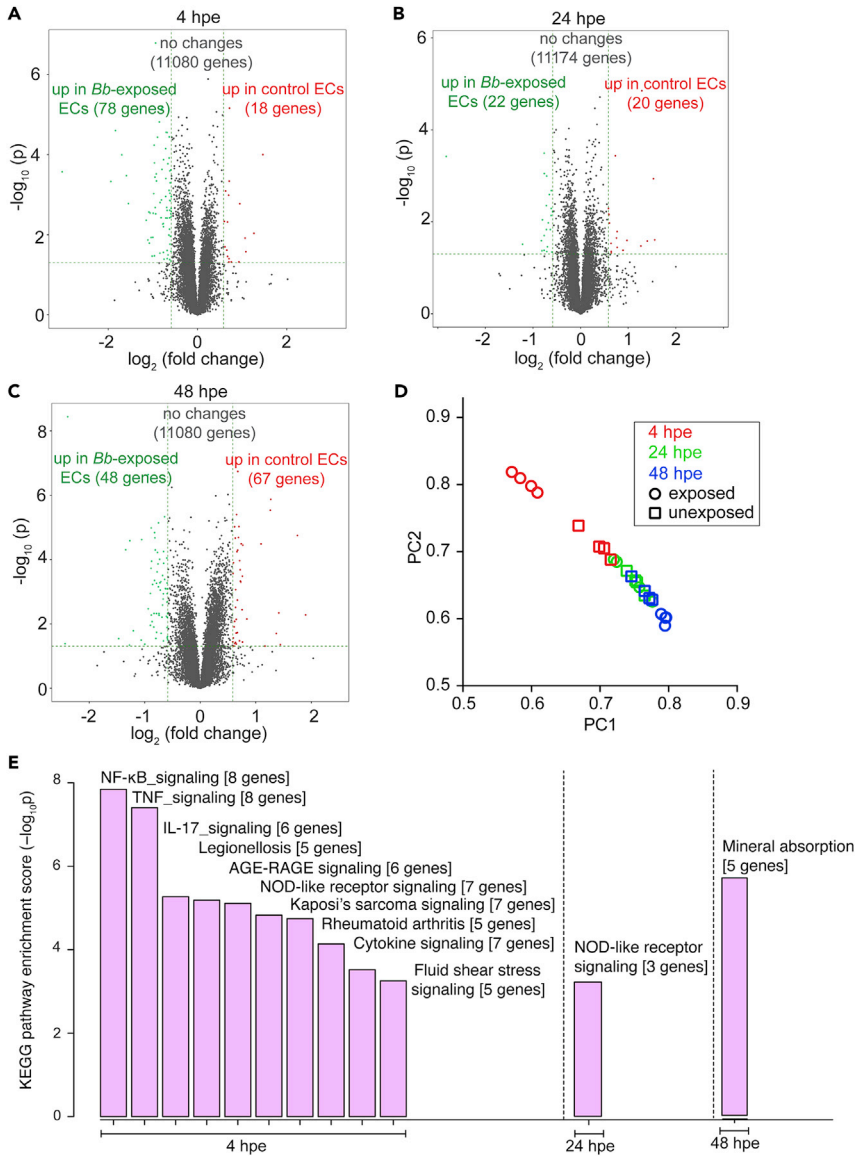

Figure 6. ECs upregulate innate immune signaling pathways at four but not 24 hpe to *Bb*

(A–C) Volcano plots of differentially expressed genes (DE-Gs). The-$\log_{10}$ pvalues are plotted against the average $\log_2$ fold changes in expression. For each pair of compared conditions the upregulated genes of each group are shown in the corresponding color. Each panel refers to a different time after exposure as indicated.

(D) PCA of top genes that have ANOVA p value $\leq$0.05 on FPKM abundance estimations. PC1 versus PC2.

(E) Pathway enrichment analysis. *Bb*-exposed ECs were compared to unexposed ECs based on their enrichment score (-log_{10}p). Resulting barplots for the different times after exposure are shown only for pathways that had-log_{10}p>3. See also Figure S6 and Table S1.

We then performed pathway enrichment analysis for the DE-Gs to revealwhich pathways were significantly perturbed when comparing the different groups (Figure 6E and Table S1, see Sheets 7–9). Compared to unexposed ECs, *Bb*-exposed ECs showed significant upregulation of 47 KEGG pathways and significant down regulation of only one pathway at 4 hpe (Table S1, see sheet 7). The pathways with an enrichment score larger than three and with at least three genes significantly upregulated in *Bb*-exposed ECs were in order of decreasing enrichment score: (1) NFκB signaling pathway; (2) TNF signaling pathway; (3) IL-17 signaling pathway; (4) Legionellosis; (5) AGE-RAGE signaling pathway in diabetic complications; (6) NOD-like receptor signaling pathway; (7) Kaposi's sarcoma-associated herpesvirus infection; (8) Rheumatoid arthritis (refer to Table S1, sheet seven for a list of the specific DE-Gs pertaining to each pathway).

Unlike *Bb*-exposed versus unexposed ECs at 4 hpe, the only KEGG pathway that complied to the criteria listed above at 24 hpe was the NOD-like receptor signaling pathway which contained only three genes differentially regulated as opposed to seven at 4 hpe. Finally, at 48 hpe the only KEGG pathway that complied to the criteria listed above was Mineral absorption, with the following five genes upregulated: *MT1F*, *MT1G*, *MT1M*, *MT1X* (genes encoding metallothioneins) and *SLC30A1* (gene encoding zinc transporter 1), all involved in copper and zinc metabolism. Metallothioneins are cysteine-rich metal binding proteins with high binding affinity for several metals, such as copper and zinc (Calvo et al., 2017), both of which have previously been shown to regulate biofilm formation (Danilova et al., 2020). In addition, metallothioneins are upregulated by host cells in response to biofilm formation by other bacterial communities (Smolentseva et al., 2017).

Given the centrality of the NFκB and TNFα signaling pathways in many types of infection and their recent involvement in modulating host cell mechanics in response to infection with intracellular bacterial pathogens (Bastounis et al., 2021), we examined in more detailed which specific genes of these two pathways were differentially expressed during *Bb*-exposure (Figure S6). At 4 hpe, we found that genes encoding a number of cytokines were significantly upregulated in *Bb*-exposed ECs, namely*: CXCL2* (gene encoding the chemokine CXCL2), *CXCL1* (gene encoding the chemokine CXCL1), *CXCL8* (gene encoding the chemokine IL-8) and *CCL2* (gene encoding the chemokine MCP1). Moreover, upregulated were also the genes encoding the cell adhesion molecule ICAM1 and EDN1, a vasoconstrictor peptide that is often released by ECs in response to TNFα or NFκB activation (Quehenberger et al., 2000; Bourque et al., 2011). Out of all those genes only *CCL2* and *CXCL1* remained significantly upregulated at later times after exposure (*i.e.,* 24 and 48 hpe) while the expression of the remaining genes returned to basal levels, *i.e.,* to those of unexposed ECs. Altogether the upregulation of immunity pathways during the early but not late stages of exposure correlates with the early changes in biomechanics we observed in *Bb*-exposed ECs and is consistent with previous findings (LaFrance et al., 2011).

Exposure of ECs to heat-inactivated *Bb* recapitulates only the early weakening of EC mechanotransduction but not the reversal at late exposure

We speculated that the time-dependent changes in EC force transduction during exposure to *Bb* could have been actively triggered by the spirochetes. However, at later time points (24 hpe) we did observe a decrease in *Bb* viability as assessed by PI staining. To rule out the possibility that the observed changes in biomechanics were simply the response of ECs to dead *Bb*, we exposed ECs to heat-inactivated *Bb-GFP* at a high (MOI = 200) or low (MOI = 22) dosage and conducted TFM and MSM 5 h prior and over 24 hpe. We discovered that irrespective of the MOI, EC traction forces and strain energy weakened to a similar extent in ECs exposed to heat-inactivated *Bb* and in those exposed to live *Bb* (Figures 7A, 7B,3A and 3B). Of interest, in response to heat-inactivated *Bb* we observed neither the transient abrupt increase in traction forces and strain energy nor their recovery at late exposure (>15 hpe), which we observed upon exposure to live *Bb*. Monolayer maximum tensile and compressive stresses of ECs were also sustainably weakened upon exposure to heat-inactivated *Bb-GFP* at both MOIs, but we did not observe the transient and abrupt increase that occurred upon exposure to live *Bb* (Figures 7A–7C,4B and 4C). Given that the weakening of EC force transduction upon early exposure to live *Bb* was accompanied by an upregulation of innate immune signaling pathways such as the NFκB pathway, we wondered whether we were to observe such an effect also in response to heat-inactivated *Bb*. To that end, we performed RT-PCR analysis on ECs exposed to heat-inactivated *Bb-GFP* at 4 and 24 hpe, to test the expression of three NF-κB target genes (namely, CXCL8, ICAM and NFKBIA) which we had found upregulated at 4 but not 24 hpe to live *Bb* through RNA sequencing analysis. Of interest, we discovered an upregulation of all those genes at both 4 and 24 hpe and the extent of upregulation (approximately 2-fold) was similar to that observed just at 4 hpe for ECs exposed to live *Bb*.

The intriguing correlation between weakening in EC mechanotransduction and upregulation of NFκB target genes led us wonder whether EC force transduction would change in response to a cytokine that is known to upregulate NFκB like tumor necrosis factor alpha (TNFα) or to muramyl dipeptide (MDP), which is found in the cell wall of many bacteria and is known to upregulate NOD signaling and NFκB in certain cell types (Stroka et al., 2012; Urbano et al., 2017; Lappas, 2013; Brandt et al., 2022). We discovered that addition of TNFα onto EC monolayers led to an immediate and sustained increase of traction and monolayer stresses while the biomechanical responses of MDP-exposed ECs appeared identical to those of non-exposed ECs (Figures S7A–S7C). When we assessed the expression of the three NF-κB target genes

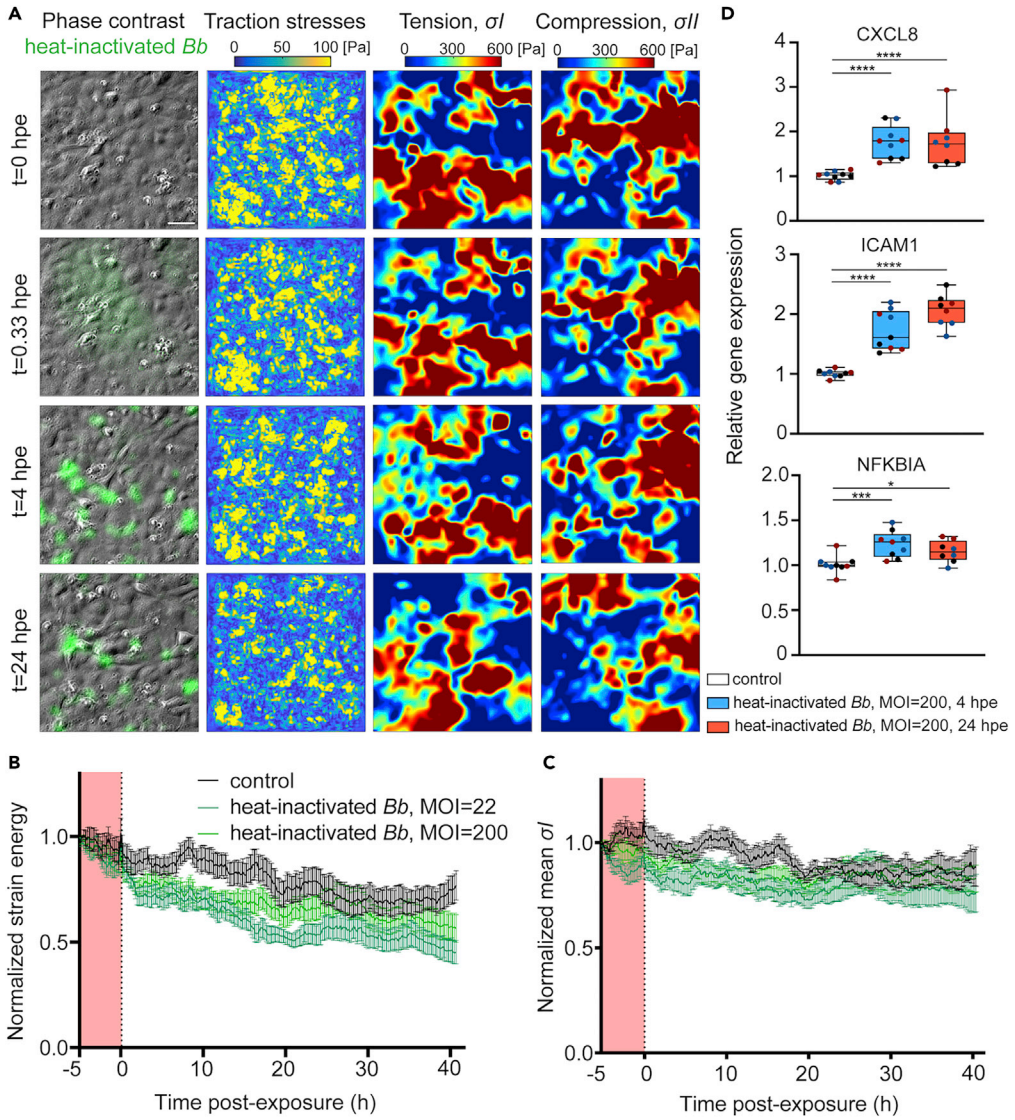

Figure 7. ECs sustainably weaken their force transduction and upregulate NF-κB target genes in response to heat-inactivated *Bb*

(A) Representative phase contrast image overlayed with heat-inactivated *Bb-GFP* fluorescence (first column), EC traction stress map (second column, Pa), monolayer tensile stresses (σ_I, third column, Pa) and absolute value of compressive stresses (σ_{II}, fourth column, Pa) for ECs in monolayer at different time points (rows) after exposure to heat-inactivated *Bb-GFP* (MOI =200). TFM was performed for ECs residing on 3 kPa ECM.

(B) Normalized strain energy imparted by ECs during a TFM recording (mean ± SEM, three independent experiments and N= 12 recordings in total). Strain energy has been normalized with respect to the first value at the beginning of each recording. Dark (light) green: ECs exposed to heat-inactivated *Bb* with an MOI = 200 (MOI= 22); black: unexposed cells. Time (h) is represented relative with respect to the time at which*Bb* was added. Time before exposure is shaded in red.

(C) Same as panel B but showing the normalized mean EC monolayer tensile stresses (σ_I) as a function of time after exposure to heat-inactivated *Bb-GFP*.

(D) Relative with respect to GAPDH expression levels of the indicated NF-κB target genes obtained by RT-PCR. N = 3 independent experiments were performed. Three conditions were tested namely ECs exposed to nothing, to heat-inactivated *Bb-GFP* with an MOI = 200 for 4 h (blue) or for 24h (red). From top to bottom normalized expression of the following genes is shown: CXCL8, ICAM1, NFKBIA. Boxplots show the mean, 25th and 75th quartiles, different colors refer to replicates from independent experiments, *: p<0.05, **: p<0.01, ***: p<0.001, ****: p<0.0001 (Wilcoxon rank-sum test run for each condition's distribution with respect to control distribution). See also Figure S7.

(CXCL8, ICAM and NFKBIA) via RT-PCR, we found a dramatic increase (10- to 100-fold compared to controls) in their expression both at 4 and 24 hpe to TNFα (Figure S7D) while there were no detectable changes in expression of those genes for cells exposed to MDP (data not shown). Thus, it appears that a dramatic upregulation of innate immune signaling as obtained in response to TNFα leads to a fast and sustained upregulation of EC force transduction. Whether TNFα is somehow related to the strong immediate upregulation of force transduction upon encounter of ECs with live *Bb* was not tested but could be the focus of future studies.

DISCUSSION

Cell-cell and cell-matrix adhesions of ECs are continuously remodeled in response to biochemical and mechanical cues. This remodeling results in dynamic alterations of the forces that cells transmit to their matrix and to each other, which are regulated to a large extent through the action of the actomyosin contractile apparatus (Komarova et al., 2017). Pro-inflammatory mediators and secreted cytokines can reinforce (Brandt et al., 2022) or alternatively release the tensile stresses between ECs, thus enhancing vascular permeability (Lee et al., 2011). A decrease in cell-ECM forces can also lead to attenuation in EC monolayer stresses as a result of the crosstalk between adherens junctions and focal adhesions (Komarova et al., 2017). Such attenuation in traction and monolayer stresses, similar to what we observed during early exposure of ECs to *Bb*, could benefit the bacteria by enhancing their transmigration through the leaky EC monolayer. However, sustained, and prolonged impairment of cellular physical forces could lead to extensive leakiness of the vessels, a feature that could harm a pathogen like *Bb* in the first place by rapidly killing the host and making a persistent infection impossible.

The weakening in EC force transduction during early *Bb* exposure which we discovered, coincides with upregulation of a number of host cell genes involved in innate immune signaling. Previous studies have demonstrated an intricate link between innate immune signaling and alterations in either intercellular stresses or permeability (Bastounis et al., 2021; Kisseleva et al., 2006; Kempe et al., 2005). We recently showed that NFκB activation in response to infection with intracellular bacterial pathogens (*L. monocytogenes* and a *Rickettsia parkeri*mutant), leads to a decrease in traction forces of epithelial cells in monolayer as compared to non-infected settings, and a decrease in monolayer stresses as measured indirectly through laser wounding (Bastounis et al., 2021). *In vivo*, NFκB activation has been explicitly linked to increased vascular EC permeability (Kisseleva et al., 2006). It is possible that *Bb* spirochetes might take advantage of the weakening in host cell mechanotransduction, which correlates with upregulation of innate immune signaling at early exposure, to facilitate their paracellular transmigration through ECs, or even their transcellular transmigration through ECs (*i.e.*, by taking advantage of the EC intracellular tension weakening). Recently, intravital imaging of the microvasculature of mice revealed that infection with *Bb* triggers local recruitment of neutrophils which, instead of killing the pathogens, leads to production of various cytokines, particularly CCL2, thereby activating ECs and increasing barrier permeability (Tan et al., 2021). This in turn facilitates transcellular but not paracellular transmigration of *Bb* to reach distant tissues. Interestingly, we also found that ECs upregulated *CCL2* expression throughout exposure to *Bb*, suggesting that some of the spirochetes we observed intracellularly may just be en route of transmigration through ECs. Production of additional cytokines, like TNFα and IL-10, was increased in the study of Tan et al., most likely because those cytokines are primarily produced by neutrophils. *In vitro* assays similar to the one we developed here but additionally involving co-culture with neutrophils could help shed more light into how ECs biomechanics in response to *Bb* exposure is altered in the presence of neutrophils. It should be noted that *Bb* might have additional ways of altering host cell mechanics, *e.g.*, by inducing changes in the mechanical properties of the ECM to which host cells are anchored directly or indirectly. For example, the *Bb* surface exposed protease BbHtrA can directly degrade ECM proteins in various tissues including the skin, joints and brain, which is expected to induce concomitant changes in host cell mechanics (Russell et al., 2013). In addition, *Bb* infection leads to the upregulation of matrix metalloproteases (MMPs, ECM degrading enzymes) by chondrocytes (Behera et al., 2005), keratinocytes and macrophages (Gebbia et al., 2001). Although MMP upregulation, ECM stiffening and changes in cell contractility are tightly correlated processes in the context of cancer metastasis (Haage and Schneider, 2014), their interplay during *Bb* infection has yet to be uncovered.

The changes we found in EC kinematics, dynamics and gene expression in response to *Bb* exposure are transient and progressively vanish as time after exposure elapses. The absence of changes in EC gene expression at late times after exposure to *Bb* is consistent with a previous microarray analysis

(LaFrance et al., 2011). However, in this study gene expression analysis of cells, including HMEC-1, at early *Bb* exposure (1 or 3 hpe) revealed upregulation of pathways related to the regulation of the actin cytoskeleton and focal adhesions which we do not find to be upregulated through RNA sequencing of HMEC-1 at 4 hpe. Rather, we found upregulation of a lot of pathways related to innate immune signaling. A possible reason for this discrepancy could be that in the LaFrance et al. study the noninfectious *Bb* strain HB19/KO1 was used while we used the infectious *Bb* strain B31 5A4 NP1. Different *Bb* strains present differences in genotype, clinical features and inflammatory potential, therefore the changes they can induce in EC gene expression and biomechanics could well be strain specific (Cerar et al., 2016).

At late EC exposure to *Bb*, we observed the formation of *Bb* aggregates, but single motile and viable spirochetes were still present in the culture medium. Past studies have suggested that multiple factors can lead to *Bb* aggregation (Anderson and Brissette, 2021; Sapi et al., 2012; Alban et al., 2000). However, in our assay we determined that this is the result of the high MOI used, since it also occurs when large amounts of spirochetes are cultured in their normal growth medium (data not shown). To determine herein, whether the lack of changes in EC gene expression and biomechanics at late exposure to live *Bb* could be related to the status of *Bb*, and to understand whether the time-dependent changes in EC force transduction represent and active or passive response to *Bb*, we exposed ECs to heat-inactivated *Bb*. We found that throughout the course of exposure EC mechanotransduction was weakened and NF-κB target genes were upregulated. It has been shown that *Bb* peptidoglycans (PG) and lipoproteins such as the outer surface protein OspC are resistant to heat and at least PG can induce NFκB activation in host cells (Jutras et al., 2016, 2019; Kumru et al., 2011) whereas other studies have shown that exposure of different cell types to dead *Bb* induce inflammatory mediators (Parthasarathy et al., 2013; Wang et al., 2008). Whether any of those components are responsible for the weakening in EC mechanotransduction could be tested in future studies experimentally by addition of recombinant proteins or PG components onto EC monolayers. However, when we added MDP onto ECs we did not observe any change in EC force transduction but also any upregulation of NFκB target genes in ECs (data not shown). On the contrary, when we exposed ECs to TNFα, NFκB target genes were dramatically upregulated (10- to 100-fold) and immediate and sustained upregulation of EC force transduction was observed, consistent with previous studies (Stroka et al., 2012; Urbano et al., 2017; Brandt et al., 2022). This result suggests that the relationship between EC physical forces and innate immune signaling is likely not monotonic. Finally, it is worth noting that the responses of ECs to live versus heat-inactivated *Bb* exposed ECs particularly differed at very early and late stages of exposure. First, upon exposure to heat-inactivated *Bb* there was no abrupt increase in EC force transduction, a feature that was observed upon exposure to live *Bb*. This result suggests that the initial signal conveyed to ECs may arise from adhesion of live *Bb* to ECs through some receptor that is possibly denatured upon heat inactivation. The late reversal of EC gene expression and biomechanics, a feature that was observed only in response to live but not heat-inactivated *Bb*, suggests that this is not a consequence of the loss of *Bb* viability because of prolonged exposure to EC culture media. Rather, it could be because of changes in the *Bb* state, including the metabolic or gene expression state. Whether this response reflects what would happen in an actual *in vivo* infection is unknown, but lack of host cell gene expression changes at one day after infection with *Bb* has previously been shown *in vitro* (LaFrance et al., 2011) while changes in gene expression of *Bb*, which have been shown to occur during actual *in vivo* infection, could well impact host cell responses in a time-dependent manner (Saputra et al., 2020).

To overcome a major limitation of *in vivo* approaches, namely, the fact that multiple parameters can change in an unpredictable manner at once limiting the strength of causal conclusions, herein we used an elaborate *in vitro* assay that enabled us to measure the spatiotemporal evolution of EC kinematics and dynamics during exposure to *Bb* in a controllable manner while tweaking one parameter at a time. This in turn allowed us to discover an intricate time-dependent link between EC innate immune signaling and biomechanics during *Bb* exposure. Our assay however is under static conditions and does not account for additional extracellular physical forces that ECs experience *in vivo*. For example, in the vasculature ECs are exposed to fluid shear stresses and gradients which can greatly impact EC behavior (*e.g.*, proliferation, motility *etc*) and mechanotransduction (Barakat and Lieu, 2003; Brandt et al., 2022; Ostrowski et al., 2014; Tan et al., 2021). The fluid shear flow regime can also impact the way *Bb* adheres on ECs (Ebady et al., 2016). It is possible that apical fluid flow might impact both innate immune signaling and physical EC forces and thus the EC responses to *Bb* exposure might present distinct features as compared to static cultures. Examination of the impact of apically exposed fluid flow on EC biomechanics and the interactions with *Bb* can be the focus of future studies. Moreover, the high MOI used in our study might not reflect what would be observed

in vivo, but we used it to be able to measure discernible effects in the EC traction-monolayer forces and signaling and thus gain new mechanistic information as it is often done in such assays. Future studies could focus on uncovering whether our conclusions are valid in *in vivo* systems.

Our discovery of the upregulation of innate immune signaling and weakening of host EC force transduction upon early but not late exposure to *Bb* underlines the importance of uncovering both the spatial and temporal changes that occur during the course of exposure. Studying how changes in host cell biomechanics and gene expression are temporally and spatially modulated will reveal how pathogens like *Bb* can subvert host physiology to their own benefit, that is, to disseminate or render infection chronic. Such studies can also lend key insights into how ECs regulate force transduction and barrier integrity in health and during bacterial infections.

Limitations of the study

Herein we used human skin microvascular ECs, HMEC-1, as our model ECs and pathogenic strains Bb1286 or GCB726, as our model *Bb* strains. Examination of additional EC types and *Bb* strains would allow assessing how generalizable or conversely EC type- or *Bb* strain-specific the mechanisms we discovered are. Moreover, in this study we assessed only the changes in the transcriptomics of host ECs. Performance of RNA sequencing to investigate the changes in gene expression that *Bb* undergoes during the course of exposure could reveal how changes in EC gene expression are linked to alterations in bacterial transcriptomics. Finally, our data suggest an active modulation of host EC mechanics and biochemistry by *Bb*. Experiments with specific *Bb*mutant strains could reveal specific *Bb* virulence factors that trigger the active responses of ECs and could facilitate the identification of the specific underlying mechanisms *Bb* employ to alter EC biomechanics. Finally, investigation of the physical and "dual" transcriptomic responses of host ECs and *Bb* in a more complex *in vitro* system which allows co-culture of ECs with professional immune cells, would have enabled examining the contribution of the host professional immune cells to *Bb*-ECs interactions, and would have thus been more physiological.

STAR★METHODS

Detailed methods are provided in the online version of this paper and include the following:

- KEY RESOURCES TABLE
- RESOURCE AVAILABILITY
  - Lead contact
  - Materials availability
  - Data and code availability
- EXPERIMENTAL MODEL AND SUBJECT DETAILS
  - Cell culture
  - Bacterial strains used in this study
- METHOD DETAILS
  - Bacterial growth conditions and exposure of ECs to *Borrelia burgdorferi*
  - Flow cytometry of ECs exposed to *Bb-GFP*
  - *Bb* segmentation and morphology-dependent classification
  - Fabrication of polyacrylamide hydrogels
  - Traction force microscopy (TFM)
  - Monolayer stress microscopy (MSM)
  - Characterization of host cell kinematics and bacterial aggregation
  - RNA isolation and RNA sequencing
  - Principal component analysis (PCA) and mRNA function enrichment analysis
  - Inside/outside bacterial labeling, immunofluorescence microscopy and image processing
  - Propidium iodide (PI) staining, imaging and quantitation of co-localization of *Bb* with PI
  - RT-PCR
- QUANTIFICATION AND STATISTICAL ANALYSIS

SUPPLEMENTAL INFORMATION

Supplemental information can be found online at https://doi.org/10.1016/j.isci.2022.104793.

ACKNOWLEDGMENTS

We are grateful to Julie A. Theriot for her insight, scientific discussions and sharing her resources. We are grateful to Joseph D. Mougous for sharing his resources and to Ben Ross for discussions, experimental support and revising the manuscript. We thank Justin Radolf and Tara Moriarty for sharing the GFP-expressing borrelial strains with us. We thank Matthew Footer for discussions and experimental support. We thank Libera Lo Presti for discussions and for revising the manuscript and rest of the materials. We acknowledge that part of our MSM codes are based on the original code (plane stress problem) written by Siva Srinivas Kolukula and we hence used some functions from his code. This research was supported by the Cell Analysis Facility Flow Cytometry and Imaging Core in the Department of Immunology at the University of Washington. RNA Seq and RT-qPCR were performed by Arraystar Inc. The graphical abstract was created with BioRender.com. This work was supported in part by the American Heart Association, Award number: 18CDA34070047 (E.E.B.), the Lyme Disease Association (E.E.B.), the Stanford Lyme Disease Seed Grant (E.E.B.) and the Deutsche Forschungsgemeinschaft (DFG, German Research Foundation) underGermany's Excellence Strategy – EXC 2124–390838134 (E.E.B., K.A., M.M., A.R.), the Erasmus+ Programme of the European Union (K.A.), the European Research Council (ICoMICS Adg grant agreement: 101018587, (R.A.-Y. and M.J.G.-B.)), the Spanish Ministry of Universities (grant FPU 20/05274 (R.A.-Y.)), grant PID2021-124271OB-I00 founded by MCIN/AEI/10.13039/501100011033 (R.A-Y, M.J.G-B) and ERDF A way of making Europe (R.A.-Y, and M.J.G.-B.). Finally, we acknowledge support by Open Access Publishing Fund of the University of Tübingen.

AUTHOR CONTRIBUTIONS

Conceptualization, E.E.B.; Methodology, E.E.B., M.J.G.-B., M.M., K.A., P.K., R.A.-Y., M.C.T.; Software, E.E.B; M.J.G.-B., M.M., R.A.-Y., A.R.; Investigation, E.E.B., P.K., M.M., K.A., R.A.-Y., A.R., B.R.; Writing – Original Draft, E.E.B.; Writing – Review & Editing, E.E.B., K.A., P.K., M.C.T., M.J.G.-B.; Resources, E.E.B., P.K., M.C.T., M.J.G.-B.; Supervision, E.E.B.

DECLARATION OF INTERESTS

The authors declare no competing interests.

Received: January 31, 2022
Revised: June 9, 2022
Accepted: July 13, 2022
Published: August 19, 2022

REFERENCES

CDC Lyme Disease. https://www.cdc.gov/lyme/index.html.

Alban, P.S., Johnson, P.W., and Nelson, D.R. (2000). Serum-starvation-induced changes in protein synthesis and morphology of Borrelia burgdorferi. Microbiology (Read.) *146*, 119–127.

Anderson, C., and Brissette, C.A. (2021). The brilliance of Borrelia: mechanisms of host immune evasion by lyme disease-causing spirochetes. Pathogens *10*, 281.

Anderson, G.G., Palermo, J.J., Schilling, J.D., Roth, R., Heuser, J., and Hultgren, S.J. (2003). Intracellular bacterial biofilm-like pods in urinary tract infections. Science *301*, 105–107.

Barakat, A., and Lieu, D. (2003). Differential responsiveness of vascular endothelial cells to different types of fluid mechanical shear stress. Cell Biochem. Biophys. *38*, 323–343.

Bastounis, E., Meili, R., Álvarez-González, B., Francois, J., del Álamo, J.C., Firtel, R.A., and Lasheras, J.C. (2014). Both contractile axial and lateral traction force dynamics drive amoeboid cell motility. J. Cell Biol. *204*, 1045–1061.

Bastounis, E.E., Ortega, F.E., Serrano, R., and Theriot, J.A. (2018). A multi-well format polyacrylamide-based assay for studying the effect of extracellular matrix stiffness on the bacterial infection of adherent cells. J. Vis. Exp. 57361.

Bastounis, E.E., Radhakrishnan, P., Prinz, C.K., and Theriot, J.A. (2022). Mechanical forces govern interactions of host cells with intracellular bacterial pathogens. Microbiol. Mol. Biol. Rev. e0009420.

Bastounis, E.E., Serrano-Alcalde, F., Radhakrishnan, P., Engström, P., Gómez-Benito, M.J., Oswald, M.S., Yeh, Y.-T., Smith, J.G., Welch, M.D., García-Aznar, J.M., and Theriot, J.A. (2021). Mechanical competition triggered by innate immune signaling drives the collective extrusion of bacterially infected epithelial cells. Dev. Cell *56*, 443–460.e11.

Bastounis, E.E., Yeh, Y.T., and Theriot, J.A. (2019). Subendothelial stiffness alters endothelial cell traction force generation while exerting a minimal effect on the transcriptome. Sci. Rep. *9*, 18209.

Bazellières, E., Conte, V., Elosegui-Artola, A., Serra-Picamal, X., Bintanel-Morcillo, M., Roca-Cusachs, P., Muñoz, J.J., Sales-Pardo, M., Guimerà, R., and Trepat, X. (2015). Control of cell–cell forces and collective cell dynamics by the intercellular adhesome. Nat. Cell Biol. *17*, 409–420.

Behera, A.K., Hildebrand, E., Scagliotti, J., Steere, A.C., and Hu, L.T. (2005). Induction of host matrix metalloproteinases by Borrelia burgdorferi differs in human and murine lyme arthritis. Infect. Immun. *73*, 126–134.

Bourque, S.L., Davidge, S.T., and Adams, M.A. (2011). The interaction between endothelin-1 and nitric oxide in the vasculature: new perspectives. Am. J. Physiol. Regul. Integr. Comp. Physiol. *300*, R1288–R1295.

Brandt, M., Gerke, V., and Betz, T. (2022). Human endothelial cells display a rapid and fluid flow dependent tensional stress increase in response to tumor necrosis factor-α. Preprint at bioRxiv. https://doi.org/10.1101/2022.01.12.476017.

Burns, M.J., Sellati, T.J., Teng, E.I., and Furie, M.B. (1997). Production of interleukin-8 (IL-8) by

cultured endothelial cells in response to Borrelia burgdorferi occurs independently of secreted [corrected] IL-1 and tumor necrosis factor alpha and is required for subsequent transendothelial migration of neutrophils. Infect. Immun. *65*, 1217–1222.

Caimano, M.J., Dunham-Ems, S., Allard, A.M., Cassera, M.B., Kenedy, M., and Radolf, J.D. (2015). Cyclic di-GMP modulates gene expression in Lyme disease spirochetes at the tick-mammal interface to promote spirochete survival during the blood meal and tick-to-mammal transmission. Infect. Immun. *83*, 3043–3060.

Calvo, J., Jung, H., and Meloni, G. (2017). Copper metallothioneins. IUBMB Life *69*, 236–245.

Cerar, T., Strle, F., Stupica, D., Ruzic-Sabljic, E., Mchugh, G., Steere, A.C., and Strle, K. (2016). Differences in genotype, clinical features, and inflammatory potential of Borrelia burgdorferi sensu stricto strains from Europe and the United States. Emerg. Infect. Dis. *22*, 818–827.

Coburn, J., Garcia, B., Hu, L.T., Jewett, M.W., Kraiczy, P., Norris, S.J., and Skare, J. (2021). Lyme disease pathogenesis. Curr. Issues Mol. Biol. *42*, 473–518.

Coburn, J., Magoun, L., Bodary, S.C., and Leong, J.M. (1998). Integrins alpha(v)beta3 and alpha5beta1 mediate attachment of lyme disease spirochetes to human cells. Infect. Immun. *66*, 1946–1952.

Coleman, J.L., Sellati, T.J., Testa, J.E., Kew, R.R., Furie, M.B., and Benach, J.L. (1995). Borrelia burgdorferi binds plasminogen, resulting in enhanced penetration of endothelial monolayers. Infect. Immun. *63*, 2478–2484.

Danilova, T.A., Danilina, G.A., Adzhieva, A.A., Vostrova, E.I., Zhukhovitskii, V.G., and Cheknev, S.B. (2020). Inhibitory effect of copper and zinc ions on the growth of Streptococcus pyogenes and Escherichia coli biofilms. Bull. Exp. Biol. Med. *169*, 648–652.

del Álamo, J.C., Meili, R., Alonso-Latorre, B., Rodríguez-Rodríguez, J., Aliseda, A., Firtel, R.A., and Lasheras, J.C. (2007). Spatio-temporal analysis of eukaryotic cell motility by improved force cytometry. Proc. Natl. Acad. Sci. USA *104*, 13343–13348.

Dev, A., Iyer, S., Razani, B., and Cheng, G. (2011). NF-kappaB and innate immunity. Curr.Top.Microbiol. Immunol. *349*, 115–143.

Dunham-Ems, S.M., Caimano, M.J., Pal, U., Wolgemuth, C.W., Eggers, C.H., Balic, A., and Radolf, J.D. (2009). Live imaging reveals a biphasic mode of dissemination of Borrelia burgdorferi within ticks. J. Clin. Invest. *119*, 3652–3665.

Ebady, R., Niddam, A.F., Boczula, A.E., Kim, Y.R., Gupta, N., Tang, T.T., Odisho, T., Zhi, H., Simmons, C.A., Skare, J.T., and Moriarty, T.J. (2016). Biomechanics of Borrelia burgdorferi vascular interactions. Cell Rep. *16*, 2593–2604.

Edelstein, A.D., Tsuchida, M.A., Amodaj, N., Pinkard, H., Vale, R.D., and Stuurman, N. (2014). Advanced methods of microscope control using μManager software. J. Biol. Methods *1*, e10.

Faralla, C., Bastounis, E.E., Ortega, F.E., Light, S.H., Rizzuto, G., Gao, L., Marciano, D.K., Nocadello, S., Anderson, W.F., Robbins, J.R., et al. (2018). Listeria monocytogenes InlP interacts with afadin and facilitates basement membrane crossing. PLoS Pathog. *14*, e1007094.

Feria-Arroyo, T.P., Castro-Arellano, I., Gordillo-Perez, G., Cavazos, A.L., Vargas-Sandoval, M., Grover, A., Torres, J., Medina, R.F., de León, A.A.P., and Esteve-Gassent, M.D. (2014). Implications of climate change on the distribution of the tick vector Ixodes scapularis and risk for Lyme disease in the Texas-Mexico transboundary region. Parasit. Vectors *7*, 199.

Gebbia, J.A., Coleman, J.L., and Benach, J.L. (2001). Borrelia spirochetes upregulate release and activation of matrix metalloproteinase gelatinase B (MMP-9) and collagenase 1 (MMP-1) in human cells. Infect. Immun. *69*, 456–462.

Girschick, H.J., Huppertz, H.I., Rüssmann, H., Krenn, V., and Karch, H. (1996). Intracellular persistence ofBorrelia burgdorferi in human synovial cells. Rheumatol. Int. *16*, 125–132.

Gui, L., and Wereley, S.T. (2002). A correlation-based continuous window-shift technique to reduce the peak-locking effect in digital PIV image evaluation. Exp. Fluids *32*, 506–517.

Haage, A., and Schneider, I.C. (2014). Cellular contractility and extracellular matrix stiffness regulate matrix metalloproteinase activity in pancreatic cancer cells. FASEB J. *28*, 3589–3599.

Hur, S.S., del Álamo, J.C., Park, J.S., Li, Y.S., Nguyen, H.A., Teng, D., Wang, K.C., Flores, L., Alonso-Latorre, B., Lasheras, J.C., and Chien, S. (2012). Roles of cell confluency and fluid shear in 3-dimensional intracellular forces in endothelial cells. Proc. Natl. Acad. Sci. USA *109*, 11110–11115.

Jutras, B.L., Lochhead, R.B., Kloos, Z.A., Biboy, J., Strle, K., Booth, C.J., Govers, S.K., Gray, J., Schumann, P., Vollmer, W., et al. (2019). Borrelia burgdorferi peptidoglycan is a persistent antigen in patients with Lyme arthritis. Proc. Natl. Acad. Sci. USA *116*, 13498–13507.

Jutras, B.L., Scott, M., Parry, B., Biboy, J., Gray, J., Vollmer, W., and Jacobs-Wagner, C. (2016). Lyme disease and relapsing fever Borrelia elongate through zones of peptidoglycan synthesis that mark division sites of daughter cells. Proc. Natl. Acad. Sci. USA *113*, 9162–9170.

Kempe, S., Kestler, H., Lasar, A., and Wirth, T. (2005). NF0ºB controls the global pro-inflammatory response in endothelial cells: evidence for the regulation of a pro-atherogenic program. Nucleic Acids Res. *33*, 5308–5319.

Kim, D., Langmead, B., and Salzberg, S.L. (2015). HISAT: a fast spliced aligner with low memory requirements. Nat. Methods *12*, 357–360.

Kisseleva, T., Song, L., Vorontchikhina, M., Feirt, N., Kitajewski, J., and Schindler, C. (2006). NF-kappaB regulation of endothelial cell function during LPS-induced toxemia and cancer. J. Clin. Invest. *116*, 2955–2963.

Koenderink, J.J., and van Doorn, A.J. (1987). Representation of local geometry in the visual system. Biol. Cybern. *55*, 367–375.

Komarova, Y.A., Kruse, K., Mehta, D., and Malik, A.B. (2017). Protein interactions at endothelial junctions and signaling mechanisms regulating endothelial permeability. Circ. Res. *120*, 179–206.

Krämer, C.E.M., Wiechert, W., and Kohlheyer, D. (2016). Time-resolved, single-cell analysis of induced and programmed cell death via non-invasive propidium iodide and counterstain perfusion. Sci. Rep. *6*, 32104.

Kumar, D., Ristow, L.C., Shi, M., Mukherjee, P., Caine, J.A., Lee, W.-Y., Kubes, P., Coburn, J., and Chaconas, G. (2015). Intravital imaging of vascular transmigration by the lyme spirochete: requirement for the integrin binding residues of the B. Burgdorferi P66 protein. PLoS Pathog. *11*, e1005333.

Kumru, O.S., Schulze, R.J., Rodnin, M.V., Ladokhin, A.S., and Zückert, W.R. (2011). Surface localization determinants of Borrelia OspC/Vsp family lipoproteins. J. Bacteriol. *193*, 2814–2825.

LaFrance, M.E., Pierce, J.V., Antonara, S., and Coburn, J. (2011). The Borrelia burgdorferi integrin ligand P66 affects gene expression by human cells in culture. Infect. Immun. *79*, 3249–3261.

Lamason, R.L., Bastounis, E., Kafai, N.M., Serrano, R., Del Álamo, J.C., Theriot, J.A., and Welch, M.D. (2016). Rickettsia Sca4 reduces vinculin-mediated intercellular tension to promote spread. Cell *167*, 670–683.e10.

Lappas, M. (2013). NOD1 and NOD2 regulate proinflammatory and prolabor mediators in human fetal membranes and myometrium via nuclear factor-kappa B. Biol. Reprod. *89*, 14.

Larsen, M., Tremblay, M.L., and Yamada, K.M. (2003). Phosphatases in cell-matrix adhesion and migration. Nat. Rev. Mol. Cell Biol. *4*, 700–711.

Leavesley, D.I., Schwartz, M.A., Rosenfeld, M., and Cheresh, D.A. (1993). Integrin beta 1- and beta 3-mediated endothelial cell migration is triggered through distinct signaling mechanisms. J. Cell Biol. *121*, 163–170.

Lee, S.Y., Zaske, A.M., Novellino, T., Danila, D., Ferrari, M., Conyers, J., and Decuzzi, P. (2011). Probing the mechanical properties of TNF-α stimulated endothelial cell with atomic force microscopy. Int. J. Nanomed. *6*, 179–195.

Livengood, J.A., and Gilmore, R.D., Jr. (2006). Invasion of human neuronal and glial cells by an infectious strain of Borrelia burgdorferi. Microbes Infect. *8*, 2832–2840.

Luo, W., Friedman, M.S., Shedden, K., Hankenson, K.D., and Woolf, P.J. (2009). GAGE: generally applicable gene set enrichment for pathway analysis. BMC Bioinf. *10*, 161.

Luo, W., Pant, G., Bhavnasi, Y.K., Blanchard, S.G., Jr., and Brouwer, C. (2017). Pathview Web: user friendly pathway visualization and data integration. Nucleic Acids Res. *45*, W501–W508.

Ma, Y., Sturrock, A., and Weis, J.J. (1991). Intracellular localization of Borrelia burgdorferi within human endothelial cells. Infect. Immun. *59*, 671–678.

Martin, M. (2011). Cutadapt removes adapter sequences from high-throughput sequencing reads. EMBnet.J. *17*, 10.

Meriläinen, L., Herranen, A., Schwarzbach, A., and Gilbert, L. (2015). Morphological and biochemical features of Borrelia burgdorferi pleomorphic forms. Microbiology *161*, 516–527.

Moriarty, T.J., Norman, M.U., Colarusso, P., Bankhead, T., Kubes, P., and Chaconas, G. (2008). Real-time high resolution 3D imaging of the lyme disease spirochete adhering to and escaping from the vasculature of a living host. PLoS Pathog. *4*, e1000090.

Murgia, R., and Cinco, M. (2004). Induction of cystic forms by different stress conditions in Borrelia burgdorferi. APMIS *112*, 57–62.

Niddam, A.F., Ebady, R., Bansal, A., Koehler, A., Hinz, B., and Moriarty, T.J. (2017). Plasma fibronectin stabilizes Borrelia burgdorferi-endothelial interactions under vascular shear stress by a catch-bond mechanism. Proc. Natl. Acad. Sci. USA *114*. E3490–e3498.

Ostrowski, M.A., Huang, N.F., Walker, T.W., VerwijleN, T., Poplawski, C., Khoo, A.S., Cooke, J.P., Fuller, G.G., and Dunn, A.R. (2014). Microvascular endothelial cells migrate upstream and align against the shear stress field created by impinging flow. Biophys. J. *106*, 366–374.

Otte, S., Ipiña, E.P., Pontier-Bres, R., Czerucka, D., and Peruani, F. (2021). Statistics of pathogenic bacteria in the search of host cells. Nat. Commun. *12*, 1990.

Oñate, E. (2013). Structural Analysis with the Finite Element Method. Linear Statics, *2* (Springer).

Parthasarathy, G., Fevrier, H.B., and Philipp, M.T. (2013). Non-viable Borrelia burgdorferi induce inflammatory mediators and apoptosis in human oligodendrocytes. Neurosci. Lett. *556*, 200–203.

Quehenberger, P., Bierhaus, A., Fasching, P., Muellner, C., Klevesath, M., Hong, M., Stier, G., Sattler, M., Schleicher, E., Speiser, W., and Nawroth, P.P. (2000). Endothelin 1 transcription is controlled by nuclear factor-kappaB in AGE-stimulated cultured endothelial cells. Diabetes *49*, 1561–1570.

Ranzato, M., Taylor, P.E., House, J.M., Flagan, R.C., Lecun, Y., and Perona, P. (2007). Automatic recognition of biological particles in microscopic images. Pattern Recogn. Lett. *28*, 31–39.

Reed, S.C.O., Lamason, R.L., Risca, V.I., Abernathy, E., and Welch, M.D. (2014). Rickettsia actin-based motility occurs in distinct phases mediated by different actin nucleators. Curr. Biol. *24*, 98–103.

Reinhart-King, C.A., Dembo, M., and Hammer, D.A. (2005). The dynamics and mechanics of endothelial cell spreading. Biophys. J. *89*, 676–689.

Replogle, A.J., Sexton, C., Young, J., Kingry, L.C., Schriefer, M.E., Dolan, M., Johnson, T.L., Connally, N.P., Padgett, K.A., and Petersen, J.M. (2021). Isolation of Borrelia miyamotoi and other Borreliae using a modified BSK medium. Sci. Rep. *11*, 1926.

Rokhzan, R., Ghosh, C.C., Schaible, N., Notbohm, J., Yoshie, H., Ehrlicher, A.J., Higgins, S.J., Zhang, R., Haller, H., Hardin, C.C., et al. (2019). Multiplexed, high-throughput measurements of cell contraction and endothelial barrier function. Lab. Invest. *99*, 138–145.

Rouse, J., Wahhab, A., Danner, R., Jutras, B., and Lochhead, R. (2021). Borrelia burgdorferi peptidoglycan triggers inflammatory responses in Lyme arthritis. J. Immunol. *206*. 52.17.

Russell, T.M., Delorey, M.J., and Johnson, B.J.B. (2013). Borrelia burgdorferi BbHtrA degrades host ECM proteins and stimulates release of inflammatory cytokines in vitro. Mol. Microbiol. *90*, 241–251.

Sapi, E., Bastian, S.L., Mpoy, C.M., Scott, S., Rattelle, A., Pabbati, N., Poruri, A., Burugu, D., Theophilus, P.A.S., Pham, T.V., et al. (2012). Characterization of biofilm formation by Borrelia burgdorferi in vitro. PLoS One *7*, e48277.

Saputra, E.P., Trzeciakowski, J.P., and Hyde, J.A. (2020). Borrelia burgdorferi spatiotemporal regulation of transcriptional regulator bosR and decorin binding protein during murine infection. Sci. Rep. *10*, 12534.

Schneider, C.A., Rasband, W.S., and Eliceiri, K.W. (2012). NIH Image to ImageJ: 25 years of image analysis. Nat. Methods *9*, 671–675. https:/doi.org/10.1038/nmeth.2089.

Shan, J., Jia, Y., Teulières, L., Patel, F., and Clokie, M.R.J. (2021). Targeting multicopy prophage genes for the increased detection of Borrelia burgdorferi sensu lato (s.l.), the causative agents of lyme disease, in blood. Front. Microbiol. *12*, 464.

Smolentseva, O., Gusarov, I., Gautier, L., Shamovsky, I., Defrancesco, A.S., Losick, R., and Nudler, E. (2017). Mechanism of biofilm-mediated stress resistance and lifespan extension in C. elegans. Sci. Rep. *7*, 7137.

Stroka, K.M., Vaitkus, J.A., and Aranda-Espinoza, H. (2012). Endothelial cells undergo morphological, biomechanical, and dynamic changes in response to tumor necrosis factor-α. Eur. Biophys. J. *41*, 939–947.

Tambe, D.T., Hardin, C.C., Angelini, T.E., Rajendran, K., Park, C.Y., Serra-Picamal, X., Zhou, E.H., Zaman, M.H., Butler, J.P., Weitz, D.A., et al. (2011). Collective cell guidance by cooperative intercellular forces. Nat. Mater. *10*, 469–475.

Tan, X., Petri, B., Devinney, R., Jenne, C.N., and Chaconas, G. (2021). The Lyme disease spirochete can hijack the host immune system for extravasation from the microvasculature. Mol. Microbiol. *116*, 498–515.

Trepat, X., Wasserman, M.R., Angelini, T.E., Millet, E., Weitz, D.A., Butler, J.P., and Fredberg, J.J. (2009). Physical forces during collective cell migration. Nat. Phys. *5*, 426–430.

Urbano, R.L., Furia, C., Basehore, S., and Clyne, A.M. (2017). Stiff substrates increase inflammation-induced endothelial monolayer tension and permeability. Biophys. J. *113*, 645–655.

Wang, G., Petzke, M.M., Iyer, R., Wu, H., and Schwartz, I. (2008). Pattern of proinflammatory cytokine induction in RAW264.7 mouse macrophages is identical for virulent and attenuated Borrelia burgdorferi. J. Immunol. *180*, 8306–8315.

Wu, J., Weening, E.H., Faske, J.B., Höök, M., and Skare, J.T. (2011). Invasion of eukaryotic cells by Borrelia burgdorferi requires beta(1) integrins and Src kinase activity. Infect. Immun. *79*, 1338–1348.

STAR★METHODS

KEY RESOURCES TABLE

REAGENT or RESOURCE	SOURCE	IDENTIFIER
Antibodies		
Rabbit polyclonal anti-*Borrelia burgdorferi* antibody	Thermo Fisher Scientific	Cat# PA1-73004, RRID:AB_1016668
Mouse monoclonal anti-integrin β1	Millipore	Cat# MAB1987; RRID:AB_94493
Mouse monoclonal anti-integrin αvβ3	Sigma	Cat# MAB1976; RRID: AB_2296419
Chemicals, peptides, and recombinant proteins		
AlexaFluor546 phalloidin	Thermo Fisher Scientific	Cat# A22283
SulfoSanpah	Thermo Fisher Scientific	Cat# 22589
Collagen I rat tail	Fisher	Cat# A1048301
Acrylamide 40% solution	Sigma	Cat# A4058
Bisacrylamide solution 2%	Fisher	Cat# BP1404250
Aminopropyltriethoxysilane	Sigma	Cat# 919302
FluoSpheres™ Carboxylate-Modified Microspheres, 0.2 μm, yellow-green fluorescent (580/605), 2% solids	Invitrogen	Cat# F8810
FluoSpheres™ Carboxylate-Modified Microspheres, 0.2 μm, yellow-green fluorescent (660/680), 2% solids	Invitrogen	Cat# F8807
MCDB131	Gibco	Cat# 10372019
Leibovitz's L-15 medium, no phenol red	Thermo Fisher Scientific	Cat# 21083027
Fetal bovine serum	Gemini Bio-Prod	Cat# 900108
Hydrocortisone	Sigma	Cat# H0888
hEGF	Sigma	Cat# EG9644
L-Glutamine	Fisher	Cat# SH3003401
Hoechst 33342, trihydrochloride	Invitrogen	Cat# H3570
BSK-H Medium	Sigma	Cat# B3528
Rabbit serum	Sigma	Cat# R4505
Gentamicin	Thermo Fisher Scientific	Cat# 15710064
Propidium iodide	Sigma	Cat# P4170
Recombinant human TNF-α	InvivoGen	Cat# rcyc-htnfa
Muramyldipeptide - MDP | NOD2 ligand	InvivoGen	Cat# tlrl-mdp
Critical commercial assays		
QIAshredder Kit	Qiagen	Cat# 79656
RNeasy Plus MicroKit	Qiagen	Cat# 74034
PrimeScript™ RT Reagent Kit	Takara Bio	Cat# RR037A
KAPA SYBR® FAST	Kapa Biosystems	Cat# KK4601
Deposited data		
RNA-seq data	This paper	GSE174545
Experimental models: Cell lines		
HMEC-1 cells	M. Welch (Reed et al., 2014)	Previously obtained from Centers for Disease Control, Biological Products Branch

(*Continued on next page*)

Continued

REAGENT or RESOURCE	SOURCE	IDENTIFIER
Experimental models: Organisms/strains		
Borrelia burgdorferi (strain Bb1286)	J. Radolph (Dunham-Ems et al., 2009)	N/A
Borrelia burgdorferi (strain GCB726)	P. Kraiczy (Moriarty et al., 2008)	N/A
Oligonucleotides		
Primers for ICAM1 (forward: 5′ GAGCTTCGTGTCCTGTATGGC -3′, reverse: 5′ ACAGAGGTAGGTGCCCTCAA -3′)	This paper	N/A
Primers for CXCL8 (forward: 5′ CAGAGACAGCAGAGCACACA -3′, reverse: 5′ GGCAAAACTGCACCTTCACA -3′)	This paper	N/A
Primers for NFKBIA (forward: 5′ ATGTCAATGCTCAGGAGCCC -3′, reverse: 5′ CAGGTGAGCTGGTAGGGAGA -3′)	This paper	N/A
Primers for GAPDH (forward: 5′ GGGAAACTGTGGCGTGAT -3′, reverse: 5′ GAGTGGGTGTCGCTGTTGA -3′)	This paper	N/A
Software and algorithms		
ImageJ	Schneider et al., 2012	https://imagej.nih.gov/ij/
MicroManager	Open Imaging	https://www.micro-manager.org/
MATLAB	MathWorks	http://www.mathworks.com/products/matlab/?requestedDomain=www.mathworks.com
GraphPad Prism v6	GraphPad	http://www.graphpad.com/scientific-software/prism/
Hisat 2	(Kim et al., 2015)	https://ccb.jhu.edu/software/hisat2/index.shtml)
Cutadapt	(Martin, 2011)	https://cutadapt.readthedocs.io/en/stable/
R package GAGE	(Luo et al., 2009)	https://bioconductor.org/packages/release/bioc/html/gage.html
R package "Pathview"	(Luo et al., 2017)	https://www.bioconductor.org/packages/release/bioc/html/pathview.html
ABAQUS	Dassault systèmes	https://www.3ds.com/products-services/simulia/products/abaqus/
QuantStudio™ Design and Analysis Software v2	Applied Biosystems	https://www.thermofisher.com/de/en/home/global/forms/life-science/quantstudio-3-5-software.html
Imaris	Bitplane	https://imaris.oxinst.com/

RESOURCE AVAILABILITY

Lead contact

Further information and requests for reagents may be directed to and will be fulfilled by the Lead Contact Effie Bastounis effie.bastounis@uni-tuebingen.de (E.E.B.).

Materials availability

Materials developed in this study are available on request to the corresponding author.

Data and code availability

Data collected and computer codes are available on request to the corresponding authors and are also publicly available at: https://github.com/ebastoun/Monolayer-Stress Microscopy (codes for calculating monolayer stresses) and https://github.com/ebastoun/borrelia_PI_colocalisation (codes for calculating

colocalization between bacteria and propidium iodide staining). The RNA sequencing data (FASTq files) generated during this study and subsequent analysis are available at the Gene Expression Omnibus (GEO) database (weblink: https://www.ncbi.nlm.nih.gov/geo/query/acc.cgi?acc=GSE174545, series record number: GSE174545). All differential expression analysis results of this study are included as supplementary tables in this article. Any additional information required to reanalyze the data reported in this paper is available from the lead contact upon request.

EXPERIMENTAL MODEL AND SUBJECT DETAILS

Cell culture

Human dermal microvascular endothelial cells HMEC-1 (generous gift from the Welch lab, University of California, Berkeley previously obtained from Centers for Disease Control, Biological Products Branch) were maintained in MCDB131 medium (Fisher Scientific; 10372-019) supplemented with 10% fetal bovine serum (GemBio, 900108), 10 ng/mL epidermal growth factor (Sigma, E9644), 1 μg/mL hydrocortisone (Sigma, H0888), and 2 mM L-Glutamine (Sigma, 56-85-9) (Reed et al., 2014). Cells were passaged 1:6 at 90% confluence.

Bacterial strains used in this study

We used *Borrelia burgdorferi* (*Bb*) constitutively expressing GFP, strain Bb1286, indicated as *Bb-GFP* throughout the main text. This strain was a generous gift from Justin Radolf's lab, University of Connecticut Health Center (Dunham-Ems et al., 2009). For the experiments involving exposure of human cells to heat-inactivated *Bb-GFP* we used strain GCB726. This strain, similar to Bb1286, was generated by electroporation of the infectious *Bb* strain B31 5A4 NP1 with the shuttle vector pTM61 that contains all plasmids except the circular plasmid cp9. The construction of this strain has been previously described (Moriarty et al., 2008). Bb1286 strain was generated also from B31 5A4 NP1 which was then electroporated with a suicide vector to produce a cp26 plasmid containing the GFP expressing gene (Caimano et al., 2015). Thus, the two strains we used are almost identical and just differ in only one plasmid.

METHOD DETAILS

Bacterial growth conditions and exposure of ECs to *Borrelia burgdorferi*

Borrelia burgdorferi (*Bb*) strain Bb1286 or GCB726 were grown to mid log phase (approximately $5x10^7$ bacteria/mL) in BSK-H media (Sigma, B3528) supplemented with 50 μg/mL gentamicin (Dunham-Ems et al., 2009). For cultivation of strain GCB726, BSK-H medium (Bio&Sell, Feucht, Germany) supplemented with 5.4% rabbit serum (Sigma, R4505), 50 μg/mL gentamicin and 100 μg/mL kanamycin was used. Briefly, 10 μL of frozen glycerol stock was added into a tube containing 1.5 mL of BSK-H media supplemented with appropriate antibiotics. The tube was placed at 37°C and until the concentration of the bacteria reached $2\text{-}5x10^6$ bacteria/mL. The bacterial solution was then diluted at $1x10^3$ bacteria/mL and bacteria were grown in fresh BSK-H with antibiotics at 37°C until a density of $5x10^7$ bacteria/mL growing as single spirochetes was reached (see Figure 1A). Bacterial concentrations were determined using a hemocytometer and a dark field microscope (generously provided by the Mougous lab, University of Washington).

The day prior to*Bb-GFP* exposure, ECs were seeded at a density of 2×10^5 cells/well on glass bottom wells of 24-well plates coated with 0.25 mg/mL rat tail collagen I (Sigma-Aldrich, C3867) or on 3 kPa polyacrylamide hydrogels also coated with 0.25 mg/mL rat tail collagen I. For microscopy recordings, cell medium was removed and, instead of MCDB131, Leibovitz's L-15 medium was used supplemented with 10% fetal bovine serum, 10 ng/mL epidermal growth factor, 1 μg/mL hydrocortisone, and 2 mM L-glutamine. For experiments involving tracking of host cell nuclei, 1 μg/mL Hoechst (Thermofisher, D1306) was added in each well to stain the cells' nuclei for 10minat 37°C. Cells were then washed once in warm media to remove excess stain. Just prior to infection bacteria were spun down, washed once in PBS and then resuspended in cell media so that minimal volumes of bacteria (1-30 μL) were added in each well to achieve the target multiplicity of infection (MOI, bacteria/host cell).

For generation of heat-inactivated *Bb-GFP*, bacteria were incubated at 56°C for 30 min as previously reported (Replogle et al., 2021). Subsequently, heat-inactivated *Bb*were stored at 4°C to avoid damage of the *Bb* membrane or morphology that can occur at lower temperatures.

Flow cytometry of ECs exposed to *Bb-GFP*

4 h post-exposure (hpe), ECs exposed to *Bb-GFP* at different MOIs were washed 4 times with sterile phosphate-buffered saline (PBS) to get rid of extracellular bacteria (Otte et al., 2021). Cells were then detached from the glass coverslip where they resided, by removing cell medium and adding 200 μL of 0.25% trypsin-EDTA in each well for 10 min at 37°C. Trypsin-EDTA cell-containing solutions in each well were then pipetted up and down 6 times to ensure single cell suspensions and 200 μL of complete medium were added to inactivate trypsin in each well. Suspensions were transferred into 35-μm cell strainers, (Falcon, 352235) and spun through at 500 x g followed by fixation in 1% paraformaldehyde for 10 min on ice. Samples were then washed once in PBS and stored in PBS with 1% BSA on ice or at 4°C. Flow cytometry analysis was performed on a BD FACS Canto RUO analyzer (University of Washington Cell Analysis Facility). 10,000-20,000 cells were analyzed per each replicate. To ensure analysis of single ECs, the bulk of the distribution of cell counts was gated using the forward versus side scatter plot and thus discarding debris or cell doublets or triplets from the analysis. In addition, a second gating step was applied after measuring the fluorescence of control, unexposed cells and gating the population of exposed cells accordingly to exclude cell autofluorescence.

Bb segmentation and morphology-dependent classification

To segment and classify bacteria depending on their morphology we used using IMARIS software (Bitplane) on the time-lapse epifluorescence images of bacteria. We opted for smoothing using surfaces detail parameter equal to 0.4 μm and thresholding was performed after background subtraction (local contrast) with the diameter of the largest sphere which fits into the object equal to 0.6 μm. An Imaris 9.6 built-in classifier was then used to classify bacteria to three distinct categories, namely: (1) single objects (spirochetes or spot-like structures); (2) bacterial networks; and (3) bacterial aggregates. For machine learning classification of surfaces Imaris 9.6 uses the existing statistics values and in addition computes more values that provide additional intensity and shape information. To provide additional shape descriptors the position and radius of the biggest sphere that fits entirely within the surface were computed and a number of features were derived from this. The original Surfaces statistics together with the machine learning statistics provide a lot of information about the shape of a surface and can be very useful for a machine learning classifier for surfaces as previously implemented elsewhere (Ranzato et al., 2007; Koenderink and van Doorn, 1987). For training, the user instigated 15 distinct objects for each class. For each instance of time the number of bacteria that fell in each category was extracted as well as average surface area (μm^2) and mean object fluorescence intensity as illustrated in Figures 2D and S2A and S2B.

Fabrication of polyacrylamide hydrogels

Polyacrylamide hydrogel fabrication was done as previously described (Bastounis et al., 2018, 2021). Glass-bottom plates with 24 wells (MatTek, P24G-1.5-13-F) were incubated for 1 h with 500 μL of 1 M NaOH, then rinsed with distilled water, and incubated with 500 μL of 2% 3-aminopropyltriethoxysilane (Sigma, 919-30-2) in 95% ethanol for 5 min. After rinsing with water, 500 μL of 0.5% glutaraldehyde were added to each well for 30 min. Wells were then rinsed with water and dried at 60°C. To prepare polyacrylamide hydrogels of 3 kPa, mixtures containing 5% acrylamide (Sigma, A4058) and 0.1% bis-acrylamide (Fisher, BP1404-250) were prepared (Bastounis et al., 2018). Two mixtures were prepared, the second of which contained 0.2 μm fluorescent beads at 0.03% (Invitrogen, F8811) for traction force microscopy (TFM) experiments. 0.06% ammonium persulfate and 0.43% TEMED were then added to the first solution to initiate polymerization. First, 3.6 μL of the first mixture without beads were added at the center of each well, capped with 12-mm untreated circular glass coverslips, and allowed to polymerize for 20 min. After coverslip removal 2.4 μL of the mixture containing tracer beads were added and sandwiched again with a 12-mm untreated circular glass coverslip and allowed to polymerize for 20 min. Next, 50 mM HEPES at pH 7.5 was added to the wells, and coverslips were removed. Hydrogels were UV-sterilized for 1 h and then activated by adding 200 μL of 0.5% weight/volume heterobifunctional cross-linker Sulfo-SANPAH (Fisher, 22589) in 1% dimethyl sulfoxide (DMSO) and 50 mM HEPES, pH 7.5, on the upper surface of the hydrogels and exposing them to UV light for 10 min. Hydrogels were washed with 50 mM HEPES at pH 7.5 and were coated with 200 μL of 0.25 mg/mL rat tail collagen I (Fisher, A1048301) in 50 mM HEPES at pH 7.5 overnight at room temperature. Next morning, the collagen coated surfaces were washed with HEPES and gels were stored in HEPES.

Traction force microscopy (TFM)

TFM was performed as previously described (del Álamo et al., 2007; Lamason et al., 2016). Briefly, in TFM, cells actively pull on their ECM depending on how well their focal adhesions are organized and connected

to the underlying cytoskeleton, and cellular force generation can be inferred from displacement of fluorescent tracer particles embedded in the deformable ECM (Bastounis et al., 2014; del Álamo et al., 2007). Prior to seeding ECs (as described above) hydrogels were equilibrated with MCDB131 medium for 30 min at 37°C. ECs were then seeded to a concentration of 2 x 10^5 cells/well directly onto the hydrogels 24 h prior to *Bb*-exposure. 1 h prior to initiation of the TFM recording, MCDB131 medium was replaced with L-15 medium supplemented appropriately. Multi-channel time-lapse sequences were acquired to image the tracer beads' fluorescence, the bacterial fluorescence, and the phase contrast image of ECs. Images were acquired using an inverted Nikon Eclipse Ti2 with an EMCCD camera (Andor Technologies) using a 40X 0.60NA Plan Fluor air objective and the MicroManager software package (Edelstein et al., 2014). The microscope was surrounded by a box type incubator (Haison) maintained at 37°C. Images were acquired every 10 min for approximately 3-8 h before *Bb-GFP* bacteria were added (or not for control wells) on the wells at an MOI of ~200*Bb*/cell. Subsequently, at each time interval we measured the 2D deformation of the substrate at each point using an image correlation technique similar to particle image velocimetry (Gui and Wereley, 2002).

We calculated the local deformation vector by performing image correlation between each image and a non-deformed reference image which we acquired by adding 10% SDS at the end of each recording to detach the cells from the hydrogels. We used interrogation windows of 32 x 16 pixels (window size x overlap). Calculations of the two-dimensional traction stresses that cell monolayers exert on the hydrogel are described elsewhere (Lamason et al., 2016; Bastounis et al., 2014). We calculated the strain energy (U_s) as the mechanical work imparted by cells to deform the hydrogel:

$$U_s = \frac{1}{2}\int_s \boldsymbol{t}(z = h)\cdot\boldsymbol{u}(z = h)ds \qquad \text{(Equation 1)}$$

where $\mathbf{u}(z = h)$ is the measured displacement vector field on the free surface of the hydrogel, $\boldsymbol{t}$ is the calculated traction stress vector field, $\int_s ds$ represents the surface integral, h is the height of the hydrogel and z the vertical coordinate. For each field of view analyzed originating from different wells we normalized the strain energy value with that of *time* = 0 min, to avoid discrepancies due to slight differences in cell confluence among wells. To quantitate how dynamic the traction adhesions of ECs is we preformed 2D cross-correlations between successive cell deformation maps (obtained via TFM) separated by different time delays using the corr2 function in MATLAB (MathWorks) that returns the 2D correlation coefficient. The resulting data shown in Figure S3 were then fitted to an exponential decay function of the form:

$$Y = (Y_0 - Plateau)\cdot\exp(-K\cdot X) + Plateau \qquad \text{(Equation 2)}$$

where Y_0 is the Y value at time equal 0, *Plateau* is the Y value at infinite times and K is the rate constant.

Monolayer stress microscopy (MSM)

We used MSM to measure the tensile and compressive stresses that ECs in monolayer experience. These stresses arise due to the cells contracting, expanding, or remaining in a resting state at different spatial locations within the monolayer and are due to reorganization of their cytoskeleton and adhesion complexes. These cytoskeletal rearrangements lead to pushing or pulling forces that affect adjacent cells, resulting in cell movements and changes in cell size and shape. Even if a given cell is also deformed due to its own remodelling and active behaviour, this cell deformation is a consequence of the stress distribution in the monolayer. This distribution is governed by the internal forces per unit of area, defining the monolayer configuration. Consequently, the stress distribution changes at each point (Figures 4A and S4). For measuring intercellular forces indirectly via MSM, we use the previously computed via TFM traction stresses that the cells in the monolayer exert on their substratum under the assumption that the traction stresses in the vertical direction are negligible, as considered previously (Lamason et al., 2016). We also assume that traction stresses in the hydrogel-monolayer interface occur only in the plane of the monolayer (i.e., there is no component of the traction stresses in the normal direction of the interface) as done previously (Trepat et al., 2009). Traction forces exerted by the cells on the hydrogel need to balance with the forces exerted by the cells to each other in the monolayer (third Newton's law). To that end, we consider idealised perfect cell-substrate adhesions.

To determine the monolayer tensile and compressive stresses, we make several simplifications. First, we consider that the thickness of the monolayer is constant and uniform. Second, regarding material properties of the monolayer, we assume perfect cell-cell adhesions (the monolayer is assumed to be a continuum)

and the properties of the monolayer are considered everywhere the same. That is all cells and adhesions in the monolayer have the same mechanical properties and the cell monolayer is considered as a linear elastic isotropic material (Tambe et al., 2011). Third, we work under the small strain assumption, so both the strains induced in the hydrogel and the configuration changes in the monolayer at each time increment (time distance between subsequent frames) are small. These assumptions dramatically simplify the formulation of the problem, since we can work in a two-dimensional framework assuming a plane stress formulation to solve the problem. Thus, the stress distribution is assumed constant through the monolayer thickness.

In this case, the equilibrium equations, compatibility, and constitutive equations yield the Beltrami differential formulation:

$$\frac{\partial^2(\sigma_x+\sigma_y)}{\partial x^2}+\frac{\partial^2(\sigma_x+\sigma_y)}{\partial y^2}=-\frac{(1+\nu)}{h}\left(\frac{\partial t_x}{\partial x}+\frac{\partial t_y}{\partial y}\right) \quad \text{(Equation 3)}$$

The advantage of using the Beltrami equation is that we can compute stresses at each point without knowing the elastic modulus of the monolayer. This equation, together with the Newton's equilibrium equations, formulated at each point of the monolayer in a differential way, yield the distribution of the stresses in the monolayer:

$$\begin{aligned}\frac{\partial\sigma_x}{\partial x}+\frac{\partial\tau_{yx}}{\partial y}+\frac{t_x}{h}=0\\ \frac{\partial\tau_{xy}}{\partial x}+\frac{\partial\sigma_y}{\partial y}+\frac{t_y}{h}=0\end{aligned} \quad \text{(Equation 4)}$$

where v is the Poisson's coefficient, t_x and $t_y$are the traction forces in the monolayer in the x and y directions, respectively (components of traction stress vector field $\boldsymbol{t}$); σ_x, σ_y are monolayer normal tension/compression stresses in the x and y directions, τ_{yx} and τ_{xy} are the monolayer shear stresses in x and y directions respectively. These shear stress components are equal (τ_{yx}=τ_{xy}) due to equilibrium. All these stresses will be different at each point of the monolayer (Figure S4A).

Although stresses in the $\boldsymbol{x}-\boldsymbol{y}$ directions are easy to retrieve, the physical meaning is difficult to interpret since the $x-y$ coordinate system is an arbitrary system, normally aligned with the image and not with the behaviour of the cell. To overcome this challenge, we transform our results into a new coordinate system (***I***, ***II***), principal coordinate system, in which there is no shear component of stress (Figure S4B). By aligning with the axis of this coordinate system, we can compute the maximum monolayer tension (σ_I) and compressions (σ_{II}) in the plane of the monolayer, (σ_I>σ_{II}). In fact, the maximum tension occurs in a perpendicular direction to the maximum compression. Both values of maximum tension and compression and their directions vary along the different points of the monolayer.

We solve the equations of the problem through a finite element formulation (Oñate, 2013) and implement the final equations into a custom-made finite element code in MATLAB (R2020b). In the simulations, the monolayer is discretized with square elements of the same size as the pixels (3.648 × 3.648 μm^2) resulting in 4225 nodes and 4096 elements. As boundary conditions, the displacements along the edge of the monolayer/image were set to zero. We choose arbitrary elastic modulus for the monolayer, since in this formulation the stresses are independent of this mechanical property of the monolayer. The Poisson's coefficient was set to 0.48. The source code is provided at https://github.com/ebastoun/Monolayer-Stress-Microscopy.

Characterization of host cell kinematics and bacterial aggregation

ECs were seeded to a concentration of 2 x 10^5 cells/well directly onto the glass coverslips coated with 0.25 mg/mL collagen I rat tail, 24 h prior to *Bb*-exposure. 1 h prior to initiation of time-lapse imaging, cells were washed with PBS and incubated with 1 μg/mL Hoechst (Thermofisher, D1306) to stain the ECs' nuclei for 10 min at 37°C. Wells were then washed with L-15 medium supplemented appropriately and 1 mL of this medium was added to each of the wells. Multi-channel time-lapse sequences were conducted to acquire at each instance of time the Hoechst-stained EC nuclear fluorescence, the bacterial fluorescence and the phase contrast image of ECs, using an inverted Nikon Eclipse Ti2 with an EMCCD camera (Andor Technologies) using a 40X 0.60NA Plan Fluor air objective and the MicroManager software package (Edelstein et al., 2014). The microscope was surrounded by a box type incubator (Haison) maintained at 37°C. Images were acquired every 10 min for approximately 7 h before *Bb* were added on the wells at an MOI of ~200.

Subsequently, at each time interval we measured the 2D displacements based on the image of the host cell nuclei using an image correlation technique similar to particle image velocimetry (Gui and Wereley, 2002). We calculated the local displacement vectors by performing image correlation between subsequent images of the nuclei. We used interrogation windows of 48 x 24 pixels (window size x overlap). We calculated the mean displacement of cells before and after *Bb*-exposure by finding the average magnitude when considering all displacements in a particular field of view.

To quantify total bacterial fluorescence overtime, we used custom-built MATLAB code to integrate the *Bb-GFP* fluorescence intensity overtime. To characterize the aggregation of bacteria observed overtime we performed segmentation using IMARIS software (Bitplane) to identify all the objects (spirochetes or aggregates) at each instance of time. All identified objects and their associated attributes (*i.e.,* area, mean *Bb* fluorescence intensity, ellipticity) were imported into MATLAB (MathWorks) for further analysis, *e.g.*, for creating scatter plots of object ellipticity *versus* object area or object mean fluorescence versus object area.

RNA isolation and RNA sequencing

For sample preparation HMEC-1 cells were cultured in MCDB 131 medium (Fisher Scientific, 10372-019) supplemented with 10% fetal bovine serum (GemBio; 900-108), 10 ng/mL epidermal growth factor (Sigma; E9644), 1 μg/mL hydrocortisone (Sigma; H0888), and 2 mM L-glutamine (Sigma; 56-85-9). To generate confluent cell monolayers, 24-well plates glass-bottom for microscopy were coated with 50 μg/mL rat-tail collagen-I (diluted in 0.2 N acetic acid) for 1hat 37°C, air-dried for 15 min, and UV-sterilized for 30 min in a biosafety cabinet. ECs were seeded at a density of 2×10^5 cells/well. 24 h post-seeding ECs were exposed to *Bb* (MOI = 200) or not. At different times post-*Bb*-exposure, namely 4 h, 24 h or 48 hpe, four replicates per condition were lysed using the QIAshredder Kit by adding 200 μL of lysis buffer in each well (Qiagen, 79656). mRNA was harvested using the RNeasy Plus MicroKit (Qiagen, 74004) and eluted in 30 μL RNAase free water. A NanoDrop ND-1000 spectrophotometer was used to determine concentration (abs 260) and purity (abs260/abs230) of total RNA samples. Total RNA from each sample was 1-2 μg. Agarose gel electrophoresis was used to check the integrity of the RNA in all the samples (performed by Arraystar Inc.).

For sequencing library preparation, the subsequent steps were followed: 1. Total RNA was enriched by oligo (dT) magnetic beads (rRNA removed); 2. RNA-seq library preparation using KAPA Stranded RNA-Seq Library Prep Kit (Illumina), which incorporates dUTP into the second cDNA strand and renders the RNA-seq library strand-specific. The completed libraries were qualified with Agilent 2100 Bioanalyzer and quantified by absolute quantification qPCR method. To sequence the libraries on the Illumina NovaSeq 6000 instrument, the barcoded libraries were mixed, denatured to single stranded DNA in NaOH, captured on Illumina flow cell, amplified *in situ*, and subsequently sequenced for 150 cycles for both ends on Illumina NovaSeq 6000 instrument. Raw sequencing data that passed the Illumina chastity filter were used for further analysis. Trimmed reads (trimmed 5′, 3′-adaptor bases) were aligned to the reference genome (GRCh37). Based on alignment statistical analysis (mapping ratio, rRNA/mtRNA content, fragment sequence bias), we determined whether the results could be used for subsequent data analysis. To examine the sequencing quality, the quality score plot of each sample was plotted. The quality score Q is logarithmically related to the base calling error probability (P): $Q = -10\log_{10}(P)$. For example, Q30 means the incorrect base calling probability to be 0.001 or 99.9% base calling accuracy. After quality control, the fragments were 5′, 3′-adaptor trimmed and filtered $\leq$20 bp reads with Cutadapt software (Martin, 2011). The trimmed reads were aligned to the reference genome with Hisat 2 software (Kim et al., 2015). In a typical experiment, it is possible to align 40 ~ 90% of the fragments to the reference genome. However, this percentage depends on multiple factors, including sample quality, library quality and sequencing quality. Sequencing reads were classified into the following classes: (1) Mapped: reads aligned to the reference genome (including mRNA, pre-mRNA, poly-A tailed lncRNA and pri-miRNA); (2) mtRNA and rRNA: fragments aligned to rRNA, mtRNA; and (3) Unmapped: reads that are not aligned.

Differentially expressed genes and differentially expressed transcripts were calculated. The novel genes and transcripts were also predicted. The expression level (fragments per kilobase of transcript per million mapped reads (FPKM) value) of known genes and transcripts were calculated using R package ballgown by estimating the transcript abundances with StringTie. The number of identified genes and transcripts per group was calculated based on the mean of FPKM in group $\geq$0.5. The FPKM value was calculated with the formula: $FPMK = \frac{C \times 10^6}{L \times N}$, where C is the number of fragments that map to a certain gene/transcript,

L is the length of the gene/transcript in Kb and N is the fragments number that maps to all genes/transcripts. Differentially expressed gene and transcript analyses were performed with R package ballgown. Fold change (cutoff 1.5), p-value ($\leq$0.05) and FPKM ($\geq$0.5 mean in one group) were used for filtering differentially expressed genes and transcripts.

Principal component analysis (PCA) and mRNA function enrichment analysis

Principal Component Analysis (PCA) and Hierarchical Clustering scatter plots and volcano plots were calculated for the differentially expressed genes in R or Python environment for statistical computing and graphics. PCA was performed using the plotPCA function in R with genes that had the ANOVA p value $\leq$0.05 on FPKM abundance estimations (Not available for samples with no replicates). Kyoto Encyclopedia of Genes and Genomes (KEGG) pathway analyses of the whole data set of DEG were performed using the R package GAGE "Generally Acceptable Gene set Enrichment" (GAGE v.2.22.0) package implemented in R (Luo et al., 2009). The analysis allowed us to determine whether the differentially expressed mRNAs were enriched in certain biological pathways. The p-values calculated by Fisher's exact test are used to estimate the statistical significance of the enrichment of the pathways between the two groups. The R package "Pathview" v.1.12.0 and KEGGraph v1.30.0 were used to visualize gene set expression data in the context of functional pathways (Luo et al., 2017).

Inside/outside bacterial labeling, immunofluorescence microscopy and image processing

Unexposed or *Bb*-exposed ECs in monolayer on glass coverslips coated with 0.25 mg/mL collagen I were washed with PBS and incubated with 1 μg/mL Hoechst (Thermofisher, D1306) to stain the cells' nuclei for 10 min at 37°C. Wells were then washed twice in PBS and then fixed with 4% EM grade formaldehyde in PBS for 10 min. Samples were washed again with PBS and stored until further processing.

For staining only extracellular *Bb* cells inside/outside labeling was performed: samples were blocked for 30 min with 5% BSA in PBS and then incubated with primary rabbit polyclonal anti-*Bb* antibody (Thermo Fisher Scientific, PA1-73004) diluted 1:100 in PBS containing 2% BSA for 1 h, at room temperature. Samples were washed in PBS three times and then incubated with Alexa Fluor 546 goat anti-rabbit secondary antibody (Invitrogen, A-11035) diluted 1:250 in PBS containing 2% BSA for 1 h. Samples were washed three times in PBS and stored in 1 mL PBS for imaging. *N*>1000 cells were analyzed per condition. For imaging, we used an inverted Nikon Diaphot 200 with a charge-coupled device (CCD) camera (Andor Technologies) and a 40× air Plan Fluor NA 0.60 objective. The microscope was controlled by the MicroManager software package. For differential immunostaining, all "green" bacteria associated with individual cells were counted as adherent (because at the time of fixation they were adhering on the host cell surface or because prior to internalization they were adherent); bacteria that were both "green" and "red" (due to antibody binding) were counted as non-internalized. Nuclei number was identified by running a custom-made script in MATLAB (Mathworks).

For immunostaining of cytoskeletal elements, fixed cells were first permeabilized for 5 min in 0.2% Triton X-100 in PBS and washed again with PBS. Samples were then blocked for 30 min with 5% BSA in PBS and then incubated with primary antibodies (mouse monoclonal anti-integrin β1, Millipore, MAB1987; mouse monoclonal anti-integrin αvβ3, Sigma, MAB1976) diluted 1:100 in PBS containing 2% BSA for 1 h. Samples were washed in PBS three times and then incubated with the appropriate secondary fluorescent antibodies (Invitrogen) diluted 1:250 in PBS containing 2% BSA for 1 h. For actin staining we used 0.2 μM AlexaFluor546 phalloidin (Thermo Fisher Scientific, A22283). Samples were washed three times in PBS and stored in 1 mL PBS for imaging. For confocal imaging we used a Yokogawa W1 Spinning Disk Confocal with Borealis upgrade on a Leica DMi6 inverted microscope with a 50um Disk pattern, a 60x 1.4NA Plan Apo oil objective and MicroManager software. Z-stacks were taken with an interval of 0.2 μm.

For quantification of the relative abundance of F-actin or integrins β1 and αvβ3 on *Bb*-exposed versus not EC monolayers on a per cell basis the pipeline described was followed. Custom made codes were written in MATLAB (Mathowrks). Briefly, the images of the Hoechst-stained nuclei were used to segment the host cell nuclei and identify their centroids. The MATLAB function voronoi2mask was used to perform centroidal voronoi tessellation and thus approximate the boundaries of each cell in the monolayer. For the area occupied by each cell the integral of fluorescence intensity of each cytoskeletal component was then calculated and depicted as a single dot on the boxplots shown in Figures 5C, 5F and S5B.

Propidium iodide (PI) staining, imaging and quantitation of co-localization of *Bb* with PI

PI (Millipore Sigma, P4170-10MG) at a concentration of 5 μM was added in ECs in monolayer exposed to *Bb* (MOI = 200) at the time of exposure, as described previously to assess dynamically bacterial death (Krämer et al., 2016). ECs were residing in wells on 24-well plates were imaged for 24hat 37 °C using the IncuCyte S3 time lapse microscopy system (Sartorius) equipped with an IncuCyte S3 20 x PLAN FLUOR objective. Phase contrast images, images of bacterial fluorescence and of PI fluorescence were acquired every 90 min. For quantification of co-localization between *Bb*-GFP and PI stain the pipeline described below was followed. Images of bacterial fluorescence were segmented so that bacterial objects were identified. Next, images of PI fluorescence were also segmented. Then the percentage of pixels occupied by bacteria that are also PI positive was determined. Co-localization index was defined as the ratio of pixels that are both occupied by bacteria and are PI-positive to the total number of pixels occupied by bacteria. The source code is provided at https://github.com/ebastoun/borrelia_PI_colocalisation.

RT-PCR

To assess expression of NFκB target genes, ECs were seeded until monolayers were formed (~$4x10^5$ cells/well of 24 well plate) as described above. At different time points, namely 4 h or 24 h post-treatment with TNFα or MDP, or post heat-killed *Bb* exposure, two to three replicates per condition per experiment were lysed using the QIAshredder Kit by adding 350 μL of lysis buffer in each well (Qiagen, 79656). mRNA was harvested using the RNeasy Plus MicroKit (Qiagen, 74034) and eluted in 30μL RNAase free water. RNA concentrations were measured spectrophotometrically (NanoDrop) and were comparable between conditions. cDNA was prepared using the PrimeScript™ RT Reagent Kit (Takara Bio, RR037A). RT-PCR was performed using the KAPA SYBR® FAST mix (Kapa Biosystems, KK4601) and the QuantStudio 3 Real-Time PCR system (Applied Biosystems). Genes of interest were amplified using the appropriate primers for ICAM1 (forward: 5′ GAGCTTCGTGTCCTGTATGGC -3′, reverse: 5′ ACAGAGGTAGGTGCCC TCAA-3′); for CXCL8 (forward: 5′ CAGAGACAGCAGAGCACACA -3′, reverse: 5′ GGCAAAACTGCACCTT CACA -3′); for NFKBIA (forward: 5′ ATGTCAATGCTCAGGAGCCC -3′, reverse: 5′ CAGGTGAGCTGGTAG GGAGA -3′); for GAPDH (forward:5′ GGGAAACTGTGGCGTGAT -3′, reverse: 5′ GAGTGGGTGTCGCTG TTGA -3′). Analysis was performed using the QuantStudio™ Design and Analysis Software v2 and the Comparative CT Method ($2^{-\Delta\Delta Ct}$). GAPDH was used as the reference gene.

QUANTIFICATION AND STATISTICAL ANALYSIS

Statistical parameters and significance are reported in the Figures and the Figure Legends. Data are determined to be statistically significant when $p < 0.05$ or $p < 0.01$ by an unpaired Student's T-Test (USTT), or Wilcoxon Rank Sum Test (WRST), where indicated. As such, asterisk denotes statistical significance as compared to indicated controls. For inside/outside labeling 20 fields of view (FOV) were analyzed consisting of an average 158 ± 60 host cell nuclei per FOV. For statistical analysis of EC kinematics a large number of cells pertained in each field of view (FOV) and average of cells' displacements were calculated in each FOV and overtime for three independent experiments. The same applies for the traction force microscopy recordings. In the boxplots and barplots midlines denote mean value and whiskers the standard deviation (vertical bars). Statistical analysis was performed in GraphPad PRISM 8.

Section 6

Spatiotemporal characterization of endothelial cell motility and physical forces during exposure to *Borrelia burgdorferi*

Marie Muenkel,[1] Raul Aparicio-Yuste,[2] Michal Caspi Tal,[3] Peter Kraiczy,[4] and Effie E. Bastounis[1,5,6,7,*]

[1]Interfaculty Institute of Microbiology and Infection Medicine, Cluster of Excellence "Controlling Microbes to Fight Infections" (CMFI, EXC 2124), University of Tübingen, 72074 Tübingen, Germany

[2]Multiscale in Mechanical and Biological Engineering (M2BE), Engineering Research Institute of Aragon (I3A), Department of Mechanical Engineering, University of Zaragoza, 50018 Zaragoza, Spain

[3]Department of Biological Engineering, Massachusetts Institute of Technology, Cambridge, MA, USA

[4]Institute of Medical Microbiology and Infection Control, University Hospital of Frankfurt, Goethe University Frankfurt, 60438 Frankfurt am Main, Germany

[5]Eberhard Karls University of Tübingen, Auf der Morgenstelle 28/E8, 72076 Tübingen, Germany

[6]Technical contact

[7]Lead contact

Published 2022 in STAR Protocols 3, 101832.

STAR Protocols

CellPress
OPEN ACCESS

Protocol

Spatiotemporal characterization of endothelial cell motility and physical forces during exposure to *Borrelia burgdorferi*

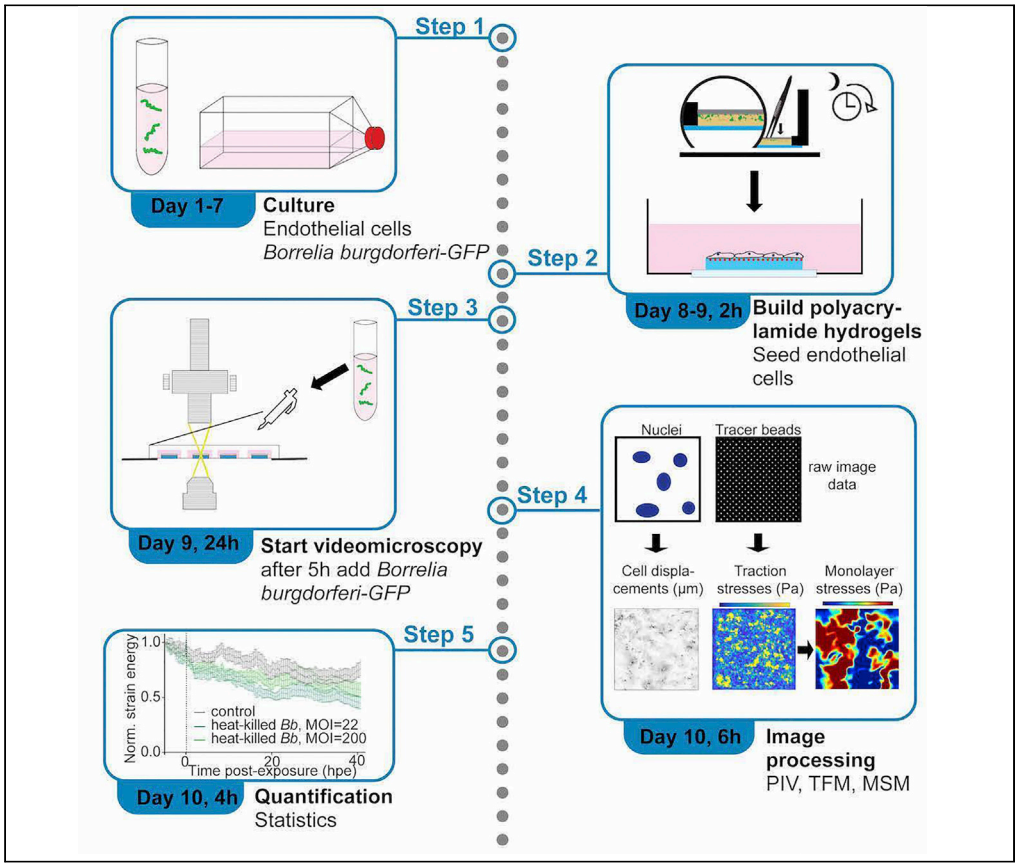

Cell motility and biomechanics are critical in various (patho)physiological processes, including the regulation of vascular barrier integrity, which can be subverted by bacterial pathogens. Here, we present a protocol on how to expose endothelial cells (ECs) to vector-borne *Borrelia burgdorferi* (*Bb*) and characterize EC kinematics and dynamics during exposure to live or heat-inactivated *Bb* through traction force and monolayer stress microscopy. Modifications to this protocol may be necessary for studying how different cell types interact with *Bb* or other microorganisms.

Publisher's note: Undertaking any experimental protocol requires adherence to local institutional guidelines for laboratory safety and ethics.

Marie Muenkel, Raul Aparicio-Yuste, Michal Caspi Tal, Peter Kraiczy, Effie E. Bastounis

effie.bastounis@uni-tuebingen.de

Highlights

Exposure of endothelial cells (ECs) to live or heat-killed *B. burgdorferi (Bb)*

Measure changes in the kinematics and dynamics of *Bb*-exposed ECs

Quantify motility of *Bb*-exposed ECs through PIV on the image of EC nuclei

TFM and MSM allow measuring *Bb*-exposed EC traction and monolayer stresses

Muenkel et al., STAR Protocols *3*, 101832
December 16, 2022
https://doi.org/10.1016/j.xpro.2022.101832

STAR Protocols

CellPress
OPEN ACCESS

Protocol

Spatiotemporal characterization of endothelial cell motility and physical forces during exposure to *Borrelia burgdorferi*

Marie Muenkel,[1] Raul Aparicio-Yuste,[2] Michal Caspi Tal,[3] Peter Kraiczy,[4] and Effie E. Bastounis[1,5,6,7,*]

[1]Interfaculty Institute of Microbiology and Infection Medicine, Cluster of Excellence "Controlling Microbes to Fight Infections" (CMFI, EXC 2124), University of Tübingen, 72074 Tübingen, Germany

[2]Multiscale in Mechanical and Biological Engineering (M2BE), Engineering Research Institute of Aragon (I3A), Department of Mechanical Engineering, University of Zaragoza, 50018 Zaragoza, Spain

[3]Department of Biological Engineering, Massachusetts Institute of Technology, Cambridge, MA, USA

[4]Institute of Medical Microbiology and Infection Control, University Hospital of Frankfurt, Goethe University Frankfurt, 60438 Frankfurt am Main, Germany

[5]Eberhard Karls University of Tübingen, Auf der Morgenstelle 28/E8, 72076 Tübingen, Germany

[6]Technical contact

[7]Lead contact

*Correspondence: effie.bastounis@uni-tuebingen.de
https://doi.org/10.1016/j.xpro.2022.101832

SUMMARY

Cell motility and biomechanics are critical in various (patho)physiological processes, including the regulation of vascular barrier integrity, which can be subverted by bacterial pathogens. Here, we present a protocol on how to expose endothelial cells (ECs) to vector-borne *Borrelia burgdorferi* (*Bb*) and characterize EC kinematics and dynamics during exposure to live or heat-inactivated *Bb* through traction force and monolayer stress microscopy. Modifications to this protocol may be necessary for studying how different cell types interact with *Bb* or other microorganisms.

For complete details on the use and execution of this protocol, please refer to Yuste et al. (2022).[1]

BEFORE YOU BEGIN

This protocol describes specific steps to measure the changes in human skin microvascular endothelial cells (HMEC-1) kinematics and dynamics before and after prolonged exposure to *Borrelia burgdorferi* (*Bb*) (Figure 1). A monolayer of HMEC-1 cells is exposed to live or heat-inactivated *Bb* and the changes in HMEC-1 kinematics and dynamics are measured via microscopy followed by image processing. Depending on the desired endothelial cell (EC) type to be used, the most appropriate culture conditions and seeding density to achieve an integral EC monolayer will have to be determined empirically and the protocol will need to be adjusted accordingly.

Preparation of *Bb* culture media

Timing: 1 h

For our studies we have been using infectious *Bb* strains Bb1286[5] and GCB726,[6] both of which were generated from the B31 5A4 NP1 *Bb* strain. Thus, both strains are cultured in the same growth medium. The difference between Bb1286 and GCB726 is in the GFP construct that was introduced to make the bacteria fluorescent.

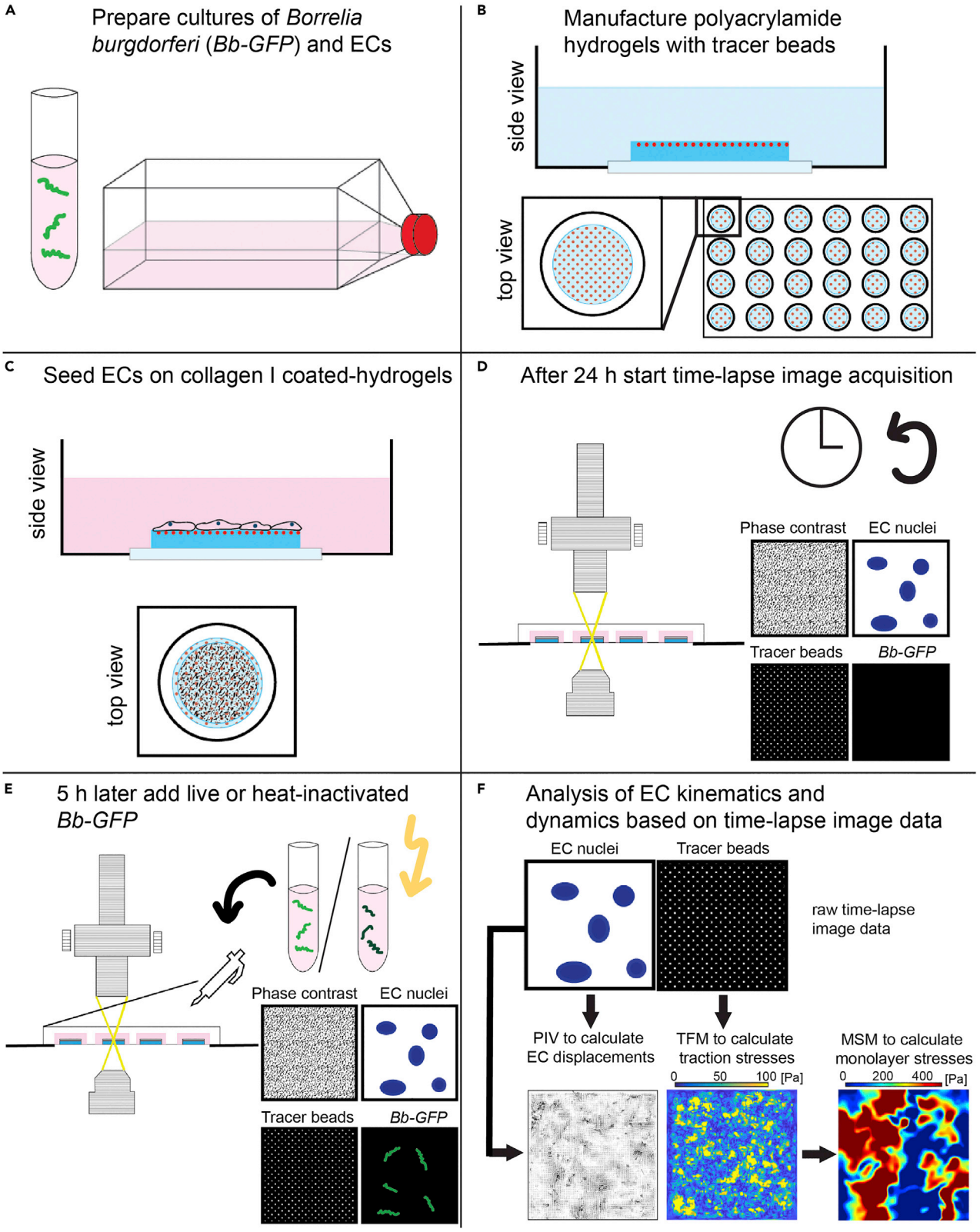
A
Prepare cultures of *Borrelia burgdorferi* (*Bb-GFP*) and ECs
B
Manufacture polyacrylamide hydrogels with tracer beads
side view
top view
C
Seed ECs on collagen I coated-hydrogels
side view
top view
D
After 24 h start time-lapse image acquisition
Phase contrast
EC nuclei
Tracer beads
Bb-GFP
E
5 h later add live or heat-inactivated *Bb-GFP*
Phase contrast
EC nuclei
Tracer beads
Bb-GFP
F
Analysis of EC kinematics and dynamics based on time-lapse image data
EC nuclei
Tracer beads
raw time-lapse image data
PIV to calculate EC displacements
TFM to calculate traction stresses
0 50 100 [Pa]
MSM to calculate monolayer stresses
0 200 400 [Pa]

Figure 1. Schematic of assay for probing EC kinematics and dynamics prior and after exposure to *Bb*

The main steps for seeding and exposing HMEC-1 cells to *Bb* and monitoring via microscopy and image processing changes in HMEC-1 kinematics and dynamics are depicted.

(A) Culture of HMEC-1 and *Bb-GFP*.

(B) Manufacturing of polyacrylamide hydrogels with embedded fluorescent tracer beads on multi-well plates.

(C) Seeding of HMEC-1 on hydrogels for 24 h.

(D) Initiation of time-lapse multi-channel and multi-positional image acquisition.

(E) Addition of live or heat-inactivated *Bb* at ~ 5 h post-initiation of videomicroscopy.

(F) Image processing to determine alterations in EC motility, traction and monolayer stresses.

1. Preparation of stock antibiotic solutions.

   Note: Type 1 ultrapure water was used for the preparation of reagents.

   a. Dissolve 0.5 g gentamicin sulfate into 10 mL of sterile water to prepare a 50 mg/mL stock solution.
   b. Dissolve 0.5 g of kanamycin into 10 mL of sterile water to prepare a 50 mg/mL stock solution.
   c. Use a 0.2-μm syringe filter to sterilize the antibiotic solutions and store stock solutions at −20°C for 1 year.

   Note: Lower grades of water may be suitable depending on your cultures.

2. Preparation of *Bb* culture media.
   a. Supplement BSK-H medium containing sodium bicarbonate with 5.4% rabbit serum.
   b. Aliquot the solution into 50 mL falcon tubes and store at −20°C for future usage.
   c. When performing experiments thaw supplemented media and add gentamicin and kanamycin from stock solutions to a final concentration of 50 μg/mL and 100 μg/mL, respectively.
   d. Store at 4°C and use for the next 2–3 months.

   Note: You should avoid repeated freezing and thawing cycles.

Preparation of HMEC-1 culture media

Timing: 1–2 h

We used HMEC-1 as model ECs because they are dermal microvascular ECs and therefore most similar to the first type of ECs *Bb* interacts with after skin infection occurs through a tick bite. Additionally, we chose those cells because we have previously characterized in great detail their mechanobiology and response to infection with intracellular bacterial pathogens.[7,8] Finally, since HMEC-1 are immortalized (i.e., cell line), they can be easily cultured or genetically manipulated.

3. Preparation of HMEC-1 cell culture media.
   a. Prepare 2 mL stocks of 250 μg/mL hydrocortisone.
      i. Weigh 25 mg of hydrocortisone.
      ii. Add 100 mL of autoclaved water and mix well.

      Note: If the hydrocortisone powder does not dissolve well in the water, place the solution briefly in a 37°C water bath.

      iii. Use 0.2 μm vacuum bottle top filters and pass through the filter the whole solution.
      iv. Aliquot 2 mL of the solution in 15 mL falcon tubes and store at −20°C for up to a year.
   b. Prepare 5 mL stocks of 200 mM L-glutamine.
      i. Weigh 2.95 g of L-glutamine.
      ii. Add 90 mL autoclaved water and mix well.

iii. Adjust to a final volume of 100 mL.
iv. Use 0.2 μm vacuum bottle top filters and pass through the filter the whole solution.
v. Aliquot 5 mL of the solution in 15 mL falcon tubes and store at −20°C for up to a year.

c. Prepare 500 μL stocks of 10 μg/mL epidermal growth factor (EGF).
i. Reconstitute 100 μg of lyophilized EGF in 10 mL autoclaved water.
ii. Mix well and use a 0.2-μm syringe filter to sterilize.
iii. Aliquot 500 μL of the solution in 1.5 mL microcentrifuge tubes and store at −20°C for up to a year.

d. Prepare HMEC-1 media using the previously made stocks.
i. In 442.5 mL of MCDB-131 medium, add 50 mL fetal bovine serum, a 5 mL stock of 200 mM L-glutamine, a 500 μL stock of 10 μg/mL EGF and a 2 mL stock of 250 μg/mL hydrocortisone.

Note: For live-microscopy media (in case you do not have a CO_2 incubator unit at your microscope) supplement instead Leibovitz's L-15 with 10% fetal bovine serum, 10 ng/mL of EGF, and 1 μg/mL hydrocortisone. L-15 already contains 2 mM L-glutamine, so you do not need to add L-glutamine.

ii. Aliquot the MCDB-131 medium with supplements (from here on referred as full MCDB-131 medium) in 50 mL falcon tubes and store at −20°C.
iii. Keep only 1–2 50 mL falcon tubes at 4°C when culturing HMEC-1 cells.

Culturing and passaging of HMEC-1 cells

Timing: 30 min to 1 h

4. Prewarm HMEC-1 culture media in a 37°C water bath.
5. Whenever cells become confluent, passage them by splitting them 1:3 to 1:6.
   a. For passaging, remove and discard the culture medium and rinse the cells once with PBS.
   b. Add 2 mL of 0.05% trypsin-EDTA in the T-75 flask and place the flask in the incubator for 5–10 min or until the cells are detached from the surface of the flask.

⚠ CRITICAL: To avoid clumping of cells do not shake the flask while waiting for the cells to detach but rather let them sit in the incubator for the appropriate amount of time until they are detached from their plastic substrate. Mechanical agitation will lift the cells, but it is possible that they might detach in clumps. This part is particularly important when seeding cells in coverslips or hydrogels where one wants to ensure homogeneous cell spatial distribution in the monolayer.

   c. When cells have detached, add culture media up to a final volume of 12 mL and mix cells by gently pipetting.
   d. Add appropriate volumes of the cell suspension to new flasks (so that the cell density as compared to the confluent flask is diluted between 1:3 and 1:6), and supplement with appropriate volumes of full culture medium.

Preparation of 10% ammonium persulfate and 0.5 M HEPES pH=7.5

Timing: 30 min

These stock solutions are needed for the preparation of the polyacrylamide hydrogels to conduct traction force microscopy (TFM).

6. Preparation of 10% ammonium persulfate.

a. Weigh 1 g of ammonium persulfate.
b. Dissolve the powder in 10 mL autoclaved water.
c. Aliquot 1 mL of the solution in 1.5 mL microcentrifuge tubes and store at −20°C.

Note: Working solutions are stored at 4°C for up to a week. This did not impact the resulting stiffness of our hydrogels as evidenced by previous atomic force microscopy (AFM) measurements performed.[7] Nevertheless, other protocols suggest always making the APS solution fresh.

7. Preparation of 0.5 M HEPES pH=7.5.
   a. Weigh 119.15 g of HEPES powder and place in a 2 L glass flask.
   b. Add 800 mL of autoclaved water.
   c. Add a magnetic stir bar and start stirring by placing the flask on a magnetic stir plate until the powder is dissolved.
   d. Adjust the pH to 7.5 by adding the appropriate volume of 10 N NaOH.

   Alternatives: Use NaOH pellets to adjust the pH.

   e. Adjust the final volume to 1 L.
   f. Use 0.2 μm vacuum bottle top filters and pass through the filter the whole solution.
   g. Prepare a working solution of HEPES 50 mM by mixing the 1:10 the 0.5 M stock solution with water and filter sterilize too.
   h. Store at 21°C–24°C the stock solution (0.5 M) and at 4°C the 50 mM HEPES solution.

KEY RESOURCES TABLE

REAGENT or RESOURCE	SOURCE	IDENTIFIER
Chemicals, peptides, and recombinant proteins		
Collagen I rat tail	Fisher	Cat# A1048301
Acrylamide 40% solution	Sigma	Cat# A4058
Bisacrylamide solution 2%	Fisher	Cat# BP1404250
Aminopropyltriethoxysilane	Sigma	Cat# 919302
FluoSpheres™ Carboxylate-Modified Microspheres, 0.2 μm, yellow-green fluorescent (580/605), 2% solids	Invitrogen	Cat# F8810
MCDB131, no glutamine	Gibco	Cat# 10372019
Leibovitz's L-15 medium, no phenol red	Thermo Fisher Scientific	Cat# 21083027
Fetal bovine serum	Gemini Bio-Products	Cat# 900108
Hydrocortisone	Sigma	Cat# H0888
hEGF	Sigma	Cat# EG9644
L-Glutamine	Fisher	Cat# SH3003401
Hoechst 33342, trihydrochloride	Invitrogen	Cat# H3570
BSK-H Medium	Sigma	Cat# B3528
Rabbit serum	Sigma	Cat# R4505
Gentamicin sulfate	MP Biomedicals	Cat# 194530
Kanamycin monosulfate	MP Biomedicals	Cat# 150029
Glycerol bidistilled (99.5%)	VWR Chemicals	Cat# 24388.295
0.05% Trypsin/EDTA	Gibco	Cat# 25300096
HEPES, Free acid	J.T. Baker	Cat# 4018-04
Ammonium persulfate (APS)	Fisher	Cat# BP17925
Tetramethylethylenediamine (TEMED)	Sigma	Cat# T9281-1 25 ML
Sulfo-SANPAH	ProteoChem	Cat# c1111-100mg
Sodium hydroxide pellets	Fisher	Cat# S318-500
Dimethyl sulfoxide (DMSO)	J.T. Baker	Cat# 9224-01

(*Continued on next page*)

Continued

REAGENT or RESOURCE	SOURCE	IDENTIFIER
Experimental models: Cell lines		
HMEC-1 cells	Reed et al.[9]	Previously obtained from Centers for Disease Control, Biological Products Branch
Experimental models: Organisms/strains		
Borrelia burgdorferi (strain Bb1286)	Dunham-Ems et al.[5]	N/A
Borrelia burgdorferi (strain GCB726)	Moriarty et al.[6]	N/A
Software and algorithms		
ImageJ	Schneider et al.[10]	https://imagej.nih.gov/ij/
MicroManager	N/A	https://www.micro-manager.org/
MATLAB	MathWorks	http://www.mathworks.com/products/matlab/?requestedDomain=www.mathworks.com
GraphPad Prism v6	GraphPad	http://www.graphpad.com/scientific-software/prism/
PIV	This paper	https://github.com/ebastoun/Correlation_length_of_movement_of_epithelial_cells_in_monolayer
TFM	Lamason et al.[2]	N/A
Monolayer stress microscopy, MSM	This paper	https://github.com/ebastoun/Monolayer-Stress-Microscopy
NIS-Elements (RRID: SCR_014329)	Nikon Instruments Inc.	https://www.microscope.healthcare.nikon.com/products/software/nis-elements
Other		
24-Well plates with glass bottom	MatTek	Cat#P24G-1.5-13-F
T-75 Flasks	Falcon	Cat#353118
50 mL Conical tubes	Falcon	Cat#352070
15 mL Conical tubes	Falcon	Cat#352196
Disposable serological pipettes (1 mL, 2 mL, 5 mL, 10 mL)	Falcon	various
Pipette tips 1–200 μL	Denville	Cat#P1122
Pipette tips 101–1,000 μL	Denville	Cat#P1126
Powder-free examination gloves	Microflex	Cat#XC-310
0.2 μm Vacuum bottle top filters	Thermo Fisher Scientific	Cat#566-0020
20 mL Syringes	BD	Cat#302830
0.2 μm Syringe filters	Thermo Fisher Scientific	Cat#723-2520
10 cm Culture plates	Falcon	Cat#351029
Biosafety cabinet	Baker	Cat#SG504
Hemocytometer	Sigma	Cat#Z359629
Bacterial incubator	Thermo Scientific	Cat#IGS180
CO_2 culture Incubator	NuAire	Cat#NU-8700
Vacuum chamber/degasser	Bel-Art	Cat#42025
Cage incubator (for the microscope)	Haison	Custom
Pipettor	Drummond	Cat#4-000-110
Pipet tips (10 μL, 200 μL, 1,000 μL)	Gilson	Cat#F144802, F123601, F123602
pH meter	METTLER TOLEDO	Cat#30019028
1 L Flask	Fisherbrand	Cat#FB5011000
Autoclave	AMSCO	Cat#3021
Stir magnet plate	Bellco	Cat#7760-06000
Magnet stirring bars	Bellco	Cat#1975-00100
Water purification system 2121B	Aqua Solutions	https://www.aquaa.com/

Note: We used an inverted Nikon Eclipse Ti2 a Prime BSI sCMOS camera (Teledyne Photometrics) for all time-lapse recording including the traction force microscopy experiments. The microscope was controlled by the NIS Elements software (Nikon). Any inverted epifluorescence or spinning disk confocal microscope (for fast time-lapse imaging) should work for the purposes of the protocol presented below.

MATERIALS AND EQUIPMENT

HMEC-1 MCDB-131-based culture media		
Reagent	Final concentration	Amount
Hydrocortisone (250 μg/mL)	1 μg/mL	2 mL
L-glutamine (200 mM)	2 mM	5 mL
EFG (10 μg/mL)	10 ng/mL	0.5 mL
FBS	10%	50 mL
MCDB-131 media	N/A	442.5 mL
Total	**N/A**	**500 mL**

Once you mix, aliquot in 50 mL falcon tubes and store at −20°C.

STEP-BY-STEP METHOD DETAILS

Culturing of *Bb* and preparation of heat-inactivated *Bb*—Days 1–7

Timing: 1 h

Bb are grown until they reach mid log phase which is approximately 5×10^7 bacteria/mL in complete BSK-H medium. Depending on the frozen stock this may require 1–2 weeks. For simplicity here we assume they require 1 week. Once they reach mid log phase, bacteria are exposed as live, highly viable bacteria to a monolayer of HMEC-1, or are first heat-inactivated and then added onto the HMEC-1.

1. Add 9 mL of complete BSK-H medium on a 15 mL falcon tube.
2. Further add 1.5 mL of frozen with glycerol *Bb* stock culture.
3. Place the tube at 33°C until the concentration of *Bb* reaches 2–5 × 10^6 bacteria/mL (mid log phase).

   Note: Typically, this will take approximately one to two weeks, but precise timing depends on the freezing method and the specific *Bb* strain used. For counting bacteria either use darkfield microscopy or (epi)fluorescence microscopy if *Bb* constitutively expresses GFP. To precisely count their number, use a hemocytometer or another type of counting chamber.

4. Once you reach that number, dilute the *Bb* solution to 1×10^3 bacteria/mL.
5. Grow *Bb* in fresh complete BSK-H at 33°C until a density of approximately 5×10^7 *Bb*/mL is reached, in which case highly viable *Bb* can be exposed to host cells.

   Note: How many *Bb* you need will ultimately depend on your desired multiplicity of infection (MOI). Herein we seed ECs on glass coverslips (or hydrogels built on them) of 24-well plates. To achieve a confluent monolayer, we aim for 4×10^5 cells the day of infection. Thus, to achieve an MOI of 10 *Bb*/cell in each well one needs to add 4×10^6 *Bb*. After counting, spirochetes should be added to ECs as quick as possible to avoid aggregation or clumping of *Bb*.

6. To prepare heat-inactivated *Bb*, incubate the desired amount of bacteria from step 5 at 56°C for 30 min.
7. Subsequently, store heat-inactivated *Bb* at 4°C.

⚠ CRITICAL: This step is critical to avoid drastic damage of the *Bb* membrane or morphology that can occur at lower temperatures (e.g., −20°C).

Manufacturing of 3 kPa polyacrylamide hydrogels for EC seeding—Days 7–8

Timing: 3–4 h

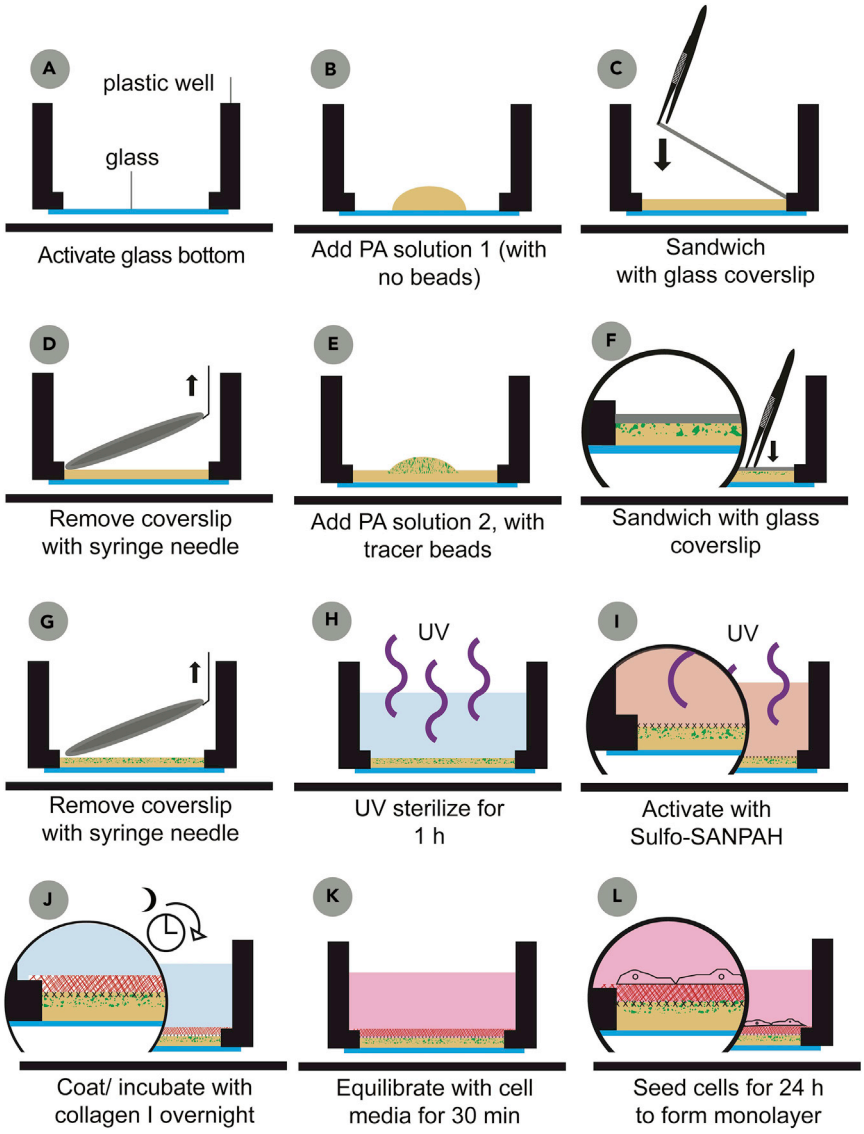

Figure 2. Schematic of the specific steps for building polyacrylamide hydrogels to perform TFM on ECs exposed to *Bb*

(A) Glass coverslips are chemically treated to allow subsequent polyacrylamide hydrogel attachment.
(B) 3.6 μL of polyacrylamide Solution 1 is placed on each glass coverslip of the multi-well plate.
(C) Solution 1 is sandwiched with a 12-mm circular glass coverslip.
(D) Coverslip is removed with a hooked needle syringe until polymerization occurs.
(E) 2.4 μL of polyacrylamide Solution 2 with tracer beads is added on top of the bottom layer.
(F) Solution 2 is sandwiched with a 12-mm circular glass coverslip.
(G) Water is added, and the coverslip is removed.
(H) UV exposure for 1 h ensures sterilization.
(I) Sulfo-SANPAH solution is added on the hydrogels and irradiation under UV for 10 min is followed.
(J) Hydrogels are washed with HEPES and incubated for 16–18 h with collagen I.
(K) Hydrogel is equilibrated with cell culture medium.
(L) HMEC-1 are seeded and allowed to form a monolayer for 24 h.

The protocol below describes how to activate glass coverslips of 24-well glass bottom plates to then build 3 kPa double-layered polyacrylamide hydrogels with embedded tracer beads to conduct traction force microscopy (TFM) as well as how to sterilize them, coat them with collagen I, and equilibrate them prior to EC seeding (Figure 2).

8. Activation of glass coverslips of 24-well glass bottom plates (Figure 2A).
   a. Add 500 μL of 1 M NaOH on glass coverslips of 24-well glass bottom plates (13 mm-diameter wells) and incubate at 21°C–24°C for 30 min.
   b. Rinse the wells once with ultrapure water.
   c. Add 500 μL of 2% (3-aminopropyl)triethoxysilane in 95% ethanol to each well and incubate at 21°C–24°C for 5 min.
   d. Rinse the wells once with ultrapure water.
   e. Add 500 μL of 0.5% glutaraldehyde in water to each well and incubate at 21°C–24°C for 30 min to 2 h.
   f. Rinse the wells once with ultrapure water.
   g. Dry the coverslips by placing the multi-well plate on a 60°C warm metal plate with the lid of the plate slightly off, or at 21°C–24°C until dry.

⚠ CRITICAL: Make sure that the temperature is not higher than 60°C, otherwise the plastic of the multi-well plate will melt.

Pause point: You can store the activated glass coverslips and build the hydrogels at a later point. In that case you do not need to dry them, water will evaporate over time.

9. Fabrication of two-layered 3 kPa polyacrylamide hydrogels and hydrogel sterilization (Figures 2A–2H).
   a. In 1.5 mL microcentrifuge tubes prepare two aqueous solutions (thereon referred as Solution 1) that contain 5% acrylamide and 0.1% bisacrylamide, by adding in a 1.5 mL microcentrifuge tube 152.6 μL water, 23.125 μL of 40% acrylamide, and 9.25 μL of 2% bisacrylamide.

Note: You can make hydrogels of different stiffnesses by adjusting the concentration of acrylamide and bisacrylamide accordingly.[7,8]

⚠ CRITICAL: The solvent can impact the final stiffness of the hydrogel as pH can impact the polymerization reaction. We used water as the solvent as in other studies[8,2,11,12] and previously performed atomic force microscopy measurements to confirm that the expected and resulting stiffness of the hydrogels is similar.[7]

   b. In 1.5 mL microcentrifuge tubes prepare two more aqueous solutions (thereon referred as Solution 2) that contain 5% acrylamide, 0.1% bisacrylamide and 0.04% of 0.2 μm tracer fluorescent beads, by adding in a 1.5 mL microcentrifuge tube 149.6 μL water, 23.125 μL of 40% acrylamide, 9.25 μL of 2% bisacrylamide and 3 μL of 0.2 μm tracer fluorescent beads.

Optional: Degas all four solutions using vacuum for 15 min to eliminate oxygen that inhibits polymerization.

   c. Pipet 1.2 μL of 10% APS stock and 0.8 μL of TEMED to Solution 1 to initiate polymerization and mix well by pipetting up and down.
   d. Immediately after add 3.6 μL of Solution 1 to the center of each glass coverslip of the 24-well dish (Figure 2B).
   e. Act fast and using your forceps cover/sandwich the polyacrylamide droplets with a 12 mm untreated circular coverslip (Figure 2C).
   f. Let Solution 1 sit for 20 min or until it fully polymerizes.

⚠ CRITICAL: If the solution in the tube polymerizes before you manage to cover all wells of the 24-well plate, then you can activate Solution 1 in the second "backup" tube you previously prepared and repeat the above steps so that all wells of the 24-well plate are processed. I.e., you can add polyacrylamide Solution 1 from the first tube to the number of

wells you can manage (e.g., 6 wells), and the "backup" tube can be used for the remaining wells.

g. Gently tap a syringe needle to a surface to create a small hook at its tip to facilitate the removal of the coverslips.
h. Lift all the coverslips using the syringe needle and your forceps (Figure 2D).

⚠ CRITICAL: Do not add water to facilitate the removal of the coverslip as you will build an additional polyacrylamide layer with tracer beads on top. To our hands the coverslip can be easily removed using the ''hooked'' syringe (see Figure 2D). Note that others pre-treat the coverslip with Sigmacote to render it hydrophobic and thus more easily be able to remove it.[13]

i. Pipet 1.2 μL of 10% APS stock and 0.8 μL of TEMED to Solution 2 (with the tracer beads) to initiate polymerization and mix well by pipetting up and down.
j. Immediately after add 2.4 μL of Solution 2 to the center of each hydrogel built on the well of the 24-well dish but without touching the gels (Figure 2E).
k. Cover Solution 2 with 12-mm circular glass coverslips and gently press downwards using a pair of forceps to ensure the thickness of the second layer is minimal (Figure 2F).

Note: You can measure the thickness of the hydrogels experimentally through phase contrast microscopy by focusing on the upper surface of the glass coverslip and on the surface of the hydrogel. On our hands thickness is 30 +/- 5 μm and is mostly attributed to the first layer since tracer beads are all focused on one focal plane at the uppermost surface of the hydrogel.

l. Let Solution 2 polymerize for 20 min.

⚠ CRITICAL: If the solution polymerizes before you cover all wells of the multi-well plate, then use the second tube you prepared of Solution 2 and repeat previous steps.

m. Add 200 μL of water to each of the wells to facilitate subsequent removal of the glass coverslips using your hooked syringe needle and forceps (Figure 2G).
n. Add 1 mL of 50 mM HEPES pH 7.5 to each of the wells to keep the hydrogels hydrated.
o. UV-expose the hydrogels for 1 h in the tissue culture hood to allow sterilization making sure the lid of the multi-well plate is inverted too (Figure 2H).

Pause point: You can store the plate with the hydrogels at 4°C indefinitely. However, it is advisable to place parafilm around the plate to avoid evaporation of the buffer and subsequent dehydration of the hydrogels.

10. Activation, protein coating and equilibration of hydrogels (Figures 2I–2K).
    a. Weigh 10 mg of sulfosuccinimidyl 6-(4′-azido-2′-nitrophenylamino)hexanoate (Sulfo-SANPAH) and place it in a 50 mL falcon tube.

Note: Sulfo-SANPAH powder should be stored at −20°C and solution should be made fresh.

    b. Add 100 μL DMSO and mix well so the Sulfo-SANPAH powder is dissolved.
    c. Add 10 mL 50 mM HEPES pH = 7.5 and mix well.
    d. Remove the HEPES buffer from the hydrogels and add 200 μL of the Sulfo-SANPAH solution on the hydrogels.
    e. Immediately expose them to UV (302 nm) for 10 min to activate them (Figure 2I).

Note: The lamp we used supplies a power of 8 Watts while the distance to the drawer where the plate with the hydrogels was placed is 5 cm. However, note that lamps "age" which leads to a reduction in resulting power.

⚠ CRITICAL: Doublecheck that UV wavelength is 302 nm. After UV exposure the solution should turn dark brown (see troubleshooting 1).

f. While UV-exposing the hydrogels, prepare 5 mL of 0.25 mg/mL solution of rat tail collagen I in 50 mM of HEPES pH=7.5.
g. Wash the hydrogels twice with 1 mL of 50 mM HEPES pH = 7.5.

Note: Repeat if needed to ensure that any excess crosslinker is removed.

h. Add 200 μL of the 0.25 mg/mL rat tail collagen I in 50 mM of HEPES on each hydrogel (Figure 2J).
i. Incubate the hydrogels, with the collagen solution on top for 16–18 h at 21°C–24°C.

Note: To prevent dehydration/evaporation, place the multi-well plates in a secondary containment and add laboratory cleaning tissues soaked in water in the inner periphery of the containment.

j. Next day wash once with PBS buffer to remove excess collagen.
k. Equilibrate hydrogels with cell culture media at 37°C for 30 min to 1 h (Figure 2K).

Note: You can use an epifluorescence or confocal microscope to measure the thickness of the hydrogels which you might need if you wish to perform TFM. To do so locate the z positions of the bottom (where the glass surface is) and top planes of the hydrogel (where the fluorescent beads' intensity is maximum). Then, subtract the z positions to determine the height. Also measure the depth of the tracer beads in reference to the upper surface of the gels, as this will affect the displacement of the beads and needs to be taken into account when performing TFM. On our hands the resulting thickness of the hydrogels is 30 μm +/- 5 μm and mainly results from the bottom layer without tracer beads. Even if a slightly higher volume of Solution I is added, the resulting thickness will be similar with this probably due to surface energy and adhesive forces between the glass and liquid solution. The second layer with the tracer beads should be thin enough so that beads are confined into a single focal plane as noted above.

Note: You can also perform atomic force microscopy (AFM) to confirm the exact stiffness of the hydrogels.

EC seeding on hydrogels, time-lapse microscopy and exposure to *Bb*—Days 8–9

Timing: 2–4 h

Once hydrogels are equilibrated, ECs are seeded on them and incubated for 24 h to form a confluent cell monolayer (Figure 2L). The multi-well plate is then transferred into the insert stage of an epifluorescence microscope and time-lapse imaging recordings are conducted. Around 5 h post-initiation of the recordings live or heat inactivated *Bb* spirochetes are added and the recording continues for 24 h post-exposure. If TFM is performed, at the end of the recording sodium dodecyl sulfate (SDS) is added to acquire a reference image of the tracer beads in undeformed hydrogels where cells have been removed from the hydrogel surface.

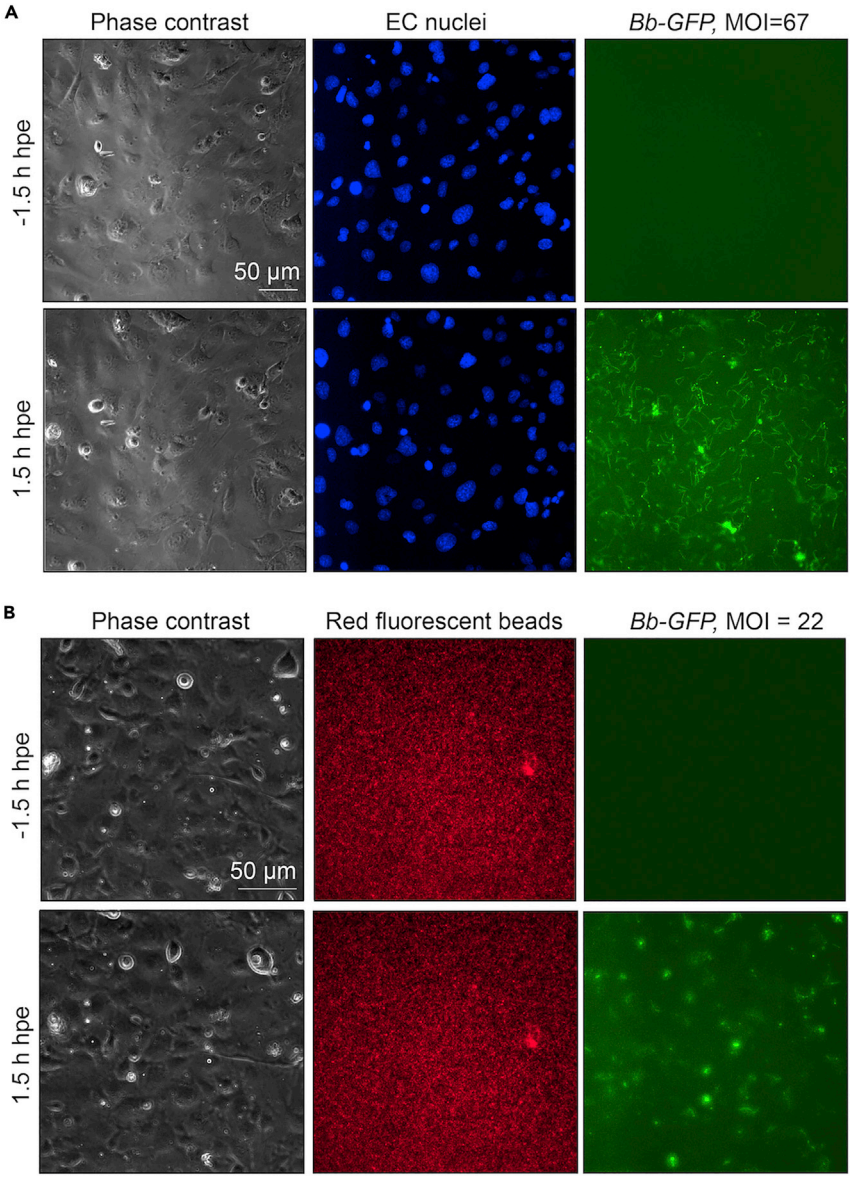

Figure 3. Multichannel images acquired prior and post-exposure to live or heat-inactivated *Bb*

(A) Columns show: phase contrast image of HMEC-1, Hoechst-stained HMEC-1 nuclei and *Bb-GFP* fluorescence before (upper row) and after (bottom row) *Bb-GFP* exposure. Times pre- and post-exposure (h post-exposure, hpe) are indicated. MOI is 67 bacteria/cell.

(B) Columns show: phase contrast image of HMEC-1, fluorescence of 0.2 µm red fluorescent tracer beads and *Bb-GFP* fluorescence before (upper row) and after (bottom row) *Bb-GFP* exposure. Times pre- and post-exposure (hpe) are indicated. MOI is 22 bacteria/cell.

11. Seeding of ECs on the hydrogels and staining of EC nuclei with Hoechst to characterize cell kinematics (Figure 3A).
    a. Detach the cells from their culture vessel using 0.25% trypsin/EDTA and seed them on the hydrogels.
        i. First wash the cells and their culture flask once with sterile PBS.
        ii. Add the appropriate amount of 0.05% trypsin/EDTA (2 mL on a 75-cm flask).
        iii. Incubate the flask at 37°C for 5–10 min to allow the detachment of the cells from their substrate.

iv. Neutralize the trypsin by adding 10 mL of cell culture medium containing FBS.
v. Pipet gently to break up the clumps of cells, and then place the solution into a conical centrifuge tube.
vi. Take out 10 μL of the solution and very gently fill out the chamber underneath the coverslip of a glass hemocytometer to count cells.
vii. Pellet down the solution of cells contained in the conical centrifuge tube using centrifugation for 5 min at 200 × *g*.
viii. During the 5 min waiting period, count the cells using the hemocytometer.

Alternatives: Use an automatic cell counter.

ix. Remove the liquid out of the conical centrifuge tube while ensuring that the cell pellet is not disrupted.
x. Resuspend the cells in the MCDB-131 full medium at a concentration of 4×10^5 cells/mL.
xi. Seed the cells in suspension on the hydrogels by first removing the medium with which the hydrogels were incubated and then adding 1 mL of cell suspension on each hydrogel.

Note: If you do not plan to do TFM and just want to characterize changes in EC motility, you can place ECs on glass coverslips coated with collagen I. Just mix 1:100 collagen I solution (stock concentration is 3.1 mg/mL) in PBS and add 500 μL of the solution in each well of the multi-well plate. Incubate for 30 min at 37°C. After one wash with PBS, you can seed the glass coverslip with ECs as you would on hydrogels.

xii. Let cells reside on the hydrogels for 24 h so they form a confluent monolayer.

b. Stain the EC nuclei with Hoechst and place live-microscopy medium on the wells.
i. Prior to the initiation of the microscopy recording prepare a solution of 1 μg/mL Hoechst in cell culture media.
ii. Remove the media from the cells and add 1 mL of Hoechst containing media.
iii. Place the multi-well plate in the incubator for 10 min.

⚠ CRITICAL: Depending on your EC type you might need to adjust the concentration of Hoechst or reduce the incubation time or both. For example, for staining the nuclei of primary HUVECs we determined that a 100-fold lower concentration of Hoechst followed by a 5 min incubation are optimal for this cell type (see troubleshooting 2).

iv. Aspirate out the Hoechst containing medium and wash the cells once with PBS.
v. Add 1 mL warm live-microscopy medium by supplementing Leibovitz's L-15 with 10% fetal bovine serum, 10 ng/mL of EGF, and 1 μg/mL hydrocortisone as indicated above.

12. Initiation of acquisition of time-lapse images of cells and tracer beads.
a. Turn on your epifluorescence (or confocal microscope) and make sure the microscope incubator's temperature is set at 37°C for at least 30 min prior to the start of the microscopy recording.
b. Place the multi-well plate on the appropriate insert on the stage of your microscope.
c. Find the focal plane where the tracer beads are located in each well and make sure they look evenly dispersed in the field of view to be imaged (see troubleshooting 3).

Note: Especially if you are beginner in TFM, you might want to consider inspecting the hydrogels immediately after they are built and prior to activation with Sulfo-SANPAH. Hydrogels where beads' are not evenly distributed can be excluded from further processing.

d. Ensure the cells form a confluent monolayer and mark the specific position.

e. Depending on how many replicate wells you want to track and how many conditions you desire to test mark different positions across the 24-well plate.

Note: We typically mark two positions per well so that a total of 48 positions are marked but that also depends on the conditions tested.

⚠ CRITICAL: Make sure your microscope's autofocus system is on to avoid potential drift in the normal (z-direction) over time. If drift occurs in the x-y direction it can be corrected, but there is no way to correct for drift in the z-direction.

f. In the acquisition settings select the time interval to be 10 min (images acquired every 10 min).
g. Select multi-channel acquisition and use a DAPI filter cube to image the cell nuclei, a GFP cube to image the GFP-expressing bacteria which will be added and an mCherry filter cube to image the tracer beads (Figures 3A and 3B).

Note: The filter cubes you will use depend on the color of the tracer beads you will choose and on the type of fluorescent protein your bacteria express. In our case power was set to 10% and the exposure time to 100 ms, when using a 40 × 0.60 NA Plan Fluor air objective. The microscope filters excitation/emission) used for DAPI, mCherry and GFP are 350/460, 470/525 nm and 530/645 nm, respectively. Note that we performed separate recordings to follow the nuclei of ECs and different ones to follow the tracer beads (Figures 3A and 3B). However, one could also simultaneously follow the tracer beads and EC nuclei. However, it might be pertinent to acquire two z-stacks at each instance of time one at the place where the tracer beads' intensity is maximum and one where the nuclei intensity is maximum.

h. Initiate the time-lapse image acquisition.

13. Exposure of ECs to *Bb-GFP* during microscopy recording.
    a. Approximately 5 h post-initiation of video-microscopy, spin down (5 min at 2,000 × *g*) the desired volume of live or heat-inactivated *Bb-GFP* depending on the MOI you want to achieve.

Note: If you want to achieve an MOI of 10 *Bb*/cell in each well and assuming your ECs have doubled in each well (i.e., you have 8×10^5 cells per well), one needs to add 8×10^6 *Bb*.

b. Wash the pellet once with PBS to remove the BSK culture media and spin down the bacteria for 5 min at 2,000 × *g*.
c. Resuspend the bacteria in such a volume of PBS so that in each well of your 24-well plate you only add 10 μL of bacterial suspension.

Note: For a MOI of 10 *Bb*/cell resuspend 8×10^6 *Bb* in 10 μL PBS.

d. When image acquisition stops and while you still have 10 min until next time point, carefully remove the lid of the multi-well plate.
e. Add 10 μL of bacterial suspension in PBS aiming to release the droplet at the center of the well without disturbing the plate.

Note: We did this because we wanted to record cells several hours prior to exposure and continue recording after exposure to pathogens too. Therefore, we wanted to avoid manipulation and displacement of the plate sitting in the microscope insert stage.

f. Add 10 μL of PBS alone on the control wells (no bacteria, vehicle control).
g. Place the lid back and allow the time-lapse imaging to continue for approximately 24 h.

Note: Be careful when removing/returning the lid, as this can disturb the focal plane along the z-axis which cannot be corrected for.

14. Acquisition of reference image of tracer beads.
    a. Once you end the microscopy recording, carefully remove the lid of your multi-well plate.
    b. Add 500 μL of 10% SDS in water in each of the wells.
    c. Through the phase contrast image make sure that the cells have detached from the surface of the hydrogel and thus, the elastic hydrogel has returned to its initial undeformed state.
    d. Take a fluorescence image of the tracer beads using the same power and exposure time as during time-lapse imaging. This will serve as the reference image of the beads in the undeformed hydrogel.

Characterization of EC kinematics and hydrogel displacements using particle image velocimetry—Days 9–10

Timing: 2–10 h

The steps herein describe how to characterize EC displacements based on the images of the host EC nuclei and the displacements of the tracer beads within the hydrogel to calculate cell traction and monolayer stresses. In both cases we use a particle image velocimetry (PIV)-like technique to find EC and extracellular matrix (ECM) displacements.[14] The codes with example data can be found at https://github.com/ebastoun. All scripts and functions are written in MATLAB (MathWorks).

15. First, use the images of the EC nuclei to characterize changes in EC kinematics before and after exposure to *Bb* (Figures 4A and 4B).
    a. Place the time-lapse images of the nuclei into a folder as individual 16-bit tiff files.
    b. Perform PIV by comparing subsequent frames by running the urapiv.m function.
        i. Use the appropriate window size and overlap depending on the objective you used and the size of your nuclei.

    Note: We followed HMEC-1 nuclei that are ~10 μm diameter, used a 40× objective and the resulting calibration factor of the images was fcal=0.18 μm/pixel. We thus used windows of 48 pixels with an overlap of 24 pixels for running the urapiv.m function.[14] The size of the windows/overlap depends on the size of the moving objects, the texture within the image and the magnitude of displacements the objects are undergoing from frame to frame. Too small windows will improve the resolution of the PIV but might introduce noise while too big windows might smoothen the resulting motions and will reduce resolution.

        ii. For each experiment run the run_PIV.m script which calls the urapiv.m function to calculate the displacement vectors and store them as .txt files.
        iii. After generating and storing the .txt files you can inspect the vector displacements (u_x and u_y) by running the script Correlation_WT.m to overlay the vector displacements with the image of cells (Figure 4A).
        iv. While running the Correlation_WT.m script you can also calculate the average magnitude of the displacements as a function of time.

    Note: If you divide by the time interval between frames you can calculate the mean speed of cells.

        v. While running the Correlation_WT.m script you can calculate the correlation length of the movement of neighboring cells.[15]

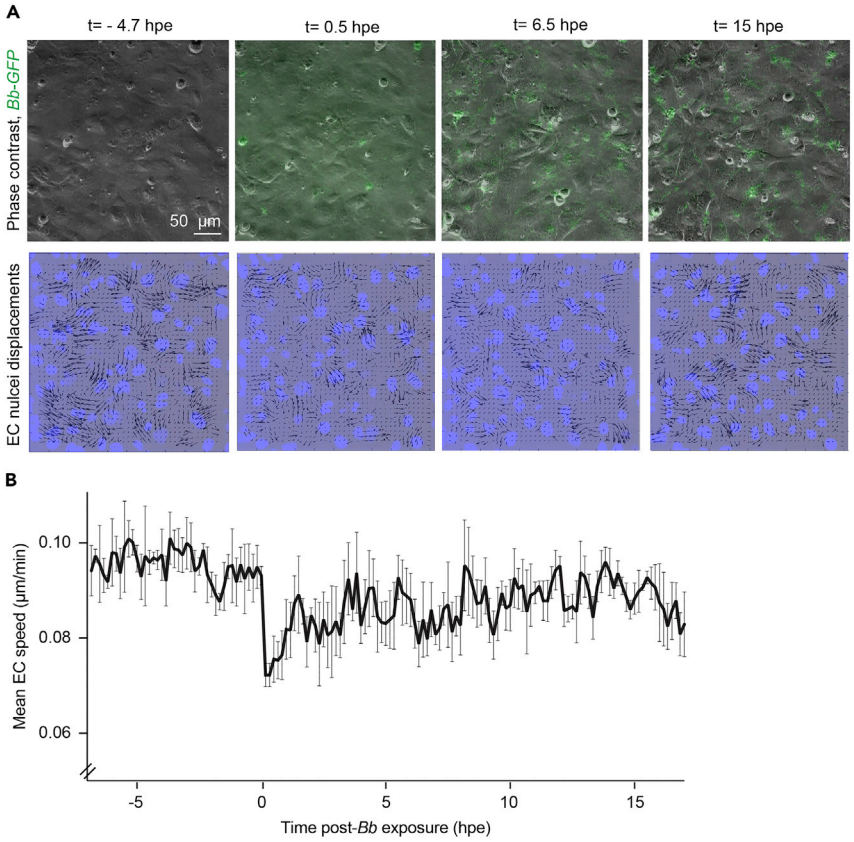

Figure 4. Analysis of HMEC-1 cell motility pre- and post-exposure to *Bb-GFP*

(A) Rows show representative: overlay of phase contrast image of HMEC-1 and *Bb-GFP* fluorescence (upper row) and overlay of Hoechst-stained HMEC-1 nuclei and HMEC-1 displacements (bottom row) determined through PIV. Columns show different time points pre- and post-*Bb* exposure. MOI is 200 bacteria per cell.

(B) Plot of mean HMEC-1 speed versus time (h) relative to the time point when host cells were exposed to *Bb* (mean+/-SEM, N=3 recordings).

c. Save the output EC kinematical analysis as a .mat file and input various parameters (e.g., speed over time, correlation length) to Prism (GraphPad) if you wish to do statistical analysis of various independent experiments (Figure 4B).

Note: You can also do the statistical analysis in MATLAB.

16. Measure the ECM displacements to perform TFM and monolayer stress microscopy (MSM).
    a. Place the time-lapse images of the fluorescent tracer beads into a folder as individual 16-bit tiff files.
    b. Add the reference image tiff file there too.

Note: If you acquired 100 frames named beads001.tiff etc., then the reference image can be saved as beads101.tiff.

    c. Using the urapiv.m file perform PIV by comparing each frame with the reference frame you acquired at the end of the recording after the addition of SDS (see troubleshooting 4).
        i. Use the appropriate window size and overlap depending on the objective you used and the size of the tracer beads.

Note: We used a 40× objective (fcal=0.18 μm/pixel) to follow 0.2 μm tracer beads and windows of 32 pixels with an overlap of 16 pixels for running the urapiv.m function.

ii. Run the urapiv.m function as before, with the exception that in this case you compare the image of the tracer beads at each time interval with the reference image of the undeformed beads.
iii. After the beads displacements are saved as .txt files you can use custom-built scripts in MATLAB (MathWorks)[2] or other TFM published codes to calculate the resulting traction stresses exerted by cells and the strain energy (mechanical work) imparted by cells over time[3] (Figure 5A).

Note: There are various sources you can find those codes to perform TFM with detailed documentation. Some examples are shown here: https://github.com/jknotbohm, https://github.com/DanuserLab/TFM.

iv. Save the strain energy overtime as a .mat file and input to Prism if you wish to do statistical analysis of various independent experiments (see troubleshooting 5) (Figure 5B).

d. Based on the calculated traction stresses you can infer also monolayer stresses built within the cellular monolayer using MSM[16] (Figures 6A and 6B).

Note: For our custom-built scripts in MATLAB (MathWorks) please refer to: https://github.com/ebastoun/Monolayer-Stress-Microscopy. Note that in order to physically interpret the stresses that cells are exposed to, we make use of the principal directions where the magnitude of stresses does not depend on the choice of the coordinate system, and there is no shear stress component.[17,18] The principal stress I (σI) is related to the maximum tensile stresses in each point of the monolayer, whereas the principal stress II (σII) is related to the maximum compressive stresses in each point of the monolayer. An extended explanation of these mechanical variables can be found elsewhere.[1]

EXPECTED OUTCOMES

With the current protocol, users will be able to culture *Bb-GFP*, generate heat-inactivated *Bb-GFP*, and expose either of those to ECs in monolayer which reside on soft physiologically-relevant deformable matrices embedded with fluorescent tracer beads. Time-lapse multi-channel microscopy imaging prior to and over the time following exposure will be used to monitor the displacements of Hoechst-stained EC nuclei concurrently with the displacements of the tracer beads. This will enable users to follow alterations of the EC motion during exposure to *Bb* as well as alterations in the displacements that ECs impart on their underlying matrix through the engagement of their focal adhesions and cytoskeleton. Moreover, using image processing and previously developed codes to conduct TFM and MSM users will learn how EC motility changes before and after exposure and how the host cell traction stresses and monolayer stresses built within the cell monolayer are dynamically modulated due to exposure to live or heat-inactivated pathogens.

QUANTIFICATION AND STATISTICAL ANALYSIS

All image processing was performed using custom-built scripts in MATLAB (MathWorks). The codes to perform PIV on the time-lapse images of Hoechst-stained cell nuclei are available at our GitHub repository together with instructions on how to run them (https://github.com/ebastoun/Correlation_length_of_movement_of_epithelial_cells_in_monolayer). Sample data are also provided to allow users to test the codes. We also used the urapiv.m function to calculate displacements of hydrogels due to EC exerting stresses onto them. TFM codes have been previously explained and published elsewhere.[2,3,4] The codes for MSM are uploaded in our gitlab repository together with instructions on how to run them https://github.com/ebastoun/Monolayer-Stress-Microscopy.[16]

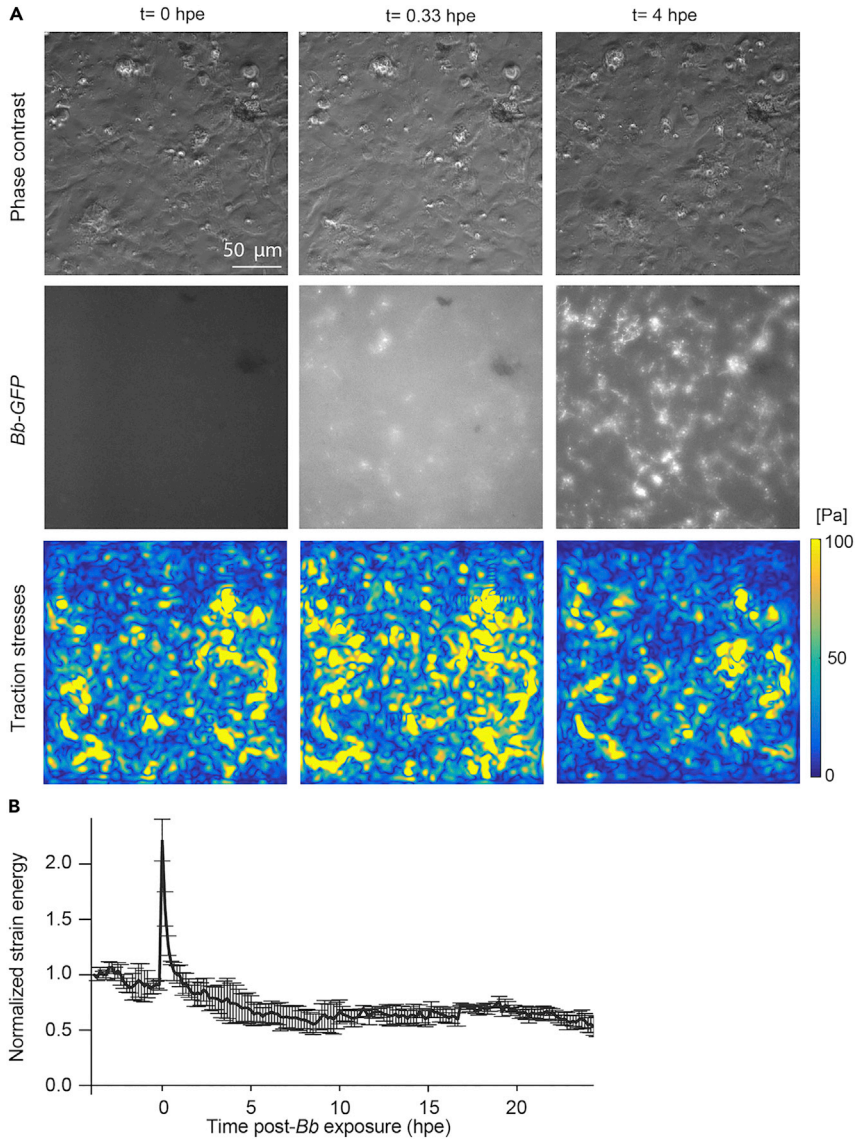

Figure 5. Traction stresses and strain energy of HMEC-1 pre- and post-exposure to *Bb-GFP*

(A) Columns show representative: phase contrast image of HMEC-1; *Bb-GFP* fluorescence; and cellular traction stresses map (3rd column, Pa) for HMEC-1 in monolayer at different time points (rows) pre- and post-exposure to *Bb-GFP*. MOI is 200 bacteria per cell and TFM was performed for cells residing on 3 kPa ECM.

(B) Normalized strain energy (mechanical work) imparted by HMEC-1 during a TFM recording pre- and post-exposure to *Bb-GFP* (mean+/-SEM, N=3 independent experiments). Strain energy has been normalized with respect to the first value at the beginning of each recording. Time (h) is represented relative to the time at which *Bb* was added.

Statistical parameters and significance are reported in the corresponding Figures and the Figure Legends. Boxplots and plots represent mean+/-SEM as indicated. Statistical analysis was performed in GraphPad PRISM 8.

LIMITATIONS

The protocol described herein concerns a particular EC type (HMEC-1) exposed to a specific extracellular bacterial pathogen (*Bb*). Its application in the context of different infection settings, e.g., different host cell types and bacterial or viral pathogens, requires optimization of different parameters. For infection protocols tailored to intracellular bacterial pathogens *Listeria monocytogenes*

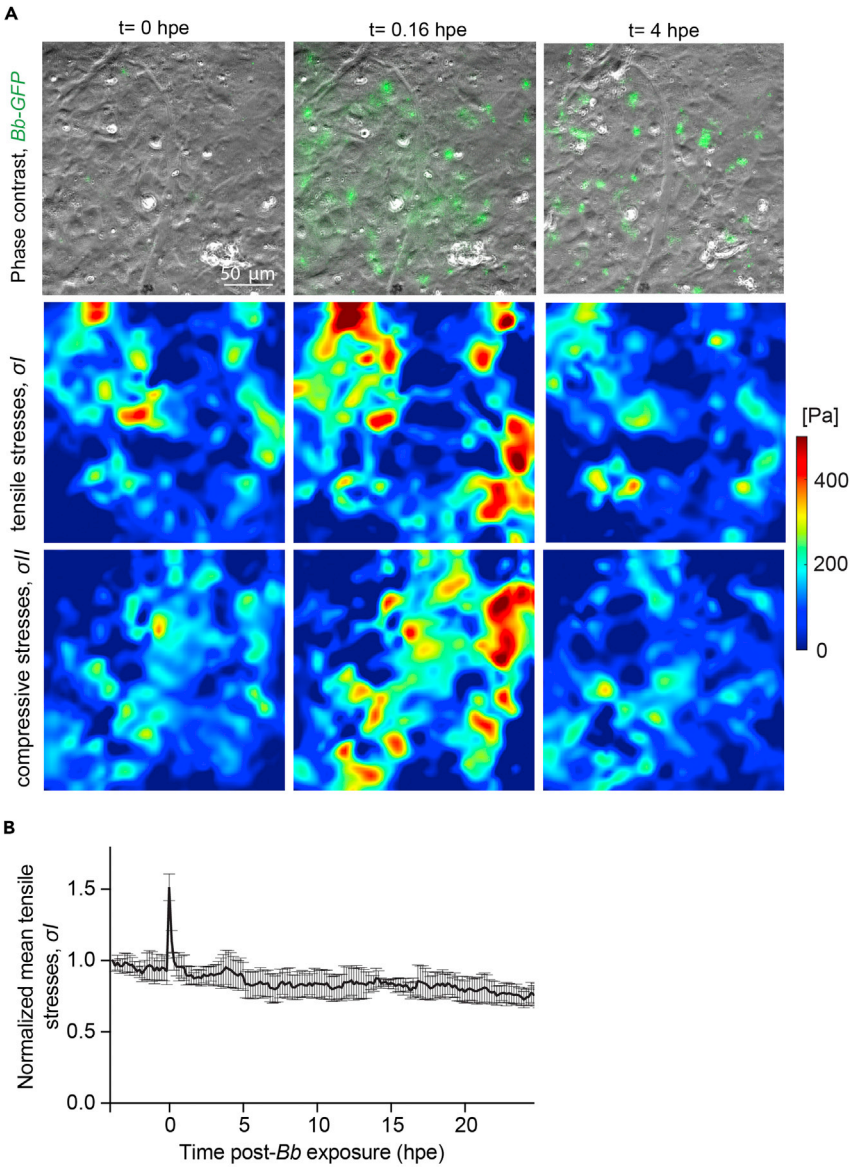

Figure 6. HMEC-1 monolayer stresses pre- and post-exposure to *Bb-GFP*

(A) Rows show representative: overlay of phase contrast image of HMEC-1 and *Bb-GFP* fluorescence (green); monolayer tensile stresses (σ_I); and compressive stresses (σ_{II}), for HMEC-1 in monolayer at different time points (columns) pre- and post-exposure to *Bb-GFP*. MOI is 200 bacteria per cell and cells reside on 3 kPa ECM.

(B) Normalized mean monolayer tensile stresses (σ_I) as a function of time post-exposure (mean+/-SEM, N=3 independent experiments). Mean σ_I has been normalized with respect to the first value at the beginning of each recording. Time (h) is represented relative to the time at which *Bb* was added.

or Rickettsia parkeri, please refer to our previous papers.[19,20] Moreover, in this particular protocol the investigation of the changes in motility of *Bb*-exposed ECs was performed for ECs residing on glass while traction forces were measured for ECs residing on soft 3 kPa hydrogels. This is due in that in our original paper, we initially placed ECs on collagen I-coated glass coverslips and followed them through microscopy prior- and post-exposure to *Bb* to evidence that shortly after exposure to pathogens ECs lower their migration speed but EC speed is recovered at later times.[1] Triggered by the observation that EC kinematics displayed time-dependent alterations post-exposure to *Bb*, we sought to investigate whether those are due to changes in cellular force transduction and thus performed TFM by placing ECs on soft 3 kPa hydrogels. We found that they do. Future studies could

address whether ECM stiffness and/or ECM-coating play a role in modulating the observed alterations in EC kinematics and dynamics upon pathogen exposure. The ECM stiffness for TFM was chosen so that it represents physiological values of subendothelial stiffness that ECs experience in small arteries.[7,21,22] However, during aging, hypertension, and atherosclerosis there are increases in subendothelial stiffness[23,24] and it could be interesting to study how increasing ECM might alter the behavior of ECs during exposure to pathogens and how that differs potentially for ECs residing on conventional glass coverslips. Finally, to estimate changes in inter- and intra-cellular stresses here we used MSM.[18,25] MSM though represents an indirect way of measuring cell monolayer tension, similar to other indirect ways such as laser ablation[26] and relies on several simplifications in terms of boundary conditions, mechanical properties, and the dimensionality of the system.[17,18] 2D MSM assumes that the intra- and inter- cellular stress components along the normal direction to the plane of the monolayer are negligible, and moreover, MSM considers perfect cell-cell and cell-ECM adhesions. All together, these previous assumptions allow to consider the simplification of the plane stress problem, where the thickness of the monolayer is assumed to be small, and it remains uniform and constant. Under this simplification, the analysis of stresses is focused on the plane of the monolayer. Therefore, MSM is based on both assumptions and does not provide an exact readout of intercellular forces which would allow to directly assess changes in barrier integrity. Continuing work on this aspect, including usage of FRET-based force sensors, could potentially facilitate a more absolute quantitation of the intercellular forces between neighboring ECs and how those directly relate to changes in barrier integrity.[27,28]

TROUBLESHOOTING

Problem 1

ECs do not attach well on the hydrogel and I cannot get a confluent monolayer.

Potential solution

First, this could be due to insufficient collagen I coating. Double check that during exposure of the hydrogels to UV, the UV wavelength is indeed 302 nm. If this is not the case, locate a transilluminator box that allows exposure to 302 nm. Alternatively, you can try doubling the concentration of the Sulfo-SANPAH to test whether that enhances collagen I coating. Make sure to wash out the remaining Sulfo-SANPAH and to proceed fast after activation with adding the collagen I solution. Finally, it could be that 3 kPa for your specific EC type is too soft and cells just do not firmly attach due to low stiffness. To assess whether that is the case build slightly stiffer hydrogels (e.g., 5 kPa).

Problem 2

I use a different EC type and Hoechst staining results in EC toxicity.

Potential solution

Depending on your EC type Hoechst or the concentration of Hoechst you use might be toxic for your ECs. First, test different conditions of Hoechst staining and assess whether they work for your EC type. Either lower the concentration of Hoechst or reduce the incubation time or both. If this does not work, you can use different EC nuclear dyes like SiR-DNA offered by Cytoskeleton. Moreover, one can also attempt to perform PIV-based kinematic analysis directly on the phase-contrast images. However, imaging the cell nuclei can be valuable in allowing one to conduct additional cell kinematical analysis like individual cellular tracking, correlation of movement of neighboring cells[29] and tracking of cellular numbers over the course of long-term live-cell imaging.

Problem 3

During the TFM image acquisition, I observe large displacements of the tracer beads to the extent that the beads move out of the focal plane imaged.

Potential solution

To perform TFM, cells must be able to displace the tracer beads embedded on the hydrogel on which cells reside as they transduce traction stresses onto it. HMEC-1 residing on 3 kPa hydrogels will definitely be able to impart deformations on the hydrogel and to our experience those are not large enough to move the beads out of the focal plane. However, if you use a higher magnification objective it is possible that this could happen. Also, if a different EC type is used that is more contractile or if cells are sub-confluent, deformations might be higher and that could lead to significant z-displacement of the beads due to cells imparting large normal deformations. In that case 2D TFM cannot be applied since the fluorescent beads will move in and out of the focal plane imaged. In that case one can either use a spinning disk confocal microscope and perform 3D TFM[30] or alternatively increase the stiffness of the hydrogel.

Problem 4

The displacements fields of the tracer beads that result after I run PIV on the TFM recordings appear rather noisy.

Potential solution

First check whether there is significant x, y or z drift. If there is x,y drift that can be corrected using image registration. However, if there is significant z drift there is nothing one can do, and the experiments need to be repeated. To avoid z drift, make sure when you remove the lid of the multi-well pate (in order to add SDS and detach the cells from the hydrogel) that you do not displace the plate. Moreover, if slight displacement is introduced in the reference image you can actually compare the position that you are imaging with the image of the tracer beads you acquired during the recording. You can correct for the slight drift which can be in x,y or even the z axis, by adjusting the focus and/or centering the image appropriately. Usually, there are some features in the texture of your tracer beads' image, like bead aggregates that are extremely bright, which can help you in performing this adjustment.

Problem 5

There is a large variation in the magnitude of cellular traction stresses from one experiment to another.

Potential solution

One potential reason for the discrepancies can be variations in cell confluency from experiment to experiment, despite seeding similar cell numbers. One way to ensure that monolayers in different experiments have similar cell numbers in the field of views images, is by staining the EC nuclei with a nuclear stain (e.g., Hoechst) and by acquiring multiple images of the cell nuclei in different fields of view. The host cell nuclei can be segmented and counted, and one can check whether indeed the density of cells is similar in the different fields of view. Another reason, that could lead to variations in the magnitude of cellular traction stresses from one experiment to another, could result from whether the beads imaged are indeed at the uppermost surface of the hydrogel or slightly below. To address this issue first endure that the upper hydrogel layer is thin and confined into a single plane. If that is the case, you should be in focus when imaging, irrespective of whether you are imaging the tracer beads' fluorescence or looking at the phase contrast image of ECs' basal surface. If the upper layer containing the tracer beads is slightly thicker (which might occur sometimes) you might be imaging deeper into the hydrogel (thus, estimating lower forces because these beads will also get displaced but to a lesser extent than beads right at the surface). Some of the TFM codes available allow you to take into account both the finite thickness of the substrate and the minute difference in height between the plane of the cells and the plane where the fluorescence of the tracer beads is maximal (in case those do not coincide).[31]

RESOURCE AVAILABILITY

Lead contact

Further information and requests for resources and reagents should be directed to and will be fulfilled by the lead contact, Effie E. Bastounis (effie.bastounis@uni-tuebingen.de).

Materials availability

This study did not generate new unique reagents.

Data and code availability

The codes generated during this study to measure EC displacements are available at https://github.com/ebastoun/Correlation_length_of_movement_of_epithelial_cells_in_monolayer (https://doi.org/10.5281/zenodo.7155531). Codes to perform TFM in cellular monolayers have been published elsewhere.[2,3,4] The codes generated during this study to measure monolayer stresses are available at https://github.com/ebastoun/Monolayer-Stress-Microscopy (https://doi.org/10.5281/zenodo.7155523).

ACKNOWLEDGMENTS

We are grateful to Joseph D. Mougous and Julie A. Theriot for previously sharing their resources and to Ben Ross for discussions and experimental support. We thank Justin Radolf and Tara Moriarty for previously sharing the GFP-expressing *Bb* strains with us. We thank Libera Lo Presti for discussions and for revising the manuscript. We acknowledge that part of our MSM codes is based on the original code (plane stress problem) written by Siva Srinivas Kolukula and we hence used some functions from his code. The graphical abstract was created with BioRender.com. This work was supported in part by the American Heart Association, award number: 18CDA34070047 (E.E.B.), the Lyme Disease Association (E.E.B.), the Stanford Lyme Disease Seed Grant (E.E.B.), the grant PID2021-124271OB-I00 funded by MCIN/AEI/10.13039/501100011033 (R.A.-Y.) and ERDF A way of making Europe (R.A.-Y.), the Spanish Ministry of Universities (grant FPU 20/05274 [R.A.-Y.]), and the Deutsche Forschungsgemeinschaft (DFG, German Research Foundation) under Germany's Excellence Strategy – EXC 2124 – 390838134 (E.E.B., M.M.).

AUTHOR CONTRIBUTIONS

E.E.B. designed and optimized the protocol for construction of polyacrylamide hydrogels on multi-well plates and for the performance of infection assays. E.E.B. performed EC kinematical analysis. E.E.B. and M.M. performed the TFM/MSM experiments. R.A.-Y. implemented the code and software to compute MSM. M.M. designed and prepared the graphical abstract and the figures presented herein under E.E.B.'s supervision. E.E.B. wrote the manuscript. P.K., M.C.T., R.A.-Y., and M.M. revised and edited the manuscript.

DECLARATION OF INTERESTS

The authors declare no competing interests.

REFERENCES

1. Yuste, R.A., Muenkel, M., Axarlis, K., Gómez Benito, M.J., Reuss, A., Blacker, G., Tal, M.C., Kraiczy, P., and Bastounis, E.E. (2022). Borrelia burgdorferi modulates the physical forces and immunity signaling in endothelial cells. iScience *25*, 104793. https://doi.org/10.1016/j.isci.2022.104793.

2. Lamason, R.L., Bastounis, E., Kafai, N.M., Serrano, R., Del Álamo, J.C., Theriot, J.A., and Welch, M.D. (2016). Rickettsia Sca4 reduces vinculin-mediated intercellular tension to promote spread. Cell *167*, 670–683.e10. https://doi.org/10.1016/j.cell.2016.09.023.

3. Saraswathibhatla, A., Galles, E.E., and Notbohm, J. (2020). Spatiotemporal force and motion in collective cell migration. Sci. Data *7*, 197. https://doi.org/10.1038/s41597-020-0540-5.

4. Teo, J.L., Lim, C.T., Yap, A.S., and Saw, T.B. (2020). A biologist's guide to traction force microscopy using polydimethylsiloxane substrate for two-dimensional cell cultures. STAR Protoc. *1*, 100098. https://doi.org/10.1016/j.xpro.2020.100098.

5. Dunham-Ems, S.M., Caimano, M.J., Pal, U., Wolgemuth, C.W., Eggers, C.H., Balic, A., and Radolf, J.D. (2009). Live imaging reveals a biphasic mode of dissemination of Borrelia burgdorferi within ticks. J. Clin. Invest. *119*, 3652–3665. https://doi.org/10.1172/JCI39401.

6. Moriarty, T.J., Norman, M.U., Colarusso, P., Bankhead, T., Kubes, P., and Chaconas, G. (2008). Real-time high resolution 3D imaging of the lyme disease spirochete adhering to and escaping from the vasculature of a living host. PLoS Pathog. *4*, e1000090. https://doi.org/10.1371/journal.ppat.1000090.

7. Bastounis, E.E., Yeh, Y.-T., and Theriot, J.A. (2018). Matrix stiffness modulates infection of endothelial cells by Listeria monocytogenes via expression of cell surface vimentin. Mol. Biol. Cell *29*, 1571–1589. https://doi.org/10.1091/mbc.E18-04-0228.

8. Bastounis, E.E., Yeh, Y.T., and Theriot, J.A. (2019). Subendothelial stiffness alters endothelial cell traction force generation while exerting a minimal effect on the transcriptome. Sci. Rep. *9*, 18209. https://doi.org/10.1038/s41598-019-54336-2.

9. Reed, S.C.O., Lamason, R.L., Risca, V.I., Abernathy, E., and Welch, M.D. (2014). Rickettsia actin-based motility occurs in distinct phases mediated by different actin nucleators. Curr. Biol. *24*, 98–103. https://doi.org/10.1016/j.cub.2013.11.025.

10. Schneider, C.A., Rasband, W.S., and Eliceiri, K.W. (2012). NIH Image to ImageJ: 25 years of image analysis. Nat. Methods *9*, 671–675. https://doi.org/10.1038/nmeth.2089.

11. Faralla, C., Bastounis, E.E., Ortega, F.E., Light, S.H., Rizzuto, G., Gao, L., Marciano, D.K., Nocadello, S., Anderson, W.F., Robbins, J.R., et al. (2018). Listeria monocytogenes InlP interacts with afadin and facilitates basement membrane crossing. PLoS Pathog. *14*, e1007094. https://doi.org/10.1371/journal.ppat.1007094.

12. Trepat, X., Wasserman, M.R., Angelini, T.E., Millet, E., Weitz, D.A., Butler, J.P., and Fredberg, J.J. (2009). Physical forces during collective cell migration. Nat. Phys. *5*, 426–430. https://doi.org/10.1038/nphys1269.

13. Subramani, R., Izquierdo-Alvarez, A., Bhattacharya, P., Meerts, M., Moldenaers, P., Ramon, H., and Van Oosterwyck, H. (2020). The influence of swelling on elastic properties of polyacrylamide hydrogels. Front. Mater. *7*. https://doi.org/10.3389/fmats.2020.00212.

14. Gui, L., and Wereley, S.T. (2002). A correlation-based continuous window-shift technique to reduce the peak-locking effect in digital PIV image evaluation. Exp. Fluids *32*, 506–517. https://doi.org/10.1007/s00348-001-0396-1.

15. Angelini, T.E., Hannezo, E., Trepat, X., Fredberg, J.J., and Weitz, D.A. (2010). Cell migration driven by cooperative substrate deformation patterns. Phys. Rev. Lett. *104*, 168104. https://doi.org/10.1103/PhysRevLett.104.168104.

16. Aparicio-Yuste, R., Muenkel, M., Clark, A.G., Gómez-Benito, M.J., and Bastounis, E.E. (2022). A stiff extracellular matrix favors the mechanical cell competition that leads to extrusion of bacterially-infected epithelial cells. Front. Cell Dev. Biol. *10*, 912318. https://doi.org/10.3389/fcell.2022.912318.

17. Tambe, D.T., Hardin, C.C., Angelini, T.E., Rajendran, K., Park, C.Y., Serra-Picamal, X., Zhou, E.H., Zaman, M.H., Butler, J.P., Weitz, D.A., et al. (2011). Collective cell guidance by cooperative intercellular forces. Nat. Mater. *10*, 469–475. https://doi.org/10.1038/nmat3025.

18. Tambe, D.T., Croutelle, U., Trepat, X., Park, C.Y., Kim, J.H., Millet, E., Butler, J.P., and Fredberg, J.J. (2013). Monolayer stress microscopy: limitations, artifacts, and accuracy of recovered intercellular stresses. PLoS One *8*, e55172. https://doi.org/10.1371/journal.pone.0055172.

19. Bastounis, E.E., Serrano-Alcalde, F., Radhakrishnan, P., Engström, P., Gómez-Benito, M.J., Oswald, M.S., Yeh, Y.-T., Smith, J.G., Welch, M.D., García-Aznar, J.M., and Theriot, J.A. (2021). Mechanical competition triggered by innate immune signaling drives the collective extrusion of bacterially infected epithelial cells. Dev. Cell *56*, 443–460.e11. https://doi.org/10.1016/j.devcel.2021.01.012.

20. Bastounis, E.E., Radhakrishnan, P., Prinz, C.K., and Theriot, J.A. (2021). Volume measurement and biophysical characterization of mounds in epithelial monolayers after intracellular bacterial infection. STAR Protoc. *2*, 100551. https://doi.org/10.1016/j.xpro.2021.100551.

21. Zieman, S.J., Melenovsky, V., and Kass, D.A. (2005). Mechanisms, pathophysiology, and therapy of arterial stiffness. Arterioscler. Thromb. Vasc. Biol. *25*, 932–943. https://doi.org/10.1161/01.atv.0000160548.78317.29.

22. Stroka, K.M., and Aranda-Espinoza, H. (2011). Endothelial cell substrate stiffness influences neutrophil transmigration via myosin light chain kinase-dependent cell contraction. Blood *118*, 1632–1640.

23. Kohn, J.C., Lampi, M.C., and Reinhart-King, C.A. (2015). Age-related vascular stiffening: causes and consequences. Front. Genet. *6*, 112. https://doi.org/10.3389/fgene.2015.00112.

24. Huynh, J., Nishimura, N., Rana, K., Peloquin, J.M., Califano, J.P., Montague, C.R., King, M.R., Schaffer, C.B., and Reinhart-King, C.A. (2011). Age-related intimal stiffening enhances endothelial permeability and leukocyte transmigration. Sci. Transl. Med. *3*, 112ra122. https://doi.org/10.1126/scitranslmed.3002761.

25. Gómez-González, M., Latorre, E., Arroyo, M., and Trepat, X. (2020). Measuring mechanical stress in living tissues. Nat. Rev. Phys. *2*, 300–317. https://doi.org/10.1038/s42254-020-0184-6.

26. Bastounis, E.E., Radhakrishnan, P., Prinz, C.K., and Theriot, J.A. (2022). Mechanical forces govern interactions of host cells with intracellular bacterial pathogens. Microbiol. Mol. Biol. Rev. *86*, e0009420. https://doi.org/10.1128/mmbr.00094-20.

27. Eder, D., Basler, K., and Aegerter, C.M. (2017). Challenging FRET-based E-Cadherin force measurements in Drosophila. Sci. Rep. *7*, 13692. https://doi.org/10.1038/s41598-017-14136-y.

28. Sim, J.Y., Moeller, J., Hart, K.C., Ramallo, D., Vogel, V., Dunn, A.R., Nelson, W.J., and Pruitt, B.L. (2015). Spatial distribution of cell–cell and cell–ECM adhesions regulates force balance while maintaining E-cadherin molecular tension in cell pairs. Mol. Biol. Cell *26*, 2456–2465. https://doi.org/10.1091/mbc.E14-12-1618.

29. Hayer, A., Shao, L., Chung, M., Joubert, L.-M., Yang, H.W., Tsai, F.-C., Bisaria, A., Betzig, E., and Meyer, T. (2016). Engulfed cadherin fingers are polarized junctional structures between collectively migrating endothelial cells. Nat. Cell Biol. *18*, 1311–1323. https://doi.org/10.1038/ncb3438.

30. del Álamo, J.C., Meili, R., Álvarez-González, B., Alonso-Latorre, B., Bastounis, E., Firtel, R., and Lasheras, J.C. (2013). Three-dimensional quantification of cellular traction forces and mechanosensing of thin substrata by fourier traction force microscopy. PLoS One *8*, e69850. https://doi.org/10.1371/journal.pone.0069850.

31. del Álamo, J.C., Meili, R., Alonso-Latorre, B., Rodríguez-Rodríguez, J., Aliseda, A., Firtel, R.A., and Lasheras, J.C. (2007). Spatio-temporal analysis of eukaryotic cell motility by improved force cytometry. Proc. Natl. Acad. Sci. USA *104*, 13343–13348. https://doi.org/10.1073/pnas.0705815104.